Bioinspired Nanofiltration Membranes by Supramolecular Self-assembly

Universität Hamburg

DER FORSCHUNG | DER LEHRE | DER BILDUNG

Dissertation

Hluf Hailu Kinfu

Hamburg, 2025

Institute of Physical Chemistry, Department of Chemistry,

Faculty of Mathematics, Informatics, and Natural Sciences,

University of Hamburg

Dissertation submitted to the University of Hamburg with the aim of achieving a doctoral degree (Dr. rer. nat.)

Prof. Dr. Volker Abetz (First reviewer)

Prof. Dr. Tobias Beck (Second reviewer)

Date of Oral Defense: 21.11.2025

Members of The Examination Commission

Examiner 1: Prof. Dr. Volker Abetz

Examiner 2: Prof. Dr. Gerrit Luinstra

Examiner 3: Priv. Doz. Dr. Christoph Wutz

This study was conducted between March 2021 and March 2024 under the guidance of Prof. Dr. Volker Abetz at the Institute of Membrane Research, Helmholtz-Zentrum Hereon (Geesthacht, Germany) and the Institute of Physical Chemistry, Department of Chemistry, Faculty of Mathematics, Informatics, and Natural Sciences, University of Hamburg (Hamburg, Germany). The dissertation, submitted as a cumulative thesis, includes reprints of the first-author publications.

List of publications

1. **Hluf Hailu Kinfu**, Md. Mushfequr Rahman, Nicolás Cevallos-Cueva, Volker Abetz. Ion Selective Metal-Phenolic Network Nanofiltration Membranes: The Role of Counterions and Predictive Modeling. Journal of Membrane Science **2025**, 733, 124320.

2. **Hluf Hailu Kinfu**, Md. Mushfequr Rahman, Nicolás Cevallos-Cueva, Volker Abetz. Metal-phenolic network-based NF membranes for nitrate removal and the utilization of DSPM-DE model. Chemical Engineering Journal **2025**, 513, 162841.

3. Nicolás Cevallos-Cueva, Md. Mushfequr Rahman, **Hluf Hailu Kinfu**, Volker Abetz. Mass transport mechanisms insights of selective sodium/magnesium separation through nanofiltration membranes. Journal of Membrane Science **2025**, 721, 123808.

4. **Hluf Hailu Kinfu**, Md. Mushfequr Rahman, Nicolás Cevallos-Cueva, Volker Abetz. Nanofiltration Membranes Containing a Metal–Polyphenol Network Layer: Using Casting Solution pH as a Tool to Tailor the Separation Performance. ACS omega **2024**, 9 (46), 45870-45883.

5. Nicolás Cevallos-Cueva, Md. Mushfequr Rahman, **Hluf Hailu Kinfu**, Volker Abetz. Mass transport mechanism of nitrate selective nanofiltration membranes on the basis of the Donnan steric pore model with dielectric exclusion (DSPM-DE). Chemical Engineering Journal **2024**, 493, 152775.

6. **Hluf Hailu Kinfu**, Md. Mushfequr Rahman, Erik Sebastian Schneider, Nicolás Cevallos-Cueva, Volker Abetz. Using the Assembly Time as a Tool to Control the Surface Morphology and Separation Performance of Membranes with a Tannic Acid–Fe^{3+} Selective Layer. Membranes **2024**, 14 (6), 133.

7. **Hluf Hailu Kinfu**, Md. Mushfequr Rahman, Erik Sebastian Schneider, Nicolás Cevallos-Cueva, Volker Abetz. Charge and size selective thin film composite membranes having tannic acid–Ferric ion network as selective layer. Journal of Membrane Science **2023**, 679, 121709.

8. **Hluf Hailu Kinfu**, Md. Mushfequr Rahman. Separation performance of membranes containing ultrathin surface coating of metal-polyphenol network. Membranes **2023**, 13 (5), 481.

9. **Hluf Hailu Kinfu**, Md. Mushfequr Rahman, Nicolás Cevallos-Cueva, Volker Abetz. Mass Transport of Dye Solutions through Porous Membrane Containing Tannic Acid/Fe^{3+} Selective Layer. Membranes **2022**, 12 (12), 1216.

List of Conference Presentations

1. **Hluf Hailu Kinfu**, Md. Mushfequr Rahman, Nicolás Cevallos-Cueva, Volker Abetz. Oral presentation of "Charge and size selective TFC membranes containing metal-polyphenol network as selective layer", 7th International Symposium on Physics of Membrane Processes & IS-START. 2024, Singapore.
2. **Hluf Hailu Kinfu**, Md. Mushfequr Rahman, Nicolás Cevallos-Cueva, Volker Abetz. Oral presentation of "Thin-film composite nanofiltration membranes having polyphenol – metal ion network selective layers", MEMDES 2023 – 6th International Conference on Desalination using Membrane Technology. 2023, Sitges, Spain.

Table of contents

List of Figures

List of Tables

List of Abbreviations

Abbreviations

EDX	Energy-dispersive X-ray spectroscopy
$FeCl_3 \cdot 6H_2O$	Iron (III) chloride hexahydrate
FO	Forward osmosis
FTIR	Fourier transform infrared spectroscopy
GPC	Gel Permeation Chromatography
HA	Humic acid
HCl	Hydrochloric acid
IP	Interfacial polymerization
MF	Microfiltration
MOF	Metal-organic framework
MPD	m-phenylenediamine
MPN	Metal-phenolic network
MPN	Metal-polyphenol network
MWCO	Molecular weight cut-off
NaOH	Sodium hydroxide
NF	Nanofiltration
NGB3-	Naphthol green B
NIPS	Non-solvent induced phase separation
OR-	Orange II
PA	Polyamide
PAN	Polyacrylonitrile
PEG	Poly(ethylene glycol)
PES	Polyethersulfone
PVDF	Poly(vinylidenedifluoride)
RB0	Riboflavin
RO	Reverse osmosis
SEM	Scanning electron microscopy
TA	Tannic Acid
TMC	Trimesoyl chloride
UF	Ultrafiltration

ZIF-8	Zeolitic imidazolate framework 8

Symbols

A	Membrane area (m^2)
A_k	Membrane porosity
C_i	Concentration of species i ($mol \cdot m^{-3}$)
C_f	Feed concentration
C_p	Concentration on the permeate side
C_r	Concentration on the retentate side
C_X	Membrane charge density ($mol \cdot m^{-3}$)
D	Diffusion coefficient ($m^2 \cdot s^{-1}$)
$D_{i,p}$	Diffusion coefficient of species i in the pore ($m^2 \cdot s^{-1}$)
$D_{i,\infty}$	Diffusion coefficient of species i in the bulk ($m^2 \cdot s^{-1}$)
e_0	Elementary charge (1.60218×10^{-19} C)
F	Faraday constant (96485.3 $C \cdot mol^{-1}$)
J_i	Solute flux for species i ($mol \cdot m^{-2} \cdot s^{-1}$)
J_V	Permeate flux ($m^3 \cdot m^{-2} \cdot s^{-1}$)
J_W	Pure water flux ($L \cdot m^{-2} \cdot h^{-1}$)
kB	Boltzmann constant (1.38065×10^{-23} $J \cdot K^{-1}$)
$K_{c,i}$	Solute mass transfer coefficient of species i ($m \cdot s^{-1}$)
$K_{i,c}$	Convection hindrance factor of species i
$K_{i,d}$	Diffusion hindrance factor of species i
L_p	Water permeability coefficient
Mw	Weight-average molecular weight ($g \cdot mol^{-1}$)
N_A	Avogadro constant ($6.02214076 \times 10^{23}$ mol^{-1})
N_c	Number of components
P_S	Solute permeability coefficient
PWP	Pure water permeance ($L \cdot m^{-2} \cdot h^{-1} \cdot bar^{-1}$)
r_p	Pore radius (m)
r_s	Solute Stokes radius for species i (m)
R	Universal gas constant (8.31446 $J \cdot mol^{-1} \cdot K^{-1}$)
R (%)	Retention of a solute (%)
R_{cal}	Calculated rejection from a model

R_{exp}	Experimentally measured rejection
R_i	Rejection ratio of species i
t	Operation time (h)
T	Temperature (K)
V	Volume of the collected permeate (L)
Z_i	Valency of species i
γ_i	Activity coefficient of species i
ΔP	Transmembrane pressure difference (Pa)
$\Delta \Pi$	Osmotic pressure difference (Pa)
ΔW_i	Born solvation energy barrier (J)
Δx	Thickness of membrane active layer (m)
ε_b	Dielectric constant of the bulk
ε_p	Dielectric constant of the pore
ε_0	Permittivity of free space
λ_i	Ratio of solute Stokes radius of solute i to effective membrane pore radius
μ	Solution viscosity (Pa·s)
ξ	Electric potential gradient at the feed/membrane interface ($V \cdot m^{-1}$)
ρ	Solution density ($kg \cdot m^{-3}$)
σ	Reflection coefficient
τ	Tortuosity
Φ_S	Steric partitioning coefficient of species
Φ_B	Born solvation coefficient (dielectric partitioning coefficient)
Φ_D	Donnan partitioning coefficient
Ψ	Electric potential (V)

Abstract

Thin-Film Composite (TFC) Membranes are a type of membrane with a thin selective layer on top of a porous support layer commonly used in water purification, desalination, and filtration processes. The selective layer controls the rejection and transport of components through the membrane and is typically a polyamide formed via interfacial polymerization (IP). However, IP uses hazardous organic solvents that are of great concern to human health and the environment. This dissertation focuses on the synthesis of a metal-phenolic network (MPN) as a selective layer for TFC nanofiltration membrane fabrication in a sustainable method, using only water as a solvent, for various applications. MPN are an emerging class of functional materials based on the self-assembly between metal ions and polyphenol ligands. Tannic acid (TA), a natural polyphenol, and metal ions (Fe^{3+}) were used to fabricate the TA-Fe^{3+} MPN selective layer over a polyacrylonitrile (PAN) porous support. This unique approach to membrane fabrication leverages supramolecular chemistry to synthesize tunable and multifunctional separation layers.

The TFC membranes were fine-tuned by systematically controlling the fabrication conditions. The influence of concentration, assembly time, pH of solutions and number of layers were investigated in detail to determine their effect on film formation, membrane microstructure, physicochemical characteristics, and separation properties. FTIR, SEM, EDX, and zeta potential measurements were used to confirm the formation of a TA-Fe^{3+} coating over the porous support. Backscattered electron (BSE) imaging shows that the thickness of the selective layer is approximately 10 nm, categorizing as an ultrathin layer for liquid separation. SEM analysis and water flux measurements illustrated that dense separation layers are fabricated at higher metal ion concentration, prolonged assembly time or alkaline solution. This demonstrates the MPN membranes exhibit tunable pore size characteristics. Moreover, the surface hydrophilicity of the membranes varied depending on the synthesis parameters. For instance, surface wettability of the TFC membrane increases for membranes fabricated at high Fe^{3+} concentration while it declines for those fabricated at high assembly time. The membranes exhibit up to 85 % flux recovery ratio during fouling tests indicating good antifouling properties.

Selective membranes are highly desirable for membrane applications. The separation properties of the fabricated membranes against small organics of 200 – 1000 g/mol molecular weight from different charge groups were investigated in detail. It is observed that the MPN layers exhibit successful charge- and size-based selectivity towards organic solutes. Anionic dyes are highly rejected while the TA-Fe^{3+} membranes show a low rejection towards neutral organic solutes in

both single solute and mixed solute filtration tests. Size exclusion and the electrostatic interactions between the negatively charged membrane surface and organic molecules in the feed solution play key roles in the rejection behavior of the TA-Fe^{3+} membranes. Mass transport mechanism of dye solutions through the MPN membranes is also analyzed using the Spiegler–Kedem–Katchalsky (SKK) model. The rejection property and selectivity to distinguish solutes based on size, charge, or chemical properties reiterate the potential of the TA-Fe^{3+} membranes for the separation and recovery of molecules from complex mixtures across various industries.

The salt rejections performance of the MPN membranes are also evaluated to analyze their rejection efficiency and monovalent/divalent ion selectivity from different feed solution compositions. The fabrication conditions significantly affect the water flux and salt retention of MPN membranes. For instance, increasing the Fe^{3+} concentration of the casting solution enhances rejection while water flux significantly declines, depicting the permeability-selectivity trade-off. The TA-Fe^{3+} thin-films generally showed good salt (NaCl, $NaNO_3$, Na_2SO_4, $MgCl_2$, $MgSO_4$, and their mixtures) rejection, demonstrating their potential for NF applications in water and wastewater treatment. The TA-Fe^{3+} membranes especially exhibited high NO_3^- removal property, outperforming commercial NF membranes. The effect of operating conditions such as pressure, feed concentration and composition on ion rejection are analyzed. In mixed salt retention tests, NO_3^-/SO_4^{2-} selectivity between 4.5 – 38.1 were obtained while 1.1 – 330 Na^+/Mg^{2+} selectivities were achieved depending on the feed composition.

The ion separation performance of the MPN membranes is elucidated using a mathematical model, the Donnan steric pore model with dielectric exclusion (DSPM-DE). Mass transport modeling of ions through the TA-Fe^{3+} NF membranes is described for various ternary and quaternary ion mixtures. It is demonstrated that the DSPM-DE can sufficiently well predict the separation properties of MPN membranes. In the cumulative part of the dissertation, insights into the dominant ion exclusion mechanisms and ion transport mechanisms that influence the selectivity and flux of ions, are provided. The effect of membrane parameters on monovalent/divalent ion selectivity (e.g., NO_3^-/SO_4^{2-}) are also explored in a sensitivity analysis. This reiterates the importance of transport models in understanding complex transport processes, predicting rejection performance, designing membranes with desired characteristics and optimization of membrane processes.

Overall, MPN membranes offer a novel platform for membrane science, moving beyond traditional polyamide chemistry for TFC NF membrane selective layers. Their coordination-driven assembly opens new pathways to create multifunctional, high-performance membranes with tunable properties suitable for desired separation applications.

Zusammenfassung

Dünnschichtkompositmembranen (TFC-Membranen) sind Membrantypen mit einer dünnen selektiven Schicht auf einer porösen Trägerschicht, die üblicherweise in der Wasseraufbereitung, Entsalzung und bei Filtrationsprozessen eingesetzt wird. Die selektive Schicht steuert die Zurückhaltung und den Transport von Komponenten durch die Membran und ist in der Regel ein Polyamid, das durch Grenzflächenpolymerisation (IP) hergestellt wird. Bei der IP werden jedoch giftige organische Lösungsmittel verwendet, die für die menschliche Gesundheit und die Umwelt sehr schädlich sind. Diese Dissertation konzentriert sich auf die Synthese eines Metall-Phenol-Netzwerks (MPN) als selektive Schicht für die Herstellung von TFC-Nanofiltrationsmembranen in einem nachhaltigen Verfahren, das nur Wasser als Lösungsmittel verwendet, für verschiedene Anwendungen. MPN sind eine aufstrebende Klasse von funktionellen Materialien, die auf der Selbstorganisation zwischen Metallionen und Polyphenol-Liganden basieren. Gerbsäure (TA), ein natürliches Polyphenol, und Metallionen (Fe^{3+}) wurden zur Herstellung der selektiven TA-Fe^{3+} MPN-Schicht auf einem porösen Polyacrylnitril (PAN)-Träger verwendet. Dieser einzigartige Ansatz zur Herstellung von Membranen nutzt die supramolekulare Chemie zur Synthese von einstellbaren und multifunktionalen Trennschichten.

Die TFC-Membranen wurden durch systematische Kontrolle der Herstellungsparameter feinabgestimmt. Der Einfluss der Konzentration, der Anordnungszeit, des pH-Werts der Lösungen und der Anzahl der Schichten wurde im Detail untersucht, um ihre Auswirkungen auf die Filmbildung, die Mikrostruktur der Membran, die physikalisch-chemischen Eigenschaften und die Trenneigenschaften zu bestimmen. FTIR-, REM-, EDX- und Zeta-Potential-Messungen wurden eingesetzt, um die Bildung einer TA-Fe^{3+}-Schicht auf dem porösen Träger zu bestätigen. Die Bildgebung mit rückgestreuten Elektronen (BSE) zeigt, dass die Dicke der selektiven Schicht etwa 10 nm beträgt, was als ultradünne Schicht für die Flüssigkeitstrennung eingestuft wird. Die REM-Analyse und Wasserflussmessungen zeigten, dass dichte Trennschichten bei höherer Metallionenkonzentration, längerer Anordnungszeit oder alkalischer Lösung entstehen. Dies zeigt, dass die MPN-Membranen einstellbare Porengrößencharakteristika aufweisen. Außerdem variierte die Oberflächenhydrophilie der Membranen in Abhängigkeit von den Syntheseparametern. So nimmt beispielsweise die Oberflächenbenetzbarkeit der TFC-Membranen bei solchen zu, die mit einer hohen Fe^{3+}-Konzentration hergestellt wurden, während sie bei Membranen, die mit einer langen Anordnungszeit hergestellt wurden, abnimmt. Die Membranen weisen bei Fouling-Tests ein

Flux-Rückgewinnungsverhältnis von bis zu 85 % auf, was auf gute Antifouling-Eigenschaften hinweist.

Selektive Membranen sind für Membrananwendungen äußerst wünschenswert. Die Trenneigenschaften der hergestellten Membranen gegenüber kleinen organischen Stoffen mit einem Molekulargewicht von 200 - 1000 g/mol aus verschiedenen Ladungsgruppen werden im Detail untersucht. Es wurde festgestellt, dass die MPN-Schichten eine erfolgreiche ladungs- und größenbasierte Selektivität gegenüber organischen Lösungsmitteln aufweisen. Anionische Farbstoffe werden in hohem Maße zurückgehalten, während die TA-Fe^{3+}-Membranen eine geringe Rückhaltung gegenüber neutralen organischen Stoffen zeigen, und zwar sowohl bei Filtrationstests für einzelne Stoffe als auch für gemischte Stoffe. Der Größenausschluss und die elektrostatischen Wechselwirkungen zwischen der negativ geladenen Membranoberfläche und den organischen Molekülen in der Zulauflösung spielen eine Schlüsselrolle für das Rückhalteverhalten der TA-Fe^{3+}-Membranen. Der Mechanismus des Massentransports von Farbstofflösungen durch die MPN-Membranen wurde zusätzlich mit Hilfe des Spiegler-Kedem-Katchalsky (SKK)-Modells analysiert. Das Rückhaltevermögen und die Selektivität bei der Unterscheidung von gelösten Stoffen auf der Grundlage von Größe, Ladung oder chemischen Eigenschaften unterstreichen das Potenzial der TA-Fe^{3+}-Membranen für die Abtrennung und Rückgewinnung spezifischer Moleküle aus komplexen Gemischen in verschiedenen Industriebranchen.

Die Salzrückhalteleistung der MPN-Membranen wurde ebenfalls bewertet, um ihre Rückhalteeffizienz und ihre Selektivität für einwertige/zweiwertige Ionen aus verschiedenen Zusammensetzungen der Einsatzlösung zu analysieren. Die Herstellungsbedingungen haben einen erheblichen Einfluss auf den Wasserfluss und die Salzrückhaltung der MPN-Membranen. So erhöht eine Erhöhung der Fe^{3+}-Konzentration der Gießlösung die Rückhaltung, während der Wasserfluss deutlich abnimmt, was den Kompromiss zwischen Durchlässigkeit und Selektivität verdeutlicht. Die TA-Fe^{3+}-Dünnschichtfilme zeigten im Allgemeinen eine gute Rückhaltung von Salzen (NaCl, $NaNO_3$, Na_2SO_4, $MgCl_2$, $MgSO_4$ und deren Mischungen), was ihr Potenzial für NF-Anwendungen in der Wasser- und Abwasseraufbereitung belegt. Die TA-Fe^{3+}-Membranen wiesen insbesondere eine hohe NO_3^--Entfernungsleistung auf und übertrafen damit kommerzielle NF-Membranen. Die Auswirkungen von Betriebsbedingungen wie Druck, Zulaufkonzentration und -zusammensetzung auf die Ionenrückhaltung wurden analysiert. In gemischten Salzrückhaltetests wurden NO_3^-/SO_4^{2-} Selektivitäten zwischen 4,5 - 38,1

beobachtet, während in Abhängigkeit von der Zusammensetzung des Feeds Na^+/Mg^{2+} Selektivitäten zwischen 1,1 - 330 erreicht wurden.

Die Ionentrennleistung der MPN-Membranen wurde mithilfe eines mathematischen Modells, dem sterischen Donnan-Porenmodell mit dielektrischem Ausschluss (DSPM-DE), erläutert. Die Modellierung des Massentransports von Ionen durch die TA-Fe^{3+} NF-Membranen wird für verschiedene ternäre und quaternäre Ionenmischungen beschrieben. Es wurde gezeigt, dass das DSPM-DE die Trenneigenschaften von MPN-Membranen ausreichend vorhersagen kann. Im kumulativen Teil der Dissertation werden Einblicke in die vorherrschenden Ionenausschluss- und Ionentransportmechanismen gegeben, die die Selektivität und den Fluss der Ionen beeinflussen. Die Auswirkungen von Membranparametern auf die Selektivität einwertiger/zweiwertiger Ionen (z. B. NO_3^-/SO_4^{2-}) wurden ebenfalls in einer Sensitivitätsanalyse untersucht. Dies unterstreicht die Bedeutung von Transportmodellen für das Verständnis komplexer Transportprozesse, die Vorhersage der Rückhalteleistung, den Entwurf von Membranen mit gewünschten Eigenschaften und die Optimierung von Membranprozessen.

Insgesamt bieten MPN-Membranen eine neuartige Plattform für die Membranforschung, die über die traditionelle Polyamidchemie für selektive TFC-NF-Membranschichten hinausgeht. Ihr koordinationsgesteuerter Aufbau eröffnet neue Wege zur Herstellung multifunktionaler Hochleistungsmembranen mit einstellbaren Eigenschaften, die für die gewünschten Trennanwendungen geeignet sind.

Chapter 1. Introduction

1.1. Overview and Objective

In 2010, an estimated 1.1 billion people lacked access to safe drinking water [1, 2]. By 2020, this figure raised to over 2 billion people [3], with projections from the World Water Council suggesting further exacerbation by 2030 [4]. The global demand for fresh water continues to grow, driven by factors that aggravate water scarcity such as rapid population growth, industrialization, rising energy demand, climate change and contamination by human activities. Addressing such demand necessitates a scientific and technological revolution in water purification and treatment. The development of innovative, affordable, and energy-efficient materials and technologies is crucial for advancing water purification methods [5]. Nowadays, membrane technology has emerged as a highly promising approach for extracting freshwater from sources such as groundwater, surface water, seawater, and even wastewater.

A membrane is a thin film of a polymeric, inorganic or hybrid material, which acts as a selective barrier between two adjacent phases. Membranes are either porous or non-porous. Technically, membranes selectively restrict the permeation of certain components. A schematic of the membrane process is illustrated in Figure 1.1. After decades of advancement, membranes are now extensively applied for industrial wastewater treatment, desalination, potable water production, water reclamation, and reuse [6]. Compared to traditional and technological separation approaches, membranes provide superior separation efficiency, minimal energy requirement, a smaller carbon footprint [7], and eliminate the tedious multistep procedures in the purification process. To effectively utilize membranes for industrial applications, the imperative nature of developing new membrane materials that exhibit enhanced flux, permselectivity, and stability has remained crucial. Membrane performance is significantly influenced by both membrane composition and morphology.

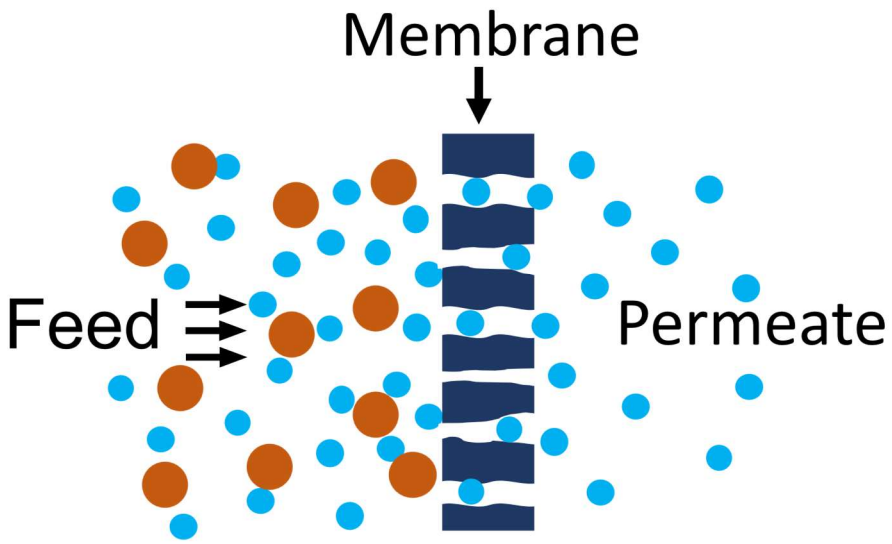

Figure 1.1 *Schematic illustration of a membrane process*

Thin-film composite (TFC) membranes, composed of an ultrathin film on top of a microporous substrate, have emerged as excellent candidates for a wide variety of separation applications, particularly nanofiltration (NF), reverse osmosis (RO), and forward osmosis (FO). The breakthrough in preparing thin-film composite membranes via interfacial polymerization was achieved by Cadotte in the late 1970s [8]. Since then, significant progress has been made that enabled interfacial polymerization to be the state-of-the-art technique of polyamide (PA) membrane synthesis for water and wastewater treatment. However, this fabrication method involves the use of toxic organic solvents and acid chlorides, raising environmental and safety concerns. Recently, polyphenol-based TFC membranes have emerged as promising alternatives, offering advancements in sustainable thin-film synthesis procedures. Tannic acid, in particular, exhibits the ability to form complexes with transition metal ions [9, 10]. Catechol or galloyl groups in polyphenols act as polydentate ligands, while metal ion centers serve as cross-linkers, similar to structures found in nature [11]. This supramolecular self-assembly process results in the formation of an ultrathin film of a metal-polyphenol network (MPN), which can be effectively utilized for the selective separation of components in nanofiltration. By using water as the solvent for both the polyphenol and metal ion casting solutions, this strategy offers a more sustainable method of selective layer fabrication. Moreover, phenolic molecules are rich in hydroxyl groups enveloping their aromatic structure. This feature imparts polyphenol-based membranes with superhydrophilic surfaces, demonstrating enhanced water permeance due to their low resistance to water transport.

Besides film fabrication, efficient membrane separation in NF relies on a thorough understanding of the rejection and transport mechanisms of components across the membrane active layer. The transport of solutes through membranes at the ionic and molecular level is a critical area of study, both in terms of its fundamentals and its industrial implications. Accurately understanding and predicting the transport of molecules, ions, and other entities across membranes is of paramount importance in, for example, optimizing membrane processes and evaluating their performance. By bridging theory with experimentation, modeling plays a vital role in providing insights and predictions about complex transport processes. These models not only guide experimental design but also accelerate the development of advanced membranes with tailored functionalities. Therefore, a comprehensive understanding of the fundamentals of transport phenomena through mathematical models is crucial [12].

Nanofiltration combines the removal of uncharged components performed at a nanoscale with the charge effects between the charged solute in a solution and the surface charge of the membrane [13]. In order to realize effective separation of neutral or charged solutes via NF, a good understanding of the synergistic effects of the partitioning mechanisms through transport models is required. A good predictive model allows the analysis of membrane performance and process optimization. Historically, several transport models including Spiegler–Kedem, space-charge model, Teorell–Mayer–Sievers model, Donnan–steric partitioning pore model (DSPM) have been developed. The most commonly adopted models for NF nowadays are based on the extended Nernst-Plank equation (ENP) [13]. The ENP is based on the assumption that ion transport inside membrane pores occurs through convection, diffusion and electromigration. The Donnan steric pore model with dielectric exclusion (DSPM-DE), which accounts for the three exclusion mechanisms, was lately introduced by Bandini and Vezzani [14] with some modifications to the DSPM model by Bowen et al. [15] Separation performance of NF was long perceived as a combination of the exclusion mechanisms of sieving (steric-hindrance) and Donnan (electrostatic) effects [16]. However, the ionic partitioning at the interface between the bulk solution and the membrane surface was shown to be influenced from a third exclusion mechanism, the dielectric effect [17], due to the decrease in the dielectric constant inside the small pores compared to the bulk solution, leading to a solvation energy barrier. Selectivity and performance of NF membranes is governed by these three exclusion mechanisms. DSPM-DE widely used to describe transport of solutes through NF membrane pores. Nevertheless, elucidation of solute transport and partitioning mechanisms through non-polyamide membranes remains to be fully established. Thus, investigation of the performance of MPN selective layers requires the description of solute transport with appropriate models.

This thesis aims to contribute to the ongoing research on fabricating low-cost, sustainable, and highly selective non-polyamide TFC membrane active layers for solute separation. The study focuses on realizing the goals – *i*) the synthesis of thin-films through metal-polyphenol self-assembly over a porous support in an ecofriendly technique via a layer-by-layer method, *ii*) investigation of MPN fabrication parameters that affect membrane structure and performance, *iii*) determination and characterization of membrane properties in detail, *iv*) provide the separation performance of the resulting MPN-based TFC membranes towards ions and small organic molecules separation, *v*) coupling experimental work with modeling and simulation to analyze solute transport across the MPN separation layer. Figure 1.2 briefly summarizes the desirable membrane process attributes.

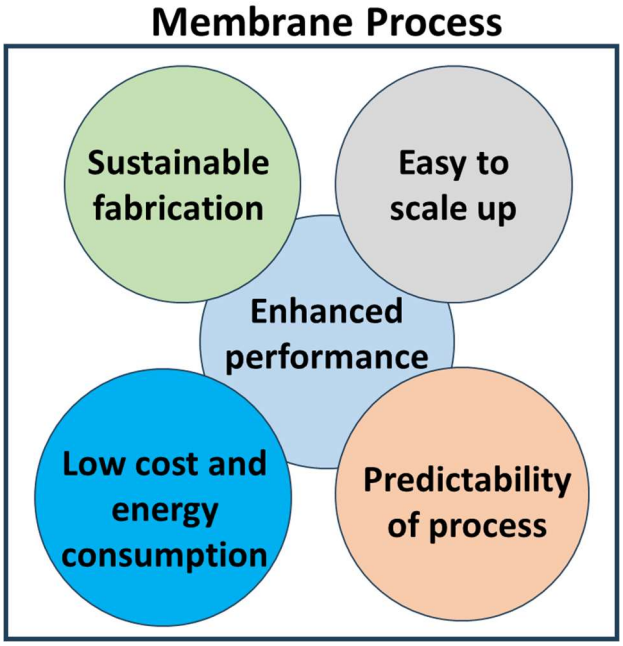

Figure 1.2 *Desirable membrane process characteristics. The membrane material, the fabrication process and the process operation should be sustainable, low cost and easy to scale up. The membrane should also exhibit improved properties such as water flux, solute rejection, selectivity, anti-fouling property, and overall stability. Furthermore, for the predictability of the membrane performance is vital that the ideal membrane has well-defined separation characteristics*

1.2. Strategy of the thesis

Membrane design and fabrication approaches are crucial in ensuring the efficiency and sustainability of membrane technology [18]. This involves innovative material selection and fabrication procedures that can effectively enhance key membrane characteristics such as

rejection, flux and stability. When we think of membrane fabrication materials and processes, it should be with high consideration that the overall process is green, fast and low cost, meeting the sustainability requirements. The first approach for sustainable membrane fabrication is the replacement of conventional toxic organic solvents, which pose significant risks to human health and the environment, with greener alternatives [19, 20].

With regard to the membrane operation efficiency and stability, reliable long-term operation of the processes is crucial. Fouling is the principal bottleneck that limits durable membrane process performance. While physical and chemical cleaning methods can partially remove foulants [21], the development of fouling-resistant membranes is a more effective strategy of controlling membrane shelf life. In general, hydrophilic and negatively charged surfaces are more prevalent in preventing membrane fouling. Thus, surface modification through coating with hydrophilic phenol containing materials such as polydopamine, tannic acid, and metal-polyphenol networks (MPNs) has been widely practiced [22-24]. MPNs are supramolecular network structures derived from the coordination between transition metal ions and phenolic ligands [25].

The tannic acid (TA)-Fe^{3+} coordination complexes are a prominent example of supramolecular metal−phenolic networks [26]. Hydroxyl-rich galloyl and catechol groups of TA provide chelating sites for transition metal ion (Fe^{3+} for example), resulting in a three-dimensional stable MPN structure [25]. This enables a rapid and low-cost conformal coating technique over diverse substrates. TA is a typical naturally occurring phenolic ligand, approved safe for use as a food additive by the US Food and Drug Administration (FDA) [27]. Its water solubility, high adhesive property, and metal chelation capability present a novel green approach to fabricate TFC membranes.

TA-Fe^{3+} networks can be constructed in a one-step (co-depostion) or multi-step procedures (sequential deposition). Co-deposition involves simultaneous deposition of both solutions over the substrate surface. In contrast, sequential deposition is analogous to layer-by-layer (LBL) film synthesis in which the support is alternately immersed in the phenolic and metal ion solutions. The later method of self-assembly prevents the formation of small complex aggregates [25], and leads to less defective membranes. Beyond the fabrication procedure, several key factors such as solution concentration, ligand-to-metal ratio, pH, ionic strength and assembly time play an important role in regulating the thin-film characteristics. These parameters allow for precise control over the membrane's physicochemical properties and separation performance. Taking this into consideration, TA-Fe^{3+} non-PA TFC membranes are fabricated in a LBL method in this study (Figure 1.3), by dissolving both constituents in a

typical green solvent, water. The impact of various synthesis parameters on the physicochemical properties and complex formation states of the fabricated TFC membranes is systematically investigated. These tannic acid–Fe^{3+} based membranes are fine-tuned to prepare organic solute selective thin-films. Furthermore, their performance in high-performance nanofiltration for salt removal is investigated.

To date, numerous studies have explored the fabrication, modification or application of both PA and non-PA thin-film composite membranes. However, non-PA membranes of new materials seem relatively overlooked in quantitative analysis and understanding of their separation performance. Description of transport phenomena via the thin-films necessitates the knowledge of membrane and solute characteristics as well as process operating conditions [28]. Different membranes exhibit different intricate structures and complex physicochemical properties that make elucidating their transport mechanisms and selectivity behavior challenging. In this thesis, the fabricated membranes are first thoroughly characterized. Then, the rejection and transport mechanisms of the analyzed solutes are evaluated with physical transport models. The validation of Spiegler–Kedem–Katchalsky model for describing the transport of aqueous solutions of organics through MPN-based membranes is examined. The ion permeation and rejection mechanisms of the NF TFC membranes having TA-Fe^{3+} selective layers are elucidated using the Donnan steric-partitioning pore model with dielectric exclusion (DSPM&DE).

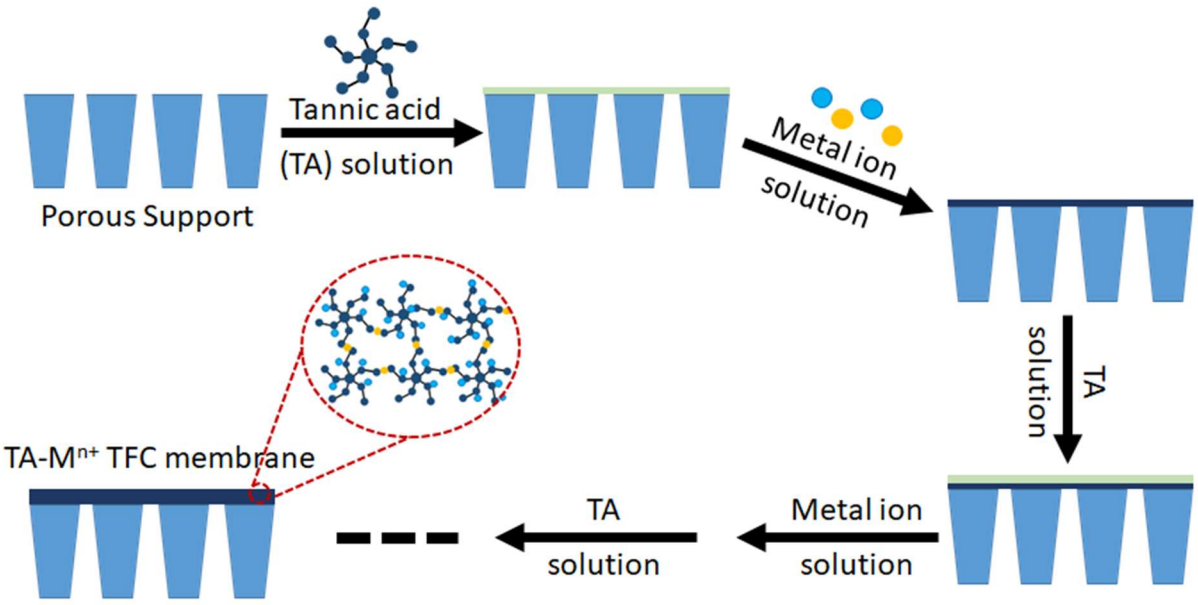

Figure 1.3 *Schematic representation of metal-polyphenol self-assembled TFC membranes via layer-by-layer technique followed in this work*

1.3. Outline of the thesis

The dissertation is organized into 11 chapters. Chapter 1 provides an overview of the general introduction, objectives and strategies of the thesis. Chapter 2 is dedicated to the literature survey. A comprehensive introduction about the membrane and membrane process classifications, methods of thin-film composite membrane fabrication, the concept of metal-polyphenol self-assembly, and the fabrication of MPN containing TFC membrane are discussed. Additionally, the key elements affecting MPN film formation, membrane structure and membrane performance are discussed. Finally, transport models that describe separation mechanisms and component transport through a porous membranes are introduced. Chapters 3 – 8 present the cumulative part of this dissertation. These chapters are part of the thesis that are published in different peer-reviewed journals. Chapter 3 deals about the successful deposition of tannic acid–Fe^{3+} thin films over a porous support and the fabrication of size- and charge-selective non-PA TFC membranes. Chapter 4 explores the effect of assembly time on tannic acid–Fe^{3+} thin films. Furthermore, the performance of the TFC membranes during single and mixed solute filtration is investigated. In chapter 5, the influence of casting solution pH on the structure and performance of MPN layers is discussed. The membrane microstructure is optimized to achieve the highest separation selectivity between small organic molecules. Chapter 6 provides insights into the mass transport mechanism of organic dye solutions through an MPN selective layer containing TFC membranes. Chapter 7 evaluates the nitrate removal efficiency of the MPN membranes from aqueous solution. The rejection of nitrate from single salt and ternary ion mixtures is investigated together with the application of the Donnan steric pore model with dielectric exclusion (DSPM-DE) to elucidate the separation performance. The rejection performance of other salts as well as the description of the transport of ions using the DSPM-DE is provided in Chapter 8. This chapter provides a fundamental understanding of ion rejection property by the tannic acid–Fe^{3+} TFC membranes and the resulting ion-ion selectivity from various mixed ion systems. Finally, the comprehensive discussion as well as the summary of this dissertation are provided in chapter 9. Chapter 10 contains the appendix parts of this dissertation in which the supporting information for the papers in the cumulative part are also included. To fit with the format in the chapters in the cumulative part, references are provided after each chapter.

References

[1] A. Nicolaï, B. G. Sumpter, and V. Meuniera, "Tunable water desalination across graphene oxide framework membranes," *Physical Chemistry Chemical Physics,* vol. 16, no. 18, pp. 8646-8654, 2014.

[2] M. A. Shannon, P. W. Bohn, M. Elimelech, J. G. Georgiadis, B. J. Mariñas, and A. M. Mayes, "Science and technology for water purification in the coming decades," *Nature,* vol. 452, no. 7185, pp. 301-310, 2008.

[3] E. O. Ezugbe and S. Rathilal, "Membrane Technologies in Wastewater Treatment: A Review," *Membranes,* vol. 10, no. 5, 2020.

[4] U. Urgency, "Water caucus summary," in *World Water Council (WWC)*, Marseille, France, 2009.

[5] S. Homaeigohar and M. Elbahri, "Graphene membranes for water desalination," *Npg Asia Materials,* vol. 9, 2017.

[6] A. Lee, J. W. Elam, and S. B. Darling, "Membrane materials for water purification: design, development, and application," *Environmental Science-Water Research & Technology,* vol. 2, no. 1, pp. 17-42, 2016.

[7] N. H. Othman *et al.*, "A Review on the Use of Membrane Technology Systems in Developing Countries," *Membranes,* vol. 12, no. 1, 2022, Art. no. 30.

[8] J. E. Cadotte, "Reverse Osmosis Membrane," US Patent 4,039,440, 1977.

[9] H. Ejima *et al.*, "One-Step Assembly of Coordination Complexes," *Science,* vol. 341, no. 6142, pp. 154-157, 2013.

[10] M. Hosseini, L. Moghaddam, L. Barner, S. Cometta, D. W. Hutmacher, and F. M. Savi, "The multifaceted role of tannic acid: From its extraction and structure to antibacterial properties and applications," *Progress in Polymer Science,* vol. 160, 2025, Art. no. 101908.

[11] M. A. Rahim *et al.*, "Coordination-driven multistep assembly of metal-polyphenol films and capsules," *Chemistry of Materials,* vol. 26, no. 4, pp. 1645-1653, 2014.

[12] N. Kaippamangalath and U. Gopalakrishnapanicker, "Chapter 8 - Transport Properties Through Polymer Membranes," in *Transport Properties of Polymeric Membranes*, S. Thomas, R. Wilson, A. K. S, and S. C. George, Eds.: Elsevier, 2018, pp. 119-158.

[13] N. Hilal, H. Al-Zoubi, N. A. Darwish, A. W. Mohammad, and M. Abu Arabi, "A comprehensive review of nanofiltration membranes: Treatment, pretreatment, modelling, and atomic force microscopy," *Desalination,* vol. 170, no. 3, pp. 281-308, 2004.

[14] S. Bandini and D. Vezzani, "Nanofiltration modeling: The role of dielectric exclusion in membrane characterization," *Chemical Engineering Science,* vol. 58, no. 15, pp. 3303-3326, 2003.

[15] W. R. Bowen, A. W. Mohammad, and N. Hilal, "Characterisation of nanofiltration membranes for predictive purposes - Use of salts, uncharged solutes and atomic force microscopy," *Journal of Membrane Science,* vol. 126, no. 1, pp. 91-105, 1997.

[16] X. L. Wang, C. Zhang, and P. Ouyang, "The possibility of separating saccharides from a NaCl solution by using nanofiltration in diafiltration mode," *Journal of Membrane Science,* vol. 204, no. 1-2, pp. 271-281, 2002.

[17] W. R. Bowen and J. S. Welfoot, "Modelling the performance of membrane nanofiltration-critical assessment and model development," *Chemical Engineering Science,* vol. 57, no. 7, pp. 1121-1137, 2002.

[18] P. S. Goh, T. W. Wong, J. W. Lim, A. F. Ismail, and N. Hilal, "Chapter 9 - Innovative and sustainable membrane technology for wastewater treatment and desalination application," in *Innovation Strategies in Environmental Science*, C. M. Galanakis, Ed.: Elsevier, 2020, pp. 291-319.

[19] A. Figoli *et al.*, "Towards non-toxic solvents for membrane preparation: A review," vol. 16, ed: Royal Society of Chemistry, 2014, pp. 4034-4059.

[20] S. A. N. Mehrabani, V. Vatanpour, and I. Koyuncu, "Green solvents in polymeric membrane fabrication: A review," *Separation and Purification Technology,* vol. 298, 2022.

[21] L. Tian *et al.*, "Insights into the properties of surface waters and their associated nanofiltration membrane fouling: The importance of biopolymers and high molecular weight humics," *Chemical Engineering Journal,* vol. 451, 2023.

[22] L. Fan *et al.*, "Green coating by coordination of tannic acid and iron ions for antioxidant nanofiltration membranes," *RSC Advances,* vol. 5, no. 130, pp. 107777-107784, 2015.

[23] J. Q. Wang *et al.*, "Fast polydopamine coating on reverse osmosis membrane: Process investigation and membrane performance study," *Journal of Colloid and Interface Science,* vol. 535, pp. 239-244, 2019.

[24] J. Zhu *et al.*, "A rapid deposition of polydopamine coatings induced by iron (III) chloride/hydrogen peroxide for loose nanofiltration," *J Colloid Interface Sci,* vol. 523, pp. 86-97, 2018.

[25] H. Ejima, J. J. Richardson, and F. Caruso, "Metal-phenolic networks as a versatile platform to engineer nanomaterials and biointerfaces," *Nano Today,* vol. 12, pp. 136-148, 2017.

[26] X. Zhu *et al.*, "Supramolecular-Based Regenerable Coating Layer of a Thin-Film Composite Nanofiltration Membrane for Simultaneously Enhanced Desalination and Antifouling Properties," *ACS Applied Materials and Interfaces,* vol. 11, no. 23, pp. 21137-21149, 2019.

[27] Z. Guo *et al.*, "Tannic acid-based metal phenolic networks for bio-applications: a review," *J Mater Chem B,* vol. 9, no. 20, pp. 4098-4110, 2021.

[28] G. Artug, *Modelling and Simulation of Nanofiltration Membranes*. Cuvillier Verlag, 2007.

Chapter 2. Theoretical Background

2.1. Membrane classification

Membranes and membrane processes can be categorized into numerous groups according to certain characteristics. The transport of components through a membrane is driven by gradients in pressure, concentration, temperature, or electrical potential gradient. Pressure driven membrane processes include microfiltration (MF), ultrafiltration (UF), nanofiltration (NF) and reverse osmosis (RO) (Figure 2.1). MF and UF are low-pressure membrane processes primarily applied for the removal of microbial contaminants and suspended particulates. These processes typically control solute transport at least partially on the basis of size-based rejection. NF and RO on the other hand operate at significantly higher pressures, and separate dissolved inorganics and small sized organics. With properties in between UF and RO, NF utilizes porous membranes of 0.5 – 2 nm pore size with molecular weight cut-off from 200 – 1000 Da [1-4]. NF ensures reducing hardness, as well as the removal of organics, particulates, and microbes. Moreover, nanofiltration membranes are distinguished for their ion selective nature. Thus, they are extensively used in water and wastewater treatment, and desalination. Other applications include the removal of micropollutants, compound refinement, organic solvent separation and pharmaceutical applications.

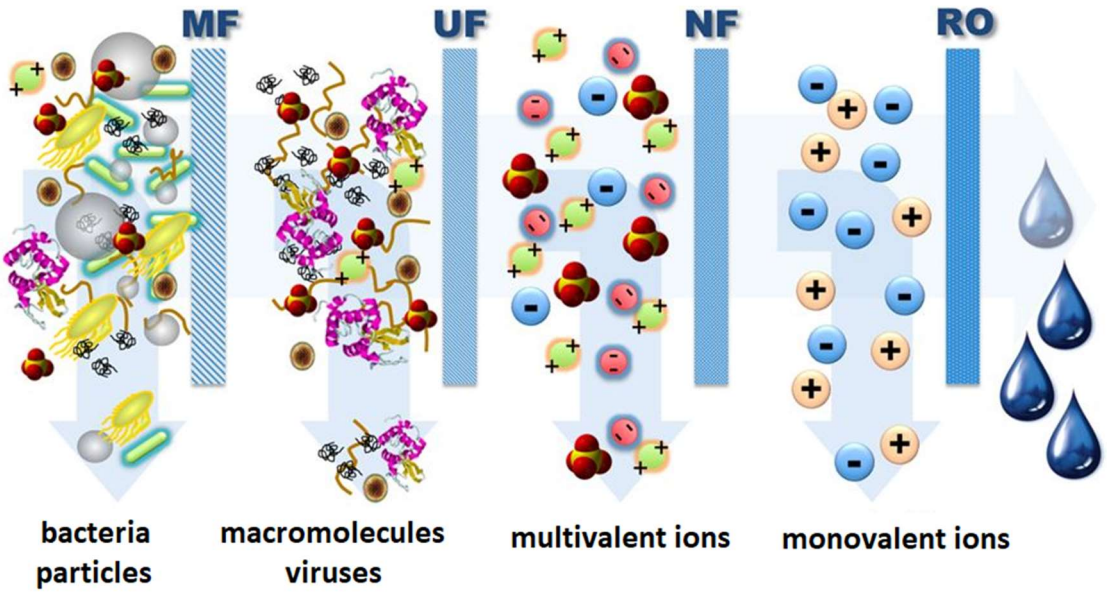

Figure 2.1 *Illustration depicting the rejection capabilities of pressure-driven membrane processes in the order of the decreasing pore size (from left); microfiltration (MF),*

ultrafiltration (UF), nanofiltration (NF), and reverse osmosis (RO). Adapted from National Research Council, 2012, National Academies Press. [5].

Synthetic membranes are classified into three groups according to their material composition: polymeric, inorganic and hybrid membranes. Inorganic membrane materials include ceramic membranes of alumina, silica, zirconia, titania, or zeolite, glass, metal, and carbon membranes. These membranes exhibit robust mechanical and chemical stability, high resistance to biofouling, and retain stable separation performance under extreme temperature and pH range [6]. Polymeric membranes are increasingly preferred in industrial applications due to their high performance and easy fabrication and modification [7]. Commonly used polymers include cellulose acetate, polysulfone (PS), polyethersulfone (PES), polyacrylonitrile (PAN), polyamide (PA), polyimide, polypropylene, polyurethane and poly(vinylidene difluoride) (PVDF). On the other hand, hybrid membranes contain materials of a composite structure combining a polymer matrix with inorganic fillers, nanoparticles, or other types of materials. Material selection is a key factor in controlling the membrane physicochemical properties as well as the permeant-membrane interaction, which influences the separation mechanisms. In addition to membrane materials, membrane morphology influences the rate of permeation and transport of species through its physical properties [7].

Over the past several decades, significant progress has been made in the fabrication of various types of membranes. According to their morphological structure, membranes can be categorized as symmetric or asymmetric membranes, as illustrated in Figure 2.2. Symmetric membranes generally consist a homogeneous morphology, with uniform structure and composition throughout their thickness [8]. Asymmetric membranes, in contrast, exhibit heterogeneous properties or structures along the membrane thickness. The introduction of anisotropic RO membranes by Loeb and Sourirajan in the early 1960s has led to the materialization of membranes for industrial application [8]. These membranes consist a thin active layer supported by a thick porous substrate of the same material. Asymmetric membranes are fabricated through the non-solvent induced phase inversion process which results in a heterogeneous structure with variations in porosity. Thin-film composite membranes, a typical membrane structure particularly in the field of RO and NF, include a ultrathin dense or microporous polymeric separation layer supported by a porous substrate in most cases composed of another material. This design maximizes water transport while maintaining mechanical support.

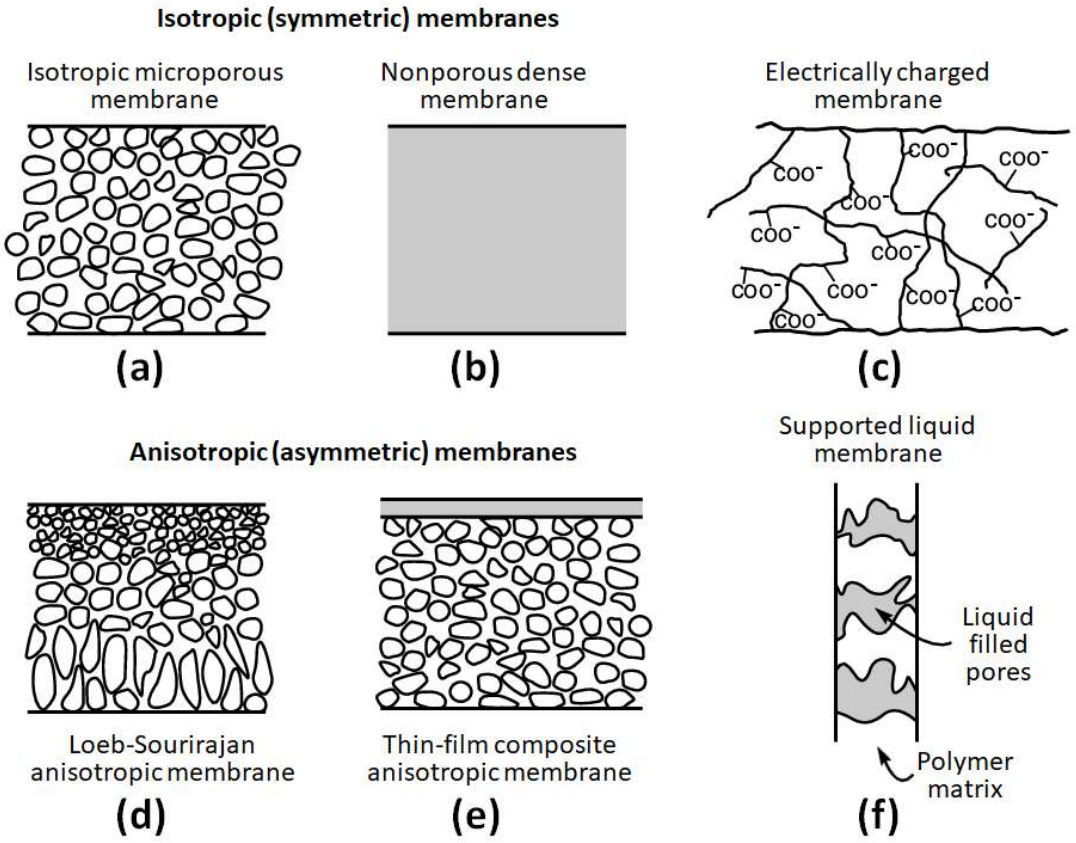

Figure 2.2 *Schematic diagrams of the principal types of membrane structures (Adapted from Richard W. Baker, 2004, Membrane Technology and Applications [8])*

2.2. Thin-film composite membranes

The emergence of TFC membranes marked a significant breakthrough in the realm of membrane technology. TFC membranes are semipermeable membranes widely used in nanofiltration, reverse osmosis, forward osmosis, gas separation, and other water reclamation applications. The thin selective layer controls membrane performance while the porous substrate underneath primarily acts as a mechanical support without hindering mass transport. Unlike the integrally skinned asymmetric membranes, TFC membranes provide the possibility of optimizing the surface chemistry and performance of the top selective layer and the porous support layer independently [9]. A possible drawback, though, is delamination between the two dissimilar materials. Therefore, the design of TFC membranes involves a careful selection of materials and fabrication methods to achieve optimal performance. The development and optimization of TFC membranes involve advancements in material science, membrane fabrication techniques, and understanding of transport phenomena. Researchers continue to explore novel polymeric materials, surface modification strategies, and innovative fabrication

methods to enhance membrane performance and expand their application range. Over the past half century, the development of high-flux, high-selectivity, fouling resistant, low-cost and scalable TFC membranes for water purification and resource recovery has attracted significant attention.

2.3. Interfacial polymerization

As introduced in the previous section, thin-film composite membranes consist of two distinct layers: a thin active layer and a porous support layer. The active layer governs membrane separation properties while the support provides mechanical stability and facilitates fluid transport. The porous support layer is commonly made of materials like polysulfone (PS), polyethersulfone (PES) or polyacrylonitrile (PAN). The top skin layer is usually a polyamide fabricated *in-situ* through interfacial polymerization (IP) reaction. Figure 2.3 illustrates the TFC membrane fabrication process through IP. IP involves a reaction between monomers at the interface between two immiscible phases, usually a diamine dissolved in the aqueous phase and acryl chloride monomer in the organic phase, to fabricate a thin dense layer on the support substrate. IP is a fast process dominated by the diffusion rate of the diamine towards the organic phase. Then, the formation of highly cross-linked polyamide film hinders further diffusion and reaction, ensuing a thin selective layer [10].

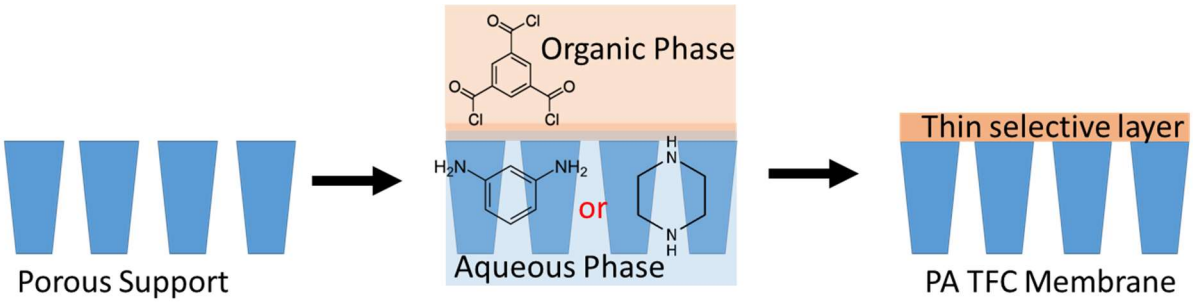

Figure 2.3 *Schematic representation of thin-film composite membrane fabrication via traditional interfacial polymerization*

Compared to other TFC membrane fabrication techniques such as coating and layer-by-layer assembly, IP allows the synthesis of ultra-thin less-defective selective layers with a thickness of around 50 nm [11]. Moreover, it is an easily scalable process, which has been widely commercialized for industrial applications. Membrane permselectivity can be effectively regulated through several procedures including optimization of the IP parameters, substrate modification, monomer selection and use of additives [12]. The thin active layer properties and performance are significantly affected by the solubility and diffusivity of the amine monomer

during IP reaction. Membrane characteristics such as pore size, thickness, surface charge, wettability, and roughness control membrane performances of flux, rejection, and selectivity. TFC membranes exhibit high solvent flux, solute rejection, and robust mechanical stability. Extensive research has been dedicated to studying and refining their structure and performance, and the fabrication process of these membranes is well developed.

However, the permeance and selectivity trade-off still remains a challenge to the efficient application of membrane processes. Moreover, TFCs have several limitations yet to be fully resolved. One of the drawbacks of TFCs is that they are very susceptible to fouling, which deteriorates membrane performance over time [13]. Polyamide TFC membranes have low chlorine resistance due to *N*-chlorination which significantly inhibits membrane performance. More importantly, the IP process requires the utilization of toxic and hazardous organic solvents [14]. These solvents raise severe concerns of health and ecological hazards to humans and ecosystems, respectively. In fact, the fabrication of polymeric membranes generates 50 billion liters of wastewater that contains harmful solvents every year [15]. Furthermore, after fabrication, the release of residual solvents during the membrane lifecycle remains an issue [16]. Therefore, it is critical to stimulate the search for alternative ecofriendly methods of synthesis. To control our ecosystem's pollution, the sustainability of membrane fabrication necessitates the replacement of organic solvents by green solvents. Hence, to address these limitations, several approaches were developed aimed at enhancing the membrane performance and sustainability. The primary focus lies in making alterations to the membrane synthesis procedure. In this dissertation, a metal-polyphenol coordination is employed to fabricate the separation layer for TFC membranes solely in water environment.

2.4. Metal−Polyphenol self-assembly based TFC membranes[(a)]

[(a)] Section 2.4 has been published as part of a review paper in a scientific journal (Kinfu H.H. and Rahman M.M., Membranes 2023, 13, 481) with slight modification. I, therefore, acknowledge that similarities with the published work exist, and declare that the published content is part of this PhD work.

Xie et al. [17] proposed five strategies to improve the sustainability of the membrane manufacturing process: *i*) polymers from renewable sources, *ii*) greener solvents, *iii*) recycling and treating wastewater generated during fabrication, *iv*) reducing fabrications steps, and *v*) dissolving casting solution at room temperature to save energy. In a quest for sustainable thin film composite membrane fabrication, coating approaches using aqueous solutions have been

practiced for preparing non-polyamide thin films. They are simple, cost-effective and ecofriendly processes through which one can easily control film thickness and structure. However, these procedures suffer from low permselectivity principally due to the increased film thickness compared to PA-TFC membranes [18]. Recently, the emergence of polyphenol-based membranes has shown promising advancements in sustainable TFC membrane synthesis procedures [19-21]. The green synthesis method and anti-fouling property of the membranes have attracted considerable attention.

This section (section 2.4) presents imperative background information about the metal-polyphenol network (MPN)-based membrane development. More focus is given to the tannic acid-metal ion (TA-M^{n+}) TFC membranes. Properties of tannic acid, the coordination chemistry between phenolic ligands and metal ions, the different practices MPNs have been utilized to form membrane structures, the techniques and factors affecting TA-M^{n+} membrane fabrication, as well as the latest application areas of MPN-based membranes are discussed.

2.4.1. Tannic acid and its property of self-assembly with metal ions

Tannic acid (TA) is a highly water-soluble [22] natural polyphenol found in plants such as oak, tea and fruits. One of the important features of tannic acid is its ability to adhere robustly onto various substrates. These include hydrophilic and hydrophobic, organic and inorganic, particle or surface substrates [23]. Adhesion occurs through different or a combination of many interactions such as hydrophobic interaction, hydrogen bond, electrostatic interactions, and coordination [24] [25]. Metal chelation is a salient feature of many polyphenols. Polyphenols act as organic polydentate ligands whilst transition metal ions play a role as crosslinkers. The coordination between tannic acid and transition metal ions, e.g. ferric ion, results in robust conformal films [26]. Natural polyphenols chelate metal ions to form metal–polyphenol network (MPN) complexes through coordination driven self-assembly. Tannic acid, a typical polyphenol, has the ability to form metal-ligand complexes by chelating many transition metal ions such as Fe^{3+}, Cr^{3+}, Co^{2+}, Zn^{2+}, Zr^{4+}, Mn^{2+}, Cu^{2+}, etc. [26-29]. Iron is the most studied metal for self-assembly with TA. At optimum conditions, coordination between catechol or galloyl groups and ferric ion forms a stable octahedral complex [26]. However, this coordination is pH dependent as the number of organic ligands coordinated with the metal ion decrease with pH. Three complex formation states are mainly recognized as presented in Figure 2.4b. However, it is worth noting that several factors such as the ligand to metal ratio, the final concentration and

the mechanism of film formation significantly influence the resulting coordination complex [30, 31].

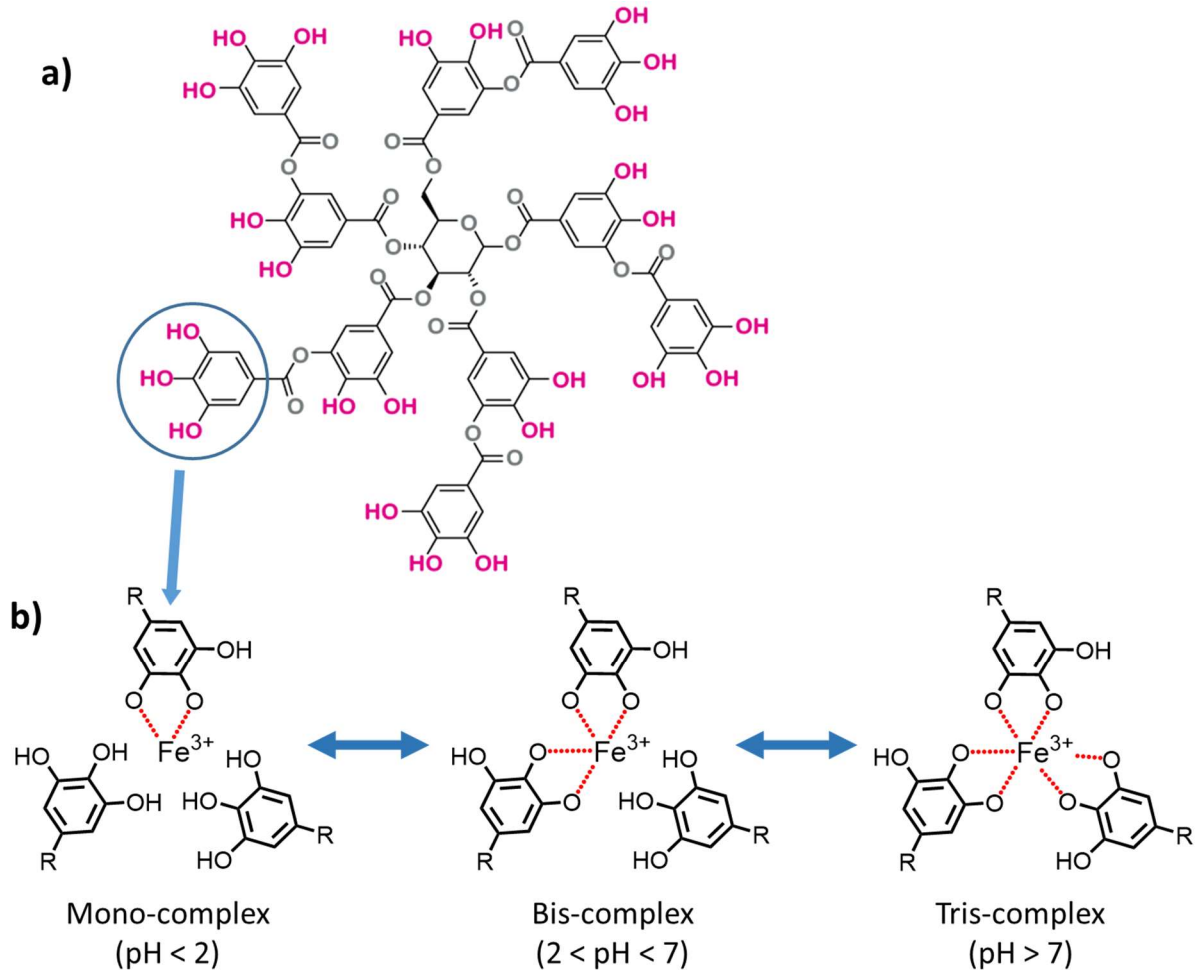

Figure 2.4 *(a) Structure of tannic acid and (b) pH-dependent tannic acid–metal ion complexation formation states.*

TA-metal ion (TA-M^{n+}) complexes have diverse applications in metal adsorption, water and wastewater treatment, drug delivery, nano-encapsulation, and many more [32, 33]. A newly introduced application for MPNs is in the field of membrane technology. TA-M^{n+} based metal-polyphenol networks are used for both membrane surface coating [23, 34, 35] and synthesis of a selective layer over a porous support [3, 18, 26]. For film synthesis, the foundation lies on polyphenol's ability to complex with metal ions though coordination reaction, or particularly supramolecular self-assembly. This self-assembly results in a thin-film of few nanometers that can be used for the selective separation of components. Tannic acid containing membranes exhibit superhydrophilic property due to their abundant hydroxyl groups enveloping the polyphenol besides their sufficient rejection towards many salts and organic components [18, 23, 36]. The nanofilm can be formed over various substrates in a simple, green, and fast facile

technique. Nevertheless, this TA−M^{n+} coordination-based membrane synthesis technique is in its early developmental phase.

2.4.2. MPN containing membranes

The use of TA for the fabrication of NF membranes is an emerging trend. The presence of catechol and gallol groups in TA provide the utilization of both non-covalent and covalently bonded layers to coat porous substrates [3]. While TA and trimesoyl chloride (TMC) have been used as monomers for interfacial polymerization to prepare TFC NF membranes [37], TA-metal coordinated layers are the most popular choice due to their environment friendly casting procedure. This approach offers several advantages; both constituents are dissolved in water, it uses naturally occurring low-cost polyphenol and simplifies the small, as well as large-scale, membrane fabrication processes. The selective layer is synthesized through different coordination methods via the self-assembly approach. Supramolecular self-assembly between metal ions and the organic ligands allows the fabrication of NF membranes without the use of reprotoxic organic solvents [18, 19, 38]. Film thickness varies from a few nanometers to approx. 30 nm. The self-assembled selective layers significantly improve membrane characteristics. Categorically, polyphenols, and tannic acid in particular, can be utilized for membrane film synthesis in three main ways depending on the chemistry and purpose: surface modification of membranes, interlayer construction and selective layer synthesis.

Membrane surface modification

Tannic acid is used for the surface modification of MF, UF, NF and RO membranes through sequential deposition or co-deposition with metal ions. The self-assembly between TA and Fe^{3+} is especially studied for coating and modifying the surface of various membranes [19, 35, 39-41]. The main advantages of TA-based surface modification include improving surface hydrophilicity, decreasing surface transport resistance and thereby enhancing water permeance [42, 43] and improving anti-fouling properties [41, 44]. Furthermore, the surface modification procedure is simple, easy and fast [41]. Polyamide membranes are prone to performance loss owing to the degradation from the exposure to the chlorine in water [45]. TA-M^{n+} networks enhance chlorine resistance by reducing the chlorine-sensitive sites. The strong free-radical scavenging effect of TA increases membrane chlorine resistance by lowering chlorine radical levels [44]. Enhanced permeability in MPN coated surfaces is associated with the abundance of -OH groups in the polyphenol.

Modification of membrane surface properties with TA-M^{n+} coating tackles the main challenges of membrane filtration; organic-, oil-, and bio-fouling, and membrane contamination by microorganisms [41]. Furthermore, surface modification of membrane active layers using MPN films can enhance salt rejection as well as divalent to monovalent ion selectivity [35]. Guo et al. [40] also showed that surface modification of commercial NF membranes with MPNs can significantly improve the rejection performance towards organic contaminants. Moreover, surface coating via self-assembly between TA and iron, copper or zinc enhances the selectivity and recovery of dye contaminants and hydrophobic micro-pollutants in 2D MXene membranes [46]. This opens a new simplistic strategy for adjusting the selectivity and efficiency of numerous types of membranes.

Interlayer construction

Over the last decade, polyphenols such as polydopamine and TA have received significant attention as bridging agents (i.e. gutter layer) between porous supports and the selective layer from IP. The primary goal of phenolic interlayers is to facilitate the wetting of the porous substrates and control the diffusion of aqueous phase components such as piperazine (PIP) during the IP process [10]. TA-based interlayers are typically co-deposited with a crosslinker or reactant such as diethylenetriamine [10], polyethyleneimine (PEI) [47], dual diazonium salt (DDS) [48] or transition ion metals. TA-Fe^{3+} intermediate layer, for instance, increases surface hydrophilicity and regulates amine monomer adsorption/diffusion during IP [49]. Furthermore, it allows the construction of smooth, ultrathin, dense PA surface structure. MPN interlayer containing membranes exhibit high separation performance and solvent permeability, presenting a potential for organic solvent nanofiltration [49].

TA-metal ion complex interlayers allow the fabrication of defect free thinner polyamide TFC membranes [10, 50]. Razavi el at. regulated the thickness, hydrophilicity, pore structure and surface roughness of a polyamide membrane by using TA-Fe^{3+} interlayer [51]. A triple-layered TFC membrane was fabricated by coating a PVDF microfiltration support with MPN before the IP reaction between MPD and TMC. The interlayer containing TFC membrane showed almost three times water flux compared to the membrane without MPN interlayer. The proposed synthesis technique ensures high controllability of chemical and physical structures and scale-up prospects for industrial applications. In a similar investigation, Yang et al. [50] constructed a TA-Fe^{3+} nanoscaffold layer over polysulfone substrate prior to interfacial polymerization of TMC and PIP, Figure 2.5a. Due to its smaller pore size, the MPN based interlayer prevents intrusion of polyamide to the pores of support substrate. Moreover, TA-Fe^{3+} interlayer enhances

uptake of amine monomers in addition to regulating their controlled release. The MPNs interlayer containing TFC membrane showed a water permeance of 19.6 $L \cdot m^{-2} \cdot h^{-1} \cdot bar^{-1}$ while that of the control TFC membrane was 2.2 $L \cdot m^{-2} \cdot h^{-1} \cdot bar^{-1}$. The rejection of salts was also improved [50]. MPN interlayers can also act as metal precursors for metal-organic framework (MOF) membrane synthesis [52]. It provides sufficient controllability of the MOF membrane synthesis, Figure 2.5b.

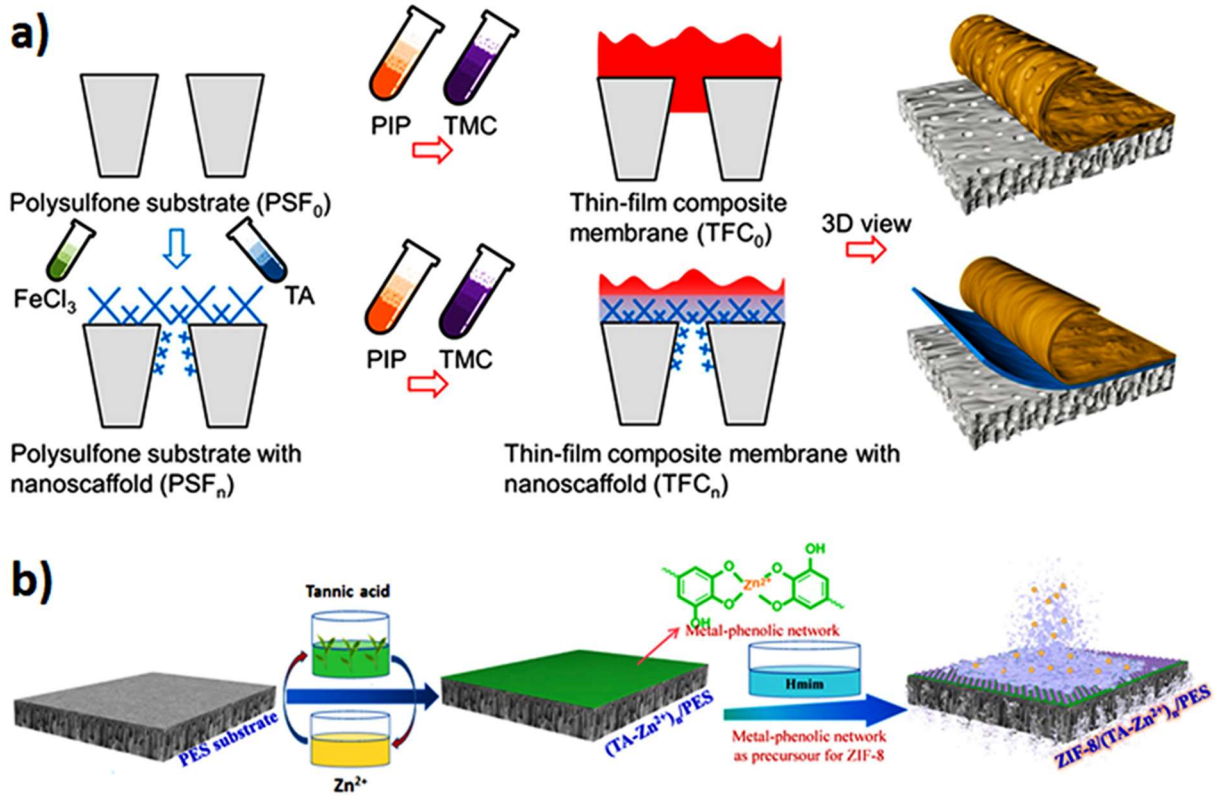

Figure 2.5 *(**a**) Schematic diagram showing the synthesis of the conventional TFC membrane (TFC_0) and the TA-Fe^{3+} nano-scaffold interlayer containing TFC membrane (TFCn). To prepare the TFCn membrane, a PSF substrate was first coated with a TA/Fe nanoporous layer, followed by interfacial polymerization of PIP and TMC. Reprinted from ref. [50] with permission from American Chemical Society. b) Schematic representation of the synthesis of ZIF-8/(TA-Zn^{2+})n/PES membrane with TA-Zn^{2+} network as interlayer and zinc precursor. Reprinted from ref. [52] with permission from Elsevier.*

Tannic Acid-Metal Ion Selective Layer

TA-metal complex layers deposited on a porous support can also act as the main separation layer in many membrane technology processes. As MPN active layer synthesis is a relatively

new topic, TA-Fe^{3+} based films dominate the research, while other transition metal ions have also been explored. A study by You et al. [53] showed that membrane properties can be tailored using different metal ion crosslinkers. NF films containing TA-Ag^{+}, TA-Cu^{2+} and TA-Fe^{3+} selective layer exhibited a relatively low water permeance compared to TA-Co^{2+} and TA-Ni^{2+} films. At 1:1 molar ratio of tannic acid molecule to metal ion, the membranes displayed a pure water flux in the range of 8 – 47 $L{\cdot}m^{-2}{\cdot}h^{-1}{\cdot}bar^{-1}$ while maintaining more than 94% rejection towards methylene blue (MB) as shown in Figure 2.6c. Additionally, the variation in molar ratio between tannic acid and Ni^{2+} can be used to fine-tune the selective layer characteristics, Figure 2.6d. Higher Ni^{2+} content decreases surface hydrophilicity as more phenolic hydroxyl groups in TA interact with Ni ions [53], limiting the available hydrophilic groups. MPN selective layers have high water/organic molecule selectivity [20]. This provides an insight into the potential of metal-polyphenol coordination chemistry as a sustainable alternative to conventional solvent-intensive TFC membrane fabrication.

Wang et al. [54] reported an in situ technique of preparing superwetting membranes for oily wastewater treatment though TA-metal ion assembly. They have proven that those metal ions with a high ionization potential, have a higher coordinating affinity with tannic acid to form stable complexes. Cu^{2+}, Zr^{4+} and Fe^{3+} based selective layers show rough surfaces with larger pore sizes compared to those from Ni^{2+}, Co^{2+} and Fe^{2+}. On the other hand, TA-Ni^{2+} and TA-Cu^{2+} complexes show a higher stability [54]. In addition to the morphological characteristics, membrane properties such as wettability, flux and rejection of TA-metal ion thin films are affected by the choice of the complexing metal ion. In another study, a TA-Cu^{2+} active layer containing membrane maintained a rather constant flux for several days [55], implying good mechanical stability. The thin layer can be fabricated from ethanolic solutions of metal ions and TA.

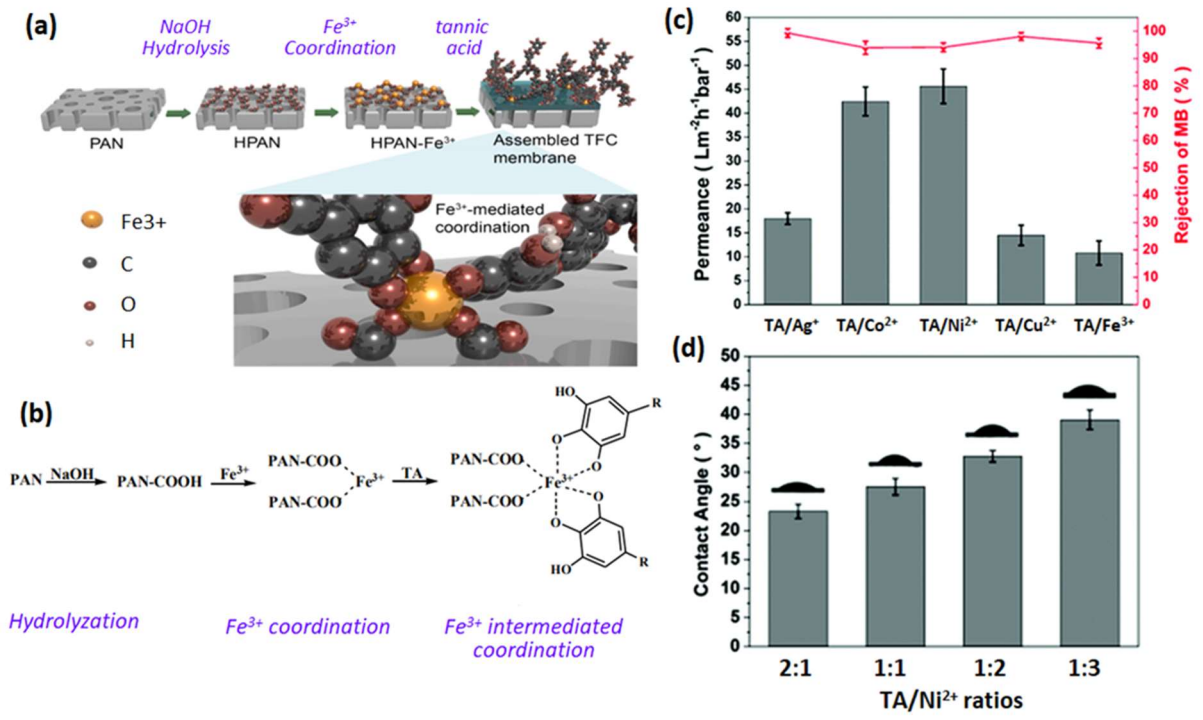

Figure 2.6 *(**a**) Schematic diagram of the preparation process of TA-Fe^{3+} self-assembled TFC membranes, and (b) reactions and the possible structure of the resultant Fe^{3+}−intermediated TA thin film, reprinted from ref. [18] with permission from Elsevier. (c) Separation performance of TA-metal ion coated composite nanofiltration membranes, and (d) the effect of TA/Ni^{2+} molar ratio on water contact angle of membrane surface, reproduced from ref. [53] with permission from The Royal Society of Chemistry.*

In coordination chemistry, it is essential to utilize the adhesion, adsorption and electrostatic interactions between the support, the polyphenol and metal ions. Consideration of the molecular interactions allows the regulation and formation of defect free thin film. For instance, in fabricating TA-Fe^{3+} TFC membranes (Figure 2.6a), the electrostatic and coordinative affinity of Fe^{3+} with the –COOH rich support layer (Figure 2.6b) facilitates the formation of homogeneous TA-Fe^{3+} selective layer and further improves the structural stability of the membrane [18]. A comprehensive investigation on the as-synthesized membrane morphology and properties revealed that the structure and performance of the selective layer can be controlled by the fabrication conditions. The rapid fabrication process makes it an ideal strategy for large-scale membrane production processes. Moreover, a variation in pH of monomer solutions showed that a slightly alkaline condition is ideal for the formation of a dense TA-Fe^{3+} selective layer due to the fact that a tris-complex of tannic acid and iron ion is established under alkaline condition [18].

A very detailed study regarding the the synthesis of superhydrophilic membrane was performed by Xiao et al. [36], who proposed LBL assembly to realize a facile process of fabricating multilayered crosslinked metal-polyphenol networks. This prevents the precipitation of metal ion, TA molecules, or TA-M^{n+} complexes as aggregates in water before depositing on the support surface, for preparing a defect free TA-Fe^{3+} selective layer. An MPN TFC membrane prepared at pH = 8 of precursor solutions resulted in the most compact selective layer with the highest retention. Similar thin selective layers for NF application were also synthesized via LBL technique in another study [38]. Alternate deposition of low concentrations of TA and $Fe(NO_3)_3 \cdot 9H_2O$ solutions generated an ultrathin and defect-free multilayered nanofilm. The tailored pore size of less than 1 nm confirmed that the films can be used for NF.MPN-based active layers prevent the decline of water flux caused by concentration polarization during operation. Table 2.1 summarizes the performance of MPN selective layers based on the self-assembly between transition metal ions and tannic acid for membrane application.

Table 2.1 *Separation performance of metal–polyphenol-coordination-based thin selective layers*

Membrane	Support	Preparation method	Permeability ($L \cdot m^{-2} \cdot h^{-1} \cdot bar^{-1}$)	Rejection (%)	Reference
TA-Cu^{2+}	PAN	Co-deposition	52	Methyl orange: 65 Brilliant blue: 99	[55]
$(TA\text{-}Fe^{3+})_5$ *	PAN	Layer-by-layer	40.9	93.9–100 towards various dyes	[36]
$(TA\text{-}Zn^{2+})_5$	PAN	Layer-by-layer	32	Static blue carmine red: 60 rose red sodium salt: 78	[36]
TA-Fe^{3+}	Polyamide TFC	Co-deposition	7.52	Na_2SO_4: 99.5	[35]
TA-Fe^{3+}	PES	Co-deposition	27.2	Congo red: 99	[19]
TA-Ni^{2+}	P84	Co-deposition	45.6	Methyl Blue: 94.1	[53]
TA-Fe^{3+}	P84	Co-deposition	9.8	Methyl Blue: 95	[53]

$(TA\text{-}Fe^{3+})_2$	PES	Layer-by-layer	12.4	Methyl orange: 90 VB12: 98.9	[38]
$TA\text{-}Fe^{3+}$	PES	Co-deposition	116	Heavy metals (Cu, Fe, Cd, Mn): 78-93	[41]
$TA\text{-}Ti^{4+}$	PSF	one-step assembly	9	Methyl blue: 96.8 Congo red: 97.2	[56]
$TA\text{-}Fe^{3+}$	Hydrolzed PAN	Co-deposition	13.6	Dyes: >99 Na_2SO_4 : 90.2, $MgSO_4$: 83.4	[18]

* Subscripts represent the number of TA-M^{n+} self-assembled layers deposited over the support.

2.4.3. Synthesis strategies of MPN membranes

Metal-polyphenol networks are spontaneously assembled with the network growing in all orientations. However, a well-structured, highly permeable and selective thin film synthesis requires a controlled and systematic fabrication procedure. So far, co-deposition and layer-by-layer self-assembly are the two widely used techniques for MPN selective layer synthesis, although interfacial polymerization (IP) has also been applied [3]. In IP, aqueous solution of TA dissolved in water and organic phase of tris(acetylacetonate)iron(III) ($Fe(acac)_3$) dissolved in *n*-hexane are used to synthesize TA-Fe^{3+} networks. However, synthesis of MPNs via IP is rare and involves toxic organic solvents.

One of the facile and fast synthesis techniques of MPNs is co-deposition, often referred to as one-step self-assembly. In this method, the top layer of a UF or MF membrane support is exposed to the aqueous solutions of the polyphenol and metal ions, either by pouring one solution shortly after the other [18, 20, 55], or immersing the support in a fresh mixture of the reagents [53]. A schematic representation of co-deposition is shown in Figure 2.7a. A thin and stable skin layer with MWCO of ~600 Da can form via one-step process of coordination using ethanolic solutions of TA and Cu^{2+} ions [55]. The reagent solutions are poured into PAN support mounted between Teflon plate and frame in 10 seconds difference and allowed to react for 10 minutes. Gou et al.'s [20] research is one of the pioneering works on metal-polyphenol based non-polyamide NF membranes synthesis via rapid assembly (less than 2 min) over a porous PES support. The obtained TA-Fe^{3+} based membranes show a potential breakage of the permeability-selectivity trade-off during pharmaceutical products removal. MPN thin-films synthesized via co-deposition generally show low salt rejection, insufficient for high performance nanofiltration. However, optimization of the separation layer via one-step self-

assembly of TA and Fe^{3+} shows that the MWCO can be finetuned to fabricate thin-films with high rejections for salts Na_2SO_4 (90.2%), $MgSO_4$ (83.4%), NaCl (50.0%) and $MgCl_2$ (35.2%) [18]. One-step assembly has also been widely used for surface modification of membranes [19, 40-42]. Membrane morphology and separation performance are regulated by several factors, which are discussed in section 2.4.4.

MPN layers can also be fabricated via sequential deposition of precursor solutions over a substrate as in layer-by-layer (LBL) self-assembly. A porous support is alternately immersed in polyphenol and metal ion solutions (Figure 2.7b). This process is analogous to synthesis of polyelectrolyte multilayer films. LBL offers better control over membrane thickness, surface porosity and pore size compared to co-deposition [38]. Layer thickness increases with the number of deposited layers. LBL mitigates the challenge of loose network formation. In contrast, co-deposition may lead to defective and loose polyphenol-metal network due to the formation of Fe^{3+} aggregates which cannot penetrate the growing the TA-Fe^{3+} layer to further crosslink with phenolic ligands. MPN NF membranes fabricated via LBL technique exhibit a narrow pore size distribution [38] and exceed the upper bound in a permeability-selectivity plot compared to other nanofilms (Figure 2.8). The LBL technique enhances surface hydrophilicity by increasing the bilayer number and subsequent introduction of abundant phenolic groups [36]. Moreover, MPN membranes synthesized via LBL show superior rejection compared to co-deposited film [36].

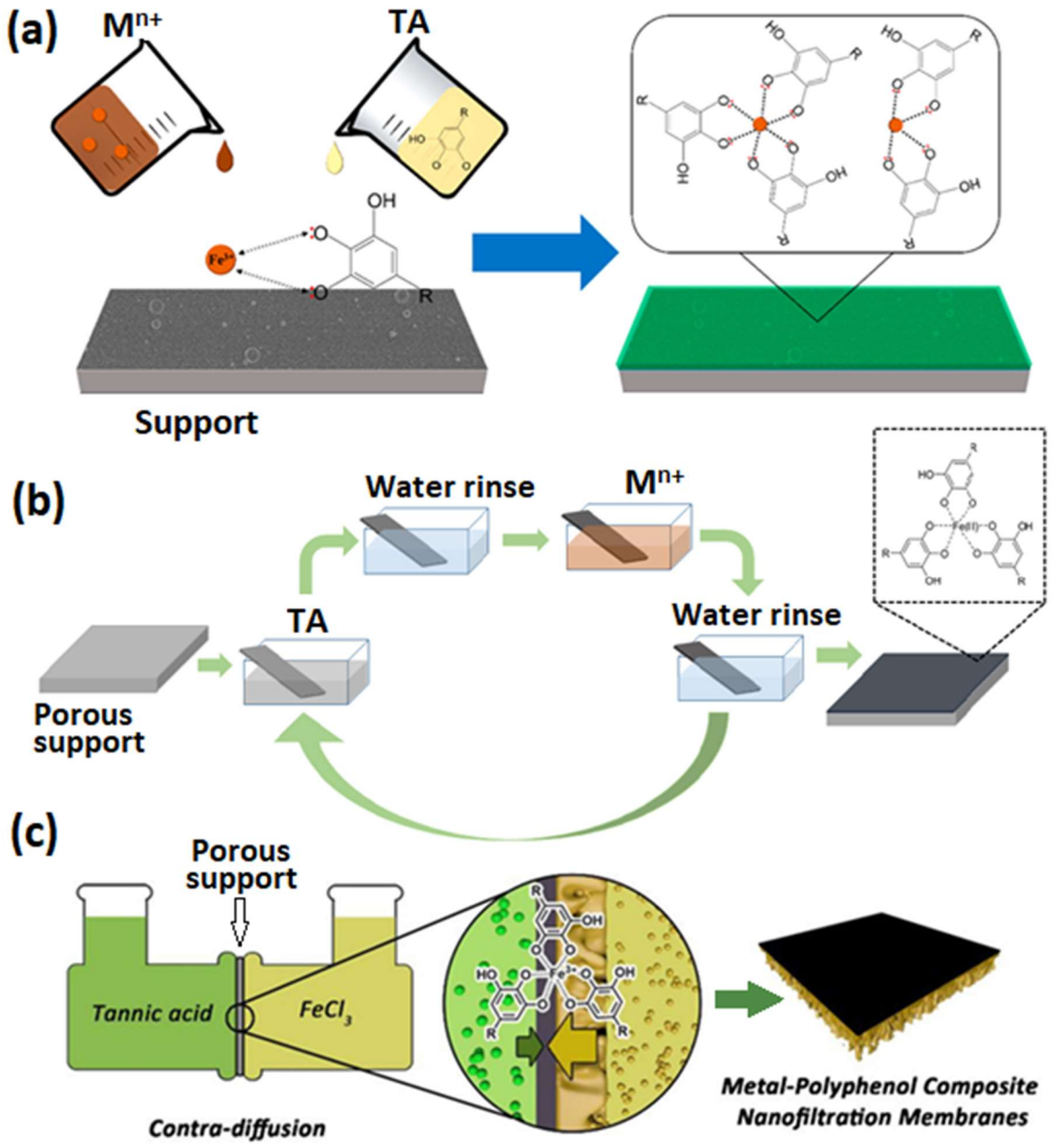

Figure 2.7 *Schematic representation of metal-polyphenol NF membrane fabrication through (a) co-deposition. Reprinted from ref. [40] with permission from American Chemical Society. (b) Layer-by-layer TA-M^{n+} membrane synthesis technique, analogous to sequential dip-coating process. c) Membranes fabrication process via confined coordination by aqueous contra-diffusion. Reprinted from ref. [57] with permission from American Chemical Society*

Another novel method of MPNs membrane synthesis is contra-diffusion that allows thin layers construction through a coordination restricted within a confined space. Unlike co-deposition and LBL, this method prevents undesired thickening of the active layer in TA-M^{n+} TFC membrane by regulating the competition between diffusion of precursors [57]. Fe^{3+} diffuses

faster than TA, and diffuses through the porous structure of the membrane to coordinate with TA at the membrane active layer side. As a result, a defect free selective layer is generated. A schematic representation of the aqueous contra-diffusion method is shown in Figure 2.7c.

MPN films can also be deposited on porous substrates through solvent/nonsolvent exchange during phase inversion process [54]. This method involves membrane support fabrication via the nonsolvent vapor-induced and liquid-induced phase separations. This allows integrating the MPN complex into the membrane matrix and coupling surface modification with pore structure and morphology control, which is challenging when using an already prepared support. Technically, TA is mixed with the casting solution and casted. Subsequently, the obtained film is immersed in non-solvent aqueous solution containing metal ion to induce precipitation as well as coordination. This technique prevents the surface pore blockage from the rapid complexation of TA and metal ions. TA-Fe^{3+} complexes are employed as additives to regulate membrane surface properties [39]. However, the dispersion of TA-M^{n+} networks in the integral membrane structure signifies increase of the selective layer thickness.

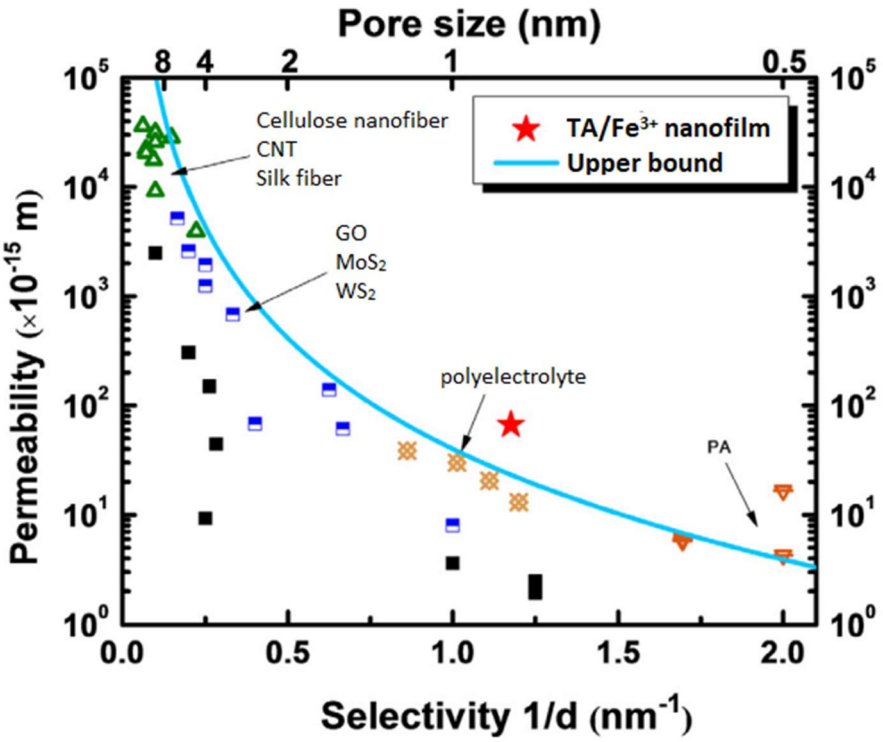

Figure 2.8 *Comparison of the selectivity−permeability between the TA/Fe^{3+} nanofilm and other nanofilms made of various materials (carbon nanotube (green triangle), graphene oxide, molybdenum disulfide, and tungsten disulfide (blue and white square), polyelectrolyte (orange square), polyamide (orange triangle), other materials (black square)). Reprinted from ref. [38], ©2018, with permission from Elsevier.*

2.4.4. Factors affecting metal–polyphenol complex formation, membrane selective layer characteristics and performance

Effect of concentration and TA to metal ion ratio

Monomer concentration significantly impacts thin-film growth via self-assembly or coordination reaction [41]. Higher monomer concentrations lead to thicker, more compact coatings by enhancing the degree of coordination. Moreover, an increase in monomer concentrations improves membrane surface hydrophilicity [18], attributed to the introduction of abundant TA hydroxyl groups. Membranes containing a TA-Fe^{3+} selective layer exhibited an increase in salt removal efficiency when the TA and Fe^{3+} concentrations of the casting solution increased [18]. The pure water flux declines as anticipated, as also observed in TA-Cu^{2+} membranes [55]. At low monomer concentrations, the selective layer is porous, while it becomes dense with the introduction of more components into the network. Higher metal ion concentrations promote more tannic acid binding on the membrane surface, resulting in thicker coatings. However, excess concentrations may result in a loose separation layer. Excessive reagents provoke rapid aggregation of TA-Fe^{3+} complexes at the membrane surface, leading to the development of particles, wrinkles, and defects in the constructed thin film [18].

At constant TA concentration, the increase in Fe^{3+} concentration leads to a decrease of water permeance with high rejection towards salts and organic molecules due to the synthesis of dense and highly crosslinked thin layers [40]. However, further increase of ferric ion concentration results in a decrease of salt rejection and an increase of pure water flux. On the other hand, an increase in TA concentration demonstrates the formation of smoother and compact membrane surfaces as revealed by SEM [19]. Increasing TA concentration from 0.5 to 1.5 g/L at a Fe^{3+} concentration of 1 g/L dramatic changes membrane performance: water flux evidently declined from 161.4 to 45.6 $L \cdot m^{-2} \cdot h^{-1}$, while orange II and Na_2SO_4 rejection increased from 71.5% to 94.8% and from 20.6% to 62.1%, respectively. Further TA concentration increases to 3 g/L had minimal impact on flux and rejection.

Effect of solution pH

Acidity or alkalinity of solutions govern the complex formation states of metal-polyphenol self-assembly. Membranes synthesized at various pH values exhibit diverse morphological characteristics. With an increase in pH value of monomer solutions, an increase in the protrusions size on membrane surfaces can be observed [36]. Oxidation of catechol groups into reactive quinones is accelerated at high pH. Quinones undergo a self-crosslinking reaction and

contribute to the TA aggregate formation (Figure 2.9). TA aggregates result in an increase in protrusion size on the surfaces of the membranes. In contrast, lower pH leads to hydroxyl group protonation, promoting TA-metal mono-complex formation and thinner selective layers. A rise in pH induces the ionization of the tannic acid functional groups (Figure 2.9), enhancing self-assembly and the formation of a dense top layer. In general, an increase in pH changes the complex formation from the mono- via bis- to tris-complex state (Figure 2.4b). Increasing solution pH also results in the fabrication of a thicker separation layer [36]. Nonetheless, in the case of ferric salt solutions, at a pH of 9 or more, generation of ferric hydroxide is facilitated [19]. This phenomenon interferes with the assembly between TA and Fe^{3+} [19, 36]. Membranes synthesized at high pH exhibit a low water contact angle [36]. This improves the membrane superhydrophilic property, increasing the interaction between membrane pore walls and water molecules that enhances water permeability by increasing the infiltration capillary force [58].

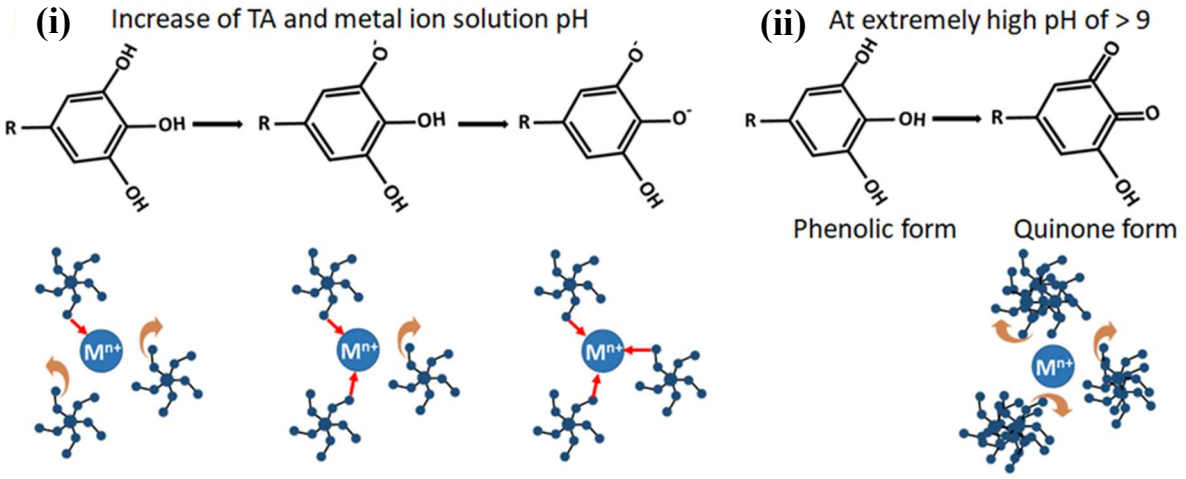

Figure 2.9 *Ionization of catechol groups of tannic acid in aqueous solutions of various pH levels and their respective coordination ability with transition metal ions. An increase in pH leads to the increase in crosslinking and the subsequent formation of thicker films with a decrease in surface porosity. However, at highly alkaline conditions, TA oxidation to quinone induces the formation of aggregate on the membrane surface.*

Assembly time

Assembly time affects MPN film formation but has minimal impact on membrane performance, as coordination occurs instantaneously and does not improve significantly with extended time [19]. Studies on TA-Cu(II) complex based film synthesis show that increasing coating time reduces water permeability until reaching a steady state [55]. TA-metal ion complex formation is a rapid process, with one minute being sufficient to create a dense selective NF membrane

layer [36]. Further prolonging assembly time slightly improves dye rejection but significantly decreases water permeance. Liu and colleagues [18] also confirmed less than two minutes were adequate for preparing TFC membrane selective layers for salt removal.

Besides coordination time, storage time of precursor solutions affects membrane structure and performance. Prolonged storage of iron solution results in aggregation [38]. Iron ion aggregation alters the TA-Fe^{3+} complex, creating defects and large pores, as illustrated in Figure 2.10c. Prolonged storage increases Fe^{3+} to TA ratio, preventing homogenous distribution of metal ions for film formation. Fe^{3+} aggregates are too large to penetrate into the growing TA films to coordinate. This results in a much looser film and large gaps (defects). Using fresh metal ion solutions ensure uniform crosslinking, leading to defect-free membranes having narrow pore size distribution with precise separation.

Number of deposited layers

Nanofilm thickness increases linearly with the number of bilayers in LBL construction, with each TA-Fe^{3+} bilayer measuring about 2.5 nm. [38]. A bilayer consists of one TA-metal ion self-assembled layer. The increase in the number of deposited layers lead to a thicker selective layer, causing flux decline. To date, research on LBL assembly has focused on ferric ions, and hence the effects associated with multilayer growth involving other metals are still unknown. Xiao et al. [36] prepared a TA-Fe^{3+} based NF membranes via LBL self-assembly technique. This method improves atom economy compared to co-deposition. In LBL, the first layer of TA adheres to the PAN support due to its substrate-independent adhesive properties, followed by ferric ion coordination with the surface-bound TA's -OH groups. For subsequent layers, incoming TA molecules self-assemble with the pre-deposited Fe^{3+} ions, continuing until the desired membrane characteristics are acquired. With an increase in the number of layers, a decrease in water contact angle to as low as 28° was achieved, due to the formation of a rough surface [36]. A single bilayer membrane exhibits low dye rejection and high water permeance, whereas increasing the number of bilayers enhances dye rejections while reducing water permeance. For example, a membrane with five bilayers deposited achieved 85.9% rejection of static blue carmine red dye (IR), 98.2% rejection of rose red sodium salt dye (RB) and a water permeance of 25.9 $L \cdot m^{-2} \cdot h^{-1} \cdot bar^{-1}$, compared to 40%, 90% and 76 $L \cdot m^{-2} \cdot h^{-1} \cdot bar^{-1}$ for single bilayer containing membrane, respectively.

The effect of ionic strength

Increasing ionic strength leads to the formation of rougher and thicker films. High salt concentration causes galloyl groups to extend out from the Fe^{3+} center and interact with other TA-metal ions complexes [59]. Further increase in salt concentration results in increase of surface roughness. At low salt concentration, TA solution is homogenous. However, when ionic strength is increased, TA particle size extends and the solution becomes turbid [3]. Electrostatic repulsion forces TA molecules to disperse well in aqueous solution. However, with severe increase of salt concentration, repulsion is screened and results in the aggregation of TA molecules and TA-M^{n+} complexes. The effect of ionic strength on TA-Fe^{3+} complex formation in solution is shown in Figure 2.10a. Individual TA-Fe^{3+} complexes agglomerate and form clusters when the salt concentration is increased. Besides, ligand-to-metal charge transfer (LMCT) depicting the formation of tris-complex of TA-Fe^{3+} increase. In this phenomenon, screening of charges plays an important role in the formation and growth of the film. MPN complexes undergo conformational changes depending on the ionic strength of the solutions [59].

Generally, change in ionic strength affects surface inhomogeneity and film thickness due to screening of charges in solution [59], leading to the deposition of more open and defected films. Shen et al. [3] studied the effect of ionic strength on TA-Fe^{3+} membrane fabricated via interfacial polymerization, finding that higher ionic strength increased VB12 rejection but decreased permeability (Figure 2.10b). At low ionic strength, steric effects limit TA-Fe^{3+} complexes to mono- and bis-complexes, while higher salt concentrations promote tri-complex formation that results in dense membranes of low porosity [3]. Nevertheless, excessive salt concentration above a threshold level causes aggregation and results in large gaps between consecutive TA-Fe^{3+} complex aggregates. Hence, defective selective layers are fabricated. Nonetheless, the impact of ionic strength on membranes formed via direct polyphenol-metal ion self-assembly in aqueous solutions remains unexplored.

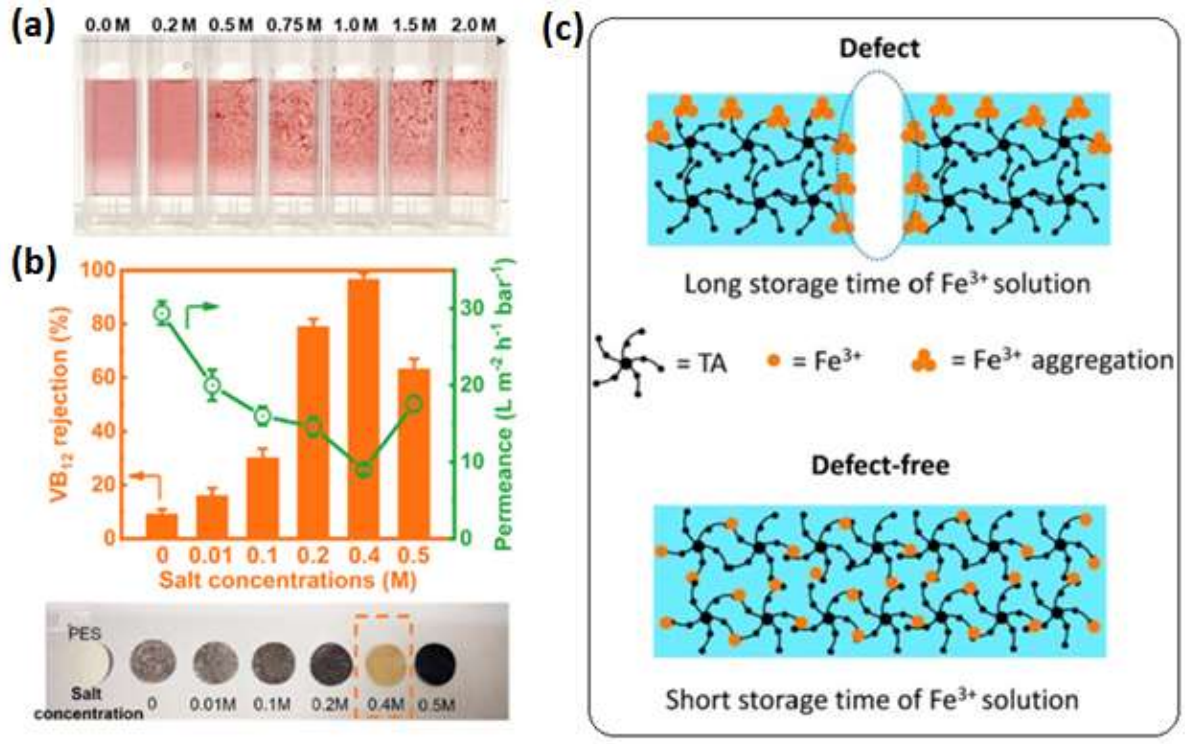

Figure 2.10 *a) Influence of salt concentration on the structure of the Fe^{3+}−TA complexes in solution. Reprinted from ref. [59] with permission American Chemical Society. b) Effect of salt concentration in aqueous solutions on the filtration performance and the appearance of PES and TA-Fe^{3+} composite membranes Reprinted from ref. [3] with permission from Elsevier, c) Schematic illustration for the effect of Fe^{3+} aggregation on the TA-Fe^{3+} nanofilms. Reprinted from ref. [38] with permission from Elsevier.*

2.4.5. Stability and applications of MPN membranes

Fouling remains a major challenge that limits the performance and cost-effectiveness of NF membranes despite various mitigation efforts [60]. Polyphenol-metal complex-based membranes offer a promising solution of safeguarding the selective layer and controlling fouling. TA-M^{n+} layers improve the stability and anti-fouling property of membranes through several mechanisms. Their hydrophilic surface forms a hydration layer that repels hydrophobic foulants like oils and proteins. The hydroxyl groups in TA adsorb H_2O molecules to form a protective thin water-layer on the surface. Studies on polyphenol-metal assembled membranes show strong resistance to fouling [18, 20, 39, 41]. Liu and his colleagues [18] demonstrated that TA-Fe^{3+} membranes achieved significant flux recovery after hydraulic washing in continuous filtration experiments with bovine serum albumin (BSA). Additionally, TA-M^{n+} selective layers show high fouling resistance towards foulants exhibiting low isoelectric point due to surface

repulsive interactions [18]. MPN membranes also exhibit strong anti-fouling property against microorganisms [41].

Metal-polyphenol films demonstrate strong adhesion to membrane supports, driven by the robust affinity of galloyl and catechol groups [26]. For example, TA-Fe^{3+} membranes remain intact exhibiting strong adhesion with PES support during an inverse filtration operation that revealed an unchanged Na_2SO_4 rejection, while it declined from 95.2% to 88.4% for commercial control PA membrane [18]. Polyphenol-metal assembly-based membranes show durable performance as summarized in Table 2.2. Metals with high ionization potential possess high coordination affinity with tannic acid to generate stable complexes [54]. According to HSAB, ionization potential is in the order of $Fe^{2+} < Co^{2+} < Ni^{2+} < Cu^{2+} < Fe^{3+} < Zr^{4+}$ [61]. While more metal content uptake upon complexation with TA were found in the cases of Cu^{2+}, Fe^{3+} and Zr^{4+} [54], TA-Cu^{2+} and TA-Ni^{2+} were the most highly stable complexes with stability constants of 21.1 and 15.3, respectively [54].

Moreover, membrane support wettability can have a significant influence on the stability of MPN layers. TA-Fe^{3+} films coated on low-wettable surface are more stable than those coated on highly-wettable surface [62]. However, the pH responsive nature of polyphenol-metal coordination makes MPN films vulnerable to acidic feed solutions. Membranes soaked in acidic solutions for 24 hours exhibited increased flux but declining rejection (Figure 2.11) due to coordination disassembly [26]. In contrast, the performance is stable for alkaline feed solutions [18]. Fang et al. [39] further confirmed that the release of Fe^{3+} from the assembled TA-Fe^{3+} complex membrane increased at low pH, while no release was observed for membranes immersed in solution of pH 5 or higher verifying their durability under alkaline condition.

Table 2.2 *Long period filtration test of membrane stability*

Membrane	Support	Length of operation	performance	reference
TA-Fe^{3+}	PAN	72 hrs.	Only <7% permeability decline	[18]
TA-Fe^{3+}	PES	30 days	Only 2% contact angle change	[39]
TA-Cu^{2+}	PAN	20 days	Slight permeability change	[55]
TA-Fe^{3+}	PES	24 hrs.	4.4% permeability decline	[19]
TA-Fe^{3+}	PES	24 hrs.	No change in permeability and rejection	[3]
TA-Fe^{3+}	PES/SPES	5 cycles	>82% flux recovery	[54]

TA-Fe^{3+}	PAN	50 hrs.	3.3% flux decline whilst no change in rejection	[36]

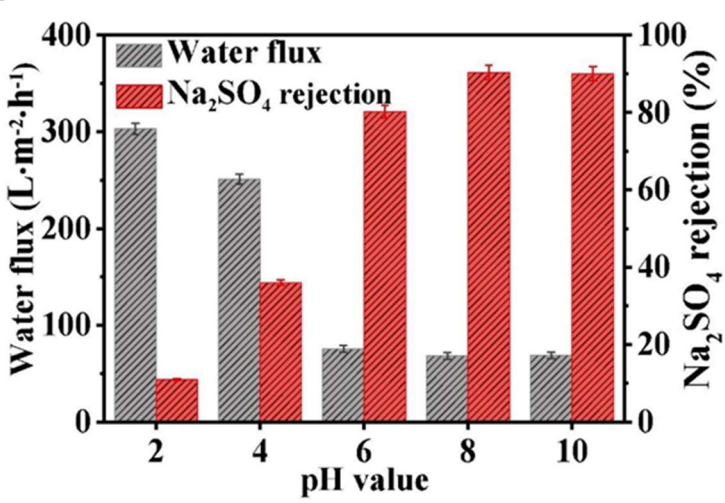

Figure 2.11 *Separation performance of TA-Fe^{3+} membrane after soaking in various solutions of distinct pH values for 24 hours prior to operation. Adopted from ref. [18] (©2020 Elsevier).*

The coordination mediated self-assembly of polyphenol and metal ions is a novel strategy for the fabrication of high performance TFC membranes [3]. With their tunable pore size [3, 38], MPN membranes have great potential in various industrial application involving liquid separation including ions or molecular separation and desalination pretreatment. Guo et al. [20] recommended non-polyamide MPN based membranes for wastewater reclamation and removal of organic contaminants. MPN-TFC NF membranes demonstrate a significantly high rejection property towards endocrine disrupting compounds (EDCs) in wastewater, presenting almost two orders of magnitude superior water/EDCs selectivity than commercial NF membranes (NF270, NF90, and XLE) despite low salt rejection [20]. Hence, polyphenol-based membranes show promise for removal of pharmaceuticals and municipal wastewater reuse.

Metal-polyphenols network-based thin films are also used for the fabrication of loose nanofiltration membranes for efficient dye/salt fractionation [36]. Ni^{2+}-polyphenol network coated nanofiltration membranes have proven effective for the treatment of dye in wastewater [53], presenting a new approach of addressing global water safety concerns from textile waste. Given that dye desalination has been a key NF membrane application over the past two decades [63], tannic acid-based membranes hold strong industrial potential. MPN based membranes could be utilized for the selective fractionation and separation of dyes in waste streams [64]. Nevertheless, the low rejection towards salts should be given a considerable attention. Although

membranes of high salt rejection could be prepared with some optimization [23], MPN membranes commonly have low salt rejection.

Another important application of MPN thin-films is the coating of UF membrane surface for fouling resistance against microorganisms and proteins [41], and enhancing anti-bacterial and algae-inhibition properties of UF membranes [65]. For instance, TA-Cu-Fe layer coating over PVDF membrane introduces an excellent biofouling resistance ability, Figure 2.12e, as tannic acid facilitates *in-situ* reduction of Cu^{2+} in situ to Cu nanoparticles, boosting bacterial and algal growth inhibition efficiency [65]. This opens a wide range of applications in food, dairy, beverage, and protein purification industries. Although RO is a popular technology for seawater and brackish water desalination [66], fouling, chlorine attack and low water flux are still major challenges of the desalination process. TA-M^{n+} self-assembly has also been extensively used for RO membrane modification through the immobilization of Ag nanoparticles for enhanced antifouling property [66, 67] and poly(*N*-vinylpyrrolidone) (PVP) to improve the hydrophilicity and fouling resistance of RO membranes [68]. The TA-M^{n+} coating also facilitates removal of pharmaceutical contaminants like metronidazole by RO [69].

MPN-based membranes play a crucial role in oil/water emulsion separation, addressing environmental concerns and resource recovery. Huang et al. [70] reviewed in detail coatings of plant polyphenols (e.g. epigallocatechin, pyrogallol, and polydopamine) and their assemblies for this purpose. A uniformly distributed coating of TA-Fe^{3+} on a polypropylene (PP) microfiltration membrane demonstrates a superhydrophilic property with high water permeance while rejecting oil droplets (Figure 2.12 a and b) [42]. Tannic acid has been the most used phenolic ligand for fabricating highly wettable thin films such as TA-Ti^{4+} [71, 72], TA-Fe^{3+} [73] and TA-Ag^{+} [74], converting hydrophobic polymeric membranes into hydrophilic, underwater oleophobic surfaces. The TFC membranes show high flux recovery ratio, reusability and long-term stability.[73] An AgNPs-TA-PVDF microfiltration membrane maintained its chemical and mechanical properties after rinsing and scratch resistance tests (Figure 2.12d) [74]. Moreover, TA-M^{n+} networks can be used to introduce additives such as PEI [75] and MOFs [76] to improve physicochemical properties of selective layers for emulsion treatment. This provides new insights into the fabrication of high efficiency membranes for oily water treatment.

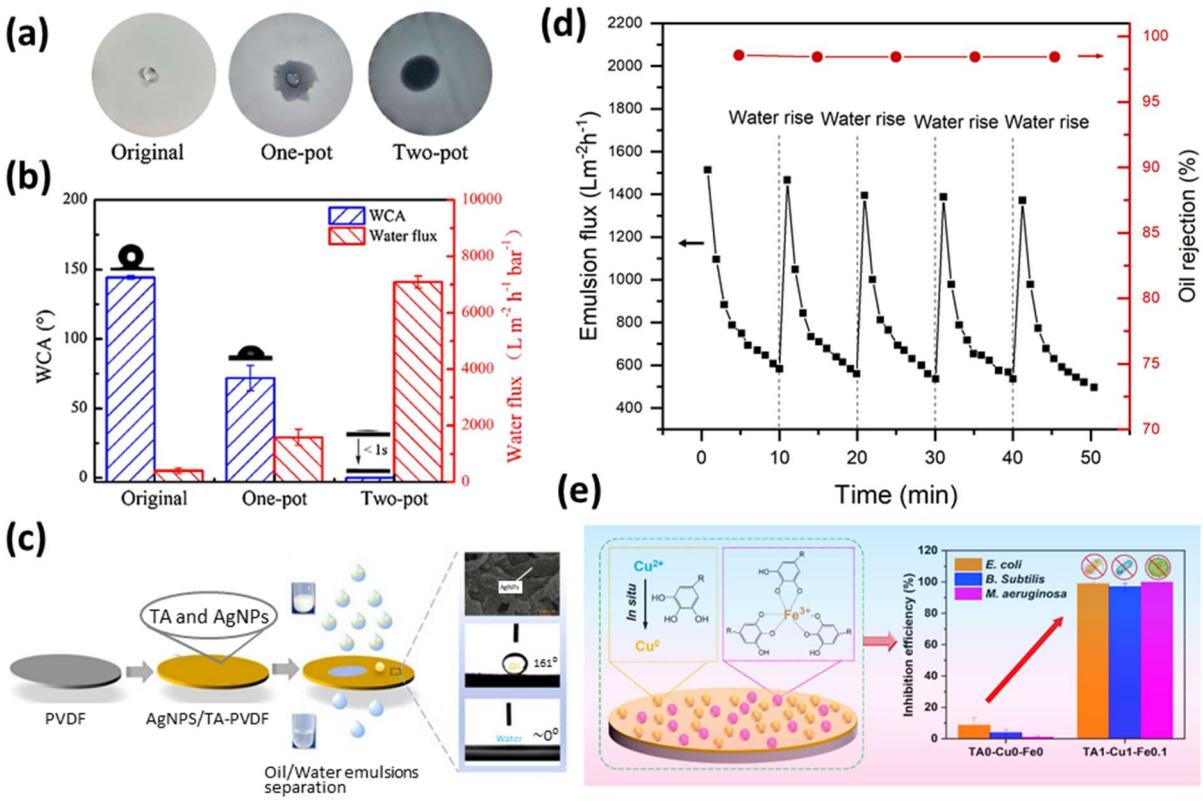

Figure 2.12 *(a) Photographic images of a water droplet (10 μL) on the membrane surface within 10 s after drop. (b) Water permeability and WCAs of superhydrophilic and underwater superoleophobic TA-Fe^{3+} coated polypropylene membrane [42] (copyright 2017, Elsevier). c) Ag-NPs/tannic acid modified PVDF membrane for efficient separation of oil and water emulsion, d) antifouling property of the Ag-NPs/tannic acid modified PVDF membranes during emulsion separation [74] (copyright 2022 Elsevier), and e) anti-bacterial and anti-algal inhibition performance of TA-Cu^{2+}-Fe^{3+} containing membranes [65] (copyright 2022, Elsevier)*

2.5. Transport models for NF membranes

A membrane is a typical permselective barrier acting as an interface between two phases, facilitating separation through the transport of components across the membrane from one phase to the other due to driving forces. The separation process and mass transport through the membrane depends on the membrane type, the properties of the separated constituents, and the theoretical framework used to describe the mechanism [77]. A systematic study and development of transport theories is fundamental for analyzing, designing, and optimizing membrane processes. Transport modeling not only enhances our understanding of rejection and

permeation mechanisms but also predicts membrane performance by analyzing component mass transfer within pores. Furthermore, it plays a crucial role in advancing membrane technology, enabling the fabrication of high-performance tailor-made membranes that demonstrate enhanced separation properties.

Transport models that describe membrane separation processes can be categorized into phenomenological and mechanistic approaches [77]. The former does not consider membrane characteristics to elucidate the separation performance while the latter associates the membrane performance to a structure-related membrane parameter. They can also be categorized as mechanism-independent or mechanism-dependant models.

Spiegler–Kedem–Katchalsky (SKK) model

A significant effort has been devoted for decades to developing transport models appropriate for small pore sized membranes such as nanofiltration membranes. One such model is the SKK model, first developed by Kedem and Katchalsky (1958) and modified by Spiegler and Kedem (1966) [78]. The SKK model is a phenomenological model based on irreversible thermodynamics. The membrane is treated as a black box without consideration of membrane characteristics. In a two-component system, solute transport is related to water permeability, solute permeance, and reflection coefficient [79]. The reflection coefficient represents the maximum attainable rejection by the membrane at high permeate flux. The SKK model considers the solvent and solute fluxes are directly related to the chemical potential gradient across the membrane.

The SKK has been applied to elucidate the separation performance of uncharged solutes without the influence of electrostatic interaction with the membrane surface [80, 81]. It was also used to describe the retention of electrolyte [82]. Schirg and Widmer extended the mathematical model to characterize the retention and selectivity of NF of aqueous dye-salt solutions [83]. The model has been widely proposed to predict the transport of components through various membrane types; nanofiltration [84], reverse osmosis [85], forward osmosis [86], and diafiltration [87].

This model defines water flux as a function of transmembrane pressure gradient.

$$J_v = L_p * (\Delta P - \sigma \Delta \pi) \qquad (2.1)$$

Where J_v is the volumetric permeate flux, and ΔP and Δπ are the applied pressure difference and osmotic pressure difference, respectively. L_p is the water permeability coefficient while σ

represents the reflection coefficient. For dilute systems, $\Delta\pi$ can be estimated using the van't Hoff's equation.

In contrast, solute transport combines the synergetic effect of diffusive and convective fluxes as shown in equation 2.2 below.

$$J_S = P_S * \frac{dC_s}{dx} + (1-\sigma) * C_S * J_v \tag{2.2}$$

Where J_S and P_S are the solute flux and the solute permeability coefficient, respectively, while C_s is the solute logarithmic mean concentration between feed and permeate. The reflection coefficient (σ) provides an insight into the separation capability of the membrane in which σ=0 and σ=1 means no separation and 100 % separation, respectively. The membrane parameters of σ and P_S are estimated using a nonlinear parameter estimation method by measuring rejection performance of the membrane at various fluxes.

By integrating the solute flux equation over the membrane thickness, the final working equation of the SKK model can be written as [88]:

$$R = \frac{\sigma(1-F)}{1-\sigma F} \tag{2.3}$$

Where R is the rejection, and F is a flux dependent constant of the following form.

$$F = exp\left(-\frac{(1-\sigma)}{P_S} * J_v\right) \tag{2.4}$$

Substituting F into the rejection expression gives a simplified SKK model of the expression:

$$ln\left[\left(\frac{1}{1-\sigma} - \frac{1}{1-R} * \frac{(1-\sigma)}{\sigma}\right)\right] = -\frac{(1-\sigma)}{P_S} * J_v \tag{2.5}$$

The SKK model can be used in combination with film theory to express several fluid flow related phenomena [89]. Concentration polarization has adverse effect on membrane performance. Considering this unavoidable phenomenon, coupling SKK with film theory allows the simultaneous estimation of model parameters using equation 2.6 [90].

$$\left(\frac{\sigma}{1-\sigma}\right)\left(1 - exp\left(-\frac{(1-\sigma)}{P_S} * J_v\right)\right)\left(ex\,p\left(\frac{-J_v}{k}\right)\right) = \frac{R_{obS}}{1-R_{obS}} \tag{2.6}$$

Where R_{obS} is the observed solute rejection and k is the mass transfer coefficient.

Despite its application for several years, the SKK model has various limitations. The model does not adequately describe the involved transport mechanisms due to its assumption of taking the membrane as a black box. Moreover, this model has limitations of describing water flux in very dilute organic solute systems [78] in which water fluxes decrease as compared to that described by the flux expression in equation 2.1. Besides, the SKK model suffers from being a mathematical perspective limited to a binary solute system. However, an extended SKK model for multiple solutes system was developed by incorporating the solute–solute interactions [91].

Teorell–Mayer–Sievers (TMS) model

TMS model is one of the oldest models for describing the transport characteristics of species and electrokinetic phenomena through charged capillaries [92]. In this case, a membrane is considered as a charged porous layer. The TMS model is a rigorous approach of estimating membrane electrical properties such as the effective charge density and electrostatic effects [93, 94]. It is also an effective method of quantitively measuring other structural factors including pore radius and the ratio of porosity to the thickness of the membrane in combination with the Steric-Hindrance Pore (SHP) model [94]. The TMS model has been adopted to estimate the membrane potential for single electrolyte as well as multivalent electrolyte solutions [92]. However, this model overestimates the membrane potential when the radius, r_p, and the dimensionless charge density in the pore wall, q_0, are more than 5.0 nm and 1.0, respectively [92].

The TMS model has been used to illuminate the transport mechanism and electrolyte permeation in NF membranes considering the electrostatic effects [93]. The fixed-charge model has been successfully applied in research employing especially ion-exchange membranes [95]. Moreover, single electrolyte and mixture of ionic rejections by charged RO membranes were well predicted by the TMS model in combination with the extended Nernst–Planck equation (ENPE) [95]. The main assumption of the TMS model is a uniform radial distribution of fixed charges in the membrane pores and mobile species [93]. This model provides a simplified mathematical analysis for the transport of ions. Mass transfer is expressed based on the extended Nernst–Planck equation. The ENPE includes the contribution of volume flux to ionic flux.

The three main working equations of TMS are [78, 92]

- The Donnan equation for the partition coefficients of ion concentrations at the interface between the membrane and the external solution
- The extended Nernst–Planck equation for mass transfer

- The electroneutrality conditions for inside the membrane and the external solutions.

Most of these equations are similar to the model equations of Donnan steric pore model and dielectric exclusion (DSPM-DE), which will be discussed later. The reflection coefficient and solute permeability derived from the TMS model are given as follows [93]:

$$\sigma = 1 - \frac{2}{(2\alpha - 1)\xi + (\xi^2 + 4)^{1/2}} \tag{2.7}$$

$$P_S = D_S(1 - \sigma)\left(\frac{A_K}{\Delta X}\right) \tag{2.8}$$

Where $\alpha = \frac{D_1}{D_1 + D_2}$ and $\xi = X_d/c$. ξ is an electrostatic effect and X_d is called the fixed charge density. A_K and ΔX are effective membrane thickness and membrane porosity, respectively. D_S is the solute diffusivity for a neutral molecule, or the generalized diffusivity for 1–1 type of electrolyte solution defined as $D_S = 2\frac{(D_1/D_2)}{D_1 + D_2}$.

The dimensionless membrane potential can be expressed as [92],

$$\Delta\bar{\Phi}_{TMS} = \frac{1}{z_2}\ln\frac{k_2^p}{k_2^f} + \frac{D_1 - D_2}{z_2 D_2 - z_1 D_1}\ln\left(\frac{T_r k_2^p - t_1\xi_f}{k_2^f + t_1\xi_f}\right) \tag{2.9}$$

Where $\Delta\bar{\Phi} = \frac{F\Delta\Phi}{R_g T}$, $t_1 = \frac{|z_1|D_1}{|z_1|D_1 + |z_2|D_2}$, $T_r = \frac{C_p}{C_f}$ and $\xi_f = \frac{|X_m|}{|z_1|\nu_1 C_f}$

$\Delta\bar{\Phi}$ represents the dimensionless form of the membrane potential, $\Delta\Phi$. X_m is the constant volume charge density of the membrane. ξ_f is the ratio of the volume charge density to equivalent salt concentration in the feed side or in the permeate side of membrane. z_i, D_i and k_i are the electrochemical valence, diffusion coefficient and partition coefficient of ion i, respectively. T_r is the transmission, denoting the ability of solute to pass through the membrane. R, R_g and T are the Faraday constant, the gas constant and the temperature, respectively.

The TMS model is generally applicable to reveal the mechanisms of transport phenomena [96]. However, as the assumption of uniform charge distribution fails to represent the pattern of distribution of fixed charges, electric potential and mobile ions, the application of TMS model is limited [95]. This especially becomes apparent for membranes with large pore size.

Space charge (SC) model

The space charge model is a modified version of the TMS model. The space charge model considers the presence of a radial distribution of the potential and concentration gradient across the membrane pores [93]. This model was proposed by Osterle et al. [97, 98] to describe the retention performance of charged capillaries [99]. The space charge model is a mechanistic model developed in terms of electrokinetic phenomena. The membrane pores are considered as straight capillaries with charges on their surface, and ions are treated as point charges.

The space charge model is one the main transport models in which ion transport is demonstrated using the Nernst–Planck equation. The Poisson–Boltzmann equation describes the radial distribution of electrical potential and ion concentration while the solvent velocity is expressed using the Navier–Stokes equation. The detailed model equations of the space charge model can be found elsewhere [95, 100, 101]. The transport of electrolytes and the accompanying salt rejection by nanofiltration membranes were successfully predicted by a space charge model [95]. However, the assumption of ions as point charges neglects the steric effects due to the size of the analyzed ions [93]. Furthermore, the complex calculation requirements, particularly in mixed electrolytes solutions, limit its application [78].

2.6. Donnan-Steric Pore Model with Dielectric Exclusion (DSPM-DE)

In recent decades, there has been extensive research in the subject of NF membrane characterization. Two procedures have been widely practiced to characterize these nanoporous membranes; direct methods and indirect methods [102]. In the direct method, pore size is for instance estimated using atomic force microscopy [103] while membrane surface zeta potential can be utilized to measure the Donnan potential [104]. The indirect method involves the application of mathematical simulations in combination with experimental rejection and flux measurements [102]. When it comes to simulations, the above reviewed transport models have been implemented. Especially models that employ the Nernst-Planck framework have become widely accepted in describing ion transport in membranes [105] and in estimating the membrane characteristics. The Donnan-Steric Pore Model with Dielectric Exclusion (DSPM-DE) is the latest and a widely adopted model in literature for simulating NF membranes. This model has been widely used to characterize these charged porous structures in terms of several parameters such as pore radius, membrane thickness, pore dielectric constant and charge density.

The following section discusses the concepts related to the transport and exclusion mechanisms according to the DSPM-DE. It also presents the main equations associated with the model besides illustrating the procedures of estimating membrane parameters.

The Donnan Steric Pore Model with Dielectric Exclusion (DSPM-DE) is a theoretical framework used to describe the mass transfer of solutes through nanoporous membranes. The DSPM-DE is particularly useful for understanding and predicting the transport of charged solutes providing insights into the selectivity of these membranes. This model is a modified version of the Donnan-Steric Pore Model (DSPM), which was first coined by Bowen et al. in the late 1990s [106, 107]. In the DSPM, solute partitioning at the interface between the membrane and the solution occurs due to the Donnan and steric effects. This model quickly became well established, and has been successful in modeling the separation of a wide range of solutions including those containing multivalent co-ions [108]. The DSPM model has gone through some revisions. DSPM-DE was introduced for effectively modeling the rejection of di- and multivalent counter-ions by the incorporation of dielectric exclusion effect although its predecessor was sufficient in elucidating the transport properties of monovalent ions. Today, DSPM-DE is the state-of-the-art transport model, and well describes the solute partitioning at the membrane-solution interfaces [109].

The partitioning mechanisms at the interface between the solution and the membrane surface occurs through the combination of steric, Donnan and dielectric exclusion effects as shown in Figure 2.13. The steric exclusion is based on the size of solutes compared to the pore size (a sieving mechanism), while Donnan exclusion occurs due to the electrostatic interaction between the charges of the solute and the fixed charges in the membrane. On the other hand, dielectric exclusion, of ions for example, accounts for the solvation energy barrier for the ion to enter the pore due to the Born effect as the dielectric constant inside the confined pores decrease compared to the bulk solution.

In DSPM-DE, the transport of ions across the membrane is described using the extended Nernst-Planck equation. Ion flux is a synergetic effect of three transport mechanisms namely diffusion, convection, and electromigration. It is assumed that the diffusive and convective fluxes are hindered due to the extremely small pore sizes in the membranes. Therefore, according to the hindered transport theory, hindrance factors are introduced to the terms of the ENP equation. The electromigrative flux is due to the gradient of membrane potential across the membrane that is developed to balance ionic fluxes. This maintains quasi-electroneutrality in the membrane process [108]. The electromigration of co-ions is in the direction towards the more

positive or high membrane potential as shown in Figure 2.14b while the counter-ions migrate in the opposite direction. Figure 2.14a schematically illustrates the local ion concentration of both the co-ion and counter ion inside the pores in a negatively membrane. The exclusion mechanisms influence the concentration profile across the membrane. The water flux and solute flux have a positive x direction from the feed to the permeate side due to the applied pressure and high solute concentration on the feed side.

The DSPM-DE is based on several fundamental assumptions. The underlying assumptions are summarized as follows.

- The membrane has straight cylindrical pores of uniform pore size, and the membrane charge distribution is uniform.
- The flow inside the pores is laminar and has reached a steady state.
- The solution is assumed to be non-ideal that the non-ideality is considered by using an activity coefficient.
- All solutes are modeled as spheres having a finite size.
- Solute-solute interaction is neglected considering a very dilute feed solution.
- Transport of solutes inside the pores is via convection, diffusion and electro-migration.
- Transports with convection and diffusion are hindered and are corrected with the respective hindrance factors.
- The concentration and potential gradient vary axially while radial variation is neglected.
- There exists a variation of solvent viscosity and dielectric constant inside the pores.
- Concentration polarization is considered on the feed side, but neglected on the permeate side as permeants are thought to be swept away instantly.
- Partial molar volume and diffusion coefficient inside the pores are independent of concentration.

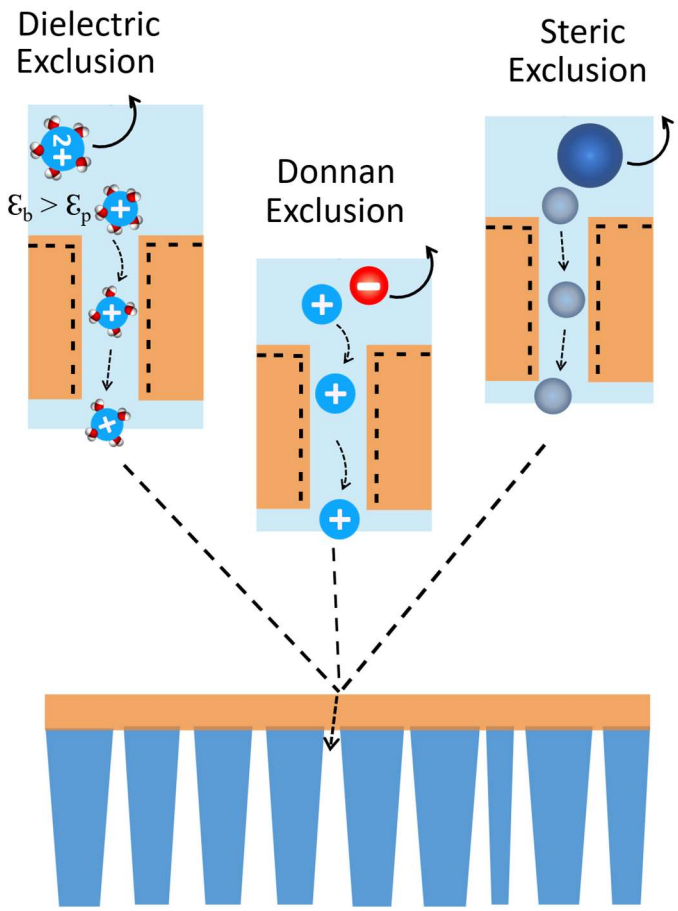

Figure 2.13 *Schematic representation of solute exclusion mechanism of NF membrane*

Model equations

At a steady state and considering a laminar flow inside the membrane pore, the Hagen-Poiseuille equation successfully describes the flux of water across the active layer. The solvent flux J_v as a function of the driving force and membrane structural parameters is expressed as:

$$J_v = \frac{\varepsilon \cdot r_p^2}{8 \cdot \mu \cdot \tau} \cdot \frac{\Delta P}{\Delta x} \qquad (2.10)$$

Where ε is membrane surface porosity, τ is the tortuosity, μ is the viscosity, and r_p is the pore radius. ΔP is the pressure difference across membrane while Δx represents the membrane thickness. In most cases, $\Delta x_e = \Delta x \cdot (\tau/\varepsilon)$ as an effective membrane thickness can be introduced that accounts for membrane porosity and tortuosity.

Solute transport inside the membrane pores is described by the extended Nernst-Planck equation. The solute flux for each ion i inside the pores of the active layer consists of the three transport mechanisms as shown in equation 2.11. The first term represents the diffusive flux of

solutes due to concentration gradient. The second and the third terms represent the advective flux (as a result of solvent flow) and the electromigrative flux (due to a potential gradient).

$$J_i = -K_{i,d} D_{i,\infty} \frac{dC_i}{dx} + K_{i,c} C_i J_v - z_i C_i K_{i,d} D_{i,\infty} \frac{F}{RT} \frac{d\Psi}{dx} \tag{2.11}$$

Where J_i is the solute flux, J_v is the permeate flux, z_i is the valence of an ion, C_i is the concentration of ion i inside the pores, F is Faraday's constant, Ψ is the electric potential, and R is the universal gas constant while T and x are temperature and selective layer thickness, respectively. $D_{i,\infty}$ is the diffusivity of a solute in a very dilute solution. $K_{i,c}$ and $K_{i,d}$ are the hindered mass transfer coefficient and the hydrodynamic coefficient for the enhanced drag of the i^{th} component inside the pores given by equation 2.12 and 2.13, respectively [105, 109].

$$K_{i,C} = \frac{\left(1 + 3.867\lambda_i - 1.907{\lambda_i}^2 - 0.834{\lambda_i}^3\right)}{\left(1 + 1.867\lambda_i - 0.741{\lambda_i}^2\right)} \tag{2.12}$$

$$K_{i,d} = \begin{cases} \dfrac{\left(1 + \left(\frac{9}{8}\right)\lambda_i ln\lambda_i - 1.560\lambda_i + 0.528{\lambda_i}^2 + 1.915{\lambda_i}^3 - 2.819{\lambda_i}^4 + 0.270{\lambda_i}^5 + 1.101{\lambda_i}^6 - 0.435{\lambda_i}^7\right)}{(1-\lambda_i)^2}, & \lambda_i \le 0.95 \\ 0.984\left(\dfrac{1-\lambda_i}{\lambda_i}\right)^{5/2}, & \lambda_i > 0.95 \end{cases} \tag{2.13}$$

Where λ is the ratio of solute radius to pore radius, $\lambda = \frac{r_s}{r_p}$, and Φ is the steric partitioning factor given by $\Phi = (1-\lambda)^2$.

As discussed earlier, the effect of concentration polarization at the feed side is considered. This gives to a rise in the concentration of ion i to $C_{i,m}$ just at the pore intrance from its $C_{i,b}$ in the bulk solution. The effect of concentration polarization is considered using the appropriate mass transfer correlations. Taking this into account, the flux of a solute at the interface between the feed-solution and the membrane is given by equation 2.14.

$$J_i = -k^*_{c,i}\left(C_{i,m} - C_{i,b}\right) + J_v C_{i,m} - \frac{z_i C_{i,m} D_{i,\infty} F}{RT} \frac{d\Psi}{dx} \tag{2.14}$$

$k^*_{c,i}$ is the mass-transfer coefficient of ion i that is a function of the stirring speed on the feed side solution [107]. The mass-transfer coefficient can be obtained from the correlation between Reynolds, Schimdt and Sherwood numbers.

Flux of component i in the permeate side is expresses as:

$$J_i = J_v C_{i,p} \tag{2.15}$$

Electroneutrality is considered and in all three domains: the feed side, inside the membrane, and the permeate. Electroneutrality in the feed and permeate side comes from the ions present in the bulk solution. However, the fixed membrane charge contributes to the overall charge electroneutrality inside the porous membrane. The following governing equations of the DSPM-DE are used for electroneutrality.

Electroneutrality condition on the feed side:

$$\sum_{i=1}^{Nc} z_i C_{i,m} = 0 \tag{2.16}$$

Electroneutrality condition within the pores:

$$C_X + \sum_{i=1}^{Nc} z_i C_i = 0 \tag{2.17}$$

Electroneutrality expression on the permeate side:

$$\sum_{i=1}^{Nc} z_i C_{i,p} = 0 \tag{2.18}$$

Where C_i and z_i are the concentration and the valence for the i^{th} ion in the system. C_X is the membrane surface charge density.

Equilibrium boundary conditions are established at the membrane-solution interfaces due to the combined effect of the three exclusion mechanisms. The partitioning of species at the interface results in an equilibrium relationship between the concentrations just inside and outside the membrane pore. Partitioning determines the rejection and permeation of solutes by the membrane as a fundamental mechanism of separation. The partitioning of ion i at the feed solution-membrane as well as at the membrane-permeate interface are expressed as:

$$\frac{\gamma_{i,1} C_{i,1}}{\gamma_{i,m} C_{i,m}} = \Phi_i \Phi_B exp\left(-\frac{z_i F}{RT} \Delta\Psi_{D,m}\right) \tag{2.19}$$

$$\frac{\gamma_{i,N} C_{i,N}}{\gamma_{i,P} C_{i,P}} = \Phi_i \Phi_B exp\left(-\frac{z_i F}{RT} \Delta\Psi_{D,P}\right) \tag{2.20}$$

Where Φ_i is the steric partitioning factor, γ_i is the activity coefficient for component i, and Ψ_D is the Donnan potential. The exponential term is the Donnan exclusion factor term. Φ_B represents the dielectric exclusion factor or the Born solvation contribution for partitioning given by:

$$\Phi_B = exp\left(-\frac{\Delta W_i}{kT}\right) \tag{2.21}$$

Where ΔW_i is the energy barrier to solvation. This is defined through the Born model [109].

$$\Delta W_i = \frac{z_i^2 e_0^2}{8\pi \mathcal{E}_0 r_s}\left(\frac{1}{\mathcal{E}_p} - \frac{1}{\mathcal{E}_b}\right) \tag{2.22}$$

Where e_0 is the electronic charge, $\mathcal{E}_0$ is the vacuum permittivity. $\mathcal{E}_p$ and $\mathcal{E}_b$ are the dielectric constants inside the pore and in the bulk solution, respectively.

The four membrane properties that are needed for the DSPM-DE simulation are effective pore radius, r_p, effective membrane thickness (Δx_e), and effective membrane charge density (C_x), pore dielectric constant ($\mathcal{E}_p$). They are determined in a step-by-step procedure by fitting of the rejection and flux performance data of the membrane in most cases. They are strongly inter-dependent as the exclusion mechanisms counter-balance to fit the rejection properties [105]. Solving the DSPM-DE equations and simulation of the process yields the concentration profiles of solutes, the potential distribution, the permeate flux, ion concentrations in the permeate as well as the ion rejection of solutes [105].

Determination of membrane parameters

The pore size of the membrane is estimated from the rejection data of uncharged solutes. The partitioning of neutral solutes at the interfaces is solely due to the steric effect. The rejection of a solute through a membrane can be expressed using the following equation [107]:

$$R_{real} = \left(1 - \frac{C_{i,p}}{C_{i,m}}\right) = 1 - \frac{K_{i,C}\Phi}{1 - \exp(Pe_m)\left(1 - K_{i,C}\Phi\right)} \tag{2.23}$$

Where Pe_m is the Peclet number, which is a function of solvent velocity.

$$Pe_m = \frac{K_{i,C}}{K_{i,d}}\frac{J_v \Delta x}{D_{i,\infty} A_k} \tag{2.24}$$

As both $K_{i,C}$ and Φ are functions of λ, the rejection of a solute through the porous membrane can be expressed as a ratio of solute radius and pore radius. Therefore, the desired pore radius can be quantified through fitting of the rejection of a known solute size. The effective membrane thickness ($\Delta xe = \frac{\Delta x}{A_k}$) can be estimated from equation 2.23 above. It can also be obtained from the Hagen-Poiseuille equation [107].

The membrane electric and water properties are determined by using the rejection of charged solutes. The pore dielectric constant of the membrane is determined by the rejection data of salts at the isoelectric point of the membrane, without the influence of electrostatic interaction. Fitting of solute rejection performance at different solvent flux, once the other parameters are determined, provides the final membrane parameter, charge density.

However, there have been several approaches of determining membrane characteristics. For instance, the pore dielectric constant can be determined on a geometric basis as [110]:

$$\varepsilon_p = 80 - 2(80 - \varepsilon^*)\left(\frac{d}{r_p}\right) + (80 - \varepsilon^*)\left(\frac{d}{r_p}\right)^2 \qquad (2.25)$$

where d is the diameter of a water molecule (0.28 nm), and ε^* is the dielectric constant of the single layer of water molecules oriented on the pore walls. Nonetheless, ε^* is strictly dependent on a solvent-membrane interaction [110]. In another study, the membrane surface charge density was determined through the Gouy–Chapman equation from streaming potential values measured using an electrokinetic analyzer [111]. Deon et al., in 2012 [112] proposed using the rejection curves of ternary ionic mixtures to numerically assess the charge density and pore dielectric constants simultaneously through extrapolation to predict the rejection of pure salt solutions. Recently, Rehman and Lienhard [113] proposed a global optimization technique to simultaneously regress all membrane parameters ($r_p, \Delta X_e, \varepsilon_p, C_x$) directly from the rejection experiments of charged species. This approach eliminates the substantial number of charged and uncharged solute rejection experiments required in the previous methods. Geraldes et al. [109] also introduced a system to overcome the numerical problems of solving the non-linear set of equations in the DSPM-DE by the discretization of ENP equations and subsequent linearization of the non-linear system of equations. The convergence problems associated with numerical instabilities were controlled using under-relaxation formula to ensure an appropriate final solution.

It is noteworthythat the membrane charge density and dielectric constant are not only dependent on membrane characteristics, but also a function of the feed solution composition [102]. For instance, a change in dielectric constant has been reported in the presence of various solutions such as NaCl, KCl and Na_2SO_4, or $MgSO_4$.[110] The types of functional groups present on the membrane surface and their chemical properties can determine the charge density. The concentration of ions in the surrounding solution significantly affects the membrane charge density. A higher concentration of ions leads to a higher charge density [111], as it can create

an electrostatic double layer on the membrane surface. The adsorption of ions and molecules onto the membrane surface can alter the charge density. Divalent ions such as Mg^{2+} and Ca^{2+} can, for instance, alter membrane charge density amounting even up to charge reversal [114].

In DSPM-DE, the assumption of parallel cylindrical pores of uniform size in the active layer differs substantially from the realistic membrane structure that contains fractal network structures having interconnected and disconnected pores of different sizes [105]. One dimensional transport of solutes also fails to represent the actual flow across the membrane phase. Furthermore, the numerical instabilities and lack of convergence limits the successful elucidation of solute rejection by DSPM-DE.

Transport models help researchers to optimize membrane materials and operating conditions for specific separation or filtration applications. They also provide a valuable tool in the field of membrane science and technology, contributing to the design of more efficient and selective membrane processes. Therefore, a continuous development of models and theories that can elucidate membrane performance are expected.

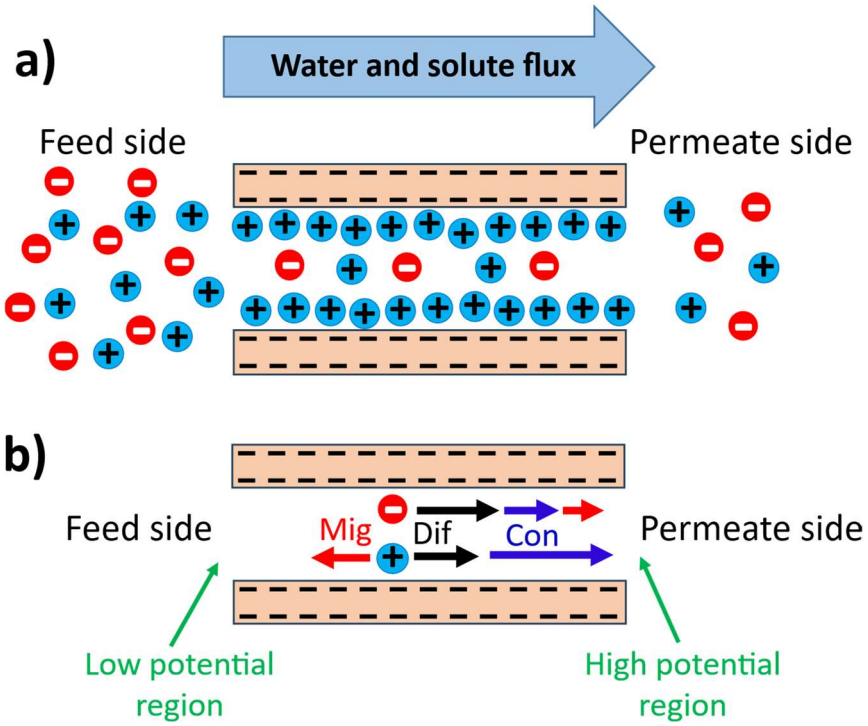

Figure 2.14 *Schematic illustration of solute transport mechanisms in the DSPM-DE as described by the Extended Nernst-Planck (ENP) equation. Solvent and solute fluxes have a one dimensional positive x direction. The local ion concentration inside a single pore in a negatively charged membrane is shown in the schematic representation. The directions of the individual transport mechanisms, i.e. diffusive flux (Dif), convective flux (Con), and electromagnetive*

flux (), are also presented. The sign of electromigrative flux and the ion concentration inside membrane pore reverses in the case of positively charged membrane surface.

References

[1] O. Aliku, "Desalination: A Means of Increasing Irrigation Water Sources for Sustainable Crop Production," InTech, 2017.

[2] P. Chuntanalerg, S. Bureekaew, C. Klaysom, W. J. Lau, and K. Faungnawakij, "Nanomaterial-incorporated nanofiltration membranes for organic solvent recovery," Elsevier, 2018, pp. 159-181.

[3] Y. J. Shen *et al.*, "Metal-organic composite membrane with sub-2 nm pores fabricated via interfacial coordination," *Journal of Membrane Science,* vol. 587, 2019, Art. no. 117146.

[4] X. M. Tan and D. Rodrigue, "A Review on Porous Polymeric Membrane Preparation. Part I: Production Techniques with Polysulfone and Poly (Vinylidene Fluoride)," *Polymers,* vol. 11, no. 8, 2019.

[5] C. National Research, *Water Reuse: Potential for Expanding the Nation's Water Supply Through Reuse of Municipal Wastewater*. Washington, DC: The National Academies Press, 2012.

[6] M. L. Chen, S. G. J. Heijman, and L. C. Rietveld, "Ceramic membrane filtration for oily wastewater treatment: Basics, membrane fouling and fouling control," *Desalination,* vol. 583, 2024, Art. no. 117727.

[7] T. A. Saleh and V. K. Gupta, "An Overview of Membrane Science and Technology," in *Nanomaterial and Polymer Membranes*: Elsevier, 2016, pp. 1-23.

[8] R. W. Baker, "Overview of Membrane Science and Technology," in *Membrane Technology and Applications*, 2004, pp. 1-14.

[9] A. F. M. Alsayed and M. A. Ashraf, "2 - Modified nanofiltration membrane treatment of saline water," in *Water Engineering Modeling and Mathematic Tools*, P. Samui, H. Bonakdari, and R. Deo, Eds.: Elsevier, 2021, pp. 25-44.

[10] X. Zhang, Y. Lv, H. C. Yang, Y. Du, and Z. K. Xu, "Polyphenol coating as an interlayer for thin-film composite membranes with enhanced nanofiltration performance," *ACS Applied Materials and Interfaces,* vol. 8, no. 47, pp. 32512-32519, 2016.

[11] C. Q. Ge *et al.*, "Recent advances of the interfacial polymerization process in gas separation membranes fabrication," *Journal of Membrane Science,* vol. 683, 2023.

[12] A. R. Hu, Y. L. Liu, J. F. Zheng, X. M. Wang, S. J. Xia, and B. van der Bruggen, "Tailoring properties and performance of thin-film composite membranes by salt additives for water treatment: A critical review," *Water Research,* vol. 234, 2023.

[13] J. N. Krishnan, K. R. Venkatachalam, O. Ghosh, K. Jhaveri, A. Palakodeti, and N. Nair, "Review of Thin Film Nanocomposite Membranes and Their Applications in Desalination," *Frontiers in Chemistry,* vol. 10, 2022.

[14] R. N. Zhang *et al.*, "Polyphenol-assisted in-situ assembly for antifouling thin-film composite nanofiltration membranes," *Journal of Membrane Science,* vol. 566, pp. 258-267, 2018.

[15] M. Razali *et al.*, "Sustainable wastewater treatment and recycling in membrane manufacturing," *Green Chemistry,* vol. 17, no. 12, pp. 5196-5205, 2015.

[16] V. Faggian, P. Scanferla, S. Paulussen, and S. Zuin, "Combining the European chemicals regulation and an (eco) toxicological screening for a safer membrane development," *Journal of Cleaner Production,* vol. 83, pp. 404-412, 2014.

[17] W. C. Xie *et al.*, "Toward the Next Generation of Sustainable Membranes from Green Chemistry Principles," *Acs Sustainable Chemistry & Engineering,* vol. 9, no. 1, pp. 50-75, 2021.

[18] D. Liu, Y. Chen, T. T. Tran, and G. Zhang, "Facile and rapid assembly of high-performance tannic acid thin-film nanofiltration membranes via Fe^{3+} intermediated regulation and coordination," *Separation and Purification Technology,* vol. 260, 2021, Art. no. 118228.

[19] L. Fan *et al.*, "Green coating by coordination of tannic acid and iron ions for antioxidant nanofiltration membranes," *RSC Advances,* vol. 5, no. 130, pp. 107777-107784, 2015.

[20] H. Guo, L. E. Peng, Z. Yao, Z. Yang, X. Ma, and C. Y. Tang, "Non-Polyamide Based Nanofiltration Membranes Using Green Metal-Organic Coordination Complexes: Implications for the Removal of Trace Organic Contaminants," *Environmental Science and Technology,* vol. 53, no. 5, pp. 2688-2694, 2019.

[21] J. Zhu *et al.*, "A rapid deposition of polydopamine coatings induced by iron (III) chloride/hydrogen peroxide for loose nanofiltration," *J Colloid Interface Sci,* vol. 523, pp. 86-97, 2018.

[22] S. H. Park, A. Alammar, Z. Fulop, B. A. Pulido, S. P. Nunes, and G. Szekely, "Hydrophobic thin film composite nanofiltration membranes derived solely from sustainable sources," *Green Chemistry,* vol. 23, no. 3, pp. 1175-1184, 2021.

[23] W. Yan, M. Shi, C. Dong, L. Liu, and C. Gao, "Applications of tannic acid in membrane technologies: A review," *Advances in Colloid and Interface Science,* vol. 284, no. 229, pp. 102267-102267, 2020.

[24] Z. Fu and R. Chen, "Study of complexes of tannic acid with Fe(III) and Fe(II)," *Journal of Analytical Methods in Chemistry,* vol. 2019, 2019.

[25] G. Ambrosi, M. Formica, V. Fusi, L. Giorgi, and M. Micheloni, "Polynuclear metal complexes of ligands containing phenolic units," vol. 252, ed: Elsevier, 2008, pp. 1121-1152.

[26] H. Ejima *et al.*, "One-Step Assembly of Coordination Complexes," *Science,* vol. 341, no. 6142, pp. 154-157, 2013.

[27] T. Liu *et al.*, "Metal Ion/Tannic Acid Assembly as a Versatile Photothermal Platform in Engineering Multimodal Nanotheranostics for Advanced Applications," *ACS Nano,* vol. 12, no. 4, pp. 3917-3927, 2018.

[28] M. A. Rahim *et al.*, "Self-Assembly of a Metal-Phenolic Sorbent for Broad-Spectrum Metal Sequestration," *ACS applied materials & interfaces,* vol. 12, no. 3, pp. 3746-3754, 2020.

[29] W. Zhang *et al.*, "Metal-dependent inhibition of amyloid fibril formation: Synergistic effects of cobalt-tannic acid networks," *Nanoscale,* vol. 11, no. 4, pp. 1921-1928, 2019.

[30] N. R. Perron and J. L. Brumaghim, "A Review of the Antioxidant Mechanisms of Polyphenol Compounds Related to Iron Binding," *Cell Biochemistry and Biophysics,* vol. 53, no. 2, pp. 75-100, 2009.

[31] M. A. Rahim *et al.*, "Coordination-driven multistep assembly of metal-polyphenol films and capsules," *Chemistry of Materials,* vol. 26, no. 4, pp. 1645-1653, 2014.

[32] B. J. Kim, S. Han, K. B. Lee, and I. S. Choi, "Biphasic Supramolecular Self-Assembly of Ferric Ions and Tannic Acid across Interfaces for Nanofilm Formation," *Advanced Materials,* vol. 29, no. 28, pp. 1-7, 2017.

[33] A. K. Koopmann *et al.*, "Tannin-Based Hybrid Materials and Their Applications: A Review," *Molecules (Basel, Switzerland),* vol. 25, no. 21, pp. 1-32, 2020.

[34] L. Pan, H. Wang, C. Wu, C. Liao, and L. Li, "Tannic-Acid-Coated Polypropylene Membrane as a Separator for Lithium-Ion Batteries," *ACS Applied Materials and Interfaces,* vol. 7, no. 29, pp. 16003-16010, 2015.

[35] X. Zhu *et al.*, "Supramolecular-Based Regenerable Coating Layer of a Thin-Film Composite Nanofiltration Membrane for Simultaneously Enhanced Desalination and Antifouling Properties," *ACS Applied Materials and Interfaces,* vol. 11, no. 23, pp. 21137-21149, 2019.

[36] Y. Xiao *et al.*, "Facile fabrication of superhydrophilic nanofiltration membranes via tannic acid and irons layer-by-layer self-assembly for dye separation," *Applied Surface Science,* vol. 515, 2020, Art. no. 146063.

[37] Y. Zhang *et al.*, "Composite nanofiltration membranes prepared by interfacial polymerization with natural material tannic acid and trimesoyl chloride," *Journal of Membrane Science,* vol. 429, pp. 235-242, 2013.

[38] C. E. Lin *et al.*, "Ultrathin nanofilm with tailored pore size fabricated by metal-phenolic network for precise and rapid molecular separation," *Separation and Purification Technology,* vol. 207, pp. 435-442, 2018.

[39] X. Fang *et al.*, "Iron-tannin-framework complex modified PES ultrafiltration membranes with enhanced filtration performance and fouling resistance," *Journal of Colloid and Interface Science,* vol. 505, pp. 642-652, 2017.

[40] H. Guo, Z. Yao, Z. Yang, X. Ma, J. Wang, and C. Y. Tang, "A One-Step Rapid Assembly of Thin Film Coating Using Green Coordination Complexes for Enhanced Removal of Trace Organic Contaminants by Membranes," *Environmental Science and Technology,* vol. 51, no. 21, pp. 12638-12643, 2017.

[41] H. J. Kim, D. G. Kim, H. Yoon, Y. S. Choi, J. Yoon, and J. C. Lee, "Polyphenol/FeIII Complex Coated Membranes Having Multifunctional Properties Prepared by a One-Step Fast Assembly," *Advanced Materials Interfaces,* vol. 2, no. 14, pp. 1-8, 2015.

[42] Y. Z. Song *et al.*, "Tannin-inspired superhydrophilic and underwater superoleophobic polypropylene membrane for effective oil/water emulsions separation," *Colloids and Surfaces A: Physicochemical and Engineering Aspects,* vol. 522, pp. 585-592, 2017.

[43] X. Yang, L. Yan, Y. Wu, Y. Liu, and L. Shao, "Biomimetic hydrophilization engineering on membrane surface for highly-efficient water purification," *Journal of Membrane Science,* vol. 589, pp. 117223-117223, 2019.

[44] X. Zhu *et al.*, "In-situ covalently bonded supramolecular-based protective layer for improving chlorine resistance of thin-film composite nanofiltration membranes," *Desalination,* vol. 474, pp. 114197-114197, 2020.

[45] R. Verbeke, V. Gómez, and I. F. J. Vankelecom, "Chlorine-resistance of reverse osmosis (RO) polyamide membranes," *Progress in Polymer Science,* vol. 72, pp. 1-15, 2017.

[46] X. Tong *et al.*, "Tannic acid-metal complex modified MXene membrane for contaminants removal from water," *Journal of Membrane Science,* vol. 622, 2021.

[47] X. Yang, "Controllable Interfacial Polymerization for Nanofiltration Membrane Performance Improvement by the Polyphenol Interlayer," *ACS Omega,* vol. 4, no. 9, pp. 13824-13833, 2019.

[48] S. C. Zhao, L. T. Li, M. Wang, L. H. Tao, Y. F. Hou, and Q. J. Niu, "Rapid in-situ covalent crosslinking to construct a novel azo-based interlayer for high-performance nanofiltration membrane," *Separation and Purification Technology,* vol. 258, 2021.

[49] H. Li *et al.*, "Tannic acid/Fe3+ interlayer for preparation of high-permeability polyetherimide organic solvent nanofiltration membranes for organic solvent separation," *Chinese Journal of Chemical Engineering,* 2022.

[50] Z. Yang *et al.*, "Tannic Acid/Fe3+ Nanoscaffold for Interfacial Polymerization: Toward Enhanced Nanofiltration Performance," *Environmental Science and Technology,* vol. 52, no. 16, pp. 9341-9349, 2018.

[51] S. R. Razavi, A. Shakeri, S. M. Mirahmadi Babaheydari, H. Salehi, and R. G.H. Lammertink, "High-Performance thin film composite forward osmosis membrane on tannic Acid/Fe3+ coated microfiltration substrate," *Chemical Engineering Research and Design,* vol. 161, pp. 232-239, 2020.

[52] Y. R. Xiao, W. T. Zhang, Y. Jiao, Y. C. Xu, and H. J. Lin, "Metal-phenolic network as precursor for fabrication of metal-organic framework (MOF) nanofiltration membrane for efficient desalination," *Journal of Membrane Science,* vol. 624, 2021.

[53] F. You, Y. Xu, X. Yang, Y. Zhang, and L. Shao, "Bio-inspired Ni2+-polyphenol hydrophilic network to achieve unconventional high-flux nanofiltration membranes for environmental remediation," *Chemical Communications,* vol. 53, no. 45, pp. 6128-6131, 2017.

[54] R. Wang, X. Zhao, Y. Lan, L. Liu, and C. Gao, "In situ metal-polyphenol interfacial assembly tailored superwetting PES/SPES/MPN membranes for oil-in-water emulsion separation," *Journal of Membrane Science,* vol. 615, no. 18, pp. 118566-118566, 2020.

[55] T. Chakrabarty, L. Pérez-Manríquez, P. Neelakanda, and K. V. Peinemann, "Bioinspired tannic acid-copper complexes as selective coating for nanofiltration membranes," *Separation and Purification Technology,* vol. 184, pp. 188-194, 2017.

[56] H. Wu, J. Xie, and L. Mao, "One-pot assembly tannic acid-titanium dual network coating for low-pressure nanofiltration membranes," *Separation and Purification Technology,* vol. 233, no. September 2019, pp. 116051-116051, 2020.

[57] Y. X. Wang *et al.*, "Metal-Polyphenol Coordination at the Aqueous Contra-diffusion "Interface": A Green Way to High-Performance Iron(III)/Tannic Acid Thin-Film-Composite Nanofiltration Membranes," *Langmuir,* vol. 38, no. 45, pp. 13793–13802, 2022.

[58] F. Xu, M. Wei, X. Zhang, Y. Song, W. Zhou, and Y. Wang, "How Pore Hydrophilicity Influences Water Permeability?," *Research,* vol. 2019, pp. 1-10, 2019.

[59] J. Guo *et al.*, "Influence of Ionic Strength on the Deposition of Metal-Phenolic Networks," *Langmuir,* vol. 33, no. 40, pp. 10616-10622, 2017.

[60] A. W. Mohammad, Y. H. Teow, W. L. Ang, Y. T. Chung, D. L. Oatley-Radcliffe, and N. Hilal, "Nanofiltration membranes review: Recent advances and future prospects," *Desalination,* vol. 356, pp. 226-254, 2015.

[61] X. You *et al.*, "Metal-coordinated sub-10 nm membranes for water purification," 2019.

[62] L. Yang, L. Han, J. Ren, H. Wei, and L. Jia, "Coating process and stability of metal-polyphenol film," *Colloids and Surfaces A: Physicochemical and Engineering Aspects,* vol. 484, pp. 197-205, 2015.

[63] J. Huang and K. Zhang, "The high flux poly (m-phenylene isophthalamide) nanofiltration membrane for dye purification and desalination," *Desalination,* vol. 282, pp. 19-26, 2011.

[64] H. H. Kinfu, M. M. Rahman, N. Cevallos-Cueva, and V. Abetz, "Mass Transport of Dye Solutions through Porous Membrane Containing Tannic Acid/Fe3+ Selective Layer," *Membranes,* vol. 12, no. 12, 2022.

[65] J. Liu *et al.*, "A combined tannic acid-copper-iron coating of ultrafiltration membrane for enhanced anti-bacterial and algal-inhibition performance," *Journal of Water Process Engineering,* vol. 50, p. 103250, 2022.

[66] C. X. Dong, Z. Wang, J. H. Wu, Y. Wang, J. X. Wang, and S. C. Wang, "A green strategy to immobilize silver nanoparticles onto reverse osmosis membrane for enhanced anti-biofouling property," *Desalination,* vol. 401, pp. 32-41, 2017.

[67] D. Suresh *et al.*, "Complexation of tannic acid/silver nanoparticles on polyamide thin film composite reverse osmosis membrane for enhanced chlorine resistance and anti-biofouling properties," *Desalination,* vol. 543, 2022.

[68] J. H. Wu, Z. Wang, W. T. Yan, Y. Wang, J. X. Wang, and S. C. Wang, "Improving the hydrophilicity and fouling resistance of RO membranes by surface immobilization of PVP based on a metal-polyphenol precursor layer," *Journal of Membrane Science,* vol. 496, pp. 58-69, 2015.

[69] E. Khodeir and M. Namvar-Mahboub, "The effect of tannic acid-based coating on performance of Ro membrane for metronidazole removal from aqueous solution," *Surfaces and Interfaces,* vol. 26, 2021.

[70] Z. Huang, S. Yin, J. Zhang, and N. Zhang, "Recent advances in membrane hydrophilic modification with plant polyphenol-inspired coatings for enhanced oily emulsion separation," *Journal of Applied Polymer Science,* vol. 138, no. 25, p. 50587, 2021.

[71] J. D. Wu *et al.*, "Facile preparation of metal-polyphenol coordination complex coated PVDF membrane for oil/water emulsion separation," *Separation and Purification Technology,* vol. 258, 2021, Art. no. 118022.

[72] H. Xie *et al.*, "Efficient oil-water emulsion treatment via novel composite membranes fabricated by CaCO(3)-based biomineralization and TA-Ti(IV) coating strategy," *Sci Total Environ,* vol. 857, no. Pt 2, p. 159183, 2023.

[73] H. L. Xie *et al.*, "Tannic acid (TA)-based coating modified membrane enhanced by successive inkjet printing of Fe^{3+} and sodium periodate (SP) for efficient oil-water separation," *Journal of Membrane Science,* vol. 660, 2022, Art. no. 120873.

[74] Y. X. Zhang, X. F. Duan, B. R. Tan, Y. C. Jiang, Y. Wang, and T. Qi, "PVDF microfiltration membranes modified with AgNPs/tannic acid for efficient separation of oil and water emulsions," *Colloids and Surfaces A: Physicochemical and Engineering Aspects,* vol. 644, 2022, Art. no. 128844.

[75] X. T. Zhao *et al.*, "Hierarchical metal-phenolic-polyplex assembly toward superwetting membrane for high-flux and antifouling oil-water separation," *Chinese Chemical Letters,* vol. 33, no. 8, pp. 3859-3864, 2022.

[76] R. Wang, X. Zhao, N. Jia, L. Cheng, L. Liu, and C. Gao, "Superwetting Oil/Water Separation Membrane Constructed from In Situ Assembled Metal-Phenolic Networks and Metal-Organic Frameworks," *ACS Appl Mater Interfaces,* vol. 12, no. 8, pp. 10000-10008, 2020.

[77] T. Leiknes, "Theory of Transport in Membranes," *PhD Thesis - TorOve Leiknes,* vol. 1, no. 0, pp. 1-17.

[78] O. Agboola, J. Maree, A. Kolesnikov, R. Mbaya, and R. Sadiku, "Theoretical performance of nanofiltration membranes for wastewater treatment," *Environmental Chemistry Letters,* vol. 13, no. 1, pp. 37-47, 2015.

[79] R. R. Nair, E. Protasova, S. Strand, and T. Bilstad, "Implementation of Spiegler-Kedem and Steric Hindrance Pore Models for Analyzing Nanofiltration Membrane Performance for Smart Water Production," *Membranes,* vol. 8, no. 3, 2018.

[80] Z. V. P. Murthy and L. B. Chaudhari, "Rejection behavior of nickel ions from synthetic wastewater containing Na2SO4, NiSO4, MgCl2 and CaCl salts by nanofiltration and characterization of the membrane," *Desalination,* vol. 247, no. 1-3, pp. 610-622, 2009.

[81] B. Van der Bruggen and C. Vandecasteele, "Modelling of the retention of uncharged molecules with nanofiltration," *Water Research,* vol. 36, no. 5, pp. 1360-1368, 2002.

[82] S. Koter, "Determination of the parameters of the Spiegler-Kedem-Katchalsky model for nanofiltration of single electrolyte solutions," *Desalination,* vol. 198, no. 1-3, pp. 335-345, 2006.

[83] P. Schirg and F. Widmer, "Characterization of Nanofiltration Membranes for the Separation of Aqueous Dye-Salt Solutions," *Desalination,* vol. 89, no. 1, pp. 89-107, 1992.

[84] A. M. Hidalgo, G. León, M. Gómez, M. D. Murcia, E. Gómez, and J. L. Gómez, "Application of the Spiegler-Kedem-Kachalsky model to the removal of 4-chlorophenol by different nanofiltration membranes," *Desalination,* vol. 315, pp. 70-75, 2013.

[85] I. Sutzkover, D. Hasson, and R. Semiat, "Simple technique for measuring the concentration polarization level in a reverse osmosis system," *Desalination,* vol. 131, no. 1-3, pp. 117-127, 2000.

[86] J. J. Wu, "On the application of the Spiegler-Kedem model to forward osmosis," *BMC Chemical Engineering,* vol. 1, no. 1, p. 15, 2019.

[87] D. Ormerod, A. Buekenhoudt, B. Bongers, T. Baramov, and J. Hassfeld, "From Reaction Solvent to Crystallization Solvent, Membrane Assisted Reaction Workup and Interpretation of Membrane Performance Results by Application of Spiegler-Kedem Theory," *Organic Process Research & Development,* vol. 21, no. 12, pp. 2060-2067, 2017.

[88] E. Nagy, "Chapter 20 - Reverse Osmosis," in *Basic Equations of Mass Transport Through a Membrane Layer (Second Edition)*, E. Nagy, Ed.: Elsevier, 2019, pp. 497-503.

[89] E. Nagy, "Chapter 15 - Nanofiltration," in *Basic Equations of Mass Transport Through a Membrane Layer (Second Edition)*, E. Nagy, Ed.: Elsevier, 2019, pp. 417-428.

[90] F. N. Ahmed, "Modified Spiegler-Kedem Model to Predict the Rejection and Flux of Nanofiltration Processes at High NaCl Concentrations," Masters of Applied Science Master thesis, University of Ottawa, 2013.

[91] A. L. Ahmad, M. F. Chong, and S. Bhatia, "Mathematical modeling and simulation of the multiple solutes system for nanofiltration process," *Journal of Membrane Science,* vol. 253, no. 1-2, pp. 103-115, 2005.

[92] W. J. Shang, X. L. Wang, and Y. X. Yu, "Theoretical calculation on the membrane potential of charged porous membranes in 1-1, 1-2, 2-1 and 2-2 electrolyte solutions," *Journal of Membrane Science,* vol. 285, no. 1-2, pp. 362-375, 2006.

[93] A. R. Hassan, N. Ali, N. Abdull, and A. F. Ismail, "A theoretical approach on membrane characterization: the deduction of fine structural details of asymmetric nanofiltration membranes," *Desalination,* vol. 206, no. 1-3, pp. 107-126, 2007.

[94] M. N. A. Seman, N. Ali, N. A. Jalanni, C. K. M. F. C. K. Yahya, and N. I. Yatim, "Characterization Assessment on Nanofiltration Membrane using Steric-Hindrance Pore (SHP) and Teorell-Meyer-Sievers (TMS) Models," *Sains Malaysiana,* vol. 52, no. 3, pp. 941-951, 2023.

[95] X. L. Wang, T. Tsuru, S. Nakao, and S. Kimura, "Electrolyte Transport through Nanofiltration Membranes by the Space-Charge Model and the Comparison with Teorell-Meyer-Sievers Model," *Journal of Membrane Science,* vol. 103, no. 1-2, pp. 117-133, 1995.

[96] Y. Tanaka, "3 - Theory of Teorell, Meyer, and Sievers (TMS Theory)," in *Ion Exchange Membranes (Second Edition)*, Y. Tanaka, Ed. Amsterdam: Elsevier, 2015, pp. 67-73.

[97] J. C. Fair and J. F. Osterle, "Reverse Electrodialysis in Charged Capillary Membranes," *Journal of Chemical Physics,* vol. 54, no. 8, pp. 3307-&, 1971.

[98] F. A. Morrison and J. F. Osterle, "Electrokinetic Energy Conversion in Ultrafine Capillaries," *Journal of Chemical Physics,* vol. 43, no. 6, pp. 2111-&, 1965.

[99] W. J. Shang, C. H. Tu, and X. L. Wang, "Theoretical calculation of reflection coefficients of single salt solutions through charged porous membranes," *Desalination,* vol. 236, no. 1-3, pp. 306-315, 2009.

[100] S. Basu and M. M. Sharma, "An improved Space-Charge model for flow through charged microporous membranes," *Journal of Membrane Science,* vol. 124, no. 1, pp. 77-91, 1997.

[101] R. J. Gross and J. F. Osterle, "Membrane Transport Characteristic of Ultrafine Capillaries," *Journal of Chemical Physics,* vol. 49, no. 1, pp. 228-&, 1968.

[102] M. Micari *et al.*, "Experimental and theoretical characterization of commercial nanofiltration membranes for the treatment of ion exchange spent regenerant," *Journal of Membrane Science,* vol. 606, 2020, Art. no. 118117.

[103] S. Singh, K. C. Khulbe, T. Matsuura, and P. Ramamurthy, "Membrane characterization by solute transport and atomic force microscopy," *Journal of Membrane Science,* vol. 142, no. 1, pp. 111-127, 1998.

[104] M. Ernst, A. Bismarck, J. Springer, and M. Jekel, "Zeta-potential and rejection rates of a polyethersulfone nanofiltration membrane in single salt solutions," *Journal of Membrane Science,* vol. 165, no. 2, pp. 251-259, 2000.

[105] R. Y. Wang and S. H. Lin, "Pore model for nanofiltration: History, theoretical framework, key predictions, limitations, and prospects," *Journal of Membrane Science,* vol. 620, 2021, Art. no. 118809.

[106] W. R. Bowen and A. W. Mohammad, "Characterization and prediction of nanofiltration membrane performance - A general assessment," *Chemical Engineering Research & Design,* vol. 76, no. A8, pp. 885-893, 1998.

[107] W. R. Bowen, A. W. Mohammad, and N. Hilal, "Characterisation of nanofiltration membranes for predictive purposes - Use of salts, uncharged solutes and atomic force microscopy," *Journal of Membrane Science,* vol. 126, no. 1, pp. 91-105, 1997.

[108] Y. Roy, D. M. Warsinger, and V. J. H. Lienhard, "Effect of temperature on ion transport in nanofiltration membranes: Diffusion, convection and electromigration," *Desalination,* vol. 420, pp. 241-257, 2017.

[109] V. Geraldes and A. M. Brites Alves, "Computer program for simulation of mass transport in nanofiltration membranes," *Journal of Membrane Science,* vol. 321, no. 2, pp. 172-182, 2008.

[110] D. L. Oatley, L. Llenas, R. Pérez, P. M. Williams, X. Martínez-Lladó, and M. Rovira, "Review of the dielectric properties of nanofiltration membranes and verification of the single oriented layer approximation," *Advances in Colloid and Interface Science,* vol. 173, pp. 1-11, 2012.

[111] A. Pérez-González, R. Ibáñez, P. Gómez, A. M. Urtiaga, I. Ortiz, and J. A. Irabien, "Nanofiltration separation of polyvalent and monovalent anions in desalination brines," *Journal of Membrane Science,* vol. 473, pp. 16-27, 2015.

[112] S. Déon, A. Escoda, P. Fievet, P. Dutournié, and P. Bourseau, "How to use a multi-ionic transport model to fully predict rejection of mineral salts by nanofiltration membranes," *Chemical Engineering Journal,* vol. 189, pp. 24-31, 2012.

[113] D. Rehman and J. H. Lienhard, "Global optimization for accurate and efficient parameter estimation in nanofiltration," *Journal of Membrane Science Letters,* vol. 2, no. 2, 2022, Art. no. 100034.

[114] S. C. Osorio, P. M. Biesheuvel, J. E. Dykstra, and E. Virga, "Nanofiltration of complex mixtures: The effect of the adsorption of divalent ions on membrane retention," *Desalination,* vol. 527, 2022.

Cumulative part of the dissertation

Chapter 3. Charge and Size Selective Thin Film Composite Membranes Having Tannic Acid–Ferric Ion Network as Selective Layer

In this chapter, a method of synthesizing TA-Fe^{3+} metal-phenolic network is introduced. A rapid complex formation between tannic acid (TA) and transition metal ions is employed to fabricate the selective layer of a thin-film composite (TFC) membrane. The MPN network is deposited over a porous polyacrylonitrile support in a layer-by-layer (LBL) self-assembly. Here, an ultrathin MPN film of around 10 nm thickness was fabricated to distinguish between solutes of different physicochemical properties for membrane separation application. The membrane structure and separation properties are fine-tuned by varying the number of layers deposited over the porous support or the TA to Fe^{3+} ratio. SEM and water contact angle analyses of the membrane surface morphologies show the formation of dense membranes at higher metal ion concentrations while the surface hydrophilicity increases. Zeta potential analyses show the fabricated membranes exhibit negative membrane surface charge. It is also demonstrated by the membranes' adsorption affinity towards positively charged solutes. High rejections towards negatively charged solutes were obtained unlike in the case of neutral solutes. The elemental composition and complexation state of the MPN thin layers are analyzed which demonstrate the TA-Fe^{3+} networks contain both bis- and mono-complexes. A step-by-step possible formation mechanism of the TA-Fe^{3+} thin-film via self-assembly in the utilized LBL technique is also presented. The fabricated membranes exhibit excellent fouling resistance mechanisms via the formation of hydration layers and repulsive electrostatic interaction with a model foulant.

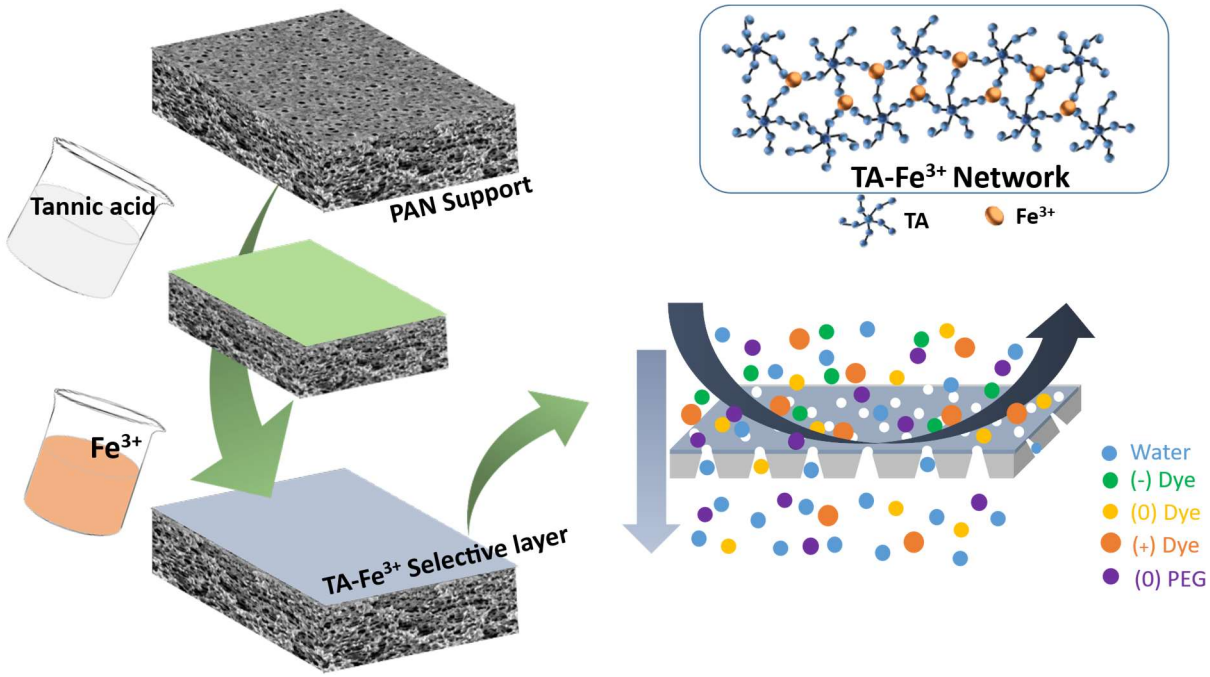
Tannic acid
PAN Support
Fe3+
TA-Fe3+ Selective layer
TA-Fe3+ Network
TA
Fe3+
Water
(-) Dye
(0) Dye
(+) Dye
(0) PEG

.

Journal of Membrane Science 679 (2023) 121709

Contents lists available at ScienceDirect

Journal of Membrane Science

journal homepage: www.elsevier.com/locate/memsci

Charge and size selective thin film composite membranes having tannic acid – Ferric ion network as selective layer

Hluf Hailu Kinfu [a], Md. Mushfequr Rahman [a,*], Erik Sebastian Schneider [a], Nicolás Cevallos-Cueva [a], Volker Abetz [a,b]

[a] Helmholtz-Zentrum Hereon, Institute of Membrane Research, Max-Planck-Straße 1, 21502, Geesthacht, Germany
[b] University of Hamburg, Institute of Physical Chemistry, Martin-Luther-King-Platz 6, 20146, Hamburg, Germany

ARTICLE INFO

Keywords:
Metal-polyphenol network
TA-Fe^{3+} membranes
Self-assembly
Thin film composite membranes
Dye selectivity

ABSTRACT

Selective membranes that can distinguish between solutes of different physicochemical properties are highly desirable for membrane applications such as nanofiltration. Rapid coordination complex formation of metals and polyphenols triggered the development of thin film composite membranes in the last decade through a green synthesis procedure, eliminating the use of toxic organic solvents. In this work, thin film composite membranes with high selectivity between organic solutes were prepared. They contain a selective layer based on a metal-polyphenol network (tannic acid – ferric ion (TA-Fe^{3+})) with a thickness of approximately 10 nm thickness. The thin layer was obtained by coating aqueous solutions of the two components on top of a microporous polyacrylonitrile support in a sequential mode. The morphological, chemical and physical properties of the membranes were investigated. The results demonstrate that hydrophilicity, surface charge, and pore size of the membranes can be fine-tuned by varying the TA/Fe^{3+} ratio of the casting solutions. The separation performance of the membranes was further analyzed by filtration tests. For instance, selectivities in the range of 3.2–20.6 were achieved between uncharged(0)/(−)charged dyes of comparable molecular size, while exhibiting a good selectivity, reaching up to 3 times, between monovalent to trivalent negatively charged dyes. This work paves a way to eco-friendly membrane synthesis for diverse applications in water and wastewater treatment.

1. Introduction

Nanofiltration membranes have a vast array of applications including potable water softening, removal of heavy metals from wastewater, desalting of dyes, removal of pesticides from agricultural wastewater etc. However, nanofiltration membranes are still underdeveloped due to drawbacks such as fouling, membrane lifetime, chemical resistance and rejection efficiency [1]. Polymeric nanofiltration membranes have either integrally skinned asymmetric or thin-film composite (TFC) structure. Most commercial nanofiltration membranes are TFC membranes where a crosslinked polyamide (PA) selective layer is prepared by *in-situ* interfacial polymerization on top of a microporous support such as the NF series from Dow® Inc., the Desal series from GE-Osmonics and the UTC series from Toray Industries, Inc. [2]. Researchers have extensively explored the interfacial polymerization in order to improve the fouling resistance and selectivity of the membranes [3]. The use of toxic organic solvents and acid chlorides in interfacial polymerization is a concern for the environment [4]. Moreover, delamination of the selective layer from the support layer can occur due to swelling degree difference as well as a weak physical adhesive interaction between PA layer and the support [5]. Most polymeric membranes are also relatively hydrophobic, limiting water permeation and making them susceptible to irreversible deposition of foulants and highly affected by the trade-off between permeability and selectivity [6]. To find an alternative of the PA layer prepared by interfacial polymerization, layer by layer assembly of oppositely charged polyelectrolytes has been extensively explored [7–9]. In recent years, the use of metal-polyphenol networks (MPNs) as selective layers of TFC membrane has received a lot of attention [6,10,11].

Deposition of two-dimensional metal-polyphenol network (MPN) thin films has been demonstrated in a pioneering work by Ejima et al. [12]. Biological systems, such as byssal threads of blue mussels particularly, contain a hard, stiff and stable thin outer protective layer of cuticle mainly assembled from catechol-metal complexes [13,14]. This

* Corresponding author.
E-mail address: mushfequr.rahman@hereon.de (Md.M. Rahman).

https://doi.org/10.1016/j.memsci.2023.121709
Received 1 March 2023; Received in revised form 13 April 2023; Accepted 30 April 2023
Available online 2 May 2023

complex formation is based on the coordination interaction between metal ions and adjacent hydroxyl groups of phenolic ligands. In the last decade, this bioinspired materials synthesis technique, i.e., deposition of MPN thin films was investigated for various applications, such as cancer treatment, imaging, drug delivery, catalysis, adsorption and membrane fabrication [15–19]. So far, tannic acid (TA) has been the most popular choice for fabrication of MPN for all of these applications. TA is a natural polyphenol found in oak trees, gall nuts, and all aerial plants. TA consists of a central glucose molecule covalently bonded to its several galloyl moieties via ester linkage. The commercially available TA contains a mixture of molecules having 2–12 galloyl moieties. This hydrolysable polyphenolic tannin exhibits a strong metal cation chelation behavior. Multiple aromatic –OH groups offer suitable sites for metal coordination [15]. Besides metal coordination bonds, it was also reported that electrostatic interactions govern tannic acid-metal interactions [20].

In the recent years, TFC membranes have been prepared by means of coordination led self-assembly of TA and different metal cations on porous supports using only water as solvent. Owing to the excellent adhesive nature, the TA-metal thin films were successfully coated on various microporous supports, e.g., polyethersulfone [10,11,21,22], polysulfone [23], polyacrylonitrile (PAN) [24–28], hydrolyzed polyacrylonitrile [28], or polyimide [29]. It was shown that TA-metal self-assembled membranes exhibit hydrophilic properties due to the catechol- and gallol-rich TA coating [11]. This decreases the interaction of a membrane with solute molecules, thus enhancing fouling resistance. However, the right conditions for self-assembly of the TA-metal layers to bridge the gap between ultrafiltration and nanofiltration and to achieve a certain molecular weight cut-off, are still unknown. In the present study, we fabricated a series of TFC membranes having TA-Fe^{3+} selective layers with a green and facile technique and investigated the influence of synthesis parameters on the membrane microstructure. Furthermore, the influence of Fe^{3+} concentration of the coating solutions on water fluxes as well as solute rejections were explored. Retentions of neutral and charged solutes having molecular weights between 200 Da and 1000 Da by the prepared membranes were thoroughly investigated.

2. Experimental

2.1. Materials

Tannic acid (TA) and iron(III) chloride hexahydrate ($FeCl_3{\cdot}6H_2O$) were purchased from Sigma-Aldrich Chemie GmbH (Germany) and Alfa Aesar GmbH & Co., respectively. Ultrafiltration polyacrylonitrile (PAN) membrane support was prepared at and supplied by Helmholtz-Zentrum Hereon. Poly(ethylene glycol) (PEG) of average molecular weight 200, 400, 600 and 1000 Da were purchased from VWR International GmbH (Germany). Hydrochloric acid (HCl, 37%) was obtained from Merck Biosciences GmbH. Sodium hydroxide (NaOH), orange II, riboflavin, naphthol green B, and rhodamine B were commercially supplied by Sigma-Aldrich. All the chemicals were used as received. All aqueous solutions were prepared with milli-Q water of high purity (0.055 μS cm^{-1}).

2.2. Preparation of TA-Fe^{3+} membranes

MPN selective layers were synthesized on the membrane supports based on the coordination self-assembly of ferric ions and TA. The membrane preparation technique used in this work is analogous to the layer-by-layer film deposition. Firstly, the PAN membrane support was pre-wetted by immersing it in milli-Q water for 3 h. Then, the support membrane was fixed onto a glass plate in a PTFE frame of 5.1 cm × 15.9 cm before exposure to TA and Fe^{3+} solutions to safeguard that the coordination reaction occurs only on the top surface. Subsequently, the PAN support was subjected to 50 ml aqueous solutions of TA and Fe^{3+} for a certain amount of time, alternately. The resulting membrane was rinsed in ultrapure water after each immersion to remove unattached as well as unstable TA molecules or Fe^{3+} from the membrane surface. The overall membrane preparation process is shown in Fig. 1a. One self-assembled layer was completed after both, TA and metal ion, solutions were deposited on the support. To produce multilayers, this procedure was then repeated. A series of membranes were prepared by varying several synthesis parameters: number of layers and TA to Fe^{3+} ratio.

2.3. Characterization of prepared membranes

Deposition of the synthesized polyphenol-metal ion-based selective layer was investigated by Fourier transform infrared spectroscopy (FTIR) using a Bruker Alpha (diamond-ATR unit) (Bruker, Karlsruhe, Germany). FTIR spectra were measured in the region of 400–4000 cm^{-1} with a resolution of 4 cm^{-1} for 64 scans. Samples were dried prior to FTIR analysis. Water contact angle (WCA) measurement was used to evaluate membrane hydrophilicity and wettability. Dynamic WCA measurements were performed using KRUESS Drop Shape Analysis System DSA 100 (FEI part of Thermo Fisher Scientific, Kawasaki, Japan) in a sessile drop mode with 3 μl of water droplets at room temperature. The reported results are averages of at least three contact angle measurements. The electrokinetic property of the membranes was determined by measuring the streaming potential with a SurPASS 3 electrokinetic analyzer (Anton Paar, Austria). A background solution of 1 mM NaCl was used in measuring the tangential streaming potential between two membrane active layers facing each other. The Helmholtz-Smoluchowski equation was used to correlate the streaming potential with the membrane zeta potential.

Morphologies of membrane surfaces and cross-sections were investigated with a Merlin scanning electron microscope (SEM) (Zeiss, Germany) at accelerating voltages between 1.5 and 3 kV using an InLens secondary electron detector and an energy selective backscattered electron (EsB) detector. Before measurement, membrane samples were dried under vacuum at 60 °C for 48–72 h and were sputter-coated with 1–1.5 nm platinum using a CCU-010 coating device (Safematic, Switzerland). In order to study the internal morphology of the membranes, cross-sectional specimens were prepared by immersing and fracturing the membranes in liquid nitrogen. For a precise measurement of the selective layer thickness, cross-sectional samples were prepared by Argon ion beam milling using a precision etching and coating system PECS II (Gatan/AMETEK, Germany). For this purpose, images were recorded by the EsB detector taking advantage of the high material contrast of the Fe-rich selective layer with respect to the underlying PAN support. Argon ion milling was performed at −120 °C and 4 kV for several hours. Before measurement, specimens were coated with 4 nm carbon using the same device and conditions. For spatially resolved elemental analysis, energy dispersive X-ray (EDX) spectroscopy was used. EDX spectroscopy was measured on membrane surfaces using an Extreme as primary and an X-max 150 as secondary EDX detector (Oxford Instruments, U.K.) at a working distance of 5.6 mm, a constant magnification of 5 kx and an acceleration voltage of 1.5 kV. The EDX analysis was performed at three different sample locations of agglomerate-free surfaces for each membrane. The reported quantitative and spectrum results are therefore averages of the individual sample data. For a quantitative comparison of Fe/O intensity ratio, the obtained spectra were normalized to the pristine PAN (support) spectrum at 0.9 keV.

2.4. Determination of permeance, retention and selectivity

Measurements of water permeance and rejection performance of the synthesized membranes were carried out in a dead-end filtration configuration. Membrane permeance tests were first performed with pure water (0.055 μS cm^{-1}). Filtrate weight was recorded after membrane flux had been stabilized. The permeance of membranes was computed with the following formula:

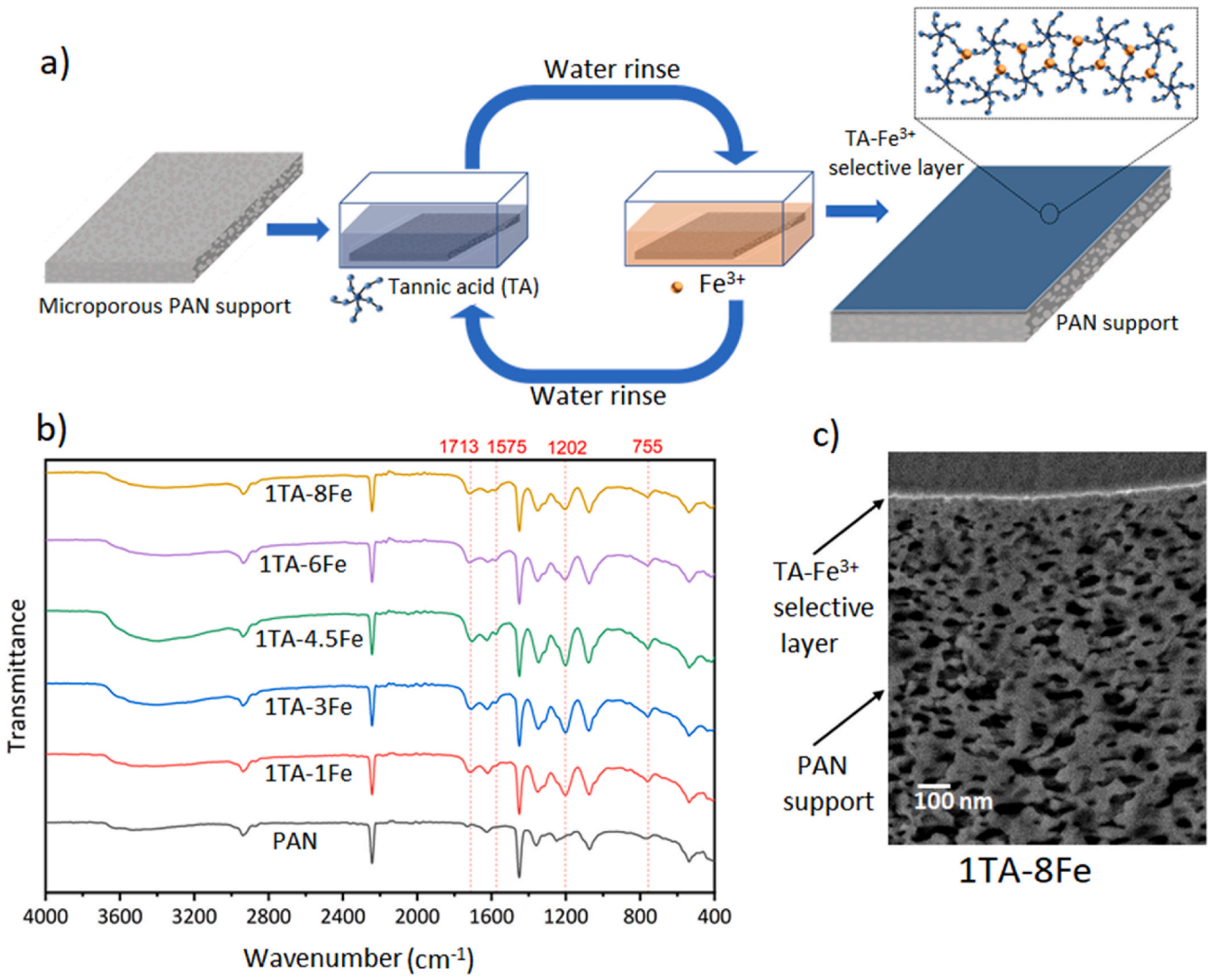

Fig. 1. a) Schematic representation of sequential deposition of TA-Fe^{3+} selective layer, b) FTIR spectra of the PAN support and the TFC membranes, and c) SEM image (backscattered electron image) of an argon ion milled cross-section of 1TA-8Fe TFC membrane.

$$J = \frac{W}{\rho * A * t * \Delta P}$$

Where J ($L{\cdot}m^{-2}\ h^{-1}\ bar^{-1}$) is water permeance, W (kg) is weight of collected permeate, ρ (kg/m^3) is density of water, A (m^2) is the effective filtration area, t (h) is the operation time, and ΔP (bar) is the applied transmembrane pressure. To determine separation performance of the synthesized membranes, PEG and dye solution filtration tests were performed using dead-end cells stirred at 350 rpm with a magnetic stirrer. The structure and molecular weight of the analyzed dyes (rhodamine B, orange II, naphthol green B, and riboflavin) are shown in Fig. 7a. The retention measurements were performed using a stirred test cell from Millipore (EMD Millipore XFUF07601) by reducing the effective membrane area to 1.77 cm^2. Permeation of ultrapure water at 3.5–4 bar transmembrane pressure, was carried out for 2 h prior to the retention measurement at 2.5–3 bar, so that, any possible compaction of the porous support layer can take place before the retention measurement. It is worth mentioning that the microporous PAN membrane support used in this work for the preparation of the TFC membranes do not show any noticeable compaction even on 15 bar feed pressure. A feed concentration of 0.1 mM was used for all single dye solutions. The absolute concentrations of the recorded dye samples were analyzed by UV–Vis spectrophotometer (GENESYS 10S, Thermo Scientific). For PEG retention tests, a feed solution of 1 g/L was used. Samples from PEG solution retention measurements, performed in the same setup, were analyzed using gel permeation chromatography (GPC) (VWR-Hitachi 2130 pump, Hitachi, Darmstadt, Germany).

The rejection of solute for all rejection measurements was calculated using the following equation:

$$R\,(\%) = \left(1 - \frac{C_p}{(C_f + C_r)/2}\right) * 100$$

Where R is solute retention, C_p, C_f and C_r are the concentrations of the permeate, feed and retentate in $mg{\cdot}L^{-1}$, respectively. The average $(C_f + C_r)/2$ is used instead of C_f for determination of R to take into account the minor change of feed concentration during the experiment. Membrane selectivity towards two solutes, both during single solute and mixed solute rejection tests, was computed using

$$Selectivity = \frac{100 - R_1(\%)}{100 - R_2(\%)}$$

In which R_1 and R_2 are rejections of solute 1 and 2, respectively.

2.5. Antifouling properties

Evaluation of the antifouling property of membranes was performed with a model foulant, Humic acid (HA). HA (100 ppm) was dissolved in aqueous NaOH solution (pH ≈ 9.5). After dissolution, the final HA solution for the filtration test was adjusted to pH 7 with aqueous HCl. The fouling test was performed by first recording pure water permeance of the membrane for 1 h followed by filtration of the HA solution for 1.5 h. Subsequently, the membrane was rinsed with pure water for 15 min to remove fouled HA molecules. Pure water permeance was then measured again. Flux recovery ratio (F_{RR}) and fouling ratio (R_t) were calculated using the following equations:

$$F_{RR}\ (\%) = \frac{W_i}{W_0} * 100$$

$$R_t\ (\%) = \left(1 - \frac{W_f}{W_0}\right) * 100$$

where F_{RR} is flux recovery ratio, W_0 is initial water permeance, W_i is water permeance after fouling and W_f is permeate flux of the fouling solution. Two cycles of fouling tests were performed for each membrane.

3. Results and discussion

3.1. Membrane morphology

Five thin film composite (TFC) membranes were prepared by deposition of TA-Fe^{3+} selective layers on top of a microporous PAN support (Fig. 1a). A series of membranes referred to as 1TA-1Fe, 1TA-3Fe, 1TA-4.5Fe, 1TA-6Fe and 1TA-8Fe were synthesized by varying the Fe^{3+} content of the casting solutions to deposit the selective layers. The acronyms of the membranes and the casting parameters are listed in Table 1. The FTIR spectra of the PAN support and the TFC membranes (Fig. 1b) prove the successful deposition of the TA-Fe^{3+} selective layer in each of these membranes. The characteristic bands from the PAN support appear at 2938, 2242 and 1450 cm^{-1}, which correspond to CH_2 stretching vibration, C≡N stretching vibration and CH_2 bending vibration, respectively. A broad OH stretching vibration is also observed in the FTIR spectrum of the PAN support in the wavenumber range 3100–3680 cm^{-1}. The –OH stretching vibration peak is stronger in the FTIR spectra of the TFC membranes due to the abundance of –OH moieties in TA. The band at 1713 cm^{-1} in the FTIR spectra of the TFC membranes corresponds to the C═O stretching vibration from ester groups of TA. A C═C stretching vibration peak from the aromatic ring of TA is observed at 1575 cm^{-1}. The absorption band at 1202 cm^{-1} is also attributed to C–O stretching vibration. Moreover, the intensified peak at 757 cm^{-1} suggests the presence of CH single bond from phenyl groups of TA. The presence of TA-Fe^{3+} layer is also visible in the SEM images of 1TA-8Fe obtained by backscattered electron (BSE) imaging mode (Fig. 1c). The image contrast in BSE imaging mode originates from the local average atomic number of the elements (material contrast). The selective layer of the TFC membranes contains Fe, which has a significantly higher atomic number compared to the elements present in PAN and TA (C, N and O). Therefore, the selective layer appears brighter in the BSE image compared to the underlying substrate. The thickness of the selective layer is approximately 10 nm (Supporting information Fig. S2). Fig. 2 shows SEM images of the surface and cross section of the PAN support and the TFC membranes obtained by secondary electron (SE) imaging mode. Unlike BSE images, the contrast in the SE images originates from the topological features of the membranes. The SE images show that the PAN support (Fig. 2a) has a porous surface and an integral asymmetric porous structure, i.e., the pore size gradually increases along the cross section towards the bottom of the membrane. From the SE images of the TFC membranes (Fig. 2b–f), it is clear that the deposition of the TA-Fe^{3+} selective layer significantly affected the surface morphology of the membranes while the open porous structure along the cross-section of the PAN support below the selective layer seems not to be affected. From Fig. 1b and c and Fig. 2b–f it is evident the ultrathin TA-Fe^{3+} selective layers are formed at the surface of the TFC membranes during the sequential deposition. There is no sign of penetration of the TA-Fe^{3+} layer in the porous substructure. The TFC membranes contains two TA-Fe^{3+} layers (Table 1). The TA-Fe^{3+} layer shows a small decrease in the water permeance compared to the PAN support after the first layer deposition. At least two deposition cycles were required to achieve a rather uniform surface coverage. The increase of deposition cycle eliminates defects at the expense of increasing the thickness of the selective layer. Consequently, the water permeance through the membranes drops significantly with the increase of the number of deposited layers (Supporting information Fig. S1). Therefore, only two deposition cycles were used to coat the TA-Fe^{3+} selective layers on PAN support. Both the size and number of open pores on the surface were reduced by the deposition of TA-Fe^{3+} self-assembled network. The selective layers of the TFC membranes become more compact and dense with increasing Fe^{3+} concentration (Fig. 2b–f). Numerous open pores are visible at the surface of 1TA-1Fe and 1TA-3Fe. Compared to these two membranes, the number of open pores is significantly lower at the surface of 1TA-4.5Fe. 1TA-8Fe has the most compact selective layer among the five TFC membranes. Determination of average pore size by SEM was not possible owing to the limited resolution (details provided in supporting information). Nanoscale protrusions appear as white spots at the SE surface image of 1TA-1Fe (Fig. 2b). Irregular agglomerates appear at the surface of membranes of high iron concentration, 1TA-6Fe (Fig. 2e) and 1TA-8Fe (Fig. 2f). EDX spectroscopy was performed to investigate the composition of the agglomerates. Fig. S3 shows the agglomerate at the surface of 1TA-8Fe is rich in Fe compared to the surrounding flat membrane surface. This indicates the formation of TA-Fe^{3+} complex aggregates over the synthesized film. Moreover, compared to the 1TA-6Fe membrane, a higher number of agglomerates was observed at the surface of 1TA-8Fe. The Fe rich TA-Fe^{3+} aggregates at the surface of the TFC membranes increase with the Fe^{3+} concentration in the casting solution.

To assess the change in the elemental composition of the thin films, EDX spectroscopy of the surfaces of the active layers was performed. Fig. 3b shows the obtained spectra of elemental composition indicating that C, N, O and Fe were the main elements observed on the membrane surfaces (full sized image can be found in Fig. S4 of the supporting material). The high intensities of carbon and nitrogen are mainly attributed to the PAN support. The analysis of the EDX spectra revealed

Table 1
TA-Fe^{3+} selective layer deposition parameters.

Membrane	Casting solution concentration (Weight %)		Casting solution concentration (Molarity in mM)		Assembly time (min)	TA solution pH	Number of TA-Fe^{3+} layers deposited
	TA	$FeCl_3{\cdot}6H_2O$	TA	$FeCl_3{\cdot}6H_2O$			
1TA-1Fe	0.02	0.02	0.1176	0.740	4	5.8	2
1TA-3Fe	0.02	0.06	0.1176	2.220	4	5.8	2
1TA-4.5Fe	0.02	0.09	0.1176	3.330	4	5.8	2
1TA-6Fe	0.02	0.12	0.1176	4.440	4	5.8	2
1TA-8Fe	0.02	0.16	0.1176	5.919	4	5.8	2

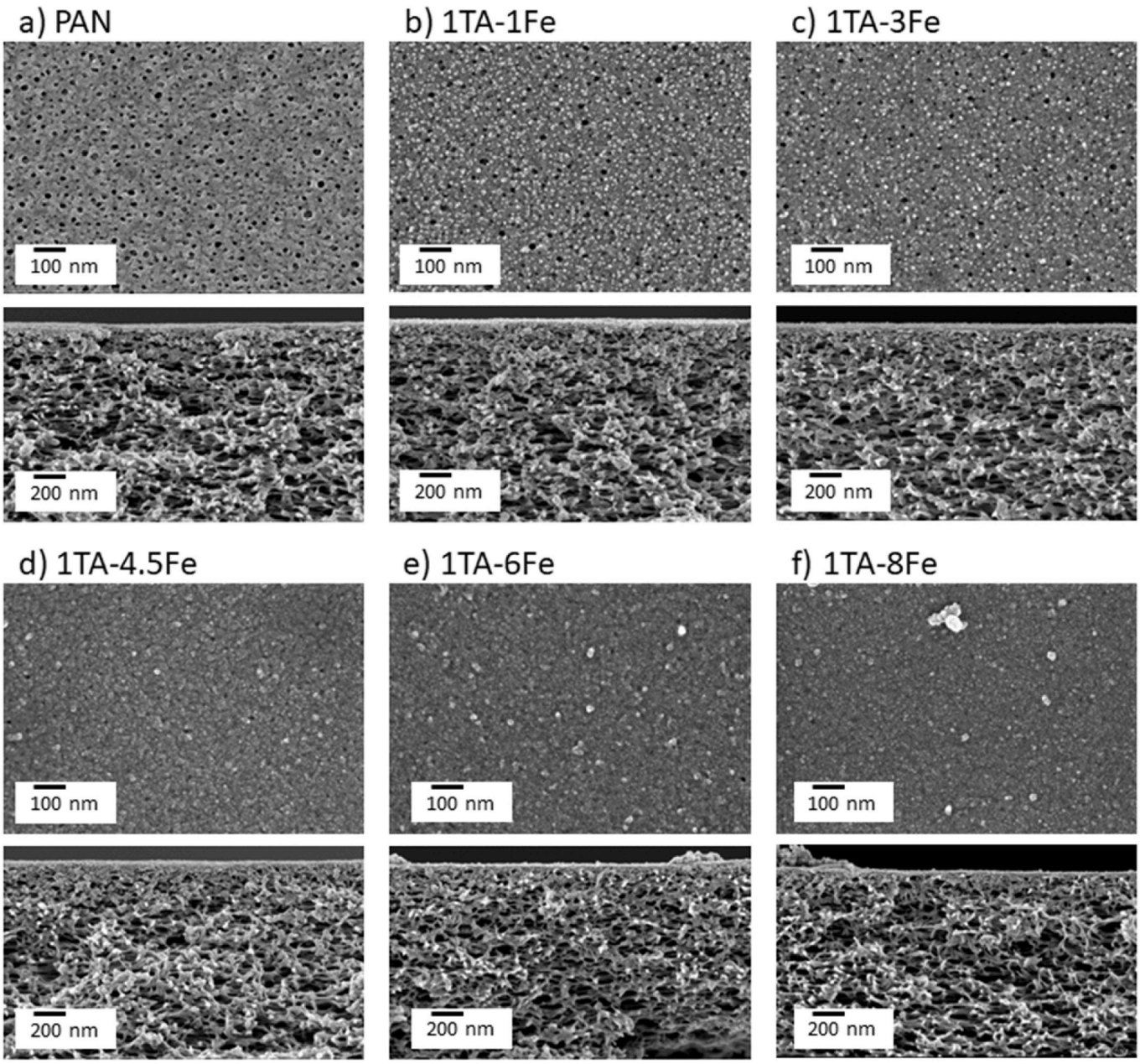

Fig. 2. SEM images of surface (top image) and cross-section (bottom image) of analyzed membranes: (a) pristine PAN support and TA-Fe^{3+} membranes at a tannic acid to $FeCl_3{\cdot}6H_2O$ ratio of (b) 1TA to 1Fe (c) 1TA to 3Fe (d) 1TA to 4.5Fe (e) 1TA to 6Fe and (f) 1TA to 8Fe.

an increase in oxygen and iron contents in the newly synthesized membranes when the concentration of Fe^{3+} was increased in the initial solution for the fabrication process. The observed elemental peak counts for Fe and O are presented in Table S1. Moreover, the elemental analysis showed a significant decrease in the intensity of C and N atoms in the TA-Fe^{3+} films compared with the bare PAN membrane (Fig. S4). This demonstrates a surface coverage of the C and N rich support by TA-Fe^{3+} self-assembled films.

A quantitative relationship of the amount of elements present in the selective layer can be estimated based on the area corresponding to each element in the EDX spectra. To overcome uncertainties on the elemental composition, three EDX spectra were taken at different spots for each membrane which showed a good conformity to each other. Three different complexes between TA and Fe^{3+} are formed in solution, namely mono-, bis-, and tris complex [12] as shown in Fig. 3a. The theoretical Fe/O ratios in these complex states are given in Table 2. Fig. 3c shows the ratio of Fe to O content in the TA-Fe^{3+} self-assembled layers. At the pH ≈ 5.8 of the milli-Q water used in this study, formation of bis-complex is likely to be favored [12]. But the metal to ligand ratio and final concentration of the solution also govern the formation of different types of metal-polyphenol complexes [30]. However, it can be observed from Fig. 3c that the Fe/O ratios of the prepared membranes lie between the theoretical Fe/O ratios expected for mono- and bis-complexes. Hence, the TA-Fe^{3+} networks of the membranes prepared at different Fe^{3+} concentrations contain both bis- and mono-complexes. Besides the pH and the concentration of the solutions, the protocol used for the preparation dictates the complexation between TA and Fe^{3+} to a large extent [30]. The protocol used in this work for formation of TA-Fe^{3+} selective layer has four basic steps as shown in Fig. 3d. At first, the TA molecules are deposited at the surface of the PAN support (step 1). Upon exposure to the Fe^{3+} solution, crosslinking between the adsorbed TA molecules takes place owing to formation of

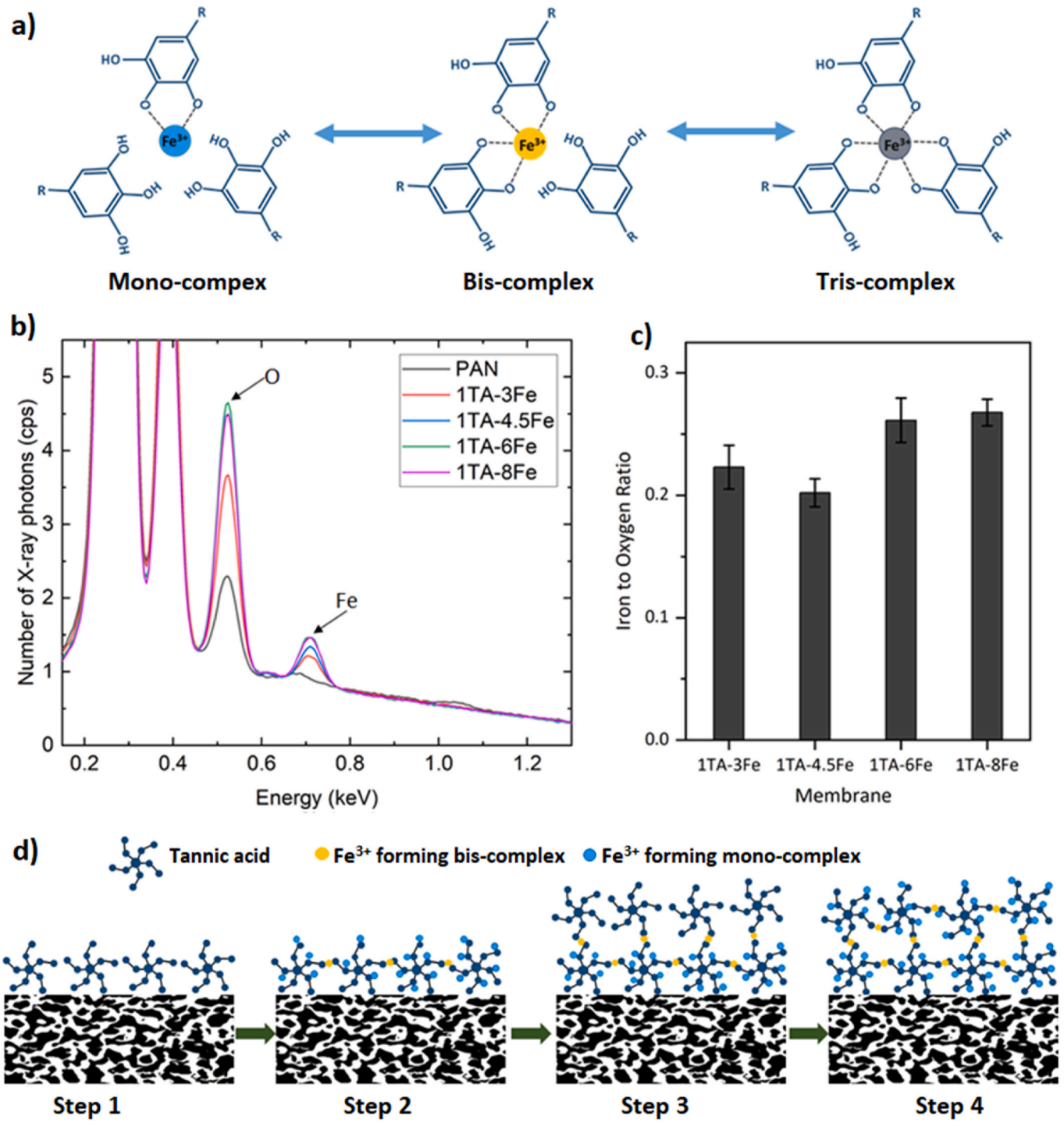

Fig. 3. a) Complex formation states of TA-Fe^{3+} coordination, b) EDX spectra of the bare PAN support and the TFC membranes containing TA-Fe^{3+}selective layers, c) Fe/O ratio of the TFC membranes, and d) possible formation mechanism of the TA-Fe^{3+} thin-film via self-assembly in a layer-by-layer technique.

Table 2
Theoretical Fe/O ratio in the three different complex states of TA-Fe^{3+} self-assembly based on Fig. 3a. Although TA contains 46 oxygen in its elemental structure, only 25 from the hydroxyl groups of catechol and gallol moieties can coordinate with metal ion centers.

Complexation state	Number of OH groups coordinating with 1 Fe center	Total oxygen in the complex state	Number of total OH groups capable of coordination	Fe centers required for total coordination of available (capable) OH groups	Fe/O ratio in the complex state
Mono-complex	2	46	25	12.5	0.27
Bis-complex	4	92	50	12.5	0.14
Tris-complex	6	138	75	12.5	0.09

bis-complex linkages. Additionally, formation of a large number of mono-complex takes place at this step (step 2). Then, the TA molecules are deposited for the second time at the membrane surface. As a result, some of the mono-complexes are converted into bis-complexes and new TA-Fe^{3+} linkages are formed (step 3). Finally, as the membranes are treated once more with Fe^{3+} solution, new bis-complex linkages form and additional mono-complexes are formed as well (step 4). From Fig. 3c, it is evident that the content of mono-complexes is higher for 1TA-6Fe and 1TA-8Fe compared to those in 1TA-3Fe and 1TA-4.5Fe.

3.2. Surface hydrophilicity and water flux

Water contact angle (WCA) at the surface of the membranes was determined to study the surface hydrophilicity. The initial WCA of the PAN support was 47.9° (Fig. 4a). Since TA has abundant hydrophilic –OH groups, it was expected that the surface of the TFC membranes was more hydrophilic and the initial WCA of the TFC membranes were lower compared to the pristine PAN membrane. For the TFC membranes, the initial WCA indeed decreased linearly when iron concentration was increased up to 1TA-6Fe. However, the initial WCA of 1TA-8Fe dropped significantly to 6.3°. Both, surface morphology and composition of the selective layer, are likely to have an impact on the change of initial WCA of the TFC membranes. Time-dependent membrane water contact angles are shown in Fig. 4b. The rate of change of the water contact angle with time is largely dependent on the surface porosity of the membranes [31]. The water droplet sinks into the pristine PAN membrane faster than the TFC membranes which is reflected by the higher change of contact angle compared to the TFC membranes. As the surface porosity of the membranes gradually decreases with increasing Fe^{3+} concentration (Fig. 2), the change of water contact angle also drops respectively. Fig. 4c shows pure water permeance through pristine PAN and the TFC membranes. The PAN support exhibited 286.6 L m^{-2}•h^{-1}•bar^{-1} water permeance. The average water permeance of 1TA-1Fe is around 165 L m^{-2}•h^{-1}•bar^{-1}. Although the surface of 1TA-1Fe is more hydrophilic compared to PAN, there is more than 50% drop of the water flux due to reduction of surface porosity (Fig. 2a and b) of the membrane. Fig. 4c

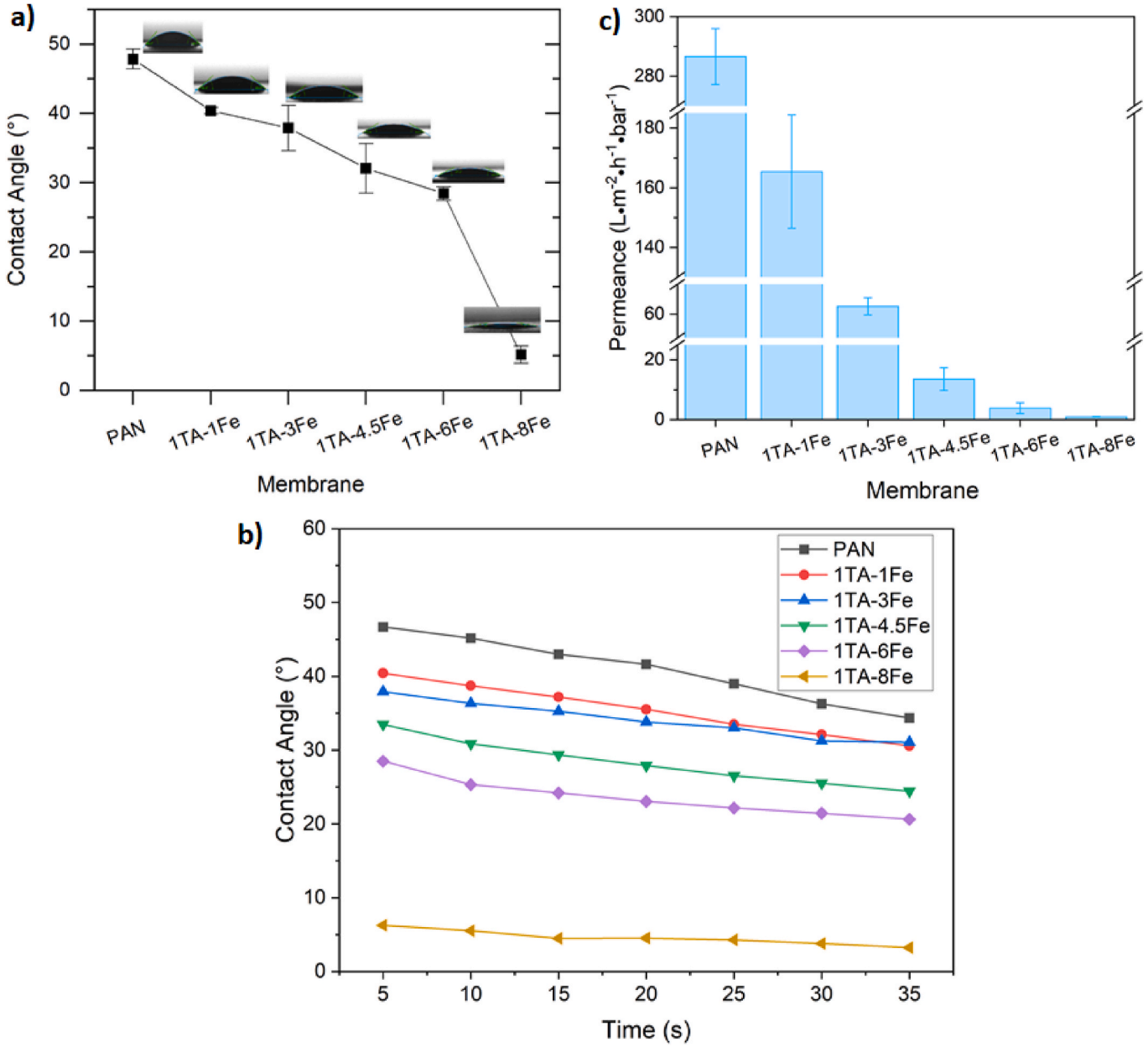

Fig. 4. a) Water contact angle b) change of water contact angle with time, and c) water permeance of the membranes.

shows the water permeance of the TFC membranes decreases with the increase of Fe^{3+} of the casting solutions which is consistent with the time dependent change of the water contact angle. However, the error bar of 1TA-1Fe is significantly high compared to other membranes. In other words, the water permeance through the membrane samples collected from different areas of the membrane have a large variation. As the selective layer of 1TA-1Fe is likely to have significant inhomogeneity, this membrane was not used for further investigations. Further investigation of the TFC membranes are performed with 1TA-3Fe, 1TA-4.5Fe, 1TA-6Fe and 1TA-8Fe membranes which have water permeances of 62.5, 13.6, 3.8 and 0.9 L m^{-2}•h^{-1}•bar^{-1}, respectively. In section 3.1, it was demonstrated that the porous structure along the cross section of the PAN support remains unchanged in the TFC membranes (Fig. 2). Therefore, it is clear that the water flux was tuned over this wide range only by tuning the surface porosity and hydrophilicity of the TFC membranes using ultrathin TA-Fe^{3+} selective layers of approximately 10 nm thickness.

3.3. Retention of neutral PEG from aqueous solution

Poly(ethylene glycol) (PEG) was used as a model neutral molecule to study the retention behavior of 1TA-3Fe, 1TA-4.5Fe, 1TA-6Fe and 1TA-8Fe. 1 g/L aqueous solutions of PEG having molecular weights (Mw) of 200, 400, 600 and 1000 Da were used as feed solutions (Fig. 5). The molecular weight dependent PEG retention behavior gives some information about the surface pore size of the membranes. An increase of Fe^{3+} concentration in the casting solution led to an increased retention of all PEGs and PEG with Mw $\geq$ 400 Da were retained by more than 90% only by the two membranes with the highest Fe^{3+} contents. This supports the observation that the surface pore sizes in the membranes decreased with an increase of Fe^{3+} content in the casting solution, i.e., the average surface pore size of 1TA-3Fe > 1TA-4.5Fe > 1TA-6Fe > 1TA-8Fe. However, there are some irregularities. For example-in case of 1TA-3Fe the retention of PEG with Mw = 1000 Da is lower than that of PEG with Mw = 600 Da. This irregularity in the retention behavior originate from the inhomogeneity of the surface pore size of the membranes. It is clear from the SEM images that the surface of PAN support is not isoporous, i.e., the distribution of surface pore size is broad (Fig. 2a). Similarly, while compared to PAN the surface porosity is lower in 1TA-3Fe pore size distribution is rather broad (Fig. 2c). Therefore, the average pore size of the 1.77 cm^2 samples (from different areas of the membrane) used for the retention measurements is not constant, but shows variations. The molecular weight cut offs of 1TA-6Fe and 1TA-8Fe membranes are around 390 Da and ~ 375 Da respectively. Other membranes show less than 40% rejection of PEG with Mw = 1000 Da.

3.4. Surface zeta potential

Along with pore size and porosity, the separation of charged molecules were also strongly influenced by the membrane surface charge. The surface charges of the PAN support and the four TFC membranes used for charged solute retention (discussed in section 3.5) were studied through streaming potential measurement in the pH range of 5–8. The Helmholtz-Smoluchowski equation was used to compute the zeta potential from the measured streaming potential. While streaming potential measurements are a popular method to study the surface charge, the discrepancy between the apparent value obtained by this method and the true surface zeta potential value has been pointed out in literature [32,33]. The pristine PAN membrane displayed a negative surface charge (Fig. 6) which is consistent with previous reports of the zeta potential of PAN membranes [34–36]. Besides PAN, there are several other polymeric surfaces which exhibit a negative zeta potential in spite of having no ionizable functional group, e.g., PTFE and polystyrene [37]. It is well established that such negative zeta potential originates from preferentially adsorbed hydroxyl ions compared to hydronium ion of the electrolyte solution at the polymer surface [37,38]. The TFC membranes also exhibited a negative zeta potential in the studied pH range. The TA-Fe^{3+} selective layers are composed of aromatic hydroxyl groups. These acidic hydroxyl groups can dissociate and form the conjugate base through an acid-base reaction with water. Hence, in a hydrated state, the TA-Fe^{3+} selective layer is likely to have a negative surface charge. Fig. 6 shows that all 4 TFC membranes have negative zeta potentials. Comparatively, the TA-Fe^{3+} membranes have a lower absolute zeta potential than the PAN pristine support. This behavior led us to a conjecture that the deposition of the hydrophilic TA-Fe^{3+} layer brings about two competing phenomena which eventually determine zeta potential values of the TFC membranes. Prevention of the preferential adsorption of hydroxide ions of the electrolyte solution at the membrane surface and dissociation of the aromatic hydroxyl groups of TA. As the Fe^{3+} content of the casting solution increases, the surface of the membranes becomes covered by a compact TA-Fe^{3+} layer and the dissociation of the aromatic hydroxyl groups becomes the only

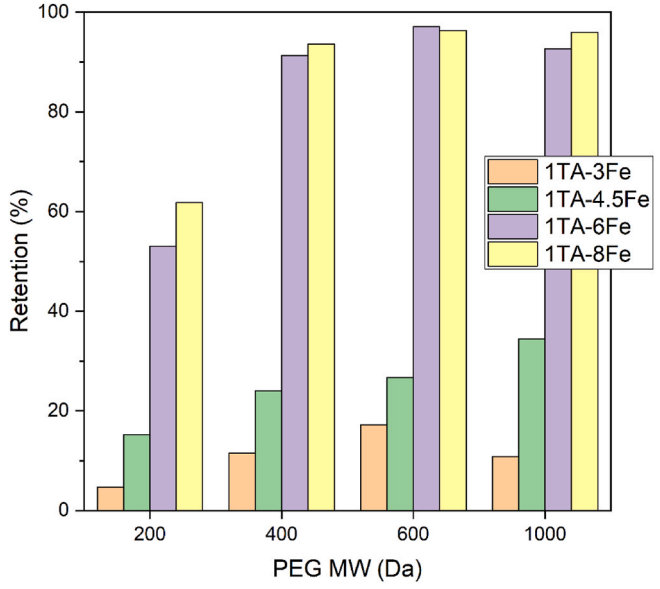

Fig. 5. Retention of PEG having molecular weight 200, 400, 600 and 1000 Da for respective 1 g/L aqueous solutions.

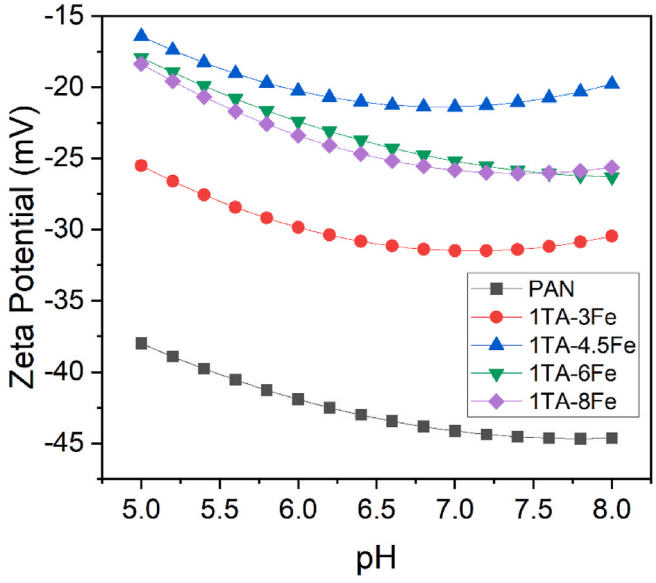

Fig. 6. Membrane zeta potential as a function of pH using 1 mM NaCl aqueous solution as electrolyte.

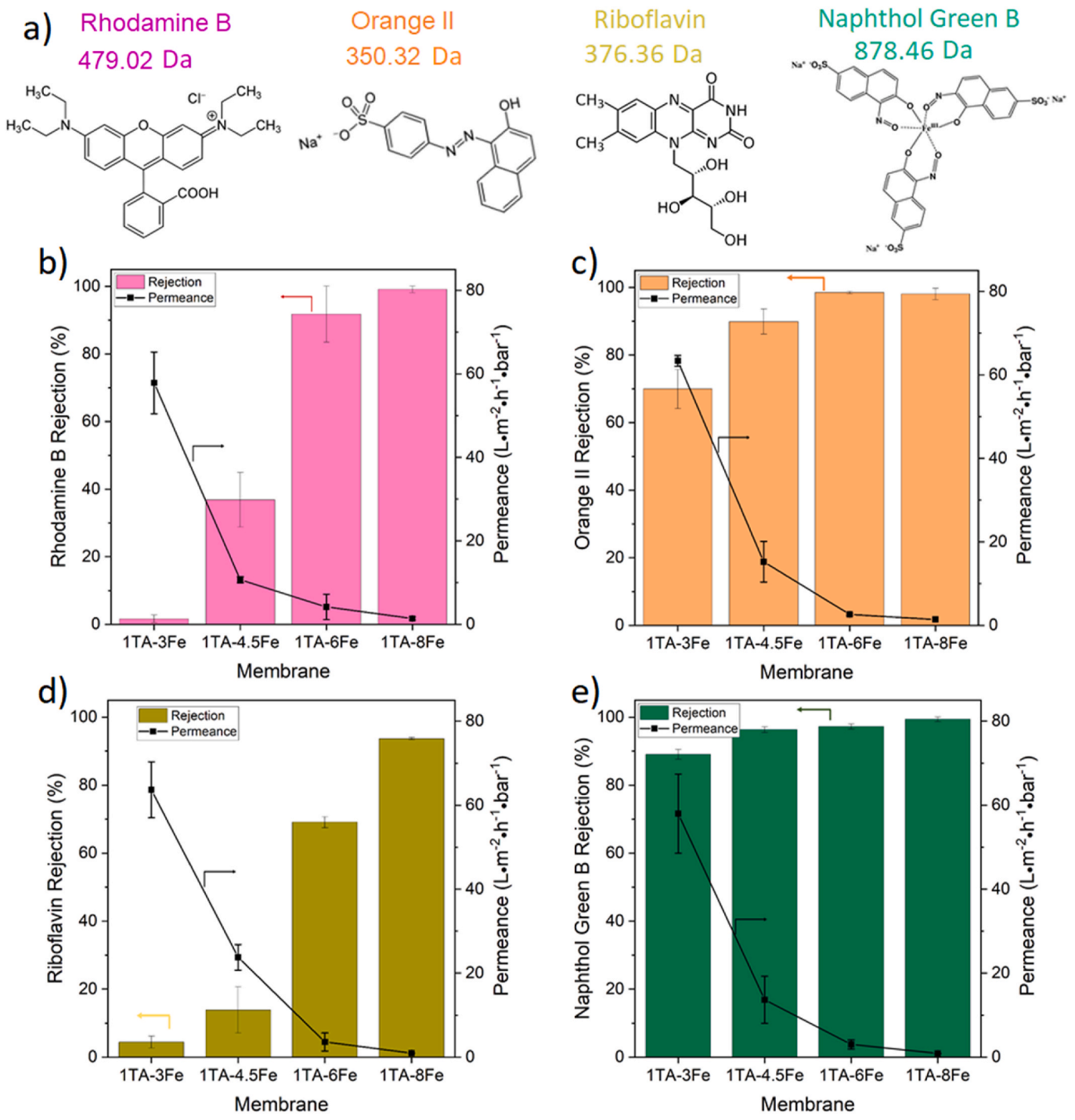

Fig. 7. a) Chemical structure of rhodamine B, orange II, riboflavin and naphthol green B. Permeance of 0.1 mM aqueous solutions and retention of b) rhodamine B, c) orange II, d) riboflavin and e) naphthol green B. (For interpretation of the references to colour in this figure legend, the reader is referred to the Web version of this article.)

determining factor of the negative zeta potential value. The dissociation of functional groups is dependent on the pH of the aqueous solution. Hence, a slightly higher pH dependence of the zeta potential was observed for 1TA-6Fe and 1TA-8Fe compared to those of PAN, 1TA-3Fe and 1TA-4.5Fe. A decrease of the absolute value of membranes' zeta potential was observed with the pH of streaming solution due to a decrease in the ionization of acidic functional groups, i.e., the aromatic hydroxyl groups of TA. However, the slightly lower negative zeta potential values of 1TA-4.5Fe compared to 1TA-6Fe and 1TA-8Fe remains unclear.

3.5. Retention of charged and neutral molecules from aqueous solution

The separation performances of the TFC membranes were further investigated through retention tests of model molecules. The retention of rhodamine B, orange II, naphthol green B and riboflavin (vitamin B2) from their respective 0.1 mM aqueous solution was investigated (Fig. 7). The permeance of these aqueous solutions gradually decreased through the TFC membranes with increasing Fe^{3+} concentration in the casting solution. The permeance of the four aqueous solutions through each of the TFC membranes did not show a substantial difference. However, the

retention of the organic molecules varies significantly based on their size and charge. In a hydrated state rhodamine B (Mw = 479.02 Da) acquires a positive charge (1+) whereas riboflavin (Mw = 376.36 Da) is neutral (0). Both orange II (Mw = 350.32 Da) and naphthol green B (Mw = 878.46 Da) are negatively charged (1- and 3-) dyes [39]. The molecular weight of rhodamine B is significantly higher than the molecular weight cut-off of 1TA-6Fe and 1TA-8Fe (section 3.3). Consequently, these two membranes retained rhodamine B almost completely from its aqueous solution. The retentions of rhodamine B by 1TA-3Fe, 1TA-4.5Fe, 1TA-6Fe and 1TA-8Fe were 2%, 37%, 97% and 99%, respectively (Fig. 7b). This trend suggests size exclusion plays an important role in the retention of rhodamine B by the TFC membranes. However, the retention of rhodamine B is only partially attributed to the pore size of membranes. Due to its counter-ionic behavior towards the surface of the selective layer, retention through adsorption cannot be overlooked. For this, the adsorption behavior of the dyes was analyzed by immersing the PAN membrane and one of the TFC membranes (i.e., 1TA-4.5Fe) in all four solutions overnight. As shown in Fig. 8, both the PAN support and the TFC membrane had a strong affinity towards rhodamine B, which led to strong adsorption. However, no adsorption of riboflavin, orange II and naphthol green B was observed in PAN and 1TA-4.5Fe.

The negatively charged dyes, orange II and naphthol green B, were highly rejected by all four membranes. 1TA-3Fe membrane exhibited 70% and 89% rejection towards orange II and naphthol green B, respectively. Orange II was retained in the range of 90–99% whilst naphthol green B was retained 96–99% by all other relatively dense membranes, prepared at higher iron concentrations. The enhanced retention of the negatively charged dyes is attributed to a combined effect of size sieving and charge repulsion. As explained, in section 3.4 the presence of aromatic hydroxyl groups induce negative charge at the membrane surface of the TFC membranes. Conversely, a low riboflavin rejection was observed for 1TA-3Fe and 1TA-4.5Fe membranes, with rejection values of 4% and 14%, respectively. Besides, 1TA-6Fe and 1TA-8Fe membranes displayed an improved rejection of 69.1% and 94%, respectively. The molecular weight of riboflavin is comparable to the molecular cut-off determined with PEG of 1TA-8Fe (~375 Da) and slightly lower than that of 1TA-6Fe (~390 Da). As the retention of the neutral riboflavin is determined only by size exclusion a significant difference of riboflavin retention by 1TA-8Fe and 1TA-6Fe is observed. The molecular weight of orange II is slightly smaller than the molecular weight of riboflavin. However, the small difference of molecular cut-off of 1TA-8Fe and 1TA-6Fe has no influence on the retention of orange II. Both 1TA-8Fe and 1TA-6Fe retain approximately 98% of orange II. As the size of orange II and riboflavin are rather similar, it is evident from Fig. 4b and c, unlike riboflavin, a combined effect of size selectivity and charge repulsion (i.e., Donnan exclusion) determines the retention of orange II by the TFC membranes. This effect can be distinguished more clearly in 1TA-3Fe and 1TA-4.5 Fe. For instance, 1TA-4.5Fe membrane displayed a retention of 90% towards the negatively charged orange II whilst uncharged riboflavin retention was only 14% despite their comparable molecular weights. Likewise, according to Fig. 5, the retention of neutral PEG with Mw = 400 Da by 1TA-4.5Fe is around 24%. The Donnan exclusion mechanism becomes more dominant at higher membrane charge density [40] and for multivalent permeating ions. While orange II is a monovalent anion, naphthol green B is a trivalent anion in aqueous solution. Moreover, the molecular weight of naphthol green B is 2.5 times higher than that of orange II. Therefore, the combined influence of Donnan exclusion and size sieving leads to the high retention of naphthol green B by the TFC membranes as depicted in Fig. 7e.

The ideal selectivity of the TFC membranes for three pairs of dyes are listed in Table 3. The riboflavin/orange II and riboflavin/naphthol green B selectivities demonstrate that these TFC membranes are capable of separating neutral and negatively charged molecules efficiently. From the above discussion, it is clear that the riboflavin/orange II selectivity is a consequence of Donnan exclusion and the riboflavin/naphthol green B originates from the combined effect of size and Donnan exclusion. 1TA-6Fe has the highest riboflavin/orange II selectivity (20.6) while 1TA-4.5 has the highest riboflavin/naphthol green B selectivity (23.4). Although the selectivity of orange II/naphthol green B is also determined by a combined size and Donnan exclusion mechanism, the selectivity values of this pair are comparatively low. Both 1TA-3Fe and 1TA-4.5Fe show a selectivity of 2.8 for orange II/naphthol green B. Among the four TFC membranes, the 1TA-4.5Fe has the best combination of permeance and selectivity of 3 pairs of molecules.

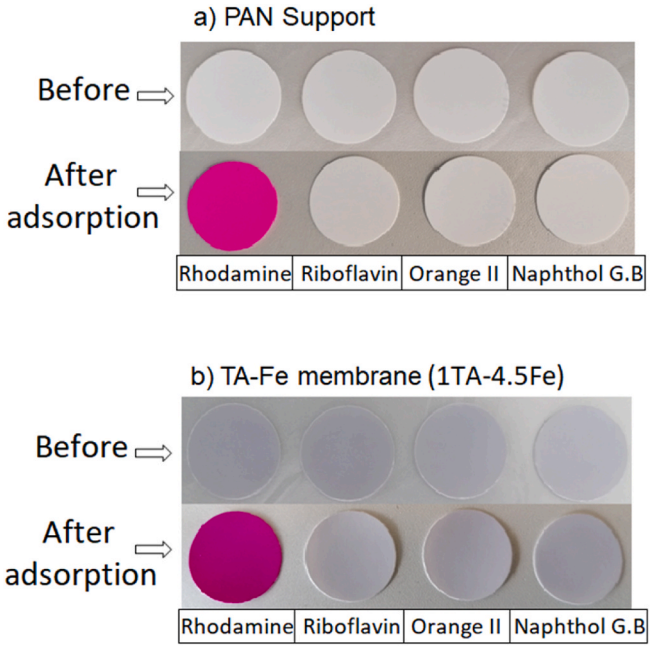

Fig. 8. Adsorption of rhodamine B, riboflavin, orange II and naphthol green B on a) PAN membrane b) 1TA-4.5Fe membrane. (For interpretation of the references to colour in this figure legend, the reader is referred to the Web version of this article.)

3.6. Antifouling behavior

The antifouling properties of 1TA-3Fe, 1TA-4.5Fe, 1TA-6Fe and 1TA-8Fe membranes were investigated using aqueous solutions of humic acid. The fouling resistance study of these membranes was comprised of five stages of filtration operation including two cycles of humic acid solution filtration. Time dependent normalized flux of the membranes is shown in Fig. 9a and b. In all cases, the membranes showed a decline in permeate flux. Large decline of fluxes during humic acid solution filtration were observed. A severe decline of the normalized flux indicates fouling of the membrane surface and pore walls. Generally, there are three main mechanisms governing fouling by humic acid; adsorption, deposition, and pore blocking by aggregate deposition [41]. Adsorption of humic acid on the membrane skin layer and infiltration of the small humic acid molecules to block pores cause initial stages flux decline [42]. A large humic acid aggregates deposited as cake layer on

Table 3
Selectivity of the different membranes obtained from single dye measurements.

Membrane prepared at →	1TA-3Fe	1TA-4.5Fe	1TA-6Fe	1TA-8Fe
Riboflavin to Orange II selectivity	3.2	8.5	20.6	3.2
Riboflavin to Naphthol green B selectivity	8.7	23.4	11.2	10.1
Orange II to Naphthol green B selectivity	2.8	2.8	0.5	3.2

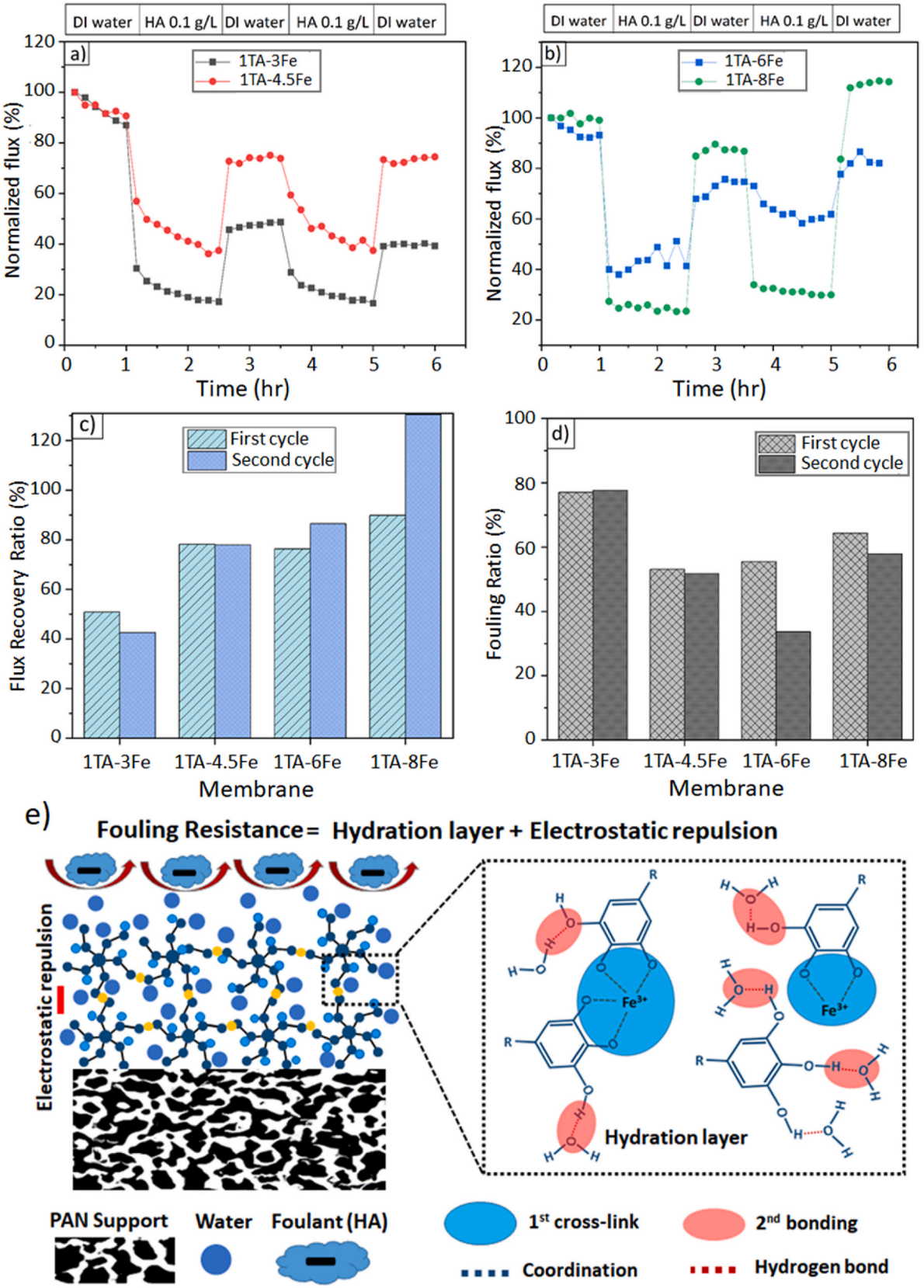

Fig. 9. Evaluation of antifouling properties of TA-Fe^{3+} selective layers. Flux versus time for TA-Fe^{3+} membranes synthesized at (a) 1TA-3Fe and 1TA-4.5Fe, and b) 1TA-6Fe and 1TA-8Fe weight ratio of tannic acid to $FeCl_3{\cdot}6H_2O$. c) Water flux recovery ratio after each cycle. d) Total fouling ratio after each cycle. e) schematic diagram on how TA-Fe complex can enhance the anti-fouling: both hydration layer formed on the TA-Fe TFC surface via hydrogen bonding interaction with TA and the negative surface charge of the membranes contribute to fouling resistance.

the upstream side the membrane especially contributes to a higher flux decline in porous membranes due to higher relative hydraulic resistance. 1TA-3Fe membrane demonstrated a poor antifouling property. A lower flux decline was observed during humic acid filtration at higher Fe ratio. 1TA-4.5Fe membranes showed a flux recovery ratio (F_{RR}) of around 81% in the first cycle while 1TA-3Fe exhibited only 51% (Fig. 9a).The flux recovery ratio increased with increase of Fe^{3+} concentration in the casting solution (Fig. 9c). This indicated an increasing antifouling performance [42]. A comparison of Figs. 2 and 9 shows that with the increase of Fe^{3+} content of the casting solution, the surface porosity of the membranes decreases while the fouling resistance increases. However, 1TA-6Fe and 1TA-8Fe membranes showed an increase in FRR during the second cycle. The flux recovery of 1TA-8Fe especially exceeded 100%. This indicates the TA-Fe layer of 1TA-8Fe layer was not stable during the second washing cycle. A TA-Fe^{3+} complex aggregates were observed during SEM and EDX analysis of this dense layer, which is discussed in detail in section 3.1 of this paper. The increase in FRR implies that these aggregates, which were blocking pores are dissociated after Humic acid filtration and membrane cleaning process. Hence, it is not desirable to use a large excess of Fe^{3+} in the casting solution.

To the general understanding, fouling is influenced by membrane characteristics, mainly hydrophilicity, surface charge and surface roughness. The membranes improved F_{RR} most probably is due to the enhancement of hydrophilicity from the abundant hydroxyl groups. Membrane hydrophilicity inhibits adsorption of foulants such as humic acid. This is due to the increase of interfacial energy of interaction between the foulant molecules and membrane surface functional groups. Catechol containing polyphenols such as dopamine and tannic acid generally exhibit excellent antifouling activity [11,43]. Moreover, hydrogen bonding sites in TA favor adsorption water molecules than the foulant, imparting fouling resistance. TA prevents fouling and concentration polarization by formation of a hydration layer. The stable hydration layer reduces formation of a stationary layer over the synthesized selective layer. Moreover, the negative charged surface of TA-Fe TFC membranes prevent fouling through electrostatic interaction with the foulant material (i.e., humic acid). The schematic diagram of fouling resistance through the synergistic effect of these two mechanisms is shown in Fig. 9e.

4. Conclusion

The coordination-based self-assembly between polyphenols and metal ions offers an ecofriendly and facile method to fabricate membranes. In this work, by using only aqueous solutions of tannic acid (TA) and $FeCl_3{\cdot}6H_2O$ (Fe^{3+}) nanofiltration TFC membranes with approximately 10 nm thick TA-Fe^{3+} selective layers were prepared with various content of Fe^{3+}. Scanning electron microscopy, infrared spectroscopy, water contact angle and zeta potential characterizations showed that the membranes' surface porosity, pore size and hydrophilicity can be fine-tuned by varying the content of Fe^{3+}. The pure water permeance of the prepared TFC membranes systematically changed between 0.93 L $m^{-2}{\bullet}h^{-1}{\bullet}bar^{-1}$ to 62 L $m^{-2}{\bullet}h^{-1}{\bullet}bar^{-1}$ due to change of the Fe^{3+} content of the casting solution. Hence the reported selectively fabrication method is an ecofriendly method to bridge the gap between ultrafiltration and nanofiltration. The retention of neutral and charged organic molecules having 200–1000 Da revealed that the synthesized TFC membranes having TA-Fe^{3+} selective layers can be used in application where either loose nanofiltration or tight nanofiltration membranes are required. While the cationic rhodamine b strongly adsorbs on the PAN support and the TFC membranes, no adsorption of the anionic orange II, naphthol green B and neutral riboflavin were observed. The results revealed that the retention of anionic dyes by the TFC membranes were dictated by a combination of size and Donnan exclusion. This work demonstrates that the controlled deposition of the ultrathin TA-Fe^{3+} selective layer on PAN allows to tune i) the retention of anionic dyes from aqueous solution, ii) the separation of anionic molecules from neutral molecules and iii) the separation of anionic molecules from each other. Moreover, the TFC membranes exhibited a good antifouling behavior and robustness towards cleaning procedures using water. This highlights the potential of the TFC membranes having TA-Fe^{3+} selective layer to be utilized for water and wastewater treatment as well as for the recovery of dyes from a mixture.

Funding

This work was funded by the Hereon-I^{2}B-Project NanoMem.

CRediT authorship contribution statement

Hluf Hailu Kinfu: Conceptualization, Methodology, Investigation, Formal analysis, Writing – original draft. **Md. Mushfequr Rahman:** Conceptualization, Writing – original draft, Writing – Review & editing, Funding acquisition, Project administration, Supervision. **Erik Sebastian Schneider:** Investigation, Writing – Review & editing. **Nicolás Cevallos-Cueva:** Methodology, Writing – Review & editing. **Volker Abetz:** Supervision, Writing – Review & editing.

Declaration of competing interest

The authors declare no conflict of interest for the paper - Charge and size selective thin film composite membranes having tannic acid – ferric ion network as selective layer.

Data availability

Data will be made available on request.

Acknowledgments

The authors acknowledge Maren Brinkmann for the PEG retention analysis in GPC, Juliana Clodt for preparing the polyacrylonitrile support and Jan Pohlmann for setting up the flux and retention measurement facilities.

Appendix A. Supplementary data

Supplementary data to this article can be found online at https://doi.org/10.1016/j.memsci.2023.121709.

References

[1] B. Van der Bruggen, M. Mänttäri, M. Nyström, Drawbacks of applying nanofiltration and how to avoid them: a review, Sep. Purif. Technol. 63 (2008) 251–263.
[2] O. Labban, C. Liu, T.H. Chong, J.H. Lienhard V, Fundamentals of low-pressure nanofiltration: membrane characterization, modeling, and understanding the multi-ionic interactions in water softening, J. Membr. Sci. 521 (2017) 18–32.
[3] A.W. Mohammad, Y.H. Teow, W.L. Ang, Y.T. Chung, D.L. Oatley-Radcliffe, N. Hilal, Nanofiltration membranes review: recent advances and future prospects, Desalination 356 (2015) 226–254.
[4] R.N. Zhang, M.R. He, D.H. Gao, Y.N. Liu, M.Y. Wu, Z.W. Jiao, Y.L. Su, Z.Y. Jiang, Polyphenol-assisted in-situ assembly for antifouling thin-film composite nanofiltration membranes, J. Membr. Sci. 566 (2018) 258–267.
[5] Y.F. Li, Y.L. Su, J.Y. Li, X.T. Zhao, R.N. Zhang, X.C. Fan, J.N. Zhu, Y.Y. Ma, Y. Liu, Z.Y. Jiang, Preparation of thin film composite nanofiltration membrane with improved structural stability through the mediation of polydopamine, J. Membr. Sci. 476 (2015) 10–19.
[6] X. Fang, J. Li, X. Li, S. Pan, X. Sun, J. Shen, W. Han, L. Wang, B. Van der Bruggen, Iron-tannin-framework complex modified PES ultrafiltration membranes with enhanced filtration performance and fouling resistance, J. Colloid Interface Sci. 505 (2017) 642–652.
[7] R.M. DuChanois, R. Epsztein, J.A. Trivedi, M. Elimelech, Controlling pore structure of polyelectrolyte multilayer nanofiltration membranes by tuning polyelectrolyte-salt interactions, J. Membr. Sci. 581 (2019) 413–420.
[8] L.Y. Ng, A.W. Mohammad, C.Y. Ng, A review on nanofiltration membrane fabrication and modification using polyelectrolytes: effective ways to develop

membrane selective barriers and rejection capability, Adv. Colloid Interface Sci. 197 (2013) 85–107.
[9] W. Yuan, G.M. Weng, J. Lipton, C.M. Li, P.R. Van Tassel, A.D. Taylor, Weak polyelectrolyte-based multilayers via layer-by-layer assembly: approaches, properties, and applications, Adv. Colloid Interface Sci. 282 (2020), 102200.
[10] L. Fan, Y. Ma, Y. Su, R. Zhang, Y. Liu, Q. Zhang, Z. Jiang, Green coating by coordination of tannic acid and iron ions for antioxidant nanofiltration membranes, RSC Adv. 5 (2015) 107777–107784.
[11] H.J. Kim, D.G. Kim, H. Yoon, Y.S. Choi, J. Yoon, J.C. Lee, Polyphenol/FeIII complex coated membranes having multifunctional properties prepared by a one-step fast assembly, Adv. Mater. Interfac. 2 (2015) 1–8.
[12] H. Ejima, J.J. Richardson, K. Liang, J.P. Best, M.P. Van Koeverden, G.K. Such, J. Cui, F. Caruso, One-step assembly of coordination complexes, Science 341 (2013) 154–157.
[13] S. Kim, D.S. Kim, S.M. Kang, Reversible layer-by-layer deposition on solid substrates inspired by mussel byssus cuticle, Chem. Asian J. 9 (2014) 63–66.
[14] J.J. Wilker, The iron-fortified adhesive system of marine mussels, Angew. Chem. Int. Ed. 49 (2010) 8076–8078.
[15] A.K. Koopmann, C. Schuster, J. Torres-Rodríguez, S. Kain, H. Pertl-Obermeyer, A. Petutschnigg, N. Hüsing, Tannin-based hybrid materials and their applications: a review, Molecules 25 (2020) 1–32.
[16] Y. Ping, J. Guo, H. Ejima, X. Chen, J.J. Richardson, H. Sun, F. Caruso, pH-responsive capsules engineered from metal–phenolic networks for anticancer drug delivery, Small 11 (2015) 2032–2036.
[17] X.-R. Song, S.-H. Li, J. Dai, L. Song, G. Huang, R. Lin, J. Li, G. Liu, H.-H. Yang, Polyphenol-Inspired facile construction of smart assemblies for ATP- and pH-responsive tumor MR/optical imaging and photothermal therapy, Small 13 (2017), 1603997.
[18] Y.Z. Song, X. Kong, X. Yin, Y. Zhang, C.C. Sun, J.J. Yuan, B. Zhu, L.P. Zhu, Tannin-inspired superhydrophilic and underwater superoleophobic polypropylene membrane for effective oil/water emulsions separation, Colloids Surf. A Physicochem. Eng. Asp. 522 (2017) 585–592.
[19] J. Wei, Y. Liang, Y. Hu, B. Kong, J. Zhang, Q. Gu, Y. Tong, X. Wang, S.P. Jiang, H. Wang, Hydrothermal synthesis of metal-polyphenol coordination crystals and their derived metal/N-doped carbon composites for oxygen electrocatalysis, Angew. Chem. 55 (2016) 12470–12474.
[20] C. Ringwald, V. Ball, Layer-by-layer deposition of tannic acid and Fe3+ cations is of electrostatic nature but almost ionic strength independent at pH 5, J. Colloid Interface Sci. 450 (2015) 119–126.
[21] C.E. Lin, M.Y. Zhou, W.S. Hung, B.K. Zhu, K.R. Lee, L.P. Zhu, L.F. Fang, Ultrathin nanofilm with tailored pore size fabricated by metal-phenolic network for precise and rapid molecular separation, Sep. Purif. Technol. 207 (2018) 435–442.
[22] Y.J. Shen, L.F. Fang, Y. Yan, J.J. Yuan, Z.Q. Gan, X.Z. Wei, B.K. Zhu, Metal-organic composite membrane with sub-2 nm pores fabricated via interfacial coordination, J. Membr. Sci. 587 (2019), 117146-117146.
[23] H. Wu, J. Xie, L. Mao, One-pot assembly tannic acid-titanium dual network coating for low-pressure nanofiltration membranes, Sep. Purif. Technol. 233 (2020), 116051-116051.
[24] S. Kasemset, A. Lee, D.J. Miller, B.D. Freeman, M.M. Sharma, Effect of polydopamine deposition conditions on fouling resistance, physical properties, and permeation properties of reverse osmosis membranes in oil/water separation, J. Membr. Sci. 425–426 (2013) 208–216.
[25] Y. Xiao, D. Guo, T. Li, Q. Zhou, L. Shen, R. Li, Y. Xu, H. Lin, Facile fabrication of superhydrophilic nanofiltration membranes via tannic acid and irons layer-by-layer self-assembly for dye separation, Appl. Surf. Sci. 515 (2020), 146063-146063.
[26] L.E. Peng, Z. Yao, J. Chen, H. Guo, C.Y. Tang, Highly selective separation and resource recovery using forward osmosis membrane assembled by polyphenol network, J. Membr. Sci. 611 (2020), 118305-118305.
[27] T. Chakrabarty, L. Pérez-Manríquez, P. Neelakanda, K.V. Peinemann, Bioinspired tannic acid-copper complexes as selective coating for nanofiltration membranes, Sep. Purif. Technol. 184 (2017) 188–194.
[28] D. Liu, Y. Chen, T.T. Tran, G. Zhang, Facile and rapid assembly of high-performance tannic acid thin-film nanofiltration membranes via Fe3+ intermediated regulation and coordination, Sep. Purif. Technol. 260 (2021), 118228-118228.
[29] F. You, Y. Xu, X. Yang, Y. Zhang, L. Shao, Bio-inspired Ni2+-polyphenol hydrophilic network to achieve unconventional high-flux nanofiltration membranes for environmental remediation, Chem. Commun. 53 (2017) 6128–6131.
[30] M.A. Rahim, H. Ejima, K.L. Cho, K. Kempe, M. Müllner, J.P. Best, F. Caruso, Coordination-driven multistep assembly of metal-polyphenol films and capsules, Chem. Mater. 26 (2014) 1645–1653.
[31] Z. Zhang, M.M. Rahman, C. Abetz, B. Bajer, J. Wang, V. Abetz, Quaternization of a polystyrene-block-poly(4-vinylpyridine) isoporous membrane: an approach to tune the pore size and the charge density, Macromol. Rapid Commun. 40 (2019), 1800729.
[32] S. Datta, A.T. Conlisk, D.M. Kanani, A.L. Zydney, W.H. Fissell, S. Roy, Characterizing the surface charge of synthetic nanomembranes by the streaming potential method, J. Colloid Interface Sci. 348 (2010) 85–95.
[33] S. Déon, P. Fievet, C. Osman Doubad, Tangential streaming potential/current measurements for the characterization of composite membranes, J. Membr. Sci. 423–424 (2012) 413–421.
[34] S. Glass, T. Mantel, M. Appold, S. Sen, M. Usman, M. Ernst, V. Filiz, Amine-terminated PAN membranes as anion-adsorber materials, Chem. Ing. Tech. 93 (2021) 1396–1400.
[35] Y. Xu, J. Lin, C. Gao, B. Van der Bruggen, Q. Shen, H. Shao, J. Shen, Preparation of high-flux nanoporous solvent resistant polyacrylonitrile membrane with potential fractionation of dyes and Na2SO4, Ind. Eng. Chem. Res. 56 (2017) 11967–11976.
[36] A.A. Kishore Chand, B. Bajer, E.S. Schneider, T. Mantel, M. Ernst, V. Filiz, S. Glass, Modification of polyacrylonitrile ultrafiltration membranes to enhance the adsorption of cations and anions, Membranes 12 (2022) 580.
[37] R. Zimmermann, U. Freudenberg, R. Schweiß, D. Küttner, C. Werner, Hydroxide and hydronium ion adsorption — a survey, Curr. Opin. Colloid Interface Sci. 15 (2010) 196–202.
[38] T. Luxbacher, The Zeta Potential for Solid Surface Analysis : a Practical Guide to Streaming Potential Measurement, first ed., 2014.
[39] Z. Zhang, M.M. Rahman, C. Abetz, A.-L. Höhme, E. Sperling, V. Abetz, Chemically tailored multifunctional asymmetric isoporous triblock terpolymer membranes for selective transport, Adv. Mater. 32 (2020), 1907014.
[40] R. Epsztein, E. Shaulsky, N. Dizge, D.M. Warsinger, M. Elimelech, Role of ionic charge density in donnan exclusion of monovalent anions by nanofiltration, Environ. Sci. Technol. 52 (2018) 4108–4116.
[41] W. Yuan, A.L. Zydney, Humic acid fouling during ultrafiltration, Environ. Sci. Technol. 34 (2000) 5043–5050.
[42] X. Zhu, H. Liang, X. Tang, L. Bai, X. Zhang, Z. Gan, X. Cheng, X. Luo, D. Xu, G. Li, Supramolecular-based regenerable coating layer of a thin-film composite nanofiltration membrane for simultaneously enhanced desalination and antifouling properties, ACS Appl. Mater. Interfaces 11 (2019) 21137–21149.
[43] S. Kasemset, A. Lee, D.J. Miller, B.D. Freeman, M.M. Sharma, Effect of polydopamine deposition conditions on fouling resistance, physical properties, and permeation properties of reverse osmosis membranes in oil/water separation, J. Membr. Sci. 425 (2013) 208–216.

Chapter 4. Using the Assembly Time as a Tool to Control the Surface Morphology and Separation Performance of Membranes with a Tannic Acid–Fe^{3+} Selective Layer

This chapter investigates how the assembly time affects the surface morphology, and filtration performance of MPN-based TFC membranes. Moreover, this chapter highlights the effectiveness of TA–Fe^{3+} selective layer in separating similarly sized small organic molecules based on their charge groups. Filtration experiments were performed in both single- and mixed-solute experiments to analyze the separation performance of the MPN active layer. The membrane fabrication method introduced in Chapter 3 is adapted. While two-TA-Fe^{3+} layers were deposited over the porous support at a fixed TA and Fe^{3+} concentrations after optimizing the TA/Fe^{3+} ratio in Chapter 3, the time for TA adsorption and complex formation is varied to fine-tune the metal-phenolic network structure and property. It was found that prolonging the assembly time leads to the formation of selective layers with smaller effective pore sizes having low water permeance indicating higher resistance to water transport. These membranes exhibited low rejection towards riboflavin and poly(ethylene glycol), but high rejection for anionic dyes orange II and naphthol green B. Excellent ideal and real selectivities in the range 2 – 27 were achieved, revealing a charge-selective nature of the prepared membranes. It is discussed that electrostatic repulsive interaction between the solutes and TA-Fe^{3+} membrane surface plays a significant role compared to size sieving. The selective removal rates for small molecular weight solutes make these membranes suitable for industrial wastewater treatment, particularly from textile plants. This work demonstrates that assembly time is a crucial parameter for controlling the permeance, rejection, and selectivity of these membranes.

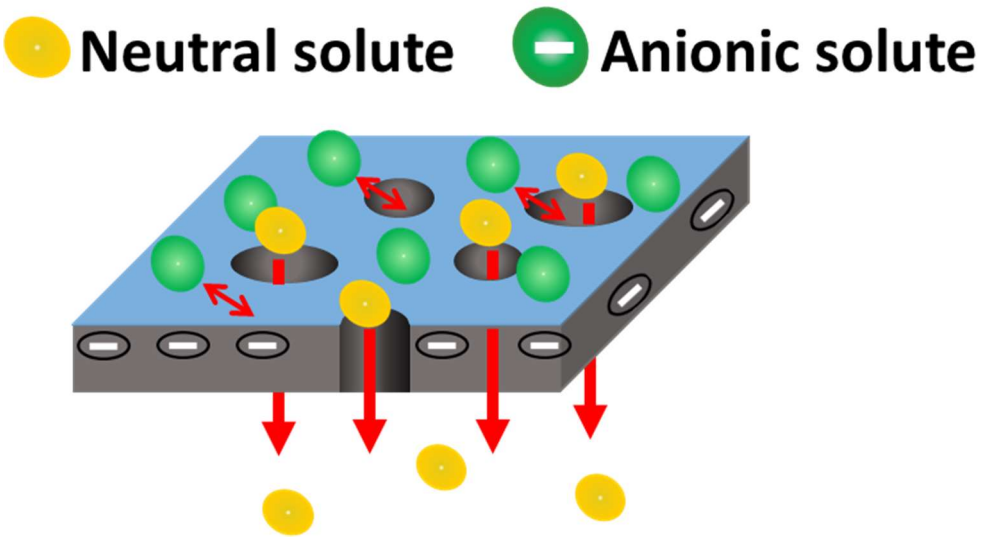

membranes

MDPI

Article

Using the Assembly Time as a Tool to Control the Surface Morphology and Separation Performance of Membranes with a Tannic Acid–Fe^{3+} Selective Layer

Hluf Hailu Kinfu [1], Md. Mushfequr Rahman [1,*], Erik S. Schneider [1], Nicolás Cevallos-Cueva [1] and Volker Abetz [1,2]

[1] Helmholtz-Zentrum Hereon, Institute of Membrane Research, Max-Planck-Straße 1, 21502 Geesthacht, Germany; hluf.kinfu@hereon.de (H.H.K.); erik.schneider@hereon.de (E.S.S.); nicolas.cevallos-cueva@hereon.de (N.C.-C.); volker.abetz@hereon.de (V.A.)

[2] Institute of Physical Chemistry, University of Hamburg, Martin-Luther-King-Platz 6, 20146 Hamburg, Germany

* Correspondence: mushfequr.rahman@hereon.de; Tel.: +49-4152872446

Abstract: Thin-film composite (TFC) membranes containing a metal–polyphenol network (MPN)-based selective layer were fabricated on a porous polyacrylonitrile support. The MPN layer was formed through coordination-based self-assembly between plant-based tannic acid (TA) and an Fe^{3+} ion. For the first time, we demonstrate that TFC membranes containing TA-Fe^{3+} selective layers can separate small organic solutes in aqueous media from equimolar mixtures of solutes. The effect of the assembly time on the characteristics and performance of the fabricated selective layer was investigated. An increase in the assembly time led to the formation of selective layers with smaller effective pore sizes. The tannic acid–Fe^{3+} selective layer exhibited a low rejection towards neutral solutes riboflavin and poly(ethylene glycol) while high rejections were observed for anionic dyes of orange II and naphthol green B. Permeation selectivities in the range of 2–27 were achieved between neutral and charged dyes in both single- and mixed-solute experiments, indicating the significant role of Donnan exclusion and the charge-selective nature of the membranes. The rejection efficiency improved with an increasing assembly time. Overall, this study demonstrates that the assembly time is a vital casting parameter for controlling the permeance, rejection and selectivity of thin-film composite membranes with a tannic acid–Fe^{3+} selective layer.

Keywords: metal–polyphenol network membranes; polyphenol; tannic acid–metal ion coordination; TFC membranes; assembly time

Citation: Kinfu, H.H.; Rahman, M.M.; Schneider, E.S.; Cevallos-Cueva, N.; Abetz, V. Using the Assembly Time as a Tool to Control the Surface Morphology and Separation Performance of Membranes with a Tannic Acid–Fe^{3+} Selective Layer. *Membranes* **2024**, *14*, 133. https://doi.org/10.3390/membranes14060133

Academic Editor: Asuncion Maria Hidalgo

Received: 26 April 2024
Revised: 26 May 2024
Accepted: 4 June 2024
Published: 6 June 2024

1. Introduction

Selectivity severely restricts the scope of separations that can be achieved through membrane-based processes [1]. Engineering membranes for molecular separation remains a challenge. An increase in the selectivity tends to significantly decrease the permeability while increasing the cost and energy consumption. Available commercial membranes remove all solutes above a given size [2]. "Chemoselective" membranes that combine size-based selectivity with a solute–functional group differentiation capability can enable researchers to design membranes for customer applications with huge potential in the separation and purification process [3]. Although there are some attempts at separating similar-sized components through electrostatic contribution, successful separation of the desired components from one another still requires further work on the manipulation of the membrane chemistry [2]. In recent years, efforts have been devoted to developing membranes capable of regulating the permeation and rejection of small molecules of similar sizes through solute–membrane interaction in addition to size-based fractionation [3–8].

Thin-film composite (TFC) membranes are typically used for nanofiltration and reverse osmosis due to their high solute rejection properties [9]. TFC membranes are fabricated by constructing a dense selective layer over a porous polymer substrate, usually via interfacial polymerization (IP). However, often, such TFC membranes demonstrate rather poor selectivity between different solutes [9]. Therefore, the development of novel membranes that offer both high permeance and adequate selectivity is required to enhance the separation efficiency. Thin-film nanocomposite (TFN) membranes with incorporated nanomaterials have recently been developed [10–13] and shown to be promising materials in addressing these issues. TFN selective layers increase the surface hydrophilicity and membrane permeability by providing water pathways and enhance perm-selectivity [14,15]. However, the synthesis of TFN films is usually complicated, involving multi-step nanomaterial synthesis, separation and purification [15]. Scaling up the fabrication of TFN membranes also remains a concern [14]. More importantly, the fabrication of both TFC and TFN selective layers via interfacial polymerization involves the use of a significant amount of toxic and hazardous solvents, which makes the process less environmentally friendly [16–18]. Hence, there is a growing demand for the production of hydrophilic TFC membranes in an ecofriendly approach.

To date, there have been various approaches developed for the fabrication of sustainable TFC membranes. Yang et al. prepared biobased TFC membranes comprising a selective layer obtained from plant-based sources [19]. A green polyamide TFC membrane was fabricated via the interfacial polymerization of natural monomers, that is, genipin in the aqueous phase and priamine in a green organic solvent. Another TFC membrane was recently fabricated using building blocks of chitosan in the aqueous phase and 2,5-furandicarboxaldehyde (FDA) dissolved in the water-immiscible ecofriendly solvent eucalyptol [20]. Park et al. also reported a green way of fabricating a high-performance TFC membrane containing a crosslinked selective layer of priamine covalently bonded through Michael addition and Schiff base reactions to tannic acid [21]. These attempts demonstrate the prospects of breaking away from the toxic monomers besides exploring the use of green solvents.

Tannic acid, a natural polyphenol, can be used for engineering new functional materials [22] such as TFC membranes [23]. Tannic acid's phenolic groups carry negative charges, making them capable of easily chelating positively charged transition metal ions [24]. The formation of tannic acid–metal ion (TA-M^{n+}) complexes arises from the strong coordination between phenolic hydroxyl groups and metal ions [25]. This coordination-driven self-assembly results in the formation of a metal–polyphenol nanofilm over a substrate surface [26], including the fabrication of thin films for membrane processes [25,27–29]. Compared with conventional water treatment membranes, metal–polyphenol network (MPN)-based membranes have several advantages: higher water flux with a comparative rejection of solutes, excellent resistance to fouling, high antimicrobial activity and efficient removal of organic contaminants [25]. More importantly, the metal–tannic acid membrane production is green and low-cost.

MPN has been used as a surface coating of ultrafiltration, nanofiltration and reverse osmosis membranes [15,27,30,31] and for the construction of the selective layer of a membrane [28,32,33]. Tannic-acid-containing membranes have shown excellent performance levels in several applications such as wastewater treatment [32], membrane fouling resistance enhancement [34,35], oil/water emulsion separation [29], desalination [36], separation of ions [33], trace organic contaminants' removal [28] and organic solute separation [33]. Moreover, tannic-acid-based MPN layers can be coated using aqueous solutions, which is ecofriendly. In recent years, the optimization of the casting parameter of TFC membranes containing a tannic acid–metal ion layer has received a lot of attention. Co-deposition and layer-by-layer (LBL) self-assembly are the two widely used procedures for the fabrication of tannic acid–metal ion-containing membranes. Despite the fact that co-deposition enables the fast synthesis of TA–metal ion films [30], the rapid self-assembly makes the process uncontrollable [33]. The LBL technique allows

a better control of the MPN layer coating synthesis and characteristics, which helps to significantly reduce the undesired defects of the selective layer of the membranes [37].

In a previous study [38], we investigated the influence of the TA-to-Fe^{3+} ratio on the surface porosity and filtration properties of the MPN selective layer containing TFC membranes. However, the impact of the assembly time on the structure and performance of TFC membranes containing TA-Fe^{3+} selective layers prepared by LBL remained to be explored. Accordingly, here, we performed a thorough study of the influence of the assembly time on the morphology and separation performance of TFC membranes containing TA-Fe^{3+} selective layers prepared by LBL. The development of membranes for effective solute–solute separation with excellent precision is still in its early phases [39]. In recent years, the development of membranes for the separation of organic solutes with dimensions of 0.5–5 nm has received a lot of attention as there is a lack of commercially available membranes to perform the task [6,7]. In this work, we demonstrate that controlling the assembly time of the formation of TA-Fe^{3+} coordination is an effective tool when performing such separation using TFC membranes containing TA-Fe^{3+} selective layers.

2. Experimental Section

2.1. Materials and Chemicals

The porous polyacrylonitrile (PAN) membrane support was prepared in-house at Helmholtz-Zentrum Hereon. Tannic acid (TA) (1701.2 g/mol), orange II (OR-) (350.32 g/mol), riboflavin (RB0) (376.36 g/mol) and naphthol green B (NGB3-) (878.46 g/mol) were commercially supplied by Sigma-Aldrich Chemie GmbH (Taufkirchen, Germany). $FeCl_3 \cdot 6H_2O$ was obtained from Alfa Aesar GmbH & Co. (Karlsruhe, Germany). Poly(ethylene glycol)s (PEGs) of average molecular weights (Mw) 200, 400, 600 and 1000 g/mol were purchased from VWR International GmbH (Darmstadt, Germany). Hydrochloric acid (HCl, 37%) and sodium hydroxide (NaOH) were supplied by Merck Biosciences GmbH (Darmstadt, Germany) and Sigma-Aldrich, respectively. All the chemicals were analytical-grade reagents and were used as received without further purification.

2.2. Membrane Selective Layer Synthesis

The TA-Fe^{3+} TFC membrane synthesis procedure was reported in our previous work [38]. Briefly, the pristine PAN support was pre-soaked in milli-Q water before further use. Then, the PAN support was fixed to a custom-designed glass plate and clapped with a PTFE frame to ensure that the MPN layer was synthesized only on the top surface of the porous support. Next, the PAN support was subjected to 50 mL TA solution (0.02 w %) for a specified time. The TA-treated porous support was then rinsed with water. Afterwards, 50 mL metal ion solution (0.09 w % $FeCl_3 \cdot 6H_2O$) was added for the same period to coordinate with the already adsorbed TA groups. The TA-Fe^{3+}-coated PAN membrane was further rinsed with pure water and subjected to both TA and Fe^{3+} solutions in the same procedure in a layer-by-layer fashion to prepare a two-TA-Fe^{3+}-layered thin film, as shown in Figure 1. The assembly time was varied to prepare a series of TFC membranes. The PAN support was exposed to both TA and Fe^{3+} solutions for the same duration, i.e., for 1 min, 2.5 min, 4 min or 6 min in each solution, and the corresponding fabricated TFC membranes are labeled MPN-1, MPN-2.5, MPN-4 and MPN-6, respectively.

2.3. Membrane Characterization

Fourier transform infrared spectroscopy (FTIR) using a Bruker Alpha (diamond-ATR unit) (Bruker, Karlsruhe, Germany) was used to analyze the functional groups and confirm the presence of TA in the TA-Fe^{3+} selective layer synthesized over the PAN support. The spectrum of each membrane was measured using 64 scans in the range of 400–4000 cm^{-1} with a resolution of 4 cm^{-1}. Membrane morphological characteristics were characterized by scanning electron microscopy (SEM) (Merlin SEM, Zeiss, Oberkochen, Germany) using accelerating voltages of between 1.5 and 3 kV. Membrane samples were vacuum dried at 60 °C for 72 h before being sputter-coated with 1–1.5 nm platinum using a CCU-010

coating device (Safematic, Switzerland). For cross-sectional image analysis, the membrane samples were prepared by immersing and fracturing them in liquid nitrogen. SEM images based on material contrast using backscattered electrons were also obtained using an in-lens EsB detector. Samples of the membrane cross-section were prepared by argon ion milling at −120 °C and 4 kV for several hours. A precision argon ion beam milling etching and coating system PECS II (Gatan/AMETEK, Pleasanton, CA, USA) was used. The samples were coated with 4 nm carbon before measurement. The hydrophilic properties of the membranes were analyzed by measuring the water contact angle (WCA) using KRUESS Drop Shape Analysis System DSA 100 (FEI part of Thermo Fisher Scientific, Kawasaki, Japan). The investigations were performed in the sessile drop mode with 3 µL of water droplets at room temperature. The membrane surface zeta potential was measured by a SurPASS 3 electrokinetic analyzer (Anton Paar, Graz, Austria) using a background electrolyte solution containing 1 mmol NaCl. The zeta potential measurements were taken in the pH range of 5–8 at room temperature. Energy-dispersive X-ray spectroscopy (EDX) was performed to determine and compare the elemental compositions of the membrane top layers using Extreme as the primary and X-max 150 as the secondary EDX detector (Oxford Instruments, Abingdon, UK). The EDX analysis was performed at a working distance of 5.6 mm, a constant magnification of 5 kx and an acceleration voltage of 1.5 kV.

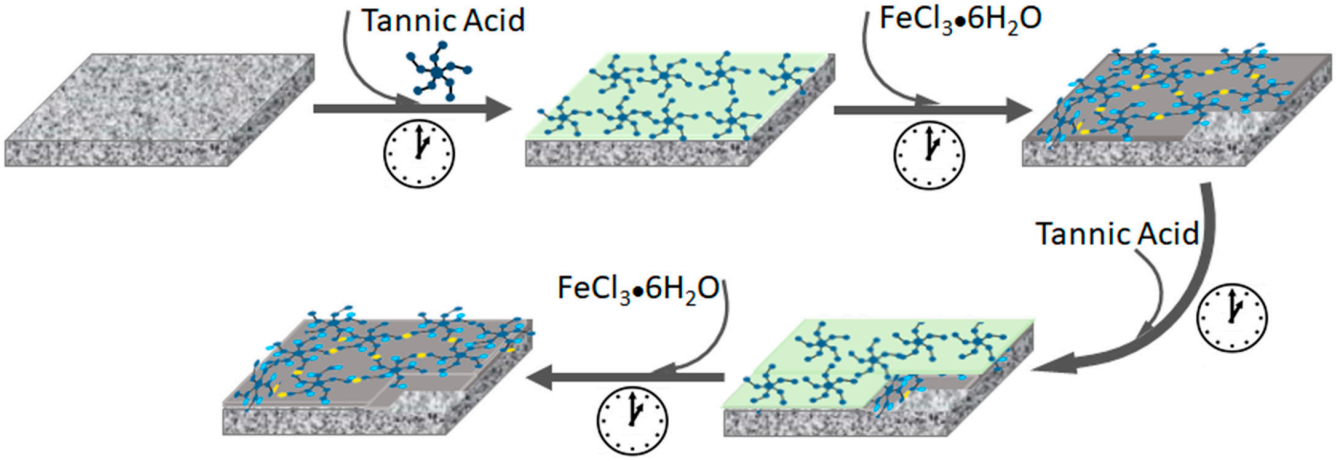

Figure 1. Schematic representation of the fabrication process of the membrane selective layer. TFC membrane containing TA-Fe^{3+} is fabricated by depositing tannic acid and iron aqueous solutions over a porous PAN support in a layer-by-layer technique.

2.4. Evaluation of Membrane Performance

The membrane filtration performance was evaluated with pure water permeance and solute rejection experiments. All experiments were performed in the dead-end filtration mode using a 2.13 cm^2 membrane active area. The membranes were compacted for at least 3 h at 4 bar transmembrane pressure. Then, the pure water permeance, P_w ($L \cdot m^{-2} \cdot h^{-1} \cdot bar^{-1}$), was measured and computed using the following equation:

$$P_w = \frac{V}{A * \Delta t * \Delta P} \quad (1)$$

where V (L) is the volume of permeate collected, A (m^2) is the effective area of the membrane, Δt (h) is the filtration time and ΔP (bar) is the applied transmembrane pressure.

Characterization of the membrane rejection performance was carried out using a stirred test cell from Millipore (EMD Millipore XFUF07601) (Merck Millipore, Darmstadt, Germany) at a stirring speed of 350 rpm in the dead-end filtration mode. The effective membrane area of the test cells was reduced to the desired size with an in-house-made reduction ring. PEG, dyes and Na_2SO_4 were used as solutes for the investigation. All rejection tests were performed at 3 bar transmembrane pressure. The concentrations

in the feed, permeate and retentate from the filtration test using PEG (1 g·L^{-1}) were analyzed using gel permeation chromatography (GPC) (VWR-Hitachi 2130 pump, Hitachi, Darmstadt, Germany). The samples from the rejection test of dyes (feed concentration of 0.1 mM) were analyzed by a UV-Vis spectrophotometer (GENESYS 10S, Thermo Scientific). The salt rejection performance of the membranes was measured with a 1 g·L^{-1} aqueous solution of Na_2SO_4, and samples were analyzed using ion chromatography (Dionex ICS600, Thermofischer Scintific Inc., Waltham, MA, USA).

To investigate the separation behavior of the synthesized membranes towards mixed solutes, 1:1 molar mixtures of the dye solutions of 0.1 mM total feed concentration were filtered with the aforementioned filtration setup. The recorded feed, permeate and retentate samples were analyzed using UV-Vis spectrophotometry.

The observed rejection was then evaluated as follows:

$$R\ (\%) = \left(1 - \frac{C_p}{\left(C_f + C_r\right)/2}\right) * 100 \quad (2)$$

where R is solute rejection, and C_p, C_f and C_r are the concentrations of the permeate, feed and retentate solutions in mg·L^{-1}, respectively. The concentrations before and after permeate collection were measured. During the test, the feed-side concentration gradually changes due to the passage of permeate solution across the membrane active layer. However, the change in the concentration is minor as the feed volume is huge compared to the permeated volume of the test solution. The average of the feed and retentate concentrations is taken into account for consideration of the small change in feed-side concentration in the dead-end filtration mode. The arithmetic mean of C_f and C_r is an approximation usually performed to measure solute retention [40]. The membrane selectivities during the rejection tests of both single solutes and mixed solutes are calculated using

$$Selectivity = \frac{100 - R_1(\%)}{100 - R_2(\%)} \quad (3)$$

where subscripts 1 and 2 represent solute 1 and solute 2, respectively.

In order to evaluate the fouling resistance potential of the TA-Fe^{3+} TFC membranes, the antifouling properties of the fabricated membranes were further assessed with the filtration of humic acid (HA) solution. A humic acid feed solution of 100 ppm at a pH of ~7, adjusted with HCl and NaOH, was used for these experiments. The experiments were conducted according to the following procedure. First, pure water flux tests were performed for 1 h to determine the initial water flux (W_i). Then, the feed solution was replaced with HA solution for the fouling studies for 1.5 h. After HA solution filtration, the fouled membrane samples were taken out and rinsed with pure water. Finally, the pure water flux of the fouled membranes (W_o) was measured again for 1 h. The procedure was repeated again for a second cycle test. All experiments were performed at 3 bar transmembrane pressure. Equations (4) and (5) were used to compute the water flux (W) and the flux recovery ratio (FRR) of the analyzed samples, respectively.

$$W = \left(\frac{V}{A * \Delta t}\right) \quad (4)$$

$$FRR = \left(\frac{W_i}{W_o}\right) * 100 \quad (5)$$

3. Results and Discussion

3.1. Influence of Assembly Time on the Membrane's Physicochemical and Morphological Properties

The general procedure of the TFC membrane fabrication followed in this work is shown in Figure 1 while the parameters used for casting the TA-Fe^{3+} selective layers on

top of a PAN porous support are listed in Table 1. Apart from the assembly time, all the other parameters were kept unchanged while coating the TA-Fe^{3+} selective layers of the TFC membranes. Table 1 shows the four TFC membranes prepared in this work, which all have double TA-Fe^{3+} layers. It should be mentioned here that the permeance through the membranes decreases with the increase in the number of deposited TA-Fe^{3+} layers [38]. The goal of this work was to achieve homogeneous TA-Fe^{3+} layers with the minimum possible number of coating cycles and to control the permeance by varying the assembly time. At least two coating cycles were required to achieve a homogeneous TA-Fe^{3+} layer using 0.1176 mM TA and 3.33 mM $FeCl_3.6H_2O$. In what follows, the TFC membranes are addressed by the assigned membrane name in Table 1, each corresponding to the assembly time used for the coating of the TA-Fe^{3+} selective layers. FTIR spectroscopy was used to investigate the deposition of TA-Fe^{3+} selective layers on the microporous PAN support. As illustrated in Figure 2a, the PAN substrate shows its absorption band for the nitrile group (C≡N stretching vibration) at 2242 cm^{-1} [41]. The bands at 2937 and 1453 cm^{-1} correspond to the CH_2 vibration peak and the bending of the C-H bond in CH_2, respectively. Conversely, the membranes containing a TA−Fe^{3+} selective layer show characteristic peaks different to those observed in the pristine PAN support. A new peak at 1202 cm^{-1} is ascribed to the C-O stretching vibration while the absorption peak at 1575 cm^{-1} is attributed to the C=C stretching vibration bond from the aromatic groups of TA. Representative peaks for the C=O stretching vibration from the ester groups of tannic acid are also shown at 1713 cm^{-1} [27]. The broad FTIR spectrum between 3100 and 3700 cm^{-1} is attributed to the phenolic -OH groups of TA. Generally, these results confirm the successful coating of the TA-Fe^{3+} layer on top of the porous PAN support. The TA-Fe^{3+} layer at the top of the microporous PAN support was also visible in a backscattered electron SEM image as a thin bright line owing to presence of electron-rich Fe in the layer. As an example, the backscattered electron SEM image of the TFC membrane sample synthesized at 6 min of assembly time (MPN-6) is provided in Figure 2b.

Table 1. TA-Fe^{3+} selective layer casting parameters.

Membrane Name	Casting Solution Concentration [Weight %]		Casting Solution Concentration [mM]		Assembly Time [min]	TA Solution pH	Number of TA-Fe^{3+} Layers Deposited
	TA	$FeCl_3.6H_2O$	TA	$FeCl_3.6H_2O$			
MPN-1	0.02	0.09	0.1176	3.330	1	5.8	2
MPN-2.5	0.02	0.09	0.1176	3.330	2.5	5.8	2
MPN-4	0.02	0.09	0.1176	3.330	4	5.8	2
MPN-6	0.02	0.09	0.1176	3.330	6	5.8	2

Figure 2c shows the EDX spectra obtained at the surfaces of the PAN support and the TFC membranes. As expected, the PAN support was composed of a significant amount of carbon and nitrogen. A small amount of oxygen is also visible in the EDX spectrum of PAN, which is in accordance with the –OH peak observed in the FTIR spectrum of PAN (Figure 2a). The EDX spectrum of the TFC membranes shows the elements that are present in the thin TA-Fe^{3+} layer as well as the PAN support owing to the penetration depth of the high-energy electron beam used to excite the samples. The EDX analysis confirmed the presence of Fe in the TFC membranes. The content of oxygen in the TFC membranes was significantly higher compared to the PAN support. The iron-to-oxygen ratio in the TA-Fe^{3+} TFC membranes was computed from the integrated area of the peaks (after correcting the peak area by subtracting that of PAN). All membranes presented ~0.2 for the Fe-to-O ratio, as shown in Figure 2d. The –OH containing pyrogallol and catechol moieties in TA acts as a bidentate ligand for the metal ion center during metal–polyphenol self-assembly to form mono, bis and/or tris complexes [26,42]. The formation of the complexation state is dictated by several factors including the pH, metal-to-ligand ratio and concentration of casting solutions [26,43,44]. Previously, we provided the possible formation mechanism of the TA-Fe^{3+} selective layer through the LBL technique [38]. The protocol involves a

four-step procedure of TA adsorption and TA–metal ion coordination, which leads to the formation of both mono- and bis-complex states. The theoretical Fe/O ratios of the three different complexation states (calculated from the chemical structure considering that a TA molecule contains 46 oxygen, out of which 25 are from –OH groups) are listed in Table S1 of the Supporting Information. The experimentally observed iron-to-oxygen ratios of the TFC membranes lie between the theoretical Fe/O ratios of the mono complex (0.27) and bis complex (0.14) for all TA-Fe^{3+} membranes. This proves that the TFC membranes contain a mixed mono-and-bis-coordinated complexed TA-Fe^{3+} layer, which is consistent with the findings of our previous study [38]. Figure 2d demonstrates that the assembly time has no significant influence on the coordination state.

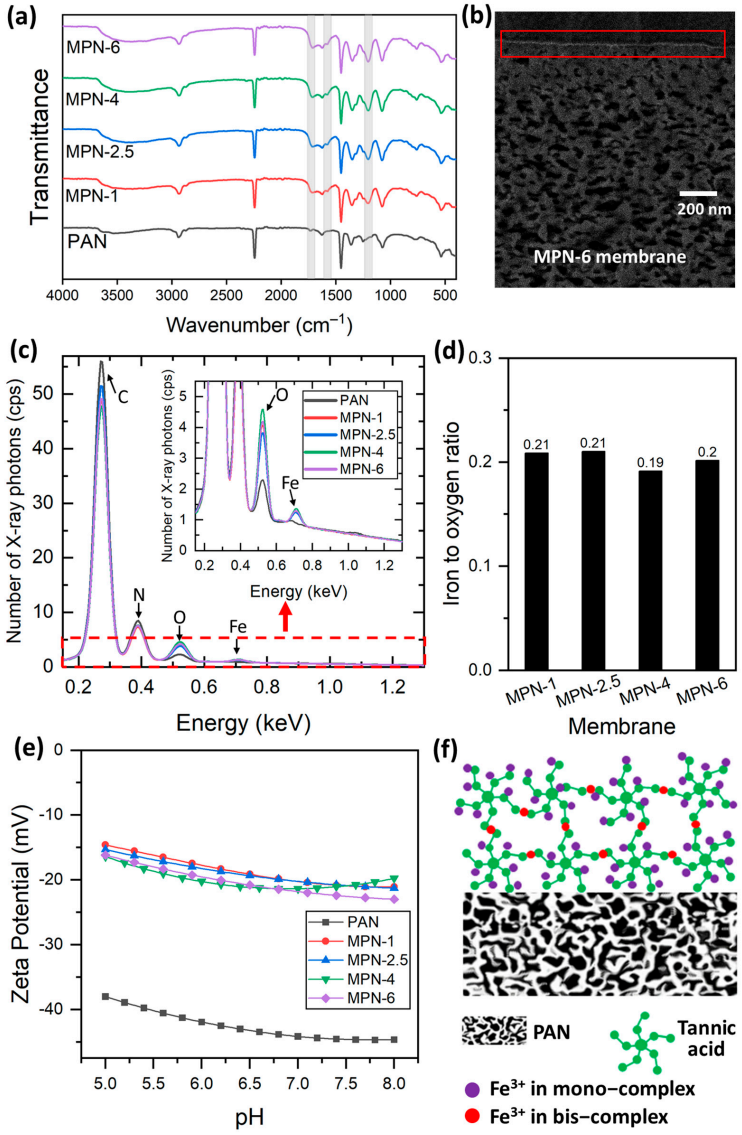

Figure 2. (**a**) FTIR spectra of the PAN and TA-Fe^{3+} membranes fabricated at different assembly times. (**b**) Backscattered electron SEM image of a TA-Fe^{3+} TFC membrane sample showing a continuous, thin, Fe-rich selective layer deposited over the porous substrate. Elemental analysis of the PAN support and the TFC membranes: (**c**) EDX spectra and (**d**) Fe/O ratio of the TFC membranes. Inset in (**c**) displays a zoomed−in figure showing the peaks for oxygen and iron. (**e**) Surface zeta potential as a function of pH for the PAN support and TA-Fe^{3+} membranes fabricated at different assembly times. (**f**) A schematic illustration of the TA–metal ion coordination for thin-film formation by the LBL technique. MPN-1, MPN-2.5, MPN-4 and MPN-6 represent TA-Fe^{3+} TFC membranes fabricated at 1 min, 2.5 min, 4 min and 6 min of assembly time, respectively.

The streaming zeta potentials at the surfaces of the membranes were measured to evaluate the surface charge property. Figure 2e demonstrates that the TFC membranes had negative zeta potentials in the investigated pH range, owing to the acidic nature of the galloyl groups in tannic acid [26]. Polyphenols possess numerous dissociable hydroxyl groups in their structure. The zeta potential profiles of the fabricated membranes showed a gradual increase with the decrease in pH. The PAN support exhibited a negative surface charge. However, the negative surface charge of the bare PAN membrane was weakened after the TA-Fe^{3+} coating. Variation in self-assembly time has no significant influence on the surface zeta potential of the membranes. It is well-established that PAN and other polymeric surfaces with no dissociable groups demonstrate a negative zeta potential owing to the preferential adsorption of –OH groups of water compared to hydronium ions [45]. Figure 2e implies the TA-Fe^{3+} coating hinders the preferential adsorption of –OH groups of water at the surface to some extent. The lower negative surface charge of the TFC membranes containing a TA-Fe^{3+} selective layer compared to that of the PAN support is consistent with the findings of our previous study [38]. While there was no significant influence on the TA-Fe^{3+} coordination state and surface charge (Figure 2), a critical influence of the assembly time on the surface morphology of the TFC membranes was observed (Figure 3). A SEM image of the PAN support is shown in Figure 3a. The pristine PAN contains a smooth and porous top surface. Figure 3b–e present the top surface and cross-sectional SEM images of the TFC membranes synthesized at various assembly times. In comparison to the PAN support, the top surface of the fabricated TFC membranes demonstrates a significant decrease in porosity due to the MPN-layer coating. From Figure 3, it is also evident that the MPN-layer coating does not penetrate the porous support, and the porosity at the spongy support layer of the membranes remains unchanged. A careful comparison of Figure 3b–e shows that the surface porosity of the TFC membranes gradually decreases with the increase in assembly time. In other words, the top layer becomes denser with the increase in the assembly time. The EDX analysis demonstrated that there is no significant influence of the assembly time on the coordination state. For the studied assembly times (i.e., 1–6 min), it was not possible to decipher any significant increase in the thickness of the TA-Fe^{3+} selective layers of the TFC membranes from the cross-sectional SEM images (Figure 3b–e). The LBL coating protocol allowed for controlled deposition of TA-Fe^{3+} on the surface of the PAN layer. TFC membranes with similar surface charges but different surface porosities were obtained by varying the assembly time.

3.2. Filtration Performance of the Membranes

3.2.1. Water Contact Angle and Pure Water Permeance of the Fabricated Membranes

The water contact angle (WCA) analyses of the polyacrylonitrile support and the TFC membranes are shown in Figure 4a. The pristine support exhibited a WCA of around 48°. The WCA of the PAN membrane declined after the TA-Fe^{3+} coating. It is important to mention here that the water contact angles are influenced by both the chemistry and porosity of the membranes. The TA-Fe^{3+} layers, owing to the presence of hydroxyl groups, are substantially more hydrophilic than the PAN. The hydrophilic nature of tannic acid [46] tends to decrease the WCA of the TFC membranes compared to that of the PAN membrane. On the other hand, for TA-Fe^{3+}-containing membranes, the loss of porosity tends to increase the WCA of the TFC membranes. Among the TFC membranes, the one fabricated using a one-minute assembly time (MPN-1) had the highest surface porosity. Therefore, it had the lowest WCA. In fact, the WCA was too low to measure. The contact angle increased from 22° to 42° when the assembly time was lengthened from 2.5 min to 6 min. The dynamic water contact angles of the membranes are provided in Figure S2 of the Supporting Information.

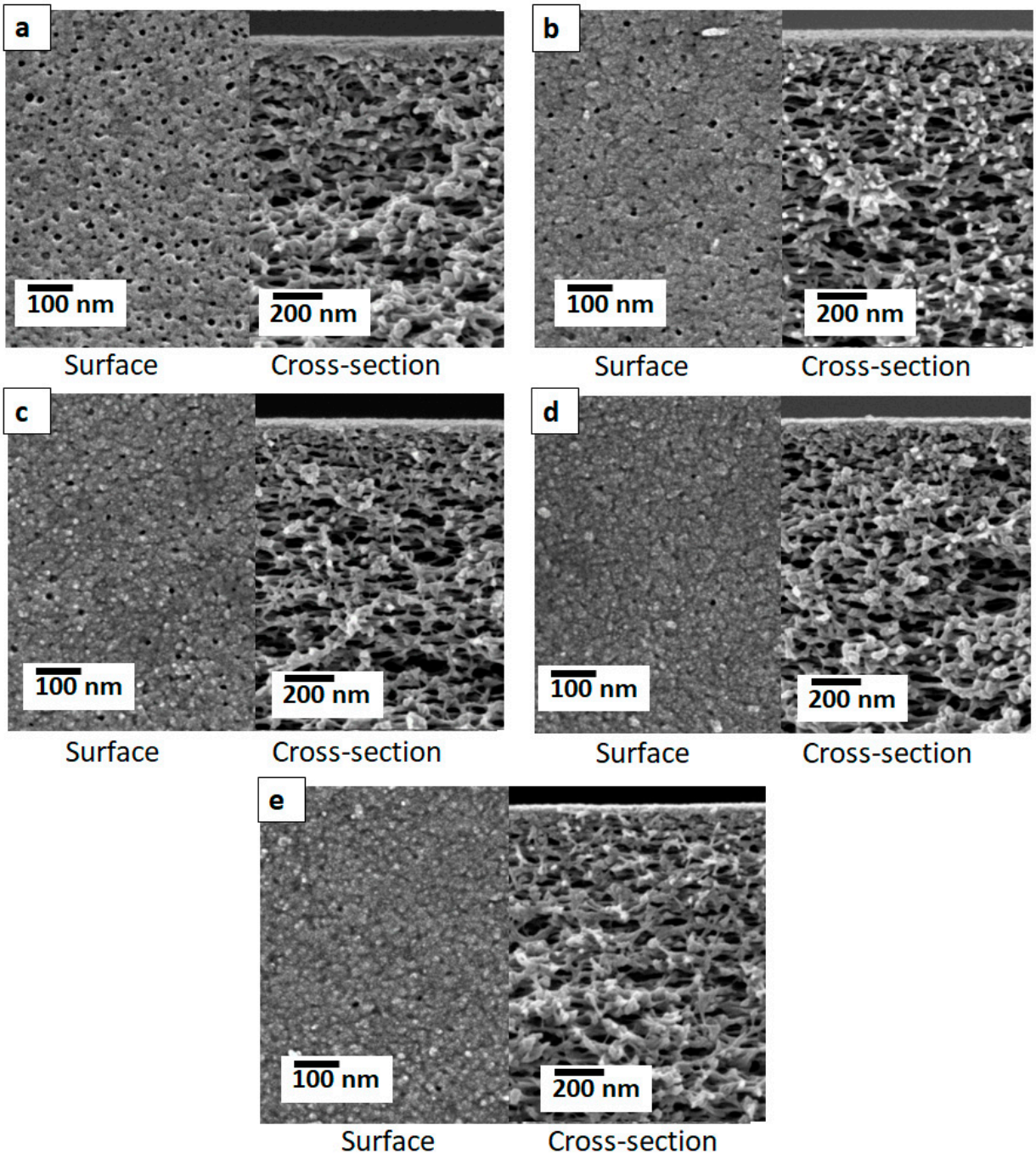

Figure 3. Top surfaces and corresponding cross-sectional SEM images of (**a**) the PAN support, and TA-Fe^{3+} TFC membranes synthesized at (**b**) 1 min (MPN-1), (**c**) 2.5 min (MPN-2.5), (**d**) 4 min (MPN-4) and (**e**) 6 min (MPN-6) of assembly time.

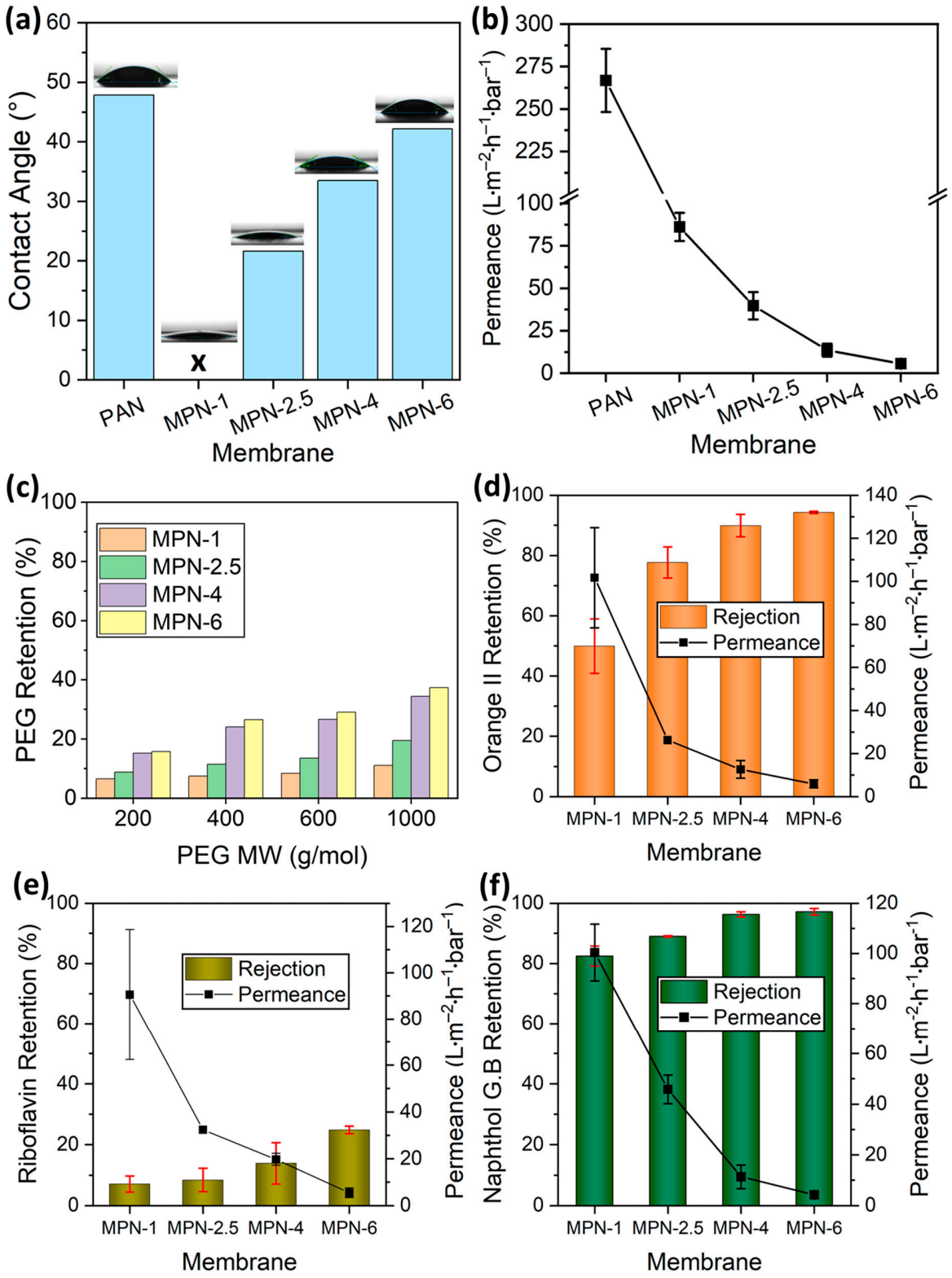

Figure 4. (**a**) Water contact angle and (**b**) pure water permeance of the PAN support and TA-Fe^{3+} membranes fabricated at different assembly times. Retention of a single solute—(**c**) poly(ethylene glycol) (neutral), (**d**) orange II (–1 charge), (**e**) riboflavin (neutral) and (**f**) naphthol green B (–3 charge)—by the TA-Fe^{3+} membranes as a function of the assembly time of the membranes. The solid line is added to guide the eye.

The pure water permeance (PWP) of the support was around 266 ± 17 $L \cdot m^{-2} \cdot h^{-1} \cdot bar^{-1}$. Figure 4b presents the PWPs of the synthesized TFC membranes. As expected, the permeance dropped significantly after the deposition of the TA-Fe^{3+} selective layer. This indicates a decrease in pore size and porosity compared to the porous pristine PAN surface. Furthermore, the membrane surface chemistry was altered after the metal–polyphenol network coating. A sharp decrease in water permeance through the TFC membranes can be observed as the assembly time is increased from 1 to 6 min (Figure 4b). The water permeance decreased owing to the lower porosity of the resulting membranes, as depicted in the SEM images presented in Figure 3. The pure water flux of the assembled membranes decreased by more than 6-fold when the assembly time was increased from 1 min to 4 min. The membrane synthesized at 6 min (MPN-6) showed a PWP of 5.6 $L \cdot m^{-2} \cdot h^{-1} \cdot bar^{-1}$. The salt rejection performance of the membranes was also investigated. The retention of Na_2SO_4 increased from 32% to 97% with the increase in assembly time from 1 to 6 min (Figure S1, Supporting Information). Overall, the fabricated membranes displayed a high Na_2SO_4 retention performance in comparison to other tannic acid–metal ion membranes published in the literature, as shown in Table S2 of the Supporting Information.

3.2.2. Organic Solute Retention Performance

Figure 4c–f show the observed organic solute rejection performance of the prepared TFC membranes. The neutral PEG and riboflavin had rather high permeances through the TFC membranes, while the anionic dyes orange II and naphthol green B were highly retained. PEG retention tests are the most commonly employed experiment to investigate the pore sizes of such membranes. We investigated the retention of PEG with molecular weights of 200, 400, 600 and 1000 g/mol by the TFC membranes. In every case, the retention of PEG of a specific molecular weight increased with the assembly time (Figure 4c), indicating the decline in the pore size of the selective layer. Hence, the findings of our morphological investigations based on SEM (Figure 3) and PEG retention were in agreement with each other. The retention rates of PEG of 1000 g/mol molecular weight by the TFC membranes prepared by using 1, 2.5, 4 and 6 min assembly times were 11%, 20%, 34% and 37%, respectively. These results confirm that although the pore size and porosity of the selective layers of the TFC membranes gradually decrease with the assembly time, each of the membranes has sufficiently large pores to allow the permeation of PEG with a molecular weight of 1000 g/mol. Hence, as expected, the retention of the neutral molecule riboflavin (molecular weight 376.76) is rather low, in the range of 7 to 25% (Figure 4e). It is worth mentioning here that for the TFC membranes prepared using 1, 2.5, 4 and 6 min assembly times, the retention rates of riboflavin were 7, 8, 14 and 25%, while the retention rates of PEG with a molecular weight of 400 g/mol were 7, 12, 24 and 27%, respectively. Hence, the retention rates of neutral molecules are in good agreement with one another. Figure 4c,e show a similar trend of rejection of neutral molecules (i.e., PEG and riboflavin). With the increase in assembly time, the rejection gradually increases due to a loss of surface porosity of the membranes. Figure 4d,f also show an increase in rejection of the anionic molecules (i.e., orange II and naphthol green B) with an increase in the assembly time. Unlike the neutral molecules, the anionic dyes orange II and naphthol green B were highly retained by the TFC membranes. For example, the retention rates of orange II and naphthol green B were 50% and 83%, respectively, for the TFC membrane prepared at 1 min of assembly time (Figure 4d,f). The naphthol green B retention rate was 97% while that of orange II was 94% when the assembly time was increased. The rejection of orange II was significantly improved when the coordination proceeded to four minutes. Surface porosity decreased only up to an assembly time of four minutes and led to an improved solute removal performance. An assembly time beyond four minutes resulted in a decline in water permeance by more than two-fold whilst no substantial variation in the anionic dyes' rejection was exhibited. Therefore, a compact selective layer can be formed within just a few minutes. Essentially, the self-assembly of polyphenols and metal ions occurs instantly [27,47]. However, as TA contains numerous –OH groups,

complete coordination between the two components is unlikely to occur. Hence, a loose network with elevated flux and relatively lower solute rejection is obtained at a short assembly time. Coordination proceeds through the involvement of more functional groups with the prolongation of the assembly time. However, the ideal selectivity of the orange II/naphthol green B pair does not change significantly with the assembly time of the studied membranes. For these anionic dyes, the ideal selectivities ranged between 2 and 3 (Table 2). On the other hand, the ideal selectivity of riboflavin/naphthol green B during a single-solute retention test increased from 5 to 27 when the assembly time increased from 1 min to 6 min (see Table 2), indicating a high permeation of neutral molecules while retaining charged groups. Similarly, the riboflavin/orange II selectivity increased from 2 to 13 with the increase in the assembly time. These results indicate that the fabricated membranes are suitable for charge-based organic/organic separation. The retention rates of the dye molecules are ordered riboflavin < orange II < naphthol green B for all membranes. Both size sieving and electrostatic exclusion play an important role in the selectivity and retention of organic solutes [48,49]. Therefore, it seems that the high retention of orange II as well as naphthol green B constitutes a combination of steric and Donnan effects. Although riboflavin and orange II have similar molecular sizes and molecular weights, the rather high retention rate of orange II suggests that Donnan exclusion predominantly affects the separation mechanism for the partitioning of solutes at the membrane–solution interface. The negatively charged TA-Fe^{3+} membrane surface (Figure 2e) rejects solutes that are smaller than the membranes' molecular weight cut-off for neutral molecules, which is due to electrostatic repulsion. This demonstrates the high uncharged dye/charged dye selectivities of the membranes. The discrepancy in retention rates between the anionic dye molecules originates from their molecular sizes and charges. Orange II (350.32 g/mol) is a smaller monovalent dye (with –1 charge) compared to the bigger naphthol green B (878.46 g/mol) (with –3 charge) in aqueous solution. Therefore, the membrane–solute electrostatic repulsive interaction is significant for naphthol green B. Moreover, for the relatively porous membranes fabricated at a short assembly time, the small molecules of orange II can permeate through the TA-Fe^{3+} active layer more easily compared to naphthol green B. This aligns with the observed high selectivity for the MPN-1 membrane obtained with a 1 min assembly time. However, as the assembly time is increased, dense membranes are fabricated, restricting the permeation of orange II through the TFC membranes, which leads to a comparable retention of the two anionic dyes at a long assembly time.

Table 2. Performance comparison of the TA-Fe^{3+} membranes with other reported studies for charge- and charge/size-based separation of small organic molecules.

Membrane Type	Small Molecules	Molecular Weight ($g.mol^{-1}$)	Molecular Charge	Selectivity Diffusion [(a)]	Selectivity Filtration		Water Permeance ($L \cdot m^{-2} \cdot h^{-1} \cdot bar^{-1}$)	Reference
					Single Solutes	Mixed Solutes		
MPN-1	RB0	376.36	0	--	5.3	6.5	86.1	This work
	NGB3-	878.45	−3					
MPN-2.5	RB0	376.36	0	--	8.3	9.3	39.8	This work
	NGB3-	878.45	−3					
MPN-4	RB0	376.36	0	--	23.4	18.4	13.6	This work
	NGB3-	878.45	−3					
MPN-6	RB0	376.36	0	--	26.7	18.4	5.6	This work
	NGB3-	878.45	−3					
MPN-1	RB0	376.36	0	--	2.0	--	86.1	This work
	OR-	350.32	−1					
MPN-2.5	RB0	376.36	0	--	4.1	--	39.8	This work
	OR-	350.32	−1					

Table 2. *Cont.*

Membrane Type	Small Molecules	Molecular Weight ($g.mol^{-1}$)	Molecular Charge	Selectivity Diffusion [a]	Selectivity Filtration		Water Permeance ($L \cdot m^{-2} \cdot h^{-1} \cdot bar^{-1}$)	Reference
					Single Solutes	Mixed Solutes		
MPN-4	RB0	376.36	0	--	8.5	--	13.6	This work
	OR-	350.32	−1					
MPN-6	RB0	376.36	0		13.2	--	5.6	This work
	OR-	350.32	−1					
MPN-1	OR-	350.32	−1	--	2.9	3.6	86.1	This work
	NGB3-	878.45	−3					
MPN-2.5	OR-	350.32	−1	--	2	2.5	39.8	This work
	NGB3-	878.45	−3					
MPN-4	OR-	350.32	−1	--	2.7	1.7	13.6	This work
	NGB3-	878.45	−3					
MPN-6	OR-	350.32	−1	--	2	1.9	5.6	This work
	NGB3-	878.45	−3					
MPN 1TA-3Fe	RB0	376.36	0	--	3.2	--	62.5	[38]
	OR-	350.32	−1					
MPN 1TA-4.5Fe	RB0	376.36	0	--	8.5	--	13.6	[38]
	OR-	350.32	−1					
MPN 1TA-6Fe	RB0	376.36	0	--	20.6	--	3.8	[38]
	OR-	350.32	−1					
MPN 1TA-8Fe	RB0	376.36	0	--	3.2	--	0.9	[38]
	OR-	350.32	−1					
Amphiphilic random copolymer membrane	Riboflavin	376.36	0	263	8.4 [b]	19.2 [b]	4.2	[3]
	Acid blue 45	474.33	−2					
Positively charged triblock copolymer SNIPS membrane (quaternized P4VP block)	RB0	376.36	0	--	21.3	28.3	11.0	[6]
	Methylene blue	319.85	+1					
Negatively charged triblock copolymer SNIPS membrane (sulfonated)	OR-	350.32	−1	--	14.7	44.6	9.5	[6]
	NGB3-	878.45	−3					
Negatively charged triblock copolymer SNIPS membrane (sulfonated)	OR-	350.32	−1	--	64.3	-	9.5	[6]
	Reactive green 19	1418.93	−6					
Isoporous block copolymer membrane	RB0	376.36	0		35.7	39.9	3.8	[50]
	Methylene blue	319.85	+1					
Negatively charged diblock copolymer SNIPS membrane (sulfonated)	OR-	350.32	−1	--	5.2	--	74	[7]
	Reactive green 19	1418.93	−6					
NP-Den hybrid membrane	Rhodamine 6G	479.02	+1	11	--		--	[51]
	Calcein	622.53	−4					
Self-assembled polyelectrolyte deposited PCTE	Rhodamine 6G	479.02	+1	3.5	--		--	[52]
	Calcein	622.53	−4					
Cationic dendrimer deposited PCTE	Calcein	622.53	−4	10	--		--	[53]
	Rhodamine 6G	479.02	+1					

[a] The selectivities were determined from a single-solute system. [b] We calculated the selectivities using the reported retention values.

3.2.3. Mixed-Solute Retention

The ideal selectivity calculated from the study of the permeation behavior when using feed solutions containing only single dyes demonstrated the potential of using the prepared TFC membranes to separate one dye from another. To check the validity of these data in order to determine the separation performance, it is important to study the permeation behavior using feed solutions containing mixtures of dyes. Coexistent substances in a feed solution can influence the retention and selectivity of solutes by membranes. For instance, plasticization of the membrane active layer by one solute may lead to a decrease in the

rejection of all solutes, while adsorption of solutes into the pores may lead to constant variation in the rejection of all components [3]. Equimolar mixtures of dye solutions of riboflavin and naphthol green B (RB0/NGB3-) as well as orange II and naphthol green B (OR-/NGB3-) were filtered through the fabricated TFC membranes. It is worth mentioning here that in our previous work [38], we reported that the anionic OR- and NGB3- did not absorb on TFC membranes containing TA-Fe^{3+} selective layers and a PAN support layer even after immersing the membranes in the dye solutions for 24 h. Figure 5a,b display the effect of the assembly time on the retention and separation of an RB0/NGB3- mixture. The UV-vis spectra of the feed and permeate solutions are plotted in Figure 5a. While the peaks for RB0 strongly appear in the UV-vis spectra of the permeate solutions, the NGB3- peak is hardly visible. Hence, as expected from the study of feed solutions containing a single dye, from the equimolar RB0/NGB3- mixture, the TFC membranes allowed RB0 to permeate rather easily and highly retained NGB3-. That is visible even in the photographs of the feed and permeate solutions (Figure 5a), which show the colors of the solutions turning from green to yellow after permeating through the TFC membranes. The intensities of the UV-vis spectra at 444 nm and 715 nm were used to determine the retention of RB0 and NGB3- from the mixture, respectively (Figure 5b). Figure 5c,d show that the TFC membranes can also separate OR- and NGB3- from a mixed solution, as anticipated from the study of the solutions containing single dyes. A color change is visible for the solution that permeated through the TFC membranes prepared using a 1 min assembly time (Figure 5c). As evident from the corresponding UV-vis spectrum (Figure 5c), this TFC membrane retains NGB3- while it allows a large portion of OR- from the mixture to permeate through. As the pore size decreases (with an increasing assembly time), the TFC membranes not only highly retain NGB3- from the mixture but also OR-. Figure 5c shows the color of the permeate solutions gradually fade away with an increasing assembly time of the TFC membranes, while the intensity of OR- in the UV-vis spectra of the corresponding permeate solutions also decreases gradually. From the retention plot in Figure 5d, it is clear that the difference in retention rates between OR- and NGB3- by the TFC membranes gradually narrows with an increasing assembly time. This is reflected in the real selectivity values (mixed solutes) of the OR-/NGB3- pair (Table 2). In general, there is a trade-off between the permeance and selectivity, i.e., the membranes with high permeances suffer from low selectivities and vice versa. However, the separation of OR- and NGB3- from their equimolar mixtures by the studied TFC membranes does not follow this trade-off. The MPN-1 TFC membrane prepared at a 1 min self-assembly time has the highest OR-/NGB3- selectivity (3.6). Owing to its large porosity, it also has the highest permeance among the four studied TF membranes. However, the TFC membranes follow the trade-off between permeance and selectivity for the RB0/NGB3- pair. Table 2 shows that, in general, there are some deviations of the real selectivity (mixed solutes) from the ideal selectivity (single solutes). For example, the studies of single-dye retention led us to a significant overestimation of the RB0/NGB3- selectivity for the TFC membranes prepared using 4 and 6 min assembly times. However, in general, in our systematic study, the ideal selectivity of the dye pairs revealed the separation potential of the membranes with sufficient accuracy. The performance of the TA-Fe^{3+} membranes for the separation of small organic molecules were compared to those from other studies in the literature, as shown in Table 2. The fabricated membranes demonstrated excellent performance considering the water permeance and selectivity in both single- and mixed-solute systems.

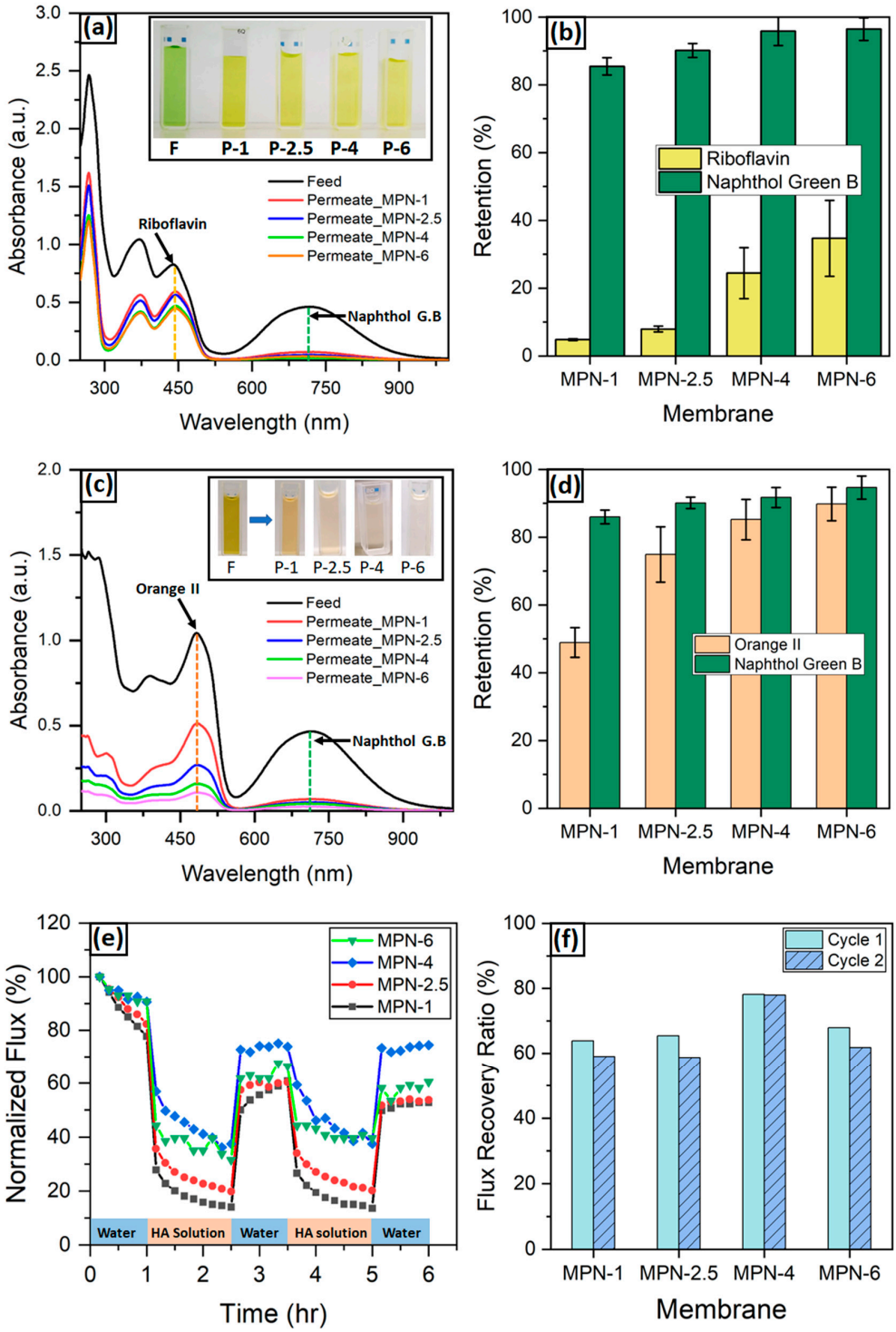

Figure 5. (**a**) UV-vis absorption spectra of the feed and permeate solutions and (**b**) retention of the 1:1 molar mixture of riboflavin and naphthol green B dyes, with peaks at 444 nm and 715 nm, respectively, through the TA-Fe^{3+} membranes synthesized at different assembly times. Inset: photographic images of the mixed dye solutions before (feed, F) and after (permeate, P) filtration experiments. Numerical values of 1, 2.5, 4 and 6 represent the assembly time (min) durations at which the membranes were fabricated by exposing the PAN surface to the TA and $FeCl_3 \cdot 6H_2O$ solutions. (**c**) UV-vis absorption spectra of the feed and permeate solutions and (**d**) retention of the dyes in the OR-/NGB3- system of the 1:1 molar mixture of orange II and naphthol green B dyes, with UV-vis absorption peaks at 482 nm and 715 nm, respectively, through the TA-Fe^{3+} membranes synthesized at different assembly times.

(**e**,**f**) Evaluation of the antifouling properties of the metal–phenolic selective layers; (**e**) normalized water and HA solution flux of the TA-Fe^{3+} membranes and (**f**) flux recovery ratios of the synthesized membranes. The investigation was performed by first recording the PWP of a membrane sample for 1 h followed by HA solution filtration for 1.5 h. Then, the membrane was rinsed with pure water to remove fouled HA molecules, after which the PWP of the fouled membrane was measured for one hour again to determine the FRR. This process was repeated for two cycles.

3.2.4. Evaluation of Membrane Antifouling Performance

Membrane fouling is a key factor for the evaluation of membrane performance. The decrease in flux during process operation due to fouling results in performance decay and increases the operational cost [54]. Therefore, we further investigated the fouling property of the fabricated membranes using humic acid (HA) as a model foulant. The study was carried out periodically to assess the changes in the flux of the MPN membranes. Figure 5e displays the normalized membrane flux during different stages. The HA solution filtration was performed in a steady state. All TA-Fe^{3+} membranes showed a decline in flux during the fouling period due to the adsorption and accumulation of HA molecules on the membrane surface and pore blockage. The membrane flux recovered to a certain extent after cleaning. In the first cycle, the flux recovery ratio (FRR) was in the range of 64–78% (Figure 5f). During the second cycle, the FRR exhibited a slight decrease due to irreversible fouling on the surface of the membranes. The antifouling property of the membranes is ascribed to the hydrophilic nature of the MPN membrane surfaces. Incorporation of tannic acid in membrane surfaces or pore walls weakens the hydrophobic interaction between the membranes and foulant molecules [55]. A protective hydration layer is formed by the preferential adsorption of water molecules on the –OH-containing self-assembled film [36,56]. This inhibition of membrane fouling prevents the decline in HA solution flux. Moreover, it enhances the FRR after membrane cleaning. Surface charge also plays a key role in affecting the membrane antifouling properties. TA contains acidic catechol groups that can tune the surface property of thin films in constructing antifouling surface substrates [57]. Generally, the fabricated membranes had a negative surface potential (Figure 3a). The antifouling property is significantly enhanced by the reversible electrostatic repulsion between HA and TA.

4. Conclusions

In this study, we investigated the influence of the assembly time on the synthesis of MPN TFC membranes fabricated via a layer-by-layer technique from aqueous solutions of low concentrated TA and a ferric ion. By varying the assembly time between 1 and 6 min, we prepared membranes with similar surface charge densities but different porosities. This work was focused on analyzing the performance of TA-Fe^{3+} TFC membranes for the separation of neutral and anionic organic molecules, both in single-solute and mixed-solute experiments. Over the years, there has been a considerable interest in the separation of small organic molecules in the nanometer dimension due to the lack of commercially viable membranes for this purpose. To the best of our knowledge, in this work, for the first time, we have demonstrated that TFC membranes containing TA-Fe^{3+} selective layers can be used for solute–solute separation with high selectivity from aqueous solutions containing a mixture of small organic solutes. Aqueous solutions containing equimolar mixtures of the riboflavin/naphthol green B pair and the orange II/naphthol green B pair were used as feed solutions. The membranes showed a high rejection of negatively charged solutes while low rejection was observed for neutral organic solutes. The electrostatic interaction between the negatively charged membrane surfaces and the organic molecules led to the selective permeation of the neutral solute riboflavin over naphthol green B. The increase in the assembly time generally improved the selectivity of the riboflavin/naphthol green B pair while the permeance decreased owing to a loss of surface porosity. This is a general trend observed in most of the separation processes, which is often referred to as the trade-off between permeance and selectivity. The results showed that the TA-Fe^{3+}

membrane fabricated at 4 min of assembly time demonstrated the best performance in terms of its high selectivity for neutral/charged dye separation and its water flux. For the orange II/naphthol green B (OR-/NGB3-) anionic dye pair, there was no trade-off between permeance and selectivity. The TFC membrane prepared using a 1 min assembly time (MPN-1) showed the highest water permeance and high selectivity for the OR-/NGB3- dye pair. The present study indicates that the self-assembled selective layers of metal–polyphenol-network-based TFC membranes obtained from a green synthesis pathway have great potential in the treatment and fractionation of a mixture of complex streams. Overall, this study proves that the assembly time is a vital tool that may be used to control the surface morphology and tune the separation performance of TFC membranes containing TA-Fe^{3+} selective layers prepared via LBL.

Supplementary Materials: The following supporting information can be downloaded at https://www.mdpi.com/article/10.3390/membranes14060133/s1, Figure S1: Sulfate ion rejection of the fabricated membranes and their respective salt solution permeance; Figure S2: Surface wettability of the pristine PAN and TA-Fe^{3+} membranes fabricated at different assembly times; Table S1: Theoretical Fe/O ratios in the three different complex states of TA-Fe^{3+} self-assembly; Table S2: Comparison of the Na_2SO_4 separation performance of the fabricated selective layers and the TA-M^{n+} membranes using porous supports in the literature.

Author Contributions: Conceptualization, H.H.K. and M.M.R.; methodology, H.H.K. and N.C.-C.; investigation, H.H.K. and E.S.S.; resources, M.M.R.; writing—original draft preparation, H.H.K.; writing—review and editing, H.H.K., N.C.-C., M.M.R., E.S.S. and V.A.; visualization, H.H.K. and M.M.R.; supervision, M.M.R. and V.A.; project administration, M.M.R.; funding acquisition, M.M.R. All authors have read and agreed to the published version of the manuscript.

Funding: This work was funded by the Hereon-I^2B-Project NanoMem.

Institutional Review Board Statement: Not applicable.

Data Availability Statement: Data are contained within the article and Supplementary Materials.

Acknowledgments: The authors acknowledge Maren Brinkmann for the PEG retention analysis in GPC, Juliana Clodt for preparing the polyacrylonitrile support and Jan Pohlmann for setting up the flux and retention measurement facilities.

Conflicts of Interest: The authors declare no conflicts of interest.

References

1. Ma, L.S.; Gutierrez, L.; Verbeke, R.; D'Haese, A.; Waqas, M.; Dickmann, M.; Helm, R.; Vankelecom, I.; Verliefde, A.; Cornelissen, E. Transport of organic solutes in ion-exchange membranes: Mechanisms and influence of solvent ionic composition. *Water Res.* **2021**, *190*, 116756. [CrossRef] [PubMed]
2. Sadeghi, I.; Kaner, P.; Asatekin, A. Controlling and Expanding the Selectivity of Filtration Membranes. *Chem. Mater.* **2018**, *30*, 7328–7354. [CrossRef]
3. Sadeghi, I.; Kronenberg, J.; Asatekin, A. Selective Transport through Membranes with Charged Nanochannels Formed by Scalable Self-Assembly of Random Copolymer Micelles. *ACS Nano* **2018**, *12*, 95–108. [CrossRef] [PubMed]
4. Bengani, P.; Kou, Y.M.; Asatekin, A. Zwitterionic copolymer self-assembly for fouling resistant, high flux membranes with size-based small molecule selectivity. *J. Membr. Sci.* **2015**, *493*, 755–765. [CrossRef]
5. Chen, M.; Yang, H.; Xu, Z.L.; Cheng, C. Separation of single and mixed anionic dyes in saline solutions using uncharged polyacrylonitrile-tris(hydroxymethyl)aminomethane (PAN-Tris) ultrafiltration membrane: Performance and mechanism. *J. Clean. Prod.* **2022**, *336*, 130471. [CrossRef]
6. Zhang, Z.Z.; Rahman, M.M.; Abetz, C.; Hohme, A.L.; Sperling, E.; Abetz, V. Chemically Tailored Multifunctional Asymmetric Isoporous Triblock Terpolymer Membranes for Selective Transport. *Adv. Mater.* **2020**, *32*, e1907014. [CrossRef] [PubMed]
7. Zhang, Z.; Rahman, M.M.; Abetz, C.; Abetz, V. High-performance asymmetric isoporous nanocomposite membranes with chemically-tailored amphiphilic nanochannels. *J. Mater. Chem. A* **2020**, *8*, 9554–9566. [CrossRef]
8. Zhang, Z.; Rahman, M.M.; Abetz, C.; Bajer, B.; Wang, J.; Abetz, V. Quaternization of a Polystyrene-block-poly(4-vinylpyridine) Isoporous Membrane: An Approach to Tune the Pore Size and the Charge Density. *Macromol. Rapid Commun.* **2019**, *40*, 1800729. [CrossRef]
9. Chen, L.Y.; Jiang, M.Y.; Zou, Q.; Xiong, S.W.; Wang, Z.G.; Cui, L.S.; Guo, H.; Zhou, T.; Gai, J.G. Highly permeable carbon nanotubes/polyamide layered membranes for molecular sieving. *Chem. Eng. J.* **2021**, *425*, 130684. [CrossRef]

10. Kim, E.S.; Hwang, G.; El-Din, M.G.; Liu, Y. Development of nanosilver and multi-walled carbon nanotubes thin-film nanocomposite membrane for enhanced water treatment. *J. Membr. Sci.* **2012**, *394*, 37–48. [CrossRef]
11. Wang, D.; Tian, M.; Han, S.; Ding, K.; Yin, L.; Zhu, J.; Zhang, Y.; Han, L. Enhanced performance of thin-film nanocomposite membranes achieved by hierarchical zeolites for nanofiltration. *J. Membr. Sci.* **2023**, *671*, 121405. [CrossRef]
12. Wei, X.X.; Liu, Y.L.; Zheng, J.F.; Wang, X.M.; Xia, S.J.; Van der Bruggen, B. A critical review on thin-film nanocomposite membranes enabled by nanomaterials incorporated in different positions and with diverse dimensions: Performance comparison and mechanisms. *J. Membr. Sci.* **2022**, *661*, 120952. [CrossRef]
13. Zhu, J.Y.; Meng, W.Q.; Xue, Q.; Zhang, K.S. Two dimensional sulfonated molybdenum disulfide (S-MoS_2) thin-film nanocomposite nanofiltration membrane for selective desalination. *J. Membr. Sci.* **2023**, *676*, 121574. [CrossRef]
14. Zhang, N.; Song, X.J.; Jiang, H.; Tang, C.Y.Y. Advanced thin-film nanocomposite membranes embedded with organic-based nanomaterials for water and organic solvent purification: A review. *Sep. Purif. Technol.* **2021**, *269*, 118719. [CrossRef]
15. Zhao, Q.; Zhao, D.L.; Ee, L.Y.; Chung, T.-S.; Chen, S.B. In-situ coating of Fe-TA complex on thin-film composite membranes for improved water permeance in reverse osmosis desalination. *Desalination* **2023**, *554*, 116515. [CrossRef]
16. Jiang, X.N.; Yong, W.F.; Gao, J.; Shao, D.D.; Sun, S.P. Understanding the role of substrates on thin film composite membranes: A green solvent approach with TamiSolve (R) NxG. *J. Membr. Sci.* **2021**, *635*, 119530. [CrossRef]
17. Ong, C.; Falca, G.; Huang, T.F.; Liu, J.T.; Manchanda, P.; Chisca, S.; Nunes, S.P. Green Synthesis of Thin-Film Composite Membranes for Organic Solvent Nanofiltration. *Acs Sustain. Chem. Eng.* **2020**, *8*, 11541–11548. [CrossRef]
18. Zhang, R.N.; He, M.R.; Gao, D.H.; Liu, Y.N.; Wu, M.Y.; Jiao, Z.W.; Su, Y.L.; Jiang, Z.Y. Polyphenol-assisted in-situ assembly for antifouling thin-film composite nanofiltration membranes. *J. Membr. Sci.* **2018**, *566*, 258–267. [CrossRef]
19. Yang, C.; Topuz, F.; Park, S.H.; Szekely, G. Biobased thin-film composite membranes comprising priamine-genipin selective layer on nanofibrous biodegradable polylactic acid support for oil and solvent-resistant nanofiltration. *Green Chem.* **2022**, *24*, 5291–5303. [CrossRef]
20. Park, S.H.; Yang, C.; Ayaril, N.; Szekely, G. Solvent-Resistant Thin-Film Composite Membranes from Biomass-Derived Building Blocks: Chitosan and 2,5-Furandicarboxaldehyde. *ACS Sustain. Chem. Eng.* **2022**, *10*, 998–1007. [CrossRef]
21. Park, S.H.; Alammar, A.; Fulop, Z.; Pulido, B.A.; Nunes, S.P.; Szekely, G. Hydrophobic thin film composite nanofiltration membranes derived solely from sustainable sources. *Green Chem.* **2021**, *23*, 1175–1184. [CrossRef]
22. Chen, C.; Yang, H.; Yang, X.; Ma, Q. Tannic acid: A crosslinker leading to versatile functional polymeric networks: A review. *RSC Adv.* **2022**, *12*, 7689–7711. [CrossRef] [PubMed]
23. Kinfu, H.H.; Rahman, M.M. Separation Performance of Membranes Containing Ultrathin Surface Coating of Metal-Polyphenol Network. *Membranes* **2023**, *13*, 481. [CrossRef] [PubMed]
24. Rahim, M.A.; Lin, G.; Tomanin, P.P.; Ju, Y.; Barlow, A.; Björnmalm, M.; Caruso, F. Self-Assembly of a Metal-Phenolic Sorbent for Broad-Spectrum Metal Sequestration. *ACS Appl. Mater. Interfaces* **2020**, *12*, 3746–3754. [CrossRef] [PubMed]
25. Yan, W.; Shi, M.; Dong, C.; Liu, L.; Gao, C. Applications of tannic acid in membrane technologies: A review. *Adv. Colloid Interface Sci.* **2020**, *284*, 102267. [CrossRef] [PubMed]
26. Ejima, H.; Richardson, J.J.; Liang, K.; Best, J.P.; Van Koeverden, M.P.; Such, G.K.; Cui, J.; Caruso, F. One-Step Assembly of Coordination Complexes. *Science* **2013**, *341*, 154–157. [CrossRef] [PubMed]
27. Fan, L.; Ma, Y.; Su, Y.; Zhang, R.; Liu, Y.; Zhang, Q.; Jiang, Z. Green coating by coordination of tannic acid and iron ions for antioxidant nanofiltration membranes. *RSC Adv.* **2015**, *5*, 107777–107784. [CrossRef]
28. Guo, H.; Peng, L.E.; Yao, Z.; Yang, Z.; Ma, X.; Tang, C.Y. Non-Polyamide Based Nanofiltration Membranes Using Green Metal-Organic Coordination Complexes: Implications for the Removal of Trace Organic Contaminants. *Environ. Sci. Technol.* **2019**, *53*, 2688–2694. [CrossRef]
29. Song, Y.Z.; Kong, X.; Yin, X.; Zhang, Y.; Sun, C.C.; Yuan, J.J.; Zhu, B.; Zhu, L.P. Tannin-inspired superhydrophilic and underwater superoleophobic polypropylene membrane for effective oil/water emulsions separation. *Colloids Surf. A Physicochem. Eng. Asp.* **2017**, *522*, 585–592. [CrossRef]
30. Guo, H.; Yao, Z.; Yang, Z.; Ma, X.; Wang, J.; Tang, C.Y. A One-Step Rapid Assembly of Thin Film Coating Using Green Coordination Complexes for Enhanced Removal of Trace Organic Contaminants by Membranes. *Environ. Sci. Technol.* **2017**, *51*, 12638–12643. [CrossRef]
31. Khodeir, E.; Namvar-Mahboub, M. The effect of tannic acid-based coating on performance of Ro membrane for metronidazole removal from aqueous solution. *Surf. Interfaces* **2021**, *26*, 101363. [CrossRef]
32. You, F.; Xu, Y.; Yang, X.; Zhang, Y.; Shao, L. Bio-inspired Ni^{2+}-polyphenol hydrophilic network to achieve unconventional high-flux nanofiltration membranes for environmental remediation. *Chem. Commun.* **2017**, *53*, 6128–6131. [CrossRef] [PubMed]
33. Xiao, Y.; Guo, D.; Li, T.; Zhou, Q.; Shen, L.; Li, R.; Xu, Y.; Lin, H. Facile fabrication of superhydrophilic nanofiltration membranes via tannic acid and irons layer-by-layer self-assembly for dye separation. *Appl. Surf. Sci.* **2020**, *515*, 146063. [CrossRef]
34. Kim, H.J.; Kim, D.G.; Yoon, H.; Choi, Y.S.; Yoon, J.; Lee, J.C. Polyphenol/Fe^{III} Complex Coated Membranes Having Multifunctional Properties Prepared by a One-Step Fast Assembly. *Adv. Mater. Interfaces* **2015**, *2*, 1500298. [CrossRef]
35. Liu, J.; Yu, X.; Yang, E.; Li, T.; Yu, H.; Wang, Z.; Dong, B.; Fane, A.G. A combined tannic acid-copper-iron coating of ultrafiltration membrane for enhanced anti-bacterial and algal-inhibition performance. *J. Water Process Eng.* **2022**, *50*, 103250. [CrossRef]
36. Liu, D.; Chen, Y.; Tran, T.T.; Zhang, G. Facile and rapid assembly of high-performance tannic acid thin-film nanofiltration membranes via Fe^{3+} intermediated regulation and coordination. *Sep. Purif. Technol.* **2021**, *260*, 118228. [CrossRef]

37. Lin, C.E.; Zhou, M.Y.; Hung, W.S.; Zhu, B.K.; Lee, K.R.; Zhu, L.P.; Fang, L.F. Ultrathin nanofilm with tailored pore size fabricated by metal-phenolic network for precise and rapid molecular separation. *Sep. Purif. Technol.* **2018**, *207*, 435–442. [CrossRef]
38. Kinfu, H.H.; Rahman, M.M.; Schneider, E.S.; Cevallos-Cueva, N.; Abetz, V. Charge and size selective thin film composite membranes having tannic acid—Ferric ion network as selective layer. *J. Membr. Sci.* **2023**, *679*, 121709. [CrossRef]
39. Wang, R.Y.; Zhang, J.W.; Tang, C.Y.Y.; Lin, S.H. Understanding Selectivity in Solute-Solute Separation: Definitions, Measurements, and Comparability. *Environ. Sci. Technol.* **2022**, *56*, 2605–2616. [CrossRef]
40. Plakas, K.V.; Karabelas, A.J.; Wintgens, T.; Melin, T. A study of selected herbicides retention by nanofiltration membranes—The role of organic fouling. *J. Membr. Sci.* **2006**, *284*, 291–300. [CrossRef]
41. Acarer, S.; Pir, I.; Tufekci, M.; Erkoc, T.; Oztekin, V.; Dikicioglu, C.; Demirkol, G.T.; Durak, S.G.; Ozcoban, M.S.; Coban, T.Y.T.; et al. Characterisation and Mechanical Modelling of Polyacrylonitrile-Based Nanocomposite Membranes Reinforced with Silica Nanoparticles. *Nanomaterials* **2022**, *12*, 3721. [CrossRef] [PubMed]
42. Kim, B.J.; Han, S.; Lee, K.B.; Choi, I.S. Biphasic Supramolecular Self-Assembly of Ferric Ions and Tannic Acid across Interfaces for Nanofilm Formation. *Adv. Mater.* **2017**, *29*, 1700784. [CrossRef] [PubMed]
43. Perron, N.R.; Brumaghim, J.L. A Review of the Antioxidant Mechanisms of Polyphenol Compounds Related to Iron Binding. *Cell Biochem. Biophys.* **2009**, *53*, 75–100. [CrossRef] [PubMed]
44. Rahim, M.A.; Ejima, H.; Cho, K.L.; Kempe, K.; Müllner, M.; Best, J.P.; Caruso, F. Coordination-driven multistep assembly of metal-polyphenol films and capsules. *Chem. Mater.* **2014**, *26*, 1645–1653. [CrossRef]
45. Glass, S.; Mantel, T.; Appold, M.; Sen, S.; Usman, M.; Ernst, M.; Filiz, V. Amine-Terminated PAN Membranes as Anion-Adsorber Materials. *Chem. Ing. Tech.* **2021**, *93*, 1396–1400. [CrossRef]
46. Fang, X.; Li, J.; Li, X.; Pan, S.; Sun, X.; Shen, J.; Han, W.; Wang, L.; Van der Bruggen, B. Iron-tannin-framework complex modified PES ultrafiltration membranes with enhanced filtration performance and fouling resistance. *J. Colloid Interface Sci.* **2017**, *505*, 642–652. [CrossRef] [PubMed]
47. Tang, C.; Amin, D.; Messersmith, P.B.; Anthony, J.E.; Prud'homme, R.K. Polymer directed self-assembly of pH-responsive antioxidant nanoparticles. *Langmuir* **2015**, *31*, 3612–3620. [CrossRef] [PubMed]
48. Li, J.; Yuan, S.S.; Zhu, J.Y.; Van der Bruggen, B. High-flux, antibacterial composite membranes via polydopamine-assisted PEI-TiO/Ag modification for dye removal. *Chem. Eng. J.* **2019**, *373*, 275–284. [CrossRef]
49. Wang, J.; Zhu, J.Y.; Tsehaye, M.T.; Li, J.; Dong, G.Y.; Yuan, S.S.; Li, X.; Zhang, Y.T.; Liu, J.D.; Van der Bruggen, B. High flux electroneutral loose nanofiltration membranes based on rapid deposition of polydopamine/polyethyleneimine. *J. Mater. Chem. A* **2017**, *5*, 14847–14857. [CrossRef]
50. Zhang, Z.Z.; Rahman, M.M.; Bajer, B.; Scharnagl, N.; Abetz, V. Highly selective isoporous block copolymer membranes with tunable polyelectrolyte brushes in soft nanochannels. *J. Membr. Sci.* **2022**, *646*, 120266. [CrossRef]
51. Park, M.H.; Subramani, C.; Rana, S.; Rotello, V.M. Chemoselective Nanoporous Membranes via Chemically Directed Assembly of Nanoparticles and Dendrimers. *Adv. Mater.* **2012**, *24*, 5862–5866. [CrossRef] [PubMed]
52. Savariar, E.N.; Krishnamoorthy, K.; Thayumanavan, S. Molecular discrimination inside polymer nanotubules. *Nat. Nanotechnol.* **2008**, *3*, 112–117. [CrossRef]
53. Savariar, E.N.; Sochat, M.M.; Klaikherd, A.; Thayumanavan, S. Functional Group Density and Recognition in Polymer Nanotubes. *Angew. Chem. Int. Ed.* **2009**, *48*, 110–114. [CrossRef] [PubMed]
54. Xie, Y.; Chen, S.Q.; Zhang, X.; Shi, Z.Q.; Wei, Z.W.; Bao, J.X.; Zhao, W.F.; Zhao, C.S. Engineering of Tannic Acid Inspired Antifouling and Antibacterial Membranes through Co-deposition of Zwitterionic Polymers and Ag Nanoparticles. *Ind. Eng. Chem. Res.* **2019**, *58*, 11689–11697. [CrossRef]
55. Wu, H.; Sun, H.; Hong, W.; Mao, L.; Liu, Y. Improvement of Polyamide Thin Film Nanocomposite Membrane Assisted by Tannic Acid-Fe(III) Functionalized Multiwall Carbon Nanotubes. *ACS Appl. Mater. Interfaces* **2017**, *9*, 32255–32263. [CrossRef] [PubMed]
56. Liu, C.; Guo, Y.Q.; Zhang, J.M.; Tian, B.; Lin, O.K.; Liu, Y.W.; Zhang, C.H. Tailor-made high-performance reverse osmosis membranes by surface fixation of hydrophilic macromolecules for wastewater treatment. *RSC Adv.* **2019**, *9*, 17766–17777. [CrossRef]
57. Zhao, L.F.; Zhang, M.; Liu, G.H.; Zhao, A.; Gong, X.S.; Shi, S.; Zheng, X.B.; Gao, J.; Jiang, Y.J. Tuning the Microstructure of a Zwitterion-Functionalized Polyethylenimine Loose NF Membrane for Dye Desalination. *Ind. Eng. Chem. Res.* **2022**, *61*, 2245–2256. [CrossRef]

Chapter 5. Nanofiltration Membranes Containing a Metal–Polyphenol Network Layer: Using Casting Solution pH as a Tool to Tailor the Separation Performance

The pH of solutions plays a crucial role in metal-polyphenol coordination. It influences the degree of ionization of polyphenols. It also affects the nature of the metal-polyphenol complex formed. Depending on pH levels, the coordination chemistry and stability of metal-polyphenol networks can vary significantly. The following chapter explores the effect of pH of the TA solution on TFC membrane fabrication in order to enhance the selectivity in solute-solute separation. MPN thin layer containing single TA-Fe^{3+} and double TA-Fe^{3+} layered TFC membranes fabricated at different pH are studied in detail. A gradient-like layer deposition in which each MPN layer is deposited at a different pH than its predecessor in a double TA-Fe^{3+} layered membranes is also explored. Here, it was found that depositing the first layer at lower pH and coating the second layer at higher pH increases mass transfer resistance compared to depositing layers at high pH followed by at low pH. Overall, changes in pH of the casting solution alter membrane characteristics such as surface porosity, water contact angle, water permeance, retention and selectivity. Highly wettable and selective membranes are generally obtained using slightly basic casting solutions. This is in agreement with the change in the complex formation state from mono-complex at acidic conditions to tris-complex at alkaline conditions. Here, the highest selectivity (around 31) for riboflavin-naphthol green B separation using MPN membranes is achieved. Analysis of salt retention properties of the MPN membranes with NaCl show a low rejection performance indicating that the selective layer could further be beneficial in organic/salt fractionation.

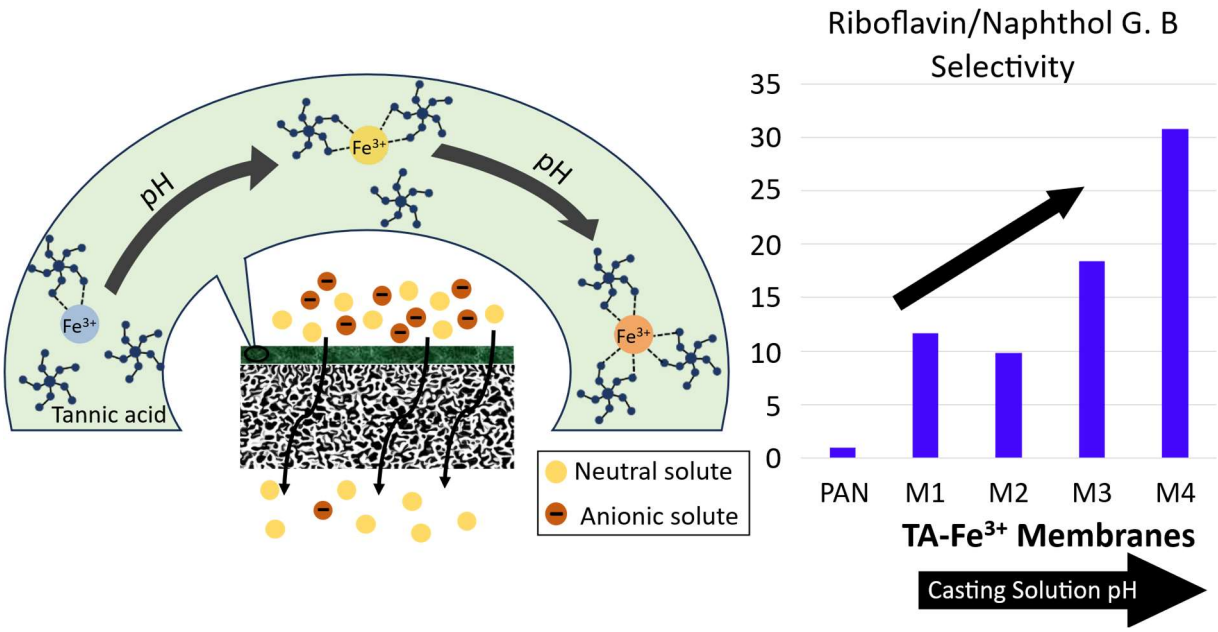
pH
pH
Fe3+
Fe3+
Fe3+
Tannic acid
Neutral solute
Anionic solute

Riboflavin/Naphthol G. B
Selectivity
35
30
25
20
15
10
5
0
PAN
M1
M2
M3
M4
TA-Fe3+ Membranes
Casting Solution pH

ACS OMEGA

Open Access

http://pubs.acs.org/journal/acsodf

Article

Nanofiltration Membranes Containing a Metal−Polyphenol Network Layer: Using Casting Solution pH as a Tool to Tailor the Separation Performance

Hluf Hailu Kinfu, Md. Mushfequr Rahman,* Nicolás Cevallos-Cueva, and Volker Abetz

Cite This: *ACS Omega* 2024, 9, 45870−45883

Read Online

ACCESS | Metrics & More | Article Recommendations | Supporting Information

ABSTRACT: Thin-film composite (TFC) membranes containing metal−polyphenol network (MPN) selective layers were fabricated using a supramolecular self-assembly between tannic acid (TA) and ferric ion (Fe^{3+}). The TA-Fe^{3+} thin film was coated on a porous polyacrylonitrile support using aqueous solutions of TA and $FeCl_3$ via a layer-by-layer deposition technique. The pH of the TA solution was used as a tool to alter the membrane characteristics. The surface porosity and water contact angle of the fabricated membranes gradually decreased as the pH of TA casting solutions was increased from 3 to 8.5 for both single-layered and double-layered TA-Fe^{3+} TFC membranes. This allowed us to tune the water permeance and the retentions of water-soluble neutral and anionic molecules by the MPN membranes by varying the pH of the casting solution. It has been shown that the water permeance decreased from 184 to 156 $L{\cdot}m^{-2}{\cdot}h^{-1}{\cdot}bar^{-1}$ for single TA-Fe^{3+} layer coated membranes when the pH was increased from 3 to 8.5, while it declined from 51 to 17 for the double TA-Fe^{3+} layer. Anionic solutes in aqueous solutions were highly retained compared to neutral components as the TFC membranes had a negative surface charge. Retentions of 95 and 90% were achieved for naphthol green B and orange II dyes by a double-layered M4 membrane fabricated at pH 8.5, while only 13% retention was found for the neutral riboflavin. The neutral dye riboflavin permeated 30.8 times higher than the anionic dye naphthol green B during a mixed dye filtration test through the TFC membrane prepared by using a TA solution of pH 8.5. To the best of our knowledge, this is the highest selectivity of a neutral/anionic dye pair so far reported for a TFC membrane having an MPN selective layer. Moreover, fouling tests have demonstrated that the MPN separation layers exhibit robust stability and adequate antifouling performance with a flux recovery ratio as high as 82%.

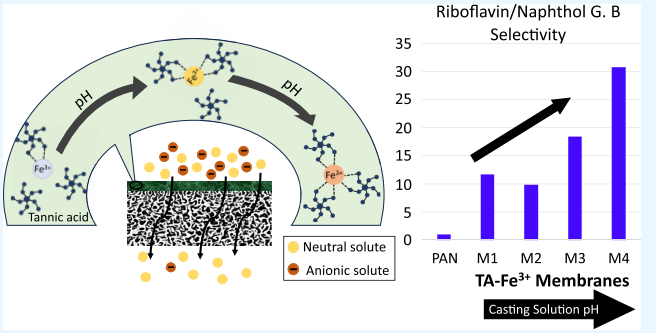

1. INTRODUCTION

Nature-inspired methods hold great potential for fabricating high-performance materials. Among them, mussel-inspired metal−polyphenol coordination is receiving high attention in engineering novel functional surfaces.[1−5] Metal−phenolic networks (MPNs) are self-assembled supramolecular structures comprising Polyphenols coordinating metal ions. Polyphenols can contain various catechol and galloyl functionalities. These are considered polydentate ligands that can chelate a vast range of transition metal ions to form highly stable MPNs.[6,7] The facile fabrication and biocompatibility of MPN coatings have increased their application for the synthesis of innovative and multifunctional materials.[8] The coating can be applied on various substrates due to the strong adhesion properties of Polyphenols through their catechol and galloyl moieties containing hydrophobic, hydrophilic, and charge shifting regions.[4] The polyphenol−metal ion complexation has been identified as an efficient and versatile platform of surface modification to engineer interfaces of novel functionalities.[4,8,9]

Bioinspired approaches toward membrane development have found a wide scope and renewed interest among scientists.[10] In the past decade, the environmentally sustainable fabrication of mussel-inspired MPN films as the separation layers of thin-film composite (TFC) membranes has attracted considerable attention in membrane separation technology.[11−13] TFC membranes composed of a thin selective layer on top of a microporous support are the industrial standard in reverse osmosis, forward osmosis, and nanofiltration. In a TFC membrane, the thin selective layer is responsible for the separation, while the porous support provides the mechanical strength.[14] Interfacial polymerization, the customary fabrication process of the thin selective layer of

Received: May 21, 2024
Revised: September 3, 2024
Accepted: October 25, 2024
Published: November 8, 2024

TFC membranes, involves the use of toxic organic solvents. The membrane industry consumes a large amount of hazardous solvents.[15,16] Substitution of these solvents with greener solvents, such as water, is thus crucial. As a result of the global challenges linked with environmental contamination, environmentally friendly, greener procedures in membrane technology have become more popular.

The strong adherent properties, alongside its low cost, fast complexation kinetics, and facile and green preparation process,[9] make the tannic acid (TA)-based MPN a suitable candidate to fabricate the selective layer of a TFC membrane. TA is a nature-derived substance.[17] Moreover, the U.S. Food and Drug Administration has recognized MPN components such as TA as safe materials.[1] TA is the most studied polyphenol and has been demonstrated to participate in various types of bondings.[18] TA is not only an excellent polyphenol that forms films via metal chelation[1] but also soluble in water.[19,20] The coordination between TA and metal ions can alleviate contemporary environmental regulations on the use of organic solvents in membrane processes. These factors have prompted considerable research into the fabrication of TFC membranes with TA−metal ion coordinated selective layers.

Separation of small organic molecules (having dimensions between 0.5 and 5 nm) from their mixtures has received a lot of attention in recent years. Emerging contaminants, particularly from pharmaceuticals and textile industries, are still a global concern.[21,22] NF membranes are becoming a reliable and potential tool for micropollutant removal.[23] MPN-based membranes have been investigated for various applications since their introduction over the past decade. For instance, Fan et al. fabricated antioxidant TA-Fe^{3+} loose nanofiltration membranes.[11] Lee and colleagues reported a facile approach to preparing antifouling MPN membranes for heavy metal removal.[13] Fang et al. fabricated a PES/Fe-TA membrane via integrating blending and interfacial coordination for enhanced dye/salt separation.[24] Several studies on the application of MPN-based thin films for oil-in-water emulsion separation have also been reported.[25−27] Moreover, these TFC membranes have been applied for the removal of trace organic contaminants[12] and dye removal.[28,29] However, the use of TFC membranes containing TA-Fe^{3+}-based selective layers for the separation of organic solutes and micropollutants from each other remains to be explored. Beyond the applications reviewed above, the implementation of TA-Fe^{3+} TFC membranes with significantly high separation efficacy for diverse applications such as pollutant removal and recovery is vital. This necessitates the development and design of a TA-Fe^{3+} layer having the right pore size and layer properties to be able to separate such small molecules from each other. Hence, it is important to explore the parameters that control the formation of ligand−metal ion complexes while casting the TA-Fe^{3+} layer. The pH of the casting solution is one of the major factors governing the MPN layer formation.[30] Polyphenol-metal stoichiometry is highly pH-dependent.[31] During TA-Fe^{3+} TFC membrane fabrication through the LBL technique, the first step is TA adsorption on the porous support. The acidity or alkalinity of the TA solution can influence its interaction with the support substrate. Second, the coordination with metal ions can be affected by solution pH[1] during the self-assembly throughout the alternate deposition of precursor solutions. This entails the need for the systematic investigation of casting solution pH on the morphology and separation performance of the MPN membranes.

In the present work, we intend to demonstrate the effect of the TA casting solution pH on the membrane morphology and performance in the separation of neutral and anionic molecules having molecular weights in the range of 200−1000 g/mol. We report the fabrication of TA-Fe^{3+} TFC membranes via a layer-by-layer (LBL) method to form the MPN active layer on a porous PAN membrane support.

2. EXPERIMENTAL SECTION

2.1. Materials. The polyacrylonitrile (PAN) ultrafiltration membrane was fabricated at Helmholtz-Zentrum Hereon. TA (1701.2 g/mol) was purchased from Sigma-Aldrich Chemie GmbH (Germany). $FeCl_3{\cdot}6H_2O$ was obtained from Alfa Aesar GmbH & Co. Hydrochloric acid (HCl, 37%) was obtained from Merck Biosciences GmbH, while sodium hydroxide (NaOH) was provided by Sigma-Aldrich. Riboflavin (RB0), orange II (OR-), and naphthol green B (NGB3-) were purchased from Sigma-Aldrich Chemie GmbH (Germany). Poly(ethylene glycol) (PEG) of 200, 400, 600, and 1000 g/mol average molecular weights were obtained from VWR International GmbH (Germany). All of the chemicals in this study were used as received without further purification.

2.2. Preparation of TA-Fe^{3+} Membranes. The TFC membranes were fabricated by depositing TA and ferric salt solution over a microporous PAN support via an LBL strategy. The TA (0.1176 mM) and $FeCl_3$ (3.330 mM) solutions were prepared separately by dissolving in water. These optimized concentrations have been chosen based on our previous rigorous study on the effect of concentration on membrane performance such as water flux and retention properties.[32] The PAN support was first wetted by immersing it in water for 3 h. Then, the prewetted support was fixed between a glass plate and a PTFE frame. Each TA-Fe^{3+} layer was formed by exposing the top surface of the PAN membrane to a solution of TA for 4 min, followed by rinsing with pure water. Here, TA is adsorbed to the surface of the substrate. Next, the TA-adsorbed support membrane is exposed to a solution containing Fe^{3+} for the same period, leading to polyphenol−metal ion coordination, followed again by rinsing with pure water. In this way, membranes coated with one layer of TA-Fe^{3+} were fabricated. The pH of the aqueous solution in which TA was dissolved was varied between 3 and 8.5 to fabricate three membranes containing a single TA-Fe^{3+} layer.

The process was repeated again to obtain double-layered TA-Fe^{3+} TFC membrane through the LBL technique. The parameters used for coating the TA-Fe^{3+} layers on the PAN support are listed in Table 1.

2.3. Membrane Characterization. Fourier transform infrared (FTIR) spectra of the membranes were measured with a Bruker Alpha (diamond-ATR unit) (Bruker, Karlsruhe, Germany). The spectra in the range of 400−4000 cm^{-1} were collected using 64 scans at a resolution of 4 cm^{-1}. The background spectrum of the PAN support was also acquired prior to TA-Fe^{3+} active layer synthesis. The zeta potential of the membranes was determined using a SurPASS 3 electrokinetic analyzer (Anton Paar, Austria). All tests were performed at room temperature using a background electrolyte solution of 1 mM NaCl. The surface hydrophilicity of the fabricated membrane was assessed through measurements of the water contact angle (WCA). The WCA measurements were performed on a KRUESS Drop Shape Analysis System

https://doi.org/10.1021/acsomega.4c04804
ACS Omega 2024, 9, 45870−45883

Table 1. Membrane Separation Layer Fabrication Parameters for Single-Layered and Double-Layered TA-Fe^{3+} Thin Films of a Self-Assembled Network Deposited over the PAN Support with Their Respective Measured Pure Water Permeance (PWP)[a]

	TA solution pH			
membrane code	first layer	second layer	number of TA-Fe^{3+} layers deposited	PWP in $L{\cdot}m^{-2}{\cdot}h^{-1}{\cdot}bar^{-1}$
S1	3		1	184
S2	5		1	167
S3	8.5		1	156
M1	3	3	2	51
M2	5	5	2	24
M3	5.8	5.8	2	21
M4	8.5	8.5	2	17
M5	3	5	2	45
M6	3	5.8	2	32
M7	3	8.5	2	26
M8	8.5	3	2	41
M9	8.5	5	2	26
M10	8.5	5.8	2	21
M11	5	8.5	2	34
M12	5	3	2	48
M13	5.8	3	2	46

[a]Casting solutions contain 0.1176 mM TA and 3.330 mM $FeCl_3$, and the assembly time was 4 min.

DSA 100 (FEI part of Thermo Fisher Scientific, Kawasaki, Japan) at room temperature. DI water of 3 μL was dropped on the top surface in the sessile drop mode. Scanning electron microscopy (SEM) (Merlin SEM, Zeiss, Germany) was used to characterize the morphologies of the membranes. Samples were vacuum-dried at 60 °C for 72 h and then coated with 1−1.5 nm Pt using a CCU-010 coating device (Safematic, Switzerland) prior to imaging. SEM images of the cross section and top surface were acquired using accelerating voltages of 1.5 and 3 kV, respectively, at a working distance between 3.4 and 3.6 mm.

2.4. Filtration Performance Test. The membrane separation performances were evaluated through filtration tests in the dead-end filtration mode. PWP and solute rejection experiments were conducted at 3 bar transmembrane pressure after compaction at 4 bar for at least 2 h.

The water flux and permeance of the membranes were evaluated according to the following equations:

$$J_w = \frac{V}{A \times t} \tag{1}$$

$$\mathrm{PWP} = \frac{J_w}{\Delta P} \tag{2}$$

where J_w ($L{\cdot}m^{-2}{\cdot}h^{-1}$) represents the water flux, while V (L) is the volume of the permeate, A (m^2) is the effective filtration area, and t (h) is the operation time. PWP ($L{\cdot}m^{-2}{\cdot}h^{-1}{\cdot}bar^{-1}$) is the pure water permeance, and ΔP (bar) is the applied transmembrane pressure.

Rejection experiments were performed using a stirred test cell from Millipore (EMD Millipore XFUF07601). The feed solution was stirred at a rate of 350 rpm. Here, we determined the rejection performance of the TA-Fe^{3+} thin film using dye (0.1 mM) and PEG (1 g/L) solutions using 300 mL feed solutions. The molecular structure and the respective molecular weight and charge in a solution of the dyes used in this study are shown in Figure 8a. Moreover, mixed solute retention tests were performed using a 1:1 molar mixture of dye solutions of 0.1 mM concentration. Salt retention performances of the fabricated membranes were also examined with 1 g/L feed solutions of NaCl and a NaCl−Na_2SO_4 mixture. The mixed salt solution was prepared at a chloride-to-sulfate molar ratio of 1:1. Solute rejections were calculated using eq 3.[33]

$$R(\%) = \left(1 - \frac{C_p}{(C_f + C_r)/2}\right) \times 100 \tag{3}$$

where R is solute retention and C_p, C_f, and C_r are the solute concentrations in the permeate, feed, and retentate solutions in $mg{\cdot}L^{-1}$, respectively. Concentrations of the feed were determined before the test, and the concentrations of the permeate and retentate were determined after running the test. Three C_p and C_r samples were collected and averaged, each collected after 10 mL of permeate had passed. For dye filtration, the concentrations of the different samples were analyzed using a UV−vis spectrophotometer (GENESYS 10S, Thermo Scientific). However, PEG samples were analyzed with gel permeation chromatography (GPC) (VWR-Hitachi 2130 pump, Hitachi, Darmstadt, Germany). Ion chromatography (Dionex ICS600, Thermofischer Scientific Inc., USA) was used to analyze the concentrations of the ions during salt rejection measurements.

Membrane selectivity toward two solutes is computed using

$$\mathrm{Selectivity} = \frac{100 - R_1(\%)}{100 - R_2(\%)} \tag{4}$$

Here, R_1 and R_2 are rejections of solutes 1 and 2, respectively.

2.5. Assessment of Membrane Antifouling Property. The antifouling property of the MPN TFC membranes was evaluated with a dynamic filtration fouling test to determine the flux decline and flux recovery ratio (FRR). Humic acid solution (100 mgL^{-1}) was used as a pollutant solution. The overall strategy involved three steps. First, the initial pure water flux (J_1) of the membranes was measured for 1 h. Next, the feed solution was replaced by the humic acid solution, and the foulant solution flux (J_f) was measured for 1.5 h. Then, the membrane was rinsed with pure water before being reinserted back into the filtration system to measure a new pure water flux (J_2). This process is repeated again to achieve a two-cycle foulant solution filtration test. The FRR is then calculated according to the following equation:

$$\mathrm{FRR}(\%) = \frac{J_2}{J_1} \times 100 \tag{5}$$

3. RESULTS AND DISCUSSION

3.1. Membrane Morphology and Water Permeance. TA bears several −OH groups. The mechanism of coordination involves the release of two hydrogen ions into solution by TA to give two electrons to metal ions, thus leading to chelate formation.[34] The complexation between TA and Fe^{3+} changes with solution acidity or alkalinity. As the dissociation of TA is pH-dependent,[35] we investigated and characterized the effect of TA solution pH on TFC membrane fabrication and performance. The pH of the TA aqueous

https://doi.org/10.1021/acsomega.4c04804
ACS Omega 2024, 9, 45870−45883

solutions was varied in the range of 3−8.5 to coat the selective layer of the TFC membranes on a microporous PAN support. At high pH, the phenolic functions of TA oxidize to quinone groups, which do not coordinate with Fe^{3+}.[36] Therefore, we have limited the study to a maximum pH value of 8.5 in this work, where no quinones have yet been formed. The pH of the $FeCl_3$ solution was kept constant while coating the selective layers. Table 1 shows the PWP of the fabricated TFC membranes containing both single (S1−S3) and double (M1−M13) TA-Fe^{3+} layers. MPN coatings of one or two layers were investigated as further deposition of TA-Fe^{3+} layers resulted in the formation of highly dense films with a significantly reduced water flux.[32] The surface chemical groups of the MPN coating and the microporous support were analyzed through FTIR analysis (Figure 2). Similar FTIR results for all of the fabricated membranes can be found in Figure S1 of the Supporting Information. Peaks at 2937 and 2242 cm^{-1} belong to the CH_2 stretching vibration and the C≡N stretching vibration of the PAN support layer, respectively. The band at 1453 cm^{-1} corresponds to the bending of the C−H bond. FTIR characteristic peaks of different functional groups unique to TA were also detected. The peaks at 1202 and 1575 cm^{-1} are ascribed to the C−O stretching vibration and the C=C stretching vibration from the aromatic groups of TA, respectively. The absorption peak attributed to C=O stretching vibration from the ester groups of TA appears at 1713 cm^{-1}, while the broad band at 3100−3700 cm^{-1} that belongs to the stretching vibration of O−H groups was enhanced in the newly synthesized double-layered membranes due to their phenolic nature. The occurrence of the above-mentioned new bands confirms the deposition of TA-Fe^{3+} films.

The PWP of the pristine PAN support was ∼266 $L{\cdot}m^{-2}{\cdot}h^{-1}{\cdot}bar^{-1}$. The TA-$Fe^{3+}$ layer coated membranes allowed significantly lower water permeances than that of the pristine PAN support. The water permeance of the membranes containing a single TA-Fe^{3+} layer (i.e., S1, S2, and S3) declined from 184 to 156 $L{\cdot}m^{-2}{\cdot}h^{-1}{\cdot}bar^{-1}$ (Table 1 and Supporting Information Figure S2) as the pH of the TA casting solution increased from 3 to 8.5. Figure 3 shows the surface and cross-section SEM micrographs of the PAN supports, S1, S2, and S3. Compared to PAN, the surfaces of S1, S2, and S3 showed a notable change in the porous structure due to the deposition of the MPN layer (Figure 3). The PAN support membrane showed a highly porous top surface structure, while the TA-Fe^{3+}-coated membranes displayed a decrease in the number and size of surface pores. The cross-section images of all membranes showed a sponge-like structure. No substantial variations in the cross-sectional morphology between the PAN support and the TFC membranes were observed. It shows the formation of a thin TA-Fe^{3+} layer on the top surface without deep penetration into the pores of the PAN support layer.

M1−M4 are double TA-Fe^{3+} layered TFC membranes in which both layers were synthesized at the same pH. The PWP of the TA-Fe^{3+} membrane synthesized at pH 3 (M1) was ∼51.5 $L{\cdot}m^{-2}{\cdot}h^{-1}{\cdot}bar^{-1}$. A sharp decline in PWP is displayed when the pH of the TA casting solution is increased from 3 to 5. The PWP of TA-Fe^{3+} membranes prepared at pH 5, pH 5.8, and pH 8.5 are 24, 21, and 17 $L{\cdot}m^{-2}{\cdot}h^{-1}{\cdot}bar^{-1}$, respectively. These results are in line with the observed SEM morphology (Figure 4a−d), which shows that the surface porosity of the assembled film decreases due to the enhanced coordination of neighboring TA-Fe complexes at high pH.

At specified concentrations, assembly times, and ionic strengths, the aqueous solution pH controls the polyphenol−metal ion complexation nature as illustrated in Figure 1. The

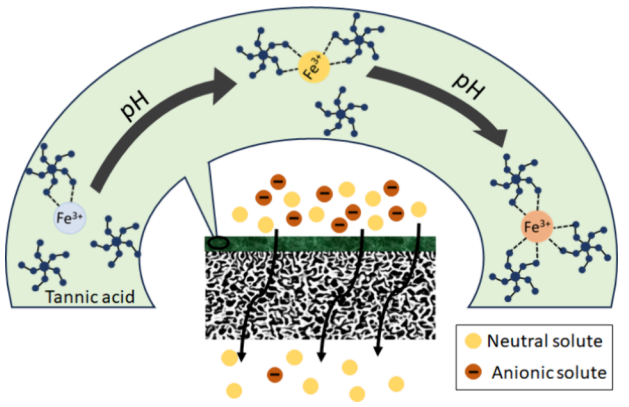

Figure 1. Schematic illustration of the TA-Fe^{3+} selective layer coating over a PAN porous membrane. The illustration shows the pH-dependent transition of the coordination between TA and Fe^{3+} ions among mono-, bis-, and tris-complex states, and the resulting thin film's selective permeation behavior toward organic solutes.

metal−polyphenol complexes comprise various stoichiometries (i.e., mono-, bis-, and tris-complex) as modulated by pH. The metal chelation behavior of catechol and galloyl ligands demonstrates that acidity or alkalinity of the solution controls the ionization of TA.[37] Essentially, several phenol groups are protonated at low pH. Phenol groups of TA only coordinate with a metal ion in the deprotonated state, i.e., when they are negatively charged. Therefore, only a small number of functional groups are available for coordination. This results in larger open pores between neighboring complexes. Hence, a low cross-linked network of the dominantly monocomplex coordination state is formed. Deprotonation of TA and the number of available metal binding sites increase with an increase in the pH of the aqueous solution. TA-Fe^{3+} coordination is predominantly in the bis-complex state in the solution pH range of 3−6.[1] However, at pH 7 and higher, a dense highly cross-linked self-assembled film of the tris-complex state displaying low water permeance is synthesized. The tris-complex elucidates three TA molecules coordinated with one metal ion center.

In the cases of M5−M13, we have also explored the interplay between the PWP and casting conditions by the deposition of each TA-Fe^{3+} layer at a different pH (Table 1). The surface and cross-sectional SEM micrographs of these membranes are provided in Figure 5. Two sets of coating solutions were analyzed in this work. For M5, M6, and M7, the first MPN layer is deposited using a TA solution of pH 3, while for the second layers, TA solutions of pH 5, 5.8, and 8.5 were used. The PWP decreases with increasing the pH of the casting solution of the second layer. The PWP of M5 (pH 3 for the first layer and pH 5 for the second layer) was 45.5 $L{\cdot}m^{-2}{\cdot}h^{-1}{\cdot}bar^{-1}$, while it declined to 26 $L{\cdot}m^{-2}{\cdot}h^{-1}{\cdot}bar^{-1}$ for M7 (pH 3 for the first layer and pH 8.5 for the second layer). The fabrication of M8, M9, and M10 involves coating the first TA-Fe^{3+} layer using a TA solution of pH 8.5 and the second layers using TA solutions of pH 3, 5, and 5.8. The PWPs of M8, M9, and M10 are 41, 26, and 21 $L{\cdot}m^{-2}{\cdot}h^{-1}{\cdot}bar^{-1}$, respectively (Table 1 and the Supporting Information, Figure S2). The comprehensive investigation allows us to analyze the role of the first and

https://doi.org/10.1021/acsomega.4c04804
ACS Omega 2024, 9, 45870−45883

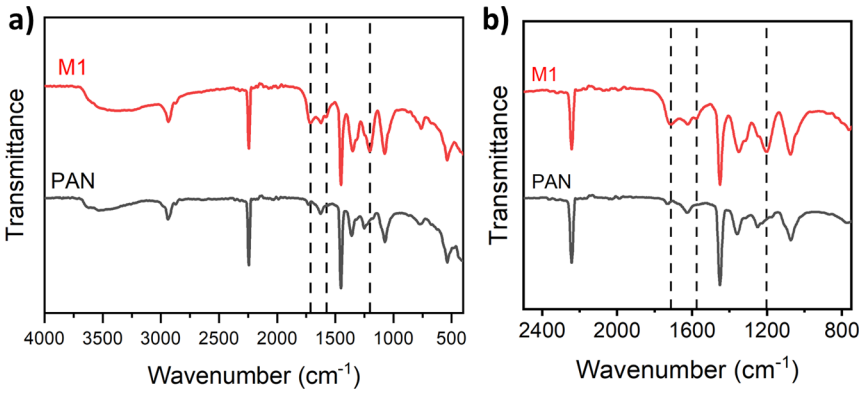

Figure 2. (a) FTIR spectra of PAN and a double TA-Fe^{3+} layered TFC membrane fabricated at pH 3 for both layers (M1), and (b) selected FTIR region illustrating the peaks specific to TA.

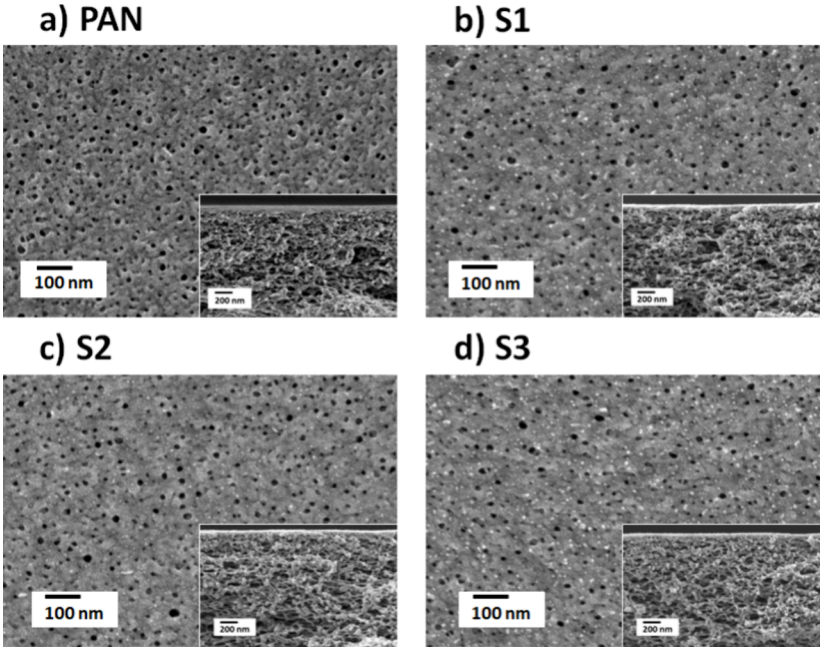

Figure 3. SEM images of single-layered TA-Fe^{3+} TFC membranes fabricated at different pHs: (a) pristine PAN support, (b) pH 3, (c) pH 5, and (d) pH 8.5. Insets show cross-sectional SEM images. The fabrication parameters can be found in Table 1.

second TA-Fe^{3+} layers in the resistance against mass transport through the membrane. Considering the PWP through the PAN support as the basis, for a TA casting solution of pH 3, the PWP dropped by 31% after coating the first TA-Fe^{3+} layer (i.e., in the case of S1), while it dropped by 81% after coating the second TA-Fe^{3+} layer (i.e., in case of M1). In the case of the pH 8.5 TA solution, the first and second coatings of the TA-Fe^{3+} layer led to 41 and 94% drops of the PWP, respectively. In the double TA-Fe^{3+} layered membranes, the second TA-Fe^{3+} layer plays the dominant role in determining the resistance against mass transport. However, an obvious difference of PWP was also observed for the membranes where the first TA-Fe^{3+} layers were coated using TA solutions of different pHs, while the second membrane was coated using the same TA solution. For example, the PWP through M8 is approximately 10 $L{\cdot}m^{-2}{\cdot}h^{-1}{\cdot}bar^{-1}$ lower than that of M1. The second TA-Fe^{3+} layer of both M1 and M8 is coated using the TA solution of pH 3. The difference in PWP in these membranes stems from the first TA-Fe^{3+} layer, which is coated using a TA solution of pH 3 and 8.5 for M1 and M8, respectively. Similarly, a 9 $L{\cdot}m^{-2}{\cdot}h^{-1}{\cdot}bar^{-1}$ difference in PWP is observed between M7 and M4 as the first TA-Fe^{3+} layers of these membranes are coated using TA solutions of pH 3 and 8.5, respectively, although the second layers for both membranes are coated using the TA solution of pH 8.5. Therefore, we also attempted to analyze the influence of reversing the pH of the TA casting solutions used to coat the first and second TA-Fe^{3+} layers of the TFC membranes. The first and second layers are reversed using TA casting solutions of pH 3 and 8.5 to coat the selective layers of M7 (first pH 3 and second pH 8.5) and M8 (first pH 8.5 and second pH 3). The PWP of M7 (26 $L{\cdot}m^{-2}{\cdot}h^{-1}{\cdot}bar^{-1}$) < M8 (41 $L{\cdot}m^{-2}{\cdot}h^{-1}{\cdot}bar^{-1}$). Similarly, the PWP of M6 (32 $L{\cdot}m^{-2}{\cdot}h^{-1}{\cdot}bar^{-1}$) < M13 (46 $L{\cdot}m^{-2}{\cdot}h^{-1}{\cdot}bar^{-1}$), which shows the influence of reversing the first and second TA-Fe^{3+} layers using TA casting solutions of pH 3 and 5.8. The PWP of M9 (26 $L{\cdot}m^{-2}{\cdot}h^{-1}{\cdot}bar^{-1}$) is slightly lower than that of M11 (34 $L{\cdot}m^{-2}{\cdot}h^{-1}{\cdot}bar^{-1}$). The influence of using TA casting solutions of pH 5 and 8.5 to reverse the first and second layer coatings on PWP can be observed from this pair. The PWP of M5 (45 $L{\cdot}m^{-2}{\cdot}h^{-1}{\cdot}bar^{-1}$)

https://doi.org/10.1021/acsomega.4c04804
ACS Omega 2024, 9, 45870−45883

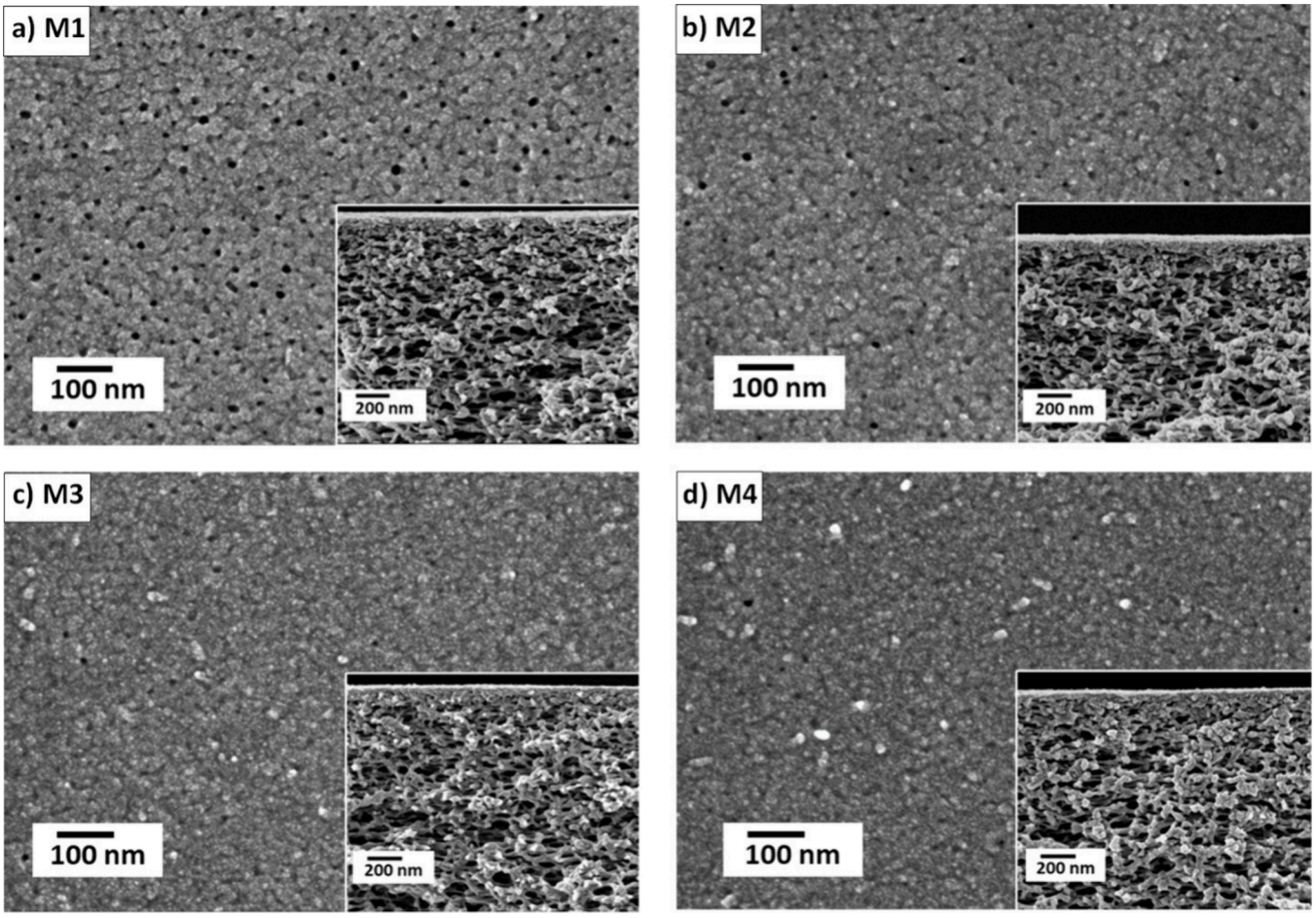

Figure 4. SEM images of double-layered MPN TFC membranes fabricated at the same pH for both TA-Fe^{3+} layers: (a) M1 at pH 3, (b) M2 at pH 5, (c) M3 at pH 5.8, and (d) M4 at pH 8.5. Insets show their cross-sectional SEM images. The fabrication parameters can be found in Table 1.

≈ M12 (48 $L{\cdot}m^{-2}{\cdot}h^{-1}{\cdot}bar^{-1}$). This pair reversed the first and second TA-Fe^{3+} layers coated using the TA casting solutions of pH 3 and 5. In general, the average PWP of the double TA-Fe^{3+} layered membranes fabricated using TA solutions of higher pH for the first layer surpassed those for which lower pH TA solutions were used to coat the first layer. When the pHs of the TA casting solutions used to coat the first and second TA-Fe^{3+} layers are far away from each other (e.g., pH 3 and 8.5), the effect of reversing is also stronger. Overall, the results show that although the PWP of the TFC membranes can be tuned for the single TA-Fe^{3+} layered membranes coated using TA solutions (0.1176 mM) of different pHs, these membranes might be useful for ultrafiltration applications. This work aims to prepare nanofiltration membranes for the separation of small organic molecules (having MW between 200 and 1000 g/mol). The PWP values of the double-layered membranes varied between 21 and 51 $L{\cdot}m^{-2}{\cdot}h^{-1}{\cdot}bar^{-1}$, which is typical for loose nanofiltration membranes with large molecular weight cutoffs suitable for the separation of organic molecules.[38,39] Hence, among the membranes listed in Table 1, only those containing a double TA-Fe^{3+} layer can be suitable for the targeted applications. For further investigations, we have selected M1, M2, M3, and M4 (i.e., the double TA-Fe^{3+} layered membranes), where both layers are coated using the TA solutions of the same pH.

3.2. WCA and Surface Zeta Potential. Mussel-inspired metal−polyphenol coatings have a reputation for producing stable and hydrophilic surfaces.[40,41] WCA was used to examine the change in hydrophilicity before and after MPN layer coating. The wettability of the membranes prepared at various pH values as revealed by WCA is presented in Figure 6b. The pristine support showed a WCA of around 47 °, illustrating its relatively low hydrophilic property. The PAN water wettability is due to the high polarity of its backbone.[42] After *in situ* fabrication of the TA-Fe^{3+} thin film, the WCA of the TFC membranes declined gradually. The widely accepted notion is that a reduced contact angle signifies increased surface energy, a stronger tendency of membrane wetting by water, and therefore enhanced hydrophilicity. An increase in the pH of the casting solution resulted in the fabrication of a comparatively hydrophilic surface. The WCA of the membrane M4 decreased to about 16 °. Time-dependent WCA from WCA tests is shown in Figure S4 of the Supporting Information. TA-based selective layers exhibit a very low WCA, indicating the fabrication of superhydrophilic membrane surfaces.[43] The low contact angles of the TFC membranes were due to the hydrophilic nature of the TA-Fe^{3+} top layer containing hydroxyl functional groups in polyphenols. The functional groups of TA on the membrane surface can form hydrogen bonds with water molecules. The nanostructured protrusions on the surface of the membrane also contribute to the overall hydrophilicity.[44] Enhancing the surface hydrophilicity is an effective approach for increasing the water permeance of membranes.[43] Hence, the synthesis of

https://doi.org/10.1021/acsomega.4c04804
ACS Omega 2024, 9, 45870−45883

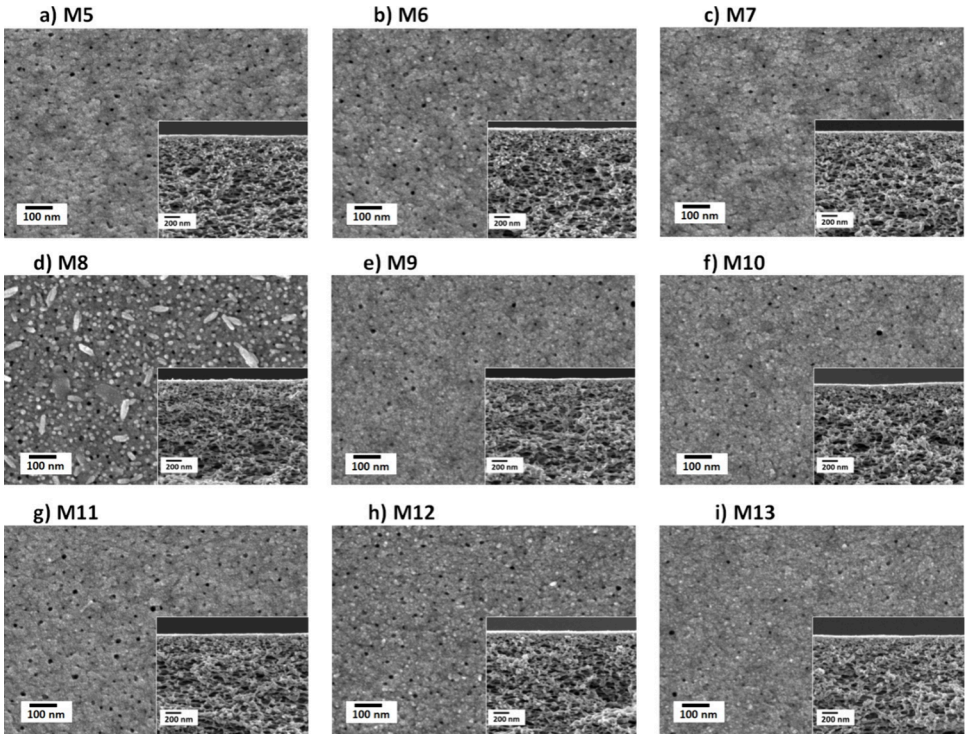

Figure 5. Surface and cross-sectional SEM images of double-layered TA-Fe^{3+} TFC membranes prepared at different pH conditions for each layer. The fabrication parameters can be found in Table 1.

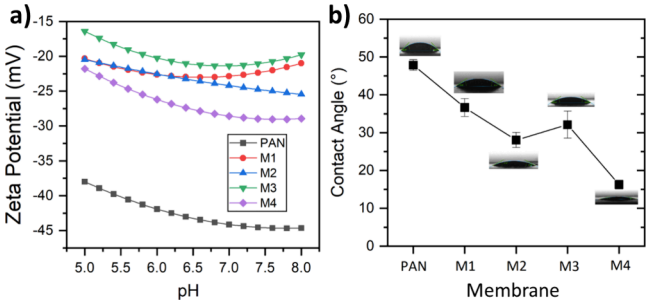

Figure 6. (a) Surface zeta potentials as a function of background electrolyte pH and (b) WCA of the membranes.

an MPN selective layer with low WCA decreases the membrane surface transport resistances toward water molecules. Moreover, hydrophilic surfaces prevent membrane fouling by inducing the formation of a hydration layer at the membrane/water interface.[45]

Membrane performance is predominantly affected by the active layer characteristics, such as surface charge and pore size. Figure 6a shows the pH dependence of the membrane surface zeta potential curves. The results of the zeta potential demonstrated that the negative surface charge of the TFC membranes was lower than that of the PAN support. This weaker negative charge of the membrane surface after MPN coating has been reported before.[32,46] However, all membranes exhibited a negative zeta potential in the pH range of 5−8. The charge of a membrane plays a crucial role in determining its ability to reject solutes during filtration processes.[47] Surface charge has a strong influence on membrane separation performance owing to the Donnan effect. Therefore, the observed negative surface charges of the TA-Fe^{3+} layer would significantly impact the membrane rejection mechanism, enhancing the subsequent anionic solute rejection and selectivity. Moreover, the negative charge of the membrane surface enables the membrane to provide better antifouling performance.[48] The observed electronegativity of the TFC membrane surface is attributed to the ionizable functional groups in the TA-containing self-assembled network.

3.3. Membrane Separation Performance. *3.3.1. PEG Retention.* Figure 7 shows the retention of PEG 200−1000 g/mol by PAN support, M1, M2, M3, and M4. As PEG is a neutral molecule, the retention of PEG of different molecular weights portrays the size sieving ability of the membranes. Figure 7 shows that the PAN membrane (which is used as a support layer for the TFC membranes) does not significantly retain PEG 200−1000 g/mol. In other words, the pores of the PAN membranes are large enough to allow a complete permeation of neutral molecules as large as PEG 1000 g/mol. Hence, the retention behavior of M1, M2, M3, and M4 solely

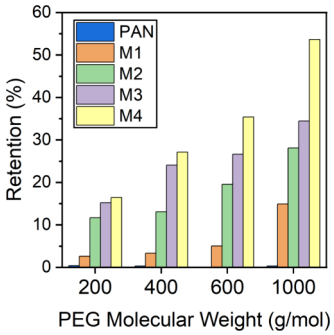

Figure 7. Neutral solute retention performance of double TA-Fe^{3+} layered membranes M1, M2, M3, and M4. Retention of 1 g/mol feed solution of PEG 200−1000 g/mol MW at 3 bar transmembrane pressure.

https://doi.org/10.1021/acsomega.4c04804
ACS Omega 2024, 9, 45870−45883

represents the size sieving property of the TA-Fe^{3+} selective layers of the TFC membranes due to the variation of pH of the TA solution between 3 and 8.5. Owing to the high surface porosity, M1 has the lowest retention of the PEG molecules among the four membranes. The retentions of PEG 200−600 g/mol by M1 are below 10%, while only that of PEG 1000 g/mol exceeds 10%. An increase of PEG retention by the membranes is observed when the pH of the TA casting solution rises. For all four studied PEG molecular weights, the retention decreased in the order of M4 > M3 > M2 > M1. It demonstrates that the size sieving ability of the TA-Fe^{3+} self-assembled thin selective layer can be controlled by varying the TA aqueous solution pH. Figure 7 also demonstrates that M1, M2, M3, and M4 allow a rather high permeation of PEG 200−1000 g/mol. Only the retention of PEG 1000 by M4 exceeds 50%. In every other case, the retention values are below 40%. In other words, in the absence of electrostatic interaction, the neutral solutes of 200−1000 g/mol can permeate rather easily through M1, M2, M3, and M4.

3.3.2. Single Dye Retention. Figure 8 shows the retention of three dyes from their respective aqueous solutions by M1, M2, M3, and M4. The molecular weights of orange II (OR-), riboflavin (RB0), and naphthol green B (NGB3-) are 350.32, 376.36, and 878.46 g/mol, respectively. Control experiments with the uncoated porous PAN membrane were performed first for analysis. Interestingly, this membrane exhibited low dye retention performances of only 1, 3, and 7% for riboflavin, orange II, and naphthol green B, respectively. The expected low rejections in the PAN likely stem from the enhanced convective transport of the dyes due to the large pore sizes of the support. The solutes encounter little to no hindrance in entering the membrane pore. However, the retention rates of the anionic dyes by the TFC membranes are significantly enhanced after MPN layer coating.

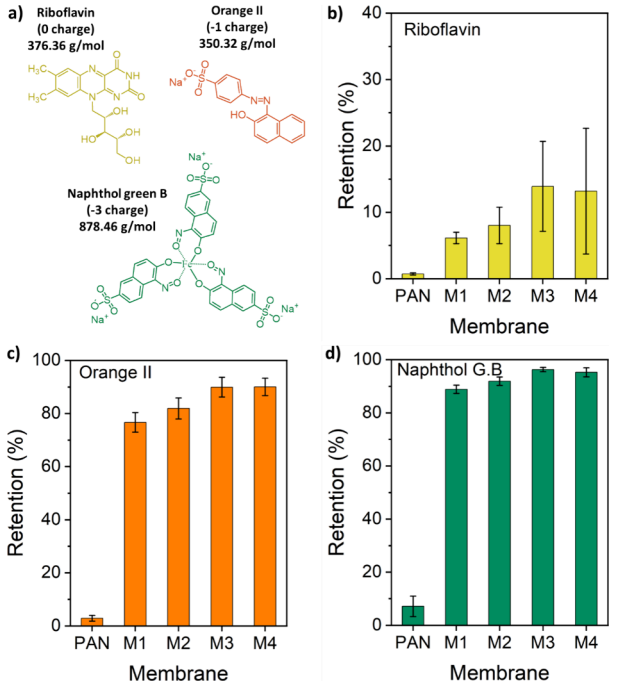

Figure 8. (a) Molecular structure of the organic solutes used for retention with their respective molecular weight and charge in aqueous solution, and single dye retention performance of the TA-Fe^{3+} membranes; (b) riboflavin, (c) orange II, and (d) naphthol green B retention.

As the TA-Fe^{3+} membranes have a negative surface charge, OR- and NGB3- are highly rejected. For example, the retentions of OR- and NGB3- by M1 are around 79 and 89%, respectively. It is noteworthy that the retention of PEG 400 g/mol by M1 is only ∼3% (Figure 7). Although OR- has a molecular weight of 350.32 g/mol, owing to the electrostatic repulsion by the surface of the membrane, the retention of OR- by M1 is approximately 24 times higher than that of PEG 400 g/mol. As expected, the neutral RB0 was hardly retained by M1 (5%) although the molecular weights of RB0 and OR- are comparable. This reiterates the charge selectivity of the MPN layer due to the Donnan effects, while the influence of size sieving on solute retention is minimal. Membranes basically reject organic solute molecules primarily through a combination of size exclusion and charge repulsion mechanisms. The size exclusion mechanism relies on the relative size of the dye molecules and the membrane pores. However, the low retention of electroneutral solutes of PEG and riboflavin in correlation with the observed SEM images illustrates the small contribution of size sieving to the overall retention mechanism. Therefore, the high retentions of the anionic dyes are due to the electrostatic repulsion interaction between the negatively charged TA-Fe^{3+} membrane surface (Figure 6a) and the charges carried by the organic solutes in solution. This exclusion mechanism supplies the MPN membranes with a charge-selective property to effectively separate and remove dye molecules from the aqueous solutions. Membranes M2, M3, and M4 also show a similar behavior, i.e., a substantially higher retention of OR- compared to RB0. The retentions of OR- by M2, M3, and M4 membranes are in the range of 82−90% (Figure 8c), while those of RB0 are only between 8 and 14% (Figure 8b). The multivalent anionic NGB3- was highly rejected by the membranes. 92−96% of the NGB3- retentions were achieved by M2, M3, and M4. These membranes displayed notable uncharged dye/charged dye selectivities, as presented in Table S1 of the Supporting Information. The RB0/NGB3- ideal selectivities of the four membranes are between 8.5 and 18.2, while the RB0/OR- selectivities are between 4.5 and 8.7. Ideal selectivities were also observed for the OR-/NGB3- dye pair owing to the larger size and valency of NGB3- compared with that of OR-.

3.3.3. Mixed Dye Retention. To investigate the separation performance of M1, M2, M3, and M4 in a mixed solute filtration, retention of a mixture of binary dyes was performed. A 1:1 molar mixture of riboflavin and naphthol green B (RB0/NGB3-) was used as an uncharged/charged dye mixture. Similarly, an equimolar mixture of negatively charged dyes, orange II and naphthol green B (OR-/NGB3-), was filtered by using the MPN membranes. During single dye retention, the membranes displayed a high riboflavin to naphthol green B ideal selectivity (Table S1 in the Supporting Information). For mixed dye solution filtration, 0.1 mM feed solutions were used. Figure 9 summarizes the results of the mixed dye solution tests. In both mixed dye experiments, the solutes easily permeated across the PAN control membrane, which showed no substantial dye retention (Figure 9). Almost no selectivities (∼1) for both RB0/NGB3- and OR-/NGB3- mixtures were obtained for the PAN membrane, and this further indicated that the support membrane has no significant influence on the retention or selectivity of the fabricated TFC membranes.

https://doi.org/10.1021/acsomega.4c04804
ACS Omega 2024, 9, 45870−45883

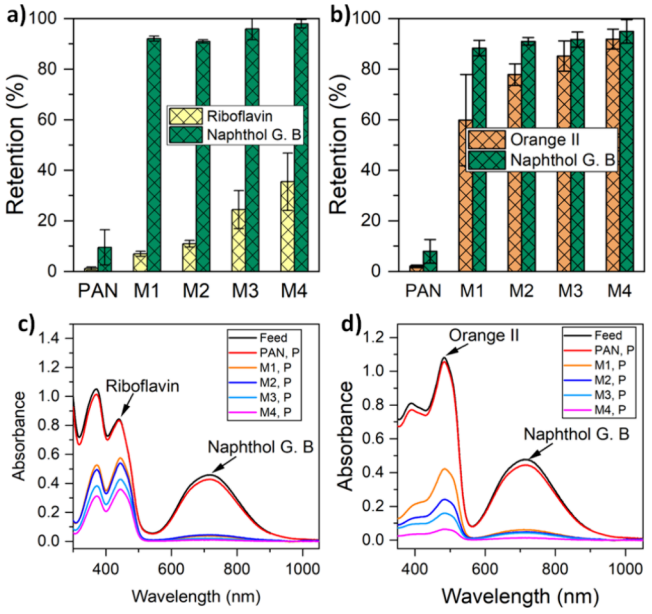

Figure 9. Mixed dye separation and selectivity of a (a) riboflavin and naphthol green B (RB0/NGB3-) mixture and (b) orange II and naphthol green B (OR-/NGB3-) mixture by double-layered membranes prepared at different pHs. M1, M2, M3, and M4 membranes were synthesized with aqueous solutions at pHs of 3, 5, 5.8, and 8.5, respectively. UV−vis spectra in (c) show riboflavin−naphthol green B separation with peaks at 444 and 715 nm, respectively, for the feed solution and the permeate samples of each membrane. The spectrum of the permeate (P) sample by the MPN membranes shows a disappearing peak attributed to naphthol green B, depicting effectual removal. (d) UV−vis spectra of the OR-/NGB3- mixture illustrating a decrease in the peaks of orange II (482 nm) and naphthol green B (715 nm) after filtration.

The MPN membranes can effectively separate the negatively charged NGB3- and neutral RB0 from the RB0/NGB3- mixture (Figure 9a). All membranes in the M1−M4 series displayed more than 90% retention toward naphthol green B. The M3 membrane that contains a double-layered TA-Fe^{3+} separation layer prepared at pH 5.8 can selectively remove 96% of the NGB3-, while the membrane synthesized at pH 8.5 (M4) removed 98% of the NGB3- from its mixture with RB0. As expected, the retentions of RB0 from the RB0/NGB3- mixture were significantly lower compared to those of NGB3-. However, a careful comparison of Figures 8b and 9a suggests that the retentions of RB0 from the feed solution containing the RB0/NGB3- mixture by the membranes were higher than those from the feed solution containing only RB0. M1, M2, M3, and M4 retained 7, 11, 25, and 35% of the RB0 from the feed solution containing the RB0/NGB3- mixture, respectively. Owing to the electrostatic exclusion, NGB3- molecules were constantly rejected from the membrane pores. Consequently, the permeation of anionic NGB3- lagged far behind the permeation of neutral RB0 through the membranes. The neutral RB0 had a substantially lower energy barrier compared to NGB3- to enter the pores of the membranes. In spite of that, RB0 had to compete with NGB3- for space to enter the pores. Such a competing effect resulted in a significant increase of RB0 retention when the feed solution contained the RB0/NGB3- mixture. The M4 membrane showed the best selective separation of neutral and anionic binary dye mixtures with a selectivity of 30.8, followed by the M3 membrane with 18.4 selectivity (Table 2). Thus, both M3 and M4 showed excellent performance in separating RB0 and NGB3- from their mixture.

Table 2. Separation Selectivity of Solutes in a Mixed Solute Retention Test

membrane	RB0/NGB3- selectivity	OR-/NGB3- selectivity
PAN	1.0	1.0
M1	11.7	3.4
M2	9.8	2.4
M3	18.4	1.8
M4	30.8	1.6

Both pore size and surface properties play a vital role during dye separation.[49] The overall membrane rejection ability arises from the combined effect of steric and Donnan exclusion. Such RB0/NGB3- separation results indicate the potential to separate small-molecule-sized dye mixtures by manipulating the membrane structure and chemistry. The zeta potential experiments showed that M4, for example, has a stronger negative charge compared to that of M3. The water flux and PEG retention results proved that the effective pore size of M4 is smaller than that of M3. A combination of these two membrane properties leads to a superior RB0/NGB3- selectivity for M4 compared to M3. However, no significant difference was observed between the OR-/NGB3- selectivities of the M1−M4 membranes. The result of the OR-/NGB3- mixture separation by the fabricated membranes is shown in Figure 9b. It can only be noted that M1 showed the best OR-/NGB3- separation property. The selectivity of OR- over NGB3- was 3.4 (Table 2). The retentions of both anionic dyes increased with an increase in solution pH during film fabrication. The decrease in pore size enhances the steric exclusion of the dyes. As a result, the selectivity between OR- and NGB3- dropped. Generally, better removal of NGB3- than OR- is observed by the TA-Fe^{3+} membranes owing to both the bigger molecular size and the three ionizable moieties in the NGB3- structure. A comparison of membrane performance for charge-based and size-based solute−solute separation of the TA-Fe^{3+} membranes with those of other studies reported in the literature for small organic molecules is presented in Table 3. A comprehensive comparison with recently published works indicates that our TA-Fe^{3+} membranes exhibit an excellent balance between water flux and solute separation selectivity. This demonstrates that the fabricated membranes hold great potential for improving the separation performances of NF membranes for small organic solutes.

3.3.4. Salt Retention. The single salt retention behavior of the prepared TFC membranes was determined with NaCl (Figure 10a). The membranes exhibited an extremely low retention of only 6−8% toward NaCl, with no significant impact of the pH at which the membranes were fabricated. The low salt rejection is mainly due to the large pore size of the membranes. The high permeation of salts indicates that the membranes can be beneficial for the separation of dye/salt mixtures since dye wastewater streams contain high concentrations of inorganic salts. To fractionate organic solutes from a saline mixture, salt extraction from the stream by a membrane is a critical issue while also achieving a high retention of the desired organic solute.[58] Furthermore, low salt retention during organic solute separation prevents an increase in the osmotic pressure of feed solutions, which can significantly reduce the driving force and permeation flux. In order to test

https://doi.org/10.1021/acsomega.4c04804
ACS Omega 2024, 9, 45870−45883

Table 3. Performance Comparison of the Fabricated TA-Fe^{3+} Membranes with Other Studies Reported for the Charge- and Size-Based Separation of Small Organic Molecules

membrane type	small organic molecules	molecular weight ($g \cdot mol^{-1}$)	molecular charge	selectivity diffusion[a]	selectivity filtration: single solutes	selectivity filtration: mixed solutes	water permeance ($L \cdot m^{-2} \cdot h^{-1} \cdot bar^{-1}$)	ref
M1	RB0	376.36	0		8.5	11.7	51	this work
	NGB3-	878.45	−3					
M4	RB0	376.36	0		18.2	30.8	17	this work
	NGB3-	878.45	−3					
M1	RB0	376.36	0		4.5		51	this work
	OR-	350.32	−1					
M4	RB0	376.36	0		8.7		17	this work
	OR-	350.32	−1					
M1	OR-	350.32	−1		1.9	3.4	51	this work
	NGB3-	878.45	−3					
M4	OR-	350.32	−1		2.1	1.6	17	this work
	NGB3-	878.45	−3					
MPN (MPN-1)	RB0	376.36	0		2.0		86.1	50
	OR-	350.32	−1					
MPN (MPN-6)	RB0	376.36	0		13.2		5.6	50
	OR-	350.32	−1					
MPN (MPN-1)	RB0	376.36	0		5.3	6.5	86.1	50
	NGB3-	878.45	−3					
MPN (MPN-6)	RB0	376.36	0		26.7	18.4	5.6	50
	NGB3-	878.45	−3					
MPN (MPN-1)	OR-	350.32	−1		2.9	3.6	86.1	50
	NGB3-	878.45	−3					
MPN (MPN-6)	OR-	350.32	−1		2	1.9	5.6	50
	NGB3-	878.45	−3					
MPN (1TA-3Fe)	RB0	376.36	0		3.2		62.5	32
	OR-	350.32	−1					
MPN (1TA-4.5Fe)	RB0	376.36	0		8.5		13.6	32
	OR-	350.32	−1					
MPN (1TA-6Fe)	RB0	376.36	0		20.6		3.8	32
	OR-	350.32	−1					
MPN (1TA-8Fe)	RB0	376.36	0		3.2		0.9	32
	OR-	350.32	−1					
amphiphilic random copolymer membrane	riboflavin	376.36	0	263	8.4[b]	19.2[b]	4.2	51
	acid blue 45	474.33	−2					
isoporous positively charged PI-*b*-PS-*b*-P4VP triblock terpolymer membrane (quaternized P4VP block)	RB0	376.36	0		21.3	28.3	11.0	52
	methylene blue	319.85	+1					
isoporous negatively charged PI-*b*-PS-*b*-P4VP triblock terpolymer membrane (sulfonated PI block)	OR-	350.32	−1		14.7	44.6	9.5	52
	NGB3-	878.45	−3					
isoporous negatively charged PI-*b*-PS-*b*-P4VP triblock terpolymer membrane (sulfonated PI block)	OR-	350.32	−1		64.3		9.5	52
	reactive green 19	1418.93	−6					
isoporous positively charged PS-*b*-P4VP diblock copolymer membrane (quaternized P4VP block)	RB0	376.36	0		35.7	39.9	3.8	53
	methylene blue	319.85	+1					
isoporous negatively charged PS-*b*-PI diblock copolymer membrane (sulfonated PI block)	OR-	350.32	−1		5.2		74	54
	reactive green 19	1418.93	−6					
NP-Den hybrid membrane	rhodamine 6G	479.02	+1	11				55
	calcein	622.53	−4					
self-assembled polyelectrolyte deposited PCTE	rhodamine 6G	479.02	+1	3.5				56
	calcein	622.53	−4					
cationic dendrimer deposited PCTE	calcein	622.53	−4	10				57
	rhodamine 6G	479.02	+1					

[a]The selectivities were determined from a single-solute system. [b]We calculated the selectivities using the reported retention values. RB0, riboflavin; NGB3-, naphthol green B; OR-, orange II; MPN, metal-polyphenol network; MPN-1, 1TA-4.5Fe assembly time 1 min; MPN-6, 1TA-4.5Fe

https://doi.org/10.1021/acsomega.4c04804
ACS Omega 2024, 9, 45870−45883

Table 3. continued

assembly time 6 min; NP-Den hybrid membrane, nanoporous membranes via chemically directed assembly of nanoparticles and dendrimers; PCTE, track etched polycarbonate membrane.

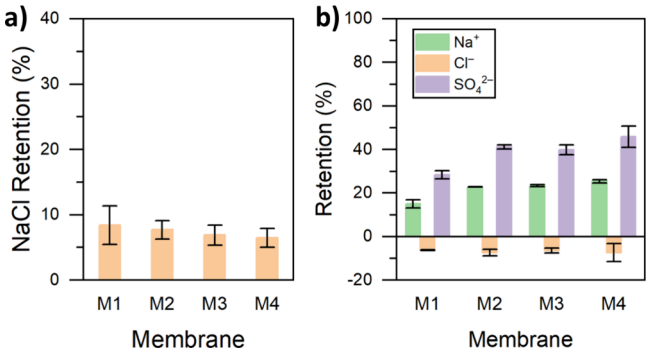

Figure 10. Salt retention performance of the MPN membranes. (a) NaCl single salt solution and (b) NaCl–Na_2SO_4 mixed salt solution. Feed solutions were fixed at 1 g/L. A Cl^-/SO_4^{2-} molar ratio of 1:1 was used for the mixed salt solution preparation.

the separation performance of the prepared membranes toward mixed ion feed solutions, filtration experiments were performed with a feed solution containing a mixture of NaCl and Na_2SO_4. It is obvious from Figure 10b that the retention of chloride by the TFC membranes is significantly lower than that of sulfate. Although the retentions of chloride by the TFC membrane from feed solutions containing only NaCl are slightly positive, in the case of the feed solution containing a mixture of NaCl and Na_2SO_4, the retentions of chloride are negative (between −6 and −7%). The sulfate retentions increased from 28 to 46% when the pH of the TA casting solution was increased from 3 (for M1) to 8.5 (for M4). Similarly, Na^+ retentions slightly improved from 15 to 25%. The higher retention of sulfate compared to that of chloride is a typical characteristic of membranes in the presence of mixed ions of the same charge. The Cl^-/SO_4^{2-} selectivity was in the range of 1.5–2, increasing with the pH of the casting solution. This membrane's selectivity toward the anions can be explained by the larger transport hindrance experienced by the divalent and less diffusive SO_4^{2-} ion with a larger hydrated size compared to the Cl^- ion.[59] The negative retention of chloride observed in the analyzed salt mixture is a consequence of the electroneutrality condition. This phenomenon has been encountered widely for ternary ion systems in the literature.[60−62] As Na^+ is a counterion to the membrane, sodium ions are transported to the permeate side due to the electrochemical potential gradient and a low exclusion by the membrane. Since the divalent and larger SO_4^{2-} is excluded by the membrane active layer, the more mobile and less charged coion, Cl^-, diffuses toward the permeate side of the membrane to neutralize the permeate solution. The transported Na^+ ions pull in the less excluded coion Cl^- so that electroneutrality is always fulfilled on both sides of the separation layer. The stirred cell dead-end filtration is performed with a large volume of feed solution compared to that of permeate solutions. Hence, there is a large quantity of chloride ions on the feed side of the membrane compared with the permeate side. The mass transfer of Cl^- leads to a higher permeate concentration relative to the feed. This resulted in the observed negative rejection of chloride from the ternary ion mixture.

3.3.5. Antifouling Performance of the TFC Membranes. Although membrane development has shown significant progress over the past half-century, membrane fouling remains a key challenge in membrane filtration. The presence of foulant organic compounds such as humic substances[63] in feed streams can lead to their adsorption on membrane surfaces. High concentrations of humic acid are found in raw wastewater and municipal wastewater effluents. As electrostatic and acid–base interactions strongly govern membrane fouling,[64] the fabrication of a separation layer with distinct membrane surface chemistry is beneficial in reducing fouling. Fouling studies demonstrate that membrane fouling is affected by hydrodynamic conditions, feedwater characteristics, and membrane properties.[65,66] The interfacial property of the membrane surface impacts the membrane–foulant interactions. Negatively charged, hydrophilic, and smooth membrane surface properties with weaker Lewis acid–base interactions between the membrane and foulant are beneficial in reducing membrane fouling.[64,65,67] Here, we investigated the fouling of humic acid on the TA-Fe^{3+} separation layer containing membranes. In order to monitor the performance of the fabricated membranes during the fouling operation, a two-cycle filtration of humic acid solution was measured. Figure 11

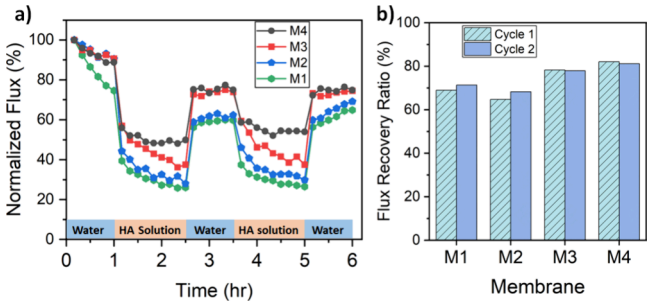

Figure 11. (a) Normalized flux variation during fouling test with HA solution and (b) FRR.

shows the normalized flux profiles and the FRRs of the membranes. The water fluxes declined slightly during the pure water filtration in the first 1 h. However, the fluxes decreased significantly when pure water was replaced by the humic acid solution. Comparatively, a small flux decline was observed for the membranes synthesized at high pH. The water flux of the thin films recovered to 69%–82% of their initial value after cleaning. A careful comparison of Figure 11a,b shows that M3 and M4 have higher FRRs compared to M1 and M2. It implies that the lower surface porosity of the TA-Fe^{3+} selective layers coated using the TA casting solutions of pH 5.8 and 8.5 leads to better antifouling properties. It must be taken into account that several factors affect the membrane fouling behavior. Strong electrostatic attractions allow the accumulation of macromolecular foulants on the membrane surface, while electrostatic repulsive forces act contrarily. The TA-Fe^{3+} TFC membrane's surface chemistry has shown that the membranes exhibit negative zeta potential in the 5–8 pH range (Figure 6a). Humic acid is also negatively charged in the aqueous solution due to the pH-dependent deprotonation of carboxylic and phenolic groups.[68] Therefore, the electrostatic repulsive

https://doi.org/10.1021/acsomega.4c04804
ACS Omega 2024, 9, 45870−45883

force contributes to the overall reduction in the deposition of humic acid on the membrane surface. Second, surface hydrophilicity influences membrane fouling. Hydrophobic membranes have a higher affinity for foulants than those comprising hydrophilic surfaces. Contact angle characterization (Figure 6b) has shown that an increase in hydrophilicity was generally observed in the order of membranes M1−M4. This supports the decrease in the flux decline as well as the increase in flux recovery for the membranes fabricated at high pH. Binding of water molecules to the surface of the hydrophilic thin films through water layer formation prevents membrane fouling.[69] Moreover, the formation of the hydration layer (water layer) makes the removal of fouled humic acid through cleaning easy.

4. CONCLUSIONS

The pH of a solution significantly affects metal−polyphenol self-assembly, influencing the structure and performance of the resulting thin film. In this work, we presented the pH of the TA solution as an effective parameter to tailor the membrane surface properties of TA-Fe^{3+} containing TFC membranes fabricated via LBL deposition. In this regard, a series of membranes have been prepared by systematically varying the pH of the TA casting solution for each deposited TA-Fe^{3+} layer or the number of layers deposited, while the other casting parameters were kept constant. The findings of this work showed that TFC membranes with high hydraulic resistance to water transport are fabricated when a TA-Fe^{3+} layer is synthesized at a higher pH on top of an already existing MPN layer synthesized at a low pH. The reverse procedure results in a porous structure with high water permeance. In general, an increase in pH led to a decrease in surface porosity due to the increase in complex formation at a higher pH. For double TA-Fe^{3+} layered TFC membranes where both layers were fabricated at the same pH, increasing the pH of the solution for coating decreased the membrane surface porosity and the water permeation rate while forming more hydrophilic surfaces. The fabricated membranes exhibited low salt retention performance, which can be beneficial for dye/salt fractionation and for reducing the osmotic pressure. In addition, the well-controlled MPN coating showed that neutral organic components PEG and riboflavin can easily permeate through the separation layer, whereas a high retention of anionic dyes by the MPN membranes was achieved. The high selectivities between anionic charged and neutral groups in both single and mixed solute retention reveal that the polyphenol-containing thin films hold great potential for charge-based solute−solute separation. The membranes prepared at different pH values showed excellent performance in separating small organics. The neutral/anionic dye selectivity from mixed dye retention tests increased with an increase in the pH during membrane fabrication. Specifically, the M4 membrane displayed the best riboflavin/naphthol green B separation selectivity of more than 30, the highest selectivity reported for a TFC membrane having an MPN selective layer. The TFC membranes also demonstrated the selective permeation of Cl^- ions over SO_4^{2-} ions from a feed solution containing a Na^+, SO_4^{2-}, and Cl^- ternary ion mixture. Furthermore, it was demonstrated that TA-Fe^{3+} selective layers coated at a higher pH led to a better FRR of the TFC membranes. It is evident that the pH of the TA casting solution is an effective tool for tuning the performance of TFC membranes having TA-Fe^{3+} selective layers.

■ ASSOCIATED CONTENT

Supporting Information

The Supporting Information is available free of charge at https://pubs.acs.org/doi/10.1021/acsomega.4c04804.

FTIR spectra of TA-Fe^{3+} membranes (Figure S1), PWP of MPN TFC membranes (Figures S2 and S3), time-dependent WCA (Figure S4), and selectivity of dyes during single dye retention tests (Table S1) (PDF)

■ AUTHOR INFORMATION

Corresponding Author

Md. Mushfequr Rahman − *Institute of Membrane Research, Helmholtz-Zentrum Hereon, 21502 Geesthacht, Germany;* orcid.org/0000-0001-9672-5556; Email: mushfequr.rahman@hereon.de

Authors

Hluf Hailu Kinfu − *Institute of Membrane Research, Helmholtz-Zentrum Hereon, 21502 Geesthacht, Germany;* orcid.org/0000-0002-7809-3345

Nicolás Cevallos-Cueva − *Institute of Membrane Research, Helmholtz-Zentrum Hereon, 21502 Geesthacht, Germany;* orcid.org/0000-0002-2600-8209

Volker Abetz − *Institute of Membrane Research, Helmholtz-Zentrum Hereon, 21502 Geesthacht, Germany; Institute of Physical Chemistry, University of Hamburg, 20146 Hamburg, Germany;* orcid.org/0000-0002-4840-6611

Complete contact information is available at: https://pubs.acs.org/10.1021/acsomega.4c04804

Author Contributions

H.H.K.: Conceptualization, methodology, investigation, writing—original draft, writing—review and editing; M.M.R.: conceptualization, writing—original draft, writing—review and editing, funding acquisition, project administration, supervision; N.C.-C.: methodology, writing—review and editing; V.A.: conceptualization, supervision, writing—review and editing. All authors have given approval to the final version of the manuscript.

Funding

This work was funded by the Hereon-I²B-Project NanoMem.

Notes

The authors declare no competing financial interest.

■ ACKNOWLEDGMENTS

The authors acknowledge Maren Brinkmann for the PEG retention analysis in GPC, Juliana Clodt for preparing the polyacrylonitrile support, Erik S. Schneider for the SEM images, and Jan Pohlmann for setting up the flux and retention measurement facilities.

■ REFERENCES

(1) Ejima, H.; Richardson, J. J.; Liang, K.; Best, J. P.; Van Koeverden, M. P.; Such, G. K.; Cui, J.; Caruso, F. One-Step Assembly of Coordination Complexes. *Science* **2013**, *341* (6142), 154−157.

(2) Holten-Andersen, N.; Harrington, M. J.; Birkedal, H.; Lee, B. P.; Messersmith, P. B.; Lee, K. Y. C.; Waite, J. H. pH-induced metal-ligand cross-links inspired by mussel yield self-healing polymer networks with near-covalent elastic moduli. *Proceedings of the National Academy of Sciences of the United States of America* **2011**, *108* (7), 2651−2655.

(3) Huang, S. Y.; Zhang, Y.; Shi, J. F.; Huang, W. P. Superhydrophobic Particles Derived from Nature-Inspired Polyphenol Chemistry for Liquid Marble Formation and Oil Spills Treatment. *Acs Sustain Chem Eng* **2016**, *4* (3), 676−681.
(4) Zhou, J.; Lin, Z.; Ju, Y.; Rahim, M. A.; Richardson, J. J.; Caruso, F. Polyphenol-Mediated Assembly for Particle Engineering. *Acc. Chem. Res.* **2020**, *53* (7), 1269−1278.
(5) Cao, X. T.; Luo, J. Q.; Woodley, J. M.; Wan, Y. H. Mussel-inspired co-deposition to enhance bisphenol A removal in a bifacial enzymatic membrane reactor. *Chem Eng J* **2018**, *336*, 315−324.
(6) Kim, S.; Kim, D. S.; Kang, S. M. Reversible Layer-by-Layer Deposition on Solid Substrates Inspired by Mussel Byssus Cuticle. *Chemistry - An Asian Journal* **2014**, *9* (1), 63−66.
(7) Saowalak, K.; Titipun, T.; Somchai, T.; Chalermchai, P. Iron(III)-Tannic Molecular Nanoparticles Enhance Autophagy effect and T(1) MRI Contrast in Liver Cell Lines. *Sci. Rep.* **2018**, *8* (1), 6647.
(8) Qin, Y.; Wang, J. P.; Qiu, C.; Hu, Y.; Xu, X. M.; Jin, Z. Y. Self-Assembly of Metal-Phenolic Networks as Functional Coatings for Preparation of Antioxidant, Antimicrobial, and pH-Sensitive-Modified Starch Nanoparticles. *Acs Sustain Chem Eng* **2019**, *7* (20), 17379−17389.
(9) Li, Z. J.; Zhao, X.; Gong, F. Y.; Lin, C. M.; Liu, Y.; Yang, Z. J.; Nie, F. D. Multilayer Deposition of Metal-Phenolic Networks for Coating of Energetic Crystals: Modulated Surface Structures and Highly Enhanced Thermal Stability. *Acs Appl Energ Mater* **2020**, *3* (11), 11091−11098.
(10) Purkait, M. K.; Sinha, M. K.; Mondal, P.; Singh, R. Biologically Responsive Membranes. In *Interface Science and Technology*; Elsevier, 2018; vol 25, pp 145-171.
(11) Fan, L.; Ma, Y.; Su, Y.; Zhang, R.; Liu, Y.; Zhang, Q.; Jiang, Z. Green coating by coordination of tannic acid and iron ions for antioxidant nanofiltration membranes. *RSC Advances* **2015**, *5* (130), 107777−107784.
(12) Guo, H.; Peng, L. E.; Yao, Z.; Yang, Z.; Ma, X.; Tang, C. Y. Non-Polyamide Based nanofiltration Membranes Using Green Metal-Organic Coordination Complexes: Implications for the Removal of Trace Organic Contaminants. *Environ. Sci. Technol.* **2019**, *53* (5), 2688−2694.
(13) Kim, H. J.; Kim, D. G.; Yoon, H.; Choi, Y. S.; Yoon, J.; Lee, J. C. Polyphenol/Fe^{III} Complex Coated Membranes Having Multifunctional Properties Prepared by a One-Step Fast Assembly. *Adv. Mater. Interfaces* **2015**, *2* (14), No. 1500298.
(14) Maruf, S. H.; Greenberg, A. R.; Pellegrino, J.; Ding, Y. F. Fabrication and characterization of a surface-patterned thin film composite membrane. *J. Membr. Sci.* **2014**, *452*, 11−19.
(15) Dong, X.; Lu, D.; Harris, T. A. L.; Escobar, I. C. Polymers and Solvents Used in Membrane Fabrication: A Review Focusing on Sustainable Membrane Development. *Membranes (Basel)* **2021**, *11* (5), 309.
(16) Razali, M.; Kim, J. F.; Attfield, M. P.; Budd, P. M.; Drioli, E.; Lee, Y. M.; Szekely, G. Sustainable wastewater treatment and recycling in membrane manufacturing. *Green Chemistry* **2015**, *17* (12), 5196−5205.
(17) Jia, Y. D.; Guan, K. C.; Zhang, P. F.; Shen, Q.; Istirokhatun, T.; Lin, Y. Q.; Matsuyama, H. Nanostructural Manipulation of Polyphenol Coatings for Superwetting Membrane Surfaces. *Acs Sustain Chem Eng* **2021**, *9* (43), 14525−14536.
(18) Li, S. J.; Chen, J. S.; Wang, J. Y.; Zeng, H. B. Anti-biofouling materials and surfaces based on mussel-inspired chemistry. *Mater Adv* **2021**, *2* (7), 2216−2230.
(19) Arul, P.; Nandhini, C.; Huang, S. T.; Gowthaman, N. S. K. Development of water-dispersible Dy(III)-based organic framework as a fluorescent and electrochemical probe for quantitative detection of tannic acid in real alcoholic and fruit beverages. *Anal. Chim. Acta* **2023**, *1274*, No. 341582.
(20) Hatami, E.; Nagesh, P. K. B.; Chowdhury, P.; Chauhan, S. C.; Jaggi, M.; Samarasinghe, A. E.; Yallapu, M. M. Tannic Acid-Lung Fluid Assemblies Promote Interaction and Delivery of Drugs to Lung Cancer Cells. *Pharmaceutics* **2018**, *10* (3), 111.
(21) Cuhorka, J.; Wallace, E.; Mikulásek, P. Removal of micro-pollutants from water by commercially available nanofiltration membranes. *Sci. Total Environ.* **2020**, *720*, No. 137474.
(22) Sontakke, A. D.; Das, P. P.; Mondal, P.; Purkait, M. K. Thin-film composite nanofiltration hollow fiber membranes toward textile industry effluent treatment and environmental remediation applications: review. *Emergent Mater* **2022**, *5* (5), 1409−1427.
(23) Xu, R.; Qin, W.; Tian, Z. S.; He, Y.; Wang, X. M.; Wen, X. H. Enhanced micropollutants removal by nanofiltration and their environmental risks in wastewater reclamation: A pilot-scale study. *Sci. Total Environ.* **2020**, *744*, No. 140954.
(24) Fang, X. F.; Wei, S. H.; Liu, S.; Li, R.; Zhang, Z. Y.; Liu, Y. B.; Zhang, X. R.; Lou, M. M.; Chen, G.; Li, F. Metal-Coordinated nanofiltration Membranes Constructed on Metal Ions Blended Support toward Enhanced Dye/Salt Separation and Antifouling Performances. *Membranes* **2022**, *12* (3), 340.
(25) Wu, J. D.; Hou, Z. Q.; Yu, Z. X.; Lang, J. H.; Cui, J. Y.; Yang, J.; Dai, J. D.; Li, C. X.; Yan, Y. S.; Xie, A. Facile preparation of metal-polyphenol coordination complex coated PVDF membrane for oil/water emulsion separation. *Separation and Purification Technology* **2021**, *258*, No. 118022.
(26) Zhang, Y. X.; Duan, X. F.; Tan, B. R.; Jiang, Y. C.; Wang, Y.; Qi, T. PVDF microfiltration membranes modified with AgNPs/tannic acid for efficient separation of oil and water emulsions. *Colloid Surface A* **2022**, *644*, No. 128844.
(27) Xie, H. L.; Shen, L. G.; Xu, Y. C.; Hong, H. C.; Yang, L. N.; Li, R. J.; Lin, H. J. Tannic acid (TA)-based coating modified membrane enhanced by successive inkjet printing of Fe3+ and sodium periodate (SP) for efficient oil-water separation. *J. Membr. Sci.* **2022**, *660*, No. 120873.
(28) Liu, Y. F.; Bai, Z. X.; Lin, G.; Xia, Y. Q.; Tong, L. F.; Li, T. R.; Liu, C. C.; Liu, S. N.; Jia, K.; Liu, X. B. Tannic acid-mediated interfacial layer-by-layer self-assembly of nanofiltration membranes for high-efficient dye separation. *Appl. Surf. Sci.* **2022**, *602*, No. 154264.
(29) Xiao, Y.; Guo, D.; Li, T.; Zhou, Q.; Shen, L.; Li, R.; Xu, Y.; Lin, H. Facile fabrication of superhydrophilic nanofiltration membranes via tannic acid and irons layer-by-layer self-assembly for dye separation. *Appl. Surf. Sci.* **2020**, *515*, No. 146063.
(30) Liu, D.; Chen, Y.; Tran, T. T.; Zhang, G. Facile and rapid assembly of high-performance tannic acid thin-film nanofiltration membranes via Fe^{3+} intermediated regulation and coordination. *Separation and Purification Technology* **2021**, *260*, No. 118228.
(31) Krogsgaard, M.; Nue, V.; Birkedal, H. Mussel-Inspired Materials: Self-Healing through Coordination Chemistry. *Chem.-Eur. J.* **2016**, *22* (3), 844−857.
(32) Kinfu, H. H.; Rahman, M. M.; Schneider, E. S.; Cevallos-Cueva, N.; Abetz, V. Charge and size selective thin film composite membranes having tannic acid−Ferric ion network as selective layer. *J. Membr. Sci.* **2023**, *679*, No. 121709.
(33) Plakas, K. V.; Karabelas, A. J.; Wintgens, T.; Melin, T. A study of selected herbicides retention by nanofiltration membranes - The role of organic fouling. *J. Membr. Sci.* **2006**, *284* (1−2), 291−300.
(34) Çakar, S.; Özacar, M. The pH dependent tannic acid and Fe-tannic acid complex dye for dye sensitized solar cell applications. *J Photoch Photobio A* **2019**, *371*, 282−291.
(35) Dultz, S.; Mikutta, R.; Kara, S. N. M.; Woche, S. K.; Guggenberger, G. Effects of solution chemistry on conformation of self-aggregated tannic acid revealed by laser light scattering. *Sci. Total Environ.* **2021**, *754*, No. 142119.
(36) Shen, Y. J.; Fang, L. F.; Yan, Y.; Yuan, J. J.; Gan, Z. Q.; Wei, X. Z.; Zhu, B. K. Metal-organic composite membrane with sub-2 nm pores fabricated via interfacial coordination. *J. Membr. Sci.* **2019**, *587*, 117146.
(37) Rahim, M. A.; Ejima, H.; Cho, K. L.; Kempe, K.; Müllner, M.; Best, J. P.; Caruso, F. Coordination-driven multistep assembly of metal-polyphenol films and capsules. *Chem. Mater.* **2014**, *26* (4), 1645−1653.

https://doi.org/10.1021/acsomega.4c04804
ACS Omega 2024, 9, 45870−45883

(38) Guo, S. W.; Wan, Y. H.; Chen, X. R.; Luo, J. Q. Loose nanofiltration membrane custom-tailored for resource recovery. *Chem Eng J* **2021**, *409*, No. 127376.
(39) Zhu, J. Y.; Tian, M. M.; Zhang, Y. T.; Zhang, H. Q.; Liu, J. D. Fabrication of a novel ″loose″ nanofiltration membrane by facile blending with Chitosan-Montmorillonite nanosheets for dyes purification. *Chem Eng J* **2015**, *265*, 184−193.
(40) Zhao, X. T.; Wang, R. X.; Lan, Y. Y.; Wang, T. Y.; Pan, J. F.; Liu, L. F. Engineering superwetting membranes through polyphenol-polycation-metal complexation for high-efficient oil/water separation: From polyphenol to tailored nanostructures. *J. Membr. Sci.* **2021**, *630*, No. 119310.
(41) Zhou, Y. Y.; Zhang, J.; Wang, Z. X.; He, F.; Peng, S. Q.; Li, Y. X. A modified TA-APTES coating: Endowing porous membranes with uniform, durable superhydrophilicity and outstanding anti-crude oil-adhesion property via one-step process. *J. Membr. Sci.* **2021**, *618*, No. 118703.
(42) Yalcinkaya, F.; Yalcinkaya, B.; Pazourek, A.; Mullerova, J.; Stuchlik, M.; Maryska, J. Surface Modification of Electrospun PVDF/PAN Nanofibrous Layers by Low Vacuum Plasma Treatment. *Int. J. Polym. Sci.* **2016**, *2016*, No. 4671658.
(43) Yan, W.; Shi, M.; Dong, C.; Liu, L.; Gao, C. Applications of tannic acid in membrane technologies: A review. *Adv. Colloid Interface Sci.* **2020**, *284* (229), No. 102267.
(44) Wang, Y. X.; Zhu, C. Y.; Lu, F.; Yu, Z. F.; Yang, H. C.; Xue, M.; Xu, Z. K. Metal-Polyphenol Coordination at the Aqueous Contra-diffusion ″Interface″: A Green Way to High-Performance Iron(III)/Tannic Acid Thin-Film-Composite nanofiltration Membranes. *Langmuir* **2022**, *38* (45), 13793−13802.
(45) Liu, C.; Guo, Y. Q.; Zhang, J. M.; Tian, B.; Lin, O. K.; Liu, Y. W.; Zhang, C. H. Tailor-made high-performance reverse osmosis membranes by surface fixation of hydrophilic macromolecules for wastewater treatment. *Rsc Advances* **2019**, *9* (31), 17766−17777.
(46) Zhu, X.; Liang, H.; Tang, X.; Bai, L.; Zhang, X.; Gan, Z.; Cheng, X.; Luo, X.; Xu, D.; Li, G. Supramolecular-Based Regenerable Coating Layer of a Thin-Film Composite nanofiltration Membrane for Simultaneously Enhanced Desalination and Antifouling Properties. *ACS Applied Materials and Interfaces* **2019**, *11* (23), 21137−21149.
(47) Bellona, C.; Drewes, J. E.; Xu, P.; Amy, G. Factors affecting the rejection of organic solutes during NF/RO treatment - a literature review. *Water Res.* **2004**, *38* (12), 2795−2809.
(48) Zarshenas, K.; Dou, H.; Habibpour, S.; Yu, A.; Chen, Z. Thin Film Polyamide Nanocomposite Membrane Decorated by Polyphenol-Assisted Ti(3)C(2)T(x) MXene Nanosheets for Reverse Osmosis. *ACS Appl Mater Interfaces* **2022**, *14* (1), 1838−1849.
(49) Chen, M.; Yang, H.; Xu, Z. L.; Cheng, C. Separation of single and mixed anionic dyes in saline solutions using uncharged polyacrylonitrile-tris(hydroxymethyl)aminomethane (PAN-Tris) ultrafiltration membrane: Performance and mechanism. *Journal of Cleaner Production* **2022**, *336*, No. 130471.
(50) Kinfu, H. H.; Rahman, M. M.; Schneider, E. S.; Cevallos-Cueva, N.; Abetz, V. Using the Assembly Time as a Tool to Control the Surface Morphology and Separation Performance of Membranes with a Tannic Acid−Fe^{3+} Selective Layer. *Membranes* **2024**, *14* (6), 133.
(51) Sadeghi, I.; Kronenberg, J.; Asatekin, A. Selective Transport through Membranes with Charged Nanochannels Formed by Scalable Self-Assembly of Random Copolymer Micelles. *Acs Nano* **2018**, *12* (1), 95−108.
(52) Zhang, Z. Z.; Rahman, M. M.; Abetz, C.; Hohme, A. L.; Sperling, E.; Abetz, V., Chemically Tailored Multifunctional Asymmetric isoporous Triblock terpolymer Membranes for Selective Transport. *Adv. Mater.* **2020**, *32* (8), DOI: .
(53) Zhang, Z. Z.; Rahman, M. M.; Bajer, B.; Scharnagl, N.; Abetz, V., Highly selective isoporous block copolymer membranes with tunable polyelectrolyte brushes in soft nanochannels. *J. Membr. Sci.* **2022**, *646*, 120266.
(54) Zhang, Z.; Rahman, M. M.; Abetz, C.; Abetz, V. High-performance asymmetric isoporous nanocomposite membranes with chemically-tailored amphiphilic nanochannels. *Journal of Materials Chemistry A* **2020**, *8* (19), 9554−9566.
(55) Park, M. H.; Subramani, C.; Rana, S.; Rotello, V. M. Chemoselective Nanoporous Membranes via Chemically Directed Assembly of Nanoparticles and Dendrimers. *Adv. Mater.* **2012**, *24* (43), 5862−5866.
(56) Savariar, E. N.; Krishnamoorthy, K.; Thayumanavan, S. Molecular discrimination inside polymer nanotubules. *Nature Nanotechnology* **2008**, *3* (2), 112−117.
(57) Savariar, E. N.; Sochat, M. M.; Klaikherd, A.; Thayumanavan, S. Functional Group Density and Recognition in Polymer Nanotubes. *Angew Chem Int Edit* **2009**, *48* (1), 110−114.
(58) Lin, J. Y.; Ye, W. Y.; Zeng, H. M.; Yang, H.; Shen, J. N.; Darvishmanesh, S.; Luis, P.; Sotto, A.; Van der Bruggen, B. Fractionation of direct dyes and salts in aqueous solution using loose nanofiltration membranes. *J. Membr. Sci.* **2015**, *477*, 183−193.
(59) Roy, Y.; Lienhard, J. H. A framework to analyze sulfate chloride selectivity in nanofiltration. *Environ Sci-Wat Res* **2019**, *5* (3), 585−598.
(60) Gao, X. R.; Li, P.; Qin, Y.; Bai, C. L.; Gu, Z. Y.; Yu, S. L. Negative rejection phenomenon in the mixed salt nanofiltration: Law and mechanism. *Desalination* **2024**, *583*, No. 117667.
(61) Labban, O.; Liu, C.; Chong, T. H.; Lienhard, V. J. H. Fundamentals of low-pressure nanofiltration: Membrane characterization, modeling, and understanding the multi-ionic interactions in water softening. *J. Membr. Sci.* **2017**, *521*, 18−32.
(62) Yaroshchuk, A. E. Negative rejection of ions in pressure-driven membrane processes. *Adv. Colloid Interface Sci.* **2008**, *139* (1−2), 150−173.
(63) Tang, C. Y.; Kwon, Y. N.; Leckie, J. O. Fouling of reverse osmosis and nanofiltration membranes by humic acid - Effects of solution composition and hydrodynamic conditions. *J. Membr. Sci.* **2007**, *290* (1−2), 86−94.
(64) Virga, E.; Zvab, K.; de Vos, W. M. Fouling of nanofiltration membranes based on polyelectrolyte multilayers: The effect of a zwitterionic final layer. *J. Membr. Sci.* **2021**, *620*, No. 118793.
(65) Tang, C. Y. Y.; Chong, T. H.; Fane, A. G. Colloidal interactions and fouling of NF and RO membranes: A review. *Adv. Colloid Interface Sci.* **2011**, *164* (1−2), 126−143.
(66) Wang, Y. N.; Tang, C. Y. Y. Protein fouling of nanofiltration, reverse osmosis, and ultrafiltration membranes-The role of hydrodynamic conditions, solution chemistry, and membrane properties. *J. Membr. Sci.* **2011**, *376* (1−2), 275−282.
(67) Meng, X. R.; Tang, W. T.; Wang, L.; Wang, X. D.; Huang, D. X.; Chen, H. N.; Zhang, N. Mechanism analysis of membrane fouling behavior by humic acid using atomic force microscopy: Effect of solution pH and hydrophilicity of PVDF ultrafiltration membrane interface. *J. Membr. Sci.* **2015**, *487*, 180−188.
(68) Ritchie, J. D.; Perdue, E. M. Proton-binding study of standard and reference fulvic acids, humic acids, and natural organic matter. *Geochim Cosmochim Ac* **2003**, *67* (1), 85−96.
(69) Choudhury, R. R.; Gohil, J. M.; Mohanty, S.; Nayak, S. K. Antifouling, fouling release and antimicrobial materials for surface modification of reverse osmosis and nanofiltration membranes. *Journal of Materials Chemistry A* **2018**, *6* (2), 313−333.

https://doi.org/10.1021/acsomega.4c04804
ACS Omega 2024, 9, 45870−45883

Chapter 6. Mass Transport of Dye Solutions through Porous Membrane Containing Tannic Acid/Fe^{3+} Selective Layer

This chapter discusses the implementation of a mass transport model for describing the transport of organic solutes through TA-Fe^{3+} membranes. For the first time, the behaviour of dye solution rejection performance of selective layers synthesized through metal-polyphenol coordination chemistry is simulated. The validity and limitations of Spiegler-Kedem-Katchalsky (SKK) model in predicting neutral and charged component transport through the pores of the metal-polyphenol film is examined. The reflection coefficient (σ) and solute permeability (P_S) were computed and showed that they strongly depend on the porous medium as well as dye molecular size and charge. The model excellently fits the experimentally measured rejections at different permeate fluxes and concentrations. However, the model underestimates dye rejection at low fluxes. This work provides mass transport insights of dye solutions through TA-Fe^{3+} layers and allows prediction of the maximum attainable dye rejection by the TFC membranes at high Peclet number (at high flux).

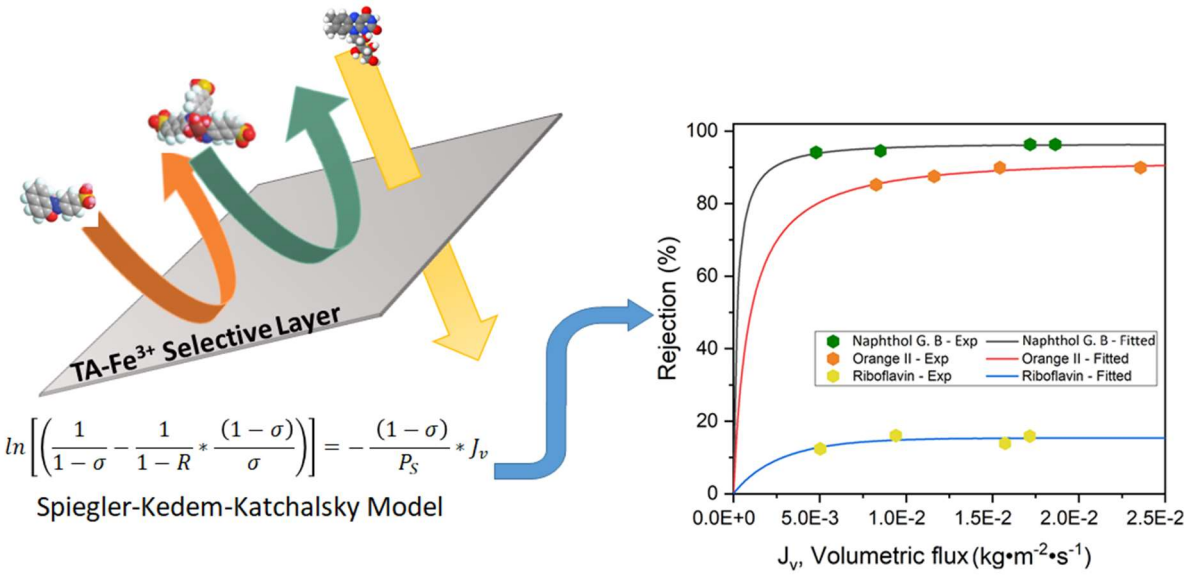

membranes

MDPI

Article

Mass Transport of Dye Solutions through Porous Membrane Containing Tannic Acid/Fe^{3+} Selective Layer

Hluf Hailu Kinfu [1], Md. Mushfequr Rahman [1,*], Nicolás Cevallos-Cueva [1] and Volker Abetz [1,2]

[1] Helmholtz-Zentrum Hereon, Institute of Membrane Research, Max-Planck-Straße 1, 21502 Geesthacht, Germany
[2] Institute of Physical Chemistry, University of Hamburg, Martin-Luther-King-Platz 6, 20146 Hamburg, Germany
* Correspondence: mushfequr.rahman@hereon.de; Tel.: +49-415-287-2446

Abstract: Tannic acid (TA)–Fe^{3+} membranes have received recent attention due to their sustainable method of fabrication, high water flux and organic solutes rejection performance. In this paper, we present a description of the transport of aqueous solutions of dyes through these membranes using the transport parameters of the Spiegler–Kedem–Katchalsky (SKK) model. The reflection coefficient (σ) and solute permeability (P_S) of the considered TA–Fe^{3+} membranes were estimated from the non-linear model equations to predict the retention of solutes. The coefficients σ and P_S depended on the porous medium and dye molecular size as well as the charge. The simulated rejections were in good agreement with the experimental findings. The model was further validated at low permeate fluxes as well as at various feed concentrations. Discrepancies between the observed and simulated data were observed at low fluxes and diluted feed solutions due to limitations of the SKK model. This work provides insights into the mass transport mechanism of dye solutions and allows the prediction of dye rejection by the TFC membranes containing a TA–Fe^{3+} selective layer using an SKK model.

Keywords: Spiegler–Kedem model; reflection coefficient; solute permeability; tannic acid–metal ion membranes; metal polyphenol complex membranes; dye retention

Citation: Kinfu, H.H.; Rahman, M.M.; Cevallos-Cueva, N.; Abetz, V. Mass Transport of Dye Solutions through Porous Membrane Containing Tannic Acid/Fe^{3+} Selective Layer. *Membranes* **2022**, *12*, 1216. https://doi.org/10.3390/membranes12121216

Academic Editor: Arian Nijmeijer

Received: 13 November 2022
Accepted: 27 November 2022
Published: 1 December 2022

1. Introduction

Wastewater, especially industrial effluents from textile plants, contains high concentration of dyes. At up to approx. 54% of the total, the textile industry is the main contributor of dye wastewater globally [1]. It is estimated that more than 15% of textile dyes used for dyeing operations ends up in wastewater streams, which is harmful to the environment [2]. Membranes offer a clean, economical and effective method of dyestuff recovery and wastewater treatment [1,3]. Due to their high retention rate, nanofiltration and reverse osmosis have been used for the treatment of industrial wastewater containing dyes [4–7]. Reverse osmosis is notorious for its high energy consumption and delivers low permeate flux. Nowadays, porous-high-flux membranes, such as ultrafiltration and loose nanofiltration membranes, which operate at low pressure gradients, appear to be more attractive [8–10]. Therefore, the development of new porous membranes with a specific focus on the removal of dyes from an aqueous solution is a vibrant research topic [11–14]. Moreover, efforts have been made to utilize porous membranes for the separation of individual dyes from an aqueous solution containing a mixture of dyes [15]. The development of new membranes and the optimization of membrane-casting parameters to find a good balance between the counteracting permeance and selectivity of the membranes is important [16]. By comparison, the comprehensive understanding of the flux and rejection behavior of a membrane using predictive mass transport models has received significantly less attention. Predictive mass transport models can be utilized to check the feasibility of separating organic solutes (e.g., dye) from a solution with a specific membrane. A good predictive

model can provide insight regarding the structural property correlations of membranes and thereby facilitate the optimization of membrane fabrication parameters. Moreover, mass transport models can be expanded to visualize the optimal design of membrane modules and even membrane-based processes to some extent. Several models have been utilized to demonstrate component transport and rejection in porous films. However, there is a lack of understanding regarding the correlations between the nature of solutes, membrane morphology and modes of transport. The availability of empirical methods for the accurate determination of a membrane's characteristics (e.g., tortuosity and surface charge density) to be used as model input parameters is a major limitation in the progress of mass transport modeling of porous membranes [17].

The Spiegler–Kedem–Katchalsky (SKK) model, a phenomenological approach defined through irreversible thermodynamics, is widely used to analyze the solute retention behavior of nanofiltration membranes. The model was first derived by Kedem and Katchalsky and was then modified by Spiegler and Kedem [18]. Being a phenomenological model, the SKK model does not take into account membrane characteristics. The membrane is considered a black box in this approach. However, the relationship between driving forces and permeate flux can be expressed explicitly [19]. The SKK model correlates the volumetric flux of a two-component (i.e., one solvent and one solute) solution with the flux of the solute. Hence, it provides a way to predict the retention and permeability of the solute in a membrane [20]. The SKK model was first employed for a reverse osmosis membrane. Since then, this phenomenological model has been extensively used to analyze and describe nanofiltration [21] and diafiltration [22] membranes. Nayak et al. [23] successfully employed the SKK model as a tool for predicting the retention of pharmaceutical pollutants from an aqueous solution using nanofiltration membranes. Furthermore, it was demonstrated that the SKK model could successfully predict dye–salt separation performance [24]. This model was further extended for the prediction of dye rejection of both monovalent and divalent charged anionic and cationic dyes [25]. A good agreement of model-calculated and experimental rejection coefficients was confirmed, and this emphasized the significance of the phenomenological model for assessing membrane separation performance.

In this work, for the first time, we examined the validity of the SKK model to predict the retention of dyes using porous thin-film composite (TFC) membranes containing a metal–polyphenol network (MPN) selective layer. In this type of membrane, the selective layer is formed by coordination networks of self-assembled polyphenols, such as tannic acid (TA) with transition metal ions. MPN selective layers are synthesized in a green way using only aqueous solutions. This novel strategy has been used for TA–Ti^{4+} [26], TA–Fe^{3+} [27] and TA–Ni^{2+} [28] selective layer preparation. MPN-containing membranes have been studied for water–oil emulsion, heavy metal removal and nanofiltration applications [26,29,30]. Fang et al. fabricated loose nanofiltration membranes by first blending Fe in PES through NIPS, and then constructing a selective layer via coordination chemistry of TA and Fe^{3+} [31]. The synthesized membrane exhibited excellent dye/salt fractionation with a high rejection to many dyes. Moreover, the introduction of TA improved the membrane hydrophilicity, negative charge and fouling resistance. The optimization of metal–polyphenol coatings and their application for low-pressure filtration is emerging. However, to the best of our knowledge, no model prediction of the component transport and solute rejection performance of TFC membranes with MPN selective layers has been reported so far. Hence, it is necessary to establish a viable method for a predictive approach to assess the solution filtration through these membranes. This study aims to elucidate the mass transport of dye solutions through a TA–Fe^{3+} thin selective layer using the SKK model. Two TFC membranes containing TA–Fe^{3+} selective layers synthesized using aqueous solutions of different pH were examined in this study. The solute transport through the membranes was considered to be a combined effect of diffusive and convective transport in the SKK model. The driving forces of diffusion and convection were the concentration gradient across the membrane and the transmembrane pressure, respectively. Therefore, we studied the dye retention behavior of the prepared TFC membranes using two sets of experiments:

(i) using a constant feed concentration and varying the transmembrane pressure, and (ii) using a constant transmembrane pressure with varying feed concentrations.

2. Materials and Methods

2.1. Chemicals

Tannic acid (TA) was purchased from Sigma-Aldrich Chemie GmbH (Schnelldorf, Germany). Iron salt of iron(III) chloride hexahydrate ($FeCl_3 \cdot 6H_2O$) was purchased from Alfa Aesar GmbH & Co. (ThermoFisher, Kandel, Germany). In-house prepared polyacrylonitrile (PAN) membranes were used as the support layer of the TFC membranes. Sodium hydroxide (NaOH), orange II (350.32 g/mol), riboflavin (376.36 g/mol) and naphthol green B (878.46 g/mol) were obtained from Sigma-Aldrich. All chemicals were used without modification.

2.2. Preparation of Tannic Acid/Fe^{3+} Selective Layer

The concept of supramolecular self-assembly between TA and transition metal ions was used to prepare the selective layers of two thin-film composite membranes. The membranes were synthesized using the sequential deposition of TA and iron salt solutions over a porous PAN support. The top surface of the support was exposed to a 50 mL aqueous solutions of 0.1176 mM of TA and 3.33 mM of $FeCl_3 \cdot 6H_2O$ alternately for 4 min. This molar concentration corresponded to 1 TA: 4.5 $FeCl_3 \cdot 6H_2O$ (1 TA–4.5 Fe in short) in weight ratio. Two layers of TA–Fe^{3+} film were deposited using a layer-by-layer technique. The pH value of the aqueous solution used for dissolving TA was varied. Two membranes, hereby named M1 and M2, were prepared with a pH of 5.8 (deionized (DI) water) and 8.5, respectively. The pH value of 8.5 for the aqueous solution of the M2 membrane was adjusted with a 1 M NaOH solution. Figure S1 shows a photograph of the PAN membrane before and after coating.

2.3. Membrane Characterization

The membrane morphology was investigated with scanning electron microscopy (SEM). SEM images were recorded on a Merlin SEM (Zeiss, Jena, Germany) at accelerating voltages between 1.5 and 3 keV using an InLens secondary electron detector. Before measurement, the samples were dried under vacuum at 60 °C for 72 h and were sputter-coated with 1–1.5 nm platinum using a CCU-010 coating device (Safematic, Zizers, Switzerland). Cross-fractured specimens were prepared in liquid nitrogen. The pure water flux of M1 and M2 membranes was measured using DI water of 0.055 μScm^{-1}. The separation performance of the membranes was analyzed with rejection experiments of three solutes: orange II, naphthol green B and riboflavin. Measurements were performed using a stirred test cell from Millipore (EMD Millipore XFUF07601) with a reduced effective membrane area of 1.77 cm^2 in a dead-end filtration mode. DI water was passed for 2 h at a transmembrane pressure of 4 bar. Then, retention measurements were performed under two sets of operating conditions: (i) a 0.1 mM feed solution concentration and variable transmembrane pressure in the range 0.2–4 bar, and (ii) a 3 bar transmembrane pressure and variable concentration in the range 0.01 mM–1 mM. The water flux (J_w) and dye rejection rate (R) were calculated using the following equations:

$$J_w = \frac{W}{\rho * A * t} \tag{1}$$

where J_w ($kg \cdot m^{-2} \cdot s^{-1}$) is the pure water flux, W (kg) is the weight of the collected permeate, A (m^2) is the effective membrane filtration area and t (s) is the operation time.

$$R\ (\%) = \left(1 - \frac{C_p}{\left(C_f + C_r\right)/2}\right) * 100 \tag{2}$$

where R is the solute retention; and C_f, C_p and C_r are the concentrations of the feed, permeate and retentate solutions, respectively. Each experimental result in this work was obtained as an average value of at least three replications.

2.4. Fitting/Prediction of Dye Rejection with Spiegler–Kedem–Katchalsky Model

Predictions of the separation performance of the membranes were performed using the Spiegler–Kedem–Katchalsky (SKK) model based on irreversible thermodynamics. In the SKK model, the characteristics of the solute (e.g., size and charge) and membrane characteristics (e.g., pore size and surface charge density) are not used as input parameters. For the transport of a two-component solution, i.e., one solvent and one solute, the governing transport equations of the SKK model are as follows:

$$J_v = L_p * (\Delta P - \sigma \Delta \pi) \tag{3}$$

$$J_S = P_S * \frac{dC_s}{dx} + (1 - \sigma) * C_S * J_v \tag{4}$$

where J_v is the volumetric permeate flux and J_S is the solute flux; ΔP and $\Delta \pi$ are the applied pressure difference and osmotic pressure difference, respectively; L_p and P_S are water permeability and solute permeability coefficients, respectively; C_s is the solute logarithmic mean concentration between the feed and permeate; and σ is the reflection coefficient of the membrane. The reflection coefficient, σ, describes the semipermeablity of the membrane. It ranges from 0 to 1, with 1 characterizing a perfectly semipermeable film (complete solute ejection). It is also a measure of rejection of the membrane at high flux. It can be observed that Equation (4) contains two parts, the first term depicting diffusion and the second representing convection.

The rejection of a solute is expressed in Equation (2). In the SKK model, the rejection of a solute can be written as follows:

$$R = \frac{\sigma(1 - F)}{1 - \sigma F} \tag{5}$$

where

$$F = exp\left(-\frac{(1 - \sigma)}{P_S} * J_v\right) \tag{6}$$

Substituting F into the rejection expression results in a simplified SKK model of the final form:

$$ln\left[\left(\frac{1}{1 - \sigma} - \frac{1}{1 - R} * \frac{(1 - \sigma)}{\sigma}\right)\right] = -\frac{(1 - \sigma)}{P_S} * J_v \tag{7}$$

The measured flux and experimental rejection results were fitted into the SKK, as shown in Equation (7). A python program was employed to solve the non-linear equation through fitting. Then, the two unknown parameters, σ and P_S, were computed using a least-squares minimization.

3. Results and Discussion

Orange II, riboflavin and naphthol green B (Figure 1) were used as model solutes to investigate the mass transport behavior through the prepared TFC membranes, M1 and M2. Orange II and naphthol green B acquire negative charges when dissolved in water, while riboflavin remains uncharged. The surface and cross-sectional morphologies of the prepared M1 and M2 TFC membranes were investigated using SEM (Figure 2). Both M1 and M2 had porous surfaces (Figure 2a,b). The cross-sectional SEM images (Figure 2c,d) demonstrate that both M1 and M2 membranes possessed a thin TA–Fe^{3+} skin layer deposited on top of the porous PAN support. The PAN support had a spongy integral asymmetric structure. For both M1 and M2, the ultrathin TA–Fe^{3+} layer only existed at the top of the membranes and the spongy porous structure of the PAN support was not blocked at all. In general, for integral asymmetric porous membranes, the resistance

against the mass transport of the permeating substance decreased from the top towards the bottom as the pore size gradually increased along the cross-section of the membrane. Figure 3a shows that the water flux through the PAN support was more than ten times higher compared to that through M1 and M2. The resistance against mass transport of the permeating substances through M1 and M2 increased significantly due to the deposition of the TA–Fe^{3+} layer on the PAN. Hence, the retention and flux through the M1 and M2 membranes were solely dictated by the TA–Fe^{3+} and the contribution of the porous PAN substructure was negligible. The top surface images of both M1 and M2 membranes (Figure 2a,b) show small pores unevenly distributed over the surface. Comparatively, the membrane prepared at higher pH (M2) had more closed pores. This was due to the fact that at a pH of 7 or higher, the complexation state of metals and polyphenols became a tris-complex, where three TA molecules coordinated with an iron center, leading to the formation of a compact layer [32–34]. It was not possible to decipher any substantial difference between the two membranes in terms of average surface pore sizes from the SEM images. The SEM image depicts only a very small area of the membrane and it is visible that the pore size distribution at the surface of M1 and M2 was rather broad. Figure 3b–d show the fluxes of riboflavin, orange II and naphthol green B aqueous solutions against the transmembrane pressure. While the fluxes of the aqueous solutions gradually increased with the transmembrane pressure in all cases, small deviations from the linear behavior were also observed. However, it is clear that the fluxes of the three aqueous solutions through M1 increased more sharply with transmembrane pressure compared to M2. Hence, it is evident that the average surface pore size of M1 was higher than that of M2. Photographs of the feed and permeate solutions investigated for M2 at a transmembrane pressure of 3 bar are shown in Figure S2.

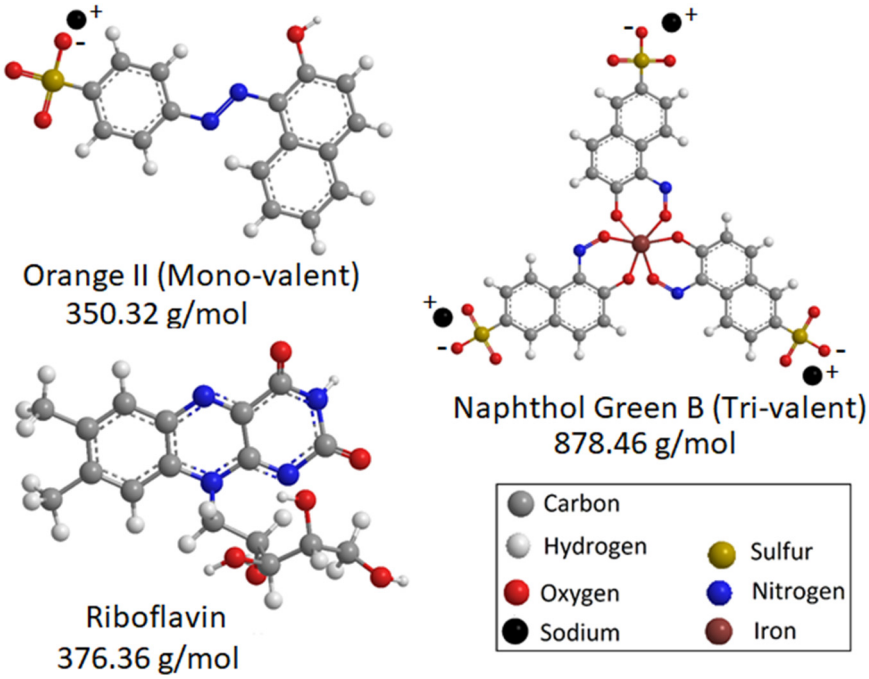

Figure 1. Chemical structure and molecular weight of the orange II, riboflavin and naphthol green B solutes.

The fluxes of the aqueous solutions over a transmembrane pressure range of 1–4 bar are plotted against the retention of the solutes (i.e., riboflavin, orange II and naphthol green B) by M1 and M2 in Figures 4a and 5a, respectively. These experimental data points were used to determine the reflection coefficient, σ, and the permeability of the solute, P_S, using the non-linear fitting of the SKK model (Tables 1 and 2). The obtained values of σ and P_S were used as input parameters in Equation (7). Consequently, the non-linear

relationship between the flux and retention of the solutes predicted by the SKK model was obtained for M1 and M2. The model algorithm used to estimate the parameters of the model is shown in Figure S3. The statistical procedure followed to fit the SKK model comprised the minimization of the residuals or error of the optimized parameters, which was a function of both the P_S and σ model parameters. According to the SKK model prediction, with an increase in the flux of the aqueous solution, the retention of the solutes increased asymptotically (Figures 4a and 5a). In order to check the validity of this prediction below the flux limit 5 $g \cdot m^{-2} \cdot s^{-1}$ (i.e., 5 $\times$ 10^{-3} $kg \cdot m^{-2} \cdot s^{-1}$), the two experimentally observed solution flux vs. solute retention points for each of the solutes were compared with the SKK predictions for M1 (Figure 4b) and M2 (Figure 5b). The experimental data points of the aqueous solutions of riboflavin showed a similar trend to the SKK model predictions for both M1 and M2. Only small deviations from the predicted values were observed. The experimental data points for orange II and naphthol green B solutions deviated substantially from the SKK model predictions for M1 (Figure 4b). Compared to that, smaller deviations between SKK model prediction and experimental data points for orange II and naphthol green B solutions were observed in the case of M2 (Figure 5b).

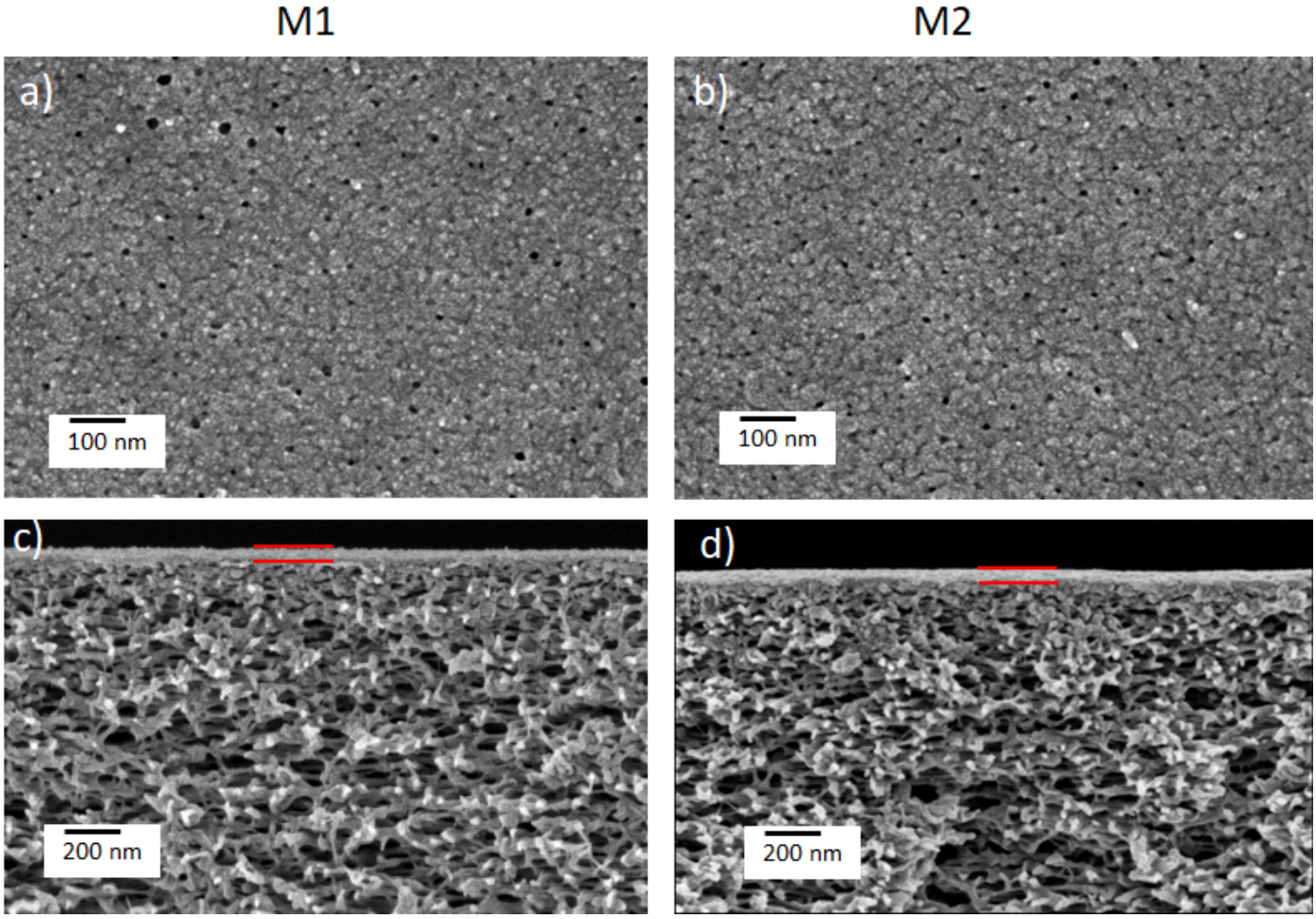

Figure 2. SEM images of top surface and cross-section (**a**,**c**) of M1 and (**b**,**d**) M2 thin-film composite membranes. In the cross-section images (**c**,**d**), the TA–Fe^{3+} selective layers are pointed out with two red lines.

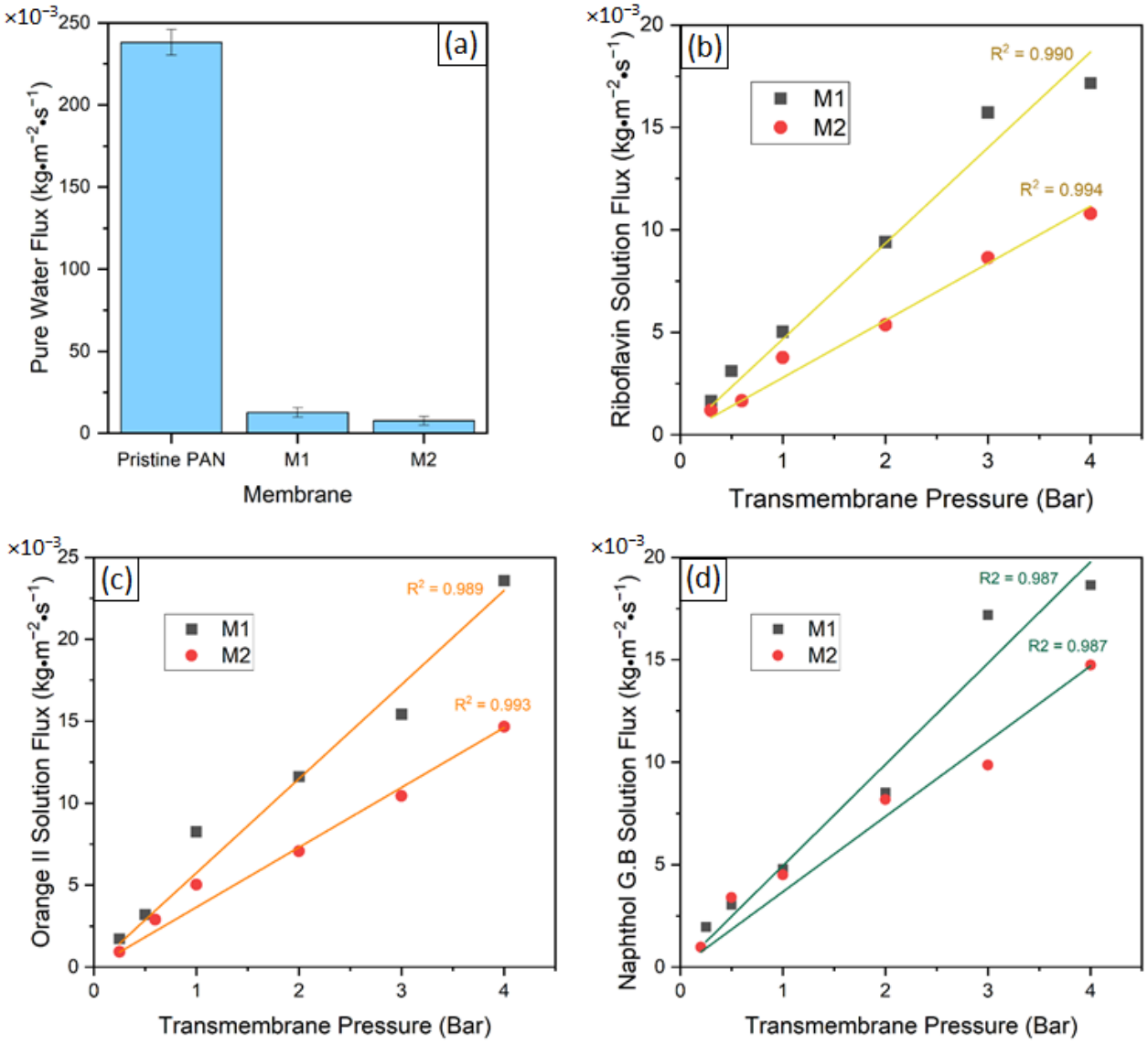

Figure 3. (**a**) Pure water flux at a pressure of 3 bar for pristine PAN support, M1 and M2 membranes; and solution flux as a function of transmembrane applied pressure for (**b**) riboflavin, (**c**) orange II and (**d**) naphthol green B.

The asymptotic increase of the retention of an uncharged solute with the increase of solution flux as a result of increasing transmembrane pressure implied that there was competition between the convective transport of water and the solutes through the selective layer of the membrane. A low transmembrane pressure means a low driving force for the convective transport of molecules through a membrane. The driving force of convection increased under a high transmembrane pressure. On the other hand, the diffusive transport reached a limiting value [35]. The permeate volumetric flux was directly proportional to the applied transmembrane pressure, while solute permeability was not. The contribution of diffusion to solute permeability declined at a high permeate volumetric flux. Moreover, when the applied pressure was increased, water and solute fluxes became uncoupled [36,37]. The porous selective layer of membranes necessarily allows the transport of the molecules based on their size. Consequently, there was a selective transport of water molecules through the selective layer of the membranes. A large number of solute molecules bounced back from the surface of the membrane or were by the membrane due to their larger size compared to the water. The fluxes of the aqueous solution increased with transmembrane pressure due to a higher driving force (Figure 3b–d). It is essential to realize that, with the

increase of transmembrane pressure, not only did a higher number of water and solute molecules move through the selective layer of the membrane per unit time, but the number of water and solute molecules that bounced back from the surface of the membranes per unit time also increased. Due to their smaller size, the water molecules had a higher probability of entering the pores of the selective layer compared to molecules of a larger uncharged solute. The asymptotically increasing solution flux vs. solute retention curves implies that there was a limiting value up to which the increase of transmembrane pressure resulted in a greater increase of the water flux compared to the solute flux. It is obvious that the limiting value of the transmembrane pressure where the solute retention vs. solution flux curve levels off would change depending on the size of the pores and solutes. The SKK model is a phenomenological model and the sizes of the pores and solutes are not used as input parameters. However, the reflection coefficient, σ, and the permeability of the solute, P_S, were calculated by fitting the experimental data points in a solution flux vs. solute rejection plot. The values of these model parameters inherently reflected the impact of the pore and solute size on the solution flux vs. solute retention curves predicted by the SKK model.

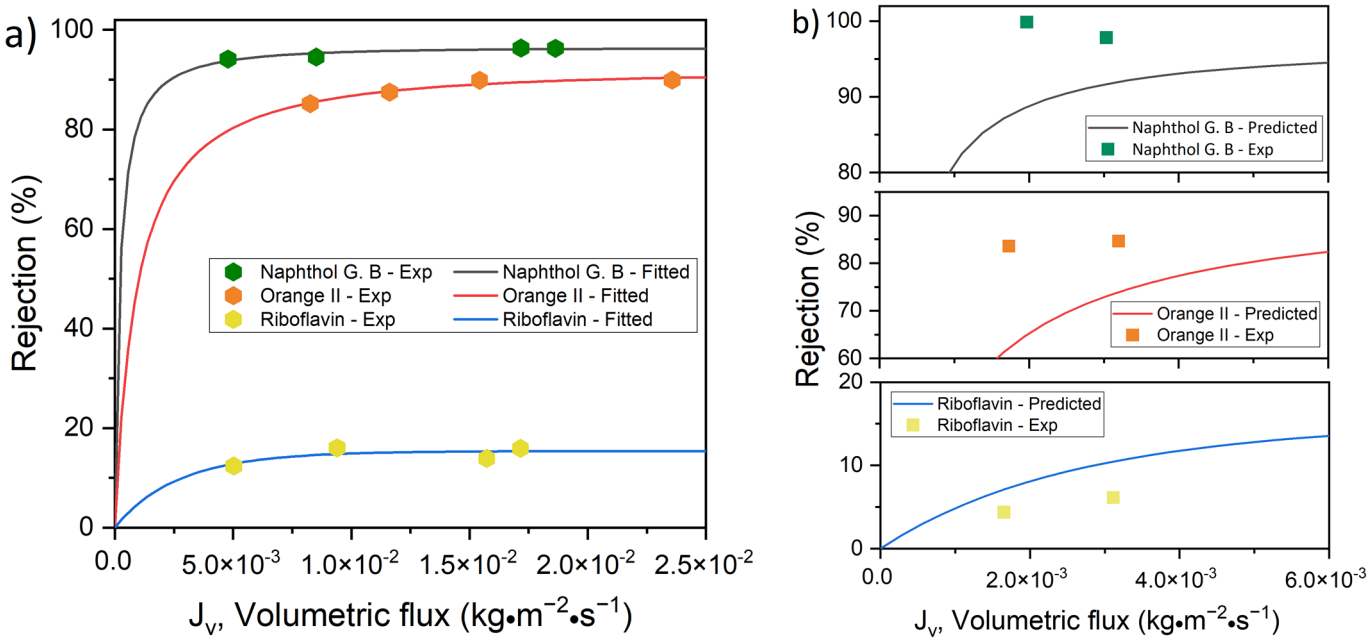

Figure 4. Dye retention versus flux for M1 (1 TA–4.5 Fe, pH 5.8) membrane; (**a**) experimental results and curve-fitting for SKK model and (**b**) validation of model through low flux experimental rejection.

Table 1. Model transfer coefficient for membrane M1.

Dye	σ	P_S (m/s)
Riboflavin	0.153822	2.57×10^{-6}
Orange II	0.911965	8.83×10^{-7}
Naphthol Green B	0.962552	2.04×10^{-7}

Table 2. Model transfer coefficient for membrane M2.

Dye	σ	P_S (m/s)
Riboflavin	0.187374	2.92×10^{-6}
Orange II	0.909181	2.65×10^{-7}
Naphthol Green B	0.954968	1.04×10^{-8}

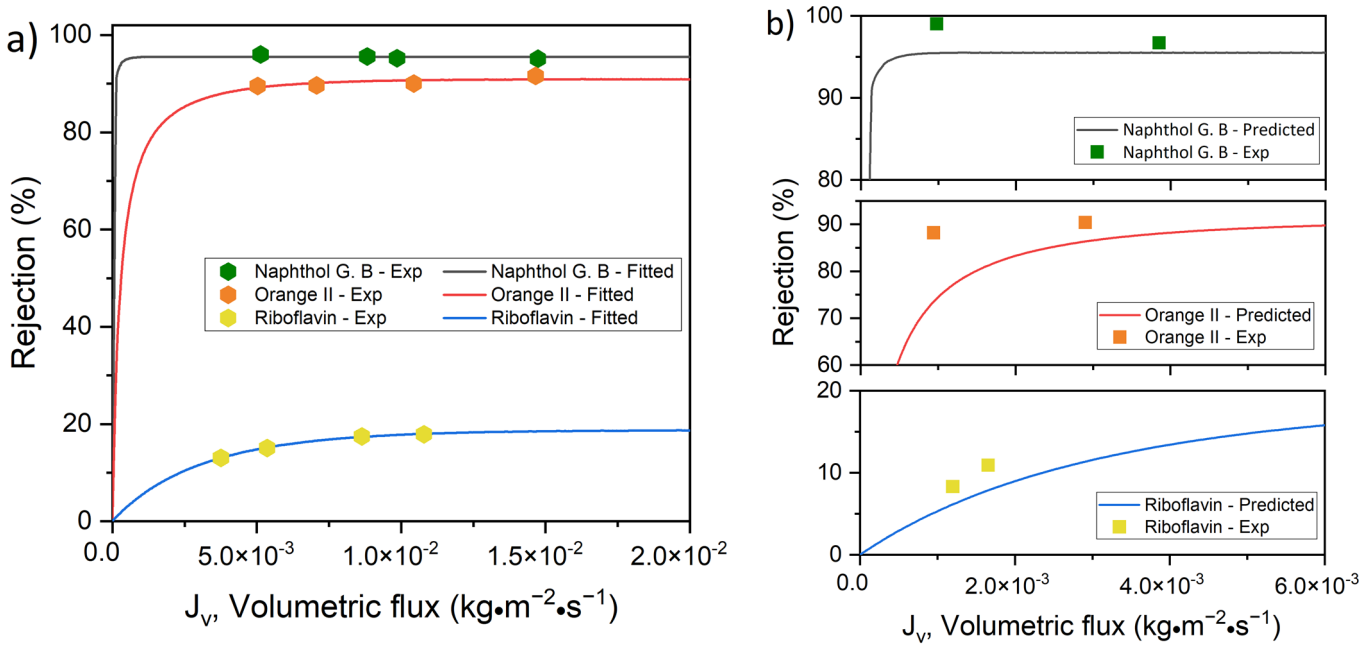

Figure 5. Dye retention versus flux for M2 (1 TA–4.5 Fe, pH 8.5) membrane; (**a**) experimental results and curve-fitting for SKK model and (**b**) validation of model through low flux experimental rejection.

The values of σ followed the order of riboflavin < orange II < naphthol green B. Although riboflavin and orange II had comparable sizes, the flux of orange II through the membranes was substantially lower than that of riboflavin. Hence, it is evident that the retention of orange II by M1 and M2 was not only a result of size exclusion. To analyze the permeation and retention of the charged solute, the influence of Donnan exclusion must also be taken into account. The 0.1 mM orange II and naphthol green B dye solutions had a pH of 6.4 and 6.5, respectively [15]. At these pH values, TA–Fe^{3+} membranes are negatively charged, with an isoelectric point of less than pH 3 [31,38]. Our membranes also showed similar negative surface charges. M1 and M2 exhibited a zeta potential of −21.0 mV and −27.3 mV at pH 6.4, respectively. At the pH of these dye solutions, the negatively charged surfaces of M1 and M2 repelled the anionic dyes, resulting in a high rejection. Hence, the charged solutes (i.e., orange II and naphthol green B) had to overcome an additional energy barrier due to the charge repulsion (i.e., Donnan exclusion) compared to the uncharged solute (i.e., riboflavin). Since the driving force for convective flow was rather low at a very low transmembrane pressure, Donnan exclusion is likely to play a stronger role in the retention of the solutes. As the transmembrane pressure increased, the driving force for convective transport of the charged solutes increased as well. This means that the charged solutes had a higher probability of overcoming the additional energy barrier of Donnan exclusion and permeate through the pores at higher transmembrane pressure. Hence, there are two competing phenomena which finally determined the influence of transmembrane pressure on the retention of a charged solute. First, similar to uncharged solutes, charged solutes also had to compete with the solvent to enter pores of the membrane, which tended to increase the solute retention with increasing transmembrane pressure. Second, the charged solutes had a higher probability of overcoming the additional energy barrier of Donnan exclusion to enter the pores with increasing transmembrane pressure, which tended to decrease the retention. The SKK model only predicted the influence of the first phenomenon. In the case of a charged solute, σ and P_S inherently reflected the influence of both size and Donnan exclusion, as they were calculated by fitting the experimental data points of the solution flux vs. solute rejection plot. However, as the SKK model failed to predict changes in retention due to the second phenomenon described above, a strong deviation of the retention behavior predicted by the SKK model from the experimentally obtained data was observed at low transmembrane

pressures (Figures 4b and 5b). According to our observation, at a low transmembrane pressure the second phenomenon had a stronger influence on the retention of orange II and naphthol green B by M1 (i.e., the membrane with a larger pore size) than M2.

It should be noted that the solute rejection increased until it stabilized when the applied pressure was increased for both M1 and M2 membranes (Figures 4a and 5a). This phenomenon was shown by orange II and riboflavin. However, the rejection of naphthol green B slightly increased in M1 and decreased in M2 with an increase of fluxes.

Aside from pressure, the feed concentration played a vital role in membrane filtration performance. An increase of the concentration of feed solution increased the driving force for solute diffusion across the membrane. Therefore, the solute flux through the membrane was expected to rise, i.e., the solute rejection was expected to decrease. On the other hand, at a constant feed pressure, a high feed concentration of solute was expected to result in a lower permeate volume flux due to an increase in the osmotic pressure. In order to investigate the influence of a high concentration, we varied the concentration of the orange II and naphthol green B feed solution in the range of 0.01 mM to 1 mM. Although the feed concentration was varied 100 fold, the volumetric fluxes through M1 and M2 did not vary substantially (e.g., standard deviations of 2.9 and 2.7 $g \cdot m^{-2} \cdot s^{-1}$ (i.e., 2.9 and 2.7 $kg \cdot m^{-2} \cdot s^{-1}$) for M1 were observed for Orange II and naphthol green B, respectively). Orange II and naphthol green B were used in this experiment while riboflavin was dropped due to its low solubility in water. Figure 6a,b present the real rejection of dyes and model-predicted results as a function of the feed concentration for both membranes. The observed rejection decreased slightly with an increase in the feed concentration in all case studies. For instance, the naphthol green B rejection declined from 98.7 to 96.3% in M1, while orange II rejection decreased from 94.0 to 90.0% in M2. However, as the concentration exceeded 0.05 mM, both membranes showed an almost constant performance with a limiting value of rejection. Hence, these results show that the diffusive transport of dyes through M1 and M2 was largely prevented owing to the size and charge exclusion mechanism. As a result, even a 100-fold change in the feed concentration did not have a substantial influence on the separation performance of the membranes. The SKK model also predicted a similar trend. A slight variation between the experimental and predicted results was observed at low feed concentrations for all dyes in both membranes. Rejection was underestimated by the SKK model. This difference was due to the fact that the driving force of diffusion (i.e., the concentration gradient) was not an input parameter in the model. The rejection was predicted from Equations (5) and (6) using the volumetric fluxes, reflection coefficients and permeability of the solutes as input parameters. The simulation was performed using the reflection coefficient and solute permeability parameters obtained in Tables 1 and 2. At a transmembrane pressure of 3 bar, the volumetric flux remained unchanged at feed concentrations of 0.01–1 mM, while the predicted rejection of the dyes was also constant. The limitation of the SKK model to adequately describe membrane performance of dilute feed systems has been reported in other studies as well [21].

Figure 7 presents the SKK model-predicted dye rejection as a function of their experimentally determined rejection values for all case studies. It also includes comparisons of rejection at different feed concentrations. An even distribution of many data points along and close to the diagonal line demonstrated the significance of the model. In accordance with these results, the applied model fitted the experimental data well. This study shows that the TA–Fe^{3+} membrane performance can be predicted using SKK model parameters and experimentally observed volumetric fluxes under the operating conditions where convection is the dominant transport mechanism.

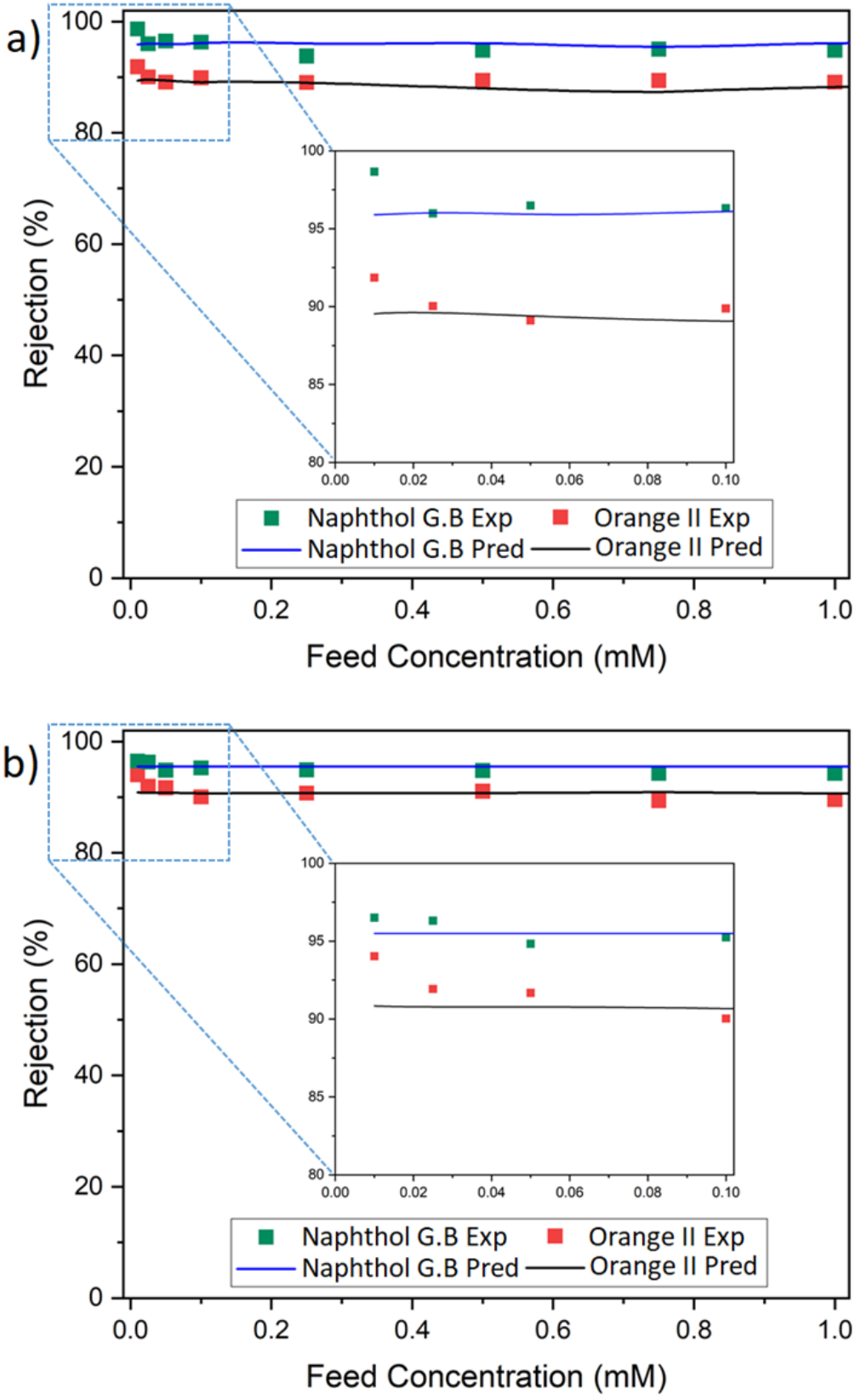

Figure 6. Dye retention prediction at different feed concentrations for 1 TA–4.5 Fe membranes prepared with (**a**) DI water of pH ~ 5.8 (M1) and (**b**) at pH 8.5 (M2). Exp denotes experimental data, while Pred implies prediction line.

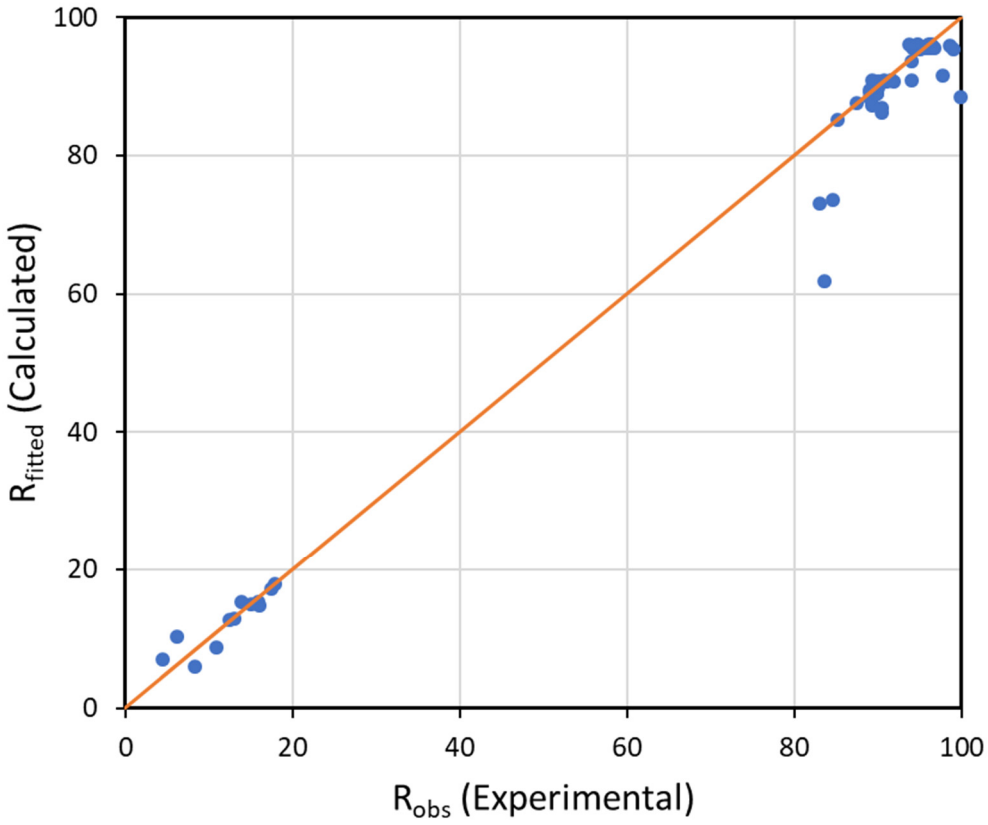

Figure 7. Comparison of experimental and model-predicted rejection for all measurements in this work.

4. Conclusions

The prediction of dye rejection performance of metal–polyphenol based membranes using the Spiegler–Kedem–Katchalsky model was investigated in this work. The membranes exhibited a high rejection towards negatively charged dyes; the reflection coefficient, σ, was in the range of 0.90–0.96 for anionic dyes of orange II and naphthol green B, while σ values of 0.15 and 0.18 were found for uncharged riboflavin. An analysis of the phenomenological model for dye transport successfully illustrated how permeate flux affects solute rejection. Experimental and predicted values were in good agreement. The validity of the model was also evaluated at low transmembrane pressure as well as using different feed concentrations. Operations at low transmembrane pressure showed a deviation between model-estimated and observed data due to the strong influence of Donnan exclusion. The volumetric fluxes through the membranes at a transmembrane pressure of 3 bar did not change significantly even with a 100-fold change in the feed concentration owing to the influence of size and Donnan exclusion. Consequently, the values of dye retention predicted by the SKK model at diluted feed concentrations deviated from the empirical values. While the overall model outcomes matched experimental data to some extent, some major limitations of the SKK model to predict the retention of charged dyes by the TFC membranes with TA–Fe^{3+} selective layers were shown in this study. These conclusions are likely to be true for other membranes as well.

Supplementary Materials: The following supporting information can be downloaded at https://www.mdpi.com/article/10.3390/membranes12121216/s1, Figure S1. Comparison of photographic images of pristine PAN membrane support and TA–Fe^{3+} membrane used for retention measurement. Color change supports the formation of metal–polyphenol selective layer on top of the porous support as confirmed with significant drop in water flux; Figure S2. Photographic images of feed and permeate samples from (a) naphthol green B, (b) orange II and (c) riboflavin 0.1 mM solution retention tests at 3 bar using M2 membrane; Figure S3. Flow chart of the simulation algorithm loop for solving non-linear equations of Spiegler–Kedem–Katchalsky model in the current study.

Author Contributions: Conceptualization, H.H.K. and M.M.R.; methodology, H.H.K. and N.C.-C.; software, H.H.K.; validation, H.H.K. and M.M.R.; formal analysis, H.H.K. and M.M.R.; investigation, H.H.K.; resources, M.M.R.; data curation, H.H.K.; writing—original draft preparation, H.H.K. and M.M.R.; writing—review and editing, H.H.K., N.C.-C., M.M.R. and V.A.; visualization, H.H.K. and M.M.R.; supervision, M.M.R. and V.A.; project administration, M.M.R.; funding acquisition, M.M.R. All authors have read and agreed to the published version of the manuscript.

Funding: This work was funded by the Hereon-I^{2}B-Project NanoMem.

Institutional Review Board Statement: Not applicable.

Informed Consent Statement: Not applicable.

Data Availability Statement: Not applicable.

Acknowledgments: The authors acknowledge J.I. Clodt for the preparation of the PAN support membranes, E.S. Schneider for the SEM characterizations and J. Pohlmann for building the flux and retention measurement facilities.

Conflicts of Interest: The authors declare no conflict of interest.

Nomenclature

C_f	Feed solute concentration ($kg \cdot m^{-3}$)
C_p	Permeate solute concentration ($kg \cdot m^{-3}$)
C_r	Retentate solute concentration ($kg \cdot m^{-3}$)
C_s	Logarithmic mean concentration of solute between the feed and permeate ($kg \cdot m^{-3}$)
J_v	Permeate flux ($kg \cdot m^{-2} \cdot s^{-1}$)
J_s	Solute flux ($kg \cdot m^{-2} \cdot s^{-1}$)
L_p	Solvent permeability constant ($m \cdot s^{-1}$)
P_s	Solute permeability constant ($m \cdot s^{-1}$)
R	Membrane rejection (%)
R_{fitted}	Membrane rejection calculated (%)
R_{obs}	Membrane rejection experimental (%)
ΔP	Transmembrane pressure (bar)
$\Delta \pi$	Osmotic pressure (bar)
σ	Reflection coefficient

References

1. Kadhim, R.J.; Al-Ani, F.H.; Al-shaeli, M.; Alsalhy, Q.F.; Figoli, A. Removal of dyes using graphene oxide (go) mixed matrix membranes. *Membranes* **2020**, *10*, 366. [CrossRef] [PubMed]
2. Sachdeva, S.; Kumar, A. Separation of dyes using composite carbon membranes. *Aiche J.* **2009**, *55*, 1712–1722. [CrossRef]
3. Majewska-Nowak, K. Ultrafiltration of dye solutions in the presence of cationic and anionic surfactants. *Env. Prot. Eng.* **2009**, *35*, 111–121.
4. Koyuncu, I.; Topacik, D.; Yuksel, E. Reuse of reactive dyehouse wastewater by nanofiltration: Process water quality and economical implications. *Sep. Purif. Technol.* **2004**, *36*, 77–85. [CrossRef]
5. Uzal, N.; Yilmaz, L.; Yetis, U. Nanofiltration and reverse osmosis for reuse of indigo dye rinsing waters. *Sep. Sci. Technol.* **2010**, *45*, 331–338. [CrossRef]
6. Van der Bruggen, B.; Daems, B.; Wilms, D.; Vandecasteele, C. Mechanisms of retention and flux decline for the nanofiltration of dye baths from the textile industry. *Sep. Purif. Technol.* **2001**, *22*, 519–528. [CrossRef]
7. Yen, H.Y.; Kang, S.F.; Yang, M.H. Separation of textile effluents by polyamide membrane for reuse. *Polym. Test.* **2002**, *21*, 539–543. [CrossRef]
8. Bielska, M.; Prochaska, K. Dyes separation by means of cross-flow ultrafiltration of micellar solutions. *Dye. Pigment.* **2007**, *74*, 410–415. [CrossRef]
9. Ghadhban, M.Y.; Majdi, H.S.; Rashid, K.T.; Alsalhy, Q.F.; Lakshmi, D.S.; Salih, I.K.; Figoli, A. Removal of dye from a leather tanning factory by flat-sheet blend ultrafiltration (uf) membrane. *Membranes* **2020**, *10*, 47. [CrossRef]
10. Oyarce, E.; Roa, K.; Boulett, A.; Sotelo, S.; Cantero-Lopez, P.; Sanchez, J.; Rivas, B.L. Removal of dyes by polymer-enhanced ultrafiltration: An overview. *Polymers* **2021**, *13*, 3450. [CrossRef]
11. Zhang, Z.; Rahman, M.M.; Abetz, C.; Bajer, B.; Wang, J.; Abetz, V. Quaternization of a polystyrene-block-poly(4-vinylpyridine) isoporous membrane: An approach to tune the pore size and the charge density. *Macromol. Rapid Commun.* **2019**, *40*, 1800729. [CrossRef] [PubMed]

12. Chen, T.; Li, B.; Huang, W.; Lin, C.; Li, G.; Ren, H.; Wu, Y.; Chen, S.; Zhang, W.; Ma, H. Highly crystalline ionic covalent organic framework membrane for nanofiltration and charge-controlled organic pollutants removal. *Sep. Purif. Technol.* **2021**, *256*, 117787. [CrossRef]
13. Zhang, W.; Zhang, L.; Zhao, H.; Li, B.; Ma, H. A two-dimensional cationic covalent organic framework membrane for selective molecular sieving. *J. Mater. Chem. A* **2018**, *6*, 13331–13339. [CrossRef]
14. Zhang, W.; Li, Y.; Xing, Z.; Zhao, M.; Fu, Y.; Wang, S.; Wu, Y.; Zeng, J.; Li, X.; Ma, H. Ionic cof composite membranes for selective perfluoroalkyl substances separation. *Macromol. Rapid Commun.* **2022**, 2200718. [CrossRef]
15. Zhang, Z.Z.; Rahman, M.M.; Abetz, C.; Hohme, A.L.; Sperling, E.; Abetz, V. Chemically tailored multifunctional asymmetric isoporous triblock terpolymer membranes for selective transport. *Adv. Mater.* **2020**, *32*, e1907014. [CrossRef]
16. Zhang, Z.; Rahman, M.M.; Abetz, C.; Abetz, V. High-performance asymmetric isoporous nanocomposite membranes with chemically-tailored amphiphilic nanochannels. *J. Mater. Chem. A* **2020**, *8*, 9554–9566. [CrossRef]
17. Mohammad, A.W.; Teow, Y.H.; Ang, W.L.; Chung, Y.T.; Oatley-Radcliffe, D.L.; Hilal, N. Nanofiltration membranes review: Recent advances and future prospects. *Desalination* **2015**, *356*, 226–254. [CrossRef]
18. Spiegler, K.S.; Kedem, O. Thermodynamics of hyperfiltration (reverse osmosis): Criteria for efficient membranes. *Desalination* **1966**, *1*, 311–326. [CrossRef]
19. Wu, F.; Feng, L.; Zhang, L.Q. Rejection prediction of isopropylantipyrine and antipyrine by nanofiltration membranes based on the spiegler-kedem-katchalsky model. *Desalination* **2015**, *362*, 11–17. [CrossRef]
20. Wu, J.J. On the application of the spiegler-kedem model to forward osmosis. *BMC Chem. Eng.* **2019**, *1*, 15. [CrossRef]
21. Agboola, O.; Maree, J.; Kolesnikov, A.; Mbaya, R.; Sadiku, R. Theoretical performance of nanofiltration membranes for wastewater treatment. *Environ. Chem. Lett.* **2015**, *13*, 37–47. [CrossRef]
22. Ormerod, D.; Buekenhoudt, A.; Bongers, B.; Baramov, T.; Hassfeld, J. From reaction solvent to crystallization solvent, membrane assisted reaction workup and interpretation of membrane performance results by application of spiegler-kedem theory. *Org. Process Res. Dev.* **2017**, *21*, 2060–2067. [CrossRef]
23. Nayak, V.; Cuhorka, J.; Mikulasek, P. Separation of drugs by commercial nanofiltration membranes and their modelling. *Membranes* **2022**, *12*, 528. [CrossRef] [PubMed]
24. Schirg, P.; Widmer, F. Characterization of nanofiltration membranes for the separation of aqueous dye-salt solutions. *Desalination* **1992**, *89*, 89–107. [CrossRef]
25. Hidalgo, A.M.; Leon, G.; Gomez, M.; Murcia, M.D.; Gomez, E.; Macario, J.A. Removal of different dye solutions: A comparison study using a polyamide nf membrane. *Membranes* **2020**, *10*, 408. [CrossRef]
26. Wu, H.; Xie, J.; Mao, L. One-pot assembly tannic acid-titanium dual network coating for low-pressure nanofiltration membranes. *Sep. Purif. Technol.* **2020**, *233*, 116051. [CrossRef]
27. Fan, L.; Ma, Y.; Su, Y.; Zhang, R.; Liu, Y.; Zhang, Q.; Jiang, Z. Green coating by coordination of tannic acid and iron ions for antioxidant nanofiltration membranes. *RSC Adv.* **2015**, *5*, 107777–107784. [CrossRef]
28. You, F.; Xu, Y.; Yang, X.; Zhang, Y.; Shao, L. Bio-inspired Ni^{2+}-polyphenol hydrophilic network to achieve unconventional high-flux nanofiltration membranes for environmental remediation. *Chem. Commun.* **2017**, *53*, 6128–6131. [CrossRef]
29. Kim, H.J.; Kim, D.G.; Yoon, H.; Choi, Y.S.; Yoon, J.; Lee, J.C. Polyphenol/Fe^{III} complex coated membranes having multifunctional properties prepared by a one-step fast assembly. *Adv. Mater. Interfaces* **2015**, *2*, 1500298. [CrossRef]
30. Song, Y.Z.; Kong, X.; Yin, X.; Zhang, Y.; Sun, C.C.; Yuan, J.J.; Zhu, B.; Zhu, L.P. Tannin-inspired superhydrophilic and underwater superoleophobic polypropylene membrane for effective oil/water emulsions separation. *Colloids Surf. A Physicochem. Eng. Asp.* **2017**, *522*, 585–592. [CrossRef]
31. Fang, X.F.; Wei, S.H.; Liu, S.; Li, R.; Zhang, Z.Y.; Liu, Y.B.; Zhang, X.R.; Lou, M.M.; Chen, G.; Li, F. Metal-coordinated nanofiltration membranes constructed on metal ions blended support toward enhanced dye/salt separation and antifouling performances. *Membranes* **2022**, *12*, 340. [CrossRef] [PubMed]
32. Ejima, H.; Richardson, J.J.; Liang, K.; Best, J.P.; Van Koeverden, M.P.; Such, G.K.; Cui, J.; Caruso, F. One-step assembly of coordination complexes. *Science* **2013**, *341*, 154–157. [CrossRef] [PubMed]
33. Liu, D.; Chen, Y.; Tran, T.T.; Zhang, G. Facile and rapid assembly of high-performance tannic acid thin-film nanofiltration membranes via Fe^{3+} intermediated regulation and coordination. *Sep. Purif. Technol.* **2021**, *260*, 118228. [CrossRef]
34. Yan, W.; Shi, M.; Dong, C.; Liu, L.; Gao, C. Applications of tannic acid in membrane technologies: A review. *Adv. Colloid Interface Sci.* **2020**, *284*, 102267. [CrossRef]
35. Fievet, P.; Labbez, C.; Szymczyk, A.; Vidonne, A.; Foissy, A.; Pagetti, J. Electrolyte transport through amphoteric nanofiltration membranes. *Chem. Eng. Sci.* **2002**, *57*, 2921–2931. [CrossRef]
36. Fang, J.; Deng, B.L. Rejection and modeling of arsenate by nanofiltration: Contributions of convection, diffusion and electromigration to arsenic transport. *J. Membr. Sci.* **2014**, *453*, 42–51. [CrossRef]
37. Ma, X.; Chen, P.L.; Zhou, M.; Zhong, Z.X.; Zhang, F.; Xing, W.H. Tight ultrafiltration ceramic membrane for separation of dyes and mixed salts (both NaCl/Na_2SO_4) in textile wastewater treatment. *Ind. Eng. Chem. Res.* **2017**, *56*, 7070–7079. [CrossRef]
38. Peng, L.E.; Yao, Z.; Chen, J.; Guo, H.; Tang, C.Y. Highly selective separation and resource recovery using forward osmosis membrane assembled by polyphenol network. *J. Membr. Sci.* **2020**, *611*, 118305. [CrossRef]

Chapter 7. Metal-phenolic Network-based NF Membranes for Nitrate Removal and The Utilization of DSPM-DE

The previous chapters were focused on studying the parameters that control MPN TFC membranes synthesis, morphology, physicochemical properties and performance. Moreover, much emphasis has been placed on the application of these membranes for the separation of small organic molecules.

In chapter 7 and 8, the applicability of TA-Fe^{3+} membranes for ion rejection is investigated along with the elucidation of ion transport using a transport model. Nitrate contamination of surface- and ground-water has become a significant global concern posing a risk to billions of people worldwide. Commercial NF membranes have low nitrate removal efficiency. In this chapter, the application of MPN containing TFC membranes via metal-polyphenol supramolecular self-assembly for nitrate removal is investigated. The in-house made thin-films present an efficient approach of effective NO_3^- removal, demonstrating 83 – 94 % nitrate rejection performance for 100 mg/L $NaNO_3$ feed solution. This highlights a high-performance NF membrane that surpass performances in the literature using commercially available membranes. A study on the effect of increasing the applied pressure shows a significant increase in nitrate retention, while increasing the feed solution concentrations leads to a decline in retention due to several factors including charge screening. Investigation of mixed ion separation behaviour of the membranes shows no NO_3^-/Cl^- selectivity while NO_3^-/SO_4^{2-} selectivity was between 4.5 – 38.1.

Additionally, the rejection mechanisms and ion transport mechanisms across the MPN active layer is elucidated using the Donnan-Steric Pore Model with Dielectric Exclusion (DSPM-DE). It is emphasized that diffusion governs the nitrate ions flux across the thin-layer. Dielectric and Donnan exclusion effects dominate its separation from a divalent anion in a ternary ion mixture ($Na^+/NO_3^-/SO_4^{2-}$) feed solution. A small variation in the pore dielectric constant especially causes a significant change in selectivity during the separation of NO_3^-/SO_4^{2-} as shown in a sensitivity analysis. This work for the first time illustrates DSPM-DE can be successfully applied for elucidating ion transport across MPN membranes. Given the increasing concerns about nitrate pollution and the demand for efficient separation technologies, this chapter presents the potential of TA-Fe^{3+} membranes for a high-performance nitrate removal.

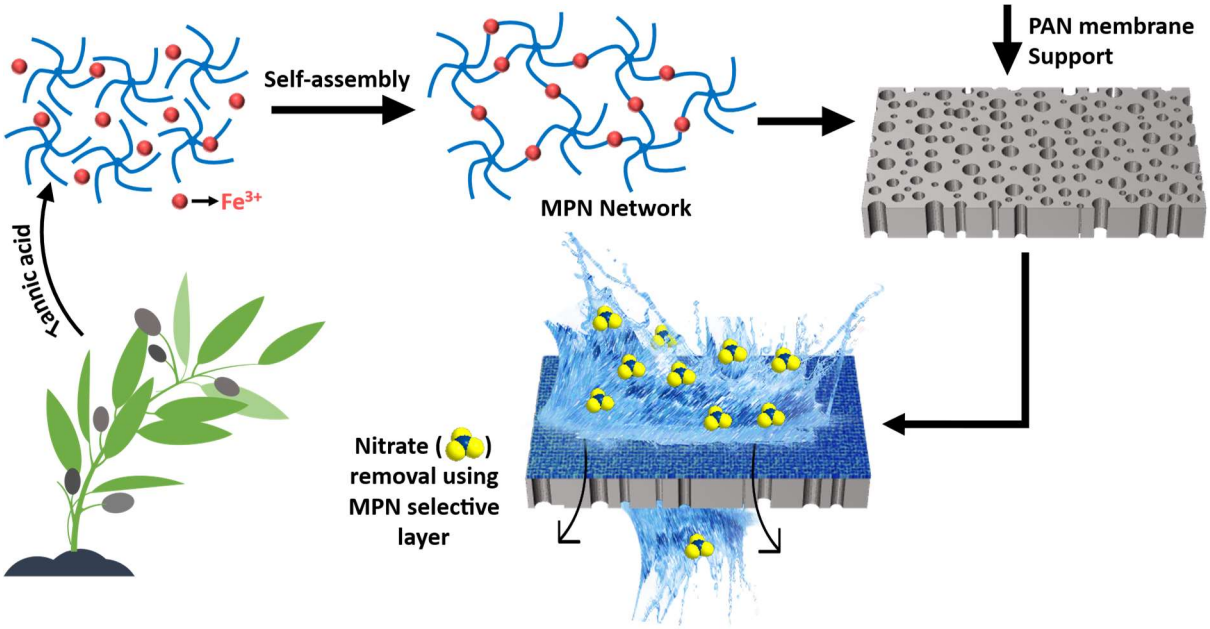
Self-assembly
Fe3+
MPN Network
PAN membrane
Support
Tannic acid
Nitrate ( )
removal using
MPN selective
layer

Chemical Engineering Journal 513 (2025) 162841

Contents lists available at ScienceDirect

Chemical Engineering Journal

journal homepage: www.elsevier.com/locate/cej

Metal-phenolic network-based NF membranes for nitrate removal and the utilization of DSPM-DE model

Hluf Hailu Kinfu [a], Md. Mushfequr Rahman [a,*], Nicolás Cevallos-Cueva [a], Volker Abetz [a,b]

[a] Helmholtz-Zentrum Hereon, Institute of Membrane Research, Max-Planck-Straße 1, 21502 Geesthacht, Germany
[b] University of Hamburg, Institute of Physical Chemistry, Martin-Luther-King-Platz 6, 20146 Hamburg, Germany

ARTICLE INFO

Keywords:
Nanofiltration
Ion separation
Metal polyphenolic network
Mass transport modelling
DSPM-DE
Nitrate removal

ABSTRACT

The rising nitrate levels in polluted surface and groundwater, often exceeding permissible limits, have created a pressing need for effective removal methods. High-throughput, low pressure nanofiltration (NF) membranes with high permselectivity are the ideal candidates for the removal of such pollutants. This work develops thin-film composite (TFC) NF membranes via supramolecular self-assembly between polyphenolic molecule of tannic acid (TA) and metal ions (Fe^{3+}) to achieve a high-performance nitrate retention. The TFC membranes exhibited an excellent NO_3^- retention property ranging from 83 – 94 %, outperforming the commercial NF membranes, and meeting the requirement for drinking water from surface water and groundwater bodies. Among the membranes, the 1TA-4.5Fe variant achieved a pure water permeance of 13.6 $L{\cdot}m^{-2}{\cdot}h^{-1}{\cdot}bar^{-1}$ and an 83 % NO_3^- rejection for a 100 mg/L feed solution. Nitrate retention improved with increased feed pressure and declined with increased nitrate concentrations in the feed solution. The thin film composite membranes having TA-Fe^{3+} selective layers also showed a good monovalent/divalent ion (NO_3^-/SO_4^{2-}) separation with a selectivity between 4.5 and 38.1. The Donnan Steric Pore Model with Dielectric Exclusion (DSPM-DE) model was used to describe the transport mechanism and rejection mechanism of ions for the feed solutions containing the ternary ion mixture ($Na^+/NO_3^-/SO_4^{2-}$). Experimental and theoretical results indicated that nitrate ion flux was primarily diffusion-driven, while ion partitioning was governed by dielectric exclusion and Donnan effects. This comprehensive evaluation underscores the high potential of these TFC membranes for advanced nitrate removal. For the first time it has been demonstrated that the DSPM-DE model can sufficiently predict the selective transport of NO_3^- over SO_4^{2-} ions through TFC membranes having TA-Fe^{3+} selective layers.

1. Introduction

Contamination of drinking water, including both surface and groundwater, has become a significant global concern. Widespread pollution of water bodies by nitrate (NO_3^-) poses risk to the human health [1,2]. Approximately 1.5 billion people worldwide rely on groundwater for irrigation and drinking [3]. In the United States, the Environmental Protection Agency (EPA), has set a maximum allowable nitrate concentration in public water supplies at 10 mg/L as nitrate-nitrogen (NO_3-N) [4]. In comparison, the European Union permits nitrate levels up to 50 mg/l (equivalent to 11.3 mg/L NO_3-N) [5,6]. However, investigations have shown that groundwater in many areas, particularly in Germany and other EU Member States, often exceeds the maximum permissible nitrate level [7,8]. Given that groundwater is a major source of drinking water, especially in countries like Germany where it accounts for 61 % of the supply, the contamination presents a significant challenge [9].

The growing use of fertilizers, pesticides and excessive farming are the main contributors of nitrate in contaminating surface and ground water [7,9–11]. Agricultural and industrial effluents contain high nitrate concentration. The high nitrate levels from these sources raise environmental and human health concerns, necessitating the development of effective nitrate removal methods. Several technologies, including ion exchange, microbial and chemical denitrification, adsorption, electrodialysis, and membrane separation processes, have been developed to remove excess NO_3^- ions from water [12–16]. Among these methods, membrane technology has emerged as a promising solution due to its cost-effectiveness, energy efficiency, simplicity, and high water recovery rates. Although reverse osmosis membranes can effectively remove almost all contaminants, the low water flux and high energy demand

* Corresponding author.
E-mail address: mushfequr.rahman@hereon.de (Md.M. Rahman).

https://doi.org/10.1016/j.cej.2025.162841
Received 11 February 2025; Received in revised form 24 March 2025; Accepted 18 April 2025
Available online 19 April 2025

remain their major drawbacks [17]. Thus, nanofiltration membranes, with characteristics between reverse osmosis and ultrafiltration, are increasingly seen as a viable alternative for water treatment [18]. However, the nitrate rejection efficiency of the available commercial NF membranes is low [19]. Hence, recent advances in membrane technology have focused on developing new materials having improved nitrate rejection without compromising the water permeance. Metal–phenolic networks (MPNs) are gaining prominence as emerging coatings in the realm of engineering functional materials [20]. MPNs are thin coating layers formed through the chelation of transition metal ions with the catechol or galloyl groups of phenolic ligands [21,22]. This coordination creates stable complexes that form robust and interconnected networks, making them suitable for synthesizing thin selective layers. Tannic acid (TA), a natural polyphenol, has been widely studied for its cost effective and rapid membrane synthesis and surface functionalization capabilities [23]. Pioneering research works have demonstrated that MPN coating layers, as a result of the TA self-assembly with various metal ions such as Fe^{3+}, Ni^{+}, Cu^{2+}, Ti^{4+} and Ag^{+}, exhibit excellent separation performance in the field of oil/water emulsion, heavy metal removal, dye separation, trace organic components removal and low-pressure NF [23–29]. MPN coatings have been reported to enhance the water permeance, rejection, and antimicrobial activity, thereby improving the overall membrane performance [20,30,31]. However, no effort has been made to study the nitrate retention properties of these membranes.

This study investigates the application of MPN containing thin-film composite (TFC) membranes for nitrate removal. Specifically, the research focuses on synthesizing an MPN-based selective layer for high nitrate retention through the supramolecular self-assembly of TA and Fe^{3+}. The TA-Fe^{3+} thin-films were deposited via layer-by-layer film synthesis method over a polyacrylonitrile (PAN) porous support to obtain the TFC membranes. The TA-Fe^{3+} layer was synthesized in an aqueous environment, by dissolving both TA and the ferric salt in water. In other words, an ecofriendly route was used to fabricate the selective layer of the TFC membranes. The nitrate removal efficiency of the TFC membranes was thoroughly investigated by performing pressure and concentration dependent retention tests as well as mixed ion filtration experiments. Furthermore, the study discusses the applicability of the Donnan Steric Pore Model with Dielectric Exclusion (DSPM-DE) [32,33] to describe nitrate separation from ionic mixtures. NF membranes contain a typically asymmetric structure in which the thin selective layer controls the mass transfer of components through the membrane while the support layer with a low resistance acts as a mechanical support. Ions undergo equilibrium partitioning at the feed solution-membrane selective layer interface [34]. DSPM-DE model effectively describes the phenomena occurring at the membrane interface and elucidates the exclusion and rejection mechanisms of an ion by the selective layer. Understanding the mass transport mechanisms governing nitrate rejection in these MPN membranes provides valuable insights into enhancing membrane performance and expanding the scope of membrane technology for sustainable water treatment.

2. Materials and methods

2.1. Materials and chemicals

A polyacrylonitrile (PAN) ultrafiltration membrane was inhouse fabricated and provided by Helmholtz-Zentrum Hereon. Tannic acid (TA) was purchased from Sigma-Aldrich Chemie GmbH (Germany). Iron (III) chloride hexahydrate ($FeCl_3{\cdot}6H_2O$) was obtained from Alfa Aesar GmbH & Co. Poly(ethylene glycol) (PEG) of 400 g/mol average molecular weight was commercially supplied by VWR International GmbH (Germany). Sodium nitrate ($NaNO_3$, 84.995 g/mol), sodium sulfate (Na_2SO_4, 142.04 g/mol), and Sodium chloride (NaCl, 58.44 g/mol) were purchased from Sigma-Aldrich Chemie GmbH (Germany). Milli-Q ultrapure water purification system was used to produce the Deionized (DI) water used in this study. Aqueous feed solutions were prepared using DI water. All chemicals were used as received.

2.2. Synthesis of the TFC membranes

The membrane fabrication method used to obtain the TFC membranes is analogous to the layer-by-layer film deposition technique. Briefly, a series of membranes were fabricated by coating the top layer of the in-house made PAN support with 50 ml aqueous solutions of tannic acid (0.02 w%) and $FeCl_3{\cdot}6H_2O$ solutions in a layer-by-layer technique. Scheme 1 illustrates the fabrication process of the TFC membrane. Firstly, the PAN was pre-soaked in pure water for at least 3 hrs. The casting solutions for the TA-Fe^{3+} coatings were dissolved in DI water. Then, a two-TA-Fe^{3+} layered coating was fabricated over the PAN substrate by depositing the TA and Fe^{3+} containing solutions alternately, each for 4 min. The membrane was rinsed with DI water after the deposition of each solution. The $FeCl_3{\cdot}6H_2O$ concentration was varied (0.09, 0.1, 0.12, and 0.16 w%) to fabricate 1TA-4.5Fe, 1TA-5Fe, 1TA-6Fe, and 1TA-8Fe TFC membranes, in the corresponding order, in which the coefficient of Fe corresponds to the weight ratio between the ferric salt and TA solutions.

2.3. Membrane characterization

Surface analyses of the membranes were performed using SEM, AFM, FTIR, and EDX. Fourier Transform Infrared Spectroscopy (FTIR) using Bruker Alpha (diamond-ATR unit) (Bruker, Karlsruhe, Germany) in the wavenumber range 4000 – 400 cm^{-1} with a resolution of 4 cm^{-1} for 64 scans was recorded to determine surface functional groups on dry samples. Energy dispersive X-ray spectroscopy (EDX) analyses were performed for elemental analysis on membrane surface. Extreme and an X-max 150 EDX (Oxford Instruments, U.K.) detectors were used as primary and secondary detectors. Analyses were performed at an acceleration voltage of 1.5 kV, a working distance of 5.6 nm and a constant magnification of 5 kx. Surface and cross-sectional morphologies of the support and fabricated TFC membranes were observed with a Merlin (Zeiss, Germany) Scanning Electron Microscopy (SEM) at an accelerating voltage of 1.5 – 3 kV. InLens secondary electron detector was used, and samples were sputter-coated with 1 – 1.5 nm platinum using a CCU-010 coating device (Safematic, Switzerland) before measurement. Atomic force microscopy (AFM) images were collected on MultiMode 8 instrument (Bruker, USA) in Tapping mode using RTESPA-150 probes (tip radius ≈ 8 nm, spring constant ≈ 5 N/m) to analyze the surface topography and roughness of the membranes. The root mean square (RMS) roughness values (R_q) and arithmetic average roughness values (R_a) of height deviations taken from the mean image data plane using a 3 μm x 3 μm scan size of membrane area were calculated with NanoScope Analysis 1.9 software. The reported roughness values are the average from three different areas for each sample. The streaming zeta potential was measured with SurPASS 3 electrokinetic analyzer (Anton Paar, Austria) using 1 mM NaCl as a background solution.

2.4. Experimental setup and operational protocol

All filtration experiments were performed in a laboratory test cell in a dead-end configuration. A stirred test cell from Millipore (EMD Millipore XFUF07601) was used for the retention experiments. A membrane area of 2.13 cm^2 was used. All the experiments were carried out at a stirring speed of 350 rpm. To evaluate the nitrate retention performances of the TA-Fe^{3+} TFC membranes, salt retention experiments were first performed with $NaNO_3$ (100 mg/L) at 3 bar transmembrane pressure. The influence of the concentration and pressure were then studied for values ranging from 100 – 4000 mg/L and 0.5 – 4.5 bar, respectively. Retentions were determined according to the following relation:

$$R(\%) = \left(1 - \frac{C_p}{(C_f + C_r)/2}\right) * 100 \quad (1)$$

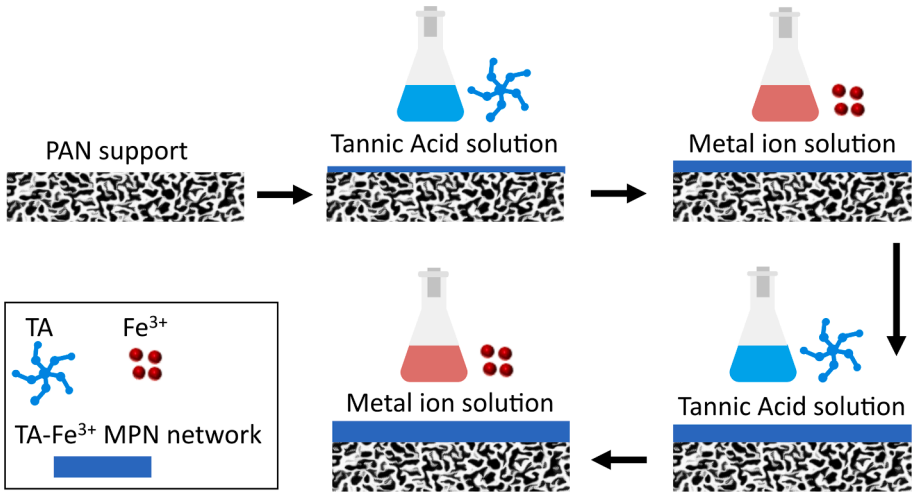

Scheme 1. Schematic illustration of the membrane fabrication technique of the MPN containing TFC membranes.

R is the solute retention, C_p, C_f and C_r are the concentrations of the permeate, feed and retentate solutions in mg/L, respectively. The average of C_f at the beginning and C_r at the end of the filtration was taken for the computation of $R(\%)$ to account for the small change in the concentration of the feed solution in a dead-end filtration system. The ionic solute concentrations in the feed, permeate and retentate were determined by ion chromatography (Dionex ICS600, Thermofischer Scientific Inc., USA) provided with a AS 14A column and a CS 12A column for the determination of anions and cations, respectively. Poly (ethylene glycol) (PEG) of 400 g/mol average molecular weight was used as neutral solute to determine the structural properties of the membranes. The concentrations of PEG in the feed, permeate and retentate were determined by gel permeation chromatography (GPC) (VWR-Hitachi 2130 pump, Hitachi, Darmstadt, Germany).

The membrane flux, J_V ($L{\cdot}m^{-2}{\cdot}h^{-1}$), was computed using equation (2).

$$J_V = \frac{V}{A^*\Delta t} \tag{2}$$

Where V (L) is the volume of the permeate collected, A (m^2) is the effective area of the membrane used for filtration, and Δt (h) is the filtration time. The pure water permeance (PWP, $L{\cdot}m^{-2}{\cdot}h^{-1}{\cdot}bar^{-1}$) was calculated as $\frac{J_V}{\Delta P}$, where ΔP (bar) is the applied transmembrane pressure.

To study the separation performance of the fabricated membranes for a mixed solute system, filtration tests of ternary ion mixtures from salts containing a common cation were performed. Two separate solutions of NaCl-$NaNO_3$ as well as $NaNO_3$-Na_2SO_4 mixtures of 10 mM total feed salt concentration in which NO_3^-/Cl^- and NO_3^-/SO_4^{2-} molar ratios of 1:1 were prepared. The retention tests were carried out at 3 bar transmembrane pressure. To work with the model proposed in this study, the retention of ions from $NaNO_3$-Na_2SO_4 mixture is measured as a function of volume flux. This was performed by varying the applied pressure driving force between 0.5 – 4.5 bar.

2.5. DSPM-DE model for elucidating the transmembrane ion transport and rejection

DSPM-DE is a practical and comprehensive model that describes the transport and rejection mechanisms of NF [33,35–37]. Evaluation of the transport mechanisms of ions through NF membranes involves mass transfer in a concentration polarization effect, followed by partitioning from the bulk solution to the membrane matrix, and then transport through the membrane active layer [38,39]. Partitioning of ions from the membrane matrix to the permeate solution occur at the membrane-permeate interface. Ionic partitioning at the solution–membrane interfaces is determined by the interplay between three exclusion mechanisms: steric (size), Donnan (charge) and dielectric exclusion effects (Scheme 2a). Steric exclusion is due to the size sieving property of the porous structure while Donnan exclusion is due to the electrostatic interaction between the charged ions in solution and the fixed membrane charge. Dielectric exclusion mechanism according to the Born effect is considered in this work. Based on the Born effect, the dielectric constant of the solvent decreases inside the pores that causes solvation energy barrier for ions to enter confined channels. The exclusion effects are accounted for using the boundary conditions at the membrane surfaces.

A comprehensive study of NF transport mechanism requires the use of the Extended Nernst–Planck (ENP) equation which involves a combination of the diffusive, convective and electro-migrative transport of species, modified by the hindered transport theory [40]. The DSPM-DE model is based on the assumption that the membrane active layer is a porous structure containing cylindrical uniformly sized pores. However, membrane structures contain tortuous pores of interconnected network of pores having a wide pore size distribution that may influence the performance predicted using the above assumption. This active layer predominantly determines the separation performance of the membrane. A method pioneered by Geraldes et al. [36] that solves the ENP equations, by first discretizing and linearizing, is followed in this work. The NF active layer is divided into equally spaced nodes and the DSPM-DE model equations are applied between each node. The non-ideality of solutions and the feed-side concentration polarization effect are considered.

Modeling of ion transport in a NF process requires the description of mass transport of each species through each region of scheme 2b: the concentration polarization layer on the feed side, the NF active layer and the permeate side. First, we start with the transport inside the pores of the membrane. Mass transport of ions across the membrane active layer through concentration gradient, inertial and electric forces is described using the ENP equation. The flux of each solute (J_i) through the membrane pore is given by equation (3) [36,41]:

$$J_i = -K_{i,d}D_{i,\infty}\frac{dC_i}{dx} + K_{i,c}C_iJ_v - z_iC_iK_{i,d}D_{i,\infty}\frac{F}{RT}\frac{d\Psi}{dx} \tag{3}$$

Where z_i is the valence, $D_{i,\infty}$ is the diffusivity, C_i is the concentration of solute i inside a pore, J_v is the solution flux, and Ψ is the electrical potential. x is the coordinate from feed towards permeate side in the direction across the membrane active layer, while F, R and T represent Faraday constant, universal gas constant and temperature, respectively. The first, second and the last terms of the right hand-side of equation (3)

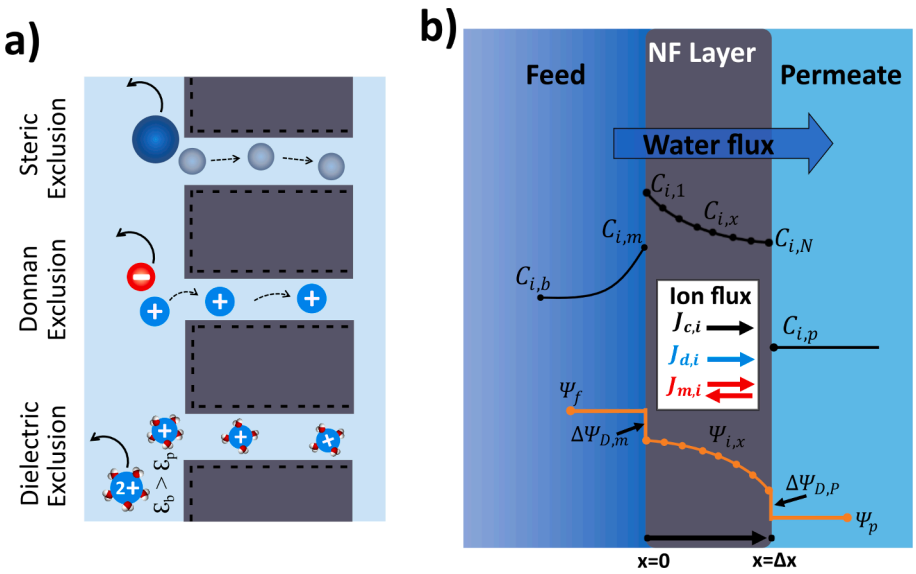

Scheme 2. Schematic illustration of NF membrane exclusion mechanisms (a) and the potential profile, the concentration profile, and the transport mechanisms in NF process (b). The membrane active layer is discretized into equally spaced nodes. For every node, one ENP equation is applied for each solute *i*.

for J_i represent the transport of ions through diffusion (diffusive flux, $J_{d,i}$), potential gradient (electromigrative flux, $J_{m,i}$), and due to convective forces (convective flux, $J_{c,i}$) respectively. The diffusion and convective transport within the small pore-sized NF membrane are hindered. $K_{i,C}$ and $K_{i,d}$ are hinderance factors for both convection and diffusion, respectively, estimated through the empirical correlations of equation (4) and (5), introduced to modify the ENP equation by the hindered transport theory [36].

$$K_{i,C} = \frac{(1 + 3.867\lambda_i - 1.907{\lambda_i}^2 - 0.834{\lambda_i}^3)}{(1 + 1.867\lambda_i - 0.741{\lambda_i}^2)} \tag{4}$$

$$K_{i,d} = \begin{cases} \dfrac{\left(1 + \left(\frac{9}{8}\right)\lambda_i ln\lambda_i - 1.560\lambda_i + 0.528{\lambda_i}^2 + 1.915{\lambda_i}^3 \right.}{(1-\lambda_i)^2} \\ \left. -2.819{\lambda_i}^4 + 0.270{\lambda_i}^5 + 1.101{\lambda_i}^6 - 0.435{\lambda_i}^7\right) \\ \qquad , \lambda_i \le 0.95 \\ 0.984\left(\dfrac{1-\lambda_i}{\lambda_i}\right)^{5/2}, \lambda_i > 0.95 \end{cases} \tag{5}$$

Where λ is the relative size of solute Stokes radius to pore size $\left(\frac{r_s}{r_p}\right)$.

Taking concentration polarization on the feed side [36] into consideration, the flux of a solute across the concentration polarization layer at the feed side of scheme 2b is be expressed as:

$$J_i = -k_{i,c}^{*}(C_{i,m} - C_{i,b}) + J_v C_{i,m} - \frac{z_i C_{i,m} D_{i,\infty} F}{RT}\frac{d\Psi}{dx} \tag{6}$$

Where $C_{i,b}$ and $C_{i,m}$ are the concentrations of ion i in the bulk solution and just at the pore entrance, respectively. $k_{i,c}^{*}$ is the permeate flux dependent mass transfer coefficient given by

$$k_{i,c}^{*} = k_{i,C}\left(\Phi_i + (1 + 0.26{\Phi_i}^{1.4})^{-1.7}\right) \tag{7}$$

Where $\Phi_i = \frac{J_i}{k_{i,C}}$. The mass transfer coefficient ($k_{i,C}$) is computed from the mass-transfer correlations as follows.

$$Sh = 0.23 Re^{0.567} Sc^{0.33} \tag{8}$$

Where $Sh = k_{i,C}L/(D_{i,\infty})$ is the Sherwood, Re is the Reynolds number and Sc is the Schmidt number which is related to viscosity and the diffusivity at infinite dilution. L is the length of the stirrer utilized.

On the other hand, the continuity equation expresses the flux of a solute on the permeate side as shown in equation (9) assuming a steady state flow.

$$J_i = J_v C_{i,p} \tag{9}$$

According to Gao et al. [42] and Wang and Lin [33], the boundary conditions are given by the equilibrium relations for partitioning at the feed-membrane interface (equation (10)) and at the membrane-permeate interface (equation (11)) as follows.

$$\frac{\gamma_{i,1}C_{i,1}}{\gamma_{i,m}C_{i,m}} = \left(1 - \frac{r_s}{r_p}\right)^2 exp\left(-\frac{\Delta W_i}{k_B T}\right) exp\left(-\frac{z_i F}{RT}\Delta\Psi_{D,m}\right) \tag{10}$$

$$\frac{\gamma_{i,N}C_{i,N}}{\gamma_{i,P}C_{i,P}} = \left(1 - \frac{r_s}{r_p}\right)^2 exp\left(-\frac{\Delta W_i}{k_B T}\right) exp\left(-\frac{z_i F}{RT}\Delta\Psi_{D,P}\right) \tag{11}$$

Where the exponential term $exp\left(-\frac{z_i F}{RT}\Delta\Psi_D\right)$ represent Donnan exclusion coefficient (Φ_D) of a solute. $\left(1 - \frac{r_s}{r_p}\right)^2$ is the steric exclusion factor (Φ_s) for ion i, while $exp\left(-\frac{\Delta W_i}{k_B T}\right)$ represents the dielectric partitioning factor (Φ_B) expressed as a function of the change in solvation energy (ΔW_i) of a solute, calculated as follows.

$$\Delta W_i = \frac{z_i^2 e_0^2}{8\pi\varepsilon_0 r_s}\left(\frac{1}{\varepsilon_p} - \frac{1}{\varepsilon_b}\right) \tag{12}$$

ε_b and ε_p are dielectric constants of water in the bulk solution and inside the pores of the active layer, e_0 is the charge of an electron, ε_0 is the vacuum permittivity. The non-ideality of the solution is considered through the introduction of an activity coefficient for an ion (γ_i) computed using [41]:

$$\ln(\gamma_i) = -Az_i\left(\frac{\sqrt{I}}{1+\sqrt{I}} - 0.3I\right) \tag{13}$$

Where I is the ionic strength of the solution given by $I = 0.5\sum_{i=1}^{Nc} z_i^2 C_i$, while A is a correction factor expressed as [41]:

$$A = \left(\frac{\sqrt{2\pi N_A}}{\ln(10)}\right)\left(\frac{e_0^2}{4\pi\varepsilon_0\varepsilon_r k_B T}\right)^{3/2} \quad (14)$$

Here, N_A, ε_r, k_B represent respectively Avogadro's number, dielectric constant of medium and the Boltzmann constant. Electroneutrality is always fulfilled in the feed side (equation (15)), permeate side (equation (16)) and inside membrane active layer (equation (17)). Inside the membrane matrix, electroneutrality is met through the contribution of the available ionic species and volumetric charge density of the NF layer.

$$\sum_{i=1}^{Nc} z_i C_{i,m} = 0 \quad (15)$$

$$\sum_{i=1}^{Nc} z_i C_{i,p} = 0 \quad (16)$$

$$C_X + \sum_{i=1}^{Nc} z_i C_i = 0 \quad (17)$$

2.5.1. Computational procedure

Only steric exclusion mechanism affects the partitioning of uncharged solutes. Therefore, rejection for neutral solutes can be expressed by solving the DSPM-DE transport equation without the dielectric and Donnan exclusion terms as follows [33,43]:

$$R_{real} = \left(1 - \frac{C_{i,p}}{C_{i,m}}\right) = 1 - \frac{K_{i,C}\Phi_s}{1 - \exp\left(-\frac{K_{i,C}}{K_{i,d}}\frac{J_v \Delta x}{D_{i,\infty} A_k}\right)\left(1 - K_{i,C}\Phi_s\right)} \quad (18)$$

Φ_s is the steric exclusion factor dependent on the solute radius and pore radius. A procedure by Bowen et al. [44] for fitting the rejection of neutral solutes to determine pore characteristics using equation (18) is followed. In this approach, the pore size (r_p) and the membrane thickness to porosity ratio ($\Delta x_e = (\frac{\Delta x}{A_k})$) were estimated using PEG retention measurements as a function of permeate flux, J_v. A 1 g/L solution of PEG of 400 g/mol molecular weight was used for this test. The feed, retentate and permeate PEG concentrations were analyzed using GPC and retention was computed as described in section 3.4 above. To estimate the pore radius and the effective thickness of each membrane, a curve fitting of rejection and J_v (in Equation (18)) was performed through minimization of the sum of squared errors (SSE) between the experimentally measured (R_{exp}) and the calculated rejection (R_{cal}) of the neutral solute. These membrane parameters were regressed using the dual annealing optimization algorithm in python. The objective function was as follows.

$$f(r_p, \Delta x_e) = SSE = \sum_{fluxes} (R_{cal} - R_{exp})^2 \quad (19)$$

Then, the observed rejection of the ternary ionic mixture (nitrate containing salt solution) a function of J_v was fitted to determine the membrane charge density (C_X) and pore dielectric constant (ε_p) by simultaneously solving the DSPM-DE system of equations. Similarly, these membrane parameters were estimated by minimizing the SSE between the measured and the calculated rejection of ions in the salt solution. Dual annealing in conjunction with the Nelder-Mead local optimizer was used to perform the optimization process in python since this regression method provides the fastest convergence as suggested by a previous study [37]. Inside the active layer, the ENP equations are discretized by dividing the membrane thickness into N number of nodes as shown in Scheme 2b. Then, the systems of equations (Equation (3) – (17)) were solved simultaneously by linearizing the discretized ENP equations and other model equations. Initial guess of potential and concentration profiles as well as under-relaxation factors for the electrical potential and concentrations inside the membrane were provided to the system to ensure that the convergence is achieved as suggested in a previous study on DSPM-DE [36]. The algorithm developed by Geraldes et al. [36] was used to solve the system of equations. The flowchart in Fig. S4 (supporting information) shows the algorithm followed in this work. The numerical parameters and operating conditions can be found in Table S1 and S2.

3. Results and discussion

This section contains two main parts. Salt retention performance of the membranes is presented and discussed in the first part of this section (subtopics 4.1 – 4.5). This involves both single and mixed salt filtration tests. The membrane characterization and the nitrate rejection behavior of the MPN membranes under different conditions is analyzed. In the second part, DSPM-DE is used to assess the ion transport properties of the TFC membranes (section 4.6). Membrane parameters are first estimated followed by the comparison of experimental and theoretical ion rejection results in multi-ionic mixtures. Finally, the implications of the exclusion coefficients and ion fluxes computed are discussed.

3.1. Characterization of the fabricated membranes

FTIR spectroscopy was used to analyze the chemical functional groups of the membranes. Peaks from the PAN support attributed to CH_2 stretching vibration (at 2936 cm^{-1}), C≡N stretching vibration (at 2242 cm^{-1}) and CH_2 bending vibration (at 1450 cm^{-1}) of the pristine support and the TFC membranes are shown in Fig. 1a. In the newly fabricated membranes, the broad spectral peak from 3700 to 3200 cm^{-1} is ascribed to the abundant phenolic –OH groups in tannic acid. Characteristic bands from the MPN layer appear at 1713 cm^{-1} and 1575 cm^{-1} in the FTIR spectra of the TFC membranes attributed to the C=O for stretching vibration in the ester groups and the C=C stretching vibration peak from the aromatic rings of TA, respectively. The peak at 1202 cm^{-1} corresponds to the C–O stretching vibration from TA. The emergence of these new spectral peaks confirms the successful deposition of the MPN layer onto the substrate surface. EDX was further carried out to validate the effective deposition of TA-Fe^{3+} layer. The characteristic peaks from the MPN coating layer clearly show the presence of oxygen and iron as component elements (Fig. S1). In comparison, the reference PAN support membrane did not exhibit any Fe peak (Fig. S1). Elemental compositions of both O and Fe increased on the 1TA-8Fe membrane surface compared to 1TA-4.5Fe membrane denoting an increased incorporation of tannic acid and metal ions in the self-assembled layer. On the contrary, the density of carbon and nitrogen in the fabricated TFC membranes decreased due to the TA-Fe^{3+} coating on the PAN surface.

AFM analysis revealed that the TA-Fe^{3+} coating at low Fe^{3+} concentration exhibit smoother surfaces compared to the pristine PAN support (Fig. 1c and 1d). The RMS roughness value (R_q) of the PAN support was 3.59 nm while the R_q for 1TA-4.5Fe and 1TA-5Fe TFC membranes slightly decreased to 3.36 and 3.35 nm, respectively. When the $FeCl_3{\cdot}H_2O$ concentration increased beyond 0.10 w%, the MPN membrane exhibit substantially rough surfaces. High metal ion concentration induces aggregation of TA-Fe^{3+} complexes on membrane surface. These aggregates are deposited over the membrane surface as a result of the binding affinity of TA [45]. This increases surface roughness and protrusions [27,46,47]. The protrusions from the complexes can be observed in Fig. 1c for 1TA-6Fe and 1TA-8Fe membranes. The RMS roughness values for these membranes were 7.15 and 6.71 nm, respectively.

To assess the impact of the MPN layer coating on the porous substrate, the surface and cross-sectional morphologies of the coated and pristine membranes were examined with SEM. The uncoated PAN membrane displayed a smooth and porous top surface as depicted in Fig. 2a. Fig. 2b-e illustrate the surface morphologies of the fabricated TFC membranes. The denser top surface structure of the TFC membranes, compared to the bare PAN membrane, is attributed to the deposition of a MPN layer, which forms rapidly due to the self-assembly of TA and Fe^{3+} [45,46]. Increasing the $FeCl_3$ concentration in the casting solution reduces the surface porosity of the TFC membranes significantly. For instance, the 1TA-4.5Fe membrane had a relatively porous

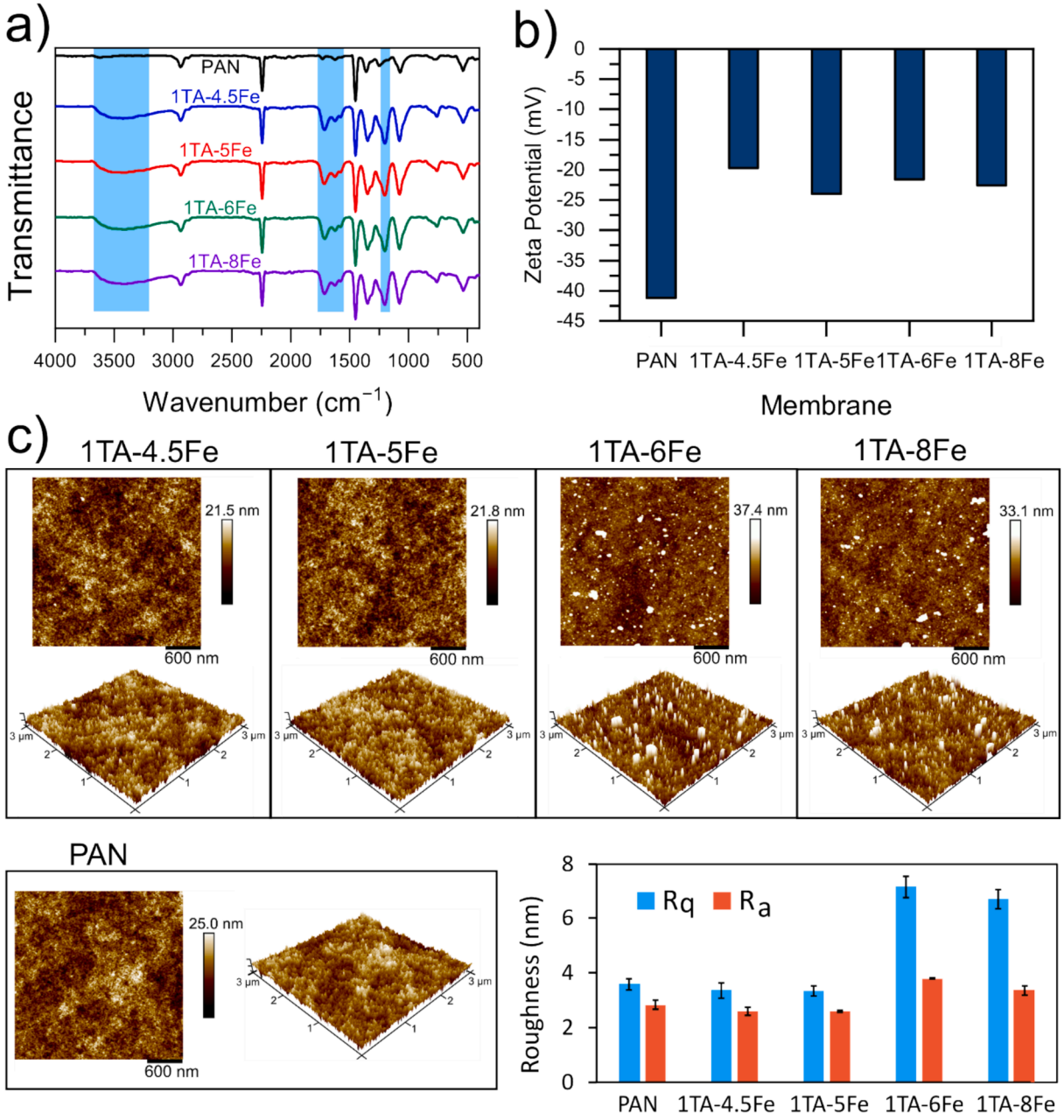

Fig. 1. Surface analysis of the PAN pristine membrane and the fabricated TA-Fe^{3+} membranes. a) FTIR, b) zeta potential at pH 5.9 of the background solution, c) 2D and 3D AFM images, and d) surface roughness of the membranes in terms of RMS (R_q) and Arithmetic average (R_a).

TA-Fe^{3+} surface coating, while 1TA-8Fe membrane exhibited the most compact surface structure. The increase in metal ion concentration during the immersion process promoted the MPN layer growth and cross-liking. Consequently, a denser top surface with low surface porosity is formed when Fe^{3+} concentration of the casting solution was increased. Furthermore, the SEM analysis of the cross-sections showed that all membranes had a spongy microporous sublayer beneath the top skin layer, which formed during the phase inversion process of the support fabrication. The high-resolution SEM images confirmed that the cross-sectional microstructure remained unobstructed, indicating that the TA-Fe^{3+} coating formed an ultrathin skin layer [45,48] only over the membrane top surface. The structure of the TFC membranes, consisting of a thin dense surface layer and a sponge-like sublayer ensures a good retention and high flux properties.

To evaluate the water flux of the MPN coated membranes, pure water permeation test was performed at 3 bar feed pressure. The pure water permeances (PWP) of the fabricated TFC membranes (Table 1) were lower than the permeance for the pristine PAN support. PWP of the PAN was 286 ± 10 $L{\cdot}m^{-2}{\cdot}h^{-1}{\cdot}bar^{-1}$. After the deposition of the TA-Fe^{3+} layer, the porous surface of the support substrate was homogeneously covered. The water permeance of the TA-Fe^{3+} membranes declined when the ferric ion concentration of the casting solution was increased. For example, the PWP of the 1TA-4.5Fe membrane was around 13.6 $L{\cdot}m^{-2}{\cdot}h^{-1}{\cdot}bar^{-1}$, whereas the 1TA-5Fe membrane, which was moderately tighter, had a PWP of 6.6 $L{\cdot}m^{-2}{\cdot}h^{-1}{\cdot}bar^{-1}$. The 1TA-8Fe TFC membrane, with its denser surface structure, showed the lowest water flux, indicating a potentially enhanced ability to retain solutes. Such a reduction in permeance is due to the formation of denser separation layers at higher Fe^{3+} concentrations, as depicted by the SEM images in Fig. 2. Similar water permeance decline was observed in our previous work for small organic molecule separation [49]. These findings underscore the importance of reagent concentration in tailoring

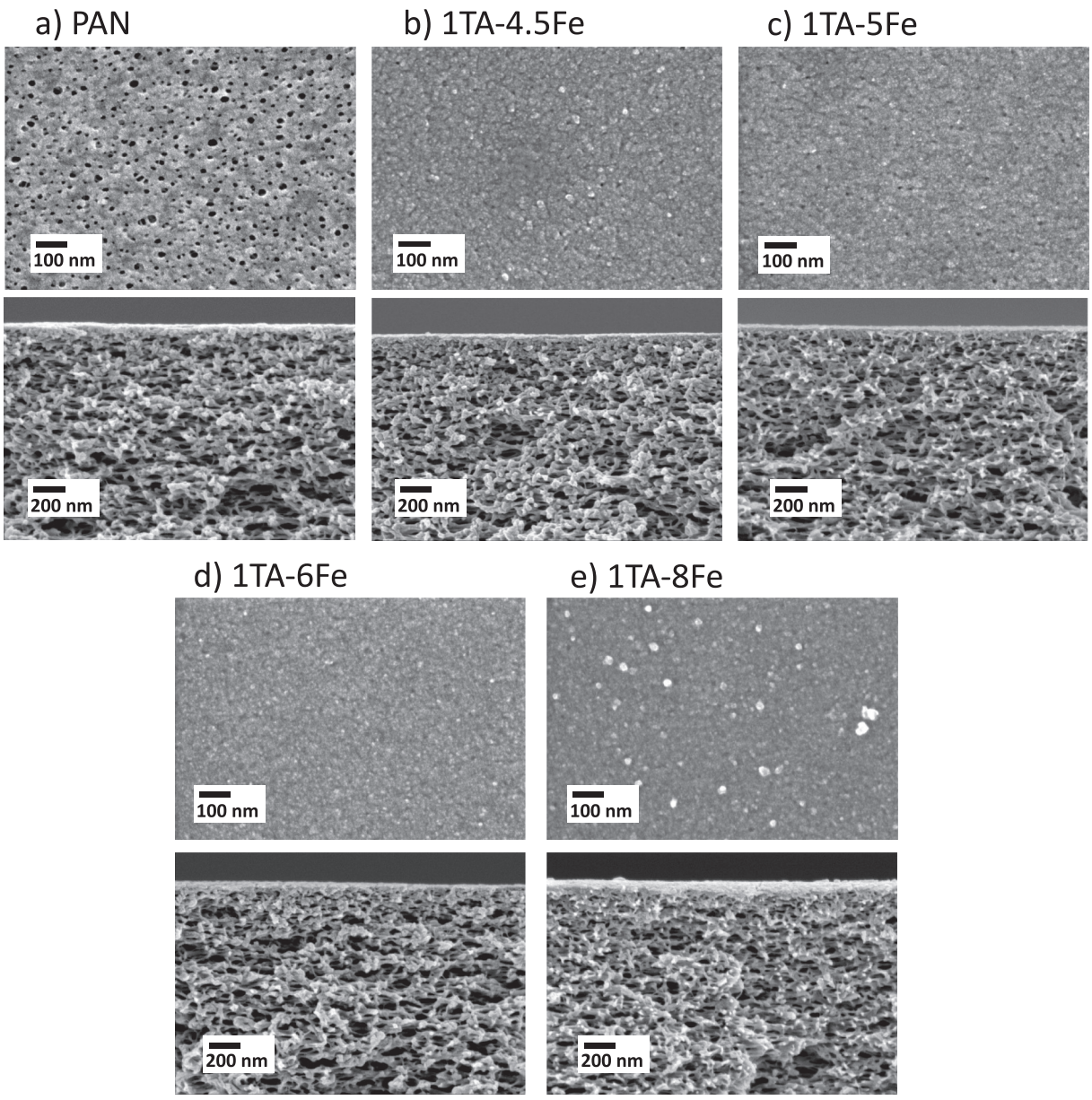

Fig. 2. Surface (top image) and cross-section (bottom image) SEM images of the analyzed support and TA-Fe^{3+} TFC membranes fabricated at different tannic acid to $FeCl_3{\cdot}6H_2O$ ratio: (a) pristine PAN support, (b) 1TA-4.5Fe, (c) 1TA-5Fe, (d) 1TA-6Fe and (e) 1TA-8Fe.

Table 1
Water permeance of the MPN based TFC membranes, fabricated at different $FeCl_3{\cdot}6H_2O$ concentration, used for nitrate retention test.

Membrane	Pure water permeance ($L{\cdot}m^{-2}{\cdot}h^{-1}{\cdot}bar^{-1}$)
PAN	286 ± 10
1TA-4.5Fe	13.6 ± 3.8
1TA-5Fe	6.6 ± 0.9
1TA-6Fe	3.8 ± 1.8
1TA-8Fe	0.9 ± 0.1

metal–phenolic network coated TFC membranes.

3.2. Nitrate retention efficiency of TA-Fe^{3+} membranes

The nitrate retention performance of the fabricated TFC membranes from aqueous solution containing $NaNO_3$ was evaluated. The nitrate removal efficiency of the membranes (Fig. 3a) increases with the increase of Fe^{3+} concentration in the casting solution. Under test conditions of 100 mg/L $NaNO_3$ concentration and 3 bar operating pressure, 1TA-8Fe membrane had the highest nitrate retention (93.8 %), outperforming 1TA-4.5Fe (82.9 %), 1TA-5Fe (89.2 %) and 1TA-6Fe (93.6 %). The ion retention mechanism involves steric exclusion, Donnan exclusion and dielectric exclusions [33]. The pH of the $NaNO_3$ feed solution was 5.9. Due to the negative surface charges of the membranes at this pH (Fig. 1b), the Donnan effect substantially contributes to the overall nitrate rejection. Steric hindrance affect ionic solute rejection, particularly in salts with hydrated ionic diameters larger than or comparable to the pore size of the membrane [50]. As Fe^{3+} concentration increased, the membrane pore size decreased, which enhanced steric hindrance and consequently improved nitrate rejection. The dielectric exclusion further enhanced the salt rejection by increasing the solvation energy barrier for ions attempting to enter the small, confined pores of the membranes.

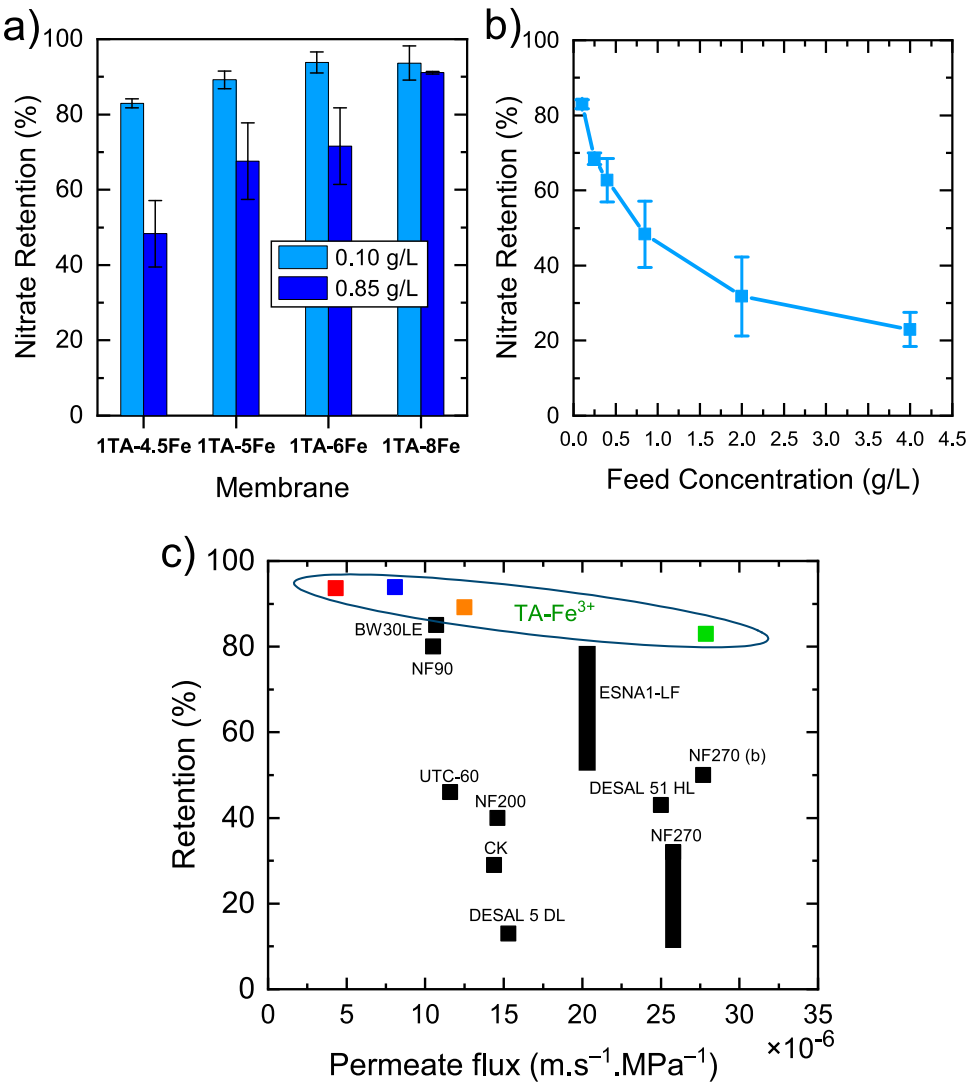

Fig. 3. (a) Nitrate ion retention performance of the TA-Fe^{3+} membranes from 100 mg/L and 850 mg/L feed concentrations. (b) Effect of feed concentration on $NaNO_3$ retention by the 1TA-4.5Fe membrane. (c) Comparison of the nitrate retention performance of the TA-Fe^{3+} membranes (Colored squares) to commercial membranes from the literature (black squares and bars). Colored squares represent 1TA-4.5Fe (green), 1TA-5Fe (orange), 1TA-6Fe (blue) and 1TA-8Fe (red) membranes. Data for 270 (b), BW30LE and CK are from ref[62], ref[63] and ref[64], respectively. Data for all other commercial membranes were taken and reconstructed from Ref. [19]. Bars represent a range of retention values. (For interpretation of the references to colour in this figure legend, the reader is referred to the web version of this article.)

3.3. *The effect of initial nitrate concentration*

Membrane performance is strongly dependent on the process operating parameters and the concentration of the feed solution is one of the most important and fundamental parameters. Fig. 3b present the effect of feed concentration on nitrate retention. The $NaNO_3$ concentration was varied between 100 mg/L – 4000 mg/L using the 1TA-4.5Fe membrane. It is observed from Fig. 3b that the salt retention decreased exponentially with the increase in salt concentration of the feed solution. Thus, a negative covariance is observed between the feed solution concentration and nitrate retention. The retention rate was 82.9 % at 100 mg/L which dropped to 68.4 % at 250 mg/L and further to 22.9 % at 4000 mg/L. This fast decline can be explained by the drop in the effects of the membrane surface charge. This behaviour is well known and is characteristic of charged membranes [51–53]. As the ion concentration in the feed increases, the electric double layer compresses [54,55]. In dilute solutions, solutes experience electrostatic repulsion from a charged membrane surface over a greater distance than in concentrated solutions [55]. At low ionic concentrations, the screening effect is weak, and electrostatic repulsion of anions plays a significant role, resulting in higher retention [56]. However, as concentration increases, the screening effect intensifies due to the shielding phenomenon [56]. Higher salt concentration leads to a stronger counter-ion screening, which gradually neutralizes the negative charge of the membrane surface. Charge neutrality in the membrane requires a balance between the volumetric charge density of the solution within the membrane pores and the fixed charges of the membrane itself. At high ionic strength, the Donnan potential developed on the membrane surface to induce the net volumetric charge density diminishes, reducing the effect of Donnan exclusion [33,57]. Therefore, retention of nitrate declines due to the weaker electrostatic interactions between the negatively charged surface of the membrane and the NO_3^- ions. Furthermore, diffusion inside the membrane is concentration dependent. Increasing the concentration of ions in the membrane pores leads to higher fluxes of ionic solutes due to the contribution of diffusive flux. All four fabricated membranes showed similar trend of ion retention owing to the change in $NaNO_3$ concentration in the feed solution (Fig. 3a). The nitrate retention of the membranes decreased from 82.9 –

93.8 % at 100 mg/L to 48.3 – 91.1 % when the feed solution was 850 mg/L, demonstrating the membranes maintained good retention even at 850 mg/L (equivalent to 10 mM of $NaNO_3$). Since the nitrate concentration in actual groundwater across European and other regions is typically lower than 100 mg/L [7], it can be concluded that the prepared MPN membranes are effective in its removal at this concentration (Fig. 3a, for 0.1 g/L) and reduce it to admissible levels.

The obtained retention results are compared with those of commercial membranes reported in the literature (Fig. 3c). The MPN membranes show a superior nitrate retention performance compared to the commercial membranes, suggesting TFC membranes with TA-Fe^{3+} selective layers are promising candidates for the denitrification of contaminated water. However, future works can focus on improving the water permeance of the MPN membranes through different strategies.

3.4. Effect of pressure on permeate flux and nitrate retention

The permeate flux increases linearly with the transmembrane pressure for all TA-Fe^{3+} membranes (Fig. 4b). Higher hydraulic pressures result in increased permeate flux, while nitrate retention is also closely tied to this flux. Fig. 4a shows the observed nitrate removal rates as a function of the applied transmembrane pressure. The nitrate retention of the membranes improves with increasing pressure, due to the increased permeate flux. This increase is most rapid at transmembrane pressures between 0.5 and 2 bars for all membranes. Relatively slower increase of retentions were observed for the increase of transmembrane pressures from 2 to 4 bars. For the 1TA-6Fe membrane, the nitrate retention was dramatically improved from 26 % at 0.5 bar to 85 % at 4 bar transmembrane pressure. The NO_3^- removal increased from 27.5, 28, 51.2, and 62 % at 1 bar to 55.9, 70.4, 85.3 and 90.1 % at 4 bar for the 1TA-4.5Fe, 1TA-5Fe, 1TA-6Fe and 1TA-8Fe membranes, respectively. Generally, it is evident that the applied pressure has a substantial and positive effect on nitrate retention. When concentration polarization is minimal, higher water permeance is observed as the applied transmembrane pressure is the only driving force for water transport through the pores [33]. The ion flux through a nanoporous membrane can be described as the sum of convective, diffusive and electromigrative fluxes [33,58,59]. Convective flux, driven by the pressure gradient across the selective layer, increases with permeate flux. At low permeate water flux, nitrate transport occurs primarily by ionic diffusion, as the contribution of convective flux is low [60]. As the applied pressure increases, the convective flux of the ions (slightly) increases. However, the overall concentration in the permeate side decreases. This decrease is due to the dilution effect in the permeate channel as a result of higher water flux [61]. Nitrate retention continues to increase with increasing flux until a limiting value for retention is reached [41,60].

3.5. Mixed salt retention

In the previous sections, we observed that MPN membranes exhibit excellent nitrate retention performance in case of feed solutions containing single salt (Fig. 3a). Here, we analyze the NO_3^- separation property of the MPN membranes from feed solutions containing mixed solution systems. These experiments assess the nitrate separation efficiency of the fabricated membranes from ternary ion solutions containing a $Na^+/Cl^-/NO_3^-$ mixture and $Na^+/NO_3^-/SO_4^{2-}$ mixture. The feed solutions contained 1:1 molar ratio of the anions. Fig. 5 presents the anion retention ability of TA-Fe^{3+} membranes, showing comparable retention of chloride and nitrate, while revealing high selectivity between NO_3^- and SO_4^{2-}. The similar charge and hydration radii (0.33 and 0.34 nm, respectively [65]) of Cl^- and NO_3^- underscores the challenge of separating these monovalent ions by NF membranes. Moreover, both of these ions exhibit similar diffusivities, 2.032 x10^{-9} $m^2 \cdot s^{-1}$ for chloride and 1.902 x10^{-9} $m^2 \cdot s^{-1}$ for nitrate [66]. However, Fig. 5a shows a small difference of the retention values, with chloride being marginally more rejected than nitrate by most membranes. This can be explained by the lower hydration energy of NO_3^- compared to Cl^-, enabling it to permeate through the membrane pores more easily by undergoing a higher degree of dehydration [64]. Furthermore, NO_3^- has a lower negative ionic charge density due to its higher ionic volume compared to Cl^- [64,66]. Therefore, nitrate is less repelled by a negatively charged membrane.

For the $NaNO_3$-Na_2SO_4 mixture (Fig. 5b), the MPN membranes showed a higher retention towards the divalent ion, SO_4^{2-}. The observed SO_4^{2-} retention was in the range of 83 – 98.8 %. The nitrate to sulfate selectivities were 4.5 – 38.1 under the operating conditions of a 1:1 molar ratio mixture of 10 mM feed solution at 3 bar transmembrane pressure and room temperature. Compared to nitrate, sulfate experiences stronger steric and Donnan exclusions by the negatively charged TA-Fe^{3+} membranes due to its higher ionic size and valence. Furthermore, nitrate is more mobile with almost twice diffusivity compared to

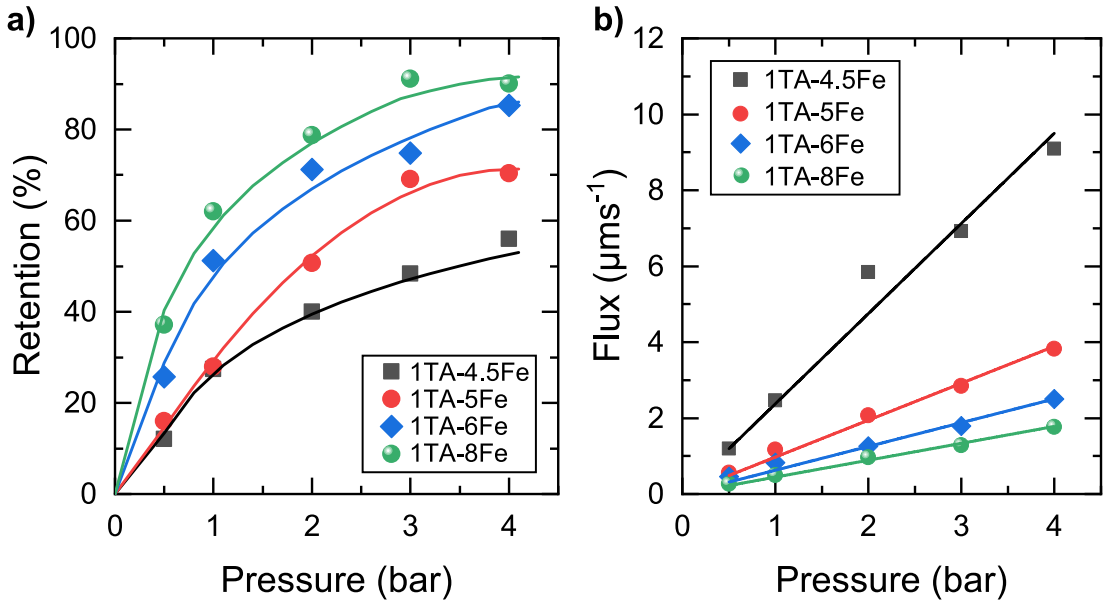

Fig. 4. Nitrate retention as a function of the applied transmembrane pressure (a), and the relationship between pressure and permeate flux variation (b) by the TA-Fe^{3+} membranes for 10 mM (≈ 850 mg/L) $NaNO_3$ feed concentration. The solid lines are added to guide the eye.

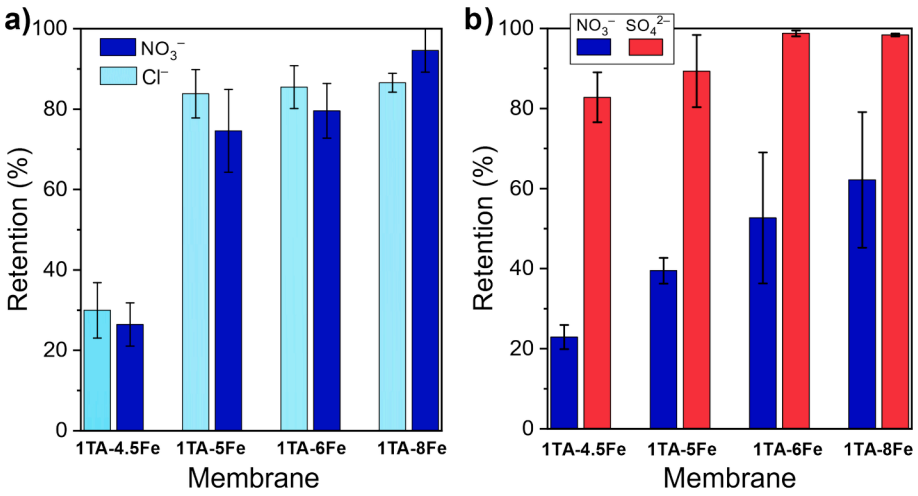

Fig. 5. The retention of anions for 1:1 molar ratio of a) NO_3^-/Cl^- and b) NO_3^-/SO_4^{2-} in 10 mM total feed concentration of $NaNO_3$–NaCl and $NaNO_3$–Na_2SO_4 mixtures, respectively.

sulfate [66]. Increasing solute radius, charge or decreasing solute diffusivity generally increase the solute retention by membranes. Due to the electrochemical potential gradient, the counter-ion (Na^+ in this case) can easily enter the membrane pores and is transported to the permeate side. Since the overall exclusion of sulfate by the membrane is higher, the other counterion (NO_3^-) permeates to neutralize the solution on the permeate side. Therefore, the transported Na^+ ions "pull in" the mobile nitrate ions to satisfy charge electroneutrality on both sides of the membrane. Overall, the TA-Fe^{3+} membranes show a good mono-/divalent anion separation from the nitrate-sulfate mixture containing feed solution.

We finally aim to correlate the observed rejection with the membrane properties through a mathematical framework. The next section discusses the applicability of the Donnan steric pore model with dielectric exclusion (DSPM-DE) to describe nitrate rejection by the TA-Fe^{3+} TFC membranes. The $NaNO_3$-Na_2SO_4 mixture was selected for this purpose since a good separation of nitrate from sulfate was observed. Besides, the experimentally measured rejection difference between chloride and nitrate cannot be described with this model [67,68].

3.6. Application of DSPM-DE for the $NaNO_3$-Na_2SO_4 system using MPN membranes

The fabrication of membranes with enhanced separation performance should be complemented by robust mass transport model to describe the NF process. These models help to understand the transport mechanisms, predict membrane performance and facilitate the design of high-performance membranes [69]. Given that MPN membranes are rather new, there has been no prior attempt to model ion transport through them. Here, we applied the DSPM-DE model to elucidate the $NaNO_3$-Na_2SO_4 mixture filtration and ion rejection properties of the TFC membranes having TA-Fe^{3+} selective layer for the first time. This approach allows us to investigate the dominant exclusion and transport mechanisms underlying the nitrate/sulfate separation.

3.6.1. Estimation of membrane parameters

Characterizing membranes in terms of parameters is an important part of membrane modeling [41]. The parameters should be articulated using simple mathematical models that allow them to be characterized with tolerable accuracy. The DSPM-DE model requires the determination of four membrane parameters. The pore radius (r_p) and effective membrane active layer thickness (Δx_e) were estimated by performing a rejection test of a neutral molecule (PEG in this case) [34,70,71]. The effective membrane thickness (Δx_e) denotes the membrane thickness to porosity ratio. The rejection of neutral molecules is attributed to the size sieving effect while the flux through the membranes is governed by a combination of diffusion and convection [71]. The r_p and Δx_e were estimated by fitting retention values (using equation (18)) at different permeate flux corresponding to different applied pressure. The rejection of PEG increased with the increase of applied pressure. The observed retentions as a function of flux and the fitted retention curves for the analyzed membranes can be found in Fig. S2 (Supporting Information).

The concentration of monomers significantly affects the growth of coating during the coordination reaction [47]. A higher Fe^{3+} concentration fosters the degree of coordination reaction to generate a more compact coating. An approximately 2 fold decrease of the r_p is observed for a 1.8 fold increase of the Fe^{3+} concentration (Fig. 6a). The r_p of the membranes gradually decreased from 1.3 nm to 0.6 nm with the increase of Fe^{3+} concentration. The Δx_e of the membranes 1TA-4.5Fe and 1TA-5Fe are rather similar. For 1TA-6Fe the Δx_e is substantially lower than for 1TA-5Fe. The Δx_e of 1TA-8Fe is slightly higher than that of 1TA-6Fe. A comparison of Fig. 4b and 6a suggests that the resistance against the mass transport through the prepared membranes is largely dictated by r_p. A small difference of Δx_e (like in case of 1TA-6Fe and 1TA-8Fe) is not reflected in the overall resistance of the membranes against mass transport.

The data obtained from the rejection test of charged solutes (a $NaNO_3$-Na_2SO_4 salt mixture) was used to estimate the membrane charge density (C_X) and pore dielectric constant (ε_p). Ion rejections, when plotted against permeate fluxes, show a linear relationship with $R^2 > 0.99$ (Fig. S3, Supporting Information). C_X and ε_p were estimated by fitting the observed rejections of the ions and simultaneously solving the DSPM-DE equations. The C_X of the membranes became more negative with increasing Fe^{3+} concentration. Theoretically, the pore dielectric constant is expected to decrease with the pore size of the membranes (i.e. with increasing the Fe^{3+} concentration). However, from Fig. 6 it is evident that although the r_p of 1TA-4.5Fe > 1TA-5Fe, there is no significant difference between the ε_p values in these two membranes. Similarly, although the r_p of 1TA-6Fe is larger than that of 1TA-8Fe the values of ε_p are rather similar. The ε_p values of 1TA-4.5Fe and 1TA-5Fe are significantly lower than those of 1TA-6Fe and 1TA-8Fe (Fig. 6b). The results indicated that the surface of the TA-Fe^{3+} membranes became more negatively charged when the concentration of ferric ion was increased (Fig. 6b). The negative surface charge is a comprehensive result of hydroxyl group adsorption on the surface and the ionization of the surface functional group, mainly through the dissociation of functional groups of the polyphenol. It is important to note that the membrane surface charge is indeed a significant parameter, dependent not

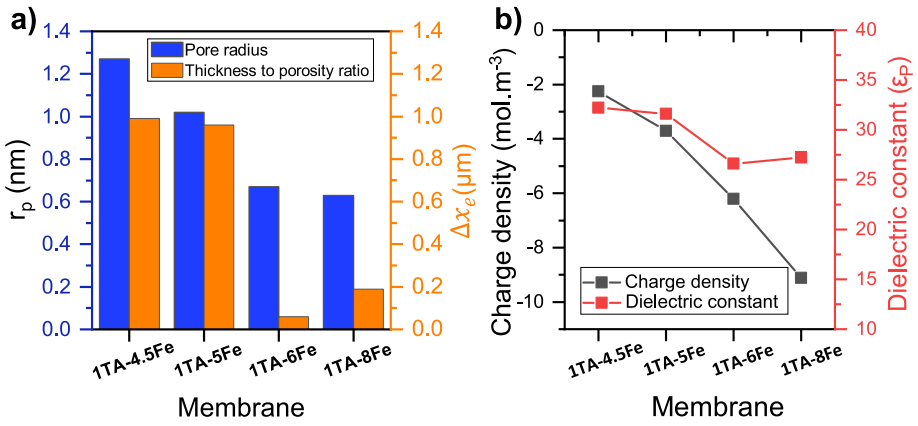

Fig. 6. Estimated membrane parameters. a) pore size (r_p) and membrane thickness to porosity ratio (Δx_e), and b) membrane charge density and pore dielectric constant.

only on the membrane material characteristics, but also on the solution composition. The type of salt and ionic strength (concentration) of the feed solution affect the charge of a membrane in contact with a solution [57,72,73]. The TA-Fe^{3+} membranes are obviously negatively charged at the testing condition.

3.6.2. *Model results and discussion*

We evaluated the DSPM-DE model's ability to predict experimental ion rejection results for the ternary ion solution. Fig. 7 shows the experimental and modeled rejection data of the ions. The rejection of ions gradually increased with the permeate flux for all membranes. The change in the flux of ions to the permeate side was minimal although the water flux increased when applied pressure was increased.

The divalent anion showed higher rejection than the monovalent anion, attributed to the overall partitioning mechanisms. Sulfate, compared to nitrate, is highly excluded by Donnan and dielectric effects due to its higher charge, and sterically due to its higher hydrodynamic radius.

Negative rejection of nitrate was observed at low permeate flux for several membranes, indicating higher nitrate concentration in the permeate relative to the feed. Due to the electrostatic interaction with the membrane, the high flux of Na^+ leads to the accelerated transport of the more mobile anion to satisfy electroneutrality on the permeate side. Therefore, the monovalent and highly diffusive nitrate easily permeates

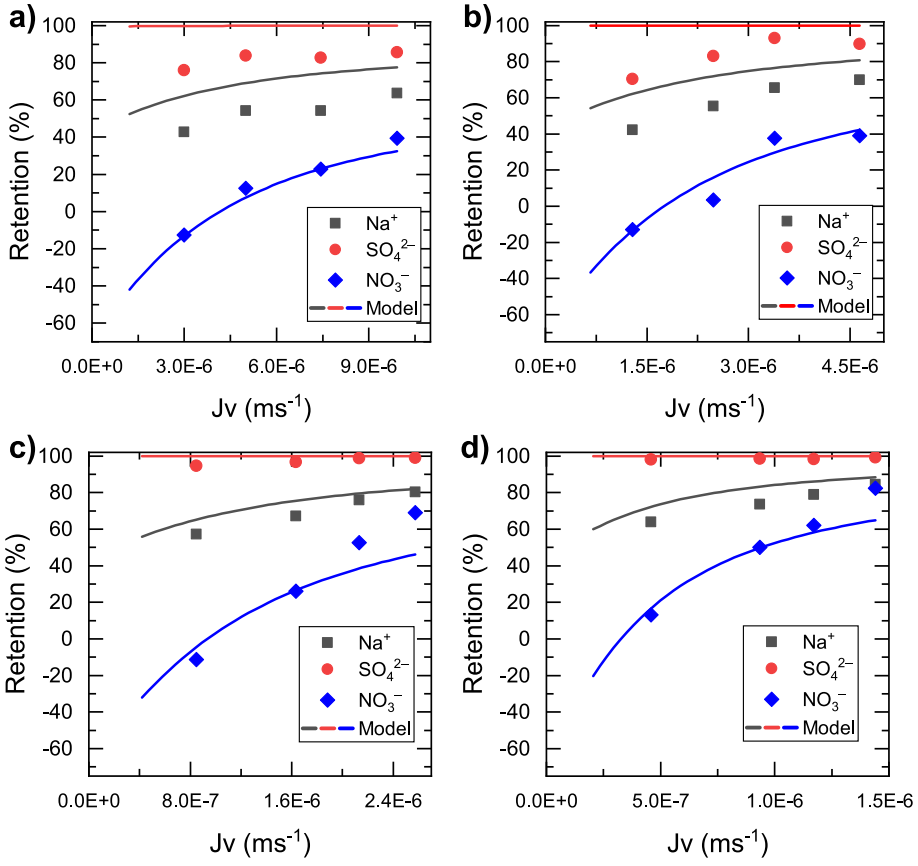

Fig. 7. Experimental and model rejections of 10 mM feed concentration of $NaNO_3$-Na_2SO_4 mixture of equimolar anions by different membranes a) 1TA-4.5Fe, b) 1TA-5Fe, c) 1TA-6Fe, and d) 1TA-8Fe.

which results in its higher concentration on the permeate side than the feed side. This phenomenon has been reported in the literature for ternary mixture of ions [41,68,74]. In a multi-ionic solution, the filtration of multiple co-ions results in the negative rejection of the less-charged co-ion at relatively low Péclet numbers [75], which is a function of the volume flux. This phenomenon occurs due to the greater relative contribution of diffusion to the overall filtration potential at low flux, which decreases as the Péclet number increases. The negative rejections for NO_3^- at low water fluxes are also observed by the DSPM-DE model.

There is especially a good agreement between the experimentally measured rejection data and the modeling results for membranes of small pore size (1TA-6Fe and 1TA-8Fe membranes). For the 1TA-4.5Fe and 1TA-5Fe membranes, the ion rejection could be better predicted at high permeate fluxes and deviates considerably at lower permeate fluxes. The deviation was higher for sulfate and better for nitrate for these membranes. The model predicts a high rejection for SO_4^{2-} although this was not achieved experimentally with the membranes of 1TA-4.5Fe and 1TA-5Fe. The obtained results indicate that the DSPM-DE model demonstrates strong potential for elucidating the nitrate removal

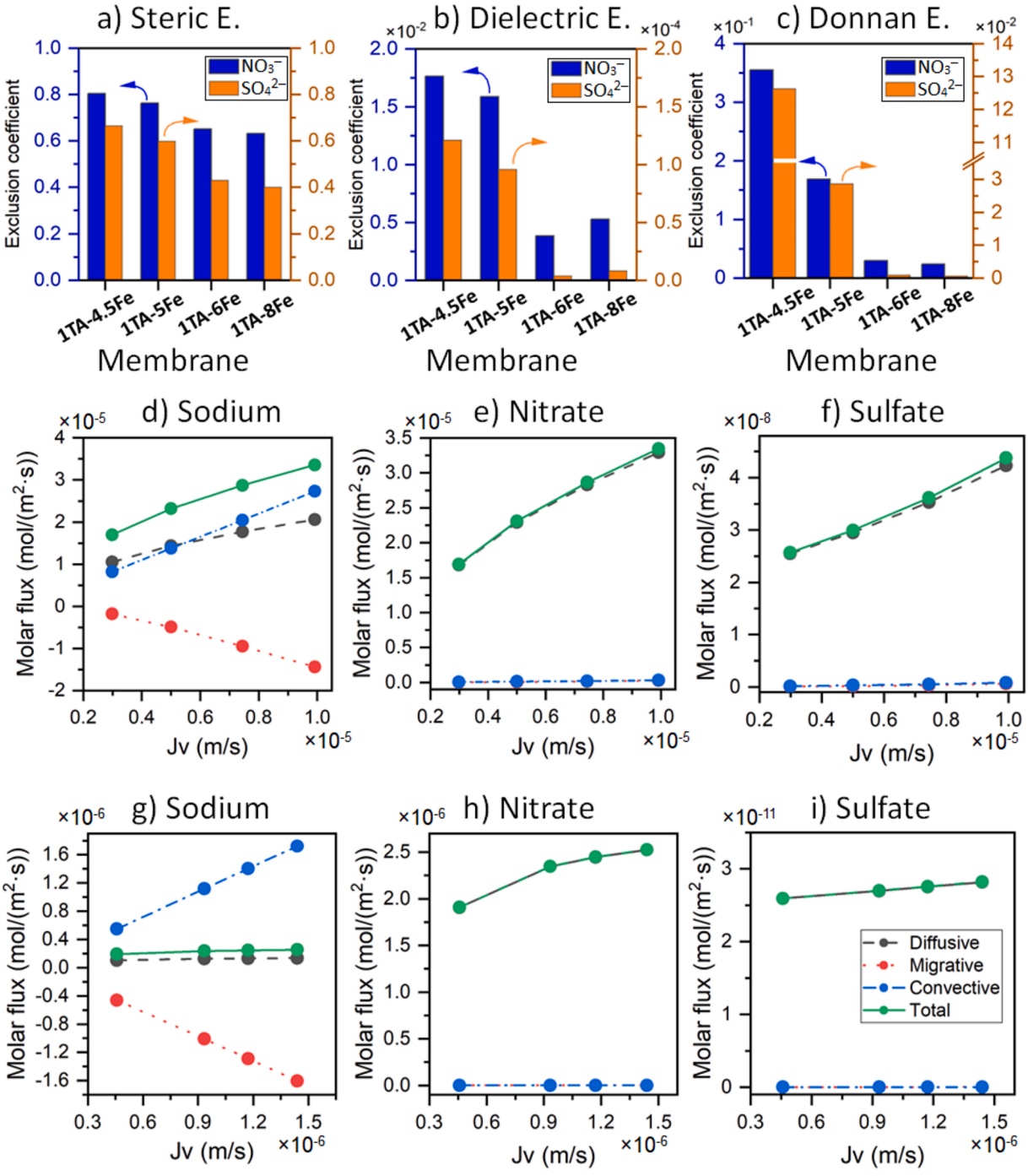

Fig. 8. Comparison of the exclusion coefficients of nitrate and sulfate ions by the MPN membranes (a-c), and ions fluxes across the membrane for 1TA-4.5Fe (d-e) and 1TA-8Fe (g-i). Legends in subplot (*i*) apply to all ion flux plots in this figure. The permeate flux (J_V) was varied by controlling the transmembrane pressure between 1 – 4 bar. Ion fluxes were computed and compared just inside the membrane from solute concentrations of $C_{i,3}$ and $C_{i,2}$ of Scheme 2b for a membrane with $C_{i,n}$ concentration regions across the film thickness, where n = 100 is the number of equally spaced nodes along the membrane thickness and *i* represents the ion.

capabilities of thin-film composite membranes with a TA-Fe^{3+} selective layer when the average pore size is below 0.7 nm. However, for pore sizes exceeding 1 nm, the DSPM-DE model proves unreliable for simulating the separation process of the TA-Fe^{3+} selective layer. In such cases, the model tends to overestimate the retention of bivalent anions and shows significant deviation from experimentally observed results. This discrepancy may be attributed to the broad pore size distribution within the selective layer. The DSPM-DE model predicts ion retention based on r_p, the average pore size estimated based the uniform pore size assumption of the model. However, membranes with an average pore size exceeding 1 nm may contain pores significantly larger than this average. These larger pores offer substantially lower resistance to the permeation of divalent anions than predicted by the DSPM-DE model. The model accurately predicts the rejection of monovalent nitrate ions even for the membranes having $r_p > 1$ nm. However, due to the electroneutrality condition, the overestimation of divalent anion retention also leads to a slight overestimation of cation rejection for the membranes having $r_p > 1$ nm.

3.6.3. Mechanism of ion exclusion

The increased rejection of ions with higher Fe^{3+} concentrations is attributed to a reduction in the values of the three exclusion coefficients at the membrane surface (Fig. 8). It is worth mentioning, as the exclusion coefficients approach zero, their contribution to ion exclusion at the interface between the feed solution and the membrane surface becomes more significant [71]. Among the three exclusion mechanisms, the steric partitioning coefficient was the highest for both nitrate and sulfate, signifying its limited role in ion exclusion at the interface. Comparatively, the computed steric factor for sulfate was lower than that for nitrate (Fig. 8a) due to the larger Stokes radius of sulfate. From Fig. 8 it is evident that dielectric exclusion is the main rejection mechanism of the membranes while Donnan exclusion also plays a significant role. The Donnan exclusion coefficient (Φ_D) of sulfate was in the range of 5.7E-4 to 1.26E-1 while that of nitrate was in the range 2.4E-2 to 3.6E-1 for all membranes. Such low Donnan partitioning factor is due to the high screening of the anions by the negatively charged membrane surface. The Donnan effect was especially pronounced for sulfate in the 1TA-6Fe and 1TA-8Fe membranes leading to enhanced ion exclusion. Conversely, the Donnan exclusion coefficients for sodium were higher than unity (Fig. S5b in the Supporting Information) due to the preferable partitioning of cations into the pores of the negatively charged membrane. The Φ_D of Na^+ increased from 2.8 to 41.9 with the increase of Fe^{3+} concentration during membrane fabrication. This is attributed to the increase in the negative membrane charge density as shown in Fig. 6b. The selectivity of polymeric membranes, which contain ionizable charged groups (such as $-O^-$, $-COO^-$, $-SO_3^-$, $-NH_4^+$), is primarily determined by the electrostatic interactions between the ions in solution and the membrane surface [58]. These interactions typically repel co-ions, excluding them at the membrane pore entrance through Donnan exclusion. The surface potential plays a critical role in shaping the ion concentration profile within the electric double layer, which influences both ion partitioning and subsequent intrapore diffusion [58]. The dielectric partitioning coefficient was the lowest of the three exclusion mechanism for the analyzed anions. The Φ_B of sulfate was 4.0E-6 to 1.2E-4 while that of nitrate was in the range 3.8E-3 to 1.8E-2 for all membranes. The exclusion factor decreased when the Fe^{3+} concentration of the casting solution was increased owing to the observed decrease in pore size of the fabricated membranes. Dielectric exclusion is more effective in smaller pores. The 1TA-4.5Fe and 1TA-5Fe membranes exhibited larger the dielectric exclusion coefficient, Φ_B, compared to those of 1TA-6Fe and 1TA-8Fe membranes. Both Donnan and dielectric effects significantly influence nitrate/sulfate selectivity. Charge-based exclusion plays a crucial role, particularly for the divalent anion SO_4^{2-} which experiences stronger electrostatic interaction due to its higher charge density. This leads to superior retention of SO_4^{2-} compared to NO_3^-, as previously discussed. Membranes that acquire a negative charge in solution are reported to be effective for the separation of divalent and monovalent anions [76]. However, dielectric exclusion was indeed more dominant for the nitrate/sulfate selectivity. The dielectric exclusion effect exhibits a difference of 2 – 3 order of magnitude between SO_4^{2-} and NO_3^-, compared to 1 – 2 orders of magnitude difference in the Donnan partitioning coefficients for these anions across all tested membranes. This disparity arises primarily from the difference in both negative charge (z_i) and ionic radius ($r_{s,i}$) of the ions. According to the Born theory the monovalent NO_3^- encounters a lower solvation energy barrier when partitioning into the confined pore dimensions of the membranes. As a result, nitrate exhibits relatively higher permeance through the TA-Fe^{3+} selective layer.

According to the transport theory of DSPM-DE, ions permeate through the nanopores of the selective layer after partitioning based on the synergistic effects of the above discussed exclusion mechanisms. Isolating and controlling a single factor to enhance ion-ion selectivity is difficult [58]. Nevertheless, membrane material selection and structural tuning (e.g., pore size and surface charge) are viable strategies to develop high-performance membranes with improved ion selectivity. The dielectric effect, attributed to a reduction in the dielectric constant within the confined pores, is primarily associated with the differences in ion solvation energy compared to the bulk solution. Therefore, decreasing the membrane pore size enhances the dielectric effect. When dielectric exclusion plays a dominant role for solute separation, narrowing the pore size or the permeation path of the NF membrane was shown to be effective [77]. Donnan interaction also plays a significant role to determine the selectivity. Therefore, the pore size and surface charge density need to be controlled simultaneously through precise control of fabrication parameters, such as, the concentration of the TA monomer. It is essential to note that the change in pore size impacts not only the steric but also the dielectric effect, especially for multivalent ions.

Fig. 8d-i illustrates the contribution of the transport mechanisms to the overall flux of ions across two membranes: the porous 1TA-4.5Fe and the dense 1TA-8Fe membranes. Similar data on the flux behavior of 1TA-5Fe and 1TA-6Fe membranes can be found in Fig. S6 of the Supporting Information. From Fig. 8d-i, it is evident that the individual fluxes of ions increased with the permeate flux of the salt solution. The increase in water flux had a stronger influence on the total transmembrane flux of ions in the membrane with bigger pore size (1TA-4.5Fe) than the 1TA-8Fe membrane. Specifically, when the applied pressure was increased from 1 to 4 bar, the total ion flux across the 1TA-4.5Fe membrane nearly doubled (Fig. 8d–f). This behavior can be attributed to the increase in driving forces for convection and electromigration (due to an electrical potential gradient) with higher applied pressure [60]. The analysis of Fig. 8e, 8f, 8h, and 8i demonstrates that the total molar flux of anions (NO_3^- and SO_4^{2-}) through both 1TA-4.5Fe and 1TA-8Fe membranes is predominantly influenced by changes in diffusive flux. As shown in Fig. 7, both ion retention and flux increase with higher applied pressure, indicating that the concentration gradient of ions between the feed and permeate sides of the membranes also increases. This elevated concentration gradient enhances the driving force for ion diffusion across the membranes at higher applied pressures.

Evidently, the contribution of the transport mechanisms to the overall solute transport of the cation (counter-ion) is different from that of the co-ions. For example, while all three transport mechanisms for the anions were oriented towards the permeate side, the electromigrative flux for Na^+ was oriented towards the feed side (Fig. 8d and 8g). The convective flux of Na^+ inside the pores was counterbalanced by the opposing electromigrative flux. Notably, diffusion dominated the transport of both NO_3^- and SO_4^{2-}, while their convective transport was negligible even at the highest tested water flux. This phenomenon is often observed for strongly charged membranes [78]. Diffusion predominates the transport of co-ions while convection dominates the transport of counter-ions towards the permeate side [59]. Among the

anions, the molar flux of NO_3^- was higher than SO_4^{2-}. This is associated to the higher diffusion coefficient (mobility) of NO_3^- as well as the higher concentration of NO_3^- inside the active layer. Although the overall ion flux increased with higher water flux, the percentage contribution of diffusive flux for NO_3^- slightly decreased (Fig. 9). This behavior arises because the diffusive flux of NO_3^- is proportional to the concentration gradient, which tends to reach a limiting value at high transmembrane flux [60]. However, the contributions of both convection and electromigration increased slightly with permeate flux. These trends were particularly pronounced in porous membranes (1TA-4.5Fe and 1TA-5Fe) compared to denser membranes fabricated at higher Fe^{3+} concentrations.

The flux of both NO_3^- and SO_4^{2-} via convection was higher than that via electromigration for the 1TA-4.5Fe membrane, but the reverse trend occurred as the Fe^{3+} concentration of the casting solution increased. This shift reflects the reduced advective transport through denser membrane. In addition, the electromigrative flux of an ion is dependent on the electrical potential gradient as well as the concentration of that ion inside the pores [79]. As the Fe^{3+} concentration increases, the negative membrane surface charge density is improved (as presented in Fig. 6b). This increase in surface charge leads to a stronger driving force for electromigration in response to the developed potential differences across the active layer which enhances the transport of ions via electromigration.

In summary, the transport of nitrate across the membrane was predominantly governed by the diffusive flux. Moreover, nitrate separation from its mixture with sulfate was influenced primarily by the dielectric exclusion. The analysis of exclusion mechanisms and fluxes by the DSPM-DE model highlighted the key factors influencing ion rejections and selectivity by the TA-Fe^{3+} membranes. Ion-membrane interactions play a critical role in solute selectivity by enabling differential diffusion of ions, in the process of transmembrane ionic transport [58]. Selectivity for nitrate removal can be improved by tailoring membrane properties like pore size and surface charge density.

To address which membrane property most significantly affects anion selectivity, a sensitivity analysis was performed by varying the membrane parameters such as charge density (−10 %, +12.5 % and +25 %). The 1TA-6Fe membrane was used for this study as the model showed a good fit of its retention performance. The influence of membrane charge density on the model predicted retention of ions is displayed in Fig. 10a. The shaded regions indicate that increasing negative surface charge density strongly improves NO_3^- retention, while SO_4^{2-} remains highly retained at all analyzed C_X. The increase of nitrate retention with negative charge density is primarily driven by the Donnan effect. A detailed analysis of charge density variations (from −2 to −20 mol/m^3) is shown in Fig. S7 of the Supporting Information. At low C_X of −2 mol/m^3, the nitrate retention was negative for all permeate volume flux, showing a high NO_3^-/SO_4^{2-} selectivity. Negative rejection in a weakly charged membrane can occur due to several mechanisms including a difference in the mobility of co-ions, the presence of non-permeating ions, and a difference in the charges of co-ion and counterion [80]. The rejection of an ion could be negative only in the presence of competing ions. In this case, as sulfate is almost completely retained, the permeation of the counter-ion (Na^+) accelerates the transport of the more mobile and monovalent NO_3^- towards the permeate side for electroneutrality. As charge density increases, electrostatic exclusion enhances nitrate retention, reducing NO_3^-/SO_4^{2-} selectivity.

The sensitivity of ion retention to the pore dielectric constant is depicted in Fig. 10b. A decrease in the dielectric constant within the pores increases ion retention by raising the solvation energy barrier. This effect is particularly significant for NO_3^- and Na^+. Increasing the dielectric constant to from 26.6 to 33 (i.e. 25 % increase) reduced nitrate retention from 14 % to −60 % at a permeate flux of 1.5E-6 m/s. The sensitivity analysis was also performed for membrane pore size and effective thickness (Fig. 10c-d). The direction of pore size shows a similar trend as in pore dielectric constant, displaying the coupled

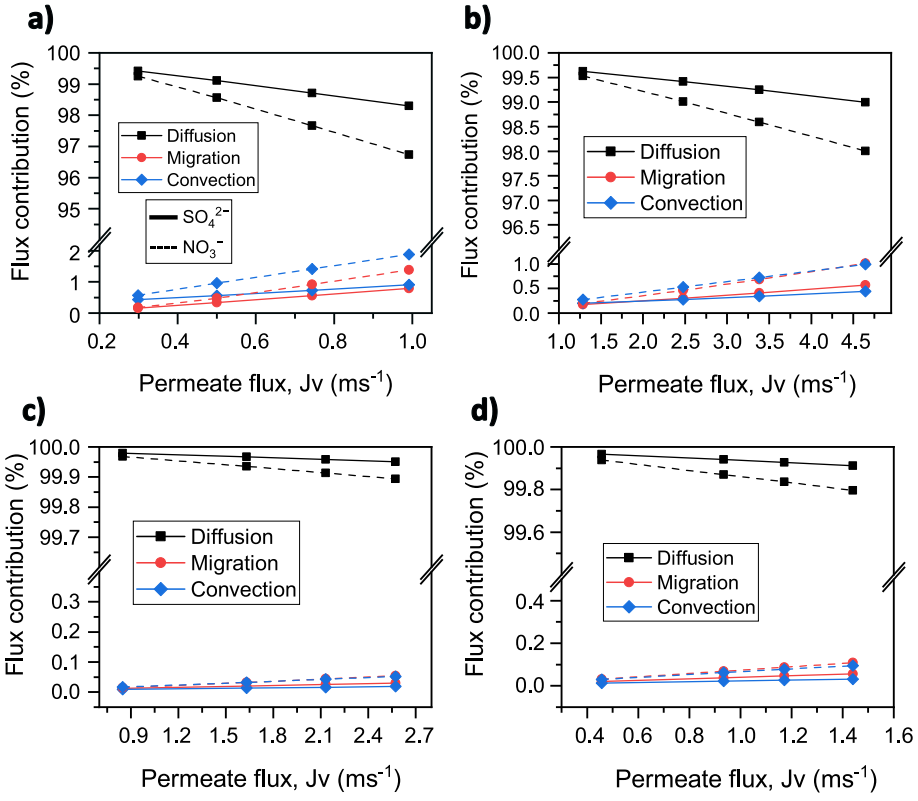

Fig. 9. Flux contributions for anions transport in $NaNO_3$-Na_2SO_4 mixed salt retention test at different permeate fluxes. a) 1TA-4.5Fe, b) 1TA-5Fe, c) 1TA-6Fe, and d) 1TA-8Fe membranes. Legend in subfigure (a) represents all; solid line is for sulfate while dash is for nitrate.

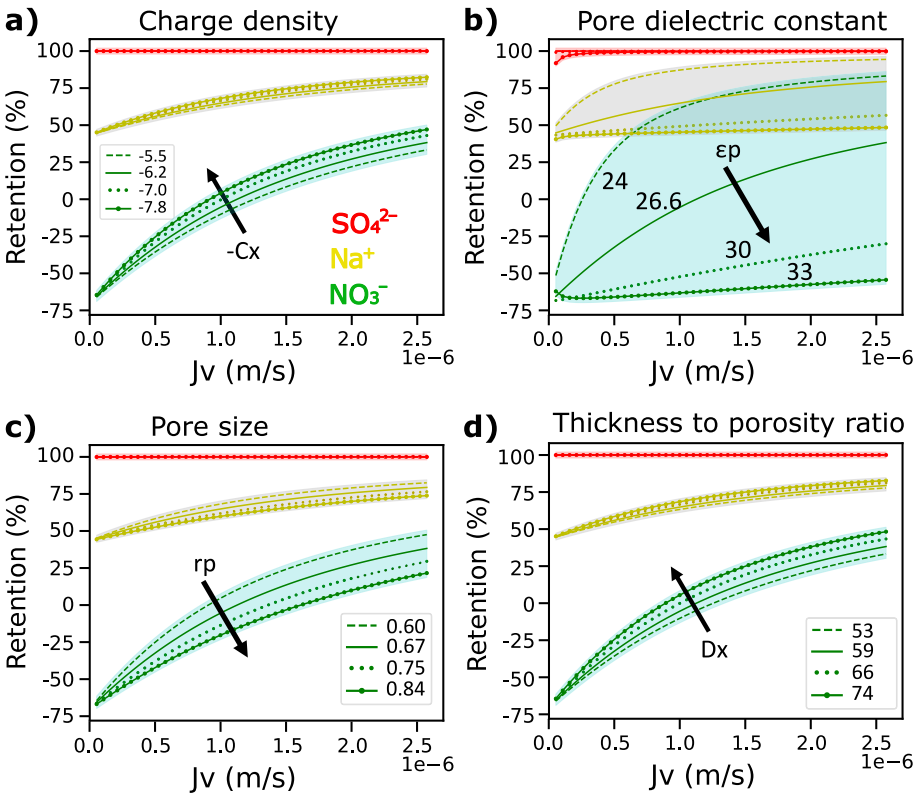

Fig. 10. Influence of membrane characteristics on the retention of ions from a $Na^+/NO_3^-/SO_4^{2-}$ ternary ion mixture for 1TA-6Fe membrane. The plots represent the model prediction for retention of nitrate (green), sodium (orange) and sulfate (red) as a function of permeate flux. The sensitivity towards the of retention for each ion is represented in the shaded areas for a −10 % up to +25 % change in the optimized membrane parameters. Optimized membrane parameters of 0.67 nm, 59 nm, −6.2 mol/m^3, and 26.6 were used as reference for pore size, thickness to porosity ratio, membrane charge density and pore dielectric constant, respectively. (For interpretation of the references to colour in this figure legend, the reader is referred to the web version of this article.)

nature of these two parameters. Larger pores led to reduced ion retention due to weaker steric exclusion, while thicker, less porous layers enhanced retention. The dielectric constant has the most significant impact on nitrate retention, followed by pore size, charge density and thickness. Excellent separation was achieved with thin, porous membranes exhibiting low negative charge density, leading to even negative nitrate retention. These findings demonstrate that the membrane physicochemical properties dictate the separation performance and can be identified using the DSPM-DE model. To enhance selective ion separation, strategies for manipulating the dielectric constant within membrane pores can be explored. For example, controlled adjustments to pore size achieved by varying factors such as concentration, assembly time, pH, solvent, or other synthesis parameters can effectively regulate ion partitioning and transport in nanofiltration membranes. However, it is important to note that variations of synthesis parameters during fabrication to control one parameter (e.g., pore size) may also influence others (e.g., charge density).

4. Conclusion

This study demonstrates that MPN TFC membranes exhibit excellent nitrate rejection properties. The selective layers of these TFC membranes were synthesized using a facile and eco-friendly technique without the use of organic solvents. FTIR, EDX, AFM and SEM characterization of the membrane surfaces show a successful deposition of TA-Fe^{3+} layer. Nitrate removal experiments revealed that the fabricated membranes display a high NO_3^- retention rates, ranging from 82.9 – 93.8 % for 100 mg/L $NaNO_3$ feed solution. The operating conditions substantially influenced the nitrate removal efficiency of the MPN membranes. An increase in feed solution concentration reduced the retention of NO_3^-. For instance, the TA-Fe^{3+} membranes exhibited nitrate rejection between 48.3 and 91.1 % when the feed solution concentration was 850 mg/L. A substantial enhancement in the nitrate removal efficiency was observed with increasing transmembrane pressure. During mixed salt retention test, the TA-Fe^{3+} membranes exhibit a NO_3^-/SO_4^{2-} selectivity ranging from 4.5 to 38.1, highlighting their effective separation capabilities for mixtures containing monovalent and divalent anions. To understand the key mechanisms governing nitrate retention, ion selectivity and ion transport, a transport model was utilized. The study investigated the applicability of the DSPM-DE model to predict rejection performance for $NaNO_3$-Na_2SO_4 mixed solution filtration. The physicochemical characteristics of the membranes were estimated by solving the model equations. During ion rejection simulations, a good agreement between the experimental and the predicted ionic rejections was observed for membranes having average pore radius below 1 nm. The model has been shown to be a valuable tool for understanding the mechanisms of ion partitioning, and transmembrane solute flux. Analysis of the exclusion mechanisms has shown that the dielectric effect was the primary exclusion mechanism for the partitioning of the ions at the membrane-solution interface. Nitrate transport across the membrane was mainly governed by diffusive flux. The contribution of diffusion to the overall transport was found to slightly decline at higher water flux. Sensitivity analysis further indicated that the dielectric constant strongly impacts nitrate retention and the corresponding NO_3^-/SO_4^{2-} separation. To the best of our knowledge this is the first study to elucidate the underlying mechanism governing selective ion transport of a TFC membrane having TA-Fe^{3+} selective layer via mass transport modelling. Through a combination of experimental demonstrations and mass transport modeling, this study showcased the potential of TFC membranes with a TA-Fe^{3+} selective layer as a highly efficient solution for nitrate removal. The findings underscore the potential utilization of these TFC membranes in water treatment applications. Moreover, it provides valuable insights

into the underlying separation mechanisms of the MPN based membranes. These insights pave the way for further advancements in TFC nanofiltration membranes with MPN-based separation layers for selective removal of ions.

5. Nomenclature

The following nomenclature applies to the equations and terms of the DSPM-DE model in this paper.

A_k	Membrane porosity
C_i	Concentration of species *i*, mol/m^3
C_X	Membrane charge density, mol/m^3
$D_{i,p}$	Diffusion coefficient of species *i* in the pore, m^2/s
$D_{i,\infty}$	Diffusion coefficient of species *i* in the bulk, m^2/s
e_0	Elementary charge, 1.60218×10^{-19}C
F	Faraday constant, 96485.3C/mol
J_i	Solute flux for species *i*, mol/m^2·s
J_V	Permeate flux, m^3/m^2·s
K_B	Boltzmann constant, 1.38065×10^{-23} J/K
$K_{c,i}$	Solute mass transfer coefficient of species *i*, m/s
$K_{i,c}$	Convection hindrance factor of species *i*
$K_{i,d}$	Diffusion hindrance factor of species *i*
N_c	Number of components
r_p	Pore radius, m
r_s	Solute Stokes radius for species *i*, m
R	Universal gas constant, 8.31446 J/mol K
R_{cal}	Calculated rejection from the model
R_{exp}	Experimentally measured rejection
R_i	Rejection ratio of species *i*
T	Temperature, K
Z_i	Valency of species *i*
γ_i	Activity coefficient of species *i*
ΔP	Applied pressure difference, Pa
$\Delta \Pi$	Osmotic pressure difference, Pa
ΔW_i	Born solvation energy barrier, J
Δx	Thickness of membrane active layer, m
ε_b	Dielectric constant of the bulk
ε_p	Dielectric constant of the pore
ε_0	Permittivity of free space
λ_i	Ratio of solute Stokes radius of species *i* to effective pore radius
μ	Solution viscosity, Pa·s
τ	Tortuosity
ξ	Electric potential gradient at the feed/membrane interface, V/m
ρ	Solution density, kg/m^3
Φ_S	Steric partitioning coefficient of species
Φ_B	Born solvation coefficient (dielectric partitioning coefficient)
Φ_D	Donnan partitioning coefficient
Ψ	Electric potential, V

The subscript *b* represents for the bulk solution in the feed, *i* for solute species, *m* is membrane or just inside the membrane pore, *p* is permeate side or just outside the pore of the membrane-permeate interface, and *real* is the real rejection considering concentration polarization.

Funding sources

This work was funded by the Hereon-I^{2}B-Project NanoMem.

CRediT authorship contribution statement

Hluf Hailu Kinfu: Writing – review & editing, Writing – original draft, Validation, Software, Methodology, Investigation, Formal analysis, Data curation, Conceptualization. **Md. Mushfequr Rahman:** Writing – review & editing, Writing – original draft, Visualization, Supervision, Resources, Funding acquisition, Formal analysis, Conceptualization. **Nicolás Cevallos-Cueva:** Writing – review & editing, Software, Methodology. **Volker Abetz:** Writing – review & editing, Supervision.

Declaration of competing interest

The authors declare that they have no known competing financial interests or personal relationships that could have appeared to influence the work reported in this paper.

Acknowledgment

The authors acknowledge Maren Brinkmann for the PEG retention analysis in GPC, Juliana Clodt for preparing the polyacrylonitrile support, Martin Held, Erik S. Schneider and Evgeni Sperling for the SEM images, Evgeni Sperling for the AFM analysis, and Jan Pohlmann for setting up the flux and retention measurement facilities.

Appendix A. Supplementary data

Supplementary data to this article can be found online at https://doi.org/10.1016/j.cej.2025.162841.

Data availability

Data will be made available on request.

References

[1] A. Rahman, N.C. Mondal, K.K. Tiwari, Anthropogenic nitrate in groundwater and its health risks in the view of background concentration in a semi arid area of Rajasthan, India, Sci. Rep. 11 (2021) 9279, https://doi.org/10.1038/s41598-021-88600-1.

[2] K. Wick, C. Heumesser, E. Schmid, Groundwater nitrate contamination: Factors and indicators, J. Environ. Manage. 111 (2012) 178–186, https://doi.org/10.1016/j.jenvman.2012.06.030.

[3] M. Reddy, V. Sunitha, Geochemical and health risk assessment of fluoride and nitrate toxicity in semi-arid region of Anantapur District, South India, Environ. Chem. Ecotoxicol. 2 (2020) 150–161, https://doi.org/10.1016/j.enceco.2020.09.002.

[4] M.H. Ward, R.R. Jones, J.D. Brender, T.M. de Kok, P.J. Weyer, B.T. Nolan, C. M. Villanueva, S.G. van Breda, Drinking Water Nitrate and Human Health: An Updated Review, Int. J. Environ. Res. Public Health 15 (2018) 1557, https://doi.org/10.3390/ijerph15071557.

[5] N. Barrabés, J. Sá, Catalytic nitrate removal from water, past, present and future perspectives, Applied Catalysis B-Environmental 104 (2011) 1–5, https://doi.org/10.1016/j.apcatb.2011.03.011.

[6] U. Prüsse, M. Hähnlein, J. Daum, K.D. Vorlop, Improving the catalytic nitrate reduction, Catal. Today 55 (2000) 79–90, https://doi.org/10.1016/S0920-5861(99)00228-X.

[7] E. Abascal, L. Gómez-Coma, I. Ortiz, A. Ortiz, Global diagnosis of nitrate pollution in groundwater and review of removal technologies, Sci. Total Environ. 810 (2022) 152233, https://doi.org/10.1016/j.scitotenv.2021.152233.

[8] G. Sundermann, N. Wägner, A. Cullmann, C.R. von Hirschhausen, C. Kemfert, Nitrate pollution of groundwater long exceeding trigger value: Fertilization practices require more transparency and oversight, DIW Weekly Report 10 (2020) 61–72, https://doi.org/10.18723/diw_dwr:2020-8-1.

[9] DVGW. *Too Many Animals – too Little Land.* https://www.dvgw.de/english-pages/topics/water/nitrates-and-drinking-water, 2023, (Accessed: 15.12.2023).

[10] R. Benkaddour, I. Merimi, T. Szumiata, B. Hammouti, Nitrates in the groundwater of the Triffa plain Eastern Morocco, Materials Today-Proceedings 27 (2020) 3171–3174, https://doi.org/10.1016/j.matpr.2020.04.120.

[11] S. Juergens-Gschwind, Chapter 4 - Ground Water Nitrates in other Developed Countries (Europe) - Relationships to Land use Patterns, in: R.F. Follett (Ed.), Developments in Agricultural and Managed Forest Ecology, Elsevier, 1989, pp. 75–138.

[12] R. Mohammadi, D.L. Ramasamy, M. Sillanpää, Enhancement of nitrate removal and recovery from municipal wastewater through single- and multi-batch electrodialysis: Process optimisation and energy consumption, Desalination 498 (2021) 114726, https://doi.org/10.1016/j.desal.2020.114726.

[13] R. Epsztein, O. Nir, O. Lahav, M. Green, Selective nitrate removal from groundwater using a hybrid nanofiltration-reverse osmosis filtration scheme, Chem. Eng. J. 279 (2015) 372–378, https://doi.org/10.1016/j.cej.2015.05.010.

[14] T.X. Liu, D.D. Chen, X.B. Luo, X.M. Li, F.B. Li, Microbially mediated nitrate-reducing Fe(II) oxidation: Quantification of chemodenitrification and biological reactions, Geochim. Cosmochim. Acta 256 (2019) 97–115, https://doi.org/10.1016/j.gca.2018.06.040.

[15] G.A. Guter, Nitrate removal from contaminated groundwater by anion exchange, in: Ion Exchange Technology (1st ed.), CRC Press, 1995, pp. 61-113.

[16] B. Ahangari, A. Eslami, M. Rafiee, A novel method for selective removal of NO_3^- from drinking water by a surface NO_3^--imprinted polymer grafted on functionalized

silica, Desalination 579 (2024) 117425, https://doi.org/10.1016/j.desal.2024.117425.
[17] L. Malaeb, G.M. Ayoub, Reverse osmosis technology for water treatment: State of the art review, Desalination 267 (2011) 1–8, https://doi.org/10.1016/j.desal.2010.09.001.
[18] J.H. Wu, M.J. Xia, Z.W. Li, L.G. Shen, R.J. Li, M.J. Zhang, Y. Jiao, Y.C. Xu, H.J. Lin, Facile preparation of polyvinylidene fluoride substrate supported thin film composite polyamide nanofiltration: Effect of substrate pore size, J. Membr. Sci. 638 (2021) 119699, https://doi.org/10.1016/j.memsci.2021.119699.
[19] L.P. Zou, S.T. Zhang, J.Y. Liu, Y. Cao, G.R. Qian, Y.Y. Li, Z.P. Xu, Nitrate removal from groundwater using negatively charged nanofiltration membrane, Environ. Sci. Pollut. Res. 26 (2019) 34197–34204, https://doi.org/10.1007/s11356-018-3829-6.
[20] X.T. Zhao, N. Jia, L.J. Cheng, L.F. Liu, C.J. Gao, Metal-polyphenol coordination networks: Towards engineering of antifouling hybrid membranes via in situ assembly, J. Membr. Sci. 563 (2018) 435–446, https://doi.org/10.1016/j.memsci.2018.06.014.
[21] A. Scarano, B. Laddomada, F. Blando, S. De Santis, G. Verna, M. Chieppa, A. Santino, The Chelating Ability of Plant Polyphenols Can Affect Iron Homeostasis and Gut Microbiota, Antioxidants 12 (2023) 630, https://doi.org/10.3390/antiox12030630.
[22] W.J. Xu, S.J. Pan, B.B. Noble, J.Q. Chen, Z.X. Lin, Y.Y. Han, J.J. Zhou, J. J. Richardson, I. Yarovsky, F. Caruso, Site-Selective Coordination Assembly of Dynamic Metal-Phenolic Networks, Angewandte Chemie-International Edition 61 (2022) e202208037, https://doi.org/10.1002/anie.202208037.
[23] C. Wei, C.L. Wang, Y.J. Hao, X. Zhang, J.S. Long, W.Z. Lang, Nature-inspired construction of poly (vinylidene fluoride) membranes through the coordination coating of tannic acid with copper ions for oil-in-water emulsions separation, J. Membr. Sci. 671 (2023) 121367, https://doi.org/10.1016/j.memsci.2023.121367.
[24] H.J. Kim, D.G. Kim, H. Yoon, Y.S. Choi, J. Yoon, J.C. Lee, Polyphenol/FeIII Complex Coated Membranes Having Multifunctional Properties Prepared by a One-Step Fast Assembly, Adv. Mater. Interfaces 2 (2015) 1–8, https://doi.org/10.1002/admi.201500298.
[25] H.H. Kinfu, M.M. Rahman, Separation Performance of Membranes Containing Ultrathin Surface Coating of Metal-Polyphenol Network, Membranes 13 (2023) 481, https://doi.org/10.3390/membranes13050481.
[26] H.L. Xie, L.G. Shen, Y.C. Xu, H.C. Hong, L.N. Yang, R.J. Li, H.J. Lin, Tannic acid (TA)-based coating modified membrane enhanced by successive inkjet printing of Fe^{3+} and sodium periodate (SP) for efficient oil-water separation, J. Membr. Sci. 660 (2022) 120873, https://doi.org/10.1016/j.memsci.2022.120873.
[27] F. You, Y. Xu, X. Yang, Y. Zhang, L. Shao, Bio-inspired Ni2+-polyphenol hydrophilic network to achieve unconventional high-flux nanofiltration membranes for environmental remediation, Chem. Commun. 53 (2017) 6128–6131, https://doi.org/10.1039/c7cc02411h.
[28] Y.X. Zhang, X.F. Duan, B.R. Tan, Y.C. Jiang, Y. Wang, T. Qi, PVDF microfiltration membranes modified with AgNPs/tannic acid for efficient separation of oil and water emulsions, Colloids Surf A Physicochem Eng Asp 644 (2022) 128844, https://doi.org/10.1016/j.colsurfa.2022.128844.
[29] R.N. Zhang, Y.C. Xu, L.G. Shen, R.J. Li, H.J. Lin, Preparation of nickel@polyvinyl alcohol (PVA) conductive membranes to couple a novel electrocoagulation-membrane separation system for efficient oil-water separation, J. Membr. Sci. 653 (2022) 120541, https://doi.org/10.1016/j.memsci.2022.120541.
[30] W. Luo, G. Xiao, F. Tian, J.J. Richardson, Y.P. Wang, J.F. Zhou, J.L. Guo, X.P. Liao, B. Shi, Engineering robust metal-phenolic network membranes for uranium extraction from seawater, Energ. Environ. Sci. 12 (2019) 607–614, https://doi.org/10.1039/c8ee01438h.
[31] X. Zhang, Z.X. Fan, W.T. Xu, Q. Meng, C. Shen, G.L. Zhang, C.J. Gao, Thin film composite nanofiltration membrane with nanocluster structure mediated by graphene oxide/metal-polyphenol nanonetwork scaffold interlayer, J. Membr. Sci. 669 (2023) 121330, https://doi.org/10.1016/j.memsci.2022.121330.
[32] R. Epsztein, E. Shaulsky, N. Dizge, D.M. Warsinger, M. Elimelech, Role of Ionic Charge Density in Donnan Exclusion of Monovalent Anions by Nanofiltration, Environ. Sci. Tech. 52 (2018) 4108–4116, https://doi.org/10.1021/acs.est.7b06400.
[33] R.Y. Wang, S.H. Lin, Pore model for nanofiltration: History, theoretical framework, key predictions, limitations, and prospects, J. Membr. Sci. 620 (2021) 118809, https://doi.org/10.1016/j.memsci.2020.118809.
[34] D.L. Oatley, L. Llenas, R. Pérez, P.M. Williams, X. Martínez-Lladó, M. Rovira, Review of the dielectric properties of nanofiltration membranes and verification of the single oriented layer approximation, Adv. Colloid Interface Sci. 173 (2012) 1–11, https://doi.org/10.1016/j.cis.2012.02.001.
[35] S. Bandini, D. Vezzani, Nanofiltration modeling: The role of dielectric exclusion in membrane characterization, Chem. Eng. Sci. 58 (2003) 3303–3326, https://doi.org/10.1016/S0009-2509(03)00212-4.
[36] V. Geraldes, A.M. Brites Alves, Computer program for simulation of mass transport in nanofiltration membranes, J. Membr. Sci. 321 (2008) 172–182, https://doi.org/10.1016/j.memsci.2008.04.054.
[37] D. Rehman, J.H. Lienhard, Global optimization for accurate and efficient parameter estimation in nanofiltration, Journal of Membrane Science Letters 2 (2022) 100034, https://doi.org/10.1016/j.memlet.2022.100034.
[38] O. Labban, C. Liu, T. Haur, J.H.L. V, O. Labban, Relating transport modeling to nanofiltration membrane fabrication : Navigating the permeability-selectivity trade-off in desalination pretreatment, (2018), 26-38. doi: 10.1016/j.memsci.2018.02.053.
[39] F. Léniz-Pizarro, C. Liu, A. Colburn, I.C. Escobar, D. Bhattacharyya, Positively charged nanofiltration membrane synthesis, transport models, and lanthanides separation, J. Membr. Sci. 620 (2021) 118973, https://doi.org/10.1016/j.memsci.2020.118973.
[40] Y. Roy, M.H. Sharqawy, J.H. Lienhard, Modeling of flat-sheet and spiral-wound nanofiltration configurations and its application in seawater nanofiltration, J. Membr. Sci. 493 (2015) 360–372, https://doi.org/10.1016/j.memsci.2015.06.030.
[41] O. Labban, C. Liu, T.H. Chong, J.H. Lienhard V, Fundamentals of low-pressure nanofiltration: Membrane characterization, modeling, and understanding the multi-ionic interactions in water softening, J. Membr. Sci. 521 (2017) 18–32, https://doi.org/10.1016/j.memsci.2016.08.062.
[42] X.R. Gao, P. Li, Y. Qin, C.L. Bai, Z.Y. Gu, S.L. Yu, Negative rejection phenomenon in the mixed salt nanofiltration: Law and mechanism, Desalination 583 (2024) 117667, https://doi.org/10.1016/j.desal.2024.117667.
[43] W.R. Bowen, A.W. Mohammad, N. Hilal, Characterisation of nanofiltration membranes for predictive purposes - Use of salts, uncharged solutes and atomic force microscopy, J. Membr. Sci. 126 (1997) 91–105, https://doi.org/10.1016/S0376-7388(96)00276-1.
[44] W.R. Bowen, A.W. Mohammad, Diafiltration by nanofiltration: prediction and optimization, AIChE J 44 (1998) 1799–1812, https://doi.org/10.1002/aic.690440811.
[45] D. Liu, Y. Chen, T.T. Tran, G. Zhang, Facile and rapid assembly of high-performance tannic acid thin-film nanofiltration membranes via Fe^{3+} intermediated regulation and coordination, Sep. Purif. Technol. 260 (2021) 118228, https://doi.org/10.1016/j.seppur.2020.118228.
[46] H. Ejima, J.J. Richardson, K. Liang, J.P. Best, M.P. Van Koeverden, G.K. Such, J. Cui, F. Caruso, One-step assembly of coordination complexes, Science 341 (2013) 154–157, https://doi.org/10.1126/science.1237265.
[47] L. Fan, Y. Ma, Y. Su, R. Zhang, Y. Liu, Q. Zhang, Z. Jiang, Green coating by coordination of tannic acid and iron ions for antioxidant nanofiltration membranes, RSC Adv. 5 (2015) 107777–107784, https://doi.org/10.1039/c5ra23490e.
[48] H. Guo, Z. Yao, Z. Yang, X. Ma, J. Wang, C.Y. Tang, A one-step rapid assembly of thin film coating using green coordination complexes for enhanced removal of trace organic contaminants by membranes, Environ. Sci. Tech. 51 (2017) 12638–12643, https://doi.org/10.1021/acs.est.7b03478.
[49] H.H. Kinfu, M.M. Rahman, E.S. Schneider, N. Cevallos-Cueva, V. Abetz, Charge and size selective thin film composite membranes having tannic acid – Ferric ion network as selective layer, J. Membr. Sci. 679 (2023) 121709, https://doi.org/10.1016/j.memsci.2023.121709.
[50] R.J. Zhang, J.Y. Tian, S.S. Gao, B. van der Bruggen, How to coordinate the trade-off between water permeability and salt rejection in nanofiltration? J. Mater. Chem. A 8 (2020) 8831–8847, https://doi.org/10.1039/d0ta02510k.
[51] F. Garcia, D. Ciceron, A. Saboni, S. Alexandrova, Nitrate ions elimination from drinking water by nanofiltration: Membrane choice, Sep. Purif. Technol. 52 (2006) 196–200, https://doi.org/10.1016/j.seppur.2006.03.023.
[52] L. Paugam, S. Taha, G. Dorange, F. Quéméneur, Influence of ionic composition on nitrate retention by nanofiltration, Chem. Eng. Res. Des. 81 (2003) 1199–1205, https://doi.org/10.1205/026387603770866380.
[53] J. Tanninen, M. Mänttäri, M. Nyström, Effect of salt mixture concentration on fractionation with NF membranes, J. Membr. Sci. 283 (2006) 57–64, https://doi.org/10.1016/j.memsci.2006.06.012.
[54] C. Kocaman, E. Bukusoglu, P.Z. Çulfaz-Emecen, Tuning electrostatic interactions for controlled structure and rejection of cellulose nanocrystal membranes, J. Membr. Sci. 661 (2022) 120932, https://doi.org/10.1016/j.memsci.2022.120932.
[55] Z.Z. Zhang, M.M. Rahman, I. Ternes, B. Bajer, V. Abetz, Engineering soft nanochannels in isoporous block copolymer nanofiltration membranes for ion separation, J. Membr. Sci. 691 (2024) 122270, https://doi.org/10.1016/j.memsci.2023.122270.
[56] L. Paugam, S. Taha, G. Dorange, P. Jaouen, F. Quéméneur, Mechanism of nitrate ions transfer in nanofiltration depending on pressure, pH, concentration and medium composition, J. Membr. Sci. 231 (2004) 37–46, https://doi.org/10.1016/j.memsci.2003.11.003.
[57] A. Pérez-González, R. Ibáñez, P. Gómez, A.M. Urtiaga, I. Ortiz, J.A. Irabien, Nanofiltration separation of polyvalent and monovalent anions in desalination brines, J. Membr. Sci. 473 (2015) 16–27, https://doi.org/10.1016/j.memsci.2014.08.045.
[58] D. Lu, Z. Yao, L. Jiao, M. Waheed, Z. Sun, L. Zhang, Separation mechanism, selectivity enhancement strategies and advanced materials for mono-/multivalent ion-selective nanofiltration membrane, Adv. Membr. 2 (2022) 100032, https://doi.org/10.1016/j.advmem.2022.100032.
[59] Y. Roy, D.M. Warsinger, V.J.H. Lienhard, Effect of temperature on ion transport in nanofiltration membranes: Diffusion, convection and electromigration, Desalination 420 (2017) 241–257, https://doi.org/10.1016/j.desal.2017.07.020.
[60] A. Szymczyk, C. Labbez, P. Fievet, A. Vidonne, A. Foissy, J. Pagetti, Contribution of convection, diffusion and migration to electrolyte transport through nanofiltration membranes, Adv. Colloid Interface Sci. 103 (2003) 77–94, https://doi.org/10.1016/S0001-8686(02)00094-5.
[61] M. Ansari, M.A. Al-Obaidi, Z. Hadadian, M. Moradi, A. Haghighi, I.M. Mujtaba, Performance evaluation of a brackish water reverse osmosis pilot-plant desalination process under different operating conditions: Experimental study, Cleaner Eng. Technol. 4 (2021) 100134, https://doi.org/10.1016/j.clet.2021.100134.

[62] A. Popova, R. Rattanakom, Z.Q. Yu, Z.L. Li, K. Nakagawa, T. Fujioka, Evaluating the potential of nanofiltration membranes for removing ammonium, nitrate, and nitrite in drinking water sources, Water Res. 244 (2023), https://doi.org/10.1016/j.watres.2023.120484.
[63] J. Joseph, Y.A. Boussouga, M. Di Vincenzo, M. Barboiu, A.I. Schäfer, Selectivity of artificial water channel-polyamide composite membranes towards inorganic contaminants, J. Membr. Sci. 664 (2022), https://doi.org/10.1016/j.memsci.2022.121019.
[64] R. Epsztein, W. Cheng, E. Shaulsky, N. Dizge, M. Elimelech, Elucidating the mechanisms underlying the difference between chloride and nitrate rejection in nanofiltration, J. Membr. Sci. 548 (2018) 694–701, https://doi.org/10.1016/j.memsci.2017.10.049.
[65] A.G. Volkov, S. Paula, D.W. Deamer, Two mechanisms of permeation of small neutral molecules and hydrated ions across phospholipid bilayers, Bioelectrochem. Bioenerg. 42 (1997) 153–160, https://doi.org/10.1016/S0302-4598(96)05097-0.
[66] D.X. Wang, M. Su, Z.Y. Yu, X.L. Wang, M. Ando, T. Shintani, Separation performance of a nanofiltration membrane influenced by species and concentration of ions, Desalination 175 (2005) 219–225, https://doi.org/10.1016/j.desal.2004.10.009.
[67] A. Santafé-Moros, J.M. Gozálvez-Zafrilla, J. Lora-García, Applicability of the DSPM with dielectric exclusion to a high rejection nanofiltration membrane in the separation of nitrate solutions, Desalination 221 (2008) 268–276, https://doi.org/10.1016/j.desal.2007.01.083.
[68] N. Cevallos-Cueva, M.M. Rahman, H.H. Kinfu, V. Abetz, Mass transport mechanism of nitrate selective nanofiltration membranes on the basis of the Donnan steric pore model with dielectric exclusion (DSPM-DE), Chem. Eng. J. 493 (2024) 152775, https://doi.org/10.1016/j.cej.2024.152775.
[69] Y.T. Liu, H. Liang, L.M. Bai, J.X. Yang, X.W. Zhu, X.S. Luo, G.B. Li, Modeling insights into the role of support layer in the enhanced separation performance and stability of nanofiltration membrane, J. Membr. Sci. 658 (2022) 120681, https://doi.org/10.1016/j.memsci.2022.120681.
[70] W.R. Bowen, J.S. Welfoot, Modelling the performance of membrane nanofiltration-critical assessment and model development, Chem. Eng. Sci. 57 (2002) 1121–1137, https://doi.org/10.1016/S0009-2509(01)00413-4.
[71] M. Micari, D. Diamantidou, B. Heijman, M. Moser, A. Haidari, H. Spanjers, V. Bertsch, Experimental and theoretical characterization of commercial nanofiltration membranes for the treatment of ion exchange spent regenerant, J. Membr. Sci. 606 (2020) 118117, https://doi.org/10.1016/j.memsci.2020.118117.
[72] S. Salgin, U. Salgin, N. Soyer, Streaming Potential Measurements of Polyethersulfone Ultrafiltration Membranes to Determine Salt Effects on Membrane Zeta Potential, Int. J. Electrochem. Sci. 8 (2013) 4073–4084, https://doi.org/10.1016/S1452-3981(23)14454-3.
[73] J. Schaep, C. Vandecasteele, A.W. Mohammad, W.R. Bowen, Analysis of the salt retention of nanofiltration membranes using the Donnan-steric partitioning pore model, Sep. Sci. Technol. 34 (1999) 3009–3030, https://doi.org/10.1081/SS-100100819.
[74] G. Hagmeyer, R. Gimbel, Modelling the salt rejection of nanofiltration membranes for ternary ion mixtures and for single salts at different pH values, Desalination 117 (1998) 247–256, https://doi.org/10.1016/S0011-9164(98)00109-X.
[75] A.E. Yaroshchuk, Negative rejection of ions in pressure-driven membrane processes, Adv. Colloid Interface Sci. 139 (2008) 150–173, https://doi.org/10.1016/j.cis.2008.01.004.
[76] Y. Roy, J.H. Lienhard, A framework to analyze sulfate chloride selectivity in nanofiltration, Environmental Science-Water Research & Technology 5 (2019) 585–598, https://doi.org/10.1039/c8ew00847g.
[77] W.H. Yu, Z.Q. Gan, J.R. Wang, Y. Zhao, J. Han, L.F. Fang, X.Z. Wei, Z.L. Qiu, B. K. Zhu, A novel negatively charged nanofiltration membrane with improved and stable rejection of Cr (VI) and phosphate under different pH conditions, J. Membr. Sci. 639 (2021) 119756, https://doi.org/10.1016/j.memsci.2021.119756.
[78] F.D. Martinez-Jimenez, V.E. Musteata, S. Cespedes-Zuluaga, B. Blankert, C. Picioreanu, Two-dimensional model of ion transport in composite membranes active layers with TEM-scanned morphology, Desalination 565 (2023) 116876, https://doi.org/10.1016/j.desal.2023.116876.
[79] P. Fievet, C. Labbez, A. Szymczyk, A. Vidonne, A. Foissy, J. Pagetti, Electrolyte transport through amphoteric nanofiltration membranes, Chem. Eng. Sci. 57 (2002) 2921–2931, https://doi.org/10.1016/S0009-2509(02)00188-4.
[80] F.Q. Mir, A. Shukla, Negative Rejection of NaCl in Ultrafiltration of Aqueous Solution of NaCl and KCl Using Socialite Octahydrate Zeolite-Clay Charged Ultrafiltration Membrane, Ind. Eng. Chem. Res. 49 (2010) 6539–6546, https://doi.org/10.1021/ie901775v.

Chapter 8. Ion Selective Metal-Phenolic Network Nanofiltration Membranes: The Role of Counterions and Predictive Modeling

This chapter presents an experimental investigation on the rejection of a range of ions by MPN TFC membrane selective layer synthesized through a green and facile technique. Their ion rejection performance from single salt solutions (NaCl, Na_2SO_4, $MgCl_2$, and $MgSO_4$) and mixed salt solutions of several combinations are analyzed. Here, the potential of salt rejection performance of the membranes is assessed to determine their potential for NF processes. By increasing the concentration of Fe^{3+} in the fabrication process, the active layer characteristics were fine-tuned to enhance the salt rejection property up to 92 % NaCl, 81 % $MgCl_2$, 99 % Na_2SO_4 and 96 % MgSO4. Moreover, the membranes exhibit good Cl^-/SO_4^{2-} separation during mixed salt retention tests. The Na^+/Mg^{2+} selectivity was higher in the case of Na_2SO_4-$MgSO_4$ mixture compared to NaCl-$MgCl_2$ mixed salt feed solution, illustrating the effect of a common anion on the retention of ions. The membranes also exhibit good monovalent/divalent ion selectivity from multi-ionic mixtures containing both anions and cations. Besides, the prediction of rejection data using the DSPM-DE was investigated. The model well describes the transport of ions as a function of trans-membrane flux through the TA-Fe^{3+} separation layer. A detailed analysis of the rejection mechanism of ions is provided in terms of the computed exclusion coefficients influencing the partitioning at the membrane-solution interface at the pore entrance. The model determines the dominant mechanisms of ion transport in terms of ions permeation flux. This analysis is also extended from ternary ion mixture to a quaternary mixture.

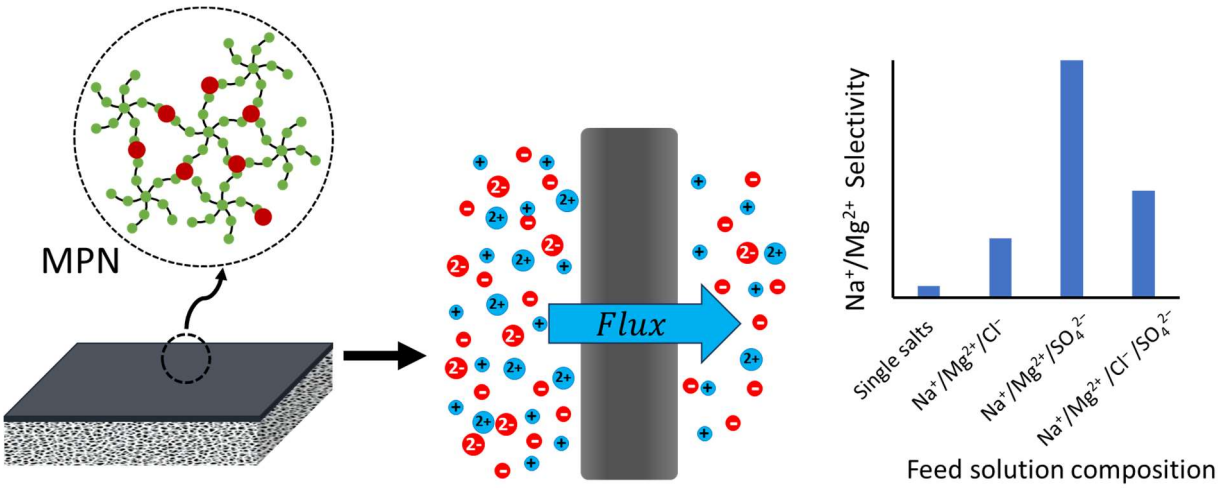

Journal of Membrane Science 733 (2025) 124320

Contents lists available at ScienceDirect

Journal of Membrane Science

journal homepage: www.elsevier.com/locate/memsci

Ion selective metal-phenolic network nanofiltration membranes: The role of counterions and predictive modeling

Hluf Hailu Kinfu [a], Md Mushfequr Rahman [a,*], Nicolás Cevallos-Cueva [a], Volker Abetz [a,b]

[a] Helmholtz-Zentrum Hereon, Institute of Membrane Research, Max-Planck-Straße 1, 21502, Geesthacht, Germany
[b] University of Hamburg, Institute of Physical Chemistry, Martin-Luther-King-Platz 6, 20146, Hamburg, Germany

A B S T R A C T

The development of high flux, selective and sustainable thin-film composite (TFC) membranes for nanofiltration (NF) is critical in addressing water purification challenges. In this work, a thin metal-phenolic network (MPN) selective layer was deposited on a porous support via a facile and scalable process, presenting a sustainable and efficient pathway for developing TFC membranes tailored for NF applications in water treatment and desalination. Here we explored the ion rejection and ion selectivity behavior of MPN membranes for various complex feed solutions. Comprehensive characterization to determine the rejection performance of the MPN selective layer for single and mixed salt solutions, including NaCl, Na_2SO_4, $MgCl_2$, and $MgSO_4$ are investigated. Furthermore, the application of the Donnan Steric Pore Model with Dielectric Exclusion (DSPM-DE) to predict the ion rejection and elucidate the transport and exclusion phenomena by a tannic acid (TA)-Fe^{3+} separation layer is explored. The findings reveal that the TA-Fe^{3+} selective layers exhibit excellent retention performance towards various salts, demonstrating the formation of a dense structure with higher retention when increasing Fe^{3+} concentration of the casting solution. The TFC membranes exhibited up to 99 % Na_2SO_4, 92 % NaCl, 96 % $MgSO_4$ and 81 % $MgCl_2$ retentions during single salt filtration tests, indicating a strong potential for high performance nanofiltration or desalting applications. Detailed analysis of the mixed salt retention properties of the MPN membranes highlights a considerable Cl^-/SO_4^{2-} and Na^+/Mg^{2+} selectivities by the TA-Fe^{3+} membranes. Computational elucidation using the DSPM-DE model indeed predicts the retention performance of $Na^+/Cl^-/Mg^{2+}$ ternary ion as well as $Na^+/Mg^{2+}/Cl^-/SO_4^{2-}$ quaternary ion mixtures, identifying dielectric and Donnan exclusions as key mechanisms for ion partitioning at the membrane-solution interface.

1. Introduction

Over the years, membrane separation processes, particularly nanofiltration (NF), have been extensively employed for the treatment of saline water and wastewaters at both the laboratory and industrial scales [1–3]. The unique attributes of NF membranes stem from their ability to effectively separate small organic and inorganic solutes while maintaining high water flux at low operating pressure. To date, thin film composite (TFC) membranes are the most popular for NF application [3]. These well-established TFC membranes primarily feature a polyamide (PA) separation layer synthesized via interfacial polymerization between a diamine (dissolved in water) and an acyl chloride (dissolved in organic solvent) on top of a porous polymer support. PA TFC membranes are particularly attractive due to their ease of synthesis and high rejection performance. However, these membranes suffer from some drawbacks, including low chlorine resistance during cleaning of the membrane and the use of highly toxic organic solvents, rendering the membrane fabrication process environmentally unsustainable [4,5]. Many of these organic solvents are classified as substances of high concern due to their detrimental environmental and human health impacts [6]. Furthermore, the utilization of organic solvents can prove costly. Therefore, eliminating the dependency on such organic solvents is vital for developing a more sustainable TFC membrane fabrication methods. The need for ecofriendly approaches for TFC membrane fabrication is increasingly recognized. One such promising technology is the deposition of a self-assembled network via metal-polyphenol coordination. Metal-phenolic networks (MPN) have emerged as a promising class of materials for the fabrication of TFC membranes over the past decade.

MPNs are supramolecular structures formed through the coordination interactions between catechol or galloyl ligands in polyphenols and transition metal-ion cross-linkers, constructed exclusively in aqueous solutions. MPN coatings are universal, multifunctional thin-films that offer tunable properties, mechanical stability and biocompatibility [7,8]. Tannic acid (TA), a star-shaped plant polyphenol, is widely studied for MPN fabrication due to its low price, availability and rich polydentate ligand structure [9]. The molecular structure of TA facilitates coordination with metal ions to form thin-films with controllable

* Corresponding author.
E-mail address: mushfequr.rahman@hereon.de (M.M. Rahman).

https://doi.org/10.1016/j.memsci.2025.124320
Received 11 April 2025; Received in revised form 29 May 2025; Accepted 7 June 2025
Available online 9 June 2025

structure. The characteristics of MPN coatings are influenced by several factors, including TA and metal ion concentrations, assembly time, solution pH, and the choice of the crosslinking metal ion [10–13]. Two primary approaches are used for synthesizing the MPN based selective layers of TFC membranes. The one-step coordination self-assembly method (co-deposition) is a rapid process of preparing TA-metal ion coatings. However, it poses challenges in controlling the rapid coordination reaction and achieving precise pore structures. In contrast, the layer-by-layer (LBL) assembly method allows the fabrication of defect-free selective layers [14], minimizing the blockage of membrane pores [10] and offering better control over the thickness and pore size of the selective layer of the TFC membranes. Coordination chemistry thus provides a facile and effective technique of constructing high-performance TFC membranes. These membranes have been studied for several applications such as separation of small organic molecules (e.g. dyes) [15–17], removal of trace organic contaminants [18], heavy metal ion removal [19,20], oil/water emulsions separation [21,22], and forward osmosis [23]. Some studies have also reported the removal of single salts from their aqueous solutions using optimized MPN membranes [18,24,25]. However, despite numerous studies on TA-Fe^{3+} MPN TFC membranes, comprehensive investigations of their ion separation performances in mixed ions systems, and the correlation of their separation mechanism and fabrication parameters through transport models have never been reported. Inspired by this gap, in this study we have fabricated TA-Fe^{3+} membranes using a layer-by-layer (LBL) technique to assess their NF performance in aqueous solutions containing both single and mixed salts. The study is focused on evaluating the salt rejections performance of MPN membranes, analyzing their monovalent/divalent ion separation efficiencies in detail, and describing the NF process through an applicable mathematical model.

The structural and physicochemical properties of membranes are critical in governing solute mass transport and separation performance. However, the characterization of nanofiltration (NF) membranes remains challenging. Due to their small pore dimensions, many techniques commonly applied to ultrafiltration (UF) membranes are not suitable to determine the pore-size of NF membranes [26]. Zeta potential measurements provide valuable insights into the surface charge characteristics which is directly related to the rejection performance of the membranes. However, the surface charge data obtained from zeta potential is highly limited for qualitative use due to the inherent limitations of the measurement technique. Electrokinetic measurements such as streaming potential, are influenced by the ionic strength and composition of solution under analysis [27]. An alternative approach to describe a NF membrane involves conducting solute rejection measurements [26], followed by application of a theoretical model to infer membrane properties. The recent approaches in modeling NF are grounded in theoretical frameworks based on the extended Nernst–Planck equation. A prominent example is the Donnan steric-pore model (DSPM) developed by Bowen and colleagues [28–30]. This model relates the transport of ions through membrane selective layer to membrane properties. DSPM model has undergone several modifications, to account for factors such as hindrance effects for ion transport through the membrane pores [30], concentration polarization [31], and the effect of dielectric exclusion [32]. Currently, the Donnan steric-pore model with dielectric exclusion (DSPM-DE), an extension of the DSPM model, is extensively utilized for the prediction of membrane performances of NF membranes for aqueous solutions containing electrolytes [32]. The DSPM-DE model effectively describes ion partitioning at the solution-membrane interface and ion transport across semi-permeable membranes. This model predicts the rejection and permeate flux of multi-ionic feed solutions as functions of membrane characteristics including pore size, membrane thickness, surface charge density and pore dielectric constant [33].

Therefore, a thorough characterization of the membrane is a prerequisite to describe the mass transport through the membrane using the DSPM-DE model. Developed through a rigorous understanding of the NF process, the DSPM-DE model has predominantly been applied to well-established polyamide (PA) TFC membranes. Yet, this approach requires more comprehensive demonstration, and further research is necessary to extend its validation beyond PA membranes. Some efforts have been made to extend the DSPM-DE model to other types of membranes. For instance, Labban et al. [34] adopted DSPM-DE model for characterizing low-pressure NF membranes from polyelectrolyte layer-by-layer-deposition. Similarly, Junker et al. [35] predicted the salt retention performance of polyelectrolyte multilayer hollow fiber membranes using DSPM-DE model. However, MPN-based membranes have been only recently introduced. There is limited understanding regarding the membrane property and its observed membrane performance correlation. The fundamental mechanisms governing ion transport and partitioning in MPN membranes remain unexplored, and there has been no attempt to model their ion retention behavior. This study aims to address this gap by modeling the filtration process of MPN membranes to elucidate their ion transport and separation efficiencies.

The performance of the MPN membranes for single and mixed salt solutions of NaCl, Na_2SO_4, $MgCl_2$, and $MgSO_4$ were analyzed. The effect of a common anion in Na^+/Mg^{2+} containing ion mixtures on the retention of ions is also explored. The DSPM-DE model was used to describe the transport and rejection of ions as a function of transmembrane flux in membranes containing TA-Fe^{3+} selective layer. This study marks the first mass transport modeling of Na^+/Mg^{2+} separation performance of the MPN membranes. The mass transport modeling enabled successful estimation of ion retention in ternary mixtures and provided insight into the dominant mechanisms of ion exclusion and transport that influence the retention and permeation of ions, respectively.

2. Experimental section

2.1. Materials and chemicals

The PAN ultrafiltration membrane was provided by Helmholtz-Zentrum Hereon. For the selective layer fabrication, tannic acid (TA, 1701.19 g/mol) and Iron (III) chloride hexahydrate ($FeCl_3{\cdot}6H_2O$, 270.33 g/mol) were purchased from Sigma-Aldrich Chemie GmbH (Germany) and Alfa Aesar GmbH & Co., respectively. Poly(ethylene glycol) (PEG) (400 g/mol) was commercially supplied from VWR International GmbH (Germany). Magnesium sulfate ($MgSO_4$, 120.366 g/mol), sodium sulfate (Na_2SO_4, 142.04 g/mol), hexahydrate form of magnesium chloride ($MgCl_2{\cdot}6H_2O$, 203.31 g/mol), and sodium chloride (NaCl, 58.44 g/mol) were obtained from Sigma-Aldrich Chemie GmbH (Germany). All casting and feed solutions were prepared using deionized (DI) water. The Milli-Q ultrapure water purification system was utilized to generate the DI water employed in this investigation. All chemicals were utilized without further purification or modification.

2.2. Synthesis of the TFC membranes

The porous PAN membrane support was first immersed in DI water for 3 h before the coating process. The TFC membranes were fabricated by a sequential layer-by-layer based self-assembly. The steps followed during the fabrication process are schematically provided in Scheme 1. The top layer of the pre-soaked PAN membrane was first immersed in 0.02 w% TA solution for 4 min. The TA molecules are coated over the PAN surface through adsorption. After draining the TA solution from the surface of the PAN membrane, the TA-coated support membrane was immediately rinsed with DI water. Then, the membrane was immersed in a certain concentration of metal ion solution ($FeCl_3$) for the same duration that results in TA-Fe^{3+} self-assembly. Again, the membrane was rinsed with DI water. This process resulted in the fabrication of one layer of TA-Fe^{3+} coating. The process was repeated once to fabricate a double TA-Fe^{3+}-layered MPN selective layer. Deposition of two TA-Fe^{3+}

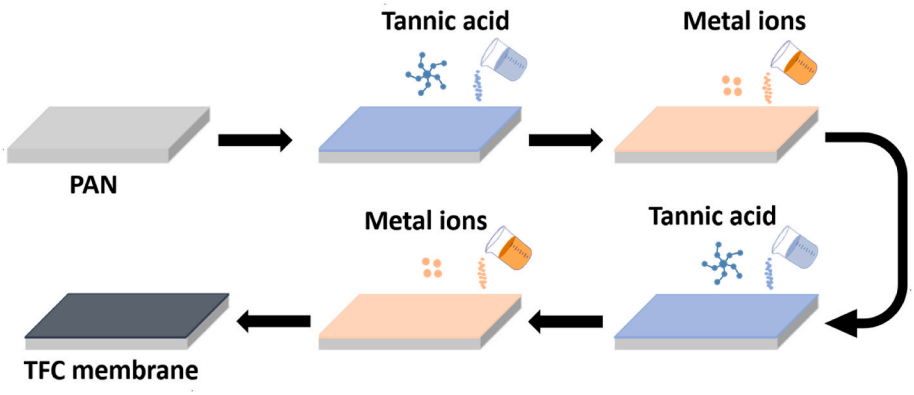

Scheme 1. Schematic of the process for the fabrication of TFC MPN membranes via layer-by-layer led supramolecular self-assembly.

layers and a 4 min assembly time were chosen based on our previous works on the effect of membrane fabrication parameters on optimizing permeance and solute rejection performances [36,37]. A series of membranes referred as 1TA-4.5Fe, 1TA-5Fe, 1TA-6Fe and 1TA-8Fe were synthesized by varying the $FeCl_3$ concentration, corresponding to 0.054, 0.06, 0.072 and 0.096 w%, respectively. Both the TA and iron salt were dissolved in water.

2.3. Ion rejection and selectivity of the MPN membranes

The separation performance of the TFC membranes were investigated with a lab-scale dead-end filtration system using a stirred test cell from Millipore (EMD Millipore XFUF07601). The surface area of the membrane was reduced to 2.13 cm^2 with an inhouse made reduction ring. The pure water flux of the membranes was determined at a transmembrane pressure between 1 and 4 bar using pure water as a feed solution. To evaluate the retention performance of the membranes, compaction of the membrane samples was initially performed at 4 bar for 2 h with DI water. Afterwards, the feed solution was replaced with a single salt or a mixed salt solution. 10 mM concentration of NaCl, $MgCl_2$, Na_2SO_4, and $MgSO_4$ aqueous solutions were used for single salt retention tests. Whereas equimolar mixtures of 10 mM total feed concentration of NaCl–Na_2SO_4, NaCl–$MgCl_2$, Na_2SO_4–$MgSO_4$, or NaCl–Na_2SO_4–$MgCl_2$–$MgSO_4$ were used as mixed salt feed solutions. The feed solutions were stirred with a magnetic stirrer at a stirring speed of 350 rpm. The membrane filtration tests were performed at 3 bar unless otherwise specified. All experiments involved three repetitions, and the average values were documented.

The permeate flux (J_V, $L{\cdot}m^{-2}{\cdot}h^{-1}$) and permeance ($PWP$, $L{\cdot}m^{-2}{\cdot}h^{-1}{\cdot}bar^{-1}$) were determined using equations (1) and (2), respectively.

$$J_V = \frac{V}{A^{*}\Delta t} \tag{1}$$

$$PWP = \frac{J_V}{\Delta P} \tag{2}$$

Where V (L) is the volume of the permeate collected, while Δt (h) and A (m^2) are the duration of filtration and the effective area of the membrane used. ΔP (bar) is the applied transmembrane pressure. The retention rate (R) was evaluated using the following equation.

$$R\ (\%) = \left(1 - \frac{C_p}{(C_f + C_r)/2}\right) {}^{*}100 \tag{3}$$

Where R is solute retention, C_p, C_f and C_r are the concentrations of the permeate, feed and retentate solutions, respectively. Ion chromatography (Dionex ICS600, Thermofischer Scientific Inc., USA) provided with a CS 12A column and a AS 14A column was used to analyze the concentrations of the cations and anion, respectively.

The ion selectivity of the membranes, for eg. the passage of a monovalent ion (A) over a divalent ion (B), was calculated using:

$$S_{A/B} = \frac{\left(C_B/C_A\right)_f}{\left(C_B/C_A\right)_p} = \frac{100 - R_A(\%)}{100 - R_B(\%)} \tag{4}$$

where R_A and R_B are the rejections of ion A and B, respectively, as computed using equation (3), while C_A and C_B are the concentrations of ion A and B, respectively, in the feed (f) solution and permeate (p) streams.

2.4. Mathematical modeling using the DSPM-DE model

2.4.1. Neutral solute retention

In characterizing NF membranes using mathematical models, the quantification of various membrane properties that govern the membrane performance is important. One procedure for the estimation of membrane structural parameters is via retention data obtained from aqueous solutions of uncharged solutes [31,32]. In this work, the pore radius and effective membrane thickness were estimated by performing a neutral solute retention test. PEG 400 g/mol molecular weight was used as a feed solution (1 g/L) and the retention tests were performed in the same procedure as described in section 2.3. The applied transmembrane pressure was varied between 0.5 and 4.5 bar to adjust the permeate fluxes of the PEG solution. The concentration of PEG in the feed, permeate and retentate samples was analyzed using gel permeation chromatography (GPC) (VWR-Hitachi 2130 pump, Hitachi, Darmstadt, Germany). The retention rates were evaluated using equation (3).

As the flux of a neutral solute is governed only by diffusion and convection, and only steric hindrance determines its partitioning at the membrane-solution interface, a well-known analytical solution of flux dependent solute rejection has been obtained [31,38] that involves the contributions of concentration polarization as shown in equation (5). Therefore, the experimentally measured real retention data at different permeate fluxes was fitted using equation (5) to determine the pore radius (r_P) and thickness to porosity ratio of the membranes $\left(\Delta x_{e=}\left(\frac{\Delta x}{A_k}\right)\right)$ simultaneously. The fitting procedure was performed using a dual annealing algorithm in python by minimizing the sum of squared errors (SSE) between experimental and calculated retention results.

$$R_{real} = \left(1 - \frac{C_{i,p}}{C_{i,m}}\right) = 1 - \frac{K_{i,C}\Phi_s}{1 - \exp\left(-\frac{K_{i,C}}{K_{i,d}}\frac{J_v \Delta x}{D_{i,\infty} A_k}\right)\left(1 - K_{i,C}\Phi_s\right)} \tag{5}$$

$$f(r_p, \Delta x_e) = SSE = \sum_{fluxes} (R_{cal} - R_{exp})^2 \quad (6)$$

2.4.2. Charged solute retention

The DSPM-DE model was adopted to describe the separation process of the TFC membranes. DSPM-DE model has been extensively used to elucidate ion retention and transport across the NF membrane active layer. Details about the development of this model can be found elsewhere [39–41]. Solute transport inside the membrane is represented by the extended Nernst-Planck equation (ENP) equation consisting of convection, diffusion and electromigration (Equation (7)). The governing model equations are provided in Table 1. Partitioning equilibrium at both sides of the membrane-solution interface are described using equations (10) and (11). The rejection data for mixed salt feed solutions were fitted using the DSPM-DE model to estimate the charge density (C_X), and pore dielectric constant (ε_p) of the membrane. Rehman and Lienhard [42] showed that the membrane input parameters can be attained using only experimental data of charged species, scrapping the traditional procedure of a step-by-step membrane parameter estimation process. Hence, in this work, these two parameters were obtained simultaneously from a fit of the retention tests of mixed ions at different flux. The function minimization is carried out using dual annealing global minimizer in python with Nelder-Mead local optimizer methods. To solve the system of equations, the algorithm developed by Geraldes et al. [40] was implemented. The SSE between experimental and calculated retention results of the ions was minimized until a tolerance of 1E-6 with the estimated C_X and ε_p was achieved. Two different cases of salt mixtures were studied: 1) the mixture of two cations at the same molar ratio having a common anion NaCl–$MgCl_2$ and 2) multi-ionic mixture containing both divalent and monovalent anions and cations (NaCl–$MgCl_2$–Na_2SO_4–$MgSO_4$). The feed concentration of the mixed salt systems was fixed in a 5 mM:5 mM mixture for case 1, while 2.5 mM of each salt was used for case two. The retention tests were conducted at various permeate fluxes by controlling the transmembrane pressure between 0.5 and 4 bar.

Table 1
Basic equations of the utilized DSPM&DE model.

Mass transport:

$$J_i = -K_{i,d} D_{i,\infty} \frac{dC_i}{dx} + K_{i,c} C_i J_v - z_i C_i K_{i,d} D_{i,\infty} \frac{F}{RT} \frac{d\Psi}{dx} \quad (7)$$

$$J_i = -k^*_{c,i}(C_{i,m} - C_{i,b}) + J_v C_{i,m} - \frac{z_i C_{i,m} D_{i,\infty} F}{RT} \frac{d\Psi}{dx} \quad (8)$$

$$J_i = J_v C_{i,p} \quad (9)$$

boundary condition equilibrium relations:

$$\frac{\gamma_{i,1} C_{i,1}}{\gamma_{i,m} C_{i,m}} = \Phi_s \Phi_B \exp\left(-\frac{z_i F}{RT} \Delta\Psi_{D,m}\right) \quad (10)$$

$$\frac{\gamma_{i,N} C_{i,N}}{\gamma_{i,P} C_{i,P}} = \Phi_s \Phi_B \exp\left(-\frac{z_i F}{RT} \Delta\Psi_{D,P}\right) \quad (11)$$

Partitioning coefficients:

$$\Phi_{s,i} = (1-\lambda_i)^2 \text{where } \lambda_i = \left(\frac{r_s}{r_p}\right) \quad (12)$$

$$\Phi_{B,i} = \exp\left(-\frac{\Delta W_i}{k_B T}\right) \text{where } \Delta W_i = \frac{z_i^2 e_0^2}{8\pi\varepsilon_0 r_s}\left(\frac{1}{\varepsilon_p} - \frac{1}{\varepsilon_b}\right) \quad (13)$$

$$\Phi_{D,i} = \exp\left(-\frac{z_i F}{RT} \Delta\Psi_{D,m}\right) \quad (14)$$

Electroneutrality:

$$\sum_{i=1}^{Nc} z_i C_{i,m} = 0 \quad (15)$$

$$C_X + \sum_{i=1}^{Nc} z_i C_i = 0 \quad (16)$$

$$\sum_{i=1}^{Nc} z_i C_{i,p} = 0 \quad (17)$$

Hindrance factors:

$$K_{i,C} = \frac{(1 + 3.867\lambda_i - 1.907\lambda_i^2 - 0.834\lambda_i^3)}{(1 + 1.867\lambda_i - 0.741\lambda_i^2)} \quad (18)$$

$$K_{i,d} = \begin{cases} \dfrac{\left(1 + \left(\frac{9}{8}\right)\lambda_i \ln\lambda_i - 1.560\lambda_i + 0.528\lambda_i^2 + 1.915\lambda_i^3 - 2.819\lambda_i^4 + 0.270\lambda_i^5 + 1.101\lambda_i^6 - 0.435\lambda_i^7\right)}{(1-\lambda_i)^2}, & \lambda_i \le 0.95 \\ 0.984\left(\dfrac{1-\lambda_i}{\lambda_i}\right)^{5/2}, & \lambda_i > 0.95 \end{cases} \quad (19)$$

* Subscripts such as b, m and p correspond to the bulk feed solution, at the membrane interface and the permeate side, respectively. See Fig. S9 in the supporting information for the coordinates of b, m and p in the membrane process. Subscript i corresponds to each solute i.

3. Results and discussion

3.1. SEM and water flux of the MPN membranes

The membranes exhibit a sponge-like cross-sectional structure (Fig. S1). Surface SEM images of the pristine support and the fabricated TFC membranes are shown in Fig. 1. The PAN substrate displays a uniformly distributed highly porous structure on its top surface, a typical surface morphology of a UF membrane. After the coating of the TA-Fe^{3+} layers, the membrane surfaces become significantly more compact, reducing the pore size and the number of pores (Fig. 1b–e). This was on account of the coordination reaction between TA and metal ions, which forms a complex network that uniformly coats the substrate surface [43]. As the Fe^{3+} concentration in the coating solution increases, a denser membrane surface is fabricated. Feed concentrations influence the stoichiometries of metal-polyphenol self-assembled layers [44]. Increasing Fe^{3+} concentration leads to a lower TA:Fe ratio in the synthesized self-assembled layer, indicating the metal-phenolic network becoming richer in iron. Since the metal ion acts as an inorganic crosslinker [25], Fe^{3+} enriched complexes result in a highly crosslinked dense thin-film. Due to its abundant hydroxyl groups, each TA molecule can coordinate with several Fe^{3+} centers. Therefore, availability of more metal ions in the solution leads to further chelation by TA [45], which leads to the formation of more compact TA-Fe^{3+} structures. Furthermore, Ejima et al., [44] observed a small increase in thickness (a few nanometers) of TA-Fe^{3+} coated capsules when the metal ion concentration was increased. This trend of decreasing pore size is consistent with the observed membrane water flux. The pure water permeance gradually decreases with the increase of the Fe^{3+} concentration.Fig. 2 shows linear increase of the pure water fluxes through the TFC membranes with increasing transmembrane pressure. The pure water permeance (PWP) through the TFC membranes were computed from Fig. 2. For reference, the PAN support exhibited PWP of 286 $L{\cdot}m^{-2}{\cdot}h^{-1}{\cdot}bar^{-1}$. Among the MPN selective layer containing TFC membranes, 1TA-4.5Fe showed the highest permeance of 15 $L{\cdot}m^{-2}{\cdot}h^{-1}{\cdot}bar^{-1}$ which progressively decreased (with increasing Fe^{3+} concentration) to 6.5, 3.2 and 1.9 $L{\cdot}m^{-2}{\cdot}h^{-1}{\cdot}bar^{-1}$ for 1TA-5Fe, 1TA-6Fe and 1TA-8Fe, respectively. These results agree with previous reports of the formation of dense membranes at high metal ion concentration [18,24] when substantially dilute casting solutions are used. These findings indicate that the morphology and the mass transport resistance of the MPN selective layer can be tuned with the concentration of Fe^{3+} in the coating solution. At low Fe^{3+} concentrations, an insufficient number of metal ion centers limits the interfacial coordination reaction, resulting in the formation of a porous skin layer [24]. However, at higher Fe^{3+} concentrations, sufficient binding sites are available for TA chelation, leading to a compact selective layer in the self-assembled TFC membrane [46].

3.2. Single salt retention performance

The retention performance of the MPN TFC membranes was first analyzed through single salt retention experiments (Fig. 3). The TFC membranes demonstrated high rejection rates towards sodium sulfate. The 1TA-4.5Fe membrane exhibited a retention of around 73 % for 10 mM Na_2SO_4 whereas $MgCl_2$ was the least retained salt (12 %) during the filtration tests. As discussed in section 3.1, increasing the Fe^{3+} concentration of casting solution leads to the formation of a denser MPN selective layer, which may lead to a higher steric hindrance. Indeed,

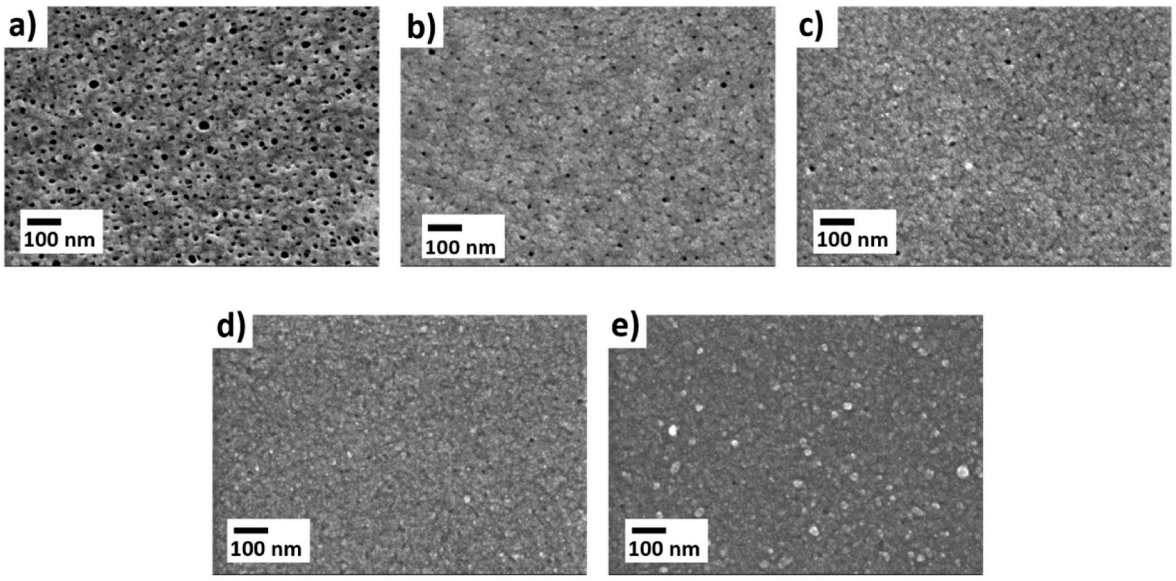

Fig. 1. SEM micrographs of the pristine support and MPN membranes: a) PAN, b) 1TA-4.5Fe, c) 1TA-5Fe, d) 1TA-6Fe, and e) 1TA-8Fe membranes.

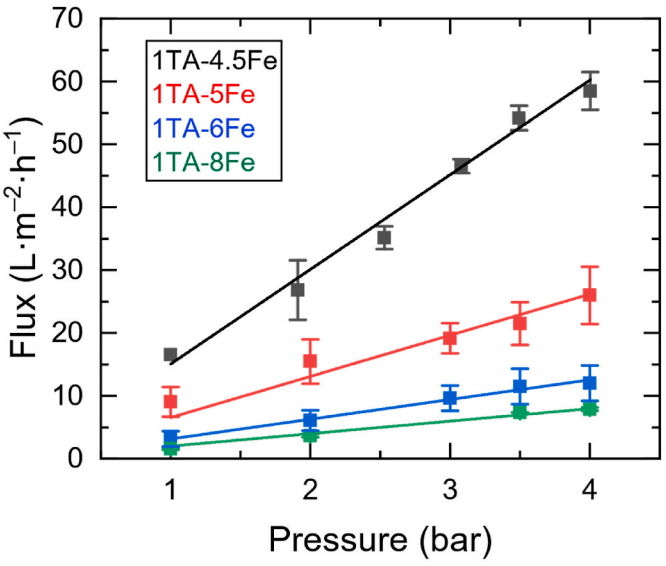

Fig. 2. Pure water flux vs pressure for the fabricated TA-Fe^{3+} membranes.

systematically increasing $FeCl_3$ concentration from 0.054 w% to 0.096 w% improved the salt retention (Fig. 3). The 1TA-8Fe membrane exhibited rejection rates exceeding 80 % for all tested salts, with Na_2SO_4 and $MgCl_2$ retentions reaching 99 % and 81 %, respectively. These results demonstrate the effectiveness of the prepared membranes in separating inorganic salts from aqueous solutions, highlighting the potential of the TFC membranes having TA-Fe^{3+} selective layer for nanofiltration applications.

All membranes displayed a higher retention towards Na_2SO_4 than $MgSO_4$. This is attributed to the negatively charged membrane surface [47]. Despite both salts sharing a common co-ion (SO_4^{2-}), Na_2SO_4, containing monovalent Na^+ as the counter-ion, was rejected more effectively than $MgSO_4$, which contains bivalent Mg^{2+}. This is due to a stronger contribution of Mg^{2+} to electroneutrality at the feed solution-membrane interface [47]. The salt retention sequence for the 1TA-4.5Fe membrane follows the order: Na_2SO_4 > NaCl > $MgSO_4$ > $MgCl_2$, indicating that size sieving plays a minimal role in its separation mechanism. Intriguingly, all magnesium salts retentions are lower than those of sodium salts for the 1TA-4.5Fe membrane. The interaction between counterions and membrane functional groups affect the membrane charge density. The presence of divalent cations such as Mg^{2+} can lower the membrane charge through adsorption or binding mechanism [48,49]. Divalent ions significantly affect the membrane zeta potential, leading to a reduced negative surface charge [50]. We hypothesize that Mg^{2+} from the magnesium containing salts interacts with the polyphenol rich selective layer, thereby decreasing the surface charge density and reducing salt retention. However, for membranes fabricated at higher Fe^{3+} concentration, the retentions of $MgSO_4$ and $MgCl_2$ were improved, indicating an increased contribution of size and dielectric exclusions to the overall rejection mechanism (discussed in detail in section 3.4.2).

We examined the effect of flux change on the salt rejection behavior of the membranes by varying the applied pressure between 0.5 and 4 bar using a Na_2SO_4 aqueous solution (Figure S2, Figure S3 of the supporting information). Fig. S2 shows the rejection of ions improved with an increase in the transmembrane flux, i.e., an increase in the applied pressure. This effect is particularly prominent at low flux zones. Overall, the analysis of the pressure effects highlights its significant influence on the salt retention properties of the TFC membranes having MPN selective layers. Intrinsically, the rejection of a solute relates to the relative transport rates between the solute and water. While the water flux linearly increases with feed pressure (Fig. S3 in the supporting information), the solute flux is only partially influenced by convection and is primarily dependent on the concentration gradient across the membrane. A comparison of the separation performance of the obtained MPN TFC membranes with commercially available NF membranes in the literature shows the membranes demonstrate competitive filtration properties (Fig. S4). Na_2SO_4 and NaCl rejections were similar to those from commercial membranes, while water flux can be further improved.

3.3. Mixed salt retention by the MPN membranes

Fig. 4 presents a comparison of the retention rates of Cl^- and SO_4^{2-} ions from an aqueous solution containing a mixture of NaCl and Na_2SO_4. Although the retention rates of both ions increased with higher ferric ion concentrations in the casting solution, the TFC membranes exhibited monovalent/divalent selectivity. When the $FeCl_3$ concentration was 0.072 w% (1TA-6Fe), sulfate was almost completely retained while chloride ions permeated relatively readily. The extent of selective transport of Cl^- over SO_4^{2-} through the TFC membranes is dictated by

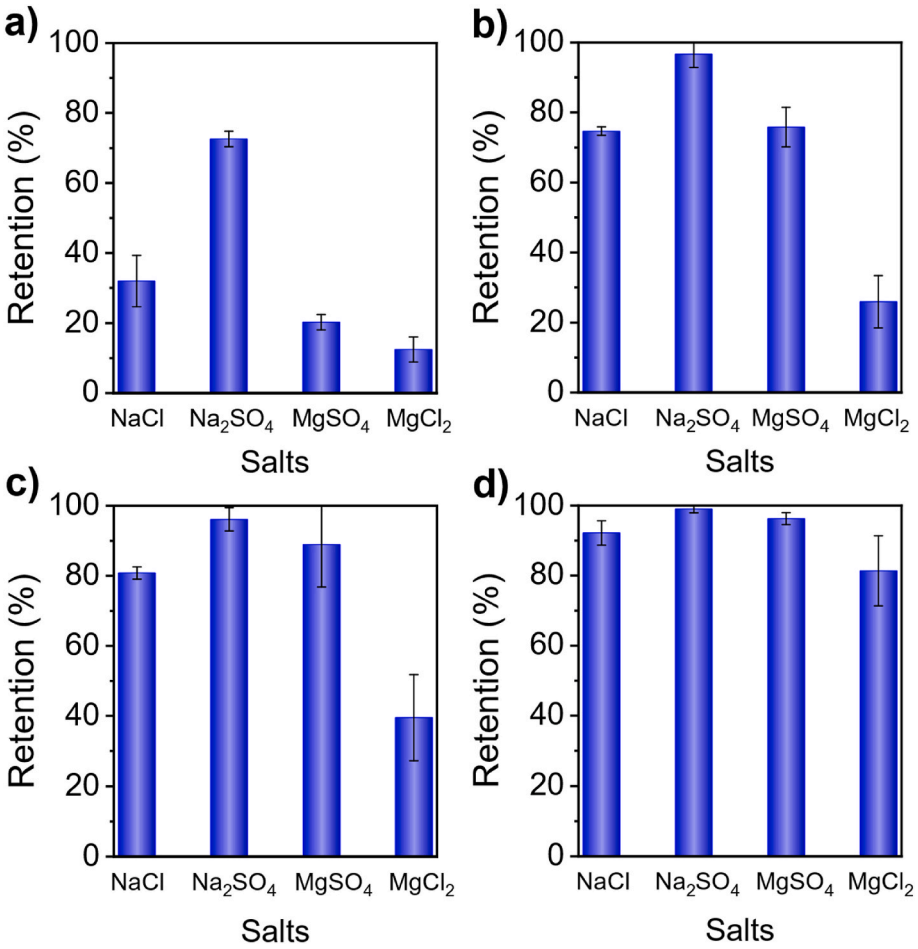

Fig. 3. Single Salts Retention results of a) 1TA-4.5Fe, b) 1TA-5Fe, c) 1TA-6Fe, and d) 1TA-8Fe membranes for 10 mM feed concentration of each salt at 3 bar transmembrane pressure.

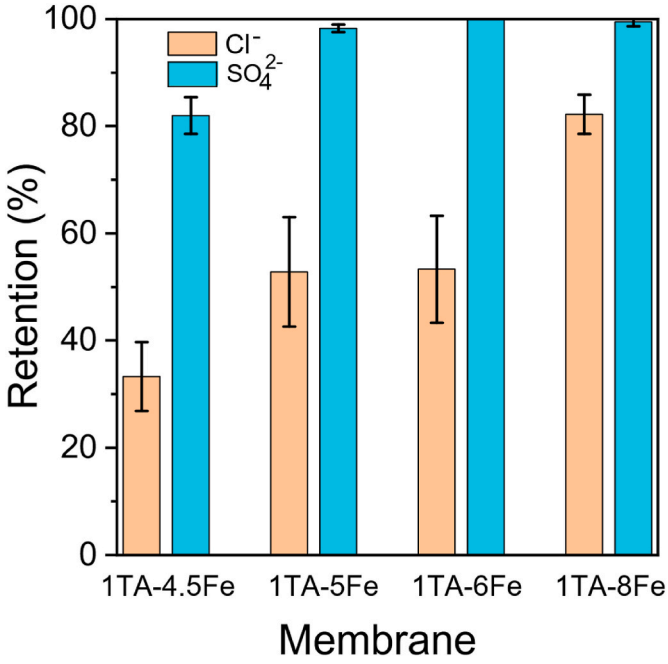

Fig. 4. The anion retentions in NaCl–Na_2SO_4 Mixed in equal molarity 10 mM total feed concentration.

the physicochemical and structural properties of the selective layer, e.g. surface charge and pore size. The Stokes radius, r_s, of SO_4^{2-} (0.231 nm) > Cl^- (0.121 nm) [51]. Being a divalent ion, SO_4^{2-} experiences a stronger electrostatic repulsion by the negatively charged MPN surfaces than monovalent Cl^-. Additionally, the solvation energy barrier for an ion to partition at the membrane-solution interface is higher for multivalent ions, which further increases SO_4^{2-} retention [32]. The selectivity of Cl^-/SO_4^{2-} was 3.7 and 27.2 for the 1TA-4.5Fe and 1TA-5Fe membranes, respectively, reaching 35.4 for the 1TA-8Fe membrane. SO_4^{2-} was completely retained by 1TA-6Fe leading to very high selectivity. The results demonstrate that a monovalent ion-rich permeate can be obtained, while concentrating sulfate on the retentate solution. Compared to the single salt Na_2SO_4 retention test discussed in section 3.2, the retention rate for SO_4^{2-} during the mixed salt NaCl–Na_2SO_4 solution was slightly higher. Conversely, the retention of the monovalent anion (Cl^-) was lower than those in single salt NaCl filtration test.

We have also evaluated the performance of the MPN membranes to separate monovalent (Na^+) and divalent (Mg^{2+}) cations from two different feed solutions containing mixture of i) NaCl–$MgCl_2$ and ii) Na_2SO_4–$MgSO_4$. The retention of the cations was first studied using Cl^- as a common anion in the NaCl–$MgCl_2$ system. Fig. 5a presents the experimental retention values of the cations at 3 bar. As expected, increasing the ferric ion concentration in the casting solution enhanced the MPN membranes' ability to retain a divalent cation. The retention of Mg^{2+} increased from 13 % to 80 % as the ferric salt concentration in the casting solution increased from 0.054 w% (1TA-4.5Fe membrane) to 0.096 w% (1TA-8Fe membrane). Unlike anion selectivity, the Donann

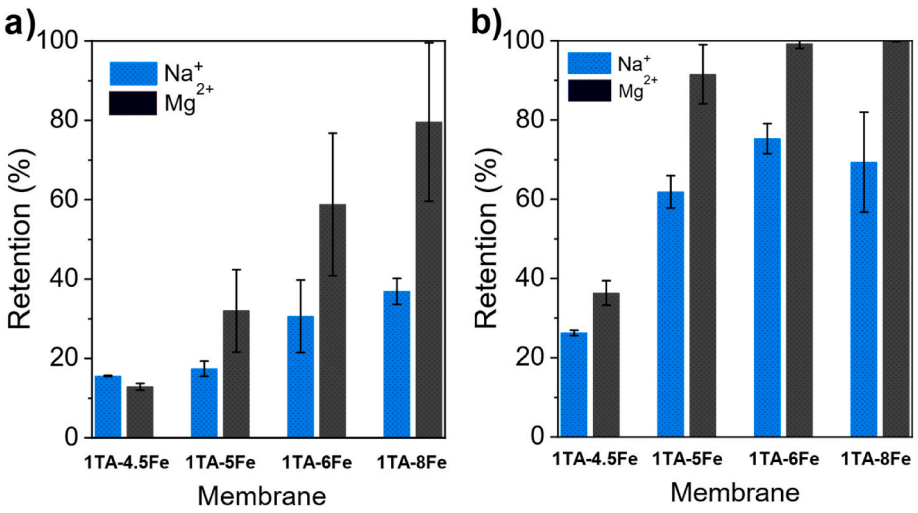

Fig. 5. Cation retentions by the MPN membranes from a) NaCl–$MgCl_2$, and b) Na_2SO_4–$MgSO_4$ equimolar mixed salt retention test using 10 mM total feed concentration.

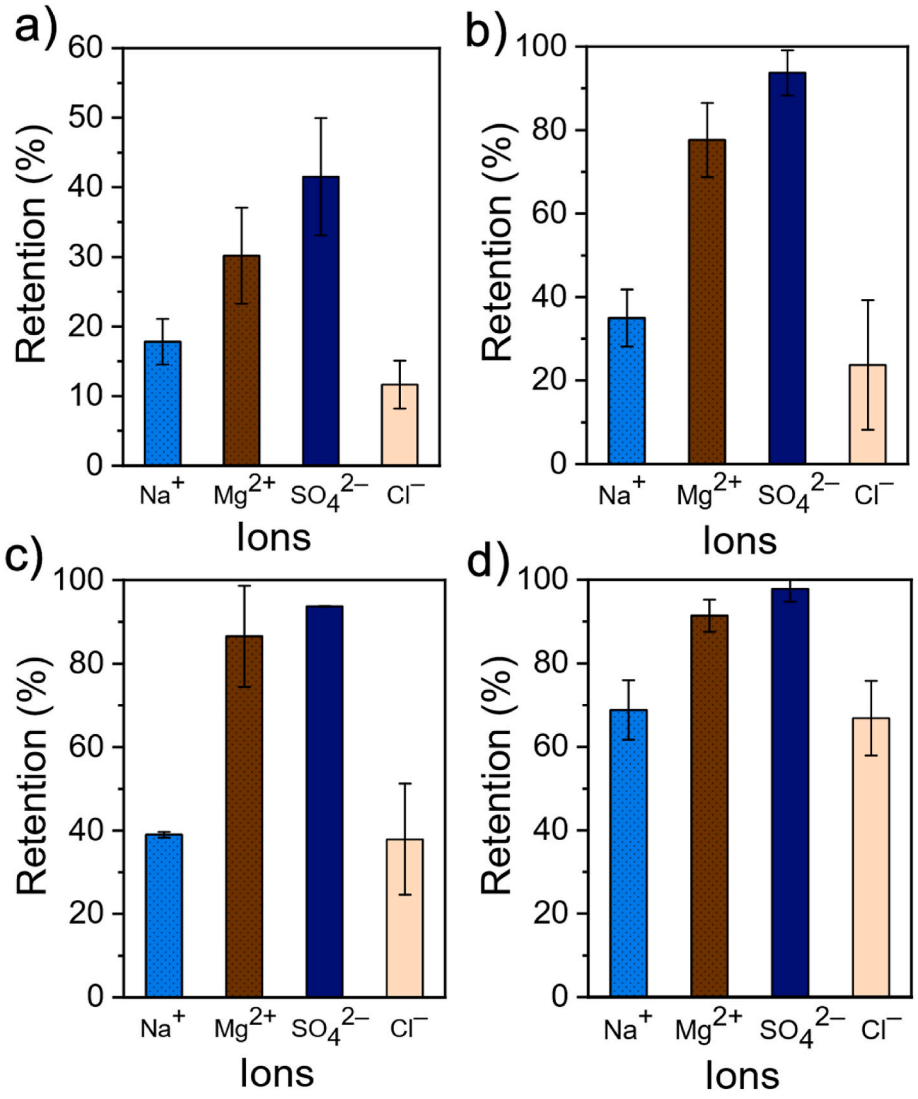

Fig. 6. The retention of ions from multi-ionic mixture. Four salts NaCl–Na_2SO_4–$MgCl_2$–$MgSO_4$ Mixed in equal molarity for 10 mM total feed concentration. a) 1TA-4.5Fe, b) 1TA-5Fe, c) 1TA-6Fe, and d) 1TA-8Fe membrane.

effect on monovalent/divalent cation selectivity is inversely related. Since both Na^+ and Mg^{2+} act as counter-ions to the negatively charged TFC membrane surface, the divalent Mg^{2+} cation more effectively counterbalances the fixed membrane charge. This effect would typically suggest a higher sodium removal rate. However, the observed retention for Mg^{2+} was significantly higher than that of Na^+, likely due to several contributing factors. Mg^{2+} has a larger hydration radius, resulting in a stronger size exclusion effect [52]. Additionally, Mg^{2+} possesses a higher ionic charge density compared to Na^+, which increases its retention due to stronger dielectric interactions. Mg^{2+} forms stronger bond with surrounding water molecules than Na^+ due to its higher hydration energy (1830 kJ/mol for Mg^{2+} and to 365 kJ/mol for Na^+) [53]. Thus, Mg^{2+} undergoes less dehydration compared to Na^+ [54]. This lower dehydration tendency hinders Mg^{2+} permeation through the TA-Fe^{3+} selective layer, whereas Na^+, with weaker hydration, enters the pores of the membrane to permeate more readily. These combined effects result in the TA-Fe^{3+} membranes exhibiting higher retention towards Mg^{2+} than Na^+ (Fig. 5a).

Next, the separation performance of the membranes was examined using SO_4^{2-} as the common anion. A substantial improvement of rejection was observed (Fig. 5b) compared to the Cl^- system (Fig. 5a). Notably, the retention of Mg^{2+} reached nearly 100 % for the 1TA-6Fe and 1TA-8Fe membranes. The observed Na^+/Mg^{2+} selectivity ($S_{Na/Mg}$) was 1.2, 4.5, 33.1, and 330 for 1TA-4.5Fe, 1TA-5Fe, 1TA-6Fe and 1TA-8Fe membranes, respectively. In contrast, the $S_{Na/Mg}$ in the chloride system ranged between 1 and 3 for all membranes. This significant variation can be attributed to the negatively charged TA-Fe^{3+} membrane surfaces, which exhibit strong SO_4^{2-} exclusion due to its higher charge density compared to Cl^-. The MPN layer effectively excludes multivalent anions such as SO_4^{2-}, which simultaneously enhances cation retention in SO_4^{2-} containing feed solutions. These findings demonstrate that the fabricated TFC membranes exhibit a strong potential for selective monovalent/divalent ion separation.

Water sources such as seawater, brackish water, and wastewater, are inherently complex, containing a diverse mixture of ions. Therefore, evaluating membrane performance using multi-ionic feed solution is essential. Here, we extended the investigation by conducting filtration tests with a multi-ionic synthetic feed solution comprising Na^+, Cl^-, Mg^{2+} and SO_4^{2-} ions at 3 bar transmembrane pressure. The observed retention of Mg^{2+} and SO_4^{2-} were higher than those of the monovalent ions (Fig. 6). For different TA-Fe^{3+} membranes, a significant increase in ion retention was observed with increasing Fe^{3+} content of TA-Fe^{3+} self-assembled layer. The average retention of Na^+ increased from 18 % to 68 %, Cl^- from 12 % to 67 % and Mg^{2+} from 30 % to 91 %. Moreover, the sulfate retention rate of the TFC membranes from the multi-ionic feed solution reached as high as 98 %. The ion retention rates of the membranes tested with a multi-ionic feed solution (Fig. 6) were slightly lower than those observed in a single salt or a ternary-ion retention test (Figs. 3 and Figs. 4–5). This finding underscores the impact of feed solution composition on membrane performance. Overall, 1TA-5Fe, 1TA-6Fe and 1TA-8Fe membranes displayed a promising retention performance, demonstrating the potential of using the fabricated MPN membranes for water softening and wastewater treatment applications.

The composition of the feed solution is hence one of the main factors governing ion retention and selectivity by membranes, necessitating ion retention study using MPN membranes at different chemical environments. Table 2 summarizes the influence of feed composition on the monovalent/divalent ion selectivity of the TA-Fe^{3+} selective layers. Na^+/Mg^{2+} selectivity is strongly dependent on the anions in the multi-component aqueous solutions (Table 2). The ideal Na^+/Mg^{2+} selectivity was <1, characteristic of negatively charged membranes as discussed in section 3.2 for single salt solutions. However, for mixed component systems, real Na^+/Mg^{2+} selectivity was higher for the SO_4^{2-} containing tertiary system than for the Cl^- containing tertiary mixed component feed solution. In contrast, the monovalent/divalent cation selectivities from Na^+, Cl^-, Mg^{2+} and SO_4^{2-} quaternary system lies between the selectivities from chloride and sulfate containing feed solutions of a tertiary mixed ion systems.

Table 2
Ideal and real monovalent/divalent selectivities by the fabricated MPN membranes. Ideal selectivity is computed from single salt retention tests of the corresponding salts. Real selectivity is computed from mixed salt retention tests of feed solution of tertiary and quaternary system.

Ideal selectivity					
	Salts	1TA-4.5Fe	1TA-5Fe	1TA-6Fe	1TA-8Fe
Na^+/Mg^{2+}	$NaCl–MgCl_2$	0.8	0.3	0.3	0.4
	$Na_2SO_4–MgSO_4$	0.3	0.1	0.4	0.3
Cl^-/SO_4^{2-}	$NaCl–Na_2SO_4$	2.5	7.6	5.0	7.9
	$MgCl_2–MgSO_4$	1.1	3.1	5.5	5.0
Real selectivity					
	Component mixture	1TA-4.5Fe	1TA-5Fe	1TA-6Fe	1TA-8Fe
Na^+/Mg^{2+}	Na^+, Mg^{2+} and Cl^-	0.96	1.2	1.7	3.1
	Na^+, Mg^{2+} and SO_4^{2-}	1.2	4.5	33.1	330.7
	Na^+, Cl^-, Mg^{2+} and SO_4^{2-}	1.1	2.9	4.5	3.6
Cl^-/SO_4^{2-}	Na^+, Cl^- and SO_4^{2-}	3.7	27.2	∞	35.4
	Na^+, Cl^-, Mg^{2+} and SO_4^{2-}	1.5	12.1	9.8	15.3

The presence of a counter-cation (Na^+ or Mg^{2+}) in the feed solution considerably affects anions (Cl^-/SO_4^{2-}) selectivity. Compared to those Na^+ containing solutions, the anion selectivity generally declines in the presence of a divalent cation (Mg^{2+}). This was observed in both single salt solutions (ideal selectivity) and mixed-salt solution (real selectivity) containing Na^+ and Mg^{2+}. The adsorption coefficient of divalent cations onto negatively charged NF membranes are 77–128 times higher than that of Na^+ [55], reducing the surface charge of the membrane. As such, the electrostatic repulsion exerted on the different anions weakens, and the membrane eventually loses selectivity. The Cl^-/SO_4^{2-} selectivity was lower when the MPN membranes were used to filter a quaternary system containing both divalent and monovalent cations, in comparison to tests with tertiary systems. Although we observe that the real selectivity increases as the Fe^{3+} concentration increases (Table 2), water permeance declines significantly (Section 3.1) attributed to the selectivity-permeability trade-off. The flux can be improved by optimizing the fabrication conditions to enhance the membrane fixed charge to reject ions without significantly hindering water transport. Future studies can also focus on integrating additives and nanomaterials that facilitate water transport in the MPN layer.

3.4. Elucidating ion transport through the MPN membranes using DSPM-DE

In this section, we adopted the well-established DSPM-DE model to elucidate ion transport and rejection properties of the MPN TFC membranes. First, we discuss the membrane input parameters estimated from neutral and charged solute retention measurements. Next, we compare the experimental retention data with the predicted values obtained using the estimated parameters. Finally, we analyze the exclusion mechanisms and ion transport processes occurring across the selective layer of the membranes.

3.4.1. Estimation of membrane parameters

The membrane structural parameters were estimated using the pore flow model, based on the retention data of PEG. In this model, the separation layer is assumed to consist of cylindrical pores of uniform

size. However, it should be noted that this simplification does not fully capture the actual wide pore size distribution and interconnected pore structure of membranes. The retention data revealed that PEG retention increased with permeate flux and stabilized at higher flux levels, indicating a limiting rejection at high applied pressure. The pore radius and effective membrane thickness were determined through the curve fitting of the experimental data (Fig. S5). The estimated membrane parameters are depicted in Table S3 of the supporting information. It was found that the fabricated TA-Fe^{3+} membranes exhibited varying pore sizes. The 1TA-4.5Fe membrane had the largest pore radius of around 1.25 nm followed by 1TA-5Fe at 1.02 nm. In contrast, the pore sizes of 1TA-6Fe and 1TA-8Fe were estimated at 0.67 nm and 0.63 nm, respectively. The concentration of Fe^{3+} in the casting solution also affects the Δx_e of the TA-Fe^{3+} selective layer of the TFC membranes. As the $FeCl_3$ concentration increased, the Δx_e decreased. However, beyond a Fe^{3+} concentration of 0.096 w%, the Δx_e began to increase.

Unlike neutral solutes, the retention properties of charged solutes, such as ions, are strongly influenced by the membrane's charge density and pore dielectric constant. Therefore, when applying the DSPM-DE model, estimation of these two membrane parameters is required, typically through fitting procedures [56]. To achieve this, ion retention experiments were conducted at different permeate fluxes by regulating the applied transmembrane pressure. A ternary ion mixture comprising Na^+ and Mg^{2+} ions with a common anion (NaCl–$MgCl_2$ system) was used for this purpose. The membrane charge density and pore dielectric constant were subsequently estimated following the procedure outlined in section 2.4.2. The obtained results are presented in Table 3. The pore dielectric constant (ε_p) indeed decreased in the 1TA-4.5Fe > 1TA-5Fe > 1TA-6Fe > 1TA-8Fe trend. A lower ε_p indicates the formation of a denser TA-Fe^{3+} separation layer. However, the membrane charge density follows a different trend for the studied salt solution system. The negative membrane charge density generally decreased as the Fe^{3+} concentration increased. The presence of divalent cations in the feed solution reduces membrane charge density through binding or complexation, which can even result in surface charge reversal [48]. Here, it can be inferred that with the increase in Fe^{3+} concentration, the amount of tannic acid assembled into the metal-polyphenol network increases. The anionic functional groups in TA act as a binding site for divalent cations, Mg^{2+}. Therefore, the small negative charge density at high Fe^{3+} concentration is further reduced due to the complexation of Mg^{2+} with the surface functional groups of the selective layer.

3.4.2. *Predicted ion retention results for NaCl–$MgCl_2$ mixed salt system*

Fig. 7 compares the experimentally determined ion retention by the TA-Fe^{3+} membranes with the values predicted by the DSPM-DE model for a feed solution containing a mixture of NaCl and $MgCl_2$. The model accurately predicts the exclusion of ions under the investigated conditions. The agreement between calculated and experimentally measured retentions by the 1TA-5Fe membrane is especially creditable with 0.90, 0.93 and 0.89 R^2 values for Na^+, Mg^{2+} and Cl^-, respectively. The 1TA-4.5Fe membrane showed the lowest rejections, between 5 and 22 % for all ions, owing to its large r_p and ε_p which reduce steric and dielectric effects, respectively. In addition, the computed high membrane charge density of 1TA-4.5Fe illustrates a higher charge interaction with the cations in the feed solutions that accelerates their partitioning into the pore entrance of the membrane. For membranes fabricated with higher Fe^{3+} concentrations, ion retention increases, as predicted by the model. Overall, the DSPM-DE model effectively quantifies the ion retention behavior of the MPN membranes across various fluxes.

Ion retention increased with permeate flux across all TA-Fe^{3+} membranes, consistent with the pressure-based rejection measurements (section 3.1). Increased applied pressure enhances the solute retention and dilutes the permeate stream, as water permeation increases linearly with pressure, while ion transport does not follow the same trend [41]. The linear relationship between permeate flux and applied pressure is shown in Fig. S6 of the supporting information.

The TA-Fe^{3+} membranes demonstrated a higher exclusion of the divalent Mg^{2+} than Na^+, a trend well predicted by the model. However, for the 1TA-4.5Fe membrane, a lower retention rate for Mg^{2+} was observed at high permeate flux, a deviation noted only in the experimental data with an unclear underlying cause. The preferential rejection of Mg^{2+} over Na^+ can be attributed to differences in ion size, valence, and physicochemical interactions which influence their exclusion coefficients. The exclusion coefficients quantify the ion rejection behavior of the MPN membranes. The partitioning coefficients governing ion exclusion were determined using equations (12)–(14). An exclusion factor of 1 represents no solute partitioning at the solution-membrane interface, whereas values greater than 1 indicate ion partitioning towards the membrane pores, and values less than 1 signify favorable partitioning toward the feed solution. Coefficients near 1 suggest weak partitioning effects, while more extreme values denote stronger exclusion mechanism. For instance, as shown in Fig. 9, the steric exclusion coefficient (Φ_s) for Na^+ was higher than for Mg^{2+}, indicating lower steric hindrance towards sodium. This results from Mg^{2+} having a larger hydration radius than Na^+ [52]. The dielectric partitioning coefficient (Φ_B) of Mg^{2+} was one order of magnitude lower than that of Na^+ for the 1TA-4.5Fe and 1TA-5Fe membranes. It increased to two orders of magnitude for the 1TA-6Fe and 1TA-8Fe membranes. In contrast, the Donnan partitioning factor (Φ_D) favored Mg^{2+} partitioning into the membrane pores. This behavior aligns with Donnan exclusion principles, where divalent counter-ions with higher ionic charge densities bind electrostatically to balance the fixed negative charges in the membrane [57]. The resulting electrical potential (i.e. Donnan potential) at the solution-membrane interface enhances counter-ion transport into the membrane pores. Despite Mg^{2+} having a higher Donnan partitioning coefficient, Na^+ consistently exhibited lower rejection across all MPN membranes. This indicates ion retention is governed by the cumulative partitioning coefficient ($\Phi = \Phi_s{}^*\Phi_D{}^*\Phi_B$). The overall Φ values for Na^+ were 0.753, 0.673, 0.685, and 0.109, while those for Mg^{2+} were 0.471, 0.352, 0.266 and 0.006 for the 1TA-4.5Fe, 1TA-5Fe, 1TA-6Fe and 1TA-8Fe membranes, respectively. For Na^+/ Mg^{2+} selectivity, both Donnan and dielectric exclusions have opposing effects. Dielectric exclusion primarily dictated Na^+ permeation selectivity, whereas Donnan exclusion negatively influenced it. Compared to these mechanisms, steric exclusion had a minimal impact due to the relatively small difference in Φ_s between Mg^{2+} and Na^+. Overall, the higher rejection of Mg^{2+} in the ternary ion mixture was largely dictated by the dielectric exclusion mechanism. Among membranes with varying Fe^{3+} concentrations, steric and dielectric partitioning coefficients followed a decreasing trend in the order 1TA-4.5Fe > 1TA-5Fe > 1TA-6Fe > 1TA-8Fe. On the other hand, the Donnan exclusion coefficient generally increased with Fe^{3+} concentration, correlating with the decreasing membrane charge density reported in Table 3.

The DSPM-DE model provides a link between various ion transport mechanisms and key physicochemical characteristics of the membrane-solution system. Ion transport across the membrane is accounted by three driving forces: fluid flow (convection), concentration gradient (diffusion), and electric potential gradient (electromigration). To identify the dominant transport mechanisms, we analyzed the relationship between ion flux and permeate flux of the NaCl–$MgCl_2$ system for all

Table 3
Membrane charge density and pore dielectric constant estimated for two different feed solutions.

Membrane	Estimated membrane parameters	
	Charge density, C_X (mol/m^3)	Pore dielectric constant, ε_p
1TA-4.5Fe	−9.8	43.4
1TA-5Fe	−8.1	38.8
1TA-6Fe	−8.5	27.4
1TA-8Fe	−0.61	25.1

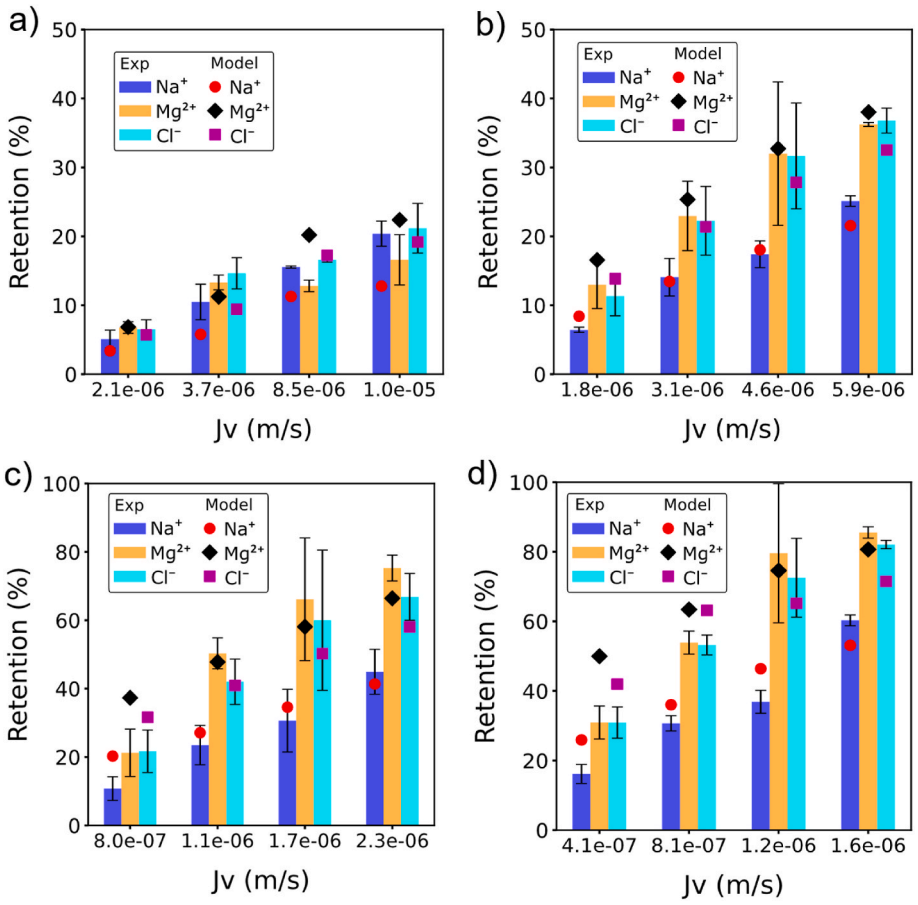

Fig. 7. Experimental (column plot) and DSPM-DE model fitted (scatter plot) retention results of a ternary ion mixture at different permeate fluxes for a) 1TA-4.5Fe, b) 1TA-5Fe, c) 1TA-6Fe, and d) 1TA-8Fe membranes. Mixed salt of 10 mM feed solution of NaCl–$MgCl_2$ was used in which the molar ratio of the cations was 1:1.

MPN membranes (Fig. 8). The total flux of each ion in the mixture decreased with an increase in Fe^{3+} concentration in the casting solution. The dense membranes (1TA-6Fe and 1TA-8Fe) displayed lower ion fluxes in agreement with the higher rejection rates observed in Fig. 7. Fig. S8 (supporting information) schematically illustrates the directions of diffusive, convective and electromigrative fluxes through a negatively charged membrane for both co-ions and counter-ions under conditions of positive retention. Notably, only the counter-ions' electromigrative flux is directed towards the feed, while both the convective and diffusive fluxes are directed towards the permeate side. Na^+ exhibits a higher diffusive flux toward the permeate compared to Mg^{2+} across all membranes. This is attributed to the higher diffusion coefficient of the more mobile Na^+ than Mg^{2+} (see Table S2). Generally, the total ion fluxes increased with permeate flux, mainly due to promoted convection. Chloride flux was mainly dominated by diffusion. For the cations in the mixture, opposing convection and electromigration fluxes were observed during ion transport. Within the nanopores of negatively charged membranes, the local concentration of cations exceeds that of anions (Fig. S9). Therefore, pressure driven flow transports more cations through the membrane via convection than anions [58]. This results in the generation of an electric field to maintain electroneutrality. This field gives rise to cation electromigration that opposes convection, while it adds to convection for anions (Figure S8a and Fig. 8). When comparing the counter-ions, sodium exhibited higher electromigrative fluxes (in absolute values) across all membranes. This is due to the fact that Na^+ is more sensitive to electrical potential gradient than Mg^{2+} [40]. In the 1TA-8Fe membrane, a different scenario was observed. Since the membrane charge density of this thin-film was very small (Table 3), the developed electric field within the membrane is weak that can be easily influenced by the local concentration of ions. Consequently, the cation electromigrative flux aligns with the concentration gradient and convection flow, driving ions toward the permeate. In this case Na^+ being the more mobile cation, diffused back to the feed side to maintain electroneutrality with the excluded chloride ions, yielding a negative diffusive flux (Fig. 8j).

3.4.3. *Predicted ion retention results for NaCl–Na_2SO_4–$MgCl_2$–$MgSO_4$ mixed salt system (quaternary ion mixture)*

While most studies in the literature focus on the application of the DSPM-DE model to ternary ion mixtures, many water and wastewater sources contain more complex compositions. Expanding membrane separation predictions to such systems is therefore essential. Here, we explore the application of the DSPM-DE model to predict the retention of a quaternary-ion mixture by the TFC membranes. The feed solution contains Na^+, Mg^{2+}, Cl^-, and SO_4^{2-}. The 1TA-5Fe membrane was selected for this study considering both its selectivity towards these ions (Fig. 6) and water flux (Fig. 2). Retentions for all ions were observed to increase with higher permeate flux, attributed to the increased transport of water at elevated pressures. Yet again, as expected the retention of divalent cation and anion (Mg^{2+} and SO_4^{2-}) by the MPN skin layer was higher compared to monovalent ions. This result highlights the efficiency of the MPN membranes in achieving sufficient ion separation. For the analysis of ion retention with the transport model, the membrane parameters of charge density (-0.54 mol·m^{-3}) and pore dielectric constant (30.8) were first estimated from the experimentally measured retentions of this system at different flux. The experimental data are then compared to DSPM-DE model predicted retentions, as shown in Fig. 10a. The model satisfactorily fit the experimental results of ion retention by

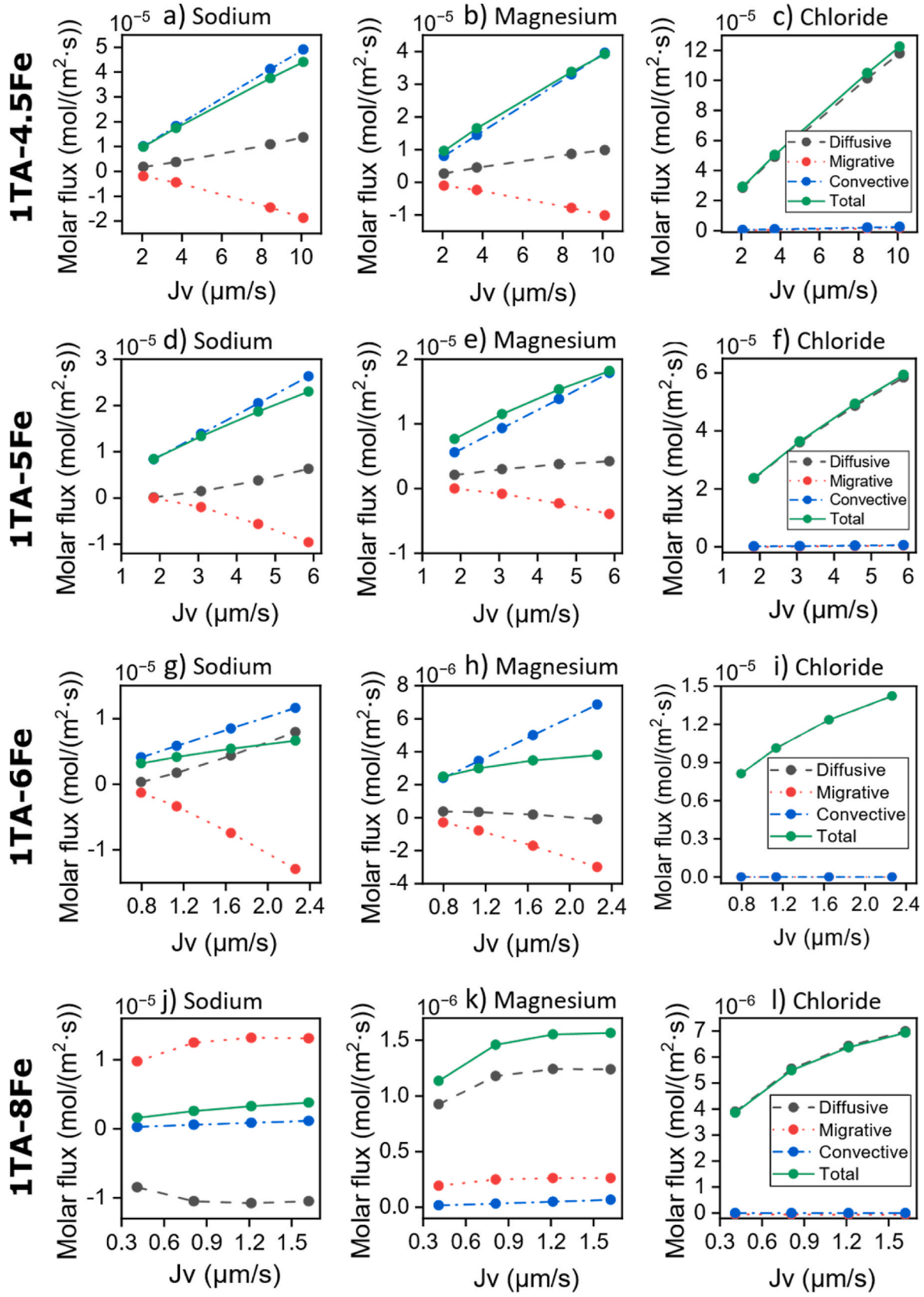

Fig. 8. Flux contributions vs permeate flux for NaCl–$MgCl_2$ mixed salt retention filtration test. Legend in chloride applies to all. The fluxes were computed inside the membrane pore between the second and third nodes after discretizing the ENP equation by dividing the obtained membrane selective layer thickness to 100 nodes. See Fig. S10 in supporting information for the location of N number of nodes and their corresponding concentration and potential profiles.

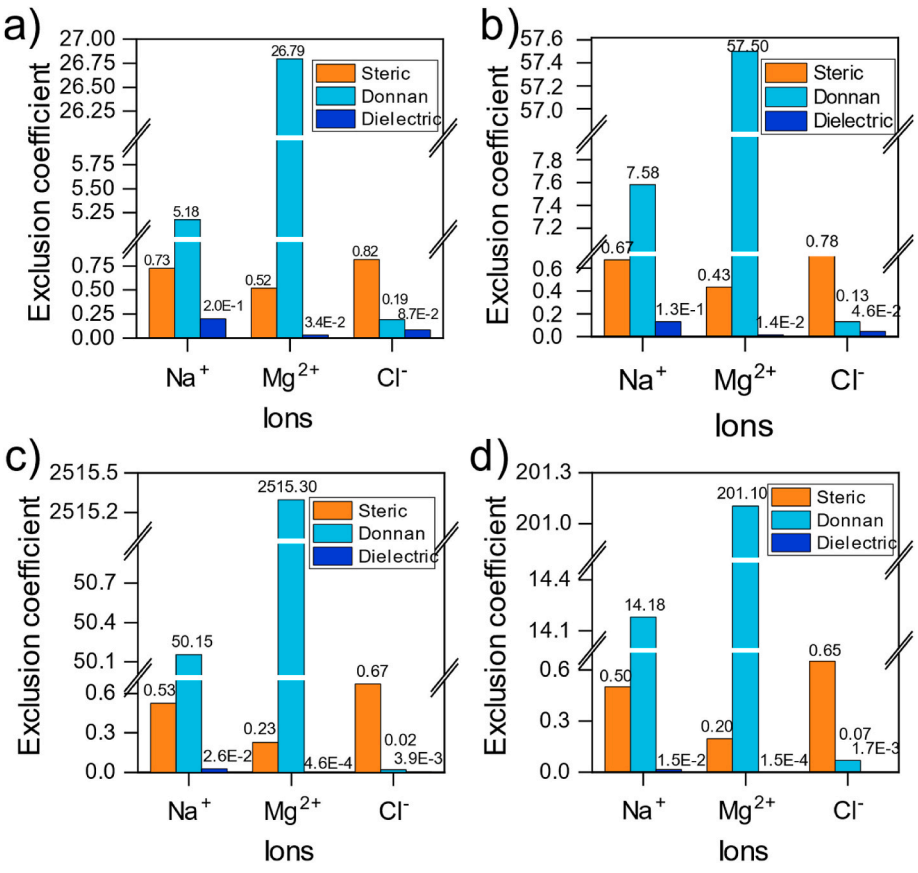

Fig. 9. Exclusion coefficients for a) 1TA-4.5Fe, b) 1TA-5Fe, c) 1TA-6Fe and d) 1TA-8Fe membranes during NaCl–$MgCl_2$ mixed salt retention.

the TA-Fe^{3+} membrane although clear deviations were found for anions: overestimating sulfate retention at low fluxes while underestimating chloride removal at high flux. The model-estimated transmembrane ionic fluxes provide valuable insights into the transport mechanisms occurring in the examined systems [41]. Fig. 10b–e illustrates the contributions of the individual fluxes to the total flux of each ion. The total flux of the ions followed the trend $Na^+ > Mg^{2+}$ and $Cl^- > SO_4^{2-}$ trend, in agreement with the observed retentions; a higher retention of an ion corresponds to a lower transmembrane ion flux. Diffusive flux was the dominant transport mechanism for both anions (Fig. 10d and e). Surprisingly, the electromigrative flux of the anions was directed toward the feed side. Given the low membrane charge density, it is assumed that the surface charges of the membranes were readily reversed through the binding of Mg^{2+} ions, creating a low potential region on the feed side, and promoting anion migration toward the feed solution. The transport of Mg^{2+} across the membrane was also primarily diffusion-driven, with electromigration and convection contributing in their respective order. In contrast, the flux of Na^+ was largely governed by electromigration (Fig. 10b). This can be explained by the higher sensitivity of Na^+ to the electrical potential gradient compared to Mg^{2+} [40].

The rejection mechanisms of ions by the MPN membrane are further visualized using exclusion coefficients (Fig. 10f–h). For exclusion coefficients greater than unity, a higher exclusion coefficient indicates an increased likelihood of partitioning into the pore channels. The partitioning coefficients for the monovalent ions were higher for all exclusion mechanisms, justifying the difference in the retention of the ions observed experimentally, except for sodium and magnesium in Donnan exclusion. The higher Donnan exclusion factor of Mg^{2+} is due to the counter-ion interaction with a negatively charged separation layer. Similar to the case of ternary ion mixtures, dielectric partitioning emerged as the critical exclusion mechanism for each ion in this system. This emphasizes the importance of including dielectric effect in the theoretical studies on ion separation, especially in the presence of divalent ions [59]. Overall, the fabricated MPN membrane demonstrated a Na^+/Mg^{2+} and Cl^-/SO_4^{2-} separation from the mixed ion system (Fig. 10a). Moreover, the DSPM-DE model provides excellent performance in modeling and illustrating the retention mechanisms of TA-Fe^{3+} membranes. The exclusion of ions by the MPN thin films at the solution-membrane interface is primarily governed by dielectric effects, driven by the reduced dielectric constant within the small confined pores of the separation layer.

4. Conclusion

Metal-phenolic network (MPN) membranes are emerging as a promising class of separation materials, offering tunable surface chemistry, strong metal-ligand coordination, and excellent stability. However, their ion retention and ion-ion selectivity in complex ionic environments for NF applications in water purification remained largely unexplored. This study provides a comprehensive analysis of ion retention behavior of MPN-based TFC membranes and extends our understanding of the NF performance using a transport model. The MPN-based TFC membranes were prepared through supramolecular self-assembly of tannic acid (TA) and Fe^{3+}. The TA-Fe^{3+} selective layer structure was fine-tuned during synthesis. This study highlights the salt retention performance of MPN membranes and evaluates their ion selectivity characteristics in both cationic and anionic mixtures. A detailed investigations into the single and mixed salt retention properties of the membranes shows the fabricated membranes exhibit excellent retention performance for various salts, underscoring their potential for NF and desalination applications. Additionally, the Cl^-/SO_4^{2-} and Na^+/Mg^{2+} selectivities were evaluated from various mixed salt systems,

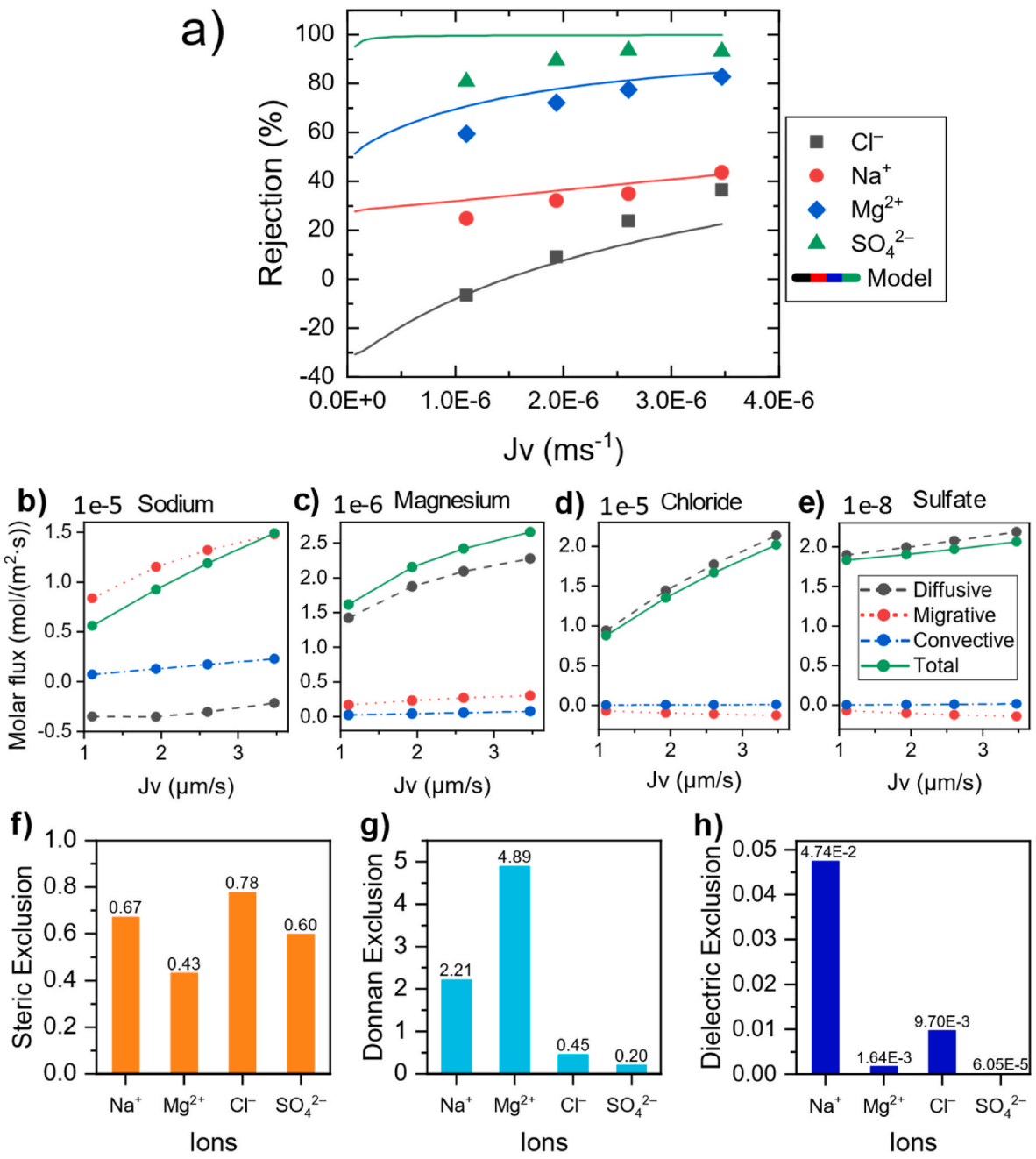

Fig. 10. a) Experimental performance and model predicted retention of a feed solution containing Na^+, Mg^{2+}, Cl^-, and SO_4^{2-} ions by the 1TA-5Fe membrane. The permeate flux vs pressure relationship is shown in Fig. S7 of the supporting information. b-e) show the contribution of the three fluxes to the total transport of each ion: b) Na^+, c) Mg^{2+}, d) Cl^-, and e) SO_4^{2-} ions. Plots (f–h) show the exclusion coefficients for steric, Donnan and dielectric effects, respectively.

including ternary ion mixtures (NaCl–Na_2SO_4, NaCl–$MgCl_2$ or Na_2SO_4–$MgSO_4$) and quaternary ion mixtures (NaCl–Na_2SO_4–$MgCl_2$–$MgSO_4$). Using sulfate as a common anion, the observed $S_{Na^+/Mg^{2+}}$ was 1.2, 4.5, 33.1, and 330 for 1TA-4.5Fe, 1TA-5Fe, 1TA-6Fe and 1TA-8Fe membranes, respectively. However, with chloride as the common anion, $S_{Na^+/Mg^{2+}}$ values ranged only between 1 and 3 for all membranes. On the other hand, an anion selectivity ($S_{Cl^-/SO_4^{2-}}$) of up 35 was achieved from a $Na^+/Cl^-/SO_4^{2-}$ ternary ion mixture retention test. The ion transport and exclusion properties of the MPN membranes were computationally elucidated using the DSPM-DE model. The model sufficiently predicts the retention performance of a ternary and quaternary ion mixtures. Dielectric and Donnan exclusion mechanisms play a key role in the partitioning of ions at the membrane-solution interface, dictating ion selectivity. While diffusion was the dominant transport mechanism for anions, convection primarily governed cation transport in most cases. This study demonstrates that the DSPM-DE model can be applied in predicting the separation properties of MPN membranes and contributes to understanding the transport and exclusion mechanisms which influence their performance. The DSPM-DE model is shown to be a valuable tool particularly in providing insight to mass transfer, membrane characteristics, and the overall efficiency of NF systems using MPN membranes.

CRediT authorship contribution statement

Hluf Hailu Kinfu: Writing – original draft, Validation, Software, Methodology, Investigation, Formal analysis, Data curation,

Conceptualization. **Md Mushfequr Rahman:** Writing – review & editing, Writing – original draft, Visualization, Supervision, Resources, Funding acquisition, Formal analysis, Conceptualization. **Nicolás Cevallos-Cueva:** Writing – review & editing, Software, Methodology. **Volker Abetz:** Writing – review & editing, Supervision, Resources.

Funding sources

This work was funded by the Hereon-I^{2}B-Project NanoMem.

Declaration of competing interest

The authors declare that they have no known competing financial interests or personal relationships that could have appeared to influence the work reported in this paper.

Acknowledgment

The authors acknowledge Maren Brinkmann for the PEG retention analysis in GPC, Juliana Clodt for preparing the polyacrylonitrile membrane support, Martin Held, Erik S. Schneider and Evgeni Sperling for the SEM images, and Jan Pohlmann for setting up the flux and retention measurement facilities.

Nomenclature

Symbol	Description
A_k	Membrane porosity
C_i	Concentration of species *i*, mol/m^3
C_X	Membrane charge density, mol/m^3
$D_{i,p}$	Diffusion coefficient of species *i* in the pore, m^2/s
$D_{i,\infty}$	Diffusion coefficient of species *i* in the bulk, m^2/s
e_0	Elementary charge, 1.60218×10^{-19} C
F	Faraday constant, 96485.3C/mol
J_i	Solute flux for species *i*, mol/m^2·s
J_V	Permeate flux, m^3/m^2·s
K_B	Boltzmann constant, 1.38065×10^{-23} J/K
$K_{c,i}$	Solute mass transfer coefficient of species *i*, m/s
$K_{i,c}$	Convection hindrance factor of species *i*
$K_{i,d}$	Diffusion hindrance factor of species *i*
N_c	Number of components
r_p	Pore radius, m
r_s	Solute Stokes radius for species *i*, m
R	Universal gas constant, 8.31446 J/mol K
R_{cal}	Calculated rejection from the model
R_{exp}	Experimentally measured rejection
R_i	Rejection ratio of species *i*
T	Temperature, K
Z_i	Valency of species *i*
γ_i	Activity coefficient of species *i*
ΔP	Applied pressure difference, Pa
$\Delta\Pi$	Osmotic pressure difference, Pa
ΔW_i	Born solvation energy barrier, J
Δx	Thickness of membrane active layer, m
ε_b	Dielectric constant of the bulk
ε_p	Dielectric constant of the pore
ε_0	Permittivity of free space
λ_i	Ratio of solute Stokes radius of species *i* to effective pore radius
μ	Solution viscosity, Pa·s
τ	Tortuosity
ξ	Electric potential gradient at the feed/membrane interface, V/m
ρ	Solution density, kg/m^3
Φ_S	Steric partitioning coefficient of species
Φ_B	Born solvation coefficient (dielectric partitioning coefficient)
Φ_D	Donnan partitioning coefficient
Ψ	Electric potential, V

The subscript *b* represents for the bulk solution in the feed, *m* is membrane or just inside the membrane pore, *p* is permeate side or just outside the pore of the membrane-permeate interface, *i* for solute species, and *real* is the real rejection considering concentration polarization.

Appendix A. Supplementary data

Supplementary data to this article can be found online at https://doi.org/10.1016/j.memsci.2025.124320.

Data availability

Data will be made available on request.

References

[1] A.W. Mohammad, Y.H. Teow, W.L. Ang, Y.T. Chung, D.L. Oatley-Radcliffe, N. Hilal, Nanofiltration membranes review: recent advances and future prospects,

Desalination (Amst.) 356 (2015) 226–254, https://doi.org/10.1016/J.DESAL.2014.10.043.
[2] D.L. Oatley-Radcliffe, M. Walters, T.J. Ainscough, P.M. Williams, A. W. Mohammad, N. Hilal, Nanofiltration membranes and processes: a review of research trends over the past decade, J. Water Proc. Eng. 19 (2017) 164–171, https://doi.org/10.1016/j.jwpe.2017.07.026.
[3] M.Q. Seah, W.J. Lau, P.S. Goh, A.F. Ismail, Greener synthesis of functionalized-GO incorporated TFN NF membrane for potential recovery of saline water from salt/dye mixed solution, Desalination (Amst.) 523 (2022), https://doi.org/10.1016/j.desal.2021.115403.
[4] X.Q. Cheng, Y.Y. Liu, Z.H. Guo, L. Shao, Nanofiltration membrane achieving dual resistance to fouling and chlorine for "green" separation of antibiotics, J. Membr. Sci. 493 (2015) 156–166, https://doi.org/10.1016/j.memsci.2015.06.048.
[5] S.L. Lin, A.C. Semiao, Y.Q. Zhang, S. Lu, C.H. Lau, Interfacial polymerization using biobased solvents and their application as desalination and organic solvent nanofiltration membranes, J. Membr. Sci. 692 (2024), https://doi.org/10.1016/j.memsci.2023.122281.
[6] W.C. Xie, T. Li, A. Tiraferri, E. Drioli, A. Figoli, J.C. Crittenden, B.C. Liu, Toward the next generation of sustainable membranes from green chemistry principles, ACS Sustain. Chem. Eng. 9 (2021) 50–75, https://doi.org/10.1021/acssuschemeng.0c07119.
[7] L. Yang, L. Han, J. Ren, H. Wei, L. Jia, Coating process and stability of metal-polyphenol film, Colloids Surf. A Physicochem. Eng. Asp. 484 (2015) 197–205, https://doi.org/10.1016/J.COLSURFA.2015.07.061.
[8] S. Kim, A. Pasc, Advances in multifunctional surface coating using metal-phenolic networks, Bull. Kor. Chem. Soc. 38 (2017) 519–520, https://doi.org/10.1002/bkcs.11123.
[9] Y.C. Xu, Y.R. Xiao, W.T. Zhang, H.J. Lin, L.G. Shen, R.J. Li, Y. Jiao, B.Q. Liao, Plant polyphenol intermediated metal-organic framework (MOF) membranes for efficient desalination, J. Membr. Sci. 618 (2021), https://doi.org/10.1016/j.memsci.2020.118726.
[10] C.M. Gao, H.Y. Chen, S.H. Liu, Y.Q. Xing, S.F. Ji, J.C. Chen, J.J. Chen, P. Zou, J. N. Cai, Preparing hydrophilic and antifouling polyethersulfone membrane with metal-polyphenol networks based on reverse thermally induced phase separation method, Surf. Interfaces 25 (2021), https://doi.org/10.1016/j.surfin.2021.101301.
[11] J. Guo, J.J. Richardson, Q.A. Besford, A.J. Christofferson, Y. Dai, C.W. Ong, B. L. Tardy, K. Liang, G.H. Choi, J. Cui, P.J. Yoo, I. Yarovsky, F. Caruso, Influence of ionic strength on the deposition of metal-phenolic networks, Langmuir 33 (2017) 10616–10622, https://doi.org/10.1021/acs.langmuir.7b02692.
[12] G. Yun, D.G. Kang, H.B. Rheem, H. Lee, S.Y. Han, J. Park, W.K. Cho, S.M. Han, I. S. Choi, Reversed anionic hofmeister effect in metal-phenolic-based film formation, Langmuir 36 (2020) 15552–15557, https://doi.org/10.1021/acs.langmuir.0c02928.
[13] M.A. Rahim, H. Ejima, K.L. Cho, K. Kempe, M. Müllner, J.P. Best, F. Caruso, Coordination-driven multistep assembly of metal-polyphenol films and capsules, Chem. Mater. 26 (2014) 1645–1653, https://doi.org/10.1021/cm403903m.
[14] H.H. Kinfu, M.M. Rahman, Separation performance of membranes containing ultrathin surface coating of metal-polyphenol network, Membranes 13 (2023) 481, https://doi.org/10.3390/membranes13050481.
[15] L. Fan, Y. Ma, Y. Su, R. Zhang, Y. Liu, Q. Zhang, Z. Jiang, Green coating by coordination of tannic acid and iron ions for antioxidant nanofiltration membranes, RSC Adv. 5 (2015) 107777–107784, https://doi.org/10.1039/c5ra23490e.
[16] F. You, Y. Xu, X. Yang, Y. Zhang, L. Shao, Bio-inspired Ni2+-polyphenol hydrophilic network to achieve unconventional high-flux nanofiltration membranes for environmental remediation, Chem. Commun. 53 (2017) 6128–6131, https://doi.org/10.1039/c7cc02411h.
[17] C.E. Lin, M.Y. Zhou, W.S. Hung, B.K. Zhu, K.R. Lee, L.P. Zhu, L.F. Fang, Ultrathin nanofilm with tailored pore size fabricated by metal-phenolic network for precise and rapid molecular separation, Separ. Purif. Technol. 207 (2018) 435–442, https://doi.org/10.1016/j.seppur.2018.06.077.
[18] H. Guo, L.E. Peng, Z. Yao, Z. Yang, X. Ma, C.Y. Tang, Non-polyamide based nanofiltration membranes using green metal-organic coordination complexes: implications for the removal of trace organic contaminants, Environ. Sci. Technol. 53 (2019) 2688–2694, https://doi.org/10.1021/acs.est.8b06422.
[19] H.J. Kim, D.G. Kim, H. Yoon, Y.S. Choi, J. Yoon, J.C. Lee, Polyphenol/FeIII complex coated membranes having multifunctional properties prepared by a one-step fast assembly, Adv. Mater. Interfac. 2 (2015) 1–8, https://doi.org/10.1002/admi.201500298.
[20] W. Luo, G. Xiao, F. Tian, J.J. Richardson, Y.P. Wang, J.F. Zhou, J.L. Guo, X.P. Liao, B. Shi, Engineering robust metal-phenolic network membranes for uranium extraction from seawater, Energy Environ. Sci. 12 (2019) 607–614, https://doi.org/10.1039/c8ee01438h.
[21] Y.Z. Song, X. Kong, X. Yin, Y. Zhang, C.C. Sun, J.J. Yuan, B. Zhu, L.P. Zhu, Tannin-inspired superhydrophilic and underwater superoleophobic polypropylene membrane for effective oil/water emulsions separation, Colloids Surf. A Physicochem. Eng. Asp. 522 (2017) 585–592, https://doi.org/10.1016/j.colsurfa.2017.03.023.
[22] X.T. Zhao, Y.Y. Jiang, L.J. Cheng, Y.Y. Lan, T.Y. Wang, J.F. Pan, L.F. Liu, Hierarchical metal-phenolic-polyplex assembly toward superwetting membrane for high-flux and antifouling oil-water separation, Chin. Chem. Lett. 33 (2022) 3859–3864, https://doi.org/10.1016/j.cclet.2021.12.017.
[23] S.R. Razavi, A. Shakeri, S.M. Mirahmadi Babaheydari, H. Salehi, R.G. H. Lammertink, High-performance thin film composite forward osmosis membrane on tannic Acid/Fe3+ coated microfiltration substrate, Chem. Eng. Res. Des. 161 (2020) 232–239, https://doi.org/10.1016/j.cherd.2020.06.032.
[24] Y.J. Shen, L.F. Fang, Y. Yan, J.J. Yuan, Z.Q. Gan, X.Z. Wei, B.K. Zhu, Metal-organic composite membrane with sub-2 nm pores fabricated via interfacial coordination, J. Membr. Sci. 587 (2019) 117146, https://doi.org/10.1016/j.memsci.2019.05.070.
[25] D. Liu, Y. Chen, T.T. Tran, G. Zhang, Facile and rapid assembly of high-performance tannic acid thin-film nanofiltration membranes via Fe^{3+} intermediated regulation and coordination, Separ. Purif. Technol. 260 (2021) 118228, https://doi.org/10.1016/j.seppur.2020.118228.
[26] J. Schaep, C. Vandecasteele, A.W. Mohammad, W.R. Bowen, Analysis of the salt retention of nanofiltration membranes using the Donnan-steric partitioning pore model, Separ. Sci. Technol. 34 (1999) 3009–3030, https://doi.org/10.1081/SS-100100819.
[27] S. Salgin, U. Salgin, N. Soyer, Streaming potential measurements of polyethersulfone ultrafiltration membranes to determine salt effects on membrane zeta potential, Int. J. Electrochem. Sci. 8 (2013) 4073–4084, https://doi.org/10.1016/S1452-3981(23)14454-3.
[28] W.R. Bowen, A.W. Mohammad, Characterization and prediction of nanofiltration membrane performance - a general assessment, Chem. Eng. Res. Des. 76 (1998) 885–893, https://doi.org/10.1205/026387698525685.
[29] W.R. Bowen, A.W. Mohammad, N. Hilal, Characterisation of nanofiltration membranes for predictive purposes - use of salts, uncharged solutes and atomic force microscopy, J. Membr. Sci. 126 (1997) 91–105, https://doi.org/10.1016/S0376-7388(96)00276-1.
[30] W.R. Bowen, H. Mukhtar, Characterisation and prediction of separation performance of nanofiltration membranes, J. Membr. Sci. 112 (1996) 263–274, https://doi.org/10.1016/0376-7388(95)00302-9.
[31] W.R. Bowen, A.W. Mohammad, Diafiltration by nanofiltration: prediction and optimization, AIChE J. 44 (1998) 1799–1812, https://doi.org/10.1002/aic.690440811.
[32] S. Bandini, D. Vezzani, Nanofiltration modeling: the role of dielectric exclusion in membrane characterization, Chem. Eng. Sci. 58 (2003) 3303–3326, https://doi.org/10.1016/S0009-2509(03)00212-4.
[33] H. Al-Zoubi, N. Hilal, N.A. Darwish, A.W. Mohammad, Rejection and modelling of sulphate and potassium salts by nanofiltration membranes: neural network and Spiegler-Kedem model, Desalination (Amst.) 206 (2007) 42–60, https://doi.org/10.1016/j.desal.2006.02.060.
[34] O. Labban, C. Liu, T.H. Chong, J.H. Lienhard V, Fundamentals of low-pressure nanofiltration: membrane characterization, modeling, and understanding the multi-ionic interactions in water softening, J. Membr. Sci. 521 (2017) 18–32, https://doi.org/10.1016/j.memsci.2016.08.062.
[35] M.A. Junker, E. te Brinke, C.M.V. Compte, R.G.H. Lammertink, J. de Grooth, W. M. de Vos, Asymmetric polyelectrolyte multilayer nanofiltration membranes: structural characterisation via transport phenomena, J. Membr. Sci. 681 (2023), https://doi.org/10.1016/j.memsci.2023.121718.
[36] H.H. Kinfu, M.M. Rahman, E.S. Schneider, N. Cevallos-Cueva, V. Abetz, Charge and size selective thin film composite membranes having tannic acid – ferric ion network as selective layer, J. Membr. Sci. 679 (2023) 121709, https://doi.org/10.1016/j.memsci.2023.121709.
[37] H.H. Kinfu, M.M. Rahman, E.S. Schneider, N. Cevallos-Cueva, V. Abetz, Using the assembly time as a tool to control the surface morphology and separation performance of membranes with a tannic Acid–Fe3+ selective layer, Membranes 14 (2024) 133, https://doi.org/10.3390/membranes14060133.
[38] V. Silva, P. Prádanos, L. Palacio, A. Hernández, Alternative pore hindrance factors: what one should be used for nanofiltration modelization? Desalination (Amst.) 245 (2009) 606–613, https://doi.org/10.1016/j.desal.2009.02.026.
[39] R.Y. Wang, S.H. Lin, Pore model for nanofiltration: history, theoretical framework, key predictions, limitations, and prospects, J. Membr. Sci. 620 (2021) 118809, https://doi.org/10.1016/j.memsci.2020.118809.
[40] V. Geraldes, A.M. Brites Alves, Computer program for simulation of mass transport in nanofiltration membranes, J. Membr. Sci. 321 (2008) 172–182, https://doi.org/10.1016/j.memsci.2008.04.054.
[41] M. Micari, D. Diamantidou, B. Heijman, M. Moser, A. Haidari, H. Spanjers, V. Bertsch, Experimental and theoretical characterization of commercial nanofiltration membranes for the treatment of ion exchange spent regenerant, J. Membr. Sci. 606 (2020) 118117, https://doi.org/10.1016/j.memsci.2020.118117.
[42] D. Rehman, J.H. Lienhard, Global optimization for accurate and efficient parameter estimation in nanofiltration, J. Membr. Sci. Lett. 2 (2022) 100034, https://doi.org/10.1016/j.memlet.2022.100034.
[43] Q.S. Yao, S.X. Li, R.R. Zhang, L.H. Han, B.W. Su, High-throughput thin-film composite membrane via interfacial polymerization using monomers of ultra-low concentration on tannic acid - copper interlayer for organic solvent nanofiltration, Separ. Purif. Technol. 258 (2021), https://doi.org/10.1016/j.seppur.2020.118027.
[44] H. Ejima, J.J. Richardson, K. Liang, J.P. Best, M.P. Van Koeverden, G.K. Such, J. Cui, F. Caruso, One-step assembly of coordination complexes, Science 341 (2013) 154–157, https://doi.org/10.1126/science.1237265.
[45] H. Wu, J. Xie, L. Mao, One-pot assembly tannic acid-titanium dual network coating for low-pressure nanofiltration membranes, Separ. Purif. Technol. 233 (2020), https://doi.org/10.1016/j.seppur.2019.116051.
[46] Y. Xiao, D. Guo, T. Li, Q. Zhou, L. Shen, R. Li, Y. Xu, H. Lin, Facile fabrication of superhydrophilic nanofiltration membranes via tannic acid and irons layer-by-layer self-assembly for dye separation, Appl. Surf. Sci. 515 (2020) 146063, https://doi.org/10.1016/j.apsusc.2020.146063.

[47] N.S. Suhalim, N. Kasim, E. Mahmoudi, I.J. Shamsudin, A.W. Mohammad, F. M. Zuki, N.L.A. Jamari, Rejection mechanism of ionic solute removal by nanofiltration membranes: an overview, Nanomaterials (Basel) 12 (2022), https://doi.org/10.3390/nano12030437.
[48] S.C. Osorio, P.M. Biesheuvel, J.E. Dykstra, E. Virga, Nanofiltration of complex mixtures: the effect of the adsorption of divalent ions on membrane retention, Desalination (Amst.) 527 (2022), https://doi.org/10.1016/j.desal.2022.115552.
[49] W.M. de Vos, S. Lindhoud, Overcharging and charge inversion: finding the correct explanation(s), Adv. Colloid Interface Sci. 274 (2019), https://doi.org/10.1016/j.cis.2019.102040.
[50] M.R. Teixeira, M.J. Rosa, M. Nyström, The role of membrane charge on nanofiltration performance, J. Membr. Sci. 265 (2005) 160–166, https://doi.org/10.1016/j.memsci.2005.04.046.
[51] W.R. Bowen, J.S. Welfoot, Modelling the performance of membrane nanofiltration-critical assessment and model development, Chem. Eng. Sci. 57 (2002) 1121–1137, https://doi.org/10.1016/S0009-2509(01)00413-4.
[52] H.L. Liu, X. Zhang, Z.X. Lv, F. Wei, Q. Liang, L.J. Qian, Z. Li, X.M. Chen, W.S. Wu, Ternary heterostructure membranes with two-dimensional tunable channels for highly selective ion separation, JACS Au 3 (2023) 3089–3100, https://doi.org/10.1021/jacsau.3c00473.
[53] Y. Marcus, A simple empirical-model describing the thermodynamics of hydration of ions of widely varying charges, sizes, and shapes, Biophys. Chem. 51 (1994) 111–127, https://doi.org/10.1016/0301-4622(94)00051-4.
[54] K. Sharma, N. Akther, Y. Choo, P.F. Zhang, H. Matsuyama, H.K. Shon, G. Naidu, Positively charged nanofiltration membranes for enhancing magnesium separation from seawater, Desalination (Amst.) 568 (2023), https://doi.org/10.1016/j.desal.2023.117026.
[55] H.Y. Guo, X.Q. Gao, K.C. Yu, X.M. Wang, S.M. Liu, Ion adsorption on nanofiltration membrane surface and its effect on rejection of charged solutes: a zeta potential approach, Separ. Purif. Technol. 326 (2023), https://doi.org/10.1016/j.seppur.2023.124830.
[56] S.B. Rutten, M.A. Junker, L.H. Leal, W.M. de Vos, R.G.H. Lammertink, J. de Grooth, Influence of dominant salts on the removal of trace micropollutants by hollow fiber nanofiltration membranes, J. Membr. Sci. 678 (2023), https://doi.org/10.1016/j.memsci.2023.121625.
[57] M. Galizia, F.M. Benedetti, D.R. Paul, B.D. Freeman, Monovalent and divalent ion sorption in a cation exchange membrane based on cross-linked poly (-styrene sulfonate–divinylbenzene), J. Membr. Sci. 535 (2017) 132–142, https://doi.org/10.1016/j.memsci.2017.04.007.
[58] C. Tang, M.L. Bruening, Ion separations with membranes, J. Polym. Sci. 58 (2020) 2831–2856, https://doi.org/10.1002/pol.20200500.
[59] D. Vezzani, S. Bandini, Donnan equilibrium and dielectric exclusion for characterization of nanofiltration membranes, Desalination (Amst.) 149 (2002) 477–483, https://doi.org/10.1016/S0011-9164(02)00784-1.

Chapter 9. Comprehensive Discussion

Membrane technology has become an emerging filtration technology for water and wastewater treatment due to its simple, low-energy and highly efficient separation. In this dissertation, the fabrication and separation performance of thin-film composite membranes comprised of metal-phenolic network selective layers have been studied in detail. This chapter provides a comprehensive discussion of the cumulative part of the dissertation.

9.1. Membrane fabrication

MPNs are synthesized via coordination interactions driven self-assembly between metal ions and phenolic ligands. MPNs offer a promising approach of membrane coating in a fast, simple, green, and cost-effective strategy. Here, a TA-Fe^{3+} selective layer is deposited over a porous support. Both TA and $FeCl_3 \cdot 6H_2O$ were dissolved in water, eliminating the use of harsh solvents for TFC membrane selective layer synthesis as in interfacial polymerization. A PAN ultrafiltration membrane was used as a porous substrate support. A layer-by-layer technique, analogous to multilayer deposition, was employed for the TA-Fe^{3+} selective layer fabrication. It was observed that the water permeance of the membranes declined as the number of layers deposited increases, indicating the formation of a dense selective layer. FTIR, EDX, SEM, AFM, zeta potential, contact angle analyses (Chapter 3 – 8) have shown a successful fabrication of the MPN layer over the porous substrate. Moreover, backscattered electron (BSE) imaging mode (Figure 1c in Chapter 3) confirms the deposition of a brighter thin layer originating from the presence of a high atomic number element (Fe). The thickness of the selective layer of the fabricated TFC membranes is around 10 nm, which can be classified as an ultrathin film in membranes for liquid separation. In addition to the selection of membrane materials, designing thin separation layers is desirable to achieve high water permeance due to their low transport resistance [1]. The MPN-based TFC membranes exhibit hydrophilic property compared to the bare PAN surface (Figure 4a in Chapter 3, Figure 4a in Chapter 4, Figure 6b in Chapter 5). Moreover, the membranes demonstrate a negatively charged surface (Figure 2a in Chapter 4, Figure 1b in Chapter 7), beneficial for charge-based separation and fouling resistance. A flux recovery ratio of up to 82 % was achieved during a fouling test with humic acid as a foulant molecule, which revealed that the MPN separation layer exhibits excellent antifouling properties. Overall, it is demonstrated that an ultrathin selective layer can be fabricated without the use of organic solvents.

9.2. Parameters that affect MPN thin-film formation and membrane fine-tuning

Polyphenols contain multiple phenolic hydroxyl groups (e.g. chemical structure of tannic acid, Figure 2.4a in Chapter 2). Through these hydroxyl groups, phenolic materials provide binding sites for the chelation of metal ions (e.g. Fe^{3+}) via coordination interaction. This leads to the formation of supramolecular metal-phenolic complexes that can be translated into a thin self-assembled layer when deposited on a surface. The nature and extent of complex formation and the subsequent structure and properties of the fabricated thin-film are dependent on coordination reaction conditions. Accordingly, in this thesis several approaches have been followed to determine the effect of each parameter on membrane structure and performance.

The influence of phenolic ligand to metal ion ratio as a synthesis parameter on membrane structure was first studied (Chapter 3). A series of TFC membranes having TA-Fe^{3+} selective layers are fabricated by varying the metal ion concentration, i.e., 0.02 – 0.16 w% of $FeCl_3 \cdot 6H_2O$ while a 0.02 w% concentration of TA was used. The deposition of the TA-Fe^{3+} MPN selective layer significantly alters the surface morphology. As the metal ion concentration increases, the top layer of the TFC membranes become denser with a compact structure of decreasing pore size (Figure 2 in Chapter 3 and Figure 2 in Chapter 7). However, surface roughness and protrusions increased in the presence of excess Fe^{3+} concentration due to the formation of TA-Fe^{3+} complex aggregates over the synthesized film (Figure 1c in Chapter 7). SEM images of the cross-section show that the sponge-like structure of the support layer is unaffected by the surface coating, illustrating fine-tuning of the membrane surface without penetration of the TA-Fe^{3+} complexes to the porous substructure. The water permeance across the fabricated membranes also decreased significantly from 165 $L \cdot m^{-2} \cdot h^{-1} \cdot bar^{-1}$ for the 1TA-1Fe membrane (0.02 w% TA and 0.02 w% $FeCl_3 \cdot 6H_2O$) to 0.9 $L \cdot m^{-2} \cdot h^{-1} \cdot bar^{-1}$ for the 1TA-8Fe membrane (0.02 w% TA and 0.16 w% $FeCl_3 \cdot 6H_2O$). For comparison, the pristine PAN support exhibits a water permeance of 286 $L \cdot m^{-2} \cdot h^{-1} \cdot bar^{-1}$ (Figure 4b in Chapter 3). The TFC membranes fabricated at higher Fe^{3+} concentration exhibit a more hydrophilic surface as observed with water contact angle measurements. This increase in hydrophilicity shows the incorporation of more TA groups, which contain abundant hydrophilic –OH groups, into the self-assembled MPN selective layer through enhanced coordination in the presence of excess metal ions. The TA-Fe^{3+} top layer exhibits a negative surface potential which is beneficial for charge selectivity towards solutes during filtration tests (see section 9.3).

The number of TA-Fe^{3+} layers deposited over the porous support determines membrane performance. Water permeance especially drops drastically when the number of deposited layers were increased from 1 to 4 layers (Figure S1 in Chapter 11 Section 11.2). This can be attributed to the fact that uniform surface coverage was not achieved with one coating cycle, while further coating leads to a compact selective layer with higher resistance to water transport.

Another parameter that controls thin-film formation is the assembly time. Although metal-polyphenol self-assembly is a rapid process, the amount of reaction time the precursors are allowed to coordinate affects the microstructure and physicochemical properties of the fabricated thin-film. For instance, the surface pore size of the TA-Fe^{3+} TFC membranes decreased significantly when the assembly time was increased from 1 min to 6 min (Figure 3 in Chapter 4). This is due to enhanced coordination with the involvement of more binding sites for coordination. The water permeance also decreased from 86.1 to 5.6 $L \cdot m^{-2} \cdot h^{-1} \cdot bar^{-1}$, indicating the synthesis of a dense separation layer. However, due to the ultrathin nature of the deposited MPN film, it was not possible to analyze whether a prolonged reaction time increases film thickness as it is observed in interfacial polymerization. On the other hand, the surface wettability of the selective layer declines for membranes fabricated at higher assembly time (Figure 4a in Chapter 4). The fabricated membranes are less prone to reversible fouling. The antifouling property of the active layer is attributed to two phenomena: 1) the electrostatic repulsive interaction between the foulant molecules and TA functional groups and 2) the formation of a hydration layer due to the preferential adsorption of water molecules on the MPN-containing self-assembled films.

The formation of coordination bonds between metal ions and polyphenols is pH dependent [2, 3]. Taking TA and Fe^{3+} as an example, MPN in the form of a mono-complex is formed under strongly acidic conditions (pH < 2). While bis-complex is formed at higher pH conditions, MPN in the form of a tris-complex is synthesized in alkaline conditions (pH > 7). To assess the effect of solution pH on membrane characteristics and separation performances, a series of membranes were fabricated by varying the pH of the solution in which TA was dissolved (Table 1 in Chapter 5). For both single TA-Fe^{3+} layered and double TA-Fe^{3+} layered TFC membrane, low solution pH results in a highly porous separation layer compared to those fabricated at a higher pH. At low pH, most of the hydroxyl groups in TA are protonated. This reduces the number of coordination sites which leads to a loose membrane. However, with the increase of the casting solution pH, the formation of bis- or tris-complexes increases, leading to highly cross-linked network of small pore sized separation layer. In addition to pore structure, the pH

of the casting solution can be used to control the surface wettability, surface charge, solute rejection performance and stability of the membranes (Figures 6 – 11 in Chapter 5). Highly selective, robust and hydrophilic TFC membranes are fabricated at 8.5 pH value. Generally, both ideal and real selectivities were enhanced for TA-Fe^{3+} layers synthesized at alkaline conditions. The membranes showed excellent performance in separating small organic solutes from aqueous solution.

Here, it should also be noted that the stability of the thin-film is also pH dependent. MPNs are extremely stable at high pH conditions, although disassembly of the network occurs when in contact with acidic feed solutions of pH < 4. This has unveiled a new approach of capsule coating for pH-responsive release mechanism in drug delivery and other applications [3]. Whereas in MPNs for membrane applications, further research on enhancing their stability under acidic feed solutions is required.

In summary, it can be concluded that the surface structure, property and performance of the TFC membranes including surface porosity, roughness, water flux, hydrophilicity, surface charge, and rejection can be tuned through these wide range of synthesis conditions. This reiterates the tunability of MPN films for membrane application. Optimizing membrane structure and properties is crucial for filtration operation. By controlling membrane morphology, surface chemistry, and mechanical properties, the performance, and membrane lifespan can be enhanced. This improves the effectiveness and sustainability of water treatment via membrane technology.

9.3. Small organic solutes separation

Selective separation of small organic solutes requires membranes with precisely tuned pore structures and surface properties. The effectiveness of these membranes depends on key factors such as membrane material, pore size, hydrophilicity, charge, and other interactions. In this regard, the removal performance of the fabricated MPN membranes towards solutes from aqueous solutions as well as from each other was investigated. The rejection and selectivity were further tailored by utilizing the TA-Fe^{3+} coating preparation procedures as a variable. Figure 9.1 summarizes the retention of small organic molecules having 200 – 1000 g/mol molecular weight (MW). The TA-Fe^{3+} selective layer demonstrated high rejection towards anionic dyes orange II (OR-) and naphthol green b (NGB3-). Conversely, low rejections were observed towards neutral solutes riboflavin (RB0) and poly(ethylene glycol) of 400 g/mol MW (PEG400). For comparison, the PAN support did not display any significant retention towards

all solutes, which indicates the retention behavior of the TFC membranes emerge entirely from the MPN coating.

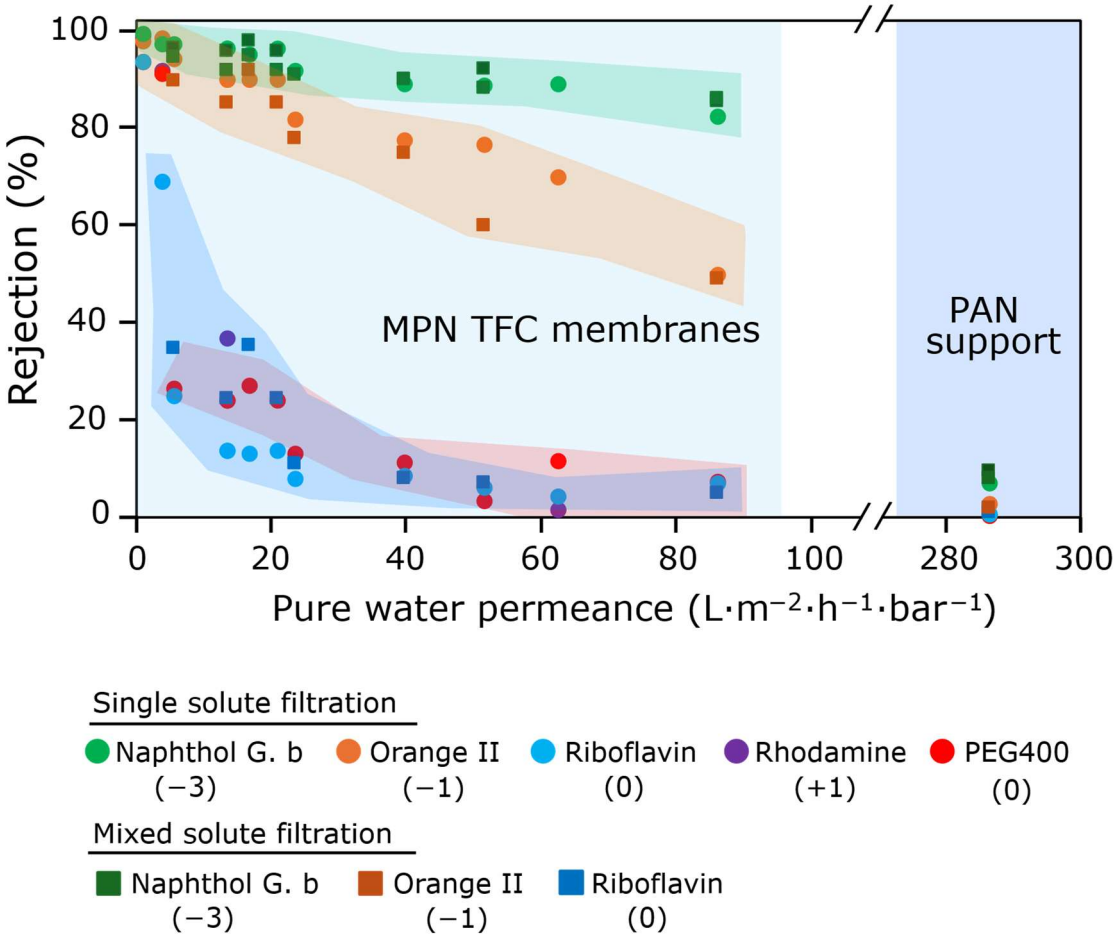

Figure 9.1 *Solute rejection performance of the TA-Fe^{3+} membranes towards different charge groups of solutes.*

In comparison to other studies in the literature, the TA-Fe^{3+} membranes perform excellent considering the selectivity-permeability trade-off (Table 2 in Chapter 4 and Table 3 in Chapter 5). A selectivity of up to 31 for neutral/charged solutes (RB0/NGB3-) were achieved, indicating the efficiency of the fabricated membranes for charge-based solute/solute separation. In general, the membranes displayed selectivities between 2 – 31 during both single solute filtration test (ideal selectivity) and mixed solute filtration test (real selectivity). For solutes of similar charge group (OR-/NGB3-), the selectivity was 2 – 4. Solute retention is governed by two phenomena: size sieving and electrostatic exclusion. These mechanisms determine the retention and selectivity of organic solutes [4, 5]. The retention behavior of the MPN selective layer and their exclusion mechanism is shown schematically in Figure 9.2.

Although RB0, PEG400 and OR- have a rather similar molecular weight and molecular size, their retention differs substantially. While OR-, the anionic dye in aqueous solution, was excluded by the TA-Fe^{3+} membrane, the neutral solutes RB0 and PEG400 permeated through the membranes with low resistance. These results demonstrate the charge-selective nature of the MPN membranes. This relies primarily on the electrostatic interactions between the sulfonate functional groups in OR- and the negatively charged surface of the MPN selective layer (Figure 9.2*i*). On the other hand, the effect of size exclusion is demonstrated in the case of similarly charged solutes, OR- and NGB3-. Naphthol green b experiences a higher steric hinderance due to its bigger size. It also experiences higher electrostatic repulsion by the TA-Fe^{3+} layer due to its trivalent charge compared to the monovalent OR-. Overall, the permeation selectivities of organic solutes constitutes a combination of steric and electrostatic effects. Here it is shown that MPN membranes are capable of separating similar-sized small organic molecules based on their charge and similar charged solutes based on size.

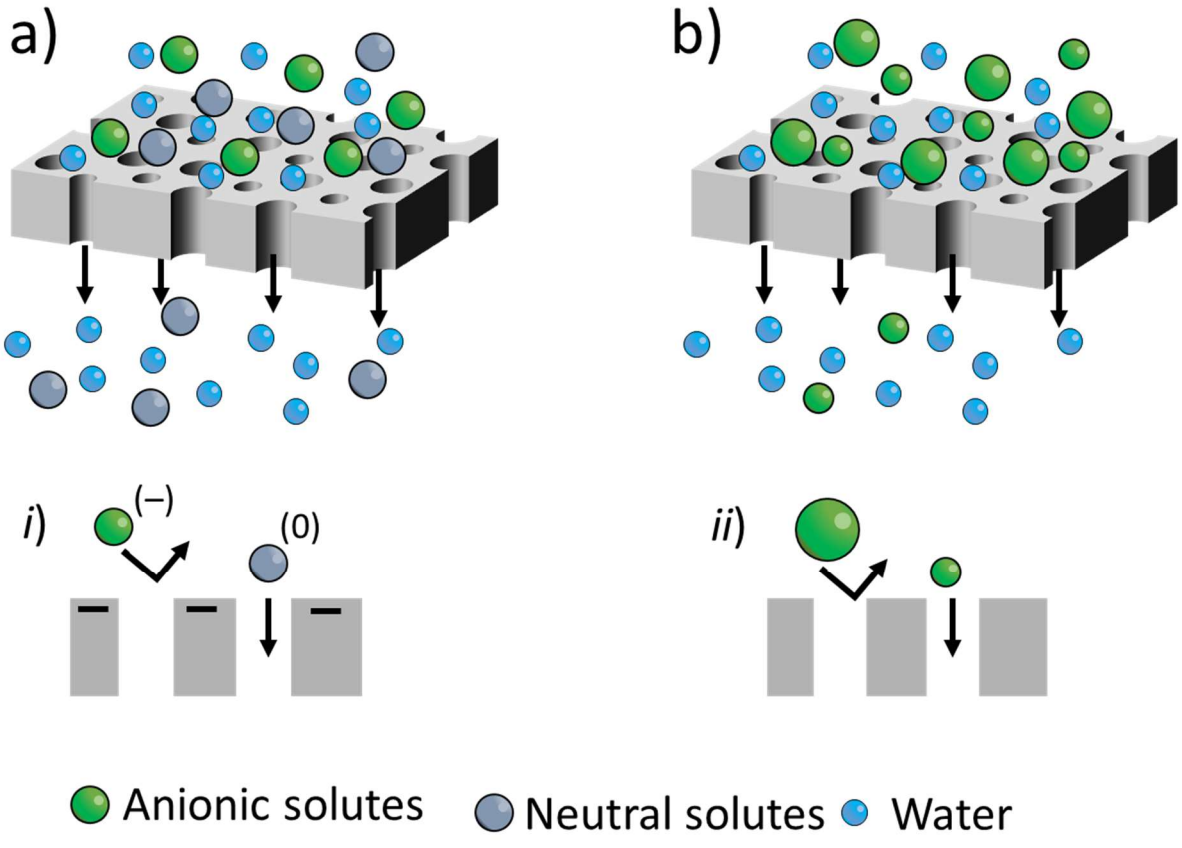

Figure 9.2 *Schematic illustration of the organic solute rejection performance of the MPN membranes with their a) charge-selective and b) size-selective behavior. The mechanism of solute exclusion at the pore entrance for each case is shown as i) charge interaction between the negatively charged membrane surface and the solutes and ii) size exclusion.*

By tuning the TA-Fe^{3+} selective layer's surface microstructure and other physicochemical properties, the selectivity towards various solute combinations were improved. For example, the RB0/NGB3- selectivities were substantially improved when the MPN coating was synthesized using slightly alkaline casting solution (pH 8.5) or at a higher assembly time (Table 2 in Chapter 5, and Table 2 in Chapter 4). The anionic dyes OR-/NGB3- selectivity slightly declines with these conditions due to the higher exclusion of both dyes. Overall, the MPN selective layers containing TFC membranes have shown great potential in fractionation of a mixture of solutes in the feed solution. Membranes that can differentiate solutes in the feed solution based on their size, their functional groups or both are essential for high-efficiency separations in water treatment and the recovery or separation of various industrial byproducts.

9.4. MPN-based membranes for inorganic ion retention

The application of membrane processes involves the removal of both organic and ionic compounds in water and wastewater treatment. NF membranes have a specific feature of ion separation by selectively rejecting multivalent ions while exhibiting a low to moderate retentions towards monovalent ions. The mechanism of ion rejection is strongly dependent on the membrane characteristics and on membrane-ion interactions.

The ion retention and ion-ion separation properties of the fabricated MPN membranes were analyzed in detail using single and mixed salt feed solutions. The separation performance of the selective layer is also correlated with the fabrication parameters during the coating process. Salt removal generally increases when the Fe^{3+} concentration in the casting solution is increased due to the formation of denser selective layer (Figure 3 in Chapter 8). This enhances the exclusion of solutes at the membrane-feed solution interface. Single salt retentions of 73 – 99 % (Na_2SO_4), and 12 – 81 % ($MgCl_2$) were achieved depending on the fabrication parameters. The salt retention behavior followed the sequence Na_2SO_4 > NaCl > $MgSO_4$ > $MgCl_2$ for relatively porous membranes, typical for a negatively charged selective layer with low steric hinderance, indicating that electrostatic interaction plays a significant in the rejection mechanism of single salts. The complexation of divalent cations (Mg^{2+} in this case) with membrane functional groups lowers the membrane charge density thereby reducing the electrostatic repulsive interaction with the co-ions. Hence, Mg^{2+} containing salts are rejected less. For membranes with 0.67 nm and 0.63 nm pore size, $MgSO_4$ overtakes NaCl indicating an increased contribution of size sieving and dielectric exclusion to the rejection mechanism. The TA-Fe^{3+} selective layer containing TFC membranes exhibited an excellent nitrate removal performance. For 100 mg/L

$NaNO_3$ feed concentration, retentions ranging from 83 – 94 % were achieved, outperforming commercial NF membranes (Figure 3 in Chapter 7). Increasing the feed concentration to 850 mg/L (10 mM $NaNO_3$) shows decline in retention to 48.3 – 91.1 %. This decline in retention is attributed to the screening effect due to the shielding phenomenon at high solute concentration, thus diminishing the Donnan potential developed at the membrane surface. On the other hand, the nitrate retention property of the membranes significantly improved when the applied transmembrane pressure increased (Figure 4 in Chapter 7). Similar behavior was observed for Na_2SO_4 retention (Figure S2 in Chapter 10, section 10.2.5). Retention increases with pressure due to the hindered transport of ions while water permeance is linearly proportional to the applied pressure, resulting in a dilute permeate stream.

Membrane characteristics such as pore size, active layer thickness, charge properties, functional groups affect the selectivity of NF membranes during mixed salt retention experiments. Here, the MPN membranes were fine-tuned to enhance their monovalent/divalent ion separation behavior. The membranes exhibit good Cl^-/SO_4^{2-} selectivity, 3.7 – 35.4, from NaCl-Na_2SO_4 mixed salt retention test (Figure 4 and section 3.3 in Chapter 8). A TA-Fe^{3+} layer fabricated at higher $FeCl_3$ casting solution concentration demonstrated a higher selectivity between ions during the filtration tests. For $NaNO_3$-Na_2SO_4 mixtures, the nitrate to sulfate selectivities were in the range 4.5 – 38.1 for different membranes (Figure 5b and section 3.5 in Chapter 7). The Cl^-/SO_4^{2-} or NO_3^-/SO_4^{2-} selectivities are attributed to the smaller ionic size and valence of the monovalent anions that result in their lower exclusion by the negatively charged MPN layer compared to the divalent anion. SO_4^{2-} experiences stronger exclusion due to steric and dielectric effects (due to its higher radius) and Donnan effects (due to its higher charge). Moreover, the monovalent ions have a higher diffusivity (2.032×10^{-9} $m^2 \cdot s^{-1}$ for Cl^- and 1.902×10^{-9} $m^2 \cdot s^{-1}$ for NO_3^-) to diffuse across the pore channels than sulfate (1.06×10^{-9} $m^2 \cdot s^{-1}$). Overall, the membranes show good monovalent/divalent anion selectivity where sulfate concentrated on the retentate stream while Cl^- or NO_3^- rich permeate passes through the membrane. However, the MPN layer does not show any significant difference between the rejection of Cl^- and NO_3^- (Figure 5a in Chapter 7) due to the similar properties of these ions. The Na^+/Mg^{2+} separation performance of the membranes was also explored under different conditions. Na^+ preferentially diffuses through the membrane leading to a low retention in the presence of a divalent cation, Mg^{2+}. The effect of the anion present in the feed solution on cation selectivity is illustrated in Figure 9.3. Up to 330 Na^+/Mg^{2+} selectivity was achieved with sulfate as the common anion, while the Na^+/Mg^{2+} selectivity was only 1 – 3 for $Na^+/Mg^{2+}/Cl^-$ system (Table 2 in Chapter 8). Furthermore, the MPN thin-films exhibited a higher retention towards divalent ions than

monovalent ions when a quaternary ion mixture was used as a feed solution (Figure 6 in Chapter 8). This reiterates their potential in ion separation from multi-ionic mixtures as found in complex streams such as seawater, brackish water, and wastewater. Generally, the TA-Fe^{3+} TFC membranes demonstrated potential for water and wastewater treatment applications.

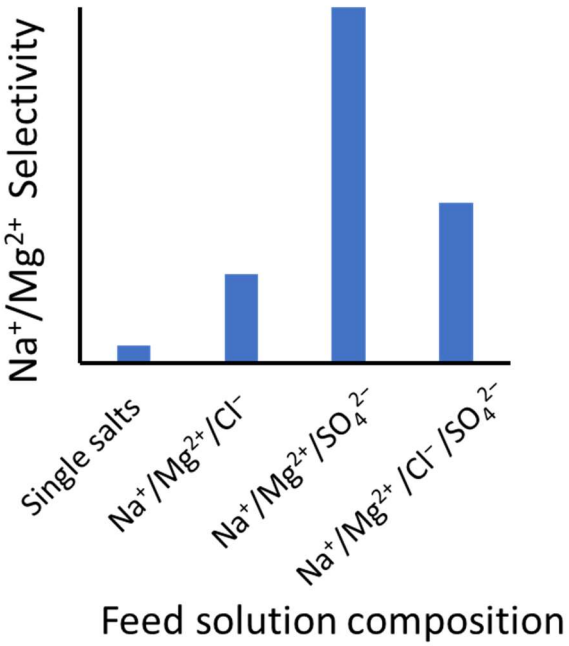

Figure 9.3 *Monovalent/divalent cation selectivity of the MPN membranes for different feed solutions. Single salt selectivity is computed from NaCl and $MgCl_2$ single salt retention tests. The tertiary ion mixtures are prepared from equimolar NaCl-$MgCl_2$ or Na_2SO_4-$MgSO_4$ mixed salt solutions.*

9.5. Modelling ion transport and exclusion

Ion transport through NF membranes is mainly described based on the extended Nernst-Planck equation. Today, Donnan Steric Pore Model with Dielectric Exclusion, DSPM-DE, is the most widely accepted model for predicting the NF performance using mixed electrolytes. This model has been used to analyze the ion separation properties of the MPN membranes in this dissertation. Three investigations have been performed: i) tertiary ion mixture of two anions with a common cation ($Na^+/NO_3^-/SO_4^{2-}$), ii) tertiary ion mixture of two cations with a common anion ($Na^+/Mg^{2+}/Cl^-$), and iii) a quaternary system of mixed ions ($Na^+/Mg^{2+}/Cl^-/SO_4^{2-}$) systems.

The model was used to determine the individual ion transport mechanisms across the membrane. For $Na^+/NO_3^-/SO_4^{2-}$ system, ion transport of the anions is governed by diffusion

(Figure 8 and 9 in Chapter 7). On the other hand, convective flux is the dominant transport mechanism for the cation (Na^+) transport. The NO_3^-/SO_4^{2-} separation analysis demonstrated that selectivity is primarily governed by dielectric exclusion followed by Donnan effects. The computed exclusion coefficients show a 2 – 3 order of magnitude difference in dielectric exclusion coefficient between the nitrate and sulfate ions while it was 1 – 2 orders of magnitude difference for the Donnan partitioning coefficients. Steric exclusion has a minimal effect on monovalent/divalent ion separation. Overall, it can be concluded that nitrate is transported across the membrane via diffusion while its separation at the pore entrance is dominated by dielectric exclusion. Furthermore, as observed from a sensitivity analysis, of the membrane characteristics, pore dielectric constant significantly influences the retention and selectivity of anions (Figure 10 in Chapter 7) followed by pore size, membrane charge density and effective film thickness. For example, a 25 % increase in pore dielectric constant leads to high NO_3^-/SO_4^{2-} selectivity. Different strategies can be followed to fine-tune membrane characteristics to achieve a high nitrate separation. For instance, the concentration, assembly time, pH, number of layers deposited can be varied to fabricate a TA-Fe^{3+} selective layer of precise pore size. This emphasizes the significance of the model in determining membrane parameters to be optimized to enhance ion separation.

During monovalent/divalent cations separation test ($Na^+/Mg^{2+}/Cl^-$ system), ion partitioning at the feed solution-membrane interface was mainly dominated by two counteracting effects. In this system, the dielectric effect leads to a higher exclusion of Mg^{2+}, which is excluded more than Na^+ due to its higher valence and ionic radius. On the other hand, due to the negative surface charge of the MPN membranes, Mg^{2+} is preferentially partitioned into the membrane pores via Donnan effect. However, the overall selectivity is determined by the cumulative effect of the exclusion mechanisms, which was reflected in the higher rejection of Mg^{2+} compared to Na^+ (Figure 7 in Chapter 8). Na^+ exhibits higher overall flux towards the permeate side, consistent with the observed rejection (Figure 8 in Chapter 8). The mass transport mechanisms governing ion transport were successfully determined, showing a convective flux dominated flux of ions from the feed side towards the permeate stream. Here, an electromigrative flux oriented towards the feed side was found for the cations due to the generation of an electric field.

The application of the DSPM-DE in describing ion retention behavior of the fabricated TFC membranes was also extended to quaternary ion mixtures. The model shows a good fit of the experimental rejection results. Ion exclusion and transport mechanisms were successfully

computed, illustrating the mechanisms of ion separation by the MPN layers. Overall, the DSPM-DE provides a comprehensive analysis of ion separation by the TA-Fe^{3+} membranes. The model sufficiently predicts and describes ion transport and illustrates the performance of the selective layers towards diverse mixtures. Mathematical transport models are essential to realize the application potential of membranes and accurately predict their performance. Such models can simplify the design of NF membranes to enhance process optimization.

References

[1] H. B. Park, J. Kamcev, L. M. Robeson, M. Elimelech, and B. D. Freeman, "Maximizing the right stuff: The trade-off between membrane permeability and selectivity," *Science,* vol. 356, no. 6343, 2017.

[2] H. Ejima *et al.*, "One-Step Assembly of Coordination Complexes," *Science,* vol. 341, no. 6142, pp. 154-157, 2013.

[3] Y. Ping *et al.*, "pH-Responsive Capsules Engineered from Metal–Phenolic Networks for Anticancer Drug Delivery," *Small,* vol. 11, no. 17, pp. 2032-2036, 2015.

[4] J. Li, S. S. Yuan, J. Y. Zhu, and B. Van der Bruggen, "High-flux, antibacterial composite membranes via polydopamine-assisted PEI-TiO2/Ag modification for dye removal," *Chemical Engineering Journal,* vol. 373, pp. 275-284, 2019.

[5] J. Wang *et al.*, "High flux electroneutral loose nanofiltration membranes based on rapid deposition of polydopamine/polyethyleneimine," *Journal of Materials Chemistry A,* vol. 5, no. 28, pp. 14847-14857, 2017.

Chapter 10. Appendix

10.1. Toxicity of Chemicals

Table 10.1 *List of chemicals used for the synthetic and analytical experiments of this PhD study with GHS symbol, H- and P-data.*

Substance	**GHS Symbol**	**Hazard Statement**	**Precautionary statement**
Orange II	GHS07	H372, H412	P260, P264, P270, P273, P314, P501
Rhodamine B	GHS07, GHS05	H302, H318, H412	P264, P273, P280, P301+P312, P305+P351+P338, P501
Riboflavin	-	-	-
Naphthol green B	-	-	-
Poly(ethylene glycol)	-	-	-
Hydrochloric acid	GHS05, GHS07	H290, H314, H335	P280, P301+P330+P331, P305+P351+P338, P308+P310
Sodium hydroxide	GHS05	H314	P280, P305+P351+P338, P310
Iron (III) chloride hexahydrate	GHS05, GHS07	H290, H302, H315, H318	P234, P264, P280, P301+P312, P302+P352, P305+P351+P338
Tannic Acid	-	-	-
Humic acid	-	-	-
Sodium chloride	-	-	-
Magnesium chloride hexahydrate	-	-	-
Magnesium sulfate	-	-	-
Sodium sulfate	-	-	-

Sodium nitrate	GHS03, GHS07	H272, H319	P210, P220, P264, P280, P305+P351+P338, P337+P313

10.2. Online accessible supporting information

10.2.1. Charge and size selective thin film composite membranes having tannic acid–Ferric ion network as selective layer

The following section contains the supplementary material to the article in chapter 3 of the cumulative part of the thesis, both available online with Doi: 10.1016/j.memsci.2023.121709

Charge and size selective thin film composite membranes having tannic acid – ferric ion network as selective layer

Hluf Hailu Kinfu[a], Md. Mushfequr Rahman[a,*], Erik Sebastian Schneider[a], Nicolás Cevallos-Cueva[a], and Volker Abetz[a,b]

[a] Helmholtz-Zentrum Hereon, Institute of Membrane Research, Max-Planck-Straße 1, 21502 Geesthacht, Germany.
[b] University of Hamburg, Institute of Physical Chemistry, Martin-Luther-King-Platz 6, 20146 Hamburg, Germany.
* Corresponding author. E-mail address: mushfequr.rahman@hereon.de

Supporting information

The number of layers constructed on the PAN substrate was increased by sequential monomer treatments. One layer of TA-Fe^{3+} self-assembled film, synthesized by immersing in TA and metal salt solution of 1:4.5 weight ratio, had a water permeance of 226 $L•m^{-2}•h^{-1}•bar^{-1}$. Compared to the PAN water flux, one layer of MPN's high flux shows almost no continuous coverage of the support materialized. However, more than two layers of deposited film displayed a very sharp drop in pure water permeance, Figure S1. Two and three layers of selective layer displayed 13.5 and 1.55 $L•m^{-2}•h^{-1}•bar^{-1}$ pure water permeance (PWP). Conversely, an exceedingly tight nanofiltration membrane of 0.37 $L•m^{-2}•h^{-1}•bar^{-1}$ water permeance was obtained for four-layered TA-ferric ion self-assembly. The concept of increasing layer number is closely related to polyelectrolyte multilayer formation. In a sense, film grows linearly in thickness with increase of layer number, which can be associated with decline in flux. Furthermore, with each cycle, newly added TA or metal ions can react with uncoordinated monomers from the already deposited film. Coordination number of TA is increased. The coordination continues resulting in an increased thickness due to longitudinal film growth provided that functional groups of –OH as well as Fe^{3+} are present on the substrate surface and in solution.

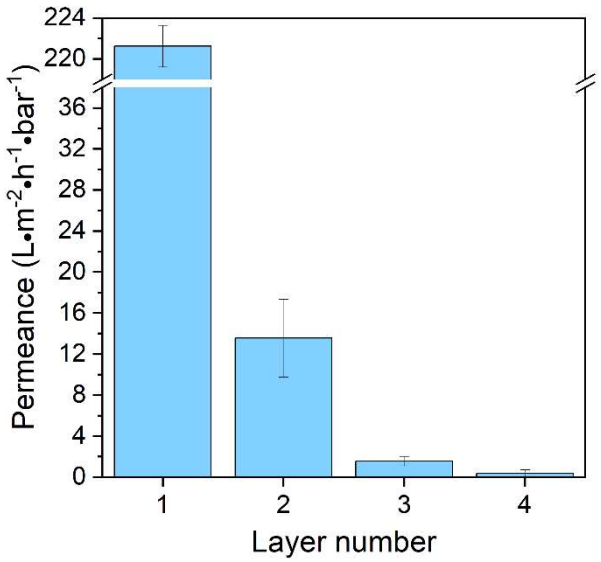

Figure S1. Influence of number of TA-Fe^{3+} layers deposited on PAN surface on pure water permeance using 1:4.5 ratio of tannic acid to $FeCl_3 \cdot 6H_2O$.

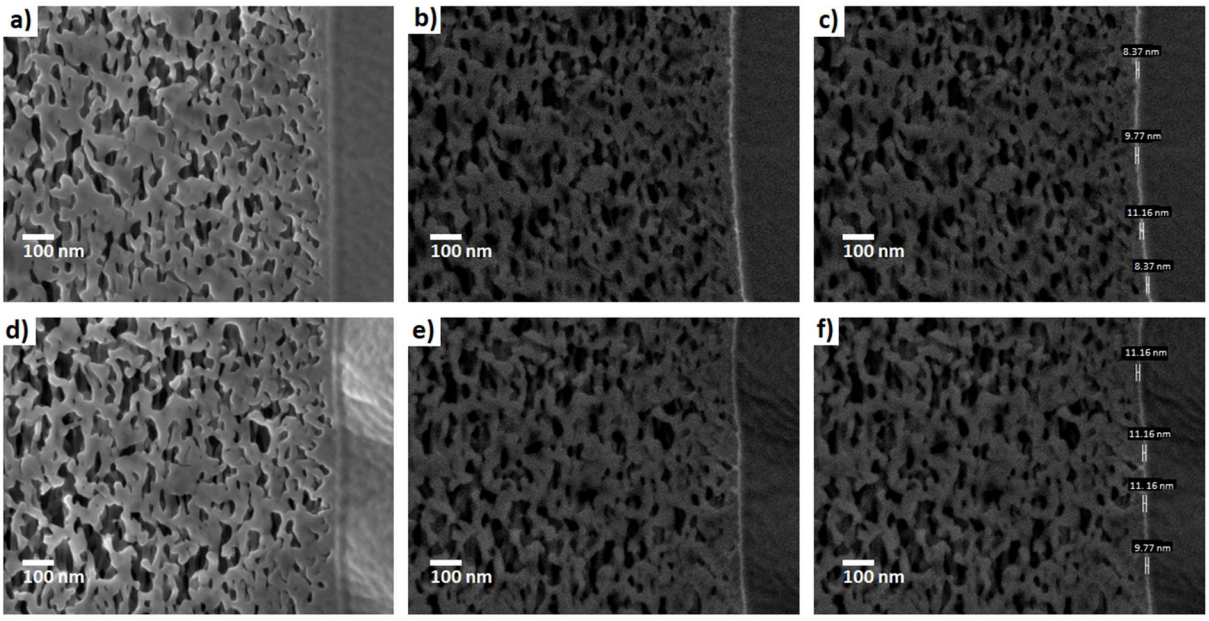

Figure S2. SEM images of Argon ion milled cross-sections. Measurement of selective layer thickness of 1TA-8Fe membrane using ESB images (b-c; e-f) showing that the average layer thickness is around 10 nm. Two samples; first raw for sample01 and second raw for sample02.

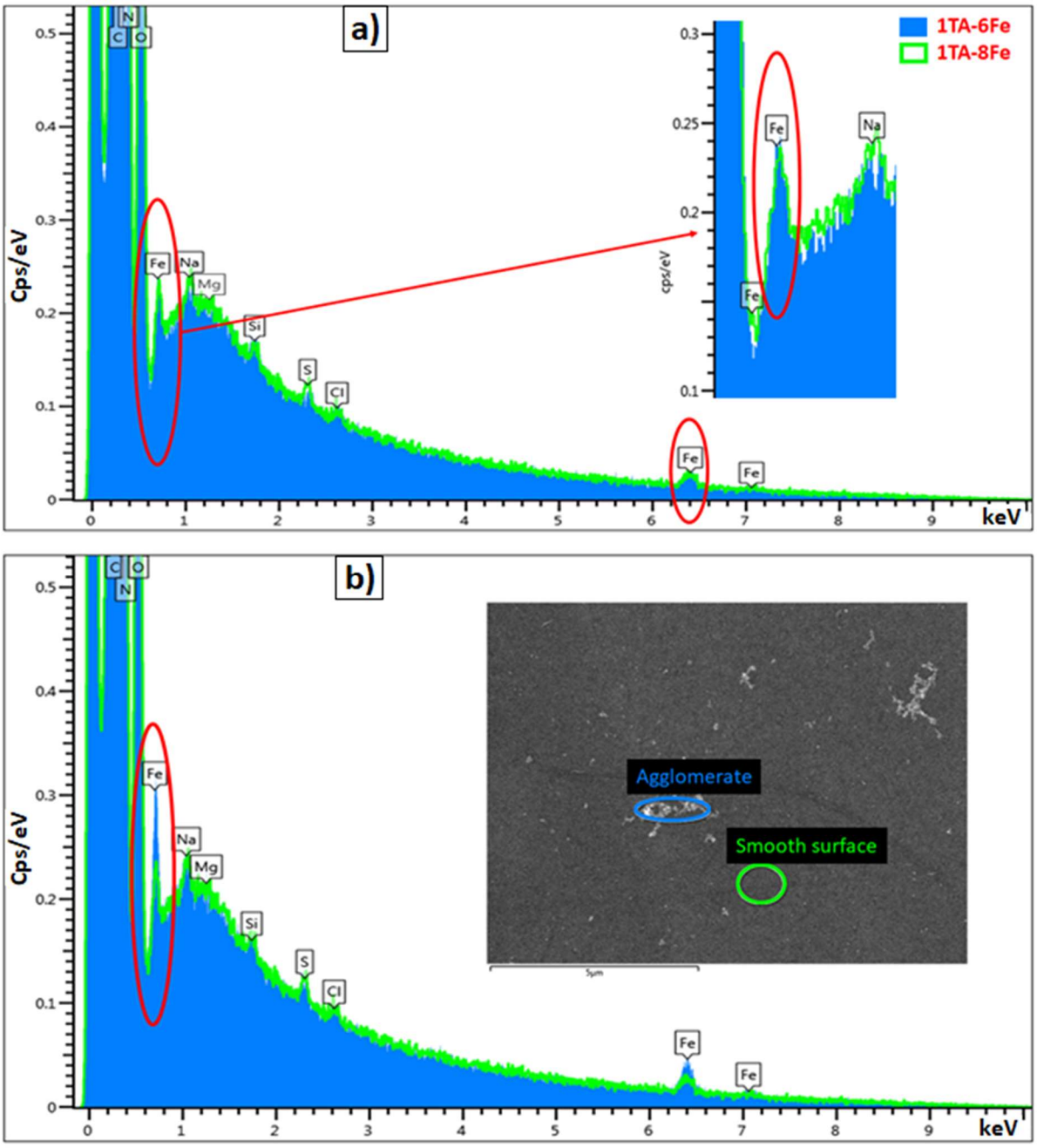

Figure S3. Energy dispersive x-ray (EDX) spectroscopy of membrane surfaces. (a) Comparison of a 1TA-6Fe and a 1TA-8Fe membrane. EDX could not show any difference between the two samples in the Fe content at agglomeration-free sites. (b) EDX analysis of a 1TA-8Fe membrane surface. Comparison of an agglomeration-free and an agglomeration-positive site; EDX revealed that the agglomerates on the sample surface do not represent any contaminants, but consist mainly of Fe.

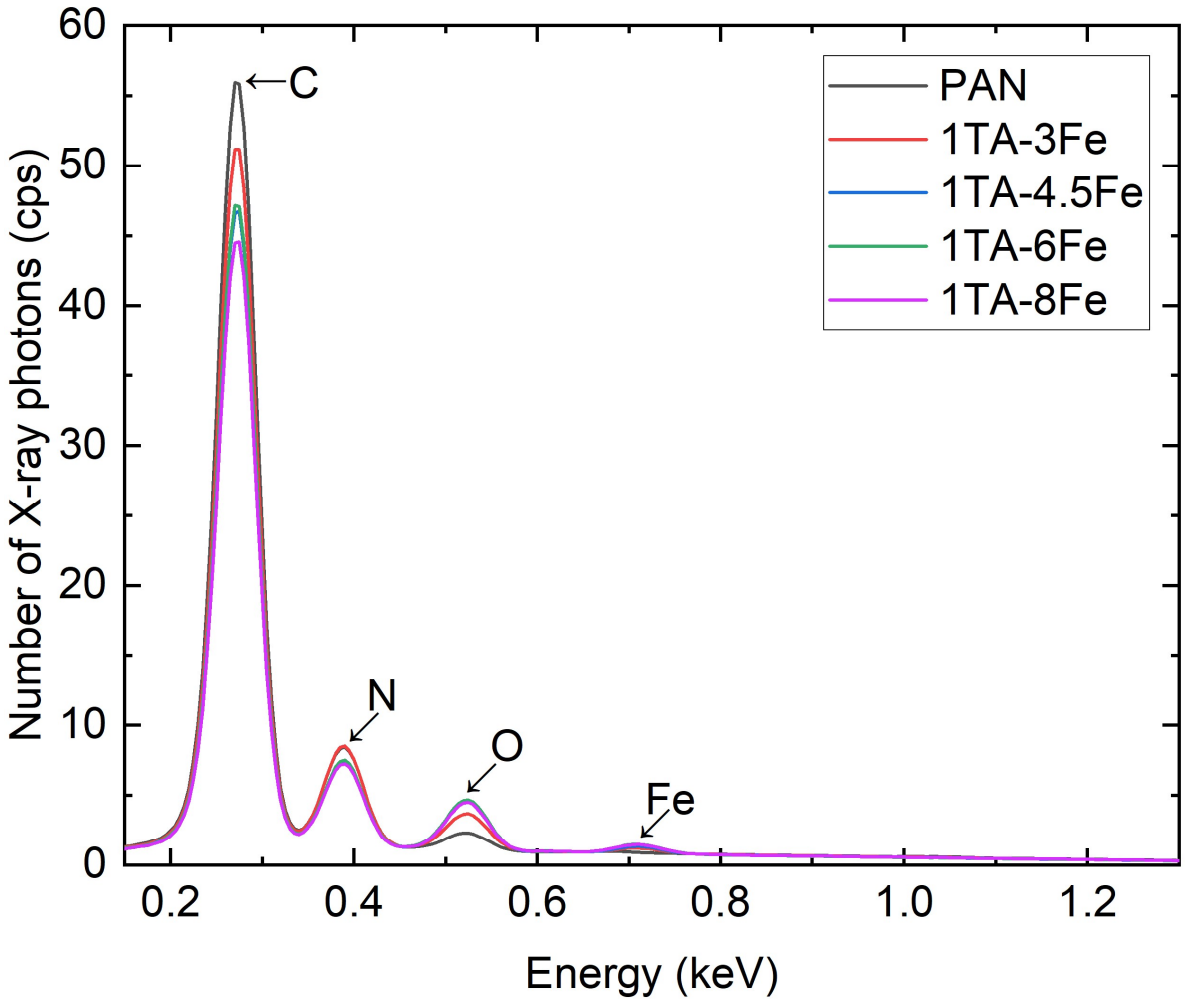

Figure S4. EDX spectra of PAN and TA-Fe^{3+} membrane synthesized at different weight ratio

Table S1. Peak intensities of Fe and O (in counts/s) from EDX analysis after normalization

	PAN	1TA-3Fe	1TA-4.5Fe	1TA-6Fe	1TA-8Fe
Fe	0.9021	1.2250	1.4107	1.5886	1.5405
O	2.2914	3.7289	4.7262	5.0420	4.7173
After Subtracting the PAN support contribution					
Fe	0.0	0.3229	0.5085	0.6865	0.6384
O	0.0	1.4375	2.4349	2.7506	2.4259

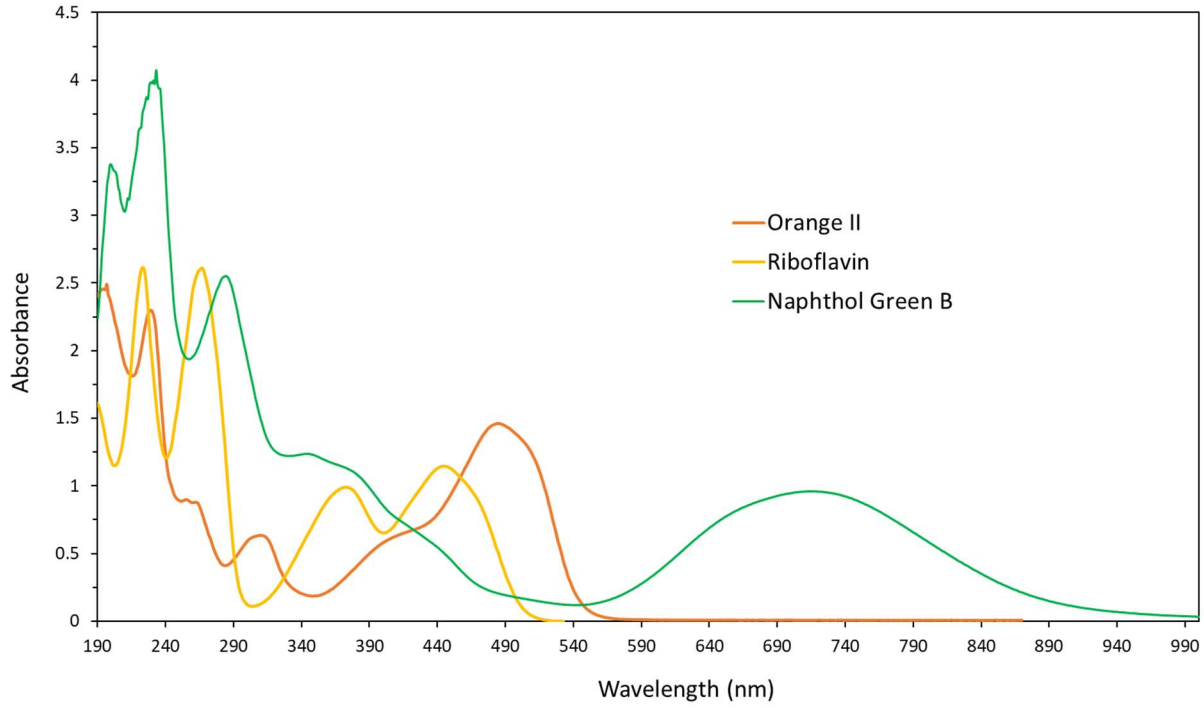

Figure S5. UV-vis light absorption spectrum of Orange II, Riboflavin, and Naphthol green B with absorption peaks at wavelength of 482 nm, 444 nm, and 715 nm, respectively.

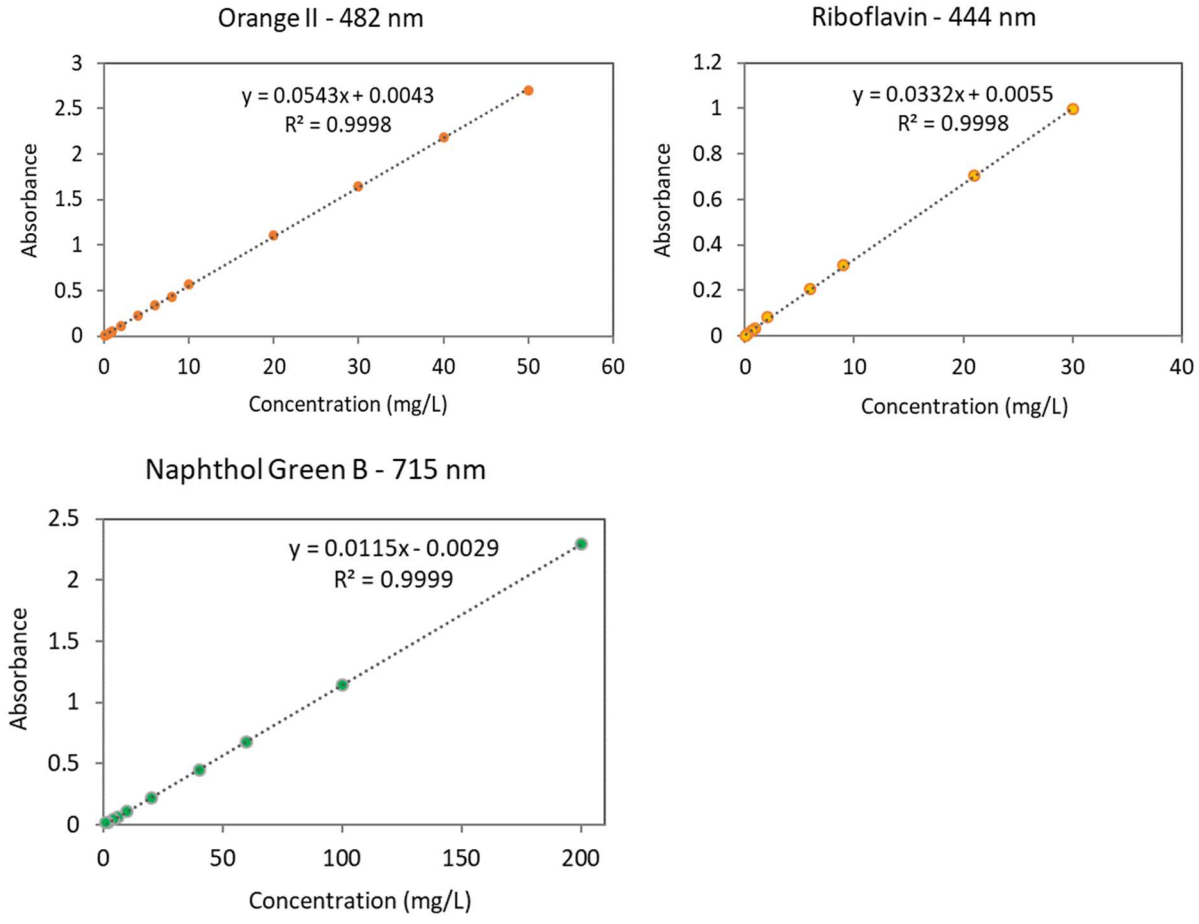

Figure S6. Calibration curves of dyes concentration using UV-vis spectrophotometer

Pore size analysis was performed with the software IMS (Imagic Bildverarbeitung AG, Switzerland). For the analysis, we recorded InLens secondary electron detector images with a magnification of 100 kx (image resolution = 1.1 nm) at four different positions for each sample. The medium pore diameter and the area ratio of open pores to the total surface (surface porosity) were determined. The generated images are shown in figure S7. Pores with an area smaller than 5 nm^2 were excluded from the analysis due to the limitations of the SEM to demonstrate a sub-nanometer or a few nanometers resolution. Figure S8 presents the pore size distribution of the analyzed membranes. The pore size analysis of top surface images revealed a shift in the pore size distribution curve towards smaller pores in the order of PAN > 1TA-1Fe > 1TA-3Fe. The number of open pores (total sum of the frequencies) was also reduced. This was in agreement with the SEM images of figure 2 of the main manuscript. However, only a few surface pores were detected in the 1TA-4.5Fe and 1TA-6Fe membranes while no pores were observed in the 1TA-8Fe membrane. It is obvious that smaller pores having less than 5 nm^2 area increase as the Fe concentration increases. However, due to the resolution limitation of the SEM, those surface pores from the images of the tight nanofiltration membranes were not recognized. The few pores for 1TA-4.5Fe (figure S8d) and 1TA-6Fe (figure S8e) membranes are therefore pinholes and do not constitute the average pore size characteristics. It can be observed from figure S7 and table S2 that the decline in the number of open pores is highly related to the increase in surface coverage of the PAN support by the metal-phenolic network at high Fe concentration. Furthermore, the porosity of the TFC membranes decreased demonstrating the formation of a dense separation layer as the Fe concentration was increased (table S2). Owing to these inherent errors involved in the values of pore size, number of pores and porosity of table S2, we did not use these values to interpret the characteristics of the membrane.

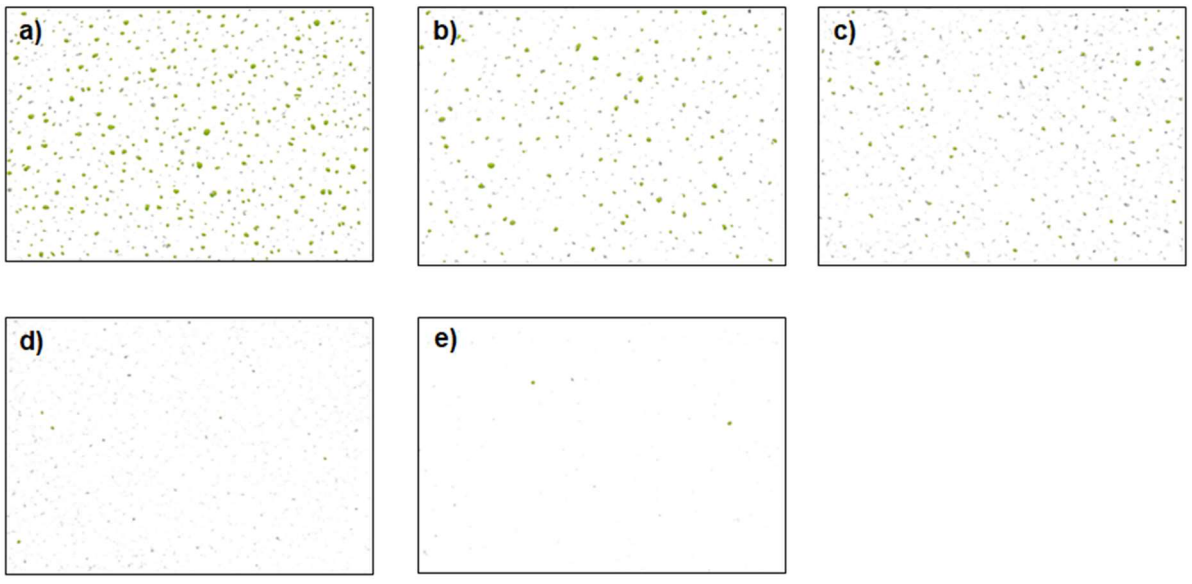

Figure S7. Surface pores of the PAN and TA-Fe^{3+} membranes as analyzed with the IMS (Imagic Bildverarbeitung AG) software from top surface SEM images; a) pristine PAN, b) 1TA-1Fe, c) 1TA-3Fe, d) 1TA-4.5Fe, and e) 1TA-6Fe membranes. Green agrea represents surface pores while the white area depicts the dense surface.

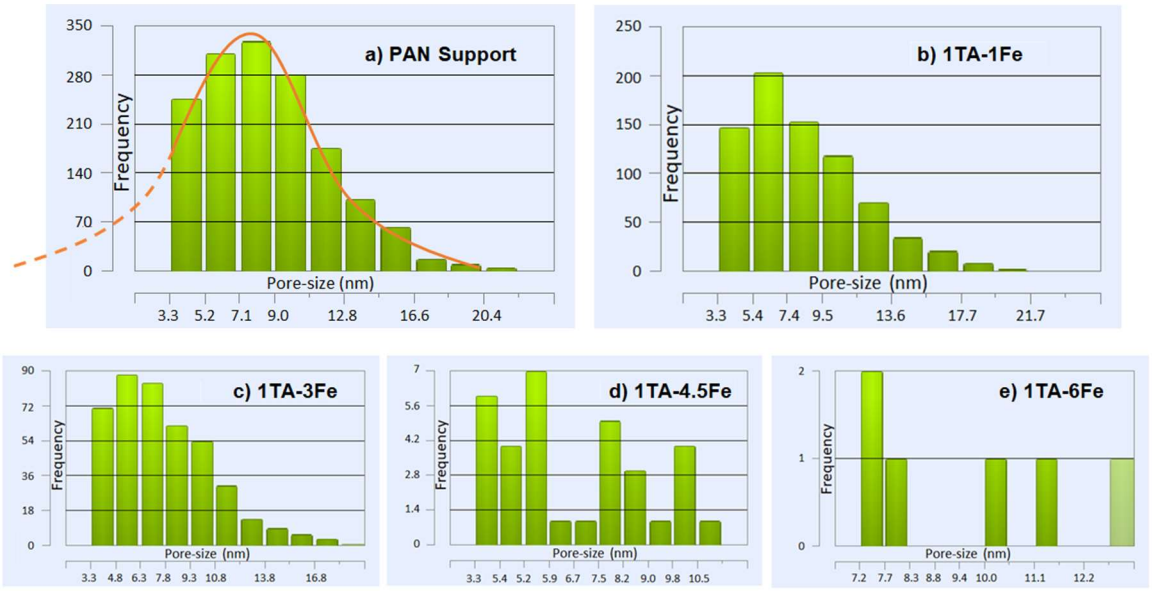

Figure S8. Pore size distribution of the porous PAN support and TA-Fe^{3+} membranes fabricated at different tannic acid to $FeCl_3 \cdot 6H_2O$ weight ratio.

Table S2. Porosity, avergae pore size, and pore count generated from the analysis

	PAN	**1TA-1Fe**	**1TA-3Fe**	**1TA-4.5Fe**	**1TA-6Fe**	**1TA-8Fe**
Number of open pores [total]	(n=1546)	(n=764)	(n=424)	(n=33)	(n=6)	(n=0)
Pore diameter [nm]	8.8 ± 3.5	8.5 ± 3.5	7.8 ± 3.0	6.7 ± 2.2	9.6 ± 2.1	n.a.
Porosity [%]	2.346 ± 0.444	1.171 ± 0.289	0.592 ± 0.224	0.025 ± 0.014	0.117 ± 0.070	0.0 ± 0.0

* Given values are mean values ± standard deviation; n= total number of pores from 4 samples of the same membrane.

10.2.2. Using the Assembly Time as a Tool to Control the Surface Morphology and Separation Performance of Membranes with a Tannic Acid–Fe^{3+} Selective Layer

The following is the supporting information to the article in chapter 4 of the cumulative part of the thesis. It is available online at Doi: 10.3390/membranes14060133/s1

Supplementary information

Using the assembly time as a tool to control the surface morphology and separation performance of membranes with a tannic acid–Fe^{3+} selective layer

Hluf Hailu Kinfu[1], Md. Mushfequr Rahman[1,*], Erik S. Schneider[1], Nicolás Cevallos-Cueva[1], and Volker Abetz[1,2]

[1] Helmholtz-Zentrum Hereon, Institute of Membrane Research, Max-Planck-Straße 1, 21502 Geesthacht, Germany.

[2] University of Hamburg, Institute of Physical Chemistry, Martin-Luther-King-Platz 6, 20146 Hamburg, Germany.

* Correspondence: mushfequr.rahman@hereon.de; Tel.: +49-415-287-2446

Salt Rejection Performance of the TA-Fe^{3+} TFC Membranes

Evaluation of Membrane Performance: The membrane rejection towards a salt solution was evaluated with a 1 g/L Na_2SO_4 filtration experiment. We used the dead-end filtration mode of a stirred test cell from Millipore (EMD Millipore XFUF07601) at a stirring speed of 350 rpm, and a 2.13 cm^2 membrane active area was used. Membrane compaction was carried out for at least 3 h at 4 bar before rejection tests were performed at 3 bar transmembrane pressure. The concentrations of the feed, permeate and retentate samples from the rejection test of the Na_2SO_4 aqueous solution were analyzed using ion chromatography (Dionex ICS600, Thermofischer Scientific Inc., USA).

The rejection characteristics of the membranes were then evaluated as follows:

$$R\ (\%) = \left(1 - \frac{C_p}{(C_f + C_r)/2}\right) * 100 \qquad (S1)$$

where R is solute retention, and C_p, C_f and C_r are the concentrations of the permeate, concentration of the feed and concentration of retentate solutions in $mg \cdot L^{-1}$, respectively. The

average of the feed and retentate concentrations was taken to account for the small change in feed-side concentration in the dead-end filtration mode.

The solution permeance, P_s ($L \cdot m^{-2} \cdot h^{-1} \cdot bar^{-1}$), was calculated using the following equation:

$$P_s = \frac{V}{A * \Delta t * \Delta P} \qquad (S2)$$

where V (L) is the volume of permeate collected, A (m^2) is the effective area of the membrane, Δt (h) is the filtration time and ΔP (bar) is the applied transmembrane pressure.

Results and Discussion

The ion rejection performance of the membranes is presented in Figure S1. Sulfate rejection by the PAN support was only 2.8 ± 1 %, which demonstrated that ions can easily permeate the porous support. The rejection of sulfate was notably higher in the self-assembled TFC membranes than the pristine support. Consistent with the large pore sizes, the TA-Fe^{3+} membranes synthesized at 1 min (MPN-1) and 2.5 min (MPN-2.5) showed relatively low rejection of Na_2SO_4. However, when the assembly time was increased, the pore size was reduced significantly, which further contributed to the enhanced rejection of SO_4^{2-} ions. The membranes fabricated at coating times of 4 min (MPN-4) and 6 min (MPN-6) had 90.4% and 97.3% sulfate rejection, respectively. Salt rejection is mainly affected by steric hindrance, dielectric exclusion and electrostatic repulsive effects [1-3]. Sulfate is a divalent anion that can be highly rejected by negatively charged surfaces due to the Donnan exclusion effect, and strong electrostatic repulsion between the negatively charged TA-Fe^{3+} surface and SO_4^{2-} anions contributes to the overall rejection of the membranes. However, as the TFC membranes showed similar surface zeta potentials (Figure 2e in the main manuscript), the differences in rejection for the membranes fabricated at different assembly times are attributed to the change in pore size, a variation that affects both steric and dielectric exclusion. The latter stems from a decreased dielectric constant of the solvent inside small confined pores and the developed solvation energy barrier [4].

A comparison of the salt retention performance levels of the membranes with those of other tannic acid–metal ion membranes published in the literature is provided in Table S2.

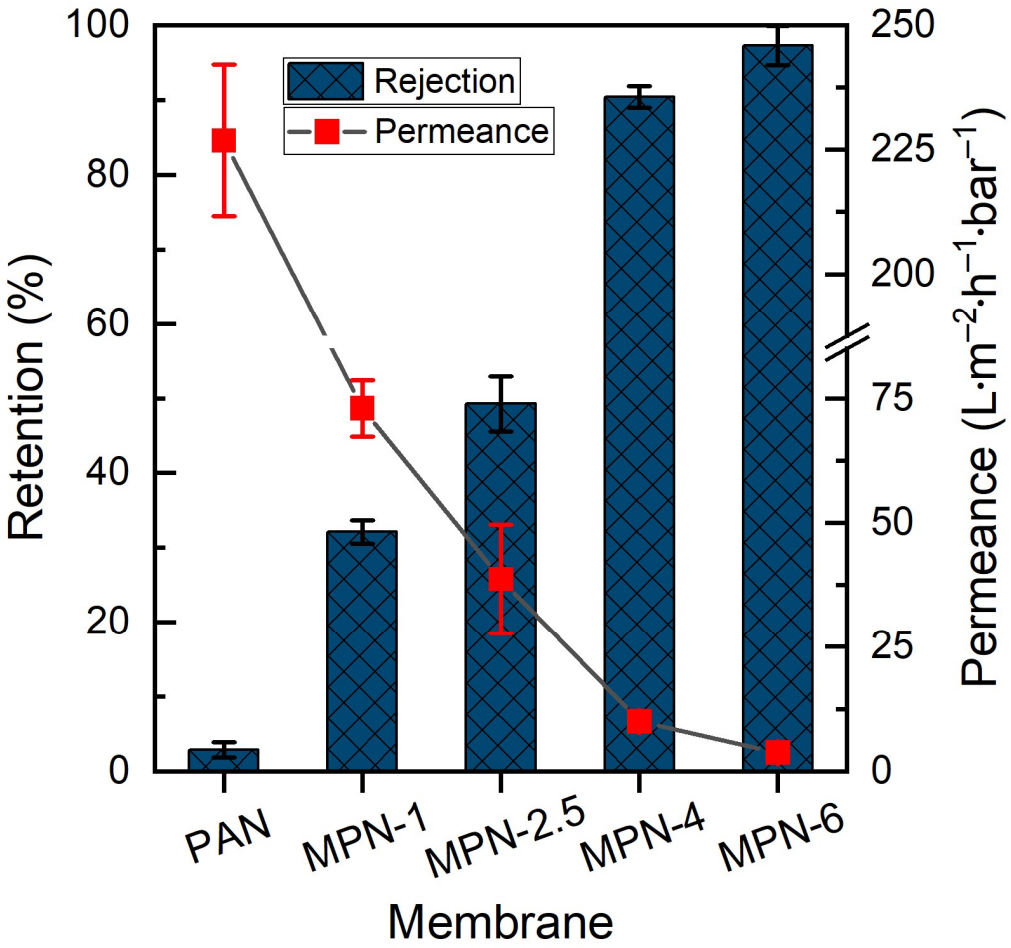

Figure S1. Sulfate ion rejection of the fabricated membranes and their respective salt solution permeance. A salt solution of 1 g/L Na_2SO_4 was used as a feed solution. The solid line is added to guide the eye.

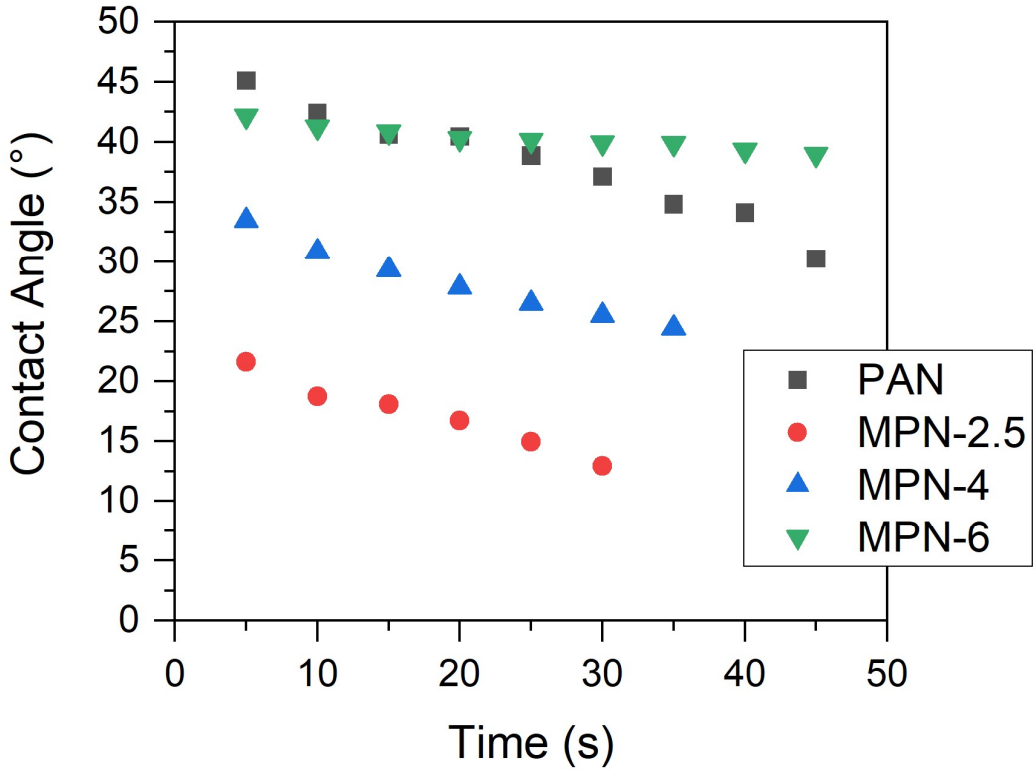

Figure S2. Surface wettability of the pristine PAN and TA-Fe^{3+} membranes fabricated at different assembly times.

Table S1. Theoretical Fe/O ratios in the three different complex states of TA-Fe^{3+} self-assembly. Although TA contains 46 oxygens in its elemental structure, only 25 from the hydroxyl groups of catechol and galloyl moieties can coordinate with metal ion centers.

Complexation state	Number of ligands and metal ions present in the complex	Total oxygen in the complex state	Number of total OH groups capable of coordination	Number of OH groups coordinating with 1 Fe center	Fe centers required for total coordination of available (capable) OH groups	Fe/O ratio in the complex state
Mono-complex	1TA-1Fe	46	25	2	12.5	0.27
Bis-complex	2TA-1Fe	92	50	4	12.5	0.14
Tris-complex	3TA-1Fe	138	75	6	12.5	0.09

Table S2. Comparison of the Na_2SO_4 separation performance of the fabricated selective layers and the TA-M^{n+} membranes using porous supports in the literature.

Membranes	Synthesis Method	Assembly time	Pure water permeance ($L \cdot m^{-2} \cdot h^{-1} \cdot bar^{-1}$)	Na_2SO_4 rejection (%)	Operating conditions	Ref.
TA−Fe^{3+}/PES	Co-deposition	1 min	5.5	89.7	3.4 mM Na_2SO_4 at 3 bar	[5]
TA−Fe^{3+}/PAN−COOH	Co-deposition	2 min	13.6	90.2	1 g/L Na_2SO_4 at 0.5 MPa	[6]
TA−Fe^{3+}/PAN	LBL	1 min	40.9	15.0	dye/ Na_2SO_4 solution at 0.2 MPa	[7]
TA−Fe^{3+}/PAN	Co-deposition	1 min	14.2	87.6	1 g/L Na_2SO_4 at 3 bar	[8]
TA−Cu^{2+}/PAN	Co-deposition	10 min	52	17	-	[9]
TA−Fe^{3+}/PES	Co-deposition	1 min	17.2	62.1	1 g/L Na_2SO_4 at 0.2 MPa	[10]
TA−Ti^{4+}/PSf	Co-deposition	9 h	9.5	70.3	5 mM Na_2SO_4 at 0.2 MPa	[11]
TA−Fe^{3+}/PAN−COOH	Contra-diffusion	7 min	7.4	95.6	1 g/L Na_2SO_4 at 25 °C and 0.6 MPa	[12]
TA−Fe^{3+}/PAN	LBL	2.5 min	39.8	49.3	1 g/L Na_2SO_4 at 3 bar	This work
		4 min	13.5	90.4	1 g/L Na_2SO_4 at 3 bar	This work
		6 min	5.6	97.3	1 g/L Na_2SO_4 at 3 bar	This work

* TA-M^{n+}, tannic acid−metal ion; PAN, polyacrylonitrile; PAN−COOH, hydrolyzed polyacrylonitrile; PSf, polysulfone; PES, polyethersulfone; LBL, layer by layer

References

[1] A. Escoda, S. Deon, and P. Fievet, "Assessment of dielectric contribution in the modeling of multi-ionic transport through nanofiltration membranes," *Journal of Membrane Science,* vol. 378, no. 1-2, pp. 214-223, 2011.

[2] P. Fievet, "Donnan Steric Pore (DSP) and Dielectric Exclusion (DE) Model," in *Encyclopedia of Membranes*, E. Drioli and L. Giorno, Eds. Berlin, Heidelberg: Springer Berlin Heidelberg, 2015, pp. 1-5.

[3] A. Szymczyk and P. Fievet, "Investigating transport properties of nanofiltration membranes by means of a steric, electric and dielectric exclusion model," *Journal of Membrane Science,* vol. 252, no. 1-2, pp. 77-88, 2005.

[4] D. L. Oatley *et al.*, "Investigation of the dielectric properties of nanofiltration membranes," *Desalination,* vol. 315, pp. 100-106, 2013.

[5] H. Guo, L. E. Peng, Z. Yao, Z. Yang, X. Ma, and C. Y. Tang, "Non-Polyamide Based Nanofiltration Membranes Using Green Metal-Organic Coordination Complexes: Implications for the Removal of Trace Organic Contaminants," *Environmental Science and Technology,* vol. 53, no. 5, pp. 2688-2694, 2019.

[6] D. Liu, Y. Chen, T. T. Tran, and G. Zhang, "Facile and rapid assembly of high-performance tannic acid thin-film nanofiltration membranes via Fe^{3+} intermediated regulation and coordination," *Separation and Purification Technology,* vol. 260, 2021, Art. no. 118228.

[7] Y. Xiao *et al.*, "Facile fabrication of superhydrophilic nanofiltration membranes via tannic acid and irons layer-by-layer self-assembly for dye separation," *Applied Surface Science,* vol. 515, 2020, Art. no. 146063.

[8] L. E. Peng, Z. Yao, J. Chen, H. Guo, and C. Y. Tang, "Highly selective separation and resource recovery using forward osmosis membrane assembled by polyphenol network," *Journal of Membrane Science,* vol. 611, pp. 118305-118305, 2020.

[9] T. Chakrabarty, L. Pérez-Manríquez, P. Neelakanda, and K. V. Peinemann, "Bioinspired tannic acid-copper complexes as selective coating for nanofiltration membranes," *Separation and Purification Technology,* vol. 184, pp. 188-194, 2017.

[10] L. Fan *et al.*, "Green coating by coordination of tannic acid and iron ions for antioxidant nanofiltration membranes," *RSC Advances,* vol. 5, no. 130, pp. 107777-107784, 2015.

[11] H. Wu, J. Xie, and L. Mao, "One-pot assembly tannic acid-titanium dual network coating for low-pressure nanofiltration membranes," *Separation and Purification Technology,* vol. 233, no. September 2019, pp. 116051-116051, 2020.

[12] Y. X. Wang *et al.*, "Metal-Polyphenol Coordination at the Aqueous Contra-diffusion "Interface": A Green Way to High-Performance Iron(III)/Tannic Acid Thin-Film-Composite Nanofiltration Membranes," *Langmuir,* vol. 38, no. 45, pp. 13793–13802, 2022.

10.2.3. Nanofiltration Membranes Containing a Metal–Polyphenol Network Layer: Using Casting Solution pH as a Tool to Tailor the Separation Performance

The Supporting Information to the article in chapter 5 of the cumulative part of the dissertation is provided next. It can also be accessed online with Doi: 10.1021/acsomega.4c04804

Nanofiltration membranes containing a metal-polyphenol network layer: using casting solution pH as a tool to tailor the separation performance

Hluf Hailu Kinfu[a], *Md. Mushfequr Rahman*[a,*], *Nicolás Cevallos-Cueva*[a], *and Volker Abetz*[a,b]

[a] Helmholtz-Zentrum Hereon, Institute of Membrane Research, Max-Planck-Straße 1, 21502 Geesthacht, Germany.

[b] University of Hamburg, Institute of Physical Chemistry, Martin-Luther-King-Platz 6, 20146 Hamburg, Germany.

* Corresponding author. E-mail address: mushfequr.rahman@hereon.de

Supporting information

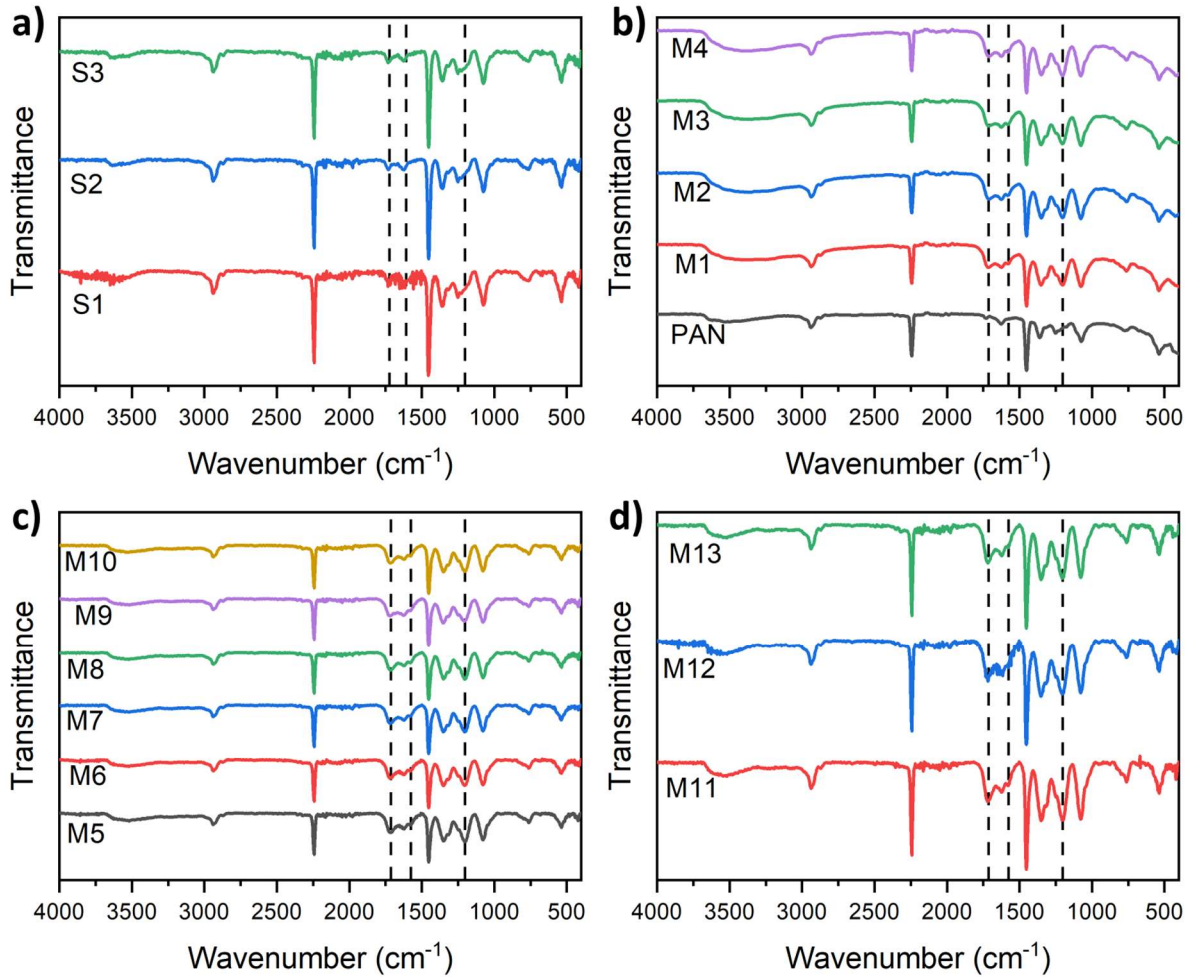

Figure S1. FTIR spectra of a) single TA-Fe^{3+} layered (S1 – S3), b-d) double TA-Fe^{3+} (M1 – M13) layered thin-film composite membranes prepared at various pH of the tannic acid solution.

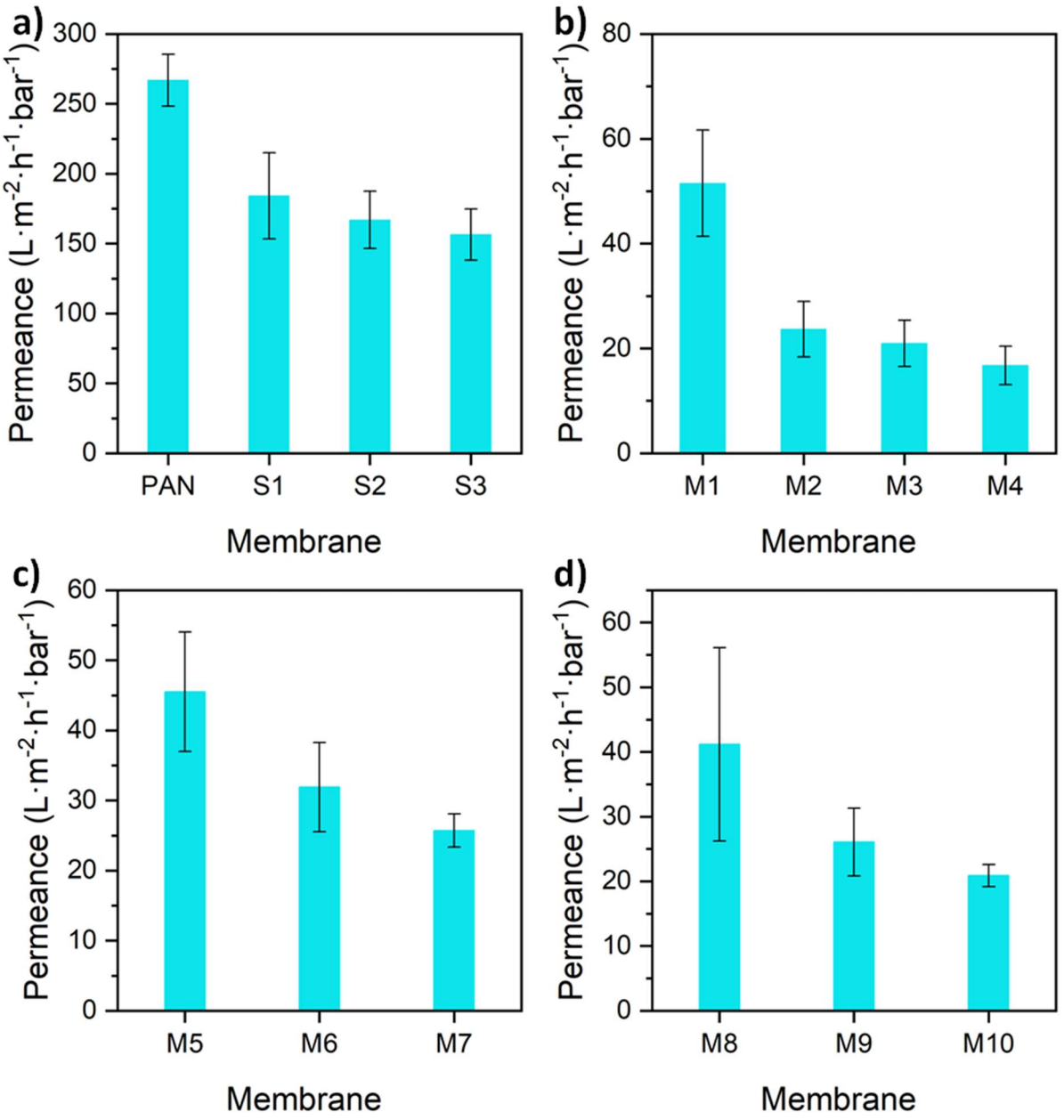

Figure S2. Pure water permeance of MPN TFC membranes: a) single TA-Fe^{3+} coating layer fabricated at different pH of TA solution, b) double TA-Fe^{3+} layered TFC membranes at which both layers were fabricated at the same pH of TA solution, c) double TA-Fe^{3+} layered TFC membranes in which the first layer was synthesized at low pH (pH 3) and the second layer at a higher pH of the TA solution, and d) double TA-Fe^{3+} layered TFC membranes in which the first layer was fabricated at high pH (pH 8.5) while the second layer was at a lower pH. For the complete fabrication conditions, the reader is referred to Table 1 of the main manuscript.

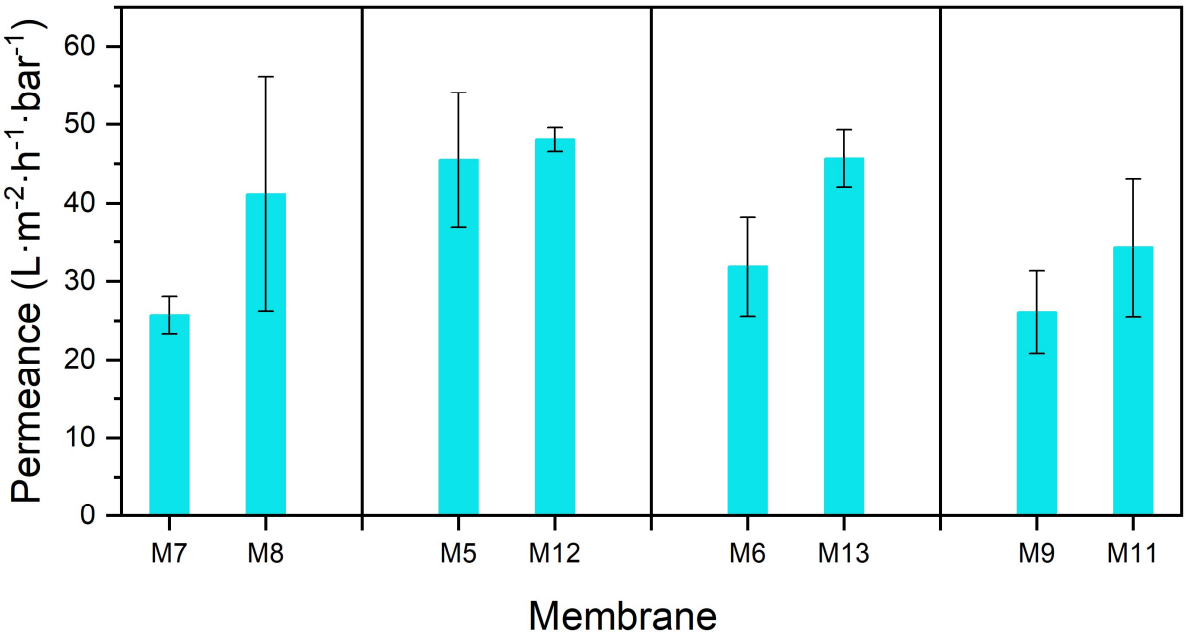

Figure S3. Comparison of pure water permeance of double TA-Fe^{3+} layered TFC membranes fabricated at different pH of TA solution for each layer. The membranes in one column are synthesized by switching the pH condition of each layer. For example, for membrane M7, the first layer is deposited at pH3 and the second layer at pH 8.5. Whereas M8 was fabricated by reversing these steps. For the complete fabrication conditions, the reader is referred to Table 1 of the main manuscript.

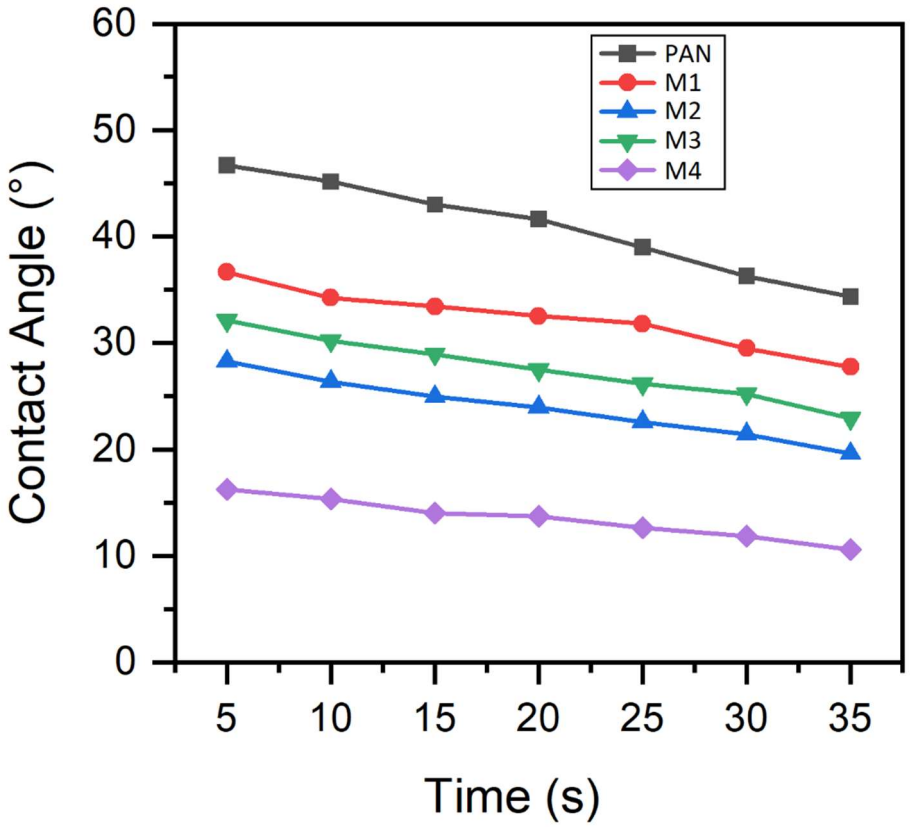

Figure S4. Time dependent variation of the water contact angle for the PAN and TA-Fe^{3+} membranes.

Table S1. Selectivity of solute permeation during single dye measurement by TA-Fe^{3+} membranes fabricated at different TA solution pH.

Ideal selectivities of dye pairs	PAN	M1	M2	M3	M4
Riboflavin to Orange II selectivity	1.0	4.5	5.1	8.5	8.7
Riboflavin to Naphthol green B selectivity	1.0	8.5	11.4	23.4	18.2
Orange II to Naphthol green B selectivity	1.0	1.9	2.2	2.8	2.1

10.2.4. Mass Transport of Dye Solutions through Porous Membrane Containing Tannic Acid/Fe^{3+} Selective Layer

The following supporting information to the article in chapter 6 of the cumulative part of the thesis is available online with Doi: 10.3390/membranes12121216/s1

Supporting Information

Mass transport of dye solutions through porous membrane containing tannic acid/Fe^{3+} selective layer

Hluf Hailu Kinfu[a], Md. Mushfequr Rahman[a,*], Nicolás Cevallos-Cueva[a], and Volker Abetz[a,b]

[a] Helmholtz-Zentrum Hereon, Institute of Membrane Research, Max-Planck-Straße 1, 21502 Geesthacht, Germany.

[b] University of Hamburg, Institute of Physical Chemistry, Martin-Luther-King-Platz 6, 20146 Hamburg, Germany.

* Corresponding author. E-mail address: mushfequr.rahman@hereon.de

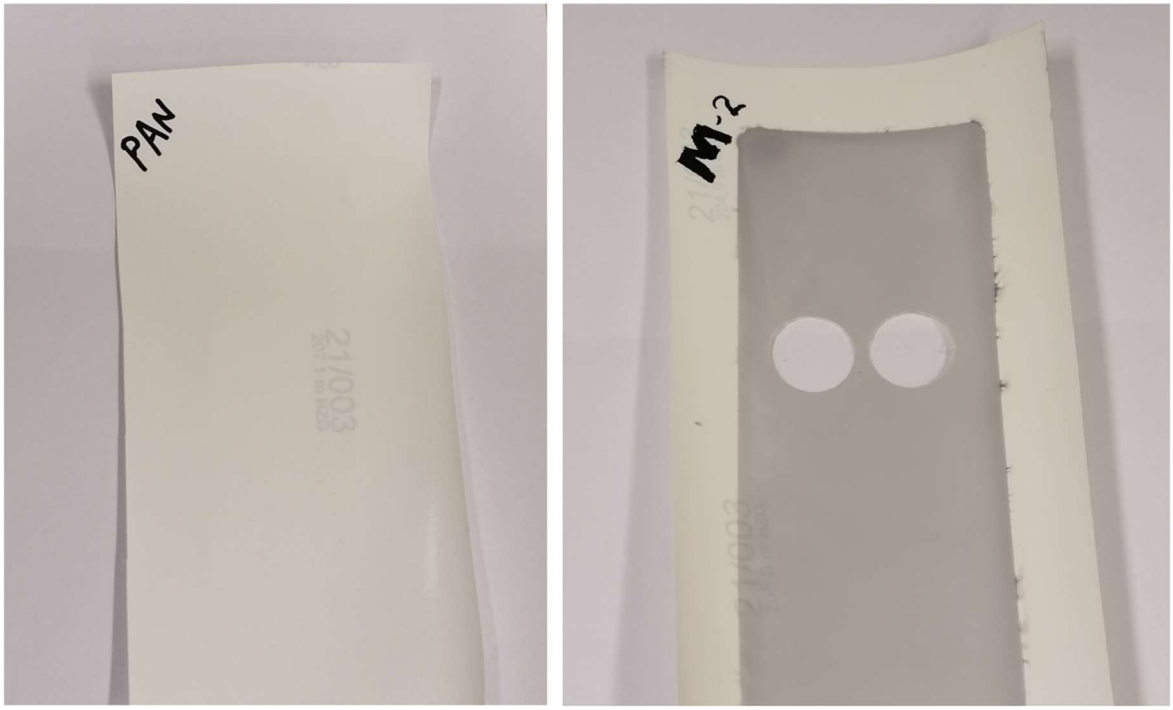

Figure S1. Comparison of photographic images of pristine PAN membrane support and TA-Fe^{3+} membrane used for retention measurement. Color change supports the formation of metal-polyphenol selective layer on top of the porous support as is also confirmed with significant drop in water flux.

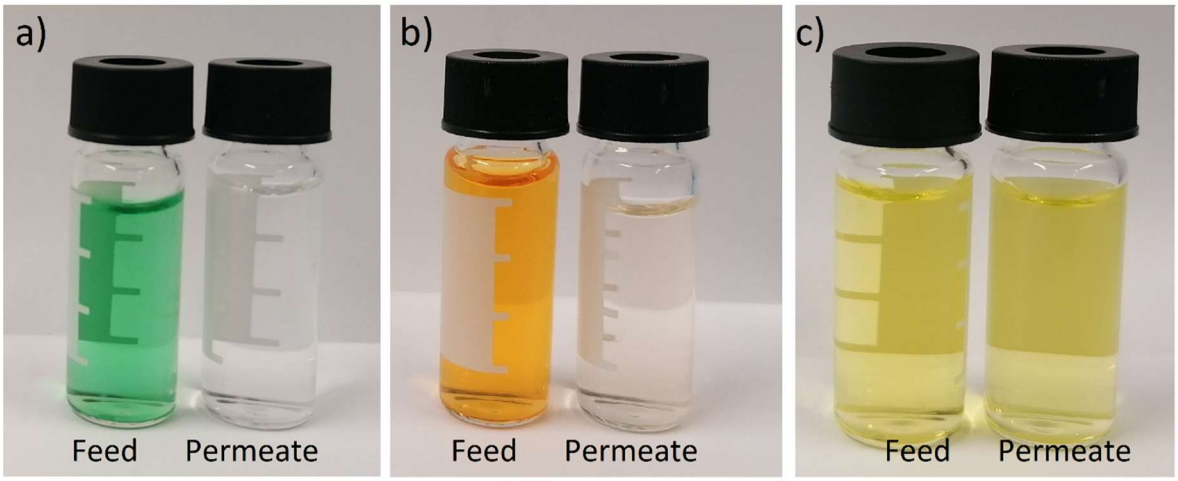

Figure S2. Photographic images of feed and permeate samples from a) naphthol green B, b) orange II and c) riboflavin 0.1mM solution retention tests at 3 bar using M2 membrane

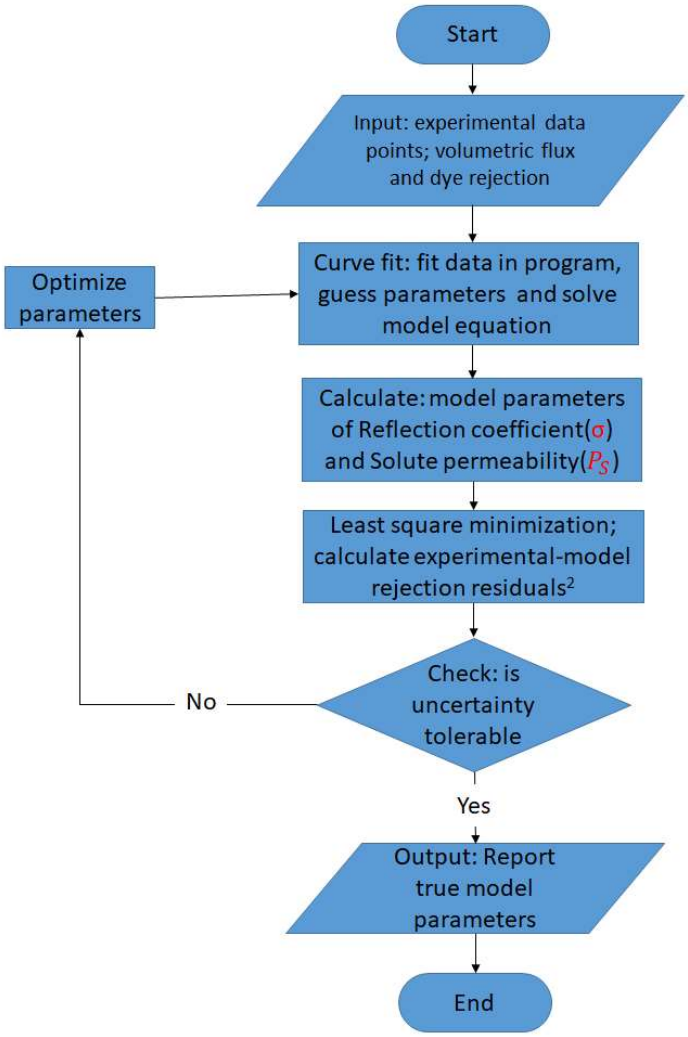

Figure S3. Flow chart of the simulation algorithm loop for solving non-linear equations of Spiegler-Kedem-Katchalsky model in the current study

10.2.5. Metal-phenolic network-based NF membranes for nitrate removal and the utilization of DSPM-DE model

The following supporting information to the article in chapter 7 of the cumulative part of the thesis is available online with Doi: 10.1016/j.cej.2025.162841

Metal–phenolic network-based NF membranes for nitrate removal and the utilization of DSPM-DE model

Hluf Hailu Kinfu[a], Md. Mushfequr Rahman[a,*], Nicolás Cevallos-Cueva[a], and Volker Abetz[a,b]

[a] Helmholtz-Zentrum Hereon, Institute of Membrane Research, Max-Planck-Straße 1, 21502 Geesthacht, Germany.

[b] University of Hamburg, Institute of Physical Chemistry, Martin-Luther-King-Platz 6, 20146 Hamburg, Germany.

* Corresponding author: mushfequr.rahman@hereon.de

Supporting Information

1. EDX analysis

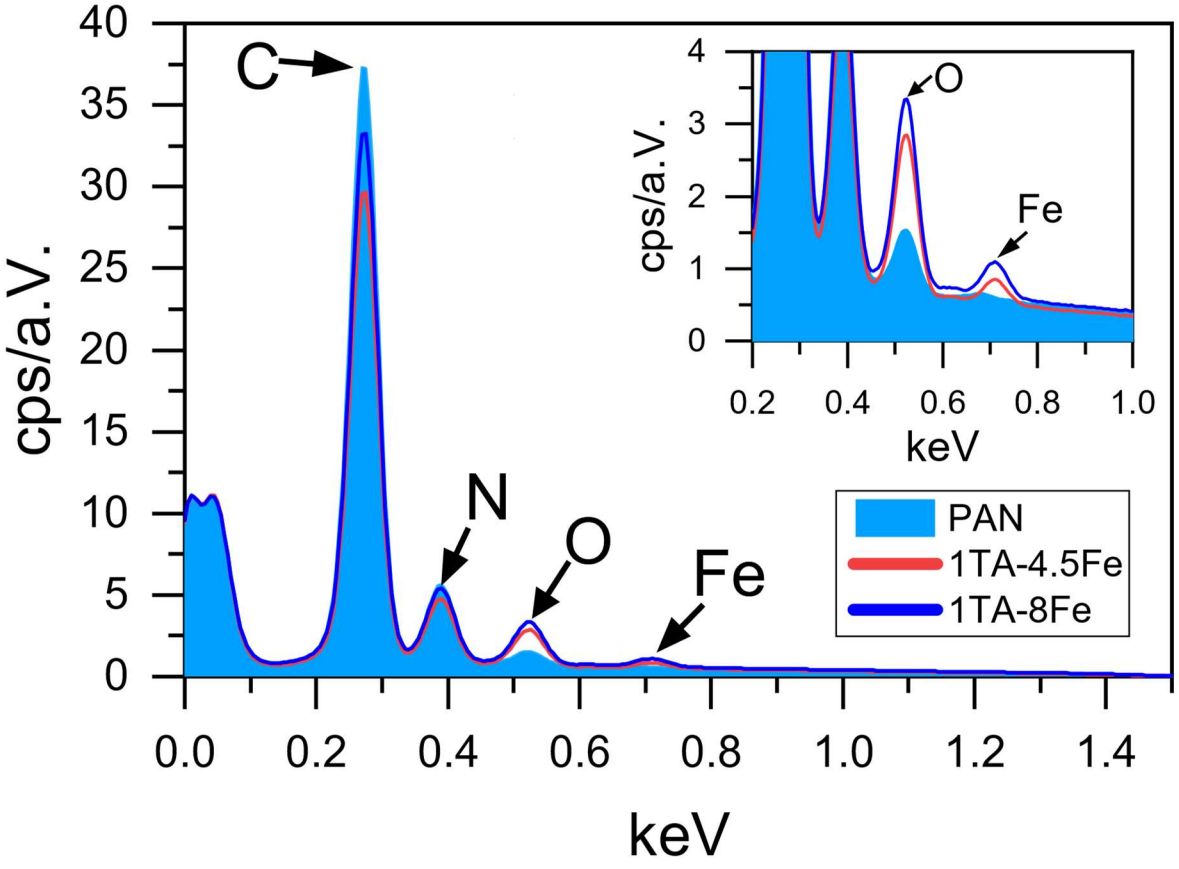

Figure S1. EDX analyses of the pristine PAN support membrane and TA-Fe^{3+} MPN membranes fabricated at the lowest and highest Fe^{3+} concentrations. The EDX spectra show that a peak for Fe emerges for the TFC MPN membranes. The oxygen peak also increases in the TFC

membranes. On the other hand, the C and N count decrease after coating the PAN surface. These results demonstrate a deposition of the TA-Fe^{3+} layer on the PAN surface.

2. Experimental rejection of PEG as a function of permeate flux

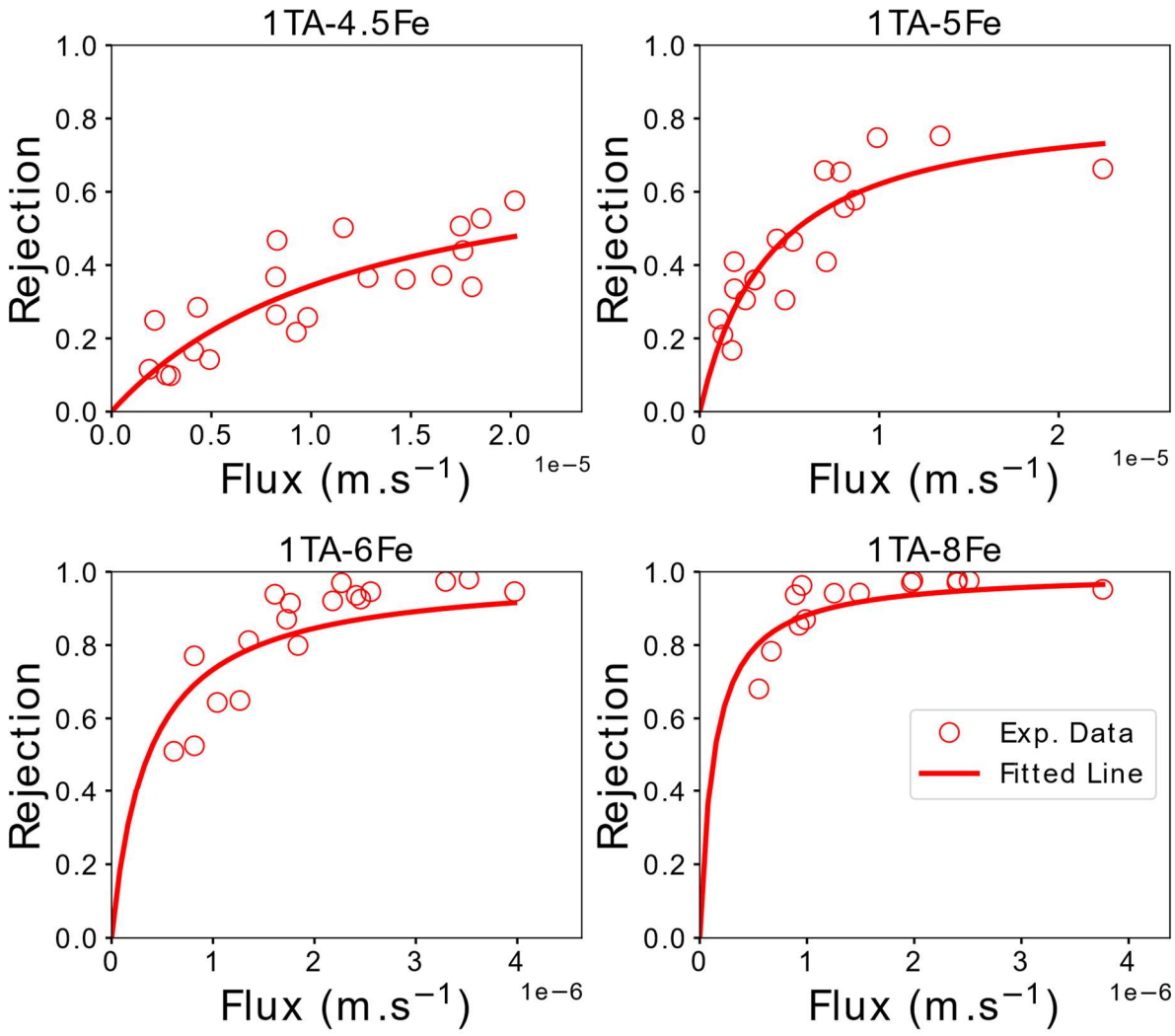

Figure S2. Poly(ethylene glycol) of 400 g/mol MW rejection of the TFC membranes. The solid lines show the retention as a function of flux obtained from the fitting of the experimental PEG rejection data using the equations described in the main manuscript for estimating the physical parameters of each membrane.

3. Flux of salt solution during mixed ion retention

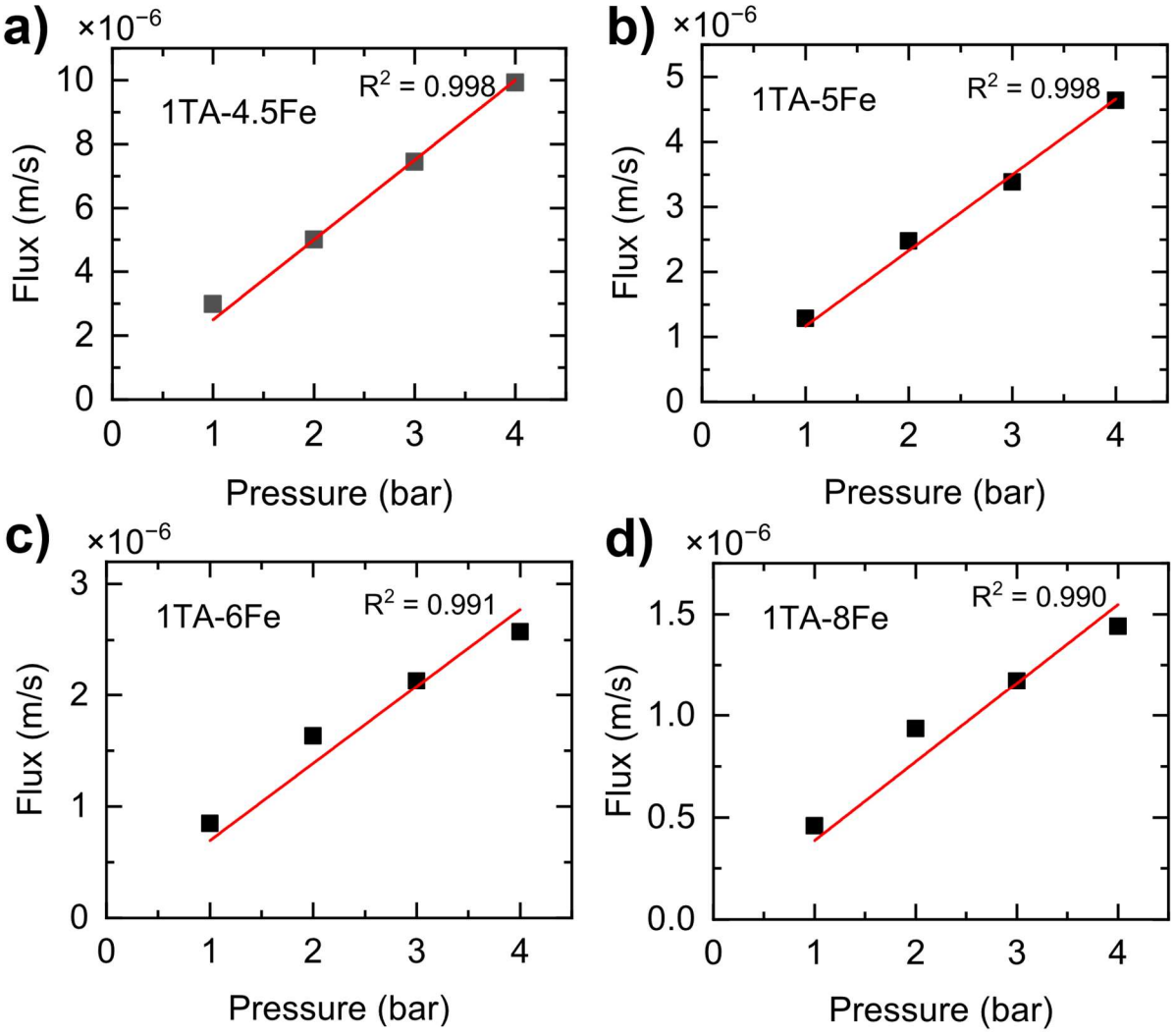

Figure S3. Measured permeate solution flux as a function of the applied pressure for $NaNO_3$-Na_2SO_4 salt mixture using the fabricated metal-polyphenol netwrok containing TFC membranes of (a) 1TA-4.5Fe, (b) 1TA-5Fe, (c) 1TA-6Fe, and (d) 1TA-8Fe.

4. Input parameters used for the fitting of ion rejection

Table S1. Solute parameters used for fitting either uncharged or salt solution rejection tests for estimating membrane parameters.

Solute	Molecular weight (Mw) ($g \cdot mol^{-1}$)	Charge	Diffusivity ($D_{i,\infty}$) ($m^2 \cdot s^{-1}$ x 10^{-9})	Stokes radius (r_s) (m x 10^{-9})	References
PEG	400	0	0.32	0.65	[1]
Sodium	23	+1	1.33	0.184	[2]

Nitrate	62	-1	1.902	0.129	[3]
Sulfate	96	-2	1.06	0.231	[2]

To solve the system of equations in DSPM-DE, the procedures followed by Geraldes and Alves [4] were implemented. The ENP equations were discretized and linearized to accurately and robustly predict the mass transfer of components in nanofiltration of multi-ionic solutions. Moreover, some parameters such as under-relaxation factor are introduced to control the numerical instabilities and ensures a smooth convergence of the iterative method to find a solution with a defined residual value. The complete set of variables and constants used in our work are listed in table S2.

Table S2. Parameters used for data fitting for the estimation of membrane parameters and the simulation of solute rejections.

Variables	**Symbol**	**Value**	**Description and unit**
Numerical parameter of the computer algorithm	**n**	100	Number of grid points (in discretization of Nernst Planck equation)
	f	0.2	Under relaxation factor
	res	1.00E-02	Normalized residuals target
	maxite	20000	maximum number of iterations
Operating parameters	**F**	96500	Faraday's constant (In SI units)
	R	8.314	Gas constant (In SI units)
	small	1.00E-15	auxiliar variable
	eps_0	8.85E-12	vacuum permittivity [F/m]
	T	298	temperature in Kelvin
	k	1.38E-23	Boltzmann constant [J/K]
	e0	1.60E-19	electronic charge [C]
	Na	6.02E-23	Avogadro number [mol-1]
	Jv	5.00E-05	Solvent flux [m/s]
Number of components	**nc**	3	Number of components (ions) in the feed solution
Water physical parameters	**d**	997	Density of water [km/m3]
	u	9.00E-04	Dynamic viscosity of water [Pa.s]
	dw	2.50E-10	Water molecule diameter [m]
	eps_b	80	Bulk dielectric constant of water
Operational variables	**L**	0.03	Characteristic length of stirrer [m]
Dimensional numbers	**Re**	3.65E+04	Computed Reynolds number

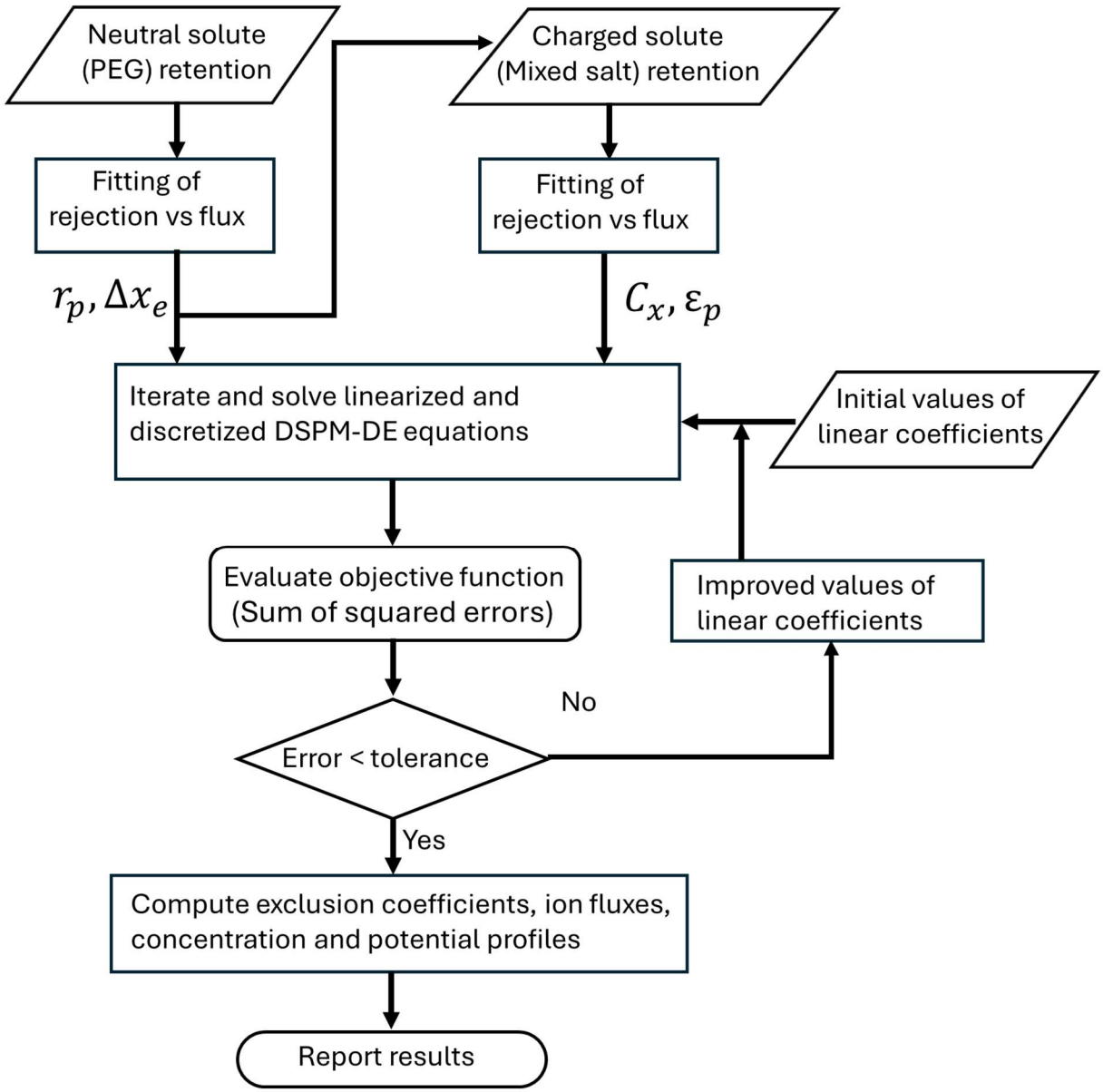

Figure S4. The flowchart followed for solving the DSPM-DE in this work.

5. Exclusion coefficients and flux of ions across the membrane active layer

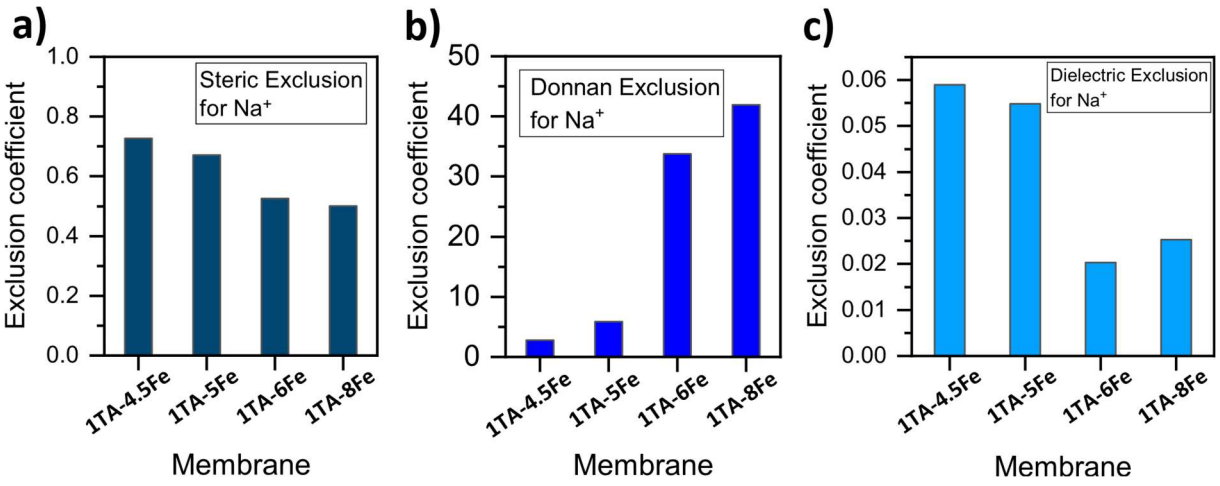

Figure S5. Exclusion coefficients for sodium in $NaNO_3$-Na_2SO_4 mixture filtration by all membranes: a) steric, b) Donnan and c) dielectric exclusion.

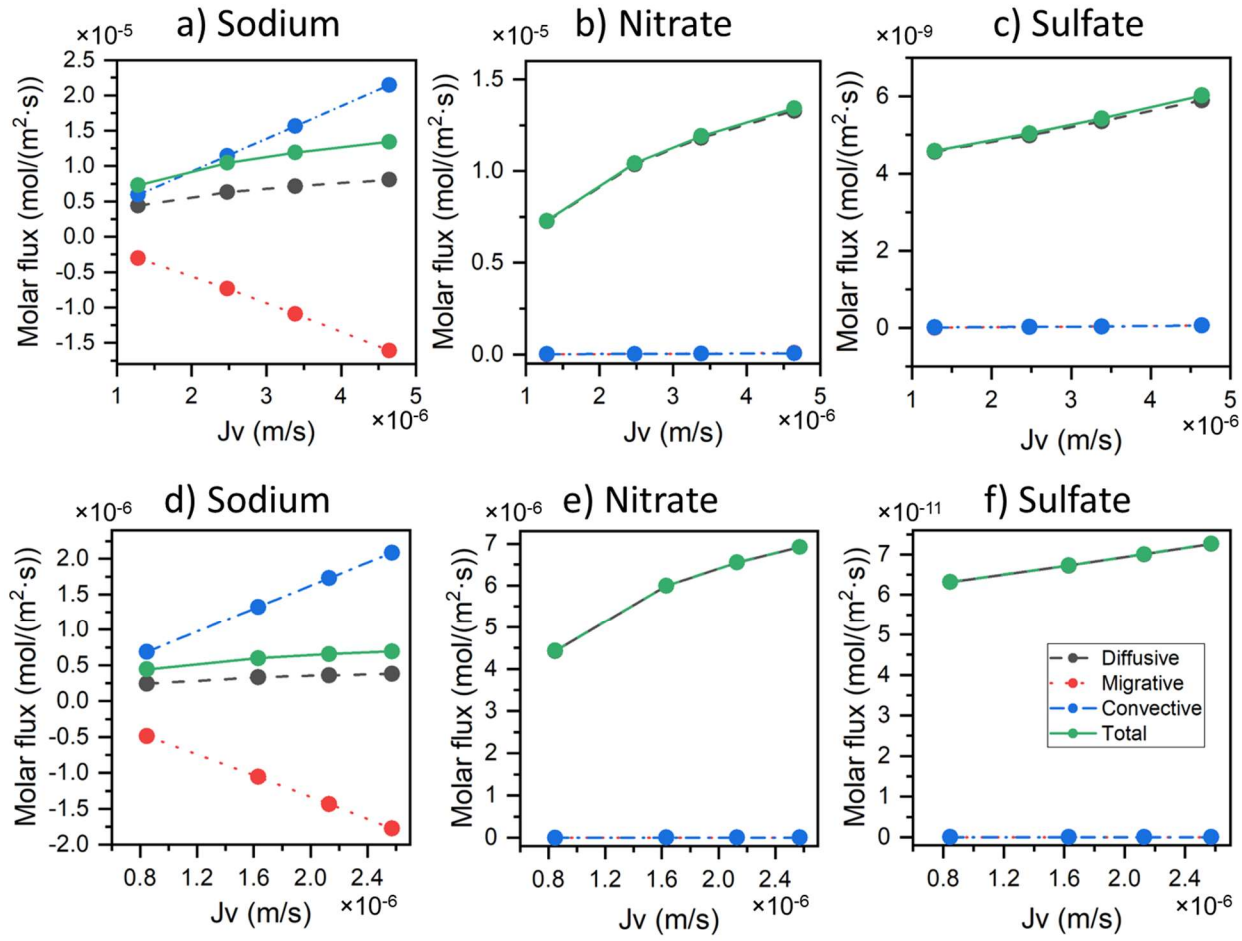

Figure S6. Flux contributions for ion transport in $NaNO_3$-Na_2SO_4 mixed salt retention test at different permeate flux, Jv, for a) 1TA-5Fe membrane and b) 1TA-6Fe membrane.

6. Sensitivity analysis with membrane charge density

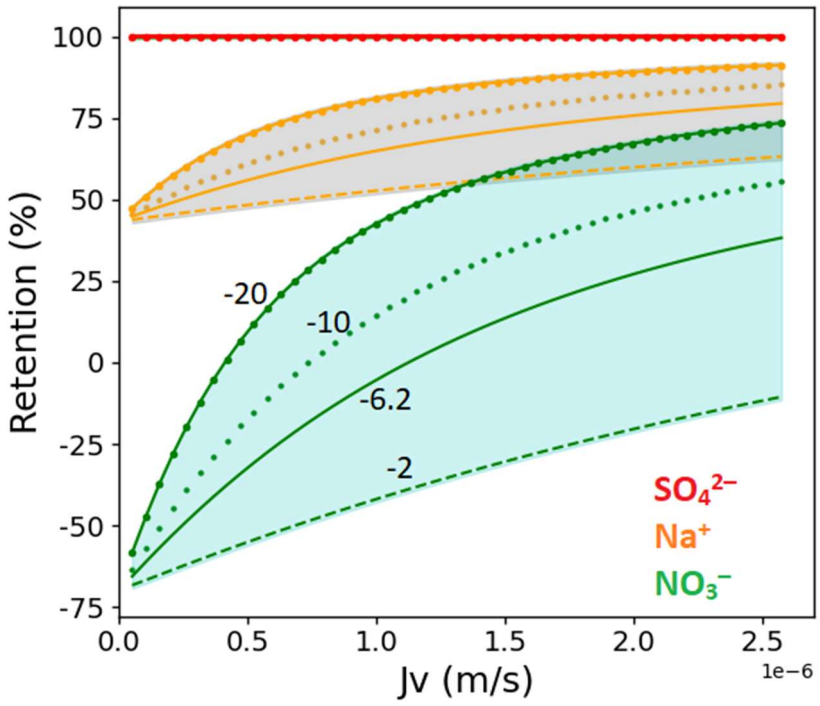

Figure S7. Influence of membrane charge density (in mol/m^3) on the retention of ions from a $Na^+/NO_3^-/SO_4^{2-}$ ternary ion mixture for the 1TA-6Fe membrane. The plots represent the model prediction for retention of nitrate (green), sodium (orange) and sulfate (red) as a function of permeate flux. The sensitivity towards the retention for each ion is represented in the shaded areas for a -10 %, 0 %, +12.5 % and +25 % change of the optimized membrane charge density parameter. Optimized membrane parameters of 0.67 nm, 59 nm, -6.2 mol/m^3, and 26.6 were used as reference for pore size, thickness to porosity ratio, membrane charge density and pore dielectric constant, respectively.

References

[1] S. Hernández, C. Porter, X. Y. Zhang, Y. N. Wei, and D. Bhattacharyya, "Layer-by-layer assembled membranes with immobilized porins," *Rsc Advances,* vol. 7, no. 88, pp. 56123-56136, 2017.

[2] W. R. Bowen and J. S. Welfoot, "Modelling the performance of membrane nanofiltration-critical assessment and model development," *Chemical Engineering Science,* vol. 57, no. 7, pp. 1121-1137, 2002.

[3] W. M. Haynes, *CRC handbook of chemistry and physics*, 95 ed. CRC press, 2014.

[4] V. Geraldes and A. M. Brites Alves, "Computer program for simulation of mass transport in nanofiltration membranes," *Journal of Membrane Science,* vol. 321, no. 2, pp. 172-182, 2008.

10.2.6. Ion Selective Metal-Phenolic Network Nanofiltration Membranes: The Role of Counterions and Predictive Modeling

The supporting information for the manuscript in Chapter 8 is provided below. It can also be accessed online at DOI: 10.1016/j.memsci.2025.124320

Ion Selective Metal-Phenolic Network Nanofiltration Membranes: The Role of Counterions and Predictive Modeling

Hluf Hailu Kinfu[a], Md. Mushfequr Rahman[a,*], Nicolás Cevallos-Cueva[a], and Volker Abetz[a,b]

[a] Helmholtz-Zentrum Hereon, Institute of Membrane Research, Max-Planck-Straße 1, 21502 Geesthacht, Germany.

[b] University of Hamburg, Institute of Physical Chemistry, Martin-Luther-King-Platz 6, 20146 Hamburg, Germany.

* Corresponding author: mushfequr.rahman@hereon.de

Supporting Information

1. Cross-sectional SEM images

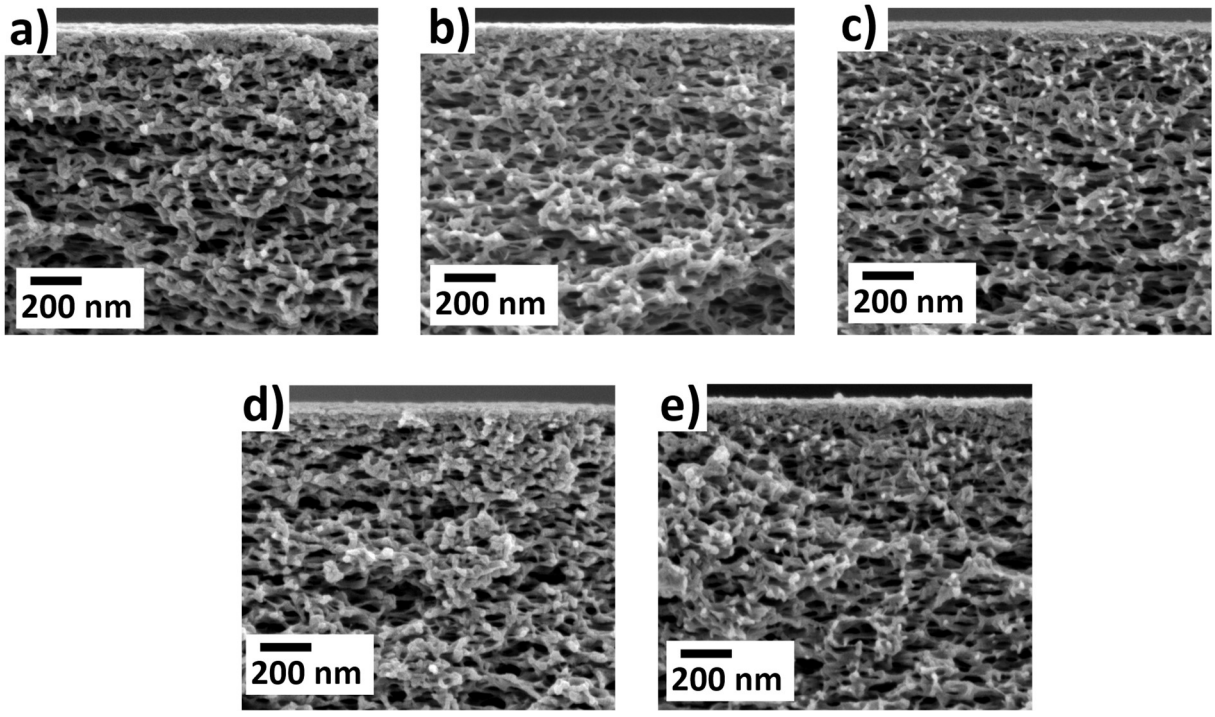

Figure S1. Cross-sectional SEM images of the pristine support and MPN membranes: a) PAN, b) 1TA-4.5Fe, c) 1TA-5Fe, d) 1TA-6Fe, and e) 1TA-8Fe membranes

2. Pressure-based salt retention test

We examined the effect of flux change on the salt rejection behavior of the membranes by varying the applied pressure between 0.5 and 4 bar using a Na_2SO_4 aqueous solution (Figure S2 and Figure S3). Figure S2 shows that the rejection of ions improved with an increase in the transmembrane flux, i.e., increase in the applied pressure. This effect is particularly prominent at low flux zones. An increase in the feed pressure only slightly improved the ion removal performance for the TFC membranes fabricated at high Fe^{3+} concentration (1TA-8Fe membrane). The 1TA-6Fe membrane maintained above 80% Na_2SO_4 retention across the investigated pressure range. But the Na_2SO_4 retention was higher than 94 % at 1 bar and almost 100 % at higher fluxes for 1TA-8Fe membrane. In contrast, the ion removal rate improved more significantly for the loose NF membranes, where the convective flux plays a substantial role. For instance, Na_2SO_4 retention in the 1TA-4.5Fe membrane increased from 25 % to 79 % under the investigated feed pressures, while the retention ranged from 54% to 95 % for the 1TA-5Fe membrane. Overall, the analysis of the pressure effects highlights its significant influence on the salt retention properties of the TFC membranes having MPN selective layers. Intrinsically, the rejection of solute relates to the relative transport rates between the solute and water. While the water flux linearly increases with feed pressure, the solute flux is only partially influenced by convection and is primarily dependent on the concentration gradient across the membrane. Moreover, the permeating ions encounter steric and electrical hinderances [1] that limit their transport across the membrane active layer. According to DSPM-DE, ion transport occurs owing to synergistic contributions of diffusion, convection and electromigration [2-4]. Diffusion dominates ion transport at low permeate volume, but its contribution decreases at high J_V values [2]. Furthermore, while diffusive and migrative fluxes are only marginally affected by feed pressure, local ion concentration across the membrane thickness can vary due to changes in permeate flux. Consequently, higher volume flux (i.e. higher applied pressure) enhances ion retention due to the dilution effect, wherein the relative increase in water transport reduces ion concentration in the permeate.

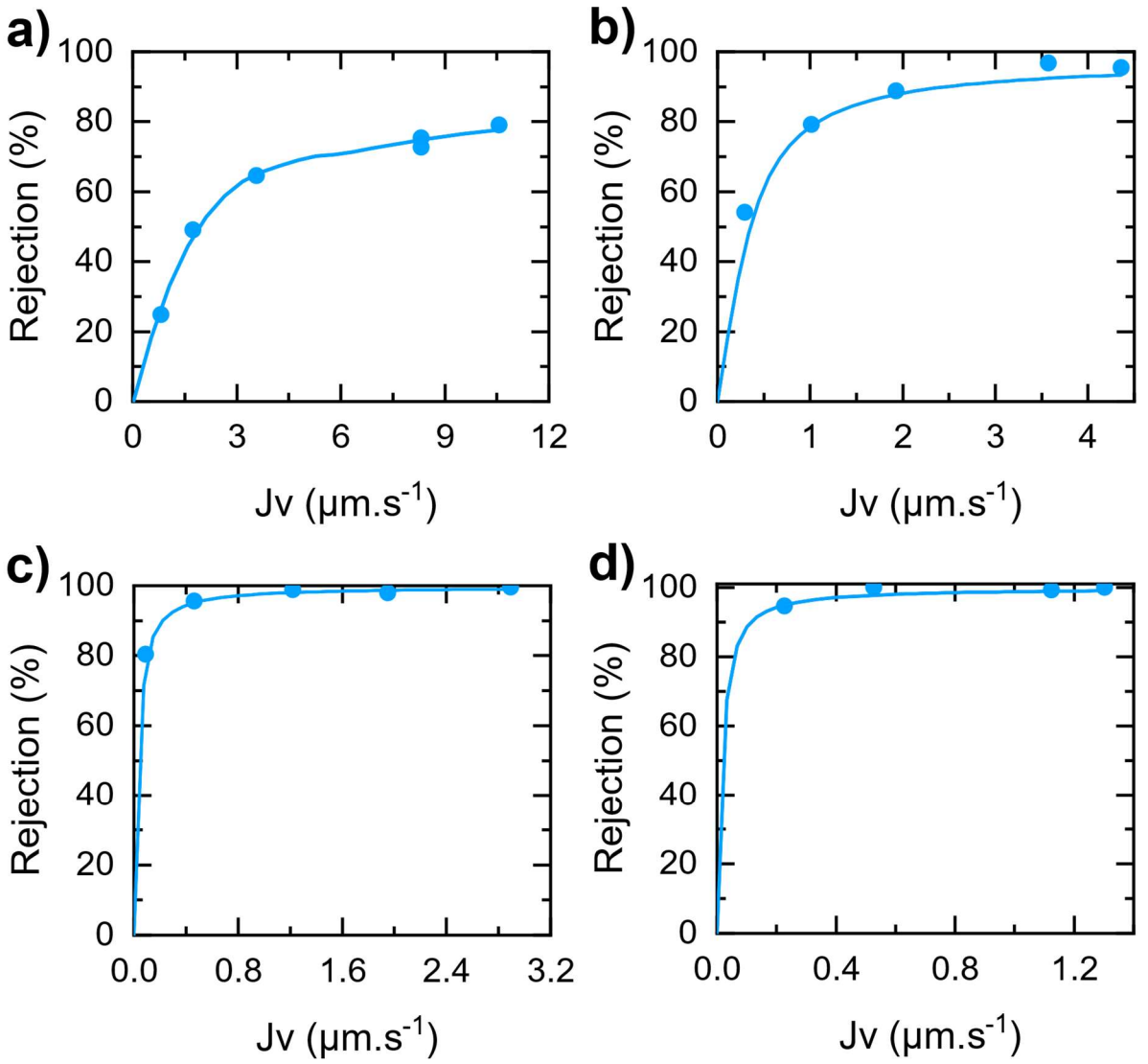

Figure S2. Na_2SO_4 retention as a function of flux for a) 1TA-4.5Fe, b) 1TA-5Fe, c) 1TA-6Fe, and d) 1TA-8Fe membranes using 10 mM feed concentration. The solid lines are added solely to guide the eye. The permeate flux (J_V) was varied due to the applied pressure variation. The linear relationship between permeate flux and applied pressure during this test can be found in Figure S3.

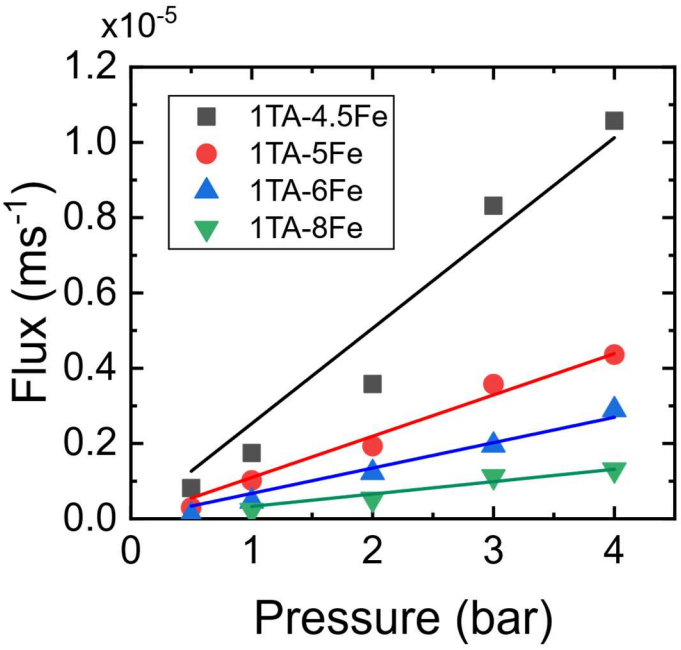

Figure S3. Permeate flux as a function of the applied transmembrane pressure in 10 mM Na_2SO_4 pressure-based rejection test of the fabricated TA-Fe^{3+} membranes.

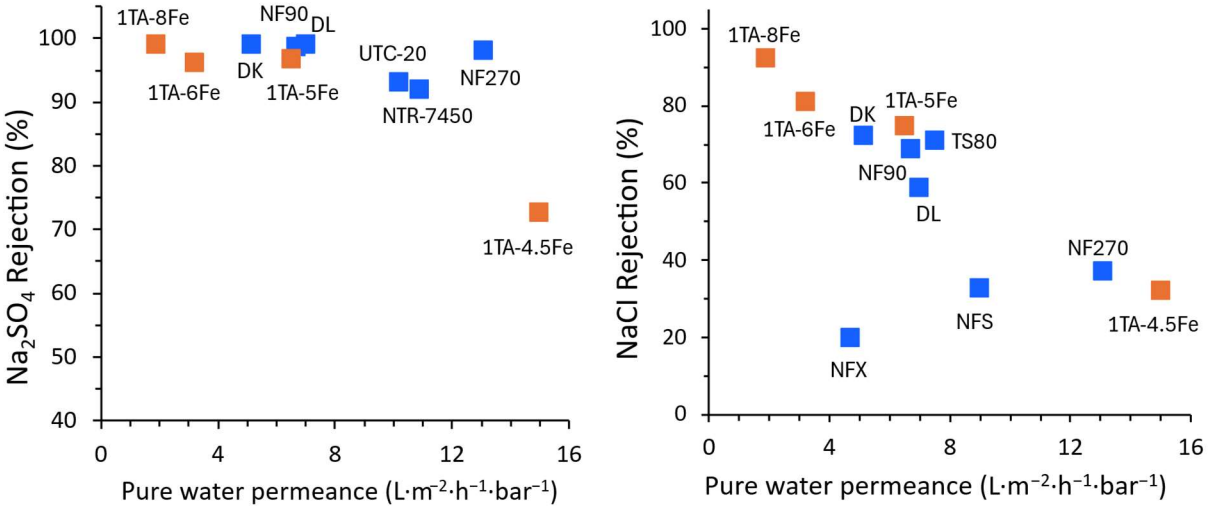

Figure S4. Comparison of the separation performance of MPN membranes (orange boxes) with those of commercially available NF membranes (blue boxes) reported in the literature. Data for the plots and their references can be found in Table S1.

Table S1. Comparison of membrane performance with commercially available membranes.

Data for Na_2SO_4 rejection						
Membrane	Manufacturer	Feed concentration	Pressure [bar]	Pure water permeance [LMH/bar]	Rejection (%)	Reference
DK	Veolia	1.0 g·L^{-1}	3.0	5.15	99.00	[5]
DL	Veolia	1.0 g·L^{-1}	3.0	7.00	99.00	[5]
NF270	Dow Filmtec™	1.0 g·L^{-1}	2	13.1	98.1	[6]
NF 90	Dow Filmtec™	1.0 g·L^{-1}	2	6.7	98.6	[6]
UTC-20	Toray	1.5 g·L^{-2}	10	10.2	93	[7]
NTR-7450	Nitto-Denko	1.0 g·L^{-1}	10	10.9	92	[7]
1TA-4.5Fe		10 mM	3	15	72.6	This work
1TA-5Fe		10 mM	3	6.5	96.7	This work
1TA-6Fe		10 mM	3	3.2	96.1	This work
1TA-8Fe		10 mM	3	1.9	99.0	This work
Data for NaCl rejection						
Membrane	Manufacturer	Feed concentration	Pressure [bar]	Pure water permeance [LMH/bar]	Rejection (%)	Reference
DK	Veolia	1.0 g·L^{-1}	3.0	5.15	72.3	[5]
DL	Veolia	1.0 g·L^{-1}	3.0	7.00	58.8	[5]
NF270	Dow Filmtec™	1.0 g·L^{-1}	2	13.1	37.1	[6]
NF 90	Dow Filmtec™	1.0 g·L^{-1}	2	6.7	68.6	[6]

TS80	Microdyn-Nadir	2.0 g·L^{-1}	7.58	7.5	71.0	[8]
NFS	Synder	2.0 g·L^{-2}	7.58	9	32.7	[8]
NFX	Synder	2.0 g·L^{-3}	7.58	4.7	19.7	[8]
1TA-4.5Fe		10 mM	3	15	32.0	This work
1TA-5Fe		10 mM	3	6.5	74.7	This work
1TA-6Fe		10 mM	3	3.2	80.8	This work
1TA-8Fe		10 mM	3	1.9	92.2	This work

3. PEG retention for pore radius and thickness to porosity ratio determination

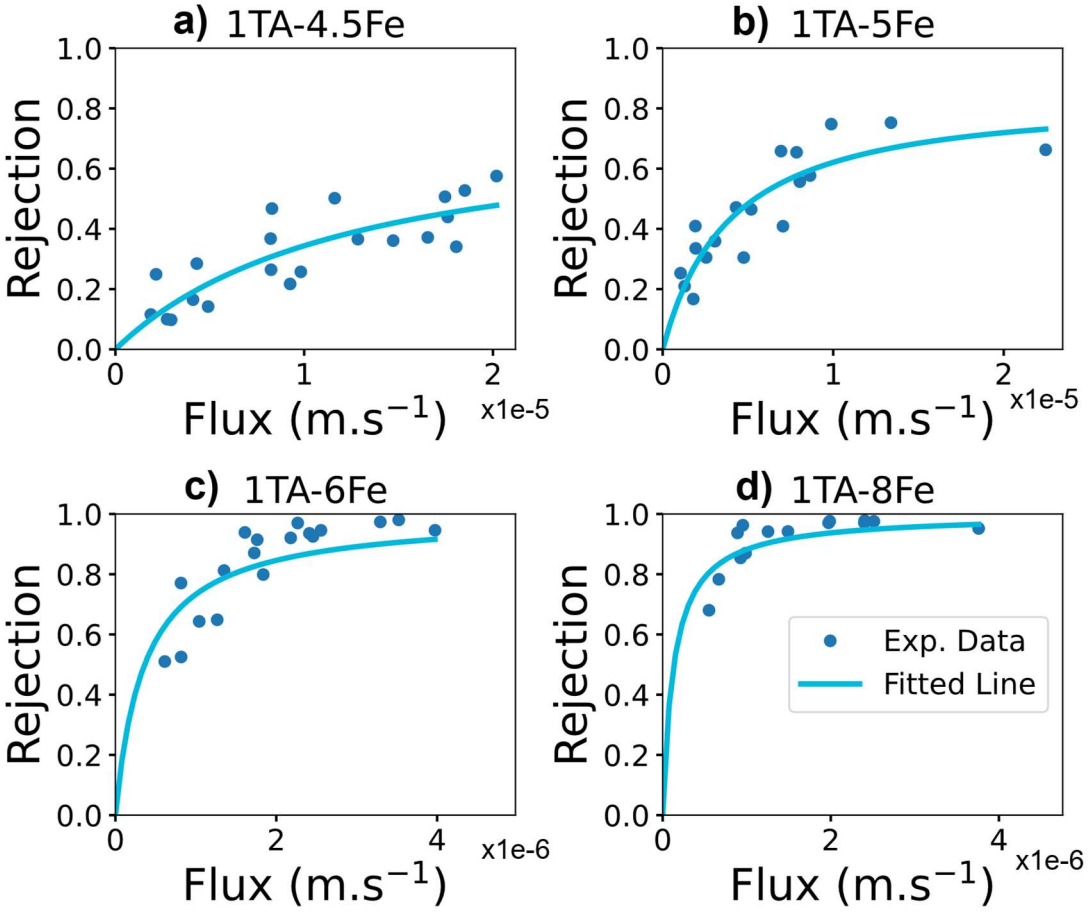

Figure S5. PEG 400 g/mol molecular weight experimental rejection as a function of permeate flux and the fitted curves for the TFC membranes. The solid lines show the fitted rejection

according to the equations described in the main manuscript for neutral solute filtration (Section 2.4.1).

4. Effect of transmembrane pressure on permeate flux during mixed salt filtration

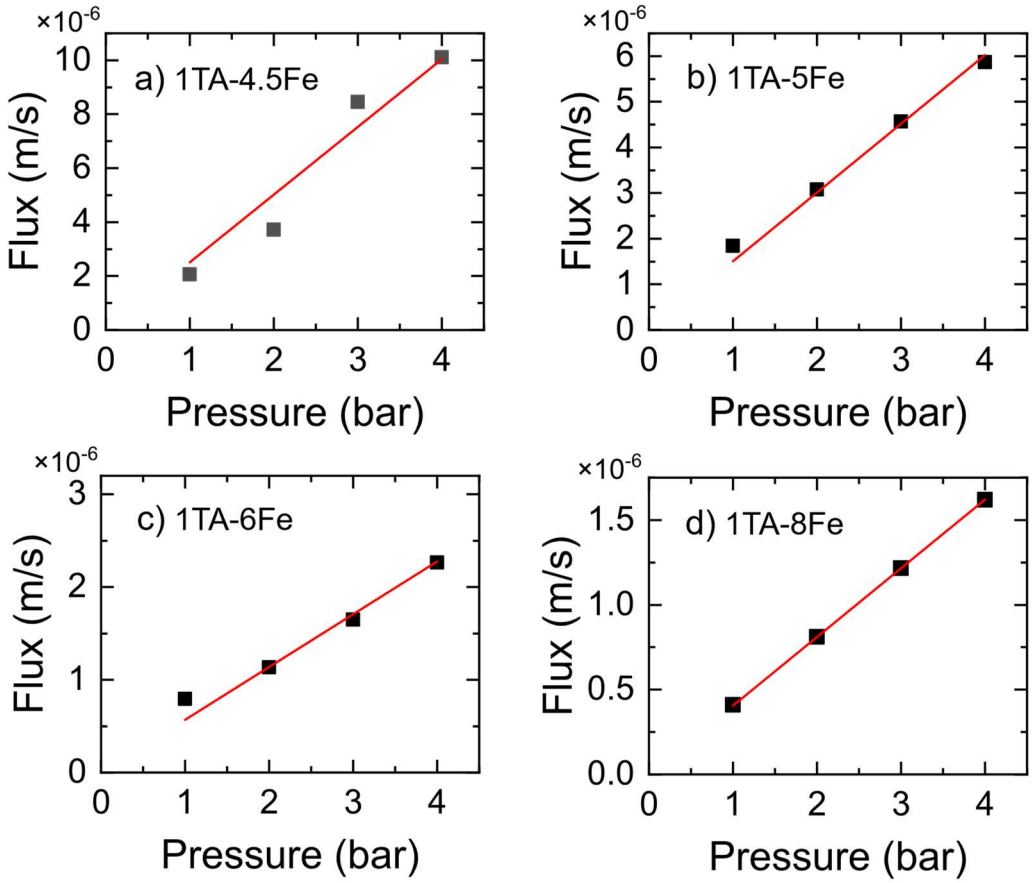

Figure S6. Solution flux dependence on transmembrane pressure for NaCl-$MgCl_2$ feed solution pressure-based retention tests.

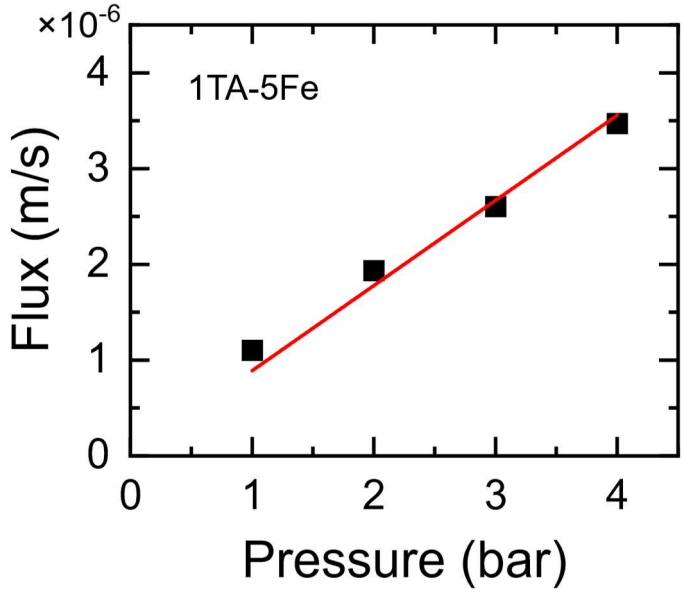

Figure S7. Pressure vs flux for pressure-based retention of NaCl-Na_2SO_4-$MgCl_2$-$MgSO_4$ mixture feed solution (quaternary system of ion mixtures) using 1TA-5Fe membrane.

5. Solute characteristics and estimated membrane structure parameters

Table S2. Solute parameters used for fitting of either uncharged or salt solution rejection tests for estimating membrane parameters.

Ion	Charge	Diffusivity ($D_{i,\infty}$) ($m^2 \cdot s^{-1}$ x 10^{-9})	Stokes radius (r_s) (m x 10^{-9})	References
Na^+	1+	1.33	0.184	[9]
Mg^{2+}	2+	0.707	0.35	[10]
Cl^-	1-	2.03	0.121	[10]
SO_4^{2-}	2-	1.06	0.231	[9]

Table S3. Estimated pore size and thickness to porosity ratio of the TFC membranes.

Membrane	r_P (nm)	Δx_e µm
1TA-4.5Fe	1.25	0.99
1TA-5Fe	1.02	0.96
1TA-6Fe	0.67	0.059
1TA-8Fe	0.63	0.180

6. Schematic illustrations of ion transport inside the pores of a negatively charged membrane

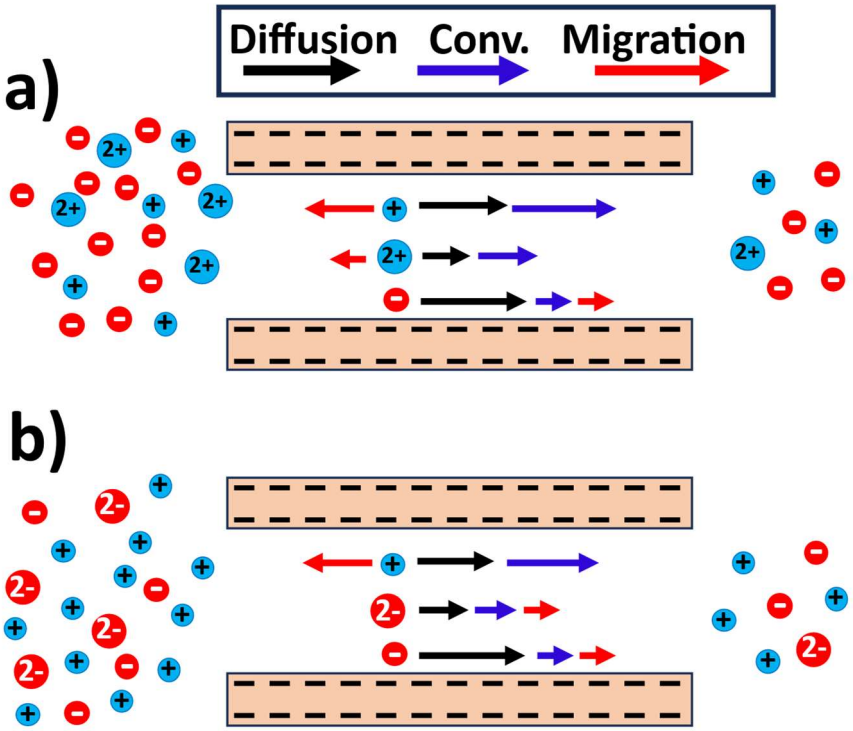

Figure S8. Schematic illustration of the direction of solute fluxes through a strongly negatively charged membrane pore. a) a mixture of monovalent and divalent cations with a common anion, and b) a mixture of monovalent and divalent anions with a common cation. The total flux is the sum of the diffusive, convective and electromigrative fluxes.

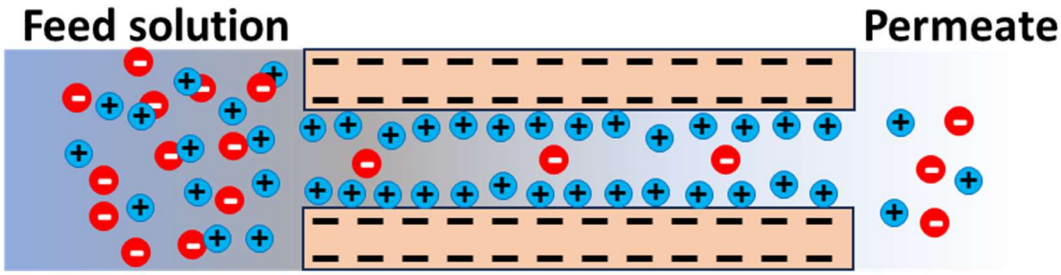

Figure S9. Schematic illustration of the local concentration of ions inside the pores of a negatively charged membrane.

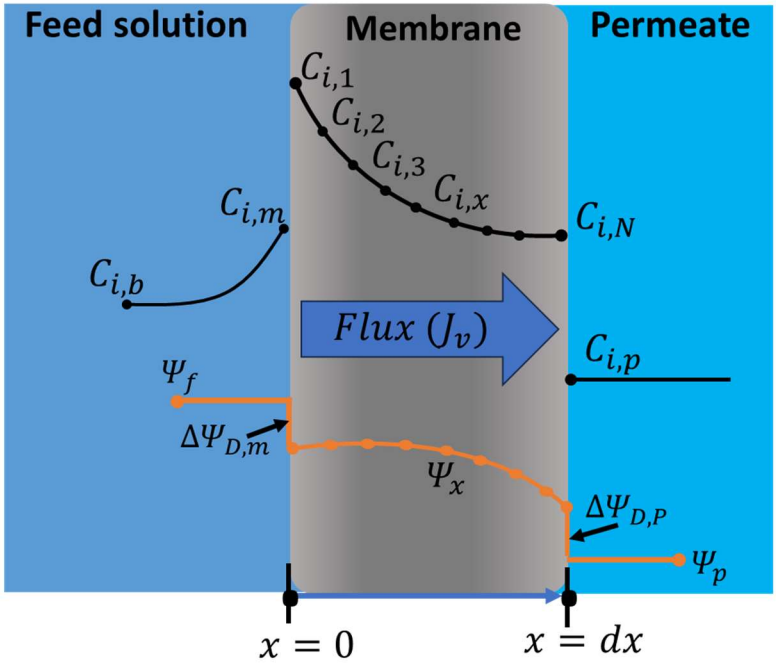

Figure S10. Schematic diagram of the three domains of the membrane process considered for modeling the mass transport ions: feed, membrane and permeate sides and their associated concentration and potential profiles. The membrane active layer is discretized into N=100 number of nodes. C_i and Ψ_i values correspond to the concentration and potential at each node inside the active layer.

References

[1] C. V. Gherasim, J. Cuhorka, and P. Mikulásek, "Analysis of lead(II) retention from single salt and binary aqueous solutions by a polyamide nanofiltration membrane: Experimental results and modelling," *Journal of Membrane Science,* vol. 436, pp. 132-144, 2013.

[2] A. Szymczyk, C. Labbez, P. Fievet, A. Vidonne, A. Foissy, and J. Pagetti, "Contribution of convection, diffusion and migration to electrolyte transport through nanofiltration membranes," *Advances in Colloid and Interface Science,* vol. 103, no. 1, pp. 77-94, 2003.

[3] M. A. Junker, E. te Brinke, C. M. V. Compte, R. G. H. Lammertink, J. de Grooth, and W. M. de Vos, "Asymmetric polyelectrolyte multilayer nanofiltration membranes: Structural characterisation via transport phenomena," *Journal of Membrane Science,* vol. 681, 2023.

[4] R. Y. Wang and S. H. Lin, "Pore model for nanofiltration: History, theoretical framework, key predictions, limitations, and prospects," *Journal of Membrane Science,* vol. 620, 2021, Art. no. 118809.

[5] P. L. Chen, X. Ma, Z. X. Zhong, F. Zhang, W. H. Xing, and Y. Q. Fan, "Performance of ceramic nanofiltration membrane for desalination of dye solutions containing NaCl and Na_2SO_4," *Desalination,* vol. 404, pp. 102-111, 2017.

[6] C. Liu, L. Shi, and R. Wang, "Crosslinked layer-by-layer polyelectrolyte nanofiltration hollow fiber membrane for low-pressure water softening with the presence of SO_4^{2-} in feed water," *Journal of Membrane Science,* vol. 486, pp. 169-176, 2015.

[7] W. X. Fang, L. Shi, and R. Wang, "Mixed polyamide-based composite nanofiltration hollow fiber membranes with improved low-pressure water softening capability," *Journal of Membrane Science,* vol. 468, pp. 52-61, 2014.

[8] A. Premachandra, S. O'Brien, N. Perna, J. McGivern, R. LaRue, and D. R. Latulippe, "Treatment of complex multi-sourced industrial wastewater - New opportunities for nanofiltration membranes," *Chemical Engineering Research & Design,* vol. 168, pp. 499-509, 2021.

[9] W. R. Bowen and J. S. Welfoot, "Modelling the performance of membrane nanofiltration-critical assessment and model development," *Chemical Engineering Science,* vol. 57, no. 7, pp. 1121-1137, 2002.

[10] V. Geraldes and A. M. Brites Alves, "Computer program for simulation of mass transport in nanofiltration membranes," *Journal of Membrane Science,* vol. 321, no. 2, pp. 172-182, 2008.

Acknowledgement

First and foremost, I would like to express my deepest gratitude to my doctoral thesis supervisor, Prof. Dr. Volker Abetz, for his guidance, supervision, invaluable insights, and unwavering support throughout the entire research journey. The regular scientific discussions have helped me immensely, and I have benefited from his expertise. His constructive feedback and diverse perspectives have been instrumental and have enriched the quality of my research. From the earliest stages of the research work to the final submission of this dissertation, Prof. Abetz's expertise and insight have played a crucial role in shaping both this dissertation and my academic development. I am grateful for the intellectual freedom I was afforded under his supervision, which allowed me to explore my ideas independently while always having the reassurance of his thoughtful mentorship. It has been a privilege to work under his supervision and I look forward to carrying on the lessons I have learned from him throughout my career.

I would like to say a special thank you to Md. Mushfequr Rahman for the invaluable mentorship, thoughtful comments, discussions and supervision, and continuous encouragement throughout my doctoral study. I am thankful for his dedication, expertise, and knowledge shared that steered me through this research work, and for his guidance in research excellence and meticulous attention to detail that inspired me to think outside the box. I extend my appreciation for creating a stimulating and collaborative research environment. The ideas, discussions, and experiences he shared and exchanged with me have contributed significantly to the research findings reflected in this dissertation. I am also sincerely thankful for his kindness, understanding, and support during times of difficulty, which have meant a great deal to me on both a personal and professional level. I am deeply indebted to the willingness and enthusiasm he showed to assist in any way he could throughout the research journey.

Next, I would like to sincerely thank Nicolás Cevallos-Cueva, who has been both a classmate during my master’s program and a colleague in our PhD journey, for his unwavering support, collaboration, and encouragement throughout the years. I am truly thankful for the positive and exciting environment he helped to create, which made each day both in the lab and in the office productive and enjoyable. The discussions we shared and the teamwork we fostered, his insights and advice during the highs and lows, and his commitment to help have played a crucial role in the completion of this project.

My sincere thanks go to Ivonne Ternes and Barbara Bajer for their unwavering support and assistance throughout the course of this work. They have introduced me to the flux and retention

measurement procedures when I arrived at Hereon, and they have continued their support in sharing their technical expertise in the laboratory work. I would also like to thank Martin Held, Erik S. Schneider and Evgeni Sperling for their continuous support in the characterizations of membranes using microscopy. Thank you for the SEM, EDX, and AFM images and analyses, for the interpretation of the results and for all the technical and scientific support regarding microscopy.

Special thanks to Maren Brinkmann for performing the GPC analysis. I truly appreciate her contribution and dedication and willingness to help even when I submit so many samples. I express my gratitude to Jan Pohlmann for his support in my work by setting up the facilities for filtration measurement, and to Juliana Clodt for preparing the polyacrylonitrile support which has been used for preparing the TFC membranes in this dissertation.

I want to take the opportunity to thank everyone at the Institute of Membrane Research who helped and supported me directly or indirectly, either by answering my quick questions during lab work or through discussions during institute seminars.

Declaration on oath / Affidavit

I hereby declare and affirm that this doctoral dissertation is my own work and that I have not used any aids and sources other than those indicated. If electronic resources based on generative artificial intelligence (gAI) were used in the course of writing this dissertation, I confirm that my own work was the main and value-adding contribution, and that complete documentation of all resources used is available in accordance with good scientific practice. I am responsible for any erroneous or distorted content, incorrect references, violations of data protection and copyright law or plagiarism that may have been generated by the gAI.

Date: 18.08.2025 Signature: 

Curriculum Vitae

CV is omitted for data protection reasons